# SCIENCE OF CLIMATE CHANGE

Volume 5.3

2025

https://scienceofclimatechange.org

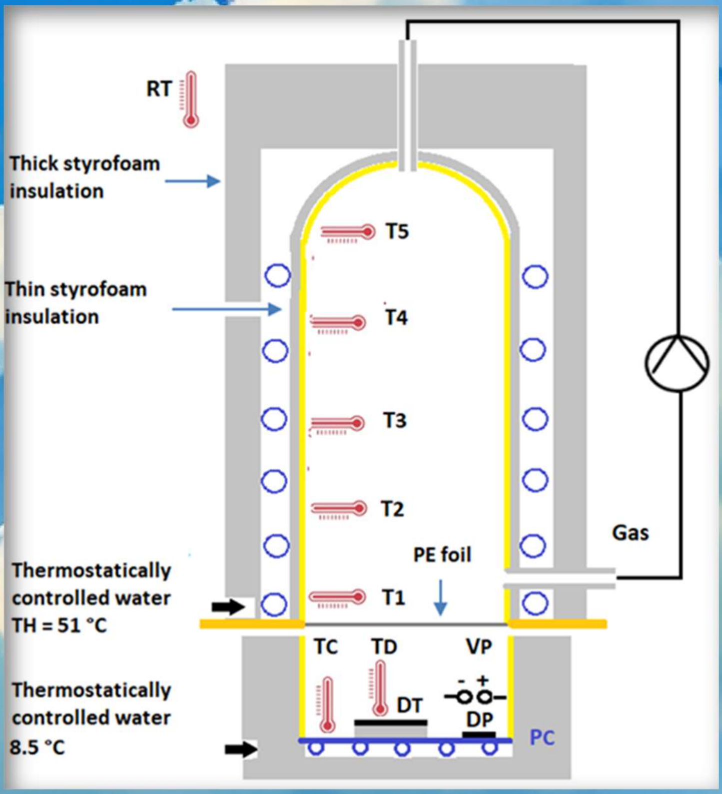

Published by: SCC Publishing (Org. no. 935 567 653)

ISSN2703-9080(print) ISNN2703-9072(online)

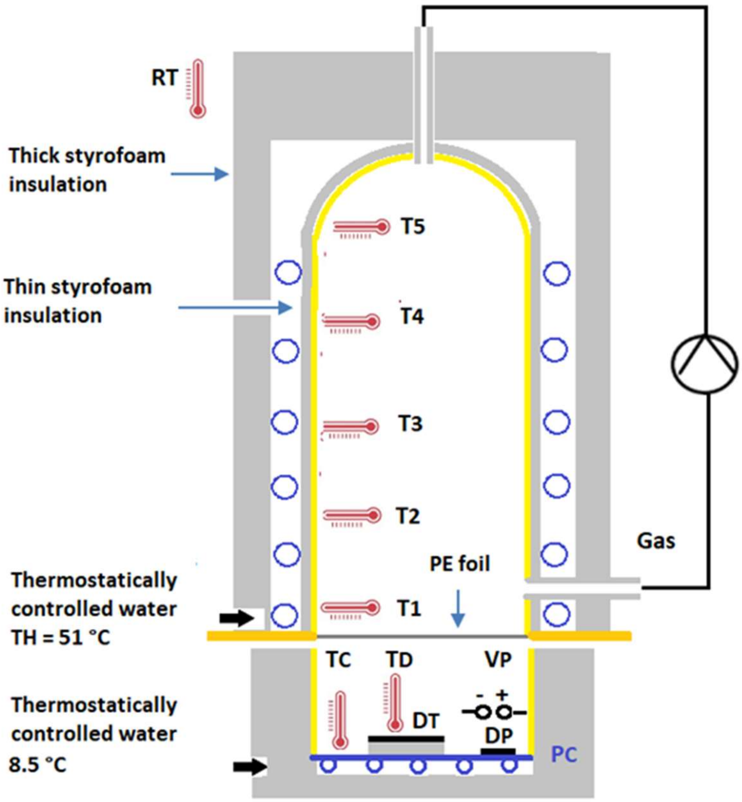

*Fig. 1: Experimental Set-Up for verification of the negative greenhouse effect.*

Figure from Harde & Schnell: The Negative Greenhouse Effect – Part II, p. 12

# Science of Climate Change

## Volume 5.3

## December 2025

**ISSN 2703 9072**

https://doi.org/10.53234/scc202510/01

SCC Publishing, Michelets vei 8 B, 1366 Lysaker, Norway
Org. no 935 567 653

# Table of Content

### Research Article

### Review Article

### Research Article

### Essay

### Commentary

# Preface

The objective of this journal is to publish peer-reviewed scientific contributions in the broad field of climate sciences. But different to many other journals we also accept research articles, essays and commentaries, which contradict the often very unilateral climate hypotheses of the IPCC and thus open the view to alternative interpretations of climate change.

The journal is a non-profit venture, in the start-up phase hosted and strongly supported by the Norwegian Climate Realists. Also, other climate organizations and their members support the journal with qualified publications or their engagement as co-editors and reviewers.

However, to be internationally better recognized as a largely independently operating journal, with the beginning of 2025 SCC is published by the SCC Publishing association.

In 2021 the journal started in the classical format, but since 2022 it is operating as an Open Access Journal with very moderate publication fees, with a new layout and new website. Since 2021 SCC could publish 5 volumes, consisting of 18 sub-volumes, mainly covering research articles, review articles, essays and discussion papers but also conference summaries and book reviews.

Within less than five years SCC could develop to an internationally recognized Journal of Climate Sciences presenting alternative views for a much broader discussion and understanding of climate phenomena.

We thank all authors for their important contributions over recent years, and we are particularly grateful to our Co-Editors, our Secretary, the many unnamed Reviewers and the Extended Board for their very trustworthy and productive cooperation over the last years.

With the end of 2025 the responsibility as Chief-Editor passes to Prof. Nikolaos Malamos.

SCC tries to continue its successful work on the wide field of climate sciences and at the same time to gain further experts, who can strengthen the editorial work and support our objectives.

| | |
|---|---|
| Stein Bergsmark | Hermann Harde |
| (SCC Publishing) | (Departing Editor-in-Chief) |

# Editorial

Volume 5 consists of two regular issues 5.1 and 5.3 with publications over the first and second half of 2025 and two extra issues 5.2 and 5.4.

Sub-volume 5.2 is a Reprint of Pattern Recognition in Physics (Special Issue 1 2013/14) – *Pattern in Solar Variability, their* Planetary *Origin and Terrestrial Impacts.*

Sub-volume 5.4 collects the Proceedings of the 6th Nordic Climate Conference in Oslo-Gardermoen (August 30–31, 2025): "*The Climate Knowledge Crisis – how does it impact Freedom of Speech, Journalism, Climate Science and Politics?*"

The actual issue 5.3 covers all publications accepted within the period July to December 2025. It contains 7 research articles, one review paper, one essay and one commentary:

- In 2 consecutive articles *Michael Schnell and Hermann Harde* describe the first experimental verification of the negative greenhouse effect in the laboratory. With a specially designed set-up they investigate the gases water vapor, $CO_2$, $CH_4$, $N_2O$, and Freon 134a at varying concentrations between 1–8% in air and at normal pressure. The radiation emitted by the gases is detected against a larger background radiation originating from the cylinder walls. All gases show strong saturation effects with increasing concentration. The measurements can be well reproduced by corresponding radiation transfer calculations. A clear influence of water vapor on the other gases is also evident as increased background radiation and partial spectral superposition with these gases, which appears as attenuated emission of these gases. Likewise, with increasing radiation—particularly for the stronger greenhouse gases—simultaneous cooling of the gases across the cylinder volume can be observed. This is explained by conversion of kinetic and thus thermal energy into radiation, which represents a negative greenhouse effect.
- *Ronald Grabyan* investigates whether atmospheric $CO_2$ precedes or lags global temperature changes over the past 2000 yr, using both visual and statistical analyses. A parallel evaluation of Total Solar Irradiance (TSI) and temperature is conducted to assess the influence of solar forcing on climate variability. Results show that atmospheric $CO_2$ consistently lags temperature by approximately 150 yr from 1 to 1850 AD, suggesting it functions as a response variable rather than a primary forcing. TSI–temperature correlations are generally strong across the full 2000 yr interval, and very strong from 1850 to present, supporting the hypothesis that solar variability plays a significant role in long-term climate change.
- *Ad Huijser* analyzes the Earth's climate system as a subsystem of the broader Earth Thermal System, allowing for the application of a "virtual balance" approach to distinguish between anthropogenic and other, natural contributions to global warming. Satellite-based Top Of the Atmosphere (TOA) radiation data from the CERES program (since 2000), in conjunction with Ocean Heat Content (OHC) data from the ARGO float program (since 2004), indicate that natural forcings must also play a significant role. Specifically, the observed warming aligns with the net increase in incoming shortwave solar radiation (SWIN), likely due to changes in cloud cover and surface albedo. Arguments suggesting that the SWIN trend is merely a feedback response to GHG-induced warming are shown to be quantitatively insufficient. This analysis concludes that approximately two-thirds of the observed global warming must be attributed to natural factors that increase incoming solar radiation, with only one-third attributable to rising GHG-concentrations. These findings imply a much lower climate sensitivity than suggested by IPCC-endorsed Global Circulation Models.
- *Frans Schrijver* evaluates in his paper whether $CO_2$ levels during historical periods of similar or more greenness as today, are consistent with the widely held view that $CO_2$ levels remained below 300 ppm over the past 800,000 years, as indicated by Antarctic ice core records. Employing Mitscherlich's Law, the research models the global Gross Primary Production (GPP) response to increasing $CO_2$, based on the mean value of eight different long-term GPP datasets. It illustrates a diminishing return of vegetation associated with rising $CO_2$, as additional factors such as nutrient and water availability impose constraints on the fertilization effect. Due to this diminishing return the average residence time of $CO_2$ in the atmosphere increases significantly with higher GPP values. High $CO_2$ levels, similar to today's, were therefore necessary for comparable GPP during green periods like 10,000 years ago. A $CO_2$ concentration of 280 ppm

would only be possible, if nature's response to $CO_2$ were fundamentally different from what we observe today, with other constraining factors exceptionally more favorable. Natural fluctuations of the atmospheric $CO_2$ concentration can be well explained, based on the strong temperature dependence of the degeneration of carbon compounds that are stored in large quantities in the soil and the oceans.

- *Les Coleman* adopts a statistical approach that examines warming from the perspective of a researcher in financial markets. The principal finding is that the central hypothesis of Anthropogenic Climate Change (ACC) seems spurious, and due to simultaneous rises in global temperature and atmospheric $CO_2$ which independently follow unrelated, time trending variables. ACC is further questioned by the existence of joint test and missing variables problems. Exploring $CO_2$'s limited ability to explain warming by incorporating unsuspected forcers shows that humidity leads temperature and explains most of its increase; further, oceanic oscillations and cereal production are stronger explanators of temperature than $CO_2$. This statistically-based study adds value to existing physics-based climate models through a complementary analytical perspective that tests the robustness of models to real world data. It concludes that human activity is contributing to global warming, but herding around the forcing role of carbon combustion has seen its influence exaggerated. This has obvious implications for the effectiveness of decarbonization as a policy to manage global warming.

- In their Review Article *Camille Veyres, Jean-Claude Maurin and Patrice Poyet* conclude from independent observations and reports that the stock-to-outflow ratio of $CO_2$ molecules in the atmosphere is about five years. Accordingly, only about 5.5% of the atmospheric $CO_2$ stock comes from fossil fuel emissions not yet absorbed by vegetation or oceans, while 94.5% originates from natural outgassing of oceans and soils. This interpretation is supported by the $\delta^{13}C$ record at Mauna Loa Observatory (MLO). The 50% increase in vegetation productivity since 1900 can be attributed to higher atmospheric $CO_2$ concentrations and a longer growing season. Decarbonization policies may therefore affect only 5.5% of atmospheric $CO_2$. Moreover, the strong month-by-month correlation, over nearly 800 months, between the increments of the $CO_2$ stock at MLO (altitude 3.4 km) and the sea-surface temperature (SST) anomaly in the inter-tropical zone shows that 94.5% of atmospheric $CO_2$ reflects the time-integrated effect of past surface temperatures, themselves determined by surface insolation. Simple models of carbon fluxes and stocks for the oceans, atmosphere, and vegetation & soils, assuming ocean degassing driven by inter-tropical SST, reproduce the observed time series atmospheric $CO_2$, $\delta^{13}C$ and vegetation productivity since 1900. In this context, IPCC theories and models based on concepts such as the Airborne Fraction, the Bern function, an adjustment time or a Revelle buffer factor, appear to be misleading constructs.

- *Antero Ollila* studies the impact of Water Vapor (WV) on global warming. In General Circulation Models (GCMs) the positive feedback of WV is the basic feature, which approximately doubles the warming impacts of any other climate drivers. However, simple climate models without this feature already show that they can simulate the temperatures of the 2000s very well. On the other hand, the observed humidity observations reveal that they vary, but not according to the water feedback theory. In this study, the radiative forcing (RF) value of WV for different atmospheric water amounts has been calculated by applying the line-by-line (LBL) method. A simple climate model by the author has been modified by implementing this dependency in the same way as for the other greenhouse (GH) gases. This model has been used for the simulations of absolute yearly temperature and humidity changes, as well as for decadal-long changes by applying CERES (Clouds and the Earth's Radiant Energy System) observations. These simulations reveal that humidity increases are strongly related to the primary energy changes of the absorbed solar radiation (ASR). The yearly temperature variations of the hemispheres show that water vapor increase has about a 14 % temperature impact and not about 100 % as assumed by the water feedback theory.

- In an Essay *Raimund Müller* considers the diverging concepts for the global $CO_2$ absorption/ emission in the various reservoirs, which significantly deviate in their respective residence times. He assumes that there exists a regular exchange of $CO_2$ between the reservoirs, both in terms of absorption and emission. Without anthropogenic emissions, absorption and emission balance each other. Consequently he follows, the same happens with any additional amount of $CO_2$ introduced into the system: it is distributed in a constant ratio among the reservoirs.

- Finally, this issue contains a Commentary from *Anthony Sadar*, which is a conflation and revision of the author's essays previously published in the *American Thinker* and the *Washington Times*. To counter climate anxiety, this treatise reflects the limited predictions of climate models, particularly the atmosphere's temperature profile, where models are not merely uncertain but also show a common warming bias relative to observations. Also, regarding the physics, how precipitation will change with warming is not sufficiently understood. This suggests that models can seriously misrepresent certain fundamental feedback processes.

We hope the above contributions will stimulate our readers to a further critical discussion of climate science, and we wish interesting reading

Tallinn/Hamburg, December 31, 2025. Hermann Harde
(Editor-in-Chief)

*Research Article*

# The Negative Greenhouse Effect – Part I:

## Experimental Studies with a Common Laboratory Set-Up

*SCC-Publishing*

*Michelets vei 8 B*
*1366 Lysaker, Norway*

*ISSN: 2703-9072*

*Correspondence:*
*harde@hsu-hh.de*

*Vol. 5.3 (2025)*
*pp. 1-9*

*Michael Schnell* [1] *, Hermann Harde* [2]

[1] *Ex Academy of Science of GDR, Berlin, Germany*

[2] *Helmut-Schmidt-University, Hamburg, Germany*

### Abstract

In two consecutive studies, the suitability of different experimental set-ups for detecting and measuring the emission of infrared-active gases is investigated, as this is of particular importance for understanding the atmospheric greenhouse effect.

The first part presents a horizontally arranged Styrofoam box, as described occasionally in the literature for such experiments. The gases are slightly heated by a heater at the bottom of the container, and the radiation—emitted by the infrared-active gases—is detected through an infrared-transparent window at the side. However, this arrangement is only suitable for demonstrating the positive or negative greenhouse effect with very strong greenhouse gases such as Freon. For weaker greenhouse gases like $CO_2$ or $CH_4$, the gas radiation can only be inadequately distinguished from the broadband background radiation of the container walls. In addition, the supplied heating power creates a circular air flow, which further complicates detection. Nevertheless, these investigations provide important clues for a significantly improved setup in the form of a vertical aluminum cylinder, which can be used to detect infrared emission under conditions such as those observed in the lower troposphere.

For a gas layer above a cooler surface, as this occurs during inversion weather conditions or can be observed in the Arctica and Antarctica during winter months, the radiation emitted by the surface and partially absorbed by the warmer gas layer is lower than the radiation emitted by the gas upward. This is known as negative greenhouse effect, which, despite the limited detection sensitivity, can be simulated for the first time in the laboratory with the presented set-up.

**Keywords:** Infrared-active gases; positive and negative greenhouse effect.

Submitted: 2025-06-12, Accepted 2025-08-19. https://doi.org/10.53234/scc202510/02

## 1. Introduction

Infrared-active gases such as water vapor (WV) or carbon dioxide ($CO_2$), along with convection and evaporation, significantly determine the vertical energy transfer in the atmosphere. Whether these gases primarily contribute to warming or cooling depends largely on the sign of the vertical temperature gradient over the atmosphere. In the troposphere, the lowest layer of the atmosphere, the temperature on average drops by 6.5°C/km. In this case, the radiation emitted into space by the infrared(IR)-active gases is lower than the radiation absorbed by them from the Earth's surface. This is known as atmospheric Greenhouse Effect (GHE)[1]. The reduced radiation at the Top of the Atmosphere (TOA) thus leads to additional warming and an increase of the long-wave radiation emitted from the Earth's surface. This happens, until—together with the directly

---

[1] Although the terms greenhouse gases and greenhouse effect are somewhat misleading and should be replaced by designations like IR-active gases and atmospheric radiative effect (see also Koutsoyiannis & Tsakalias, 2025 [1]), here we still use the conventional terminology as established over 150 years.

absorbed solar radiation—an equilibrium is adjusted between the energy supply and removal at TOA.

However, in some parts of the troposphere, the temperature gradient can also be reversed, e.g., during inversion weather conditions or during the winter months in central parts of the Arctic and Antarctic. During these winter months, the surface of the poles can be colder than the troposphere, which is warmed by currents from the equator to higher latitudes, thus potentially reversing the GHE (see Schmithüsen et al., 2015 [2]). Then the radiation emitted by the warmer air is more intense than the thermal radiation coming from the Earth's surface and absorbed in the atmosphere.

However, one of the most common objections against the GHE–whether positive or negative–is that the IR-active molecules under the conditions of the lower atmosphere transfer the absorbed radiation energy almost completely to other air molecules, known as thermalization, and according to physical reasons suppress any gas emission.

The "thermalization" hypothesis was already refuted in a previous study by laboratory experiments (Harde & Schnell, 2022 [3]). Our actual experiments show, in agreement with theoretical considerations (Harde, 2013 [4]) that IR-active gases can also draw their radiation energy from the kinetic energy of the gas mixture, thereby lowering the temperature of the gas.

Such an effect can only be observed experimentally, if a heated gas container is in radiation exchange with a cooled radiation receiver, and the radiation emitted by the container walls is weaker than the gas radiation of the Greenhouse-Gases (GH-gases). This requires container walls made of polished metal, which have extremely low emission coefficients. Under this condition, addition of a GH-gas leads to an increase in IR radiation while simultaneously cooling the gas volume. This corresponds to conditions as found for a negative GHE. Such conditions can directly be replicated in the laboratory with a set-up as presented in Section 2 (for further details of an improved set-up see: Harde & Schnell, 2025, Part II [5], Subsection 4.4).

An unexpected air circulation in the set-up is discussed in Section 3, and despite some limitations in the sensitivity, we can demonstrate in Section 4 that GH-gases not only emit in higher altitudes but also under conditions similar to those in the lower troposphere, while deriving their radiation energy from the gas's kinetic energy. The decreasing gas temperature and altered distribution also lead to a slightly reduced wall temperature and thus cooling at constant heating power. The particular challenge, however, lies in detecting the increased radiation component of the molecular bands against the broad background radiation, which clearly predominates due to the large surface area of the container walls.

Our initial investigations using a horizontally positioned Styrofoam box were inspired by the experiments of Seim and Olsen in 2023 [6]. The authors used such a set-up to verify our previous experiments on the $CO_2$ GHE (Harde & Schnell, 2022 [3]). They found a slight *temperature increase* with increasing $CO_2$, but much smaller than expected. This could not be explained.

It is likely that these deficiencies are due to the nature of the experimental set-up, which introduce unnecessary complications such as multiple reflections and air currents. Therefore, the first part of our investigations presented here, primarily addresses the question, how far such a box is really suitable for demonstrating a positive or negative greenhouse effect.

In Part II, it is shown that with a vertical experimental setup—consisting of a cylinder with polished Aluminum walls—not only the negative GHE of the most important greenhouse gases water vapor (WD), $CO_2$ , methane ($CH_4$) and nitrous oxide ($N_2O$) can be reliably detected, but it is also experimentally confirmed that water vapor can attenuate the effect of the other gases by superposition and saturation on the spectral bands (see also Harde, 2014 [7]).

## 2. Experimental Set-Up

Based on the experimental set-up of Seim and Olsen [6], a horizontally arranged, rectangular-shaped Styrofoam box is used with the heating and temperature distribution in the box (Fig. 1).

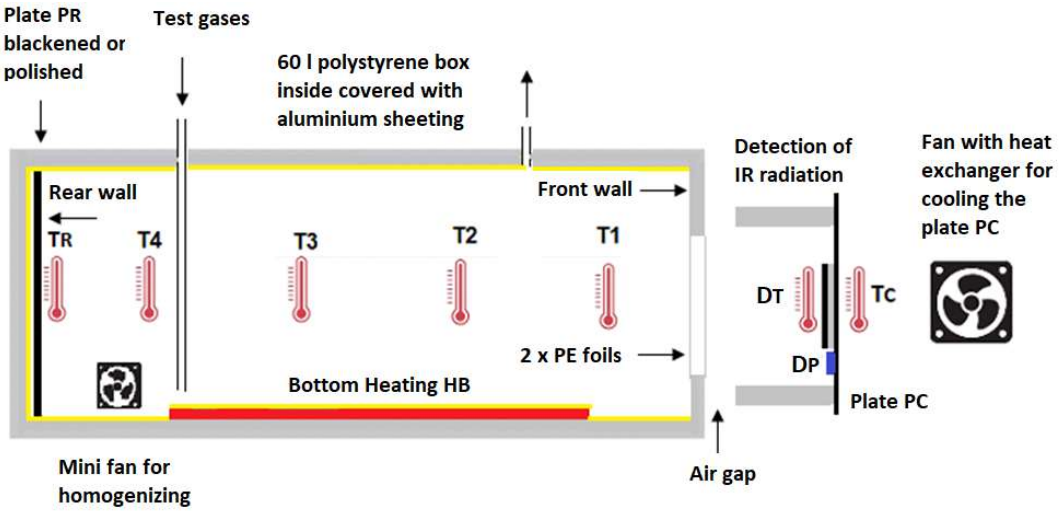

*Fig. 1: Schematic experimental setup*

The air inside the box is slowly heated to 36°C by a floor heating. Every 5 minutes, four temperature sensors T1 to T4 record the temperature profile inside the box and store the values in data loggers (see Appendix).

The infrared radiation emanating from the inner surfaces of the box is directed outwards through a large opening in the right-hand wall onto a cooled plate $P_C$ at constant temperature $T_C$. The cooled plate $P_C$ is an essential part of the experimental concept, because it creates an energy sink that enables a measurable energy flow by infrared radiation and/or heat conduction from the inside to the outside.

The opening is sealed inside and out with two thin Polyethylene (PE) foils that allow infrared radiation to pass through but retain the sample gases and virtually eliminate mechanical heat conduction to the outside.

If the box is filled with GH-gases, infrared radiation is generated by two sources: the radiation from the box's interior walls and the IR-active gases. GH-gases can only noticeably increase the emitted radiation intensity, if they generate a higher radiance on their absorption-emission bands than the inner walls. This requires the walls to have the lowest possible emissivity $\varepsilon << 1$. To ensure this, all interior surfaces of the box are covered with polished aluminum plates, so that these surfaces emit a significantly lower radiation intensity than a blackbody radiator.

The radiation passing through the opening is detected by two independent detector systems located on the cooled plate $P_C$ ( Fig. 2b). In the center of the plate is a blackened aluminum disc, separated from plate $P_C$ by 8 mm thick Styrofoam insulation . The disc reacts to IR radiation with a temperature increase, which is measured by the temperature sensor $D_T$. In addition, four Peltier elements $D_P$ are glued directly to the $P_C$ plate. They generate a voltage in the mV range when there is a temperature difference between the top and bottom (Seebeck effect).

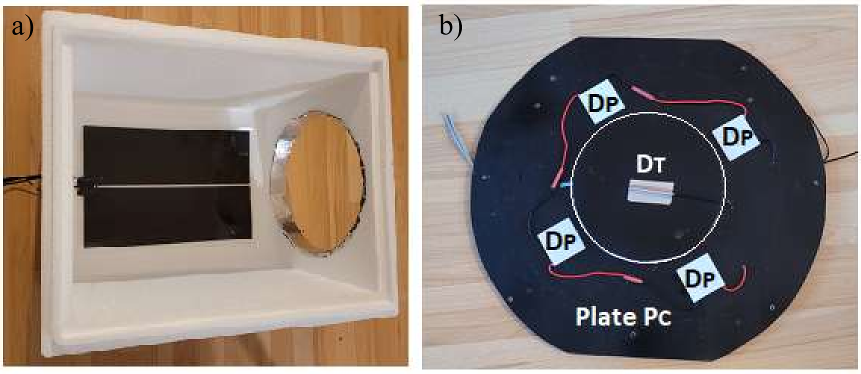

*Fig. 2: a) Styrofoam box in its raw state (without lid and aluminum plates on the side walls) with heating foil $H_B$ and radiation opening, b) detection of the IR radiation on the inside of the cooled plate $P_C$ with the temperature sensor $D_T$ and 4 Peltier elements $D_P$ before its blackening.*

A DC amplifier and data logger is recording and storing the data. In this set-up, the temperature and voltage changes are purely qualitative parameters of the radiation flux to the $P_C$ plate and only represent trends for the investigations presented here. To derive the actual radiation intensities from these data, calibration is required, which is presented in Part II of this study [5].

The rear wall (left side) is covered with a polished or blackened aluminum plate $P_R$ and its temperature $T_R$ is recorded by a data logger. Since only this plate is aligned plane-parallel to the plate $P_C$, it can be used to demonstrate the radiation exchange with the cooled plate (see Section 3).

## 3. A Metastable Air Circulation

Without heating, all temperatures in the Styrofoam box are approximately 18°C, and the air is at rest. When the floor heating $H_B$ is switched on, the air warms up, initially creating a surprising temperature distribution. The sensor $T_1$ has the highest temperature, and the rear wall $P_R$ – polished or blackened – has the lowest temperature: $T_1 > T_2 > T_3 > T_4 > T_R$ (Fig. 3). This phenomenon cannot be explained by heat conduction. Then, for $T_1$ the exact opposite would be expected due to the large opening to the cooled sensors.

The unusual temperature gradient is an indication that the heat is mainly dissipated by IR radiation. Only the rear wall $P_R$ in the box is aligned plane-parallel to the cooled plate $P_C$ and thus can optimally exchange infrared radiation with the cooled plate $P_C$. As a result, the temperature $T_R$ (green line) is up to 2°C lower than all other measuring points within the box, and the blackened rear wall is further 1.9°C colder than the polished rear wall (Fig. 3, Tab. 1).

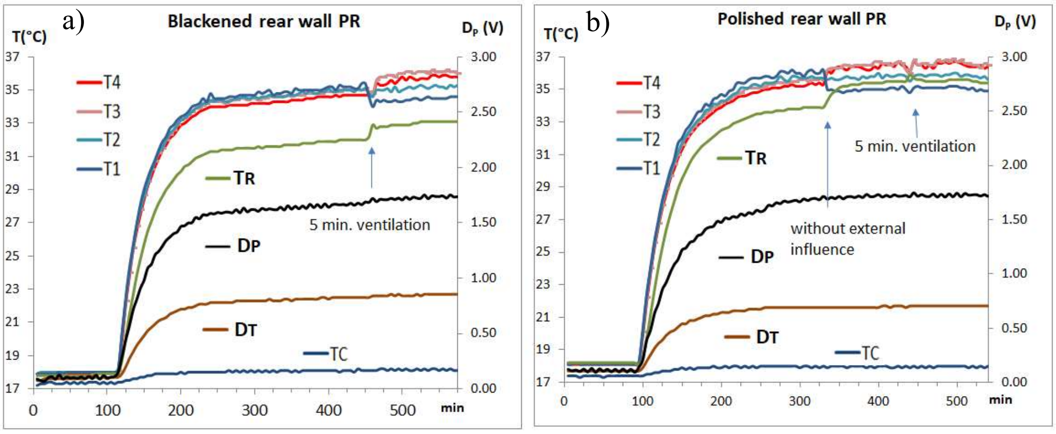

*Fig. 3: Temperatures during heating of the Styrofoam box: a) Stop of the metastable air circulation by short-term ventilation at min 450, b) spontaneous stop of the air circulation without external intervention at min 330. Short-term ventilation in the stable state at min 450 has no effect on the temperature curve of the individual measuring points.*

The colder rear wall $P_R$ causes the adjacent air to flow downwards, creating counterclockwise air circulation in the box. The air passes the floor heating $H_B$ and absorbs additional heat, which is transferred to $T_1$. Thus sensor $T_1$ (blue line) becomes the warmest point in the box (Fig. 3, Table 1). This phenomenon is a metastable air circulation that immediately stops when the internal fan is switched on for a short time. The fan then heats the rear wall, increasing its temperature $T_R$ by up to 1.5°C and eliminating the downward flow as the driving force of the air circulation. A new and now stable temperature gradient $T_4 \sim T_3 > T_2 > T_1$ is formed, which corresponds to the expected heat flow from the warm box to the cold plate $P_C$. For the blackened back wall, the temperature $T_R$ remains significantly below the air temperatures $T_1 - T_4$ (Fig. 3a), while the polished back wall is close to the air temperatures $T_1 - T_4$ (Fig. 3b).

With the polished back wall, from beginning the temperature $T_R$ is higher than with the blackened wall, so that the abnormal air circulation can stop automatically after some time even without external influence (Fig. 3b).

Air circulation has no or only a negligible influence on the energy transport to the plate $P_C$, as can be seen from the sensors $D_P$ and $D_T$ (Fig. 3, Table 1). However, since air temperatures are an important indicator of a negative GHE, a stable circulation and temperature distribution must be established before adding a GH-gas. Therefore, the mini-fan in the box is switched on for 5 minutes approximately 3 hours before adding a GH-gas to ensure that the stable condition is achieved (see Fig. 4, min 230). When stable circulation has already been established, the ventilation has no influence on the temperatures, as shown in Fig. 3b.

Table 1: Influence of air circulation on temperatures and energy transport, HB = 21 W.

| Condition<br>the change | $T_C$<br>°C | $T_R$<br>°C | $T_4$<br>°C | $T_3$<br>°C | $T_2$<br>°C | $T_1$<br>°C | $D_T$<br>°C | $D_P$<br>V |
|---|---|---|---|---|---|---|---|---|
| | | | | Polished back panel: | | | | |
| Metastable | 18.0 | 33.9 | 35.3 | 35.6 | 35.7 | 36.0 | 21.6 | 1.70 |
| Stable | 18.0 | 35.4 | 36.3 | 35.6 | 35.8 | 35.0 | 21.6 | 1.70 |
| difference | 0.0 | 1.5 | 1.0 | 0.0 | 0.1 | -1.0 | 0.0 | 0.0 |
| | | | | Back wall blackened: | | | | |
| Metastable | 18.1 | 32.0 | 34.7 | 35.0 | 35.0 | 35.2 | 22.5 | 1.70 |
| Stable | 18.1 | 32.9 | 35.6 | 36.0 | 35.1 | 34.3 | 22.6 | 1.73 |
| difference | 0.0 | 0.9 | 0.9 | 1.0 | 0.1 | -0.9 | 0.1 | 0.03 |

## 4. Evidence of Gas Radiation and the Negative Greenhouse Effect

Before starting an experiment as described in Section 2, the air in the Styrofoam box with the polished back wall is heated to 35 to 43 °C (heating power $H_B$ between 21 and 28 W), and a stable condition is ensured by ventilation. After further 200 minutes, the greenhouse gas is poured in near the floor using a mini pump with a rate of about 1 l/min. Then the gas and air are homogenized for 5 minutes using the internal fan. The temperature changes measured 30 minutes before and after adding the GH-gas are used as averages of the recorded data (Table 2). As a control measurement, the IR-inactive noble gas argon is also examined to check whether mechanical heat conduction has an influence on the measurements. For the sake of simplicity, only data for the medium heating level $H_B$ = 25 W are shown in Fig. 4 and Table 2.

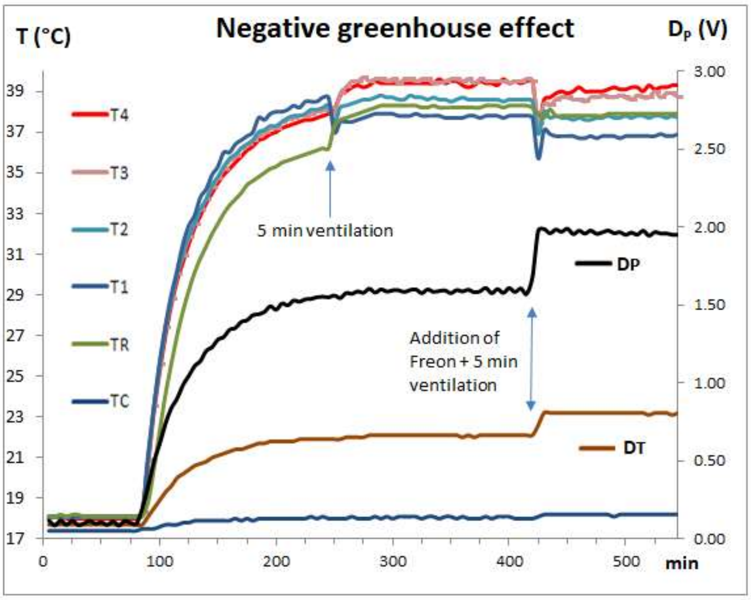

*Fig. 4: Verification of the negative GHE with 2 vol.% Freon 134a,* $H_B$ = 25 W.

Table 2: Influence of sample gases on temperatures and IR radiation, $H_B = 25$ W

| Gas<br>Vol.-% | $\Delta T_C$<br>°C | $\Delta T_R$<br>°C | $\Delta T_4$<br>°C | $\Delta T_3$<br>°C | $\Delta T_2$<br>°C | $\Delta T_1$<br>°C | $\Delta D_T$<br>°C | $\Delta D_P$<br>V |
|---|---|---|---|---|---|---|---|---|
| Freon 2% | 0.0 | -0.5 | -0.4 | -0.9 | -0.9 | -1.0 | 1.1 | 0.38 |
| $N_2O$ 2 % | 0.0 | -0.1 | -0.3 | -0.2 | -0.2 | -0.2 | 0.2 | 0.06 |
| $CO_2$ 2 % | 0.0 | -0.1 | -0.1 | 0.0 | -0.1 | -0.1 | 0.2 | 0.07 |
| Argon 2% | 0.0 | 0.1 | 0.0 | 0.1 | 0.0 | 0.1 | 0.0 | 0.00 |
| Argon 5% | 0.0 | 0.1 | 0.0 | 0.1 | 0.0 | 0.0 | 0.0 | 0.00 |

The addition of Freon 134a (1,1,1,2-tetrafluoroethane), a very strong greenhouse gas, leads to a significant increase in detectable radiation, which can be seen as increase of the measured values $\Delta D_T$ and $\Delta D_P$. At the same time the air in the box cools down by up to 1.0°C.

This counter-reaction is the result of molecular collisions, which lead to a continuous repopulation of excited rotational-vibrational states of the Freon molecules (see, e.g.: Harde, 2013, Subsection 2.3 and 2.5 [4]). In this way the radiated energy due to spontaneous emission of the molecules occurs at the expense of the air's kinetic energy. Control measurements with Ar or He show no changes, so specific heat conduction can be ruled out for the measured temperature decrease.

The observed temperature drop over the box is a clear indication of a negative GHE, which can be demonstrated with this experimental set-up in a laboratory and under normal pressure conditions.

However, for other IR-active gases such as $CO_2$, $CH_4$ or $N_2O$, the described set-up only gives very weak or even no measurable radiation changes at the sensors or in the gas temperature. This shows, apparently, a simple Styrofoam box is not sufficiently suitable for detecting the GHE for these gases (Table 2).

Furthermore, these studies show that a blackened back wall is counterproductive for detecting the negative GHE. To this end, the Freon measurements were repeated with both a polished and a blackened back wall $P_R$ at a heating $H_B = 21$ W (Table 3).

Table 3: Polished vs. blackened back panel, measured temperatures and radiation with respective changes when adding 2 vol.% Freon, $H_B = 21$ W

| Adding Freon | $T_R$<br>°C | $T_C$<br>°C | $T_4$<br>°C | $T_3$<br>°C | $T_2$<br>°C | $T_1$<br>°C | $D_T$<br>°C | $D_P$<br>V |
|---|---|---|---|---|---|---|---|---|
| Polished back panel = Variant A | | | | | | | | |
| Average | 35.20 | 18.30 | 36.20 | 36.00 | 35.10 | 34.20 | 22.90 | 1.70 |
| the change | -0.34 | 0.10 | -0.36 | -0.66 | -0.79 | -0.83 | 0.89 | 0.30 |
| Back panel blackened = variant B | | | | | | | | |
| Average | 34.10 | 18.40 | 35.40 | 35.40 | 34.60 | 33.80 | 23.30 | 1.90 |
| the change | 1.04 | 0.10 | -0.36 | -0.74 | -0.70 | -0.77 | 0.30 | 0.12 |
| Difference Var. B - A | 1.38 | 0.00 | 0.00 | -0.09 | 0.09 | 0.06 | -0.59 | -0.17 |

While the changes in air temperatures are almost identical, there are significant differences in the IR radiation ($D_T$ and $D_P$). To understand this, one must examine the temperature changes $\Delta T_R$ of the various back panels. The polished panel (variant A) largely reflects the Freon radiation, preventing heat transfer and dissipating the heat output primarily through IR radiation to the $P_C$ plate. The slight temperature decrease $\Delta T_R = -0.34$ °C is caused by heat conduction to the cooler adjacent air layers.

In contrast, the blackened rear wall (variant B) absorbs the Freon radiation almost completely and thus experiences a significant temperature increase of $\Delta T_R = 1.04$ °C despite the cooled ambient air. As a result, part of the Freon radiation is converted into heat and partly disappears through the rear polystyrene wall to the room. This is lost as the IR radiation towards the $P_C$ plate with the sensors $D_T$ and $D_P$ and results in a lower increase for variant B than variant A.

The experiment with the blackened back wall demonstrates, why proving the negative GHE is quite difficult and so far, has only been successful with the super GH-gas Freon. To detect the gas radiation of IR-active gases, the container and the GH-gases are both heating up. Even with polished walls and a small emission coefficient, due to the relatively large surface of a cuboid box it is difficult to distinguish the gas radiation from the background radiation of the container. Therefore, the set-up with a Styrofoam box is not sensitive enough to clearly detect the relatively weak IR radiation from $CO_2$ and nitrous oxide on this background. Especially a horizontal set-up with disruptive convection and multiple reflections is difficult to control.

In contrast, a cylindrical, vertically mounted radiation channel with polished Al-walls can be used, not only to measure the negative GHE of $CO_2$ and nitrous oxide, but also that of the weaker GH-gas methane (Harde & Schnell, 2025, Part II [5]).

## 5. Summary

In this contribution we demonstrate that IR-active gases are transferred to excited states through thermal excitation and convert the kinetic energy of their surrounding into infrared radiation by spontaneous emission. Due to inelastic collisions in the gas mixture, the lost radiation energy is continuously extracted from the thermal energy of the gas and observed as a temperature drop in the compartment. The hypothesis that collision processes of the gases in the lower troposphere prevent IR emission and that greenhouse gases cannot generate back-radiation is thus once again refuted.

However, with the presented set-up this effect could only clearly be demonstrated using the particularly potent greenhouse gas tetrafluoroethane (Freon 134a). Apparently, this limitation is caused by the set-up, consisting of a horizontally placed Styrofoam box, which is only partially suitable for radiation transfer. Multiple reflections of the infrared radiation from the parallel interior walls impede the radiation transfer to the cooled $P_C$ plate and are overlaid by the wall radiation. Furthermore, the horizontal arrangement leads to complications due to the resulting air circulation. Part II of this study [5] shows that these problems can be overcome with a vertically arranged cylindrical radiation channel with polished Al-walls.

**Funding:** No funding of the work.

**Co-Editor**: Stein Bergsmark; **Reviewer 1**: Anonymous, **Reviewer 2:** Prof. D. Koutsoyiannis.

## References

1. D. Koutsoyiannis, G. Tsakalias, 2025: *Unsettling the settled: Simple musings on the complex climatic system*, Front. Complex Syst., Vol. 3, https://doi.org/10.3389/fcpxs.2025.1617092
2. H. Schmithüsen, J. Notholt , G. König-Langlo, P. Lemke, T. Jung, 2015: *How increasing $CO_2$ leads to an increased negative greenhouse effect in Antarctica* , Geophys . Res. Lett., 42, pp. 10, 422–10,428, doi:10.1002/2015GL066749.
3. H. Harde, M. Schnell, 2022: *Verification of the Greenhouse Effect in the Laboratory* , Science of Climate Change, Vol. 2.1, pp. 1-33. https://doi.org/10.53234/scc202203/10
4. H. Harde, 2013: *Radiation and Heat Transfer in the Atmosphere: A Comprehensive Approach on a Molecular Basis* , International Journal of Atmospheric Sciences (Open Access), vol. 2013, http://dx.doi.org/10.1155/2013/503727

5. H. Harde, M. Schnell, 2025: *The Negative Greenhouse Effect – Part II: Studies of Infrared Gas Emission with an Advanced Experimental Set-Up*, Science of Climate Change, Vol. 5.3, pp. 10 – 34, https://doi.org/10.53234/scc202510/03
6. T. O. Seim, B. T. Olsen, 2023: *The Influence of Heat Source IR Radiation on Black-Body Heating/Cooling with Increased $CO_2$ Concentration* , Atmospheric and Climate Sciences, 13, pp. 240-254, https://doi.org/10.4236/acs.2023.132014
7. H. Harde, 2014: *Advanced Two-Layer Climate Model for the Assessment of Global Warming by $CO_2$*, Open Journal of Atmospheric and Climate Change, Vol. 1, No. 3, p. 1, https://web.archive.org/web/20160429061756/http://www.scipublish.com/journals/ACC/papers/download/3001-846.pdf.

## Appendix

The laboratory is thermostatted at 18 °C ± 0.3 °C to prevent perturbations caused by fluctuating room temperatures.

To supply the $H_B$ heating foil, the current from the socket is stabilized at 230 V via a digital voltage regulator. It is then rectified by another digital voltage regulator and adjusted to the desired heating output $H_B$ using a percentage setting from 52 to 70%. The hole (diameter Ø = 28.5 cm) in the Styrofoam box is cut using an electric cutter. Commercially available aluminum plates are polished to a high gloss with polishing paste or blackened with "Matt Black" paint spray. Back panel = 36 x 32 cm, $P_C$ plate Ø = 41 cm, IR detector plate Ø = 16.7 cm.

The housing for the IR detector is made of polystyrene wallpaper: length = 13 cm, outer diameter = 41 cm, inner diameter = 30 cm. The housing is connected to the front wall and the cooled $P_C$ plate by four threaded rods, leaving a 2 cm air gap between the box and the housing.

The PE foils are glued to a wooden frame 37 x 33 cm and a hole with Ø = 29 cm and fixed to the front wall from both sides with silicone rubber.

Table A1: Distances of the temperature measuring points from the front wall of the box

| Sensor | $T_R$ | $T_4$ | $T_3$ | $T_2$ | $T_1$ | $T_C$ | $D_T$ | $D_P$ |
|---|---|---|---|---|---|---|---|---|
| Distance (cm) | 49 | 45 | 34 | 23 | 11.5 | -20 | -19.5 | -19.5 |

Table A2: Compilation of materials used.

| Device | Source |
|---|---|
| Styrofoam box = Thermobox 60 liters<br>Internal dimensions: 49.0 x 37.0 x 33.0 cm<br>External dimensions L/W/H: 57 x 45 x 41 cm | Amazon/Terra Exotica |
| Styrofoam plate for additional insulation of the lid 57 x 45 x 2 cm | hardware store |
| Heating foil 2x20 W NEKOSUKI reptile terrarium heating mats 42 x 28 cm | Amazon/Terra Exotica Terrarium |
| PE film , cling film 45 cm x 300 m | Amazon/Packaging Team |
| Thermocouple TEC1 12706 12V 6A 40x40mm | Amazon/ shenzhenshiyaoxingmaoyi |
| Digital voltage regulator 4000W AC 220V SCR | Amazon/ Luoyuuk |
| Digital voltage regulator KEMOT SER-2000 | Amazon |
| Elitech Temperature Data Logger, RC-4 | Amazon |

| | |
|---|---|
| Voltage data logger VOLTCRAFT VC-11015505 DL-250V | Conrad Electronic SE |
| DC 3-12V iHaospace AD620 DC Power Amplifier | Amazon/ iHaospace |
| Heat exchanger, ASHATA 120mm aluminum radiator | Amazon/Richer-R123 |
| Fan Sunon 80 x 80 x 25mm | Amazon/ kessler -electronic |
| Mini fan 30 x 30 x 10mm | Amazon/CHEER CHAMP |

*SCC-Publishing*

*Michelets vei 8 B*
*1366 Lysaker, Norway*

*ISSN: 2703-9072*

*Correspondence:*
*harde@hsu-hh.de*

*Vol. 5.3 (2025)*
*pp. 10-34*

# The Negative Greenhouse Effect – Part II:

## Studies of Infrared Gas Emission with an Advanced Experimental Set-Up

*Hermann Harde [1], Michael Schnell [2]*

*[1] Helmut-Schmidt-University, Hamburg, Germany*

*[2] Ex Academy of Science of GDR, Berlin, Germany*

## Abstract

For our studies of the greenhouse gas emission – different to a simpler experimental set-up with a horizontally positioned Styrofoam box described in Part I – here we use an arrangement consisting of a vertically placed cylinder with uniformly heated walls and an opening at the bottom, which is sealed by an infrared-transparent foil. Below this foil are two calibrated radiation sensors on a cooled plate, which measure the radiation emerging from the cylinder. At the same time, the temperature distribution in the container is recorded before and after adding a greenhouse gas.

With this set-up we have investigated the gases water vapor, $CO_2$, $CH_4$, $N_2O$, and Freon 134a at varying concentrations between 1–8% in air and at normal pressure. The radiation emitted by the gases can be detected against a larger background radiation originating from the cylinder walls. All gases show strong saturation effects with increasing concentration. The measurements can be well reproduced by corresponding radiation transfer calculations. A clear influence of water vapor on the other gases is also evident as increased background radiation and partial spectral superposition with these gases, which appears as attenuated emission of these gases. Likewise, with increasing radiation—particularly for the stronger greenhouse gases—simultaneous cooling of the gases across the cylinder volume can be observed. This is explained by conversion of kinetic and thus thermal energy into radiation, which can escape through the infrared transparent foil.

For a gas layer located above a cooler subsurface, as known from inversion weather conditions or as observed in the Arctic and Antarctic during the winter months, the radiant power emitted by the surface and partially absorbed by the warmer gas layer, is lower than the power emitted upward. This corresponds to a negative greenhouse effect, which with the presented set-up can be reproduced for the first time in the laboratory.

**Keywords:** Greenhouse effect; greenhouse gases; negative greenhouse effect.

Submitted 2025-06-12, Accepted 2025-08-19; https://doi.org/10.53234/scc202510/03

## 1. Introduction

The main components of our atmosphere, nitrogen and oxygen, do not interact with the radiation emitted from the Earth's surface, radiation which is assigned to the mid-infrared (IR) spectral range (3 - 50 µm) and is also referred to as thermal radiation or simply heat radiation. It is undisputed that certain IR-active gases absorb this heat radiation, as demonstrated by numerous measurements with these so-called Greenhouse-(GH)-gases. The spectra, with extensive data on temperature dependence and pressure broadening due to collisions between these gases, are available in the HITRAN-database (Rothman et al, 2025 [1]). Critics of the Greenhouse Effect (GHE) disagree that GH-gases can partially or even completely release the absorbed energy as IR emission. Opinions differ widely, although the physical basis for this was already developed in the middle and end of the 19th century (Kirchhoff, 1859 [2]; Clausius, 1887 [3]).

One of the most common objections to IR emission of GH-gases is that under the conditions of the lower atmosphere, IR-active molecules transfer the absorbed radiation energy almost completely to other air molecules via collision processes (thermalization), and the collisions prevent any spontaneous emission, especially back-radiation to the Earth's surface.

In previous studies, we used a special apparatus to simulate the radiative transfer between the Earth's surface and a cloud layer at an altitude of 5-6 km (Harde & Schnell, 2022 [4]). We could show that GH-gases increase the temperature of a heated plate that is arranged plane-parallel to a cooled plate. These measurements allowed us to experimentally determine the radiative forcings $\Delta F_{2xGas}$ for the gases carbon dioxide, nitrous oxide, and methane, which are in excellent agreement with Line-by-Line Radiation Transfer (LBL-RT) calculations.

Using a modified set-up, in this contribution we investigate how the GH-gases water vapor (WV-$H_2O$), carbon dioxide ($CO_2$), methane ($CH_4$), nitrous oxide ($N_2O$) and Freon 134a (1,1,1,2-tetrafluoroethane, $CFH_2CF_3$) can influence the temperature of a warmer air layer located above a cooler background – here a cooled plate.

In contrast to the *usual* atmospheric GHE, which primarily affects the lower troposphere, with the new set-up there is only a heat flux from a warmer to a colder body. A violation of the second law of thermodynamics [3], as often cited by critics, is thus per se ruled out.

It is shown that even at normal pressure GH-gases act as emitters, and in their presence an additional heat flow is generated by radiative exchange. Since the energy for this heat transport is extracted from the direct environment, a *negative* GHE occurs (see Section 4.4), which cools the air and simultaneously increases the heat flow dissipated by radiation. If the GH-gases were pure absorbers, they could only increase the air temperature, what is not observed.

Heat transport by IR radiation requires that IR-active gases absorb energy through inelastic collisions with nitrogen and oxygen molecules at the expense of the kinetic energy of their surroundings and release this energy as IR radiation, thus enabling continuous emission (Harde, 2013 [5]).

However, the experimental detection of gas radiation in the laboratory is anything but simple (see also: Schnell & Harde, 2025 [6]), as a gas can't simply be placed in an empty space; this always requires a container to enclose the gas. Despite the use of inner walls with a particularly low emissivity $\varepsilon$, such containers (hereafter referred to as cylinders) emit IR radiation that is sometimes significantly more intense than the gases, which can only be detected on a higher background. Therefore, only that fraction of the gas radiation can be measured, which has a higher intensity at a specific wavelength than the background radiation of the container. Like an iceberg, only a portion of the gas radiation is visible due to this superposition.

This issue requires some preparatory studies of the set-up before investigating the GH-gases:

1. A calibration of the radiation sensors to quantify the outgoing heat flux.
2. Blind tests, which demonstrate that short-term temperature fluctuations during the addition of gases have no influence on the final temperatures and heat flows.
3. Control tests with the IR-inactive noble gases argon and helium to exclude heat conduction as a cause of a possible additional heat flux.
4. Detection and quantification of the background radiation and losses.

Only with these preparatory steps can it be ensured that the experiments demonstrate the physical principles of gas radiation. Of course, these are not experiments on a planetary scale, but rather a fundamental proof that GH-gases can convert the heat of their surroundings into IR radiation even at normal pressure, and thus that they significantly influence the heat flows in the atmosphere through upward or downward radiation.

## 2. Experimental Set-Up

### *2.1 General Concept*

The core of the experimental setup consists of a vertically positioned, heated aluminum cylinder, enclosed at the top by a dome and at the bottom by a Polyethylene (PE) foil. Below the cylinder, a separate energy sink in form of a cooled plate $P_C$ is located. It is equipped with radiation detectors

$D_T$ and $D_P$ (Figs. 1 and 2). The cylinder and $P_C$ plate are not rigidly connected, allowing calibration of the radiation detectors with a heat source.

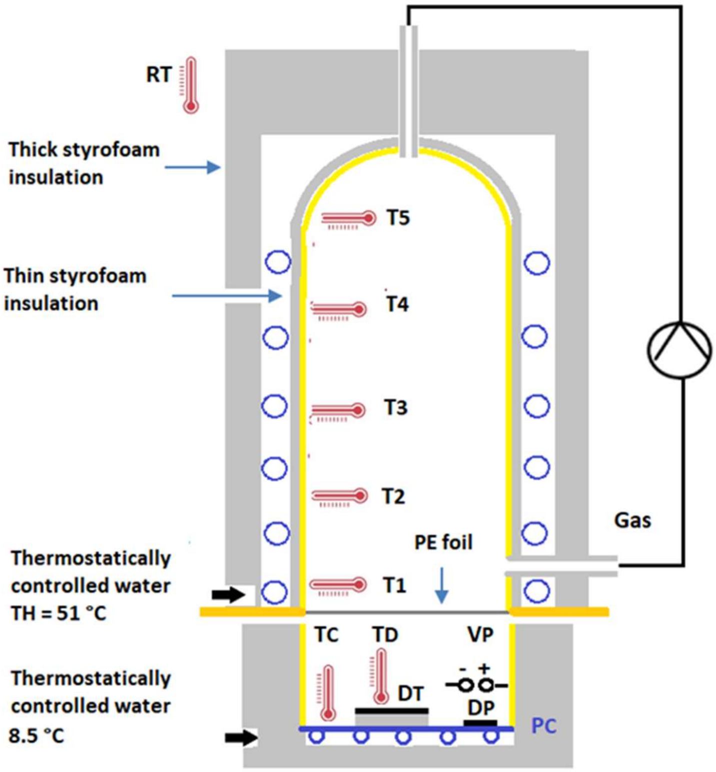

Fig. 1: Schematic experimental setup.

The interior surfaces of the cylinder and dome are highly polished to minimize their IR emissions. Temperature sensors at various distances from the PE foil measure the cylinder temperatures $T_1$ - $T_5$ , which are recorded by data lockers.

To uniformly heat the aluminum cylinder, water at a constant temperature of $T_H = 51°C$ is passed through a PVC hose that wraps around the cylinder along its entire length (Fig. 2a). A 2 mm thick insulating tape is placed between the hose and the cylinder, which plays an important role in detecting gas radiation. As a result, the cylinder temperatures $T_1 – T_5$ are significantly lower than the water temperature $T_H$ . This cooling effect depends on the heat losses to the $P_C$ plate and is thus an indicator of the intensity of this heat flow (see also Table 1 and Fig. 5).

The vertical positioning of the cylinder ensures a stable air stratification, eliminating convection as a means of heat transfer. Heat conduction losses to the $P_C$ plate are minimized because stagnant air is a very poor conductor of heat, and the cylinder is separated from the cooled $P_C$ plate with its detectors by the PE foil. At the same time, this foil is highly transparent for IR radiation in the spectral range of interest and, together with the radiation detectors $D_T$ and $D_P$, ensures detection of the IR radiation emitted by the gas and the cylinder walls.

The detector $D_T$ consists of a small, blackened disc, whose temperature $T_D$ is measured, and which is glued to an 8 mm thick insulating layer in the middle of the $P_C$ plate; parallel as detector $D_P$ is the voltage $V_P$ of 10 (mini) Peltier elements recorded, which are fixed on the $P_C$ plate and are electrically connected in series (Fig. 2c).

Underneath the $P_C$ plate is a copper coil embedded in concrete, which dissipates the transferred heat by flowing water at a constant temperature of 8.5°C.

Test gases can be poured in through two openings, one in the dome and one at the bottom of the cylinder. To ensure loss-free filling, the light gases methane and helium are metered into the upper opening and all other gases into the lower opening. A pump is then used to circulate the gas mixture for 15 minutes to achieve a homogeneous mixture.

Since water vapor is a strong GH-gas that can influence the measurement, the water vapor concentration in the cylinder is reduced to a minimum with a desiccant before the test gases are added.

*Fig. 2: Left: Gas cylinder with insulating wallpaper and PVC hose for heating with 51°C warm water, before the external thermal insulation was applied. Top right: View into the interior of the gas cylinder with the PE foil clamped between two wooden panels as the lower end. Bottom right: The blackened* $P_C$ *plate beneath the gas cylinder with the thermal radiation sensors* $D_T$ *and* $D_P$*, thermally insulated by a Styrofoam block with a mirrored aluminum inner wall.*

## *2.2 Calibration of Radiation Detectors*

The detectors $D_T$ and $D_P$ measure the IR radiation emitted by the cylinder through a temperature or voltage increase. To derive the radiation output in Watts from these values, the detectors are calibrated using a defined heat emission. Heat conduction plays only a minor role here (see subsection 3.3).

For this purpose, the cylinder above the radiation detector is replaced by a Styrofoam block containing an electrically heated plate $P_W$. Like the cylinder, it is separated from the radiation detector by a PE Foil (Fig. 3). The radiation detector itself remains unchanged.

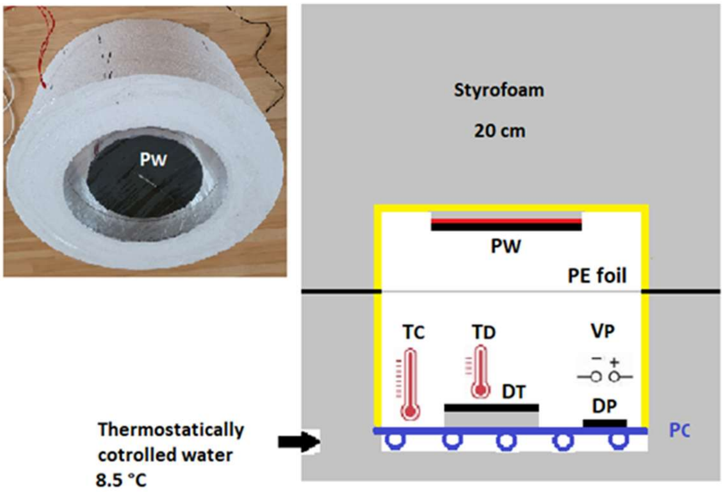

*Fig. 3: Calibration of the radiation detectors* $D_T$ *and* $D_P$*. Left: Styrofoam block with heating plate and PE foil. Right: Schematic experimental setup.*

When gradually increasing the heating for plate $P_W$, the respective temperature $T_D$ and voltage $V_P$ of the sensors are measured. They are established within 1 hour of constant heating per heating stage (Appendix, Table A3). Fig. 4 shows the strictly linear relationship between power and the measured temperature $T_D$ or voltage $V_P$. Since the detectors are separated from the heating plate by the PE foil, they measure almost exclusively the IR radiation emitted by the plate (see Subsection 3.3).

With reference to the cylinder's radiation cross-section of $A = 0.0855$ m², the received radiation intensity is specified in W/m². This is important for further analysis to compare the measurements with the theoretically expected intensities. For the temperature sensor, the relationship is:

$$I_T(T_D) = (0.935 \cdot T_D - 8.512)/A \ \ [\mathrm{W/m^2}] \ , \qquad (1a)$$

for the Peltier elements:

$$I_P(V_P) = (5.069 \cdot V_P - 2.283)/A \ \ [\mathrm{W/m^2}] \ . \qquad (1b)$$

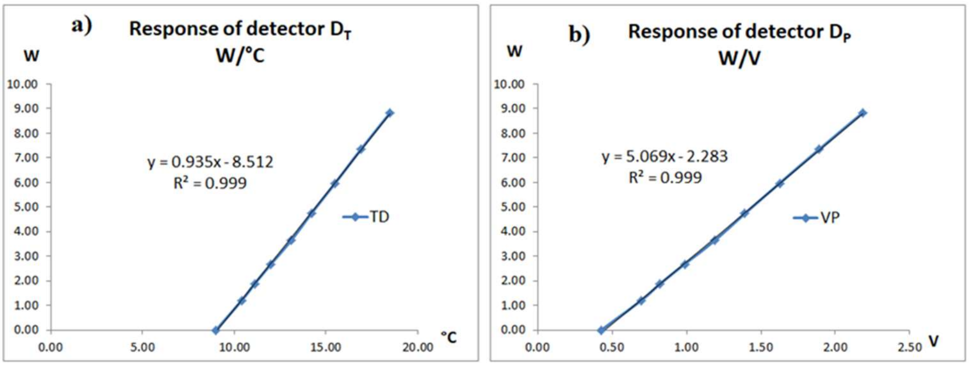

*Fig. 4: Correlation of a) temperature $T_D$ and radiant power $I_T$ , b) voltage $V_P$ and radiant power $I_P$.*

When measuring the gas- and superimposed background-radiation, a slight difference of about 5% is observed between the detectors when converting the measured temperature or voltage into corresponding intensities according to (1a) and (1b). For the further data analysis and the comparison with theory, the average value $I_{av}$ of both measurements is considered. At the same time, this reduces minor fluctuations between individual values.

## 3. Preliminary Tests

### *3.1 Measurement with Test Gases*

Filling the cylinder with a test gas and subsequent circulation (homogenization) leads to a brief cooling of the inside air and appears as a stronger dip in the $T_1$ temperature curve (Fig. 5). This raises the question, how far the lower temperature of the freshly added test gases can influence the measurements of the cylinder temperatures $T_1 - T_5$. Preliminary tests with dried air as test gas demonstrate that these mechanical interventions do not affect the long-term measurements. All temperature differences $\Delta T$ before and after pouring in air, are zero or close to zero (Table 1), if the system is allowed approximately 40 minutes to return to thermal equilibrium. The measurement phases over 60 minutes before and after adding the sample gases reduce smaller temperature fluctuations and give reliable average values.

Also the background intensity $I_0$ from the cylinder walls, as registered by the detectors $D_T$ and $D_P$, are only minimally influenced by this filling and pumping procedure (see Table 1 and Fig. 5b).

Table 1: Preliminary test with dried air ($H_2O$ ~ 0.15 vol.%).

| Dry Air | $T_W$ °C | $T_C$ °C | $T_5$ °C | $T_4$ °C | $T_3$ °C | $T_2$ °C | $T_1$ °C | $T_D$ °C | $V_P$ V | $I_0$ W/m² |
|---|---|---|---|---|---|---|---|---|---|---|
| Final values | 51.0 | 10.0 | 44.3 | 44.2 | 43.8 | 43.9 | 41.5 | 16.2 | 1.82 | 79.5 |
| $\Delta T_D / \Delta V_P / \Delta I$ | 0.0 | 0.0 | 0.0 | 0.0 | 0.0 | 0.0 | 0.0 | 0.0 | 0.01 | 0.5 |

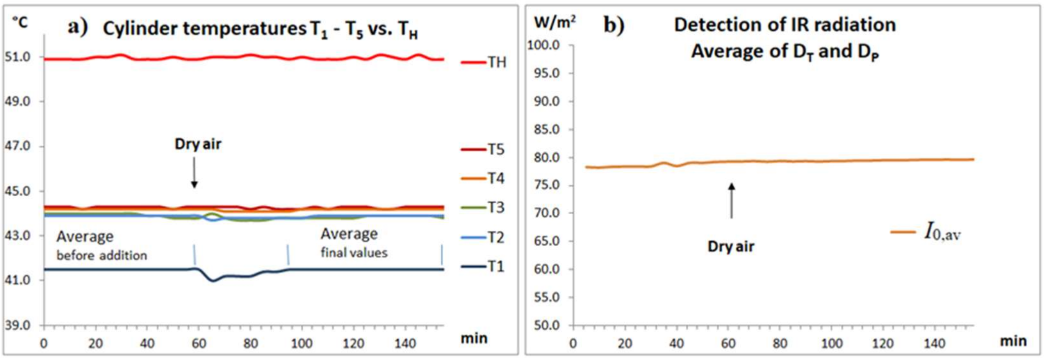

*Fig. 5: Preliminary test with dried air, a) water temperature $T_H$ and temperatures $T_1$ – $T_5$ in the cylinder, b) background radiation $I_{0,av}$ as average of the detectors $D_T$ and $D_P$ at $H_2O$ ~ 0.15 vol.%.*

## *3.2 Control Tests with Argon and Helium*

Since the specific thermal conductivity of the air in the cylinder changes after adding a GH-gas, it is necessary to check whether the *internal* thermal conductivity $\lambda_{gas}$ influences the measured values. Note, this refers to heat flows within the cylinder up to the final PE foil. *External* heat conduction refers to heat from the PE foil to the $P_C$ plate (Subsection 3.3).

Control experiments with the IR-inactive noble gases argon ($\lambda_{Ar}$ = 0.01772 W/m/K) and helium ($\lambda_{He}$ = 0.1513 W/m/K), which have significantly different values than air ( $\lambda_{air}$ = 0.0262 W/m/K), show no observable changes in temperatures or background radiation (Table 2, Fig. 6). This refutes another potential objection that the radiation of the GH-gases could be caused by heat conduction effects inside the cylinder.

Table 2: Effects of argon and helium, each 8 vol.%, $H_2O$ ~ 0.15 vol.%.

| Noble gas | $\Delta T_W$ °C | $\Delta T_C$ °C | $\Delta T_5$ °C | $\Delta T_4$ °C | $\Delta T_3$ °C | $\Delta T_2$ °C | $\Delta T_1$ °C | $\Delta T_D$ °C | $\Delta V_P$ V | $\Delta I_{0,av}$ W/m² |
|---|---|---|---|---|---|---|---|---|---|---|
| Argon | 0.0 | 0.0 | 0.0 | 0.0 | 0.0 | -0.1 | -0.1 | 0.0 | 0.0 | 1.2 |
| Helium | 0.1 | 0.0 | 0.2 | 0.1 | 0.2 | 0.1 | 0.0 | 0.0 | 0.0 | 0.4 |

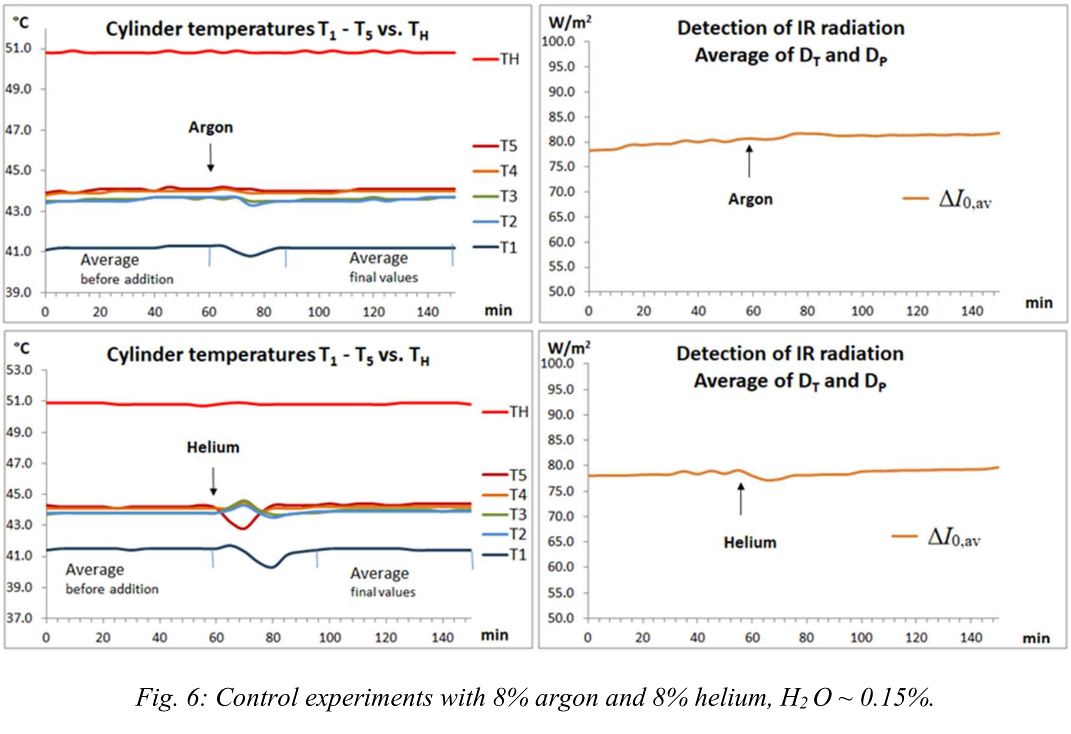

*Fig. 6: Control experiments with 8% argon and 8% helium, $H_2O$ ~ 0.15%.*

### 3.3 Background Radiation of the Cylinder

The cylinder is made of polished aluminum, which with an emissivity of $\varepsilon = 5\%$ would suggest a low-emission surface. However, this is too short-sighted, since the cylinder as a cavity radiator with efficient multiple reflections and an inner surface of more than 10 times the size of the exit surface to the sensors, emits a significantly higher intensity than a flat plate made of the same material and with the cross-section of the cylinder. This can be demonstrated by continuously heating the cylinder. When the water temperature $T_H$ increases, the difference to the cylinder temperatures $T_1 - T_5$ increases, which is caused by a rising radiation loss to the plate $P_C$ and observed as increasing intensity at the detectors $D_T$ and $D_P$ (Fig. 7).

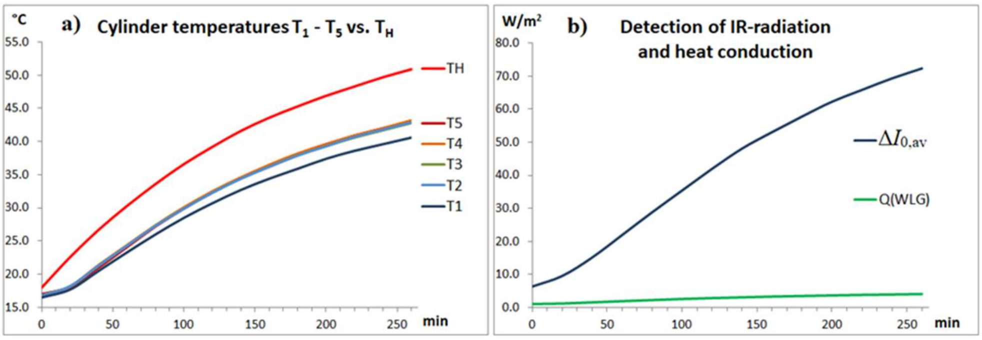

*Fig. 7: a) Increase of the temperatures $T_1 - T_5$ with increasing jacket heating $T_H$, b) detection of the background radiation $I_0$ of the cylinder with increasing temperature, and calculation of the mechanical heat conduction $Q_{WLG}$ to the $P_C$ plate, $H_2O$ ~ 0.15%.*

This radiation is 2 to 10 times higher than that observed when GH-gases are added (Section 4), indicating a considerable background radiation.

A significantly smaller fraction (around 6%) of heat losses is caused by heat conduction between the cylinder and the $P_C$ plate (outside), which are separated by 15 cm (Fig. 7b, green graph). For calculating the heat conduction, the thermal conductivity $\lambda_{air} = 0.0262$ W/m/K and an area $A = 0.0855$ m$^2$ are used. As temperature difference from the adjacent $T_1$ measuring point to the cooled plate $P_C$ with $\Delta T = T_1 - T_C$ a distance of $L = 0.2$ m is assumed. Additional thermal insulation provided by the very thin PE film can be neglected.

Stagnant air is a very poor conductor of heat. These studies demonstrate once again how important it is to use a vertically arranged cylinder and to avoid convection that inevitably occurs with a horizontal arrangement (see Part I [6]).

This is different when a GH-gas is added. In this case, no mechanical heat conduction can contribute to the external heat flow, since cylinder temperatures are not increasing but are actually decreasing slightly. This means when a GH-gas is added, external mechanical heat conduction per se cannot raise the outgoing flux. In other words: the intensity $I_0$ before adding the test gases, still may contain a small portion of mechanical conduction, while the additional heat flux of the GH-gases $I_{Gas}$ is exclusively the result of the radiative transfer (Fig. 17 and following).

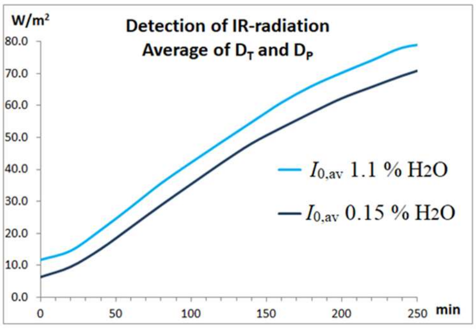

*Fig. 8: Background radiation $I_{0,av}$ measured by the detectors $D_T$ and $D_P$ with increasing jacket heating $T_H$ for two water vapor concentrations of 1.1 and ~ 0.15%.*

The background radiation also depends on the humidity of the cylinder air. Fig. 8 shows a comparison of the measured intensity $I_{0,av}$ of the sensors $D_T$ and $D_P$ for two different water vapor contents of ~ 0.15 and 1.1% while continuously heating the cylinder jacket.

## 4. Some Theoretical Aspects

### 4.1. Spectral Properties of Greenhouse Gases

Unlike nitrogen, oxygen or the noble gases, GH-gases can absorb and re-emit radiation in the mid- and long-wave IR spectral range. This spectral range of so-called thermal radiation extends on a wavelength scale $\lambda$ from approximately 4 µm to the cm range, or in reciprocal wavelengths[1] over a range of 1 to 2500 $cm^{-1}$.

Within this spectral interval, the main GH-gases in the atmosphere, such as water vapor (WV-$H_2O$), carbon dioxide ($CO_2$), methane ($CH_4$), nitrous oxide ($N_2O$), and ozone ($O_3$), have a total of 722,000 spectral lines, many of them very weak in intensity, but over the long propagation paths in the atmosphere they also contribute to a significant interaction with radiation. The strength of this radiative interaction on a line is defined by the effective cross section—or as integral over the line profile of such a spectral line—by the spectral line intensity (see, e.g., Harde 2013 [5], Subsection 2.2.2). Fig. 9 provides an overview over the line intensities of $H_2O$, $CO_2$, $CH_4$ and $N_2O$ according to the HITRAN database [1].

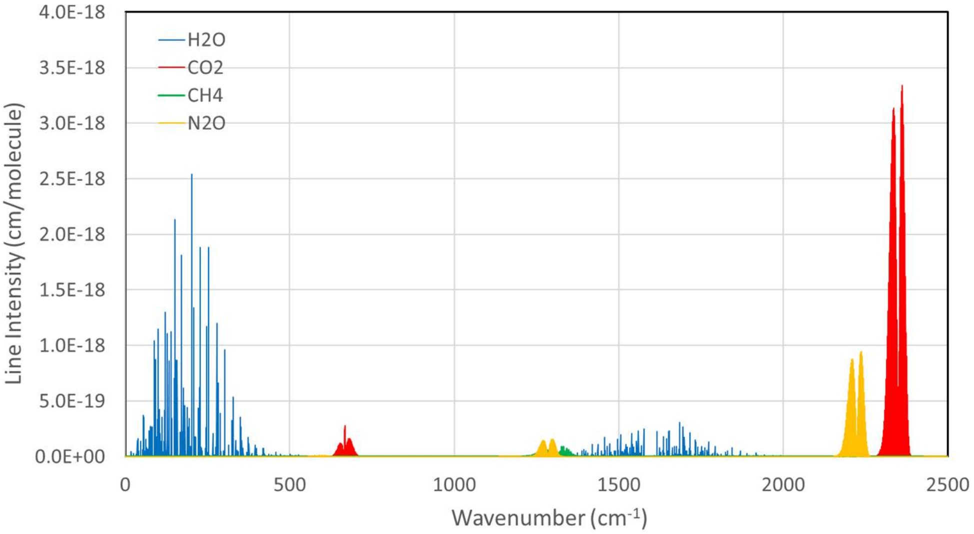

*Fig. 9: Spectral line intensities of the greenhouse gases water vapor, $CO_2$, $CH_4$ and $N_2O$ over the spectral range of 0 - 2500 $cm^{-1}$. This corresponds to a wavelength range of ∞ - 4 µm. The values apply to a gas temperature of T = 44°C.*

Tetrafluoroethane ($CFH_2CF_3$), also known as HFC-134a or Freon 134a, is not available as a 'line-by-line' dataset in the HITRAN database, but the absorption cross section is listed for specific spectral ranges, temperatures and ambient pressures (Harrison 2016 [7]). Freon has been used as an efficient coolant for many years, but according to an EU regulation, its use is to be gradually phased out by 2030 due to its high global warming potential.

For our investigations the very high IR activity is particularly well suited for demonstrating the GHE. Fig. 10 shows the absorption cross section of the particularly dominant spectral bands between 800 and 1500 $cm^{-1}$ for the relevant spectral range. Because the spectrum consists of a multitude of closely spaced lines, it is virtually impossible to derive spectroscopic line parameters for

---

[1] Instead representing spectra in wavelength units, it is very common in spectroscopy to use reciprocal wavelengths $\tilde{\nu} = 1/\lambda$ in units of $cm^{-1}$. This corresponds to a frequency scale $\nu = c/\lambda$, divided by the speed of light $c$, and is expressed as wavenumbers per cm.

it and to perform comparable simulations of the absorption-emission spectra as for the other gases. Therefore, the following discussion on Freon is limited to a qualitative comparison of the measurements with the other gases.

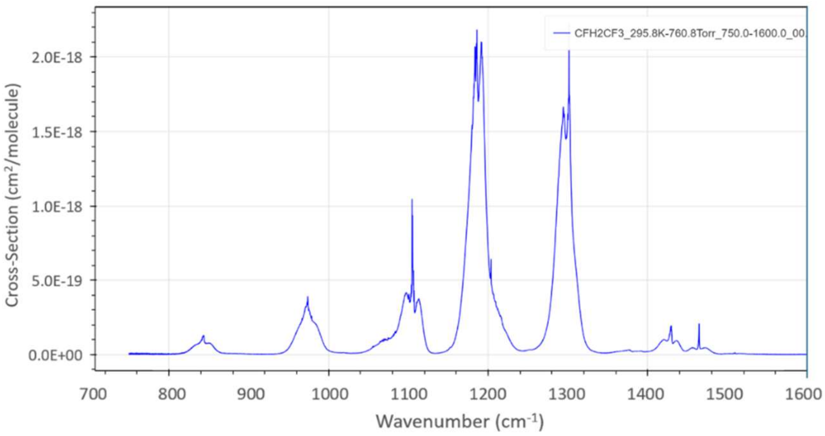

*Fig. 10: IR absorption cross section of tetrafluoroethane ($CFH_2 CF_3$) at 296 K and 1014 hPa in air (Harrison 2016 [7]).*

## *4.2 Emissions of Greenhouse Gases*

The actual maximum absorption and emission at the molecular bands is determined not only by the line intensities or cross sections but essentially depends also on the thermal excitation by collision according to a Boltzmann distribution (see Harde 2013 [5], Subsection 2.3). For the GH-gases, displayed in Fig. 9, the spectral intensities (not to be confused with the line intensities) are shown in Fig. 11, each calculated for a gas concentration of 2% in air, a total pressure of $p = 1013$ hPa, a gas temperature of $T_G = 44°C$, and a temperature gradient from the dome to the PE foil of 0.047°C/cm.

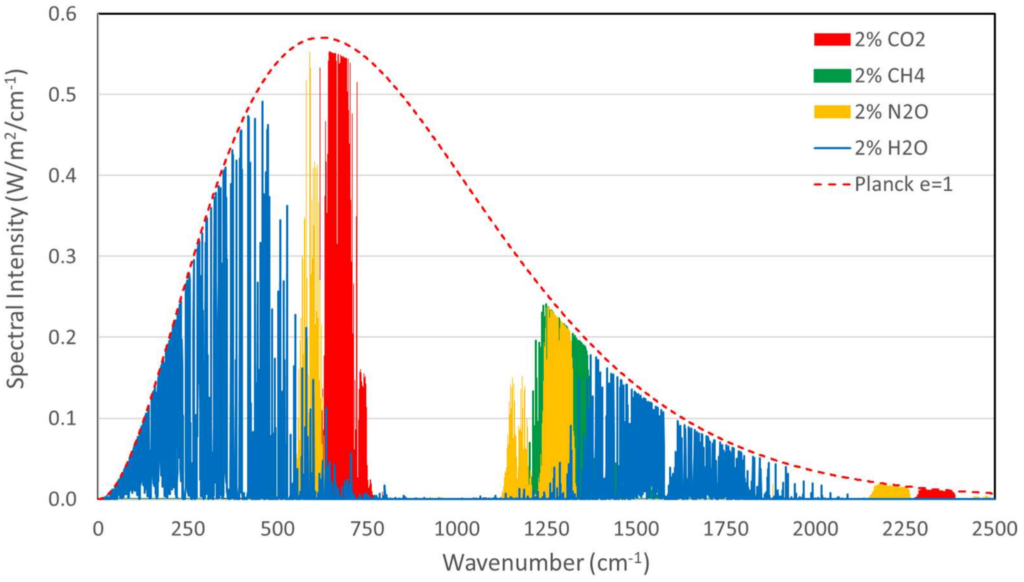

*Fig. 11: Emission spectra of WV, $CO_2$, $CH_4$ and $N_2O$ each for concentrations of 2% in air at a gas temperature $T_G = 44°C$ and a pressure of 1013 hPa.*

Due to the reduced thermal excitation of higher lying molecular states the significantly stronger spectral band of $CO_2$ (red) around 2300 $cm^{-1}$ (see also Fig. 9) plays a subordinate role with a contribution of only 1.3 $W/m^2$ compared to a total emission for $CO_2$ of 28.8 $W/m^2$. On the other hand the bending mode with attached rotation lines around 670 $cm^{-1}$ practically coincides with the maximum of a Planckian radiator at 44°C (red dotted line), and thus, mainly determines the

$CO_2$ GHE. The small intensity difference of the $CO_2$ band to the blackbody distribution is the result of a radiative transfer calculation with a temperature gradient across the cylinder (lapse rate) of $\lambda_R = 0.047$°C/cm.

It is also clearly visible, not $CO_2$ but WV (blue) is the dominating GH-gas with a total emission of 42.2 $W/m^2$, which covers larger parts of the other gases. This is already evident under the conditions prevailing here, with the same concentrations for all gases. In the atmosphere, with a WV concentration 30–40 times that of $CO_2$ and a significantly larger superposition, this results in a substantially reduced impact of the other gases.

$N_2O$ (orange), with an emission of 29.2 $W/m^2$, is additionally masked by $CH_4$ (green) with 11.1 $W/m^2$, and the strongest band of $N_2O$ around 2250 $cm^{-1}$ has hardly any influence on the total emission.

While the individual contributions of the gases add up to a total intensity of 111.3 $W/m^2$, this intensity is reduced by 32% to 75.8 $W/m^2$ due to the spectral superposition and an increased saturation on the bands.

### *4.3 Background Radiation and Transmission Losses*

The greater challenge in measuring the respective emitted intensities of a gas undoubtedly lies in separating this component from the higher background caused by the radiation from the cylinder walls. As already explained in Section 3.3, the inner surface of the cylinder, which stores the gases, is good 10 times larger than the cross-sectional area to the sensors. Therefore, despite a very low emissivity of the walls of only approximately 5%, due to efficient multiple reflection, the cylinder acts like a cavity radiator, emitting a significantly higher radiation intensity than a flat plate made of the same material (see also cavity radiator, e.g., Atkins & Friedman 2011[8]).

For our further analysis and comparison with the measurements, a Planckian radiator with an effective emissivity $\varepsilon_{eff}$ of 42% is used as the background. In addition, radiation emerging from the cylinder acts as a volume radiator with the sensors only detecting a limited aperture angle compared to the heat plate $P_W$ used for calibration. In our calculations this is incorporated by a loss factor $V_\Omega$.

Further slight losses are caused by reflection at the front and back side of the PE foil, and also by selective absorption bands of polyethylene. Figure 12 shows the transmission of a PE foil measured with a Fourier spectrometer over the relevant spectral range (Asgari et al. 2014 [9]).

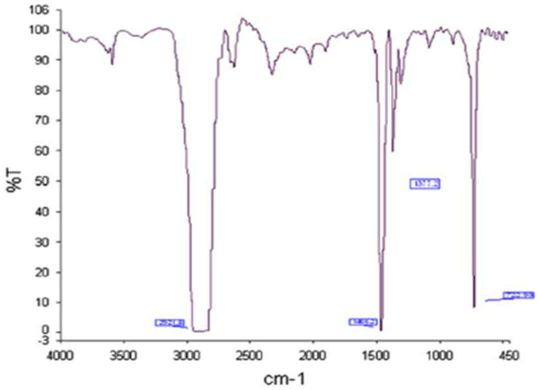

*Fig. 12: Fourier transmission spectrum of a PE foil (see Asgari et al. 2014 [9] ). The wavenumber scale runs from right to left.*

The CH-bending vibration around 690–900 $cm^{-1}$ (at the right side) with the center at 722.9 $cm^{-1}$ partially overlaps with the emission range of $CO_2$. For the further calculations, we use a wavenumber-dependent transmission

$$T(\tilde{\nu}) = V_\Omega \cdot \tau_0 \left[1 - \sum\nolimits_1^3 n_i \frac{(d\tilde{\nu}/2)^2}{(\tilde{\nu} - \tilde{\nu}_i)^2 + (d\tilde{\nu}/2)^2}\right] \tag{2}$$

with a Lorentz profile around the absorption centers $\tilde{\nu}_1 = 722.9$ cm$^{-1}$, $\tilde{\nu}_2 = 1377.2$ cm$^{-1}$ and $\tilde{\nu}_3 = 1456.2$ cm$^{-1}$ (Fig. 13). The transmission factor $\tau_0$ with 0.9 takes into account the reflections at the foil. The line widths are chosen uniformly for all absorptions with $d\tilde{\nu} = 30$ cm$^{-1}$, while the absorption depths are determined by the amplitudes $n_i$ and vary between 40 and 98%. With $V_\Omega = 0.4$, the total transmission is shown in Fig. 13.

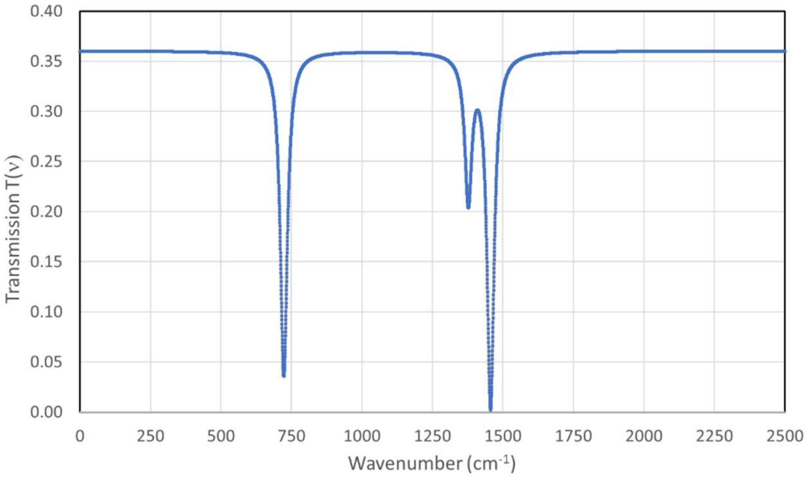

*Fig. 13: Total spectral transmission through the PE foil and limited aperture of the detectors.*

For example, with $CO_2$ at a concentration of 2% and an effective emissivity of the cylinder with $\varepsilon_{eff} = 42\%$, this results in an expected spectral intensity at the detectors, as shown in Fig. 14. A residual humidity (blue) of 1% is also considered. The actual $CO_2$ emission (red) with 28.8 W/m$^2$ (see Fig. 11) contributes only 5.3 W/m$^2$ compared to the wall emission (grey) and water vapor, together with 90.3 W/m$^2$. This is not more than 5.5% of the total intensity with 95.6 W/m$^2$. These calculations show that with a laboratory experiment, similar to an iceberg, we can basically only measure the tip of the gas radiation.

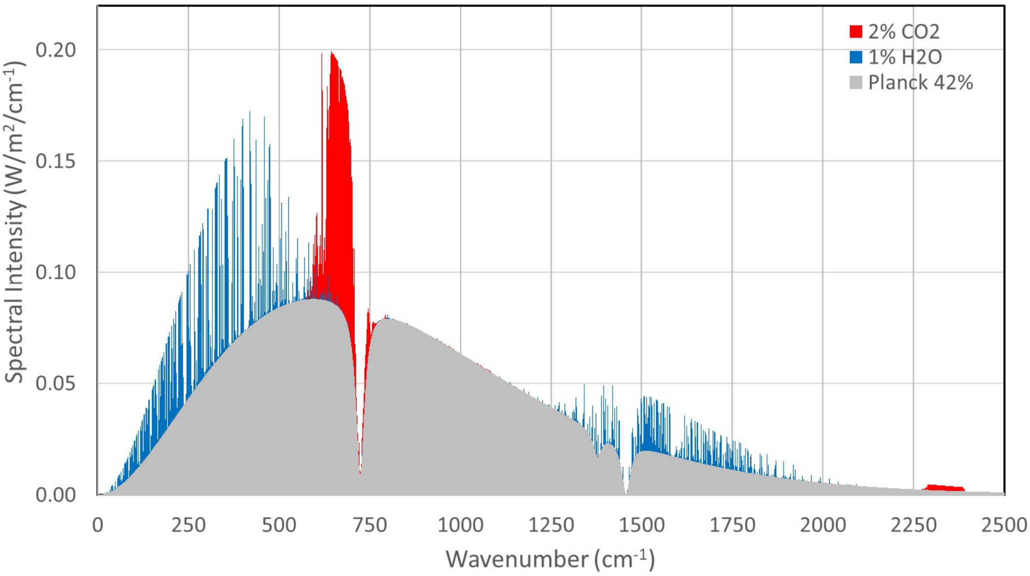

*Fig. 14: Spectral intensity as a function of wavenumber for 2% $CO_2$, 1% $H_2O$, L=70 cm, $\lambda_R = 0.047$ °C/cm, $\varepsilon_{eff} = 42\%$ and $V_\Omega = 0.4$ at a total intensity of 95.6 W/m$^2$.*

## 4.4 The Negative Greenhouse Effect

If the radiation emitted by a warmer gas layer leads to a cooling of this layer, because IR-active gases are excited through collision processes and the required emission energy is extracted from the kinetic energy of the gas, we can already speak of this process in a simplified manner as a negative GHE. However, more general and fundamental is to refer to the definition of the GHE.

According to Thomas & Stamnes (1999) [10] and in accordance with the current IPCC assessment report, AR6 [11], the difference in the intensities on the one hand emitted from the Earth's surface and on the other hand radiated at TOA to space, is defined as the atmospheric GHE.

With Stefan-Boltzmann, then the intensity emitted by a surface element of the Earth is

$$F_\mathrm{s} = \varepsilon_\mathrm{s}\,\sigma\,T_\mathrm{s}^4, \tag{3}$$

with $\varepsilon_\mathrm{s}$ as the emissivity, $\sigma$ as the Stefan-Boltzmann constant and $T_\mathrm{S}$ as the temperature of this surface. The radiative forcing at TOA can be derived from a simplified two-layer model as:

$$F_\mathrm{TOA} = \varepsilon_\mathrm{s}\,(1-\alpha_\mathrm{A})\,\sigma\,T_\mathrm{s}^4 + \varepsilon_\mathrm{A}\,\sigma\,T_\mathrm{A}^4 = \varepsilon_\mathrm{s}\,\sigma\,T_\mathrm{s}^4 - \varepsilon_\mathrm{A}\,\sigma\,(\varepsilon_\mathrm{s}\,T_\mathrm{s}^4 - T_\mathrm{A}^4)\,, \tag{4}$$

with an atmospheric temperature $T_\mathrm{A}$ and an atmospheric absorptivity $\alpha_\mathrm{A}$ equal to the atmospheric emissivity $\varepsilon_\mathrm{A}$. This gives for the GHE:

$$\mathrm{GHE} = \varepsilon_\mathrm{A}\,\sigma\,(\varepsilon_\mathrm{s}\,T_\mathrm{s}^4 - T_\mathrm{A}^4). \tag{5}$$

The emissivity $\varepsilon_A$ includes all IR-active gases and depends on their concentration.

For $\left(\varepsilon_\mathrm{s}\,T_\mathrm{s}^4 - T_\mathrm{A}^4\right) < 0$, or for $\varepsilon_\mathrm{s} = 1$ and a colder surface than the atmosphere, the GHE becomes negative, and the Earth loses more energy to space with GH-gases than without, at least locally.

Also with a continuous temperature increase from ground to higher altitudes–thus a negative lapse rate (the regular lapse rate over the troposphere is normally given as +6.5°C/km)–the same applies with a higher emission to space than radiation from the Earth is absorbed by the atmosphere (see also: Schmithüsen et al., 2015 [12]; van Wijngaarden & Happer, 2025 [13]).

In the set-up presented here, the cylinder walls on the one hand serve to transfer kinetic energy to the gas via mechanical heat conduction, which in the real atmosphere is caused by air currents, e.g., from equatorial zones to the poles. On the other hand, they emit the background radiation comparable to the long-wave radiation emitted by the Earth's surface. Although the walls have the highest temperature, their emitted intensity with an emissivity $\varepsilon \approx 5\%$ and an effective emissivity $\varepsilon_\mathrm{eff} = 42\%$ (see Subsec. 4.3) is weaker than the radiation emitted by the gas on the emission bands. Substituting $\varepsilon_\mathrm{s}$ by $\varepsilon_\mathrm{eff}$ in (5) and with $T_\mathrm{S}$ and $T_\mathrm{A}$ now representing the wall and gas temperature in the cylinder, this corresponds to conditions similar to those for a negative GHE, where the gas absorbs less background radiation than it emits.

The additionally emitted energy of the IR-active molecules is drawn from the thermal energy of the gas and, while the heating power remains constant, leads to a changed temperature distribution and reduction across the cylinder with slightly reduced wall temperatures and thus cooling.

## 5. Measurements and Calculations of Greenhouse Gas Emissions

This section summarizes the measurements and corresponding calculations for the radiation of the GH-gases water vapor, carbon dioxide, methane, nitrous oxide and Freon 134a. All investigations are performed under atmospheric pressure conditions, and additionally to the actual detection of IR radiation, the cooling of the gases due to their emission and their impact on the cylinder temperature are recorded.

The strongest cooling occurs at position $T_1$ and gradually decreases towards the dome. This cooling gradient determines the radiation transfer according to the Schwarzschild equation and the layer model (Schwarzschild 1906 [14], Harde 2013 [5]). The $T_1$ gas layer, which is only 5 cm away from the PE foil, can transmit its IR radiation almost unhindered to the $P_\mathrm{C}$ plate and the detectors. All more distant layers must transport the energy via absorption and remission, which hinders the radiation transfer through the lower gas layers. This effect is particularly evident for nitrous oxide and Freon, since these gases influence all five temperatures $T_1 - T_5$ (Subsections 5.4 and 5.5).

$T_\mathrm{D}$ and $V_\mathrm{P}$ are the temperatures and voltages measured by the radiation detectors before adding the GH-gases, and $\Delta T_D$ and $\Delta V_P$ are the changes caused by these gases. With equation (1) the respective data are expressed as intensities, and the fraction caused by the gases is given by the difference with and without GH-gases. However, the spectral superposition with the background radiation results in a significantly reduced signal component for the gas to be detected (see Subsection 4.3).

For control purposes, the heating temperature $\Delta T_H$ and the cooling temperature $\Delta T_C$ are also specified. $\Delta T_H = 0$ excludes that any cooling of the cylinder temperature is caused by the wall heating $T_H$. For the stronger GH-gases Freon 134a and $N_2O$ the cooling temperature $\Delta T_C$ shows a noticeable increase in the experiments, which can be attributed to an increase in gas radiation and can only be dissipated from the $P_C$ plate by a rising temperature. Such increase is a further indication of an ascending gas radiation.

### *5.1 Water Vapor*

Preliminary measurements with different air humidity already demonstrated the significant influence of WV on the background radiation (Fig. 8). Therefore, first measurements for three different air humidities are presented, and their influence on the other gases is considered in the following subsections.

If the gas cylinder is filled directly with humid air from the laboratory, this corresponds to a water vapor concentration of approximately 1.1%. However, the humidity can be changed within limits using the connected air circulation pump (Fig. 1). Either the air in the compartment passes a desiccant, which can reduce the WV concentration to a minimum of ~ 0.15%, or it is pumped through a water container, increasing the humidity to a maximum of 1.9%.

The measurements are listed in Table 3 and shown in Fig. 15. Despite the comparatively small concentration variation, significant changes with humidity are evident. While the temperatures $T_1$ and $T_2$ are slightly decreasing, the values for $T_D$ and $V_P$, and thus the mean total intensity $I_T$, are clearly increasing (Table 3, last column).

Table 3: Measurements with air of different humidity

| W-Vapor % | $T_W$ °C | $T_C$ °C | $T_5$ °C | $T_4$ °C | $T_3$ °C | $T_2$ °C | $T_1$ °C | $T_D$ °C | $V_P$ V | $I_T$ W/m² |
|---|---|---|---|---|---|---|---|---|---|---|
| 0.15 | 51.0 | 10.0 | 44.3 | 44.2 | 43.8 | 43.9 | 41.5 | 16.2 | 1.82 | 79.4 |
| 1.1 | 51.1 | 10.1 | 44.3 | 44.2 | 43.8 | 43.8 | 41.4 | 16.6 | 1.88 | 83.4 |
| 1.9 | 51.2 | 10.1 | 44.3 | 44.2 | 43.8 | 43.7 | 41.2 | 16.7 | 1.92 | 85.1 |

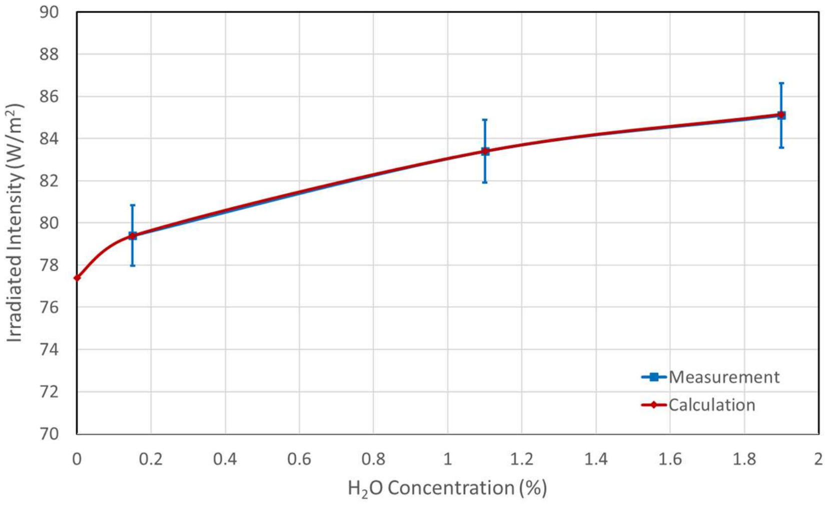

*Fig. 15: Measured mean intensity (Rectangles, blue) and calculated intensity (Diamonds, red) of water vapor emission as a function of concentration at a background radiation from the cylinder of 77.4 W/m² for* $\lambda_R = 0.043$ - $0.046$ °C/cm, $\varepsilon = 42\%$, $V_\Omega = 37.9$ %.

The measurements (blue squares) can well be reproduced by radiative transfer calculations (red diamonds), for the minimum WV concentration of 0.15% with a temperature gradient of $\lambda_R$ = 0.043 °C/cm, for the concentration of 1.9 vol.% with a value of 0.046 °C/cm due to the slightly increased temperature gradient. The emissivity of the background radiation is $\varepsilon_{eff}$ = 42% and the loss factor $V_\Omega$ = 37.9%.

The WV portion compared to the total signal is only 2.5% (2.0 $Wm^{-2}$ / 79.4 $Wm^{-2}$) for a concentration of 0.15% and increases to 9% (7.7 / 85.1) for a 1.9% WV fraction. In any case, this requires an extremely careful and sophisticated experimental technique, as can be achieved with the presented set-up.

Without the background, the WV emission would be 10.5 W/m² at a concentration of 0.15% and would reduce to 3.5 W/m² at the detectors. It increases to 41.3 W/m² at a concentration of 1.9% and is still 13.6 W/m² at the detectors (Fig. 16: WV - blue; Planck - dashed gray, $\varepsilon_{eff}$ = 42%).

The interaction of WV with other greenhouse gases is of particular interest from the perspective of the so-called *water vapor feedback*. The overlap and influence on the emission behavior of the other gases will therefore be considered in more detail in the following Subsections.

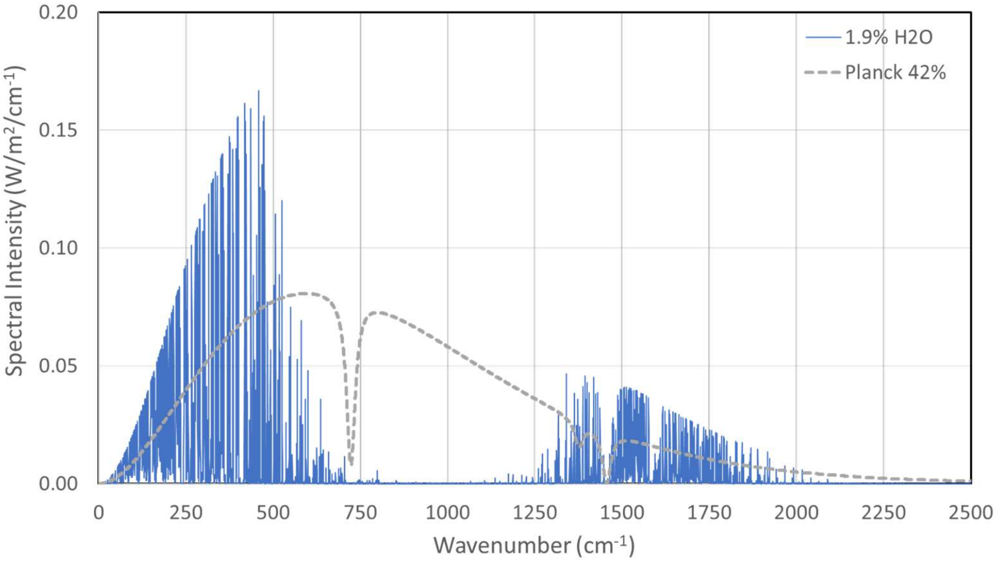

*Fig. 16: Calculated intensity for 1.9% WV (blue) at the detectors without background radiation from Planck radiators (grey for $\varepsilon_{eff}$ = 42%).*

## 5.2 $CO_2$ Measurements

$CO_2$ radiation is measured for three standard concentrations of 2, 4, and 8%. Addition of $CO_2$ leads to a significant cooling of the gas temperatures $T_1$ and $T_2$ with a simultaneous increase in the measured IR radiation intensity $I_{0,av}$ (Fig. 17).

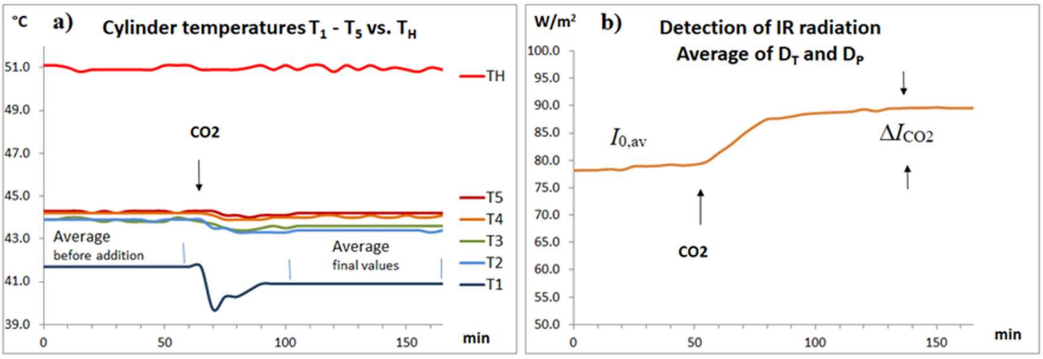

*Fig. 17: Effects of 8% $CO_2$. a) Decrease in cylinder temperatures, b) increase in IR radiation after adding $CO_2$ (WV concentration about 0.15%).*

These effects not only depend on the $CO_2$ concentration but are also determined by the respective WV concentration. Therefore, each of the $CO_2$ measurements is carried out for the three WV concentrations 0.15%, 1.1% and 1.9%. The temperature changes are listed in Table 4a, and the IR radiation detected by the sensors is displayed in Table 4b. Here, $I_{0,\mathrm{av}}$ is the mean background radiation before addition of $CO_2$ and $\Delta I_{CO2}$ is the change in intensity due to $CO_2$. The absolute fluctuations in $I_{0,\mathrm{av}}$ from measurement to measurement are on average less than 3% and have no noticeable influence on the difference measurements of $\Delta I_{CO2}$.

Table 4a: Influence of $CO_2$ and WV on the gas temperatures $T_1 - T_5$ .

| W-Vapor % | $\Delta T_H$ °C | $\Delta T_C$ °C | $\Delta T_5$ °C | $\Delta T_4$ °C | $\Delta T_3$ °C | $\Delta T_2$ °C | $\Delta T_1$ °C |
|---|---|---|---|---|---|---|---|
| **$CO_2$: 2%** | | | | | | | |
| 0.15 % $H_2O$ | 0.0 | 0.1 | -0.1 | -0.2 | -0.2 | -0.5 | -0.5 |
| 1.1 % $H_2O$ | 0.0 | 0.1 | -0.1 | -0.2 | -0.2 | -0.3 | -0.4 |
| 1.9 % $H_2O$ | 0.0 | 0.1 | -0.1 | -0.1 | -0.2 | -0.3 | -0.3 |
| **$CO_2$: 4%** | | | | | | | |
| 0.15 % $H_2O$ | 0.0 | 0.1 | -0.2 | -0.2 | -0.4 | -0.6 | -0.6 |
| 1.1 % $H_2O$ | 0.0 | 0.1 | -0.1 | -0.1 | -0.2 | -0.3 | -0.5 |
| 1.9 % $H_2O$ | 0.0 | 0.1 | -0.1 | -0.1 | -0.2 | -0.3 | -0.4 |
| **$CO_2$: 8%** | | | | | | | |
| 0.15 % $H_2O$ | 0.0 | 0.2 | -0.1 | -0.2 | -0.3 | -0.5 | -0.8 |
| 1.1 % $H_2O$ | 0.0 | 0.2 | -0.1 | -0.1 | -0.2 | -0.4 | -0.5 |
| 1.9 % $H_2O$ | 0.0 | 0.2 | 0.0 | -0.1 | -0.2 | -0.4 | -0.4 |

Table 4b: Measurement of the IR radiation at the sensors, $I_{0,\mathrm{av}}$ = background radiation before addition of $CO_2$, $\Delta I_{CO2}$ = change in intensity due to $CO_2$ radiation.

| W-Vapor % | $T_D$ °C | $\Delta T_D$ °C | $V_P$ V | $\Delta V_P$ V | $I_{0,\mathrm{av}}$ W/m $^2$ | $\Delta I_{CO2}$ W/m$^2$ |
|---|---|---|---|---|---|---|
| **$CO_2$: 2%** | | | | | | |
| 0.15 % $H_2O$ | 16.4 | 0.7 | 1.86 | 0.14 | 81.7 | 7.7 |
| 1.1 % $H_2O$ | 16.6 | 0.5 | 1.89 | 0.10 | 83.9 | 5.9 |
| 1.9 % $H_2O$ | 16.7 | 0.5 | 1.93 | 0.10 | 85.4 | 5.7 |
| **$CO_2$: 4%** | | | | | | |
| 0.15 % $H_2O$ | 16.2 | 0.8 | 1.82 | 0.15 | 79.4 | 8.8 |
| 1.1 % $H_2O$ | 16.5 | 0.7 | 1.88 | 0.12 | 82.9 | 7.3 |
| 1.9 % $H_2O$ | 16.6 | 0.6 | 1.91 | 0.12 | 84.6 | 6.5 |
| **$CO_2$: 8%** | | | | | | |
| 0.15 % $H_2O$ | 16.2 | 0.9 | 1.80 | 0.19 | 78.8 | 10.5 |
| 1.1 % $H_2O$ | 16.5 | 0.8 | 1.87 | 0.14 | 82.6 | 8.3 |
| 1.9 % $H_2O$ | 16.7 | 0.7 | 1.91 | 0.13 | 84.8 | 7.7 |

The measurements of the averaged total intensity are compared in Fig. 18 with the corresponding radiative transfer calculations for $CO_2$ and $H_20$. The background radiation is included according to Figs. 14 and 16. The measurements are indicated by squares with error bars of ±1.2% of the measured values, the corresponding calculations by diamonds and dashed lines. The data for the WV concentration of 0.15% are in blue, for 1.1% in green, and for 1.9% in magenta. For a better comparison of the data, the initial intensities $I_{0,\mathrm{av}}$ are uniformly related to the values listed in Table 3.

With increasing WV concentration, it is evident that not only the background radiation is continuously increasing, but simultaneously this leads to a further attenuation of the $CO_2$ radiation. This is particularly noticeable for the lower concentrations of WV and $CO_2$, as can be seen from the different gradients after adding $CO_2$. For example, an $H_2O$ concentration of 0.15% results in an increase of 7.7 W/m$^2$, whereas for 1.9% WV the intensity is only increasing by 5.7 W/m$^2$ (see Table 4b, last column). This is only 74% of the original intensity.

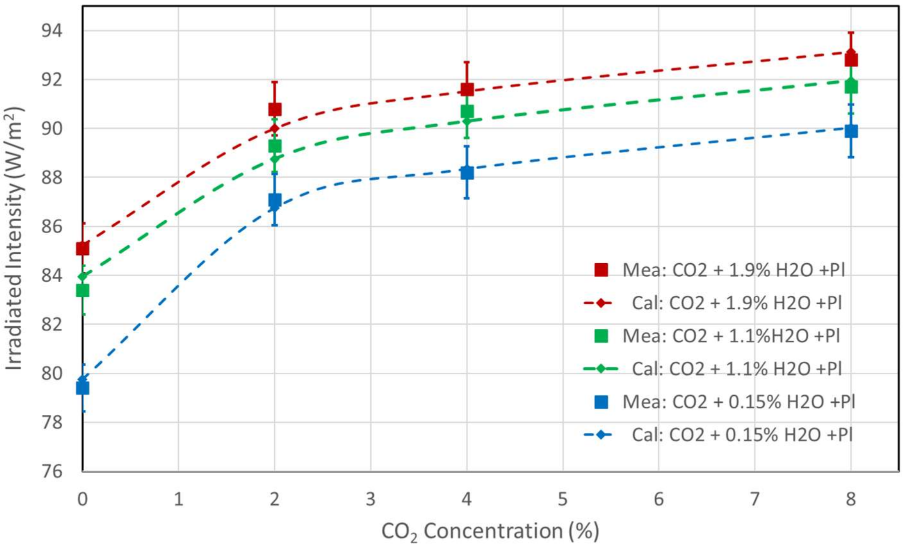

*Fig. 18: Measurements (Squares with error bars) and calculations (Diamonds, dashed line) for the IR radiation of $CO_2$ at different WV concentrations (0.15% blue, 1.1% green, 8% red) and background radiation by cylinder walls.*

The attenuation is mainly due to a further increase in the background and thus an increased saturation of the $CO_2$ line-wings. So, a calculation for 2% $CO_2$ alone – without background radiation of the cylinder walls – results in an emission of 28.8 W/m$^2$ and for 1.9% WV alone of 41.2 W/m$^2$, thus a total of 70 W/m$^2$, whereas also considering the overlap, the intensity is only 0.13 W/m$^2$ smaller. The only slight overlap of the spectra around 670 cm$^{-1}$ is obvious from Fig. 11 and also Fig. 14.

However, due to the long propagation paths in the atmosphere and the 30 – 40 times higher WV concentration, the weak overlap of the spectra leads to a significant limitation of the $CO_2$ climate sensitivity and also to a reduced WV-feedback (Harde 2014 [15], Harde 2017 [16]). For further detailed considerations of WV as the dominating GH-gas see also: Koutsoyiannis & Vournas 2024 [17] and Koutsoyiannis 2024 [18].

Also striking is the different increase in $CO_2$ radiation intensity at concentrations below and above 2%, which changes from an almost linear to a logarithmic curve and reflects the clear saturation of the absorption and emission processes of the vibration-rotation band around 670 cm$^{-1}$. For concentrations above 2%, the further increase in intensity is primarily determined by its unsaturated wings and weaker bands.

The kink with increasing intensity is observed for all GH-gases and is the reason why comparing $CO_2$ with GH-gases at very low concentrations, as done for the so-called greenhouse potential, is like comparing apples and pears.

### 5.3 Methane

Methane is classified as a particularly dangerous GH-gas with a global warming potential 25 times higher than $CO_2$. This classification arises from the low atmospheric methane concentration of approximately 2 ppm, at which the optical density is still very low compared to $CO_2$, and thus there is still considerable potential for an increase. But global warming potential can easily be confused with effectiveness. In fact, methane gas radiation has been measured to be less effective than $CO_2$ (Fig. 19).

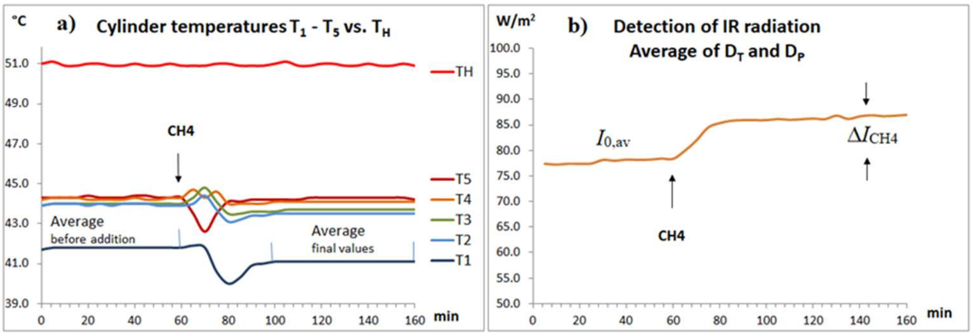

*Fig. 19: Effects of 8% methane, a) decrease in cylinder temperatures, b) increase in IR radiation after addition of $CH_4$, $H_2O$ ~ 0.15%.*

Tables 5a and b show the measurements of the gas temperature and $CH_4$ emission for the concentrations 2%, 4% and 8% at two WV concentrations.

Table 5a: Influence of $CH_4$ and WV on the gas temperatures $T_1 – T_5$ .

| W-Vapor % | $\Delta T_H$ °C | $\Delta T_C$ °C | $\Delta T_5$ °C | $\Delta T_4$ °C | $\Delta T_3$ °C | $\Delta T_2$ °C | $\Delta T_1$ °C |
|---|---|---|---|---|---|---|---|
| **$CH_4$ : 2 %** | | | | | | | |
| 0.15 % $H_2O$ | 0.0 | 0.1 | 0.0 | -0.1 | -0.1 | -0.4 | -0.5 |
| 1.1 % $H_2O$ | 0.0 | 0.1 | 0.0 | -0.1 | -0.1 | -0.2 | -0.2 |
| **$CH_4$ : 4 %** | | | | | | | |
| 0.15 % $H_2O$ | 0.0 | 0.1 | -0.1 | -0.2 | -0.3 | -0.4 | -0.5 |
| 1.1 % $H_2O$ | 0.0 | 0.1 | 0.0 | -0.1 | -0.2 | -0.3 | -0.4 |
| **$CH_4$ : 8 %** | | | | | | | |
| 0.15 % $H_2O$ | 0.0 | 0.2 | -0.1 | -0.1 | -0.3 | -0.5 | -0.7 |
| 1.1 % $H_2O$ | 0.0 | 0.1 | 0.0 | 0.0 | -0.2 | -0.3 | -0.6 |

Table 5b: Measurement of IR radiation at the sensors, before and after addition of $CH_4$.
$\Delta I_{CH4}$ = intensity change due to $CH_4$ radiation.

| W-Vapor % | $T_D$ °C | $\Delta T_D$ °C | $V_P$ V | $\Delta V_P$ V | $I_{0,av}$ W/m$^2$ | $\Delta I_{CH4}$ W/m$^2$ |
|---|---|---|---|---|---|---|
| **CH4 : 2 %** | | | | | | |
| 0.15 % $H_2O$ | 16.1 | 0.6 | 1,795 | 0.116 | 78.6 | 6.3 |
| 1.1 % $H_2O$ | 16.4 | 0.3 | 1,825 | 0.074 | 80.8 | 4.0 |
| **CH4 : 4 %** | | | | | | |
| 0.15 % $H_2O$ | 16.1 | 0.6 | 1,801 | 0.116 | 78.4 | 6.6 |
| 1.1 % $H_2O$ | 16.4 | 0.5 | 1,831 | 0.104 | 80.9 | 5.9 |
| **CH4 : 8 %** | | | | | | |
| 0.15 % $H_2O$ | 16.1 | 0.8 | 1,793 | 0.144 | 78.0 | 8.5 |
| 1.1 % $H_2O$ | 16.7 | 0.7 | 1,919 | 0.111 | 85.3 | 6.8 |

Methane is oxidized to $CO_2$ in the atmosphere under the influence of ozone and UV light and has a relatively short residence time of approximately nine years. An increase in the $CO_2$ concentration of 2 ppm within nine years does not appear very significant.

As with $CO_2$, methane radiation also depends on the WV concentration. Due to the increase in the background and partial overlap of the bands, this again attenuates the $CH_4$ signal. The greatest methane effect is achieved at a $H_2O$ concentration of 0.15% and is only 78% of the original effect at 1.1% WV (Table 5b).

Also for methane together with WV the measurements can very well be reproduced by the radiative transfer calculations (Fig. 20). The measurements are again indicated by squares with error bars, and the corresponding calculations by diamonds and dashed lines, for a WV concentration of 0.15% in blue, for 1.1% in green. The initial intensities $I_{0,\mathrm{av}}$ are consistently referenced to the values listed in Table 3.

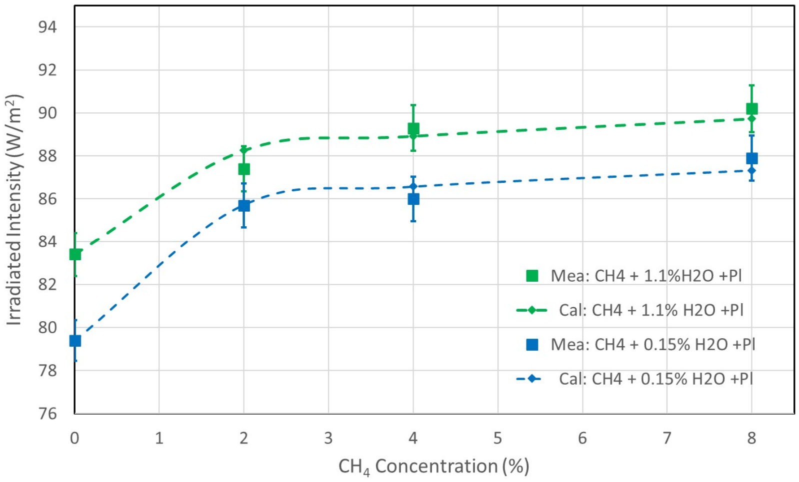

*Fig. 20: Measurements (squares with error bars) and calculations (diamonds, dashed line) of the IR radiation of $CH_4$ for two WV concentrations (0.15% blue, 1.1% green) and background radiation by cylinder walls.*

## *5.4 Nitrous Oxide*

Nitrous oxide ($N_2O$), the third most important long-lived greenhouse gas, is thought to contribute significantly to global warming due to its long atmospheric residence time and its approximately 300 times higher greenhouse potential relative to $CO_2$. In the radiation experiment, the effect of $N_2O$ is higher than that of $CO_2$, but only by a factor of 1.5 (see Fig. 21b compared to Fig. 17b).

As with $CO_2$ and $CH_4$, nitrous oxide radiation also depends on the WV concentration. The greatest effect is again achieved at an $H_2O$ concentration of 0.15% and is reduced to 86% of the original effect at 1.1% water vapor (Table 6b).

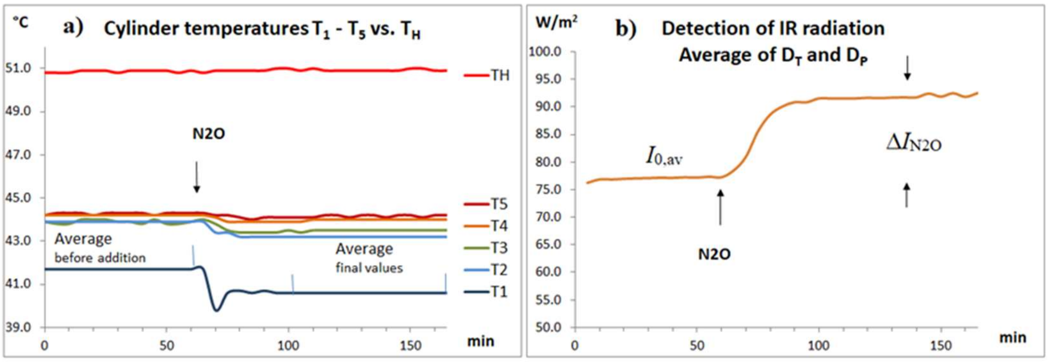

*Fig. 21: Effects of 8% nitrous oxide, a) decrease in cylinder temperatures, b) increase in IR radiation after addition of $N_2O$ at a WV concentration of 0.15%.*

Table 6a: Influence of $N_2O$ on the temperatures $T_1 - T_5$ .

| W-Vapor % | $\Delta T_H$ °C | $\Delta T_C$ °C | $\Delta T_5$ °C | $\Delta T_4$ °C | $\Delta T_3$ °C | $\Delta T_2$ °C | $\Delta T_1$ °C |
|---|---|---|---|---|---|---|---|
| **$N_2O$ : 2 %** | | | | | | | |
| 0.15 % $H_2O$ | 0.0 | 0.2 | -0.2 | -0.3 | -0.4 | -0.6 | -0.7 |
| 1.1 % $H_2O$ | 0.0 | 0.2 | -0.1 | -0.2 | -0.2 | -0.5 | -0.5 |

| | | | | | | | |
|---|---|---|---|---|---|---|---|
| **$N_2O$ : 4 %** | | | | | | | |
| 0.15 % $H_2O$ | 0.0 | 0.2 | -0.2 | -0.3 | -0.4 | -0.7 | -0.9 |
| 1.1 % $H_2O$ | 0.0 | 0.2 | -0.2 | -0.2 | -0.3 | -0.5 | -0.7 |
| **$N_2O$ : 8 %** | | | | | | | |
| 0.15 % $H_2O$ | 0.1 | 0.3 | -0.1 | -0.2 | -0.4 | -0.7 | -1.1 |
| 1.1 % $H_2O$ | 0.0 | 0.2 | -0.1 | -0.2 | -0.3 | -0.6 | -0.8 |

Table 6b: Measurement of IR radiation at the sensors, before and after addition of $N_2O$. $\Delta I_{N2O}$ = intensity change due to $N_2O$ radiation.

| W-Vapor % | $T_D$ °C | $\Delta T_D$ °C | $V_P$ V | $\Delta V_P$ V | $I_{0,av}$ W/m$^2$ | $\Delta I_{N2O}$ W/m$^2$ |
|---|---|---|---|---|---|---|
| **$N_2O$ : 2 %** | | | | | | |
| 0.15 % $H_2O$ | 16.2 | 1.0 | 1,809 | 0.189 | 79.0 | 10.7 |
| 1.1 % $H_2O$ | 16.6 | 0.8 | 1,890 | 0.156 | 83.8 | 9.1 |
| **$N_2O$ : 4 %** | | | | | | |
| 0.15 % $H_2O$ | 16.0 | 1.1 | 1,779 | 0.220 | 77.3 | 12.5 |
| 1.1 % $H_2O$ | 16.7 | 1.0 | 1,910 | 0.187 | 84.8 | 11.0 |
| **$N_2O$ : 8 %** | | | | | | |
| 0.15 % $H_2O$ | 16.0 | 1.3 | 1,777 | 0.255 | 77.1 | 14.8 |
| 1.1 % $H_2O$ | 16.7 | 1.2 | 1,921 | 0.207 | 85.2 | 12.5 |

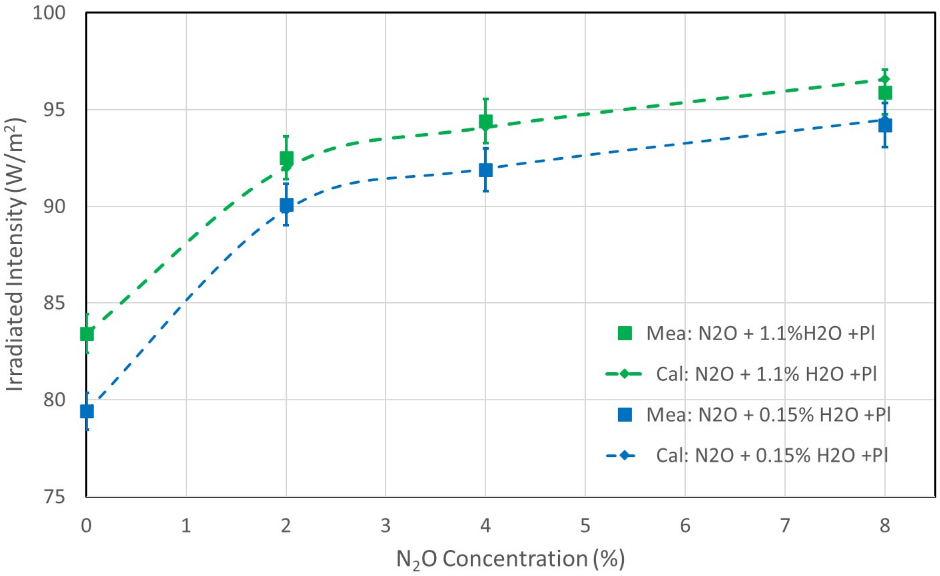

*Fig. 22: Measurements (squares with error bars) and calculations (diamonds, dashed lines) of the IR radiation of $N_2O$ for two WV concentrations (0.15% blue, 1.1% green) and background radiation from cylinder walls.*

## *5.5 Freon*

If doubters of the GHE – whether the positive or negative effect – still need to be convinced that GH-gases are emitting radiation and at the same time are cooling their environment, this even under conditions as found in the lower troposphere, they should take a closer look at the measurements of Freon 134a (1,1,1,2-Tetrafluoroethane) (Fig. 23).

Freon, a very strong greenhouse gas, which already allowed to observe the radiation with an unsuitable Styrofoam box (see Part I [6]), shows cooling of the cylinder air of over 2°C at a concentration of only 1 vol.% (Fig. 23a). The gas radiation attains such high intensities (see Fig. 23b) that the heat can only be dissipated from the plate $P_C$ with a significant increase in the $T_C$ temperature. The illusion that GH-gases are merely absorbers at normal pressure and do not emit IR radiation, and therefore do not generate back-radiation, is clearly refuted in view of these unambiguous data.

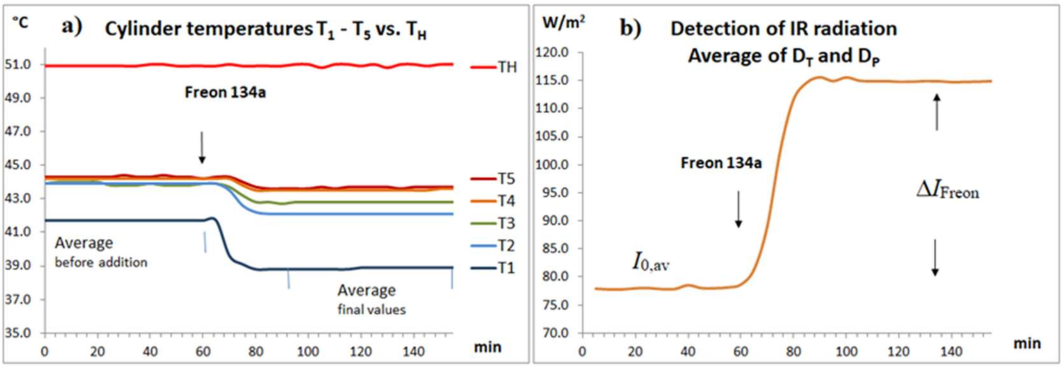

*Fig. 23: Effects of 1% Freon 134a, a) decrease in cylinder temperatures, b) increase in IR radiation after addition of Freon, $H_2O$ ~ 0.15%.*

The greatest Freon effect is achieved at a WV concentration of 0.15% and is only about 88% of the original effect at 1.1% water vapor (Table 7b).

Table 7a: Influence of Freon 134a on the temperatures $T_1 - T_5$.

| W-Vapor % | $\Delta T_H$ °C | $\Delta T_C$ °C | $\Delta T_5$ °C | $\Delta T_4$ °C | $\Delta T_3$ °C | $\Delta T_2$ °C | $\Delta T_1$ °C |
|---|---|---|---|---|---|---|---|
| **Freon: 1%** | | | | | | | |
| 0.15% $H_2O$ | 0.0 | 0.6 | -0.6 | -0.7 | -1.1 | -1.8 | -2.8 |
| 1.1% $H_2O$ | 0.0 | 0.5 | -0.5 | -0.6 | -0.9 | -1.5 | -2.4 |
| **Freon: 2%** | | | | | | | |
| 0.15% $H_2O$ | 0.1 | 0.7 | -0.5 | -0.4 | -0.9 | -1.9 | -3.1 |
| 1.1% $H_2O$ | 0.0 | 0.6 | -0.3 | -0.3 | -0.7 | -1.6 | -2.7 |
| **Freon: 4%** | | | | | | | |
| 0.15% $H_2O$ | 0.0 | 0.7 | -0.2 | -0.3 | -0.8 | -1.8 | -3.5 |
| 1.1% $H_2O$ | 0.0 | 0.6 | -0.1 | -0.2 | -0.5 | -1.5 | -3.0 |

Table 7b: Measurement of IR radiation at the sensors, before and after addition of Freon 134a.
$\Delta I_{Freon}$ = change in intensity due to Freon radiation.

| W-Vapor % | $T_D$ °C | $\Delta T_D$ °C | $V_P$ V | $\Delta V_P$ V | $I_{0,av}$ W/m² | $\Delta I_{Freon}$ W/m² |
|---|---|---|---|---|---|---|
| **Freon: 1%** | | | | | | |
| 0.15% $H_2O$ | 16.1 | 3.3 | 1,789 | 0.636 | 78.3 | 36.6 |
| 1.1% $H_2O$ | 16.5 | 2.9 | 1,870 | 0.550 | 82.7 | 32.1 |
| **Freon: 2%** | | | | | | |
| 0.15% $H_2O$ | 16.1 | 3.6 | 1,769 | 0.692 | 77.3 | 40.1 |
| 1.1% $H_2O$ | 16.6 | 3.2 | 1,881 | 0.612 | 83.4 | 35.6 |
| **Freon: 4%** | | | | | | |
| 0.15% $H_2O$ | 16.0 | 3.8 | 1,764 | 0.733 | 76.9 | 42.5 |
| 1.1% $H_2O$ | 16.6 | 3.3 | 1,878 | 0.629 | 83.4 | 36.8 |

The measured intensities before and after pouring in Freon according to Table 7b are graphically represented in Fig. 24. Within the assumed error limits of 2.5%, they show virtually no further increase with Freon concentrations larger than 1% and only a slight difference for a WV content of 0.15% (blue) compared to 1.1% (green). Interpolated equilibration values are shown as dotted graphs. The emission is already so strongly saturated at 1% Freon that even an increased WV content shows only a minimal correction.

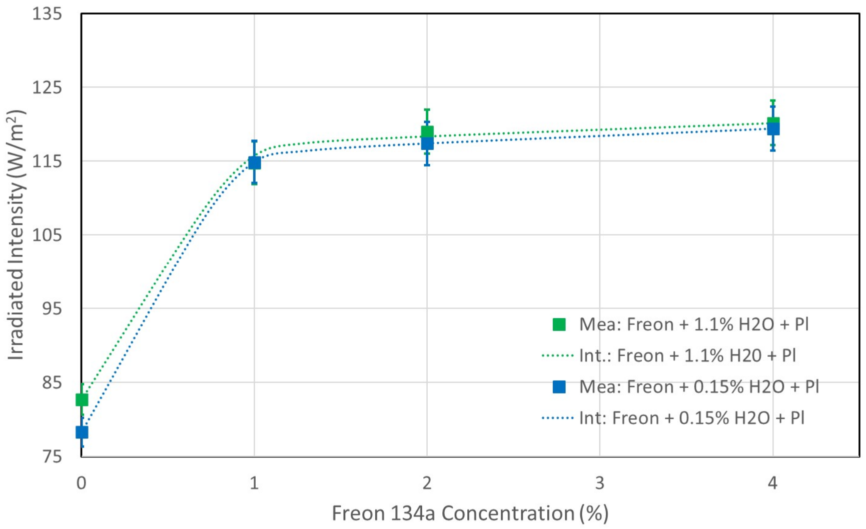

*Fig. 24: Measurements (squares with error bars) and interpolation of the data (dotted lines) for the IR radiation of Freon 134a for two WV concentrations (0.15% blue, 1.1% green) with background radiation from the cylinder walls.*

## 6. Summary

Using a new experimental setup with only two temperature poles—a warm gas and a cooler radiation receiver—it can be shown that GH-gases are emitters even at normal pressure. These gases absorb energy through inelastic collisions with the nitrogen and oxygen molecules in air at the expense of the kinetic energy of their surroundings, and they release this energy as IR radiation. Such a process is a negative greenhouse effect and results in the ambient air cooling and increasing IR radiation, when $CO_2$, methane, nitrous oxide and Freon 134a are added. These experiments demonstrate once again that the so-called back-radiation is not ominous but actually exists.

A violation of the second law of thermodynamics per se doesn't exist, since these experiments only investigate the heat flow from a warm gas to a cooler plate. Control experiments with the IR-inactive noble gases argon and helium show no effect, thus ruling out heat conduction as a likely cause of the temperature changes.

The detection of gas radiation is not entirely straightforward, as the IR radiation from the container significantly overwhelms the radiation from the gases, meaning that, like an iceberg, only the tip of the effect is visible. However, the above investigations are not just a simple demonstration of this effect; they also confirm the underlying theory through the good agreement between measurements and calculations, thus allowing a direct comparison of the different effects of the GH-gases studied.

The concept of *radiative potential* must be critically examined, as methane is a weaker emitter than $CO_2$ (see also Harde & Schnell [4]), and the radiation intensity of nitrous oxide is only 1.5 times greater. A 25- or 300-times higher radiation potential compared to $CO_2$ is misleading, as it is an apples-to-pears comparison and also includes the residence time. Radiative potential is a political term and should not be confused with effectiveness.

The measured gas radiation depends on the concentration of these gases, but also on any remaining residual water vapor concentration. As the $H_2O$ concentration increases, the gas radiation of the other GH-gases is overlaid, and their effectiveness is correspondingly reduced.

Warm air above a colder surface is not only of theoretical interest, but also occurs in nature, for example, during inversion weather conditions, but especially at the poles during persistent darkness. Here, $CO_2$ causes a negative greenhouse effect, which satellite measurements also show as a hump in the 15 µm wavelength range, or around 670 $cm^{-1}$, instead of the familiar $CO_2$ funnel (Schmithüsen et al., 2015 [12]; van Wijngaarden & Happer 2025 [13]).

The negative greenhouse effect and the ability of GH-gases to convert heat from their surrounding into infrared radiation is of fundamental importance for the Earth's climate. It supports global heat transport between the equator and the poles, as well as vertical exchange through convection and evaporation. Through these mechanisms, heat in various forms can be efficiently transported to the tropopause and beyond, where it is ultimately radiated into space. Without this heat transport, the radiation balance of incoming and outgoing radiation at the upper edge of the atmosphere could not be maintained; and at the same time, by radiating GH-gases towards the Earth's surface, they protect the Earth from further cooling. Only through this can plant and animal life on Earth be ensured.

**Funding:** No funding of the work.

**Co-Editor**: Stein Bergsmark; **Reviewer 1**: Anonymous, **Reviewer 2**: Prof. D. Koutsoyiannis.

**Acknowledgement:** We thank the Co-Editor and the Reviewers for their critical reports of the two articles and particularly Reviewer 2 for his detailed and very constructive comments.

## References

1. L. S. Rothman et al., 2025: HITRAN database: https://hitran.org/
2. G. Kirchhoff, 1859: *Monthly reports of the Academy of Sciences in Berlin* , Sessions of Dec. 1859, 1860, Berlin, pp. 783-787).
3. R. Clausius, 1887: The Mechanical Theory of Heat, Volume I, https://archive.org/details/diemechanischewr00clau/page/n5/mode/2up?view=theater
4. H. Harde, M. Schnell, 2022: *Verification of the Greenhouse Effect in the Laboratory* , Science of Climate Change, Vol. 2.1, pp. 1- 33, https://doi.org/10.53234/scc202203/10
5. H. Harde, 2013: *Radiation and Heat Transfer in the Atmosphere: A Comprehensive Approach on a Molecular Basis* , International Journal of Atmospheric Sciences (Open Access), vol. 2013, http://dx.doi.org/10.1155/2013/503727
6. M. Schnell, H. Harde, 2025: *The Negative Greenhouse Effect – Part I: Experimental Studies with a Common Laboratory Set-Up*, Science of Climate Change, Vol. 5.3, pp. 1 – 9, https://doi.org/10.53234/scc202510/02
7. J. J. Harrison, 2015: *Infrared absorption cross sections for 1,1,1,2-tetrafluoroethane* , Journal of Quantitative Spectroscopy and Radiative Transfer 151, 210-216, https://doi.org/10.1016/j.jqsrt.2014.09.023,
   HITRAN: https://hitran.org/data/xsec/CFH2CF3_295.8K-760.8Torr_750.0-1600.0_00.xsc
8. P. Atkins, R. Friedman, 2011: *Molecular Quantum Mechanics* , 5th Edition, Oxford University Press, Oxford, ISBN 978-0-19-954142-3 , Black Body Radiation | tec science
9. P. Asgari, O. Moradi, B. Tajeddin, 2014: *The effect of nanocomposite packaging carbon nanotube base on organoleptic and fungal growth of Mazafati brand dates* , Int. Nano Lett. 4, 98 https://doi.org/10.1007/s40089-014-0098-3

10. G. E. Thomas, K. Stamnes, 1999: *Radiative Transfer in the Atmosphere and Ocean*, Cambridge Univ. Press, Cambridge, UK, equation 12.19.
11. IPCC Sixth Assessment Report (AR6), 2021: V. Masson-Delmotte, P. Zhai, A. Pirani et al.: *Climate Change 2021: The Physical Science Basis. Contribution of Working Group I to the Sixth Assessment Report of the Intergovernmental Panel on Climate Change*, Cambridge University Press.
12. H. Schmithüsen , J. Notholt , G. König-Langlo, P. Lemke, T. Jung, 2015: *How increasing $CO_2$ leads to an increased negative greenhouse effect in Antarctica* , Geophys . Res. Lett., 42, pp. 10, 422–10,428, https://doi.org/10.1002/2015GL066749 .
13. W. A. van Wijngaarden, W. Happer, 2025: *Radiation Transport in Clouds*, Science of Climate Change, Vol. 5.1, pp. 1- 12, https://doi.org/10.53234/scc202501/02.
14. K. Schwarzschild, 1906: *On the Equilibrium of the Solar Atmosphere* . In: News of the Royal Society of Sciences at Göttingen, Mathematical-Physical Class, 1906, Issue 1, pp. 41–53 (January 13, 1906).
15. H. Harde, 2014: *Advanced Two-Layer Climate Model for the Assessment of Global Warming by $CO_2$* , Open Journal of Climate Change, Vol. 1, No. 3, ISSN(Print): 2374-3794, https://web.archive.org/web/20160429061756/http://www.scipublish.com/journals/ACC/papers/download/3001-846.pdf
16. H. Harde, 2017: *Radiation Transfer Calculations and Assessment of Global Warming by $CO_2$,* International Journal of Atmospheric Sciences, Volume 2017, Article ID 9251034, pp. 1-30, https://doi.org/10.1155/2017/9251034.
17. D. Koutsoyiannis, C. Vournas, 2024: *Revisiting the greenhouse effect—a hydrological perspective,* Hydrological Sciences Journal, Vol. 69 (2), pp. 151–164, https://doi.org/10.1080/02626667.2023.2287047.
18. D. Koutsoyiannis, 2024: *Relative importance of carbon dioxide and water in the greenhouse effect: Does the tail wag the dog?*, Science of Climate Change, 4 (2), 36–78, https://doi.org/10.53234/scc202411/01.

## Appendix

The laboratory is thermostatically controlled at 17°C ± 0.3 °C to prevent interference from fluctuating room temperatures. The hot and cold water temperatures for heating the cylinder and cooling the $P_C$ plate, respectively, are stabilized within ±0.1°C. To establish thermal equilibrium, heating and cooling are switched on 5 hours before data recording.

Some data show a wave-like pattern, caused by the thermostat's temperature control. These fluctuations are compensated for by averaging over a period of one hour before and after the addition of a sample gas.

To generate cylinder air with varying humidity levels, either the laboratory air with a relative humidity of 64% is used, or the cylinder air is passed over solid caustic soda or damp paper for four hours. The water vapor content is measured with a hygrometer outside the cylinder as relative humidity and converted to absolute humidity g/m³.

Table A1: Technical data

| | Length/Height | Ø: | | Length/Height | Ø: |
|---|---|---|---|---|---|
| **Cylinder** | 57 cm | 33 cm | **Calibration** | | |
| Dome | 13 cm | 33 | Radiation opening | | 34.5 cm |
| heating hose | 25 m | 8x12 mm | aluminum cover | 0.8 mm | 33.5 cm |
| Styrofoam top | 20 cm | 50 cm | Plate $P_W$ | 0.8 mm | 22 cm |

| | | | | | |
|---|---|---|---|---|---|
| Styrofoam wall | 66 cm | 50 cm | PI- polyimide film heater | | 22 cm |
| | | | Styrofoam over $P_W$ | 20 cm | 50 cm |
| **Plate $P_C$** | 0.8 mm | 36 cm | Styrofoam under $P_W$ | 5 cm | 50 cm |
| soft copper pipe | 5 m | 8x1 mm | Laboratory power supply Korad ka3005d 0-30 V | | |
| Styrofoam | 15 cm | 50 cm | | | |
| Radiation opening | - | 34.5 cm | **Data logger** | | |
| | | | temperature | Elitech RC4 | |
| **IR detectors** | | | Tension: | VOLTCRAFT DL-250V | |
| Plate $D_T$ | 0.8 mm | 11.8 | | | |
| Styrofoam | 0.8 cm | 11.8 | **Thermostat:** | ES-10 ± 0.1°C | |
| Peltier elements 10 x TES1-3104Q | 15x15x3.4 mm | | **DC amplifier:** | AD620 | |

Table A2: Distance of the sensors from the PE foil.

| sensor | $T_5$ | $T_4$ | $T_3$ | $T_2$ | $T_1$ | $D_T$ | $D_P$ | $T_C$ |
|---|---|---|---|---|---|---|---|---|
| cm | 64 | 47 | 33 | 19 | 5 | -14 | -15.5 | -15 |

Table A3: Calibration of the IR sensors.

| Heating W | $T_C$ °C | $T_D$ °C | $V_P$ V |
|---|---|---|---|
| 0.000 | 8.5 | 9.0 | 0.427 |
| 1,202 | 8.8 | 10.4 | 0.694 |
| 1,873 | 8.9 | 11.1 | 0.820 |
| 2,685 | 9.1 | 12.0 | 0.987 |
| 3,644 | 9.3 | 13.1 | 1,190 |
| 4,740 | 9.5 | 14.2 | 1,392 |
| 5,972 | 9.7 | 15.5 | 1,626 |
| 7,340 | 9.9 | 16.9 | 1,891 |
| 8,833 | 10.1 | 18.5 | 2,185 |

Table A4: Heating of the cylinder, $H_2O$ ~ 0.15 vol.%.

| min | $T_H$ °C | $T_C$ °C | $T_5$ °C | $T_4$ °C | $T_3$ °C | $T_2$ °C | $T_1$ °C | $T_D$ °C | $V_P$ V |
|---|---|---|---|---|---|---|---|---|---|
| 0 | 18 | 8.8 | 17 | 16.8 | 16.8 | 16.8 | 16.5 | 10.3 | 0.44 |
| 20 | 22.6 | 8.9 | 18.1 | 18.2 | 18.2 | 18.2 | 17.7 | 10.5 | 0.51 |
| 40 | 26.7 | 9 | 21 | 21.4 | 21.3 | 21.3 | 20.5 | 10.9 | 0.63 |
| 60 | 30.3 | 9 | 24.1 | 24.4 | 24.3 | 24.3 | 23.3 | 11.5 | 0.75 |
| 80 | 33.6 | 9.1 | 27.2 | 27.4 | 27.3 | 27.3 | 26 | 12.1 | 0.87 |
| 100 | 36.6 | 9.2 | 29.9 | 30.1 | 29.9 | 29.9 | 28.5 | 12.6 | 1.00 |
| 120 | 39.2 | 9.3 | 32.3 | 32.5 | 32.3 | 32.3 | 30.7 | 13.1 | 1.13 |
| 140 | 41.6 | 9.5 | 34.5 | 34.6 | 34.4 | 34.4 | 32.7 | 13.6 | 1.24 |
| 160 | 43.6 | 9.5 | 36.3 | 36.5 | 36.2 | 36.2 | 34.4 | 14 | 1.34 |
| 180 | 45.3 | 9.6 | 38.1 | 38.2 | 37.9 | 37.9 | 35.9 | 14.4 | 1.42 |
| 200 | 46.9 | 9.7 | 39.6 | 39.6 | 39.3 | 39.3 | 37.4 | 14.8 | 1.50 |

| | | | | | | | | | |
|---|---|---|---|---|---|---|---|---|---|
| 220 | 48.3 | 9.7 | 40.9 | 40.9 | 40.6 | 40.7 | 38.6 | 15.1 | 1.56 |
| 240 | 49.7 | 9.8 | 42 | 42 | 41.7 | 41.8 | 39.6 | 15.4 | 1.63 |
| 260 | 50.9 | 9.8 | 43.1 | 43.2 | 42.8 | 42.9 | 40.6 | 15.6 | 1.69 |

Table A5: Heating of the cylinder, $H_2O$ = 1.1 vol.%.

| min | $T_H$ °C | $T_C$ °C | $T_5$ °C | $T_4$ °C | $T_3$ °C | $T_2$ °C | $T_1$ °C | $T_D$ °C | $V_P$ V |
|---|---|---|---|---|---|---|---|---|---|
| 0 | 19.3 | 8.9 | 18.2 | 17.9 | 17.9 | 17.9 | 17.6 | 10.8 | 0.53 |
| 20 | 23.9 | 9 | 19.3 | 19.2 | 19.3 | 19.2 | 18.7 | 11 | 0.59 |
| 40 | 28.1 | 9 | 22.2 | 22.3 | 22.3 | 22.2 | 21.4 | 11.5 | 0.72 |
| 60 | 31.8 | 9.2 | 25.3 | 25.4 | 25.3 | 25.3 | 24.3 | 12.1 | 0.85 |
| 80 | 35.1 | 9.3 | 28.2 | 28.4 | 28.2 | 28.2 | 27 | 12.7 | 0.99 |
| 100 | 38.1 | 9.4 | 30.9 | 31 | 30.8 | 30.8 | 29.4 | 13.2 | 1.12 |
| 120 | 40.7 | 9.5 | 33.4 | 33.4 | 33.2 | 33.1 | 31.6 | 13.7 | 1.24 |
| 140 | 43.1 | 9.6 | 35.7 | 35.7 | 35.4 | 35.4 | 33.6 | 14.2 | 1.36 |
| 160 | 45.2 | 9.7 | 37.6 | 37.6 | 37.4 | 37.3 | 35.5 | 14.7 | 1.47 |
| 180 | 47.1 | 9.8 | 39.4 | 39.4 | 39 | 39 | 37.1 | 15.1 | 1.57 |
| 200 | 48.8 | 9.8 | 40.9 | 40.9 | 40.6 | 40.6 | 38.5 | 15.5 | 1.64 |
| 220 | 50.3 | 9.9 | 42.3 | 42.3 | 41.9 | 41.9 | 39.7 | 15.8 | 1.72 |

Klimarealistene
Vollsveien 109
1358 Jar, Norway
ISSN: 2703-9072

Correspondence:
rgrabyan@cox.net

Vol. 5.3 (2025)
pp. 35-80

Research Article

# Global Atmospheric $CO_2$ Lags Temperature by 150 yr between 1 and 1850 AD

Ronald Grabyan

Irvine, California, USA

## Abstract

This study investigates whether atmospheric $CO_2$ precedes or lags global temperature changes over the past 2000 yr, using both visual and statistical analyses. A parallel evaluation of Total Solar Irradiance (TSI) and temperature was conducted to assess the influence of solar forcing on climate variability.

Temperature, $CO_2$, and TSI data were drawn from many well-established publications and international climate data repositories. Original, unsmoothed series were used to identify visual markers—such as peak–trough alignments, correlative clusters, and trend concordance—while smoothed series (using 50-yr and 100-yr running averages and Loess filters) were employed to emphasize large-scale patterns and reduce local variability. Correlation analysis, conducted within a statistical validation framework, was applied across all data variants.

Results show that atmospheric $CO_2$ consistently lags temperature by approximately 150 yr from 1 to 1850 AD. After applying this lag correction ($CO_{2Lag}$), Pearson correlation coefficients ($r_{PCC}$) between $CO_{2Lag}$ and temperature reached Very Strong values ranging from 0.85 to 0.99. TSI–temperature correlations were generally Strong across the full 2000 yr interval, and Very Strong from 1850 to present. A prominent alignment among $CO_{2Lag}$, TSI, and temperature occurs around 1460 AD.

These findings indicate that atmospheric $CO_2$ does not precede, nor appear to drive, global temperature trends. Rather, $CO_2$ consistently lags temperature, suggesting it functions as a response variable rather than a primary forcing. In addition, TSI exhibits Strong to Very Strong temporal alignment with temperature, supporting the hypothesis that solar variability plays a significant role in long-term climate change.

**Keywords:** $CO_2$; temperature; $CO_2$ lags temperature; total solar irradiance; last 2000 yr

Submitted 2024-12-17, Accepted 2025-08-20. https://doi.org/10.53234/scc202510/04

## 1. Introduction

Understanding the role of atmospheric $CO_2$ in climate dynamics is a critical scientific and policy concern. If $CO_2$ is a primary driver of global temperature change, then reducing anthropogenic emissions becomes essential. Conversely, if $CO_2$ plays a lagging role, the rationale for large-scale mitigation strategies deserves reexamination. A rigorous, evidence-based evaluation of this relationship is needed.

The prevailing consensus in climate science maintains that increased atmospheric $CO_2$—primarily from fossil fuel combustion—drives warming of the Earth's surface and lower atmosphere. This conclusion is supported by numerous studies linking rising $CO_2$ levels to temperature trends across multiple timescales. However, other peer-reviewed studies challenge this causality, suggesting that temperature changes lead $CO_2$ changes, rather than follow them (e.g., Humlum et al., 2013; Chylek et al., 2018a; Sharma & Karamanev, 2021). Some of these studies show temperature leading $CO_2$ by centuries in paleoclimate records, while others find leads of months in the instrumental era and millions of years in the distant paleoclimate records.

Recent publications further support the hypothesis that temperature changes precede atmospheric $CO_2$ fluctuations. Several studies by Koutsoyiannis and collaborators (2020, 2022a, 2022b, 2023, 2024a, 2024b) suggest that global air temperature may act as leading indicators or drivers of $CO_2$ concentration changes.

In addition to the $CO_2$-temperature relationship, a wide array of natural factors has been proposed to explain historical temperature variability. These include:

1. Solar variability: Total Solar Irradiance (TSI), magnetic modulation of cosmic rays, UV-induced atmospheric chemistry, and weakening of the jet stream (Easterbrook, 2016a; Svensmark and collaborators, 1999, 2007, 2016, 2021, 2022; Ogurtson et al., 2002; Shaviv et al., 2023; Scafetta, 2023; Gray et al., 2010; Moffa-Sanchez et al., 2014; Ineson et al., 2011).
2. Oceanic oscillations: The Atlantic Multidecadal Oscillation (AMO), thermohaline circulation, and ENSO-like cycles (Knudsen et al., 2011; Lin & Qian, 2022; Gray, 2012; Gray et al., 2003; D'Aleo & Easterbrook, 2016; Doos et al., 2012; Toggweiler & Key, 2001).
3. Planetary and orbital forcing: Changes in Earth's eccentricity, axial tilt, and precession (Milankovitch cycles), as well as planetary gravitational influences (Scafetta & Bianchini, 2022; Stefani et al., 2004; Wanner et al., 2022; Morner, 2012; Lourens & Tuenter, 2016; Marsh, 2014; Roe, 2006; Shackleton, 2000; Imbrie et al., 1992).
4. Volcanism, tectonics, and extraterrestrial impacts: Volcanic aerosols, plate tectonics, and meteor strikes as agents of climate change (Covey et al., 1994; Dekan, 2021; Komitov & Kaftan, 2020; Wanner et al., 2022; Vinos, 2024a; Vinos, 2024b; Vevard & Veizer, 2019).

Multiple studies across diverse timescales have found that $CO_2$ tends to lag temperature. For instance:

1. Ice core records from the last 420 kyr show lags of 300 to 2300 yr (Mudelsee, 2001; Caillon et al., 2003).
2. Monnin et al. (2001) reported a lag of ~410,000 yr between 11.2 and 17 kyr BP.
3. Sharma and Karamanev (2021) found $CO_2$ lagging temperature by 1020–1080 yr over the last 650 kyr.
4. Middleton (2011) postulated a 250-yr lag of $CO_2$ to temperature during the Little Ice Age.
5. Instrumental records from 1980–2011 show $CO_2$ lagging SST and air temperatures by 9 to 12 mo (Humlum et al., 2013).
6. Monthly datasets for the 1960–2016 period show average lags of 4 to 5 mo (Adams & Piovesan, 2005; Chylek et al., 2018b).
7. Koutsoyiannis (2024a) synthesized findings across multiple geological intervals, reporting that $CO_2$ consistently lagged temperature, with lag duration increasing with timescale:
    7.1. Phanerozoic: ~2.3 million yr
    7.2. Cenozoic: ~800,000 yr
    7.3. Late Quaternary: ~1200 yr
    7.4. Common Era (1–1700 AD): ~33 yr
    7.5. Instrumental Period: 3–8 months

The consistent pattern of temperature leading $CO_2$ invites a reevaluation of cause-and-effect assumptions in climate science. This study focuses on the Common Era, analyzing the lag relationship between $CO_2$ and temperature using 16 global temperature proxies and 4 $CO_2$ proxies over the past 2000 yr. Both visual and statistical methods (e.g., statistically validated Pearson correlation, lag testing) are employed.

Results show that $CO_2$ consistently lags temperature by approximately 150 yr across the 1–1850 AD period. These findings hold for both the pre-1600 and post-1600 segments of the data, even accounting for structural breaks or regime shifts.

Given the robust pattern of temperature leading $CO_2$, this analysis is extended to evaluate potential drivers of temperature change. Numerous studies have pointed to solar variability as a plausible mechanism, including changes in TSI (Scafetta, 2023; D'Aleo, 2016; Whiteet al., 1997; White, 2000; Hoyt & Schatten, 1993; Soon, 2009; Soon & Legates, 2013; Soon et al., 2015, Li, 2022; Wang et al., 2020; Schmutz, 2021; Usoskin et al., 2005; Douglass & Clader, 2002; Abdussamatov, 2016; Lean, 2000), solar magnetic activity (Lockwood & Stamper, 1999), and radiative forcing beyond TSI alone (Shaviv, 2008). Though satellite measurements since 1978 show only ~0.1% variation in TSI over an 11 yr solar cycle (Willson & Hudson, 1988), longer-term changes since the Maunder Minimum may be as high as 0.4–0.5% (Willson, 1997; Hoyt & Schatten, 1997; Solanki & Fligge, 2000; Willson & Mordvinov, 2003).

In addition to variations in TSI, several studies have proposed more indirect solar influences on climate. These include solar eruptions such as flares, coronal mass ejections, and high-speed wind streams from coronal holes (D'Aleo, 2016). Since 2001, the total magnetic flux emitted by the Sun has reportedly increased by a factor of 2.3, which may influence Earth's climate through two primary mechanisms: (1) enhanced ozone chemistry in the upper atmosphere triggered by ultraviolet radiation (Bard & Frank, 2006; Gray et al., 2010; Haigh et al., 2010; Ermolli et al., 2013), and (2) ionization at higher latitudes during geomagnetic storms (D'Aleo, 2016; Lockwood & Stamper, 1999). In parallel, variations in cloud formation linked to galactic cosmic rays and solar modulation have been suggested as additional contributors to climate variability (Svensmark & Friis-Christensen, 1997; Svensmark, 1999, 2007, 2016, 2022; Svensmark et al., 2021; Shaviv et al., 2023).

Abdussamatov (2015) further argued that Earth's temperature is influenced by the annual energy balance, incorporating factors such as TSI, oceanic thermal inertia, albedo feedback, and greenhouse gas concentrations. According to D'Aleo (2016), these indirect solar effects may significantly amplify the Sun's role in modulating climate.

This study evaluates solar irradiance records from multiple sources and compares them to global temperature over the last two millennia and selected modern periods (1659, 1850, 1880 to present). While causation cannot be definitively established, the correlations observed suggest that solar energy input—direct and indirect—plays a substantial role in global temperature variability.

Four Appendices for this study are incorporated in the Supplementary Material, including Appendices A–D: (A) Data – Correlation Analysis of $CO_2$ vs. temperature, (B) Statistical Validation Framework, (C) Structural Break or Regime Shift at 1600 AD, and (D) Total Solar Irradiance and Temperature.

## 2. Methods

Published data from 18 studies of air temperature and five studies of $CO_2$ across the last 2000 yr were used in this investigation. Multiple proxies from across the world were utilized in these published studies of $CO_2$ and temperature. For $CO_2$, ice cores from Antarctica were used in this study. For temperature, ice cores, tree rings, marine and lake sediment, speleothem, pollen, Mg/Ca in fossil shells, and stalagmites, and others, were also used in these studies.

Data from the published studies were either obtained from the respective authors, downloaded from public repositories or digitized from the published papers utilizing an online digitizing program, Graph Grabber v2.0.2 (Quintessa Limited, 2020) – all with permission. Each temperature study was compared to each $CO_2$ study (64 pairs in the main body of this report – Data Set A and Data Set B).

Results of $r_{PCC}$ data analysis for Data Set A and Data Set B, for data ranges of 200-1600 AD and 1000-1600 AD are presented in Supplementary Material, Appendix A.

The research plan of this paper includes using Pearson Correlation Coefficients obtained by evaluating each pair of $CO_2$ and temperature time-series data obtained from various published studies, both in original form, data smoothing transformations, and with $CO_2$ at a range of lags from -200 to +200 yr in an interval of 10 yr. Therefore, it is important to discuss the potential weaknesses of this approach as presented by Koskinas et al. (2022) and Koutsoyiannis (2024c), as well as the potential strengths. These studies address the strong time-dependence of such data, especially of long-range memory type (Hurst-Kolmogorov dynamics) where the probability distribution of $r_{PCC}$ is potentially heavily modified by the presence of long-range dependence (LRD). Long memory processes imply persistent autocorrelation that can inflate apparent statistical significance of cross-correlations and cause unreliable p-values.

The well-described concerns regarding long-range dependence (LRD) in paleoclimate $CO_2$ and temperature data — as outlined by Koskinas et al. (2022) and Koutsoyiannis (2024c) — are fully acknowledged, and these concerns center on the potential inflation of correlation coefficients when applied to nonstationary or persistent time series. However, based on a structured series of diagnostic tests and methodological guard rails (herein termed Statistical Validation Framework, as described below), I consider the conditional use of Pearson Correlation Coefficient ($r_{PCC}$) both acceptable and informative within the context of this study and pending the results of the SVF (Beran, 1994; Granger & Joyeux, 1980). The following measures support this judgment:

1. Alignment of time-series by calendar-year, with a consistent shift 150 yr earlier in time applied to $CO_2$, testing the hypothesized delayed or lagged response to temperature
2. Multiple smoothing levels (Original, RA 100, multiple Loess) applied to isolate persistent structure while at the same time observing inflation risk
3. Visual inspection of $CO_2$ and temperature curve alignment which in most cases depicts strong shape and change similarity consistent with lagged response, including alignment of peaks and troughs
4. Max-r-lag testing across a broad range of lag intervals (-200 to +200 yr) to identify the peak r-correlations with physical lags (generally at an interval of 10 yr)
5. Statistical Validation Framework:
    - 5.1 Autocorrelation Tests:
        - 5.1.1 Durbin-Waston Test (Durbin & Watson, 1950)
        - 5.1.2 Breusch-Godfrey Test (Breusch, 1978; Godfrey, 1978)
        - 5.1.3 Ljung-Box Q-Test (Ljung & Box, 1978)
    - 5.2 Hurst Exponent Analysis:
        - 5.2.1 Rescaled Range (R/S) (Hurst, 1951)
        - 5.2.2 Detrended Fluctuation Analysis (DFA) (Peng et al., 1994)
        - 5.2.3 Geweke-Porter-Hudak Spectral Estimation (GPH) (Geweke & Porter-Hudak, 1983)
    - 5.3 Heteroskedasticity and Autocorrelation Consistent Standard Errors (HAC SE) (Newey & West, 1987)
    - 5.4 Effective Sample Size (Neff) (Newey & West, 1987; Bretherton et al., 1999)
    - 5.5 Block Permutation Results (Politis & Romano, 1994)
    - 5.6 False Discovery Rate Methods (Globally Grouped) (Benjamini & Hochberg, 1995)

A complete discussion of these tests with their results can be found in Supplementary Material, Appendix B, in the context of the Statistical Validation Framework (SVF) -- validation of correlation significance under dependence, autocorrelation, and long-memory conditions.

Total Solar Irradiance (TSI) data were analyzed and compared to the temperature data utilized in this study in order to observe potential correlations. 11 TSI studies were included, and six temperature studies from 1659, 1850 and 1880 were included to address the near-term timeframe of 200 to 400 yr as well as the last 2000 yr timeframe.

Visual graphical analysis, in conjunction with various smoothing algorithms, assisted in the qualitative and semi-quantitative search for understanding the relationship in our climate of:

$CO_2$ and temperature
TSI and temperature

The methods process of this study is identified and followed as shown in detail below:

1. Each data set (from published sources) was evaluated in its original state and processed with a straight-line interpolation algorithm resulting in a data set of whole number years with an interval of one, unless it was already presented as such.
2. Each resulting data set was graphed as comparison graphs of every $CO_2$-temperature pair. Vertical axes adjustments were made to overlay the graphs to similar curve amplitudes in order to visually compare the curves.
3. The average lag of $CO_2$ to temperature was determined to be about 150 yr, based on a max-lag analysis with a range of -200 to +200 yr – the $CO_{2Lag}$ curves were added to the charts with original non-smoothed $CO_2$ and non-smoothed temperature.
4. In order to remove noise and other more granular data influences, and reveal larger trends, each data set was smoothed in Excel Professional 2019, using 4 algorithms:
    - 4.1. Running Average, centered on 50 yr (RA 50)
    - 4.2. Running Average, centered on 100 yr (RA 100)
    - 4.3. Loess Smoothing Algorithm – less smoothing (Loess 1)
    - 4.4. Loess Smoothing Algorithm – more smoothing (Loess 2)

    Loess (Locally Estimated Scatterplot Smoothing) is an Excel plugin, non-parametric locally weighted smoothing algorithm, with a smoothing parameter and the number of years for the quadratic moving regression (Peltier Tech, 2024).
5. Several iterations of selecting the appropriate Loess smoothing parameters were constructed in order to have resulting curves which had similar amplitude and frequency. If these two elements of the curves are not compatible, they may not reflect the true relationship of the curves, and statistical correlation could be poor and misleading. Note a larger number of data points (yr) in the Loess smoothing parameter will remove noise and other local features providing a broader, more regional view of the data. When smoothing data, the smoothed result is reflecting the impact of up to several hundred yr surrounding each data point (yr), and the localized nature of the original data will influence the smoothed curves. Thus, detailed temporal analysis with smoothed curves should be conducted with caution.
6. Pearson Correlation Coefficient ($r_{PCC}$) was calculated conditionally for each data pair of $CO_2$ and temperature, where there were data values at each year of both curves (64 sets for Data Set A and Data Set B)—data ranges 200-1600 AD, 1000-1600 AD, and 1600-1850 AD. An in-depth lag analysis approach was implemented where an $r_{PCC}$ was calculated for each lag between -200 yr and +200 yr, and the maximum $r_{PCC}$ was selected with its corresponding lag, along with an $r_{PCC}$ at 0-lag, as well as $r_{PCC}$. These calculations resulted in tables and graphs of $r_{PCC}$ as a function of lag correction, thus identifying the $CO_2$ lag year with the highest correlation. All $r_{PCC}$ values are considered conditional as previously

mentioned. For this study the following correlation coefficient strength ranges are utilized for general strength of correlation:

| | |
|---|---|
| $r_{PCC} > 0.00$ and $r_{PCC} < 0.20$ | None |
| $r_{PCC} > 0.20$ and $r_{PCC} < 0.40$ | Weak |
| $r_{PCC} > 0.40$ and $r_{PCC} < 0.60$ | Moderate |
| $r_{PCC} > 0.60$ and $r_{PCC} < 0.80$ | Strong |
| $r_{PCC} > 0.80$ and $r_{PCC} < 1.00$ | Very Strong |

7. Based on the general outline of the Statistical Validation Framework (SVF) described above, the detailed methodology and results are presented in Supplementary Material, Appendix B.
8. All statistical analyses were conducted using R (R Core Team, 2024) and Python 3.10 (Python Software Foundation). Analyses utilized the following libraries: numpy, scipy, pandas, and matplotlib in Python, and zoo, car, and nlme in R (Harris et al., 2020; Hunter, 2007; McKinney, 2010; Virtanen et al., 2020; Wickham, 2016; Zeileis & Grothendieck, 2005; Zeileis & Hothorn, 2002). Data alignment and preliminary Pearson correlation analyses were also implemented in Microsoft Excel using custom Visual Basic for Applications (VBA) scripts, which matched paired $CO_2$ and temperature values by calendar year (Microsoft Corporation, 2022). These routines served as independent verification of the primary results computed in R and Python. All figures in this study were created using Microsoft Excel's charting tools.
9. The data was separated into three main categories: (1) range 200-1600 AD, (2) range 1000-1600, and (3) range 1600-1850 AD. This is due to the presence of a structural break, possibly the result of a regime-shift at 1600 AD. This is discussed in Section 3.2 and in Supplementary Material, Appendix C. The data in the range 1600-1850 AD was treated more rigorously due to the character of $CO_2$ post-1600 AD. The following data transformation steps applied to both $CO_2$ and temperature for this range, except where noted, are followed:
   - 9.1. 50-yr centered running average – applied to suppress short-term fluctuation and emphasize low-frequency variability (Jones & Mann, 2004).
   - 9.2. Cubic Transformation – utilized to amplify long-term fluctuations and nonlinearly enhance larger variations in the $CO_2$ time series. This emphasizes major deviations while preserving the sign of the data, a paleoclimate technique used to highlight signal dynamics (Moberg et al., 2005).
   - 9.3. Standard Linear Detrending – fits a straight line to the data using least squares regression which isolates the stationary fluctuation component at the same time eliminating monotonic drift (Mann, 2004; Mudelsee, 2010)
   - 9.4. Normalization (min-max, 0-1) – Each series was subsequently normalized to the (0,1) interval using min-max scaling. This process allows for direct visual and statistical comparison of series with different magnitudes while preserving the relative shape of each curve (Wilkes, 2011).

This data was then processed for $r_{PCC}$ and lag values prior to tabulating and charting the results. Results are tabulated in Supplementary Material, Appendix A, Table A23.

10. Graphs of the original curves were produced showing the original curves and lagged original curves. Graphs of the smoothed curves were produced showing smoothed $CO_2$, smoothed temperature, and smoothed lagged $CO_2$ by the amount identified by the strongest correlation analysis and related lag, which usually corresponded to the visual correlation. Smoothing included Running Average (RA 50 and RA 100) and a matrix of Loess (level 1 and level 2). Documented on each graph is the recording of conditional $r_{PCC}$ (max at lag) and $r_{PCC}$ at 0-lag, as well as significance qualification from the SVF.

11. For the data range 200-1600 AD, a composite graph was produced with the top 8 smoothed temperature curves; all 4 of the ice-core-based lag-corrected $CO_2$ curves; an average curve of the temperature curves; and an average of the $CO_{2Lag}$ curves.
12. Pearson Correlation Coefficient ($r_{PCC}$) was calculated conditionally between the two average curves of temperature and lag-corrected $CO_2$ (at the peak of $CO_{2lag}$ correction).
13. TSI data and temperature data were utilized in this study in order to observe potential correlations and possible causation (correlation does not automatically equate to causation) (Supplementary Material, Appendix D). Visual graphics and statistical correlation techniques were applied to this data as described previously.

## 3. Results

### 3.1 Data Results - $CO_2$ vs. Temperature (200-1600 AD and 1000-1600 AD)

Pearson Correlation Analysis, $r_{PCC}$, and lag analysis were conducted on all pairs of $CO_2$ and temperature data analyzed in this study – both Data Set A and Data Set B (Supplementary Material, Appendix A). This included calculating $r_{PCC}$ for all combinations of four published $CO_2$ data sets and 16 published temperature data sets (eight in each set) covering varying ranges between two major data ranges (200- 1600 AD, and 1000-1600 AD) for five smoothing transformation algorithms:

1. Original data (Orig)
2. Running Average – 50 (RA 50)
3. Running Average – 100 (RA 100)
4. Loess Smoothing 1 (Loess 1) less smoothed
5. Loess Smoothing 2 (Loess 2) more smoothed

This approach calculated the following for each transformation level of the data:

1. $r_{PCC}$ (no lag of $CO_2$ to temperature)
2. $r_{PCC}$ (maximum $r_{PCC}$) (calculated from -200 to +200 lag yr in 10-yr intervals)
3. lag (lag interval at the maximum $r_{PCC}$)
4. Averages of each calculated parameter per $CO_2$ and temperature source

In Supplementary Material, Appendix A, Fig. A1 shows the lag value at the maximum $r_{PCC}$ depicted for a pair of $CO_2$ and temperature series – Rubino et al. (2019) and Yang et al. (2002). Typical of almost every pair of $CO_2$ and temperature lag analysis curve analyzed in this study, the curve resembles a normal or slightly log-normal curve where the correlation-lag values climb rather smoothly from 0, or negative, $r_{PCC}$ to a peak of maximum $r_{PCC}$ at a lag in the general average range of +150 yr. The curve then declines at a similar pace to the incline to 0, or negative $r_{PCC}$. This pattern is extremely consistent. While the average is about a 150 yr $CO_2$ lag, various data combinations at different smoothing transformations range from about 100 to about 200 $CO_2$ lag to temperature.

The following tables in Supplementary Material, Appendix A, contain the results organized as follows:

| Data Set A Table | Data Set B Table | Transformation | Range |
|---|---|---|---|
| Table A1 | Table A12 | Original | 200-1600 AD |
| Table A2 | Table A13 | Original | 1000-1600 AD |
| Table A3 | Table A14 | RA 50 | 200-1600 AD |
| Table A4 | Table A15 | RA 50 | 1000-1600 AD |
| Table A5 | Table A16 | RA 100 | 200-1600 AD |
| Table A6 | Table A17 | RA 100 | 1000-1600 AD |
| Table A7 | Table A18 | Loess 1 | 200-1600 AD |

| | | | |
|---|---|---|---|
| Table A8 | Table A19 | Loess 1 | 1000-1600 AD |
| Table A9 | Table A20 | Loess 2 | 200-1600 AD |
| Table A10 | Table A21 | Loess 2 | 1000-1600 AD |

Tables A11 (Data Set A) and A22 (Data Set B) (as shown in Supplementary Material, Appendix A) identify the smoothing transformation parameters utilized, specifically the parameters for the Loess method. A general overview of the data in Tables A1 through A11 (as shown in Supplementary Material, Appendix A) are summarized in Table 1. The separation of results into the ranges (200-1600 AD and 1000-1600 AD) are predicated on a couple of factors:

1. Two of the four $CO_2$ data sets have data from well-before 1000 AD and the other two commence at around 1000 AD. Likewise, 10 of the 16 temperature data sets begin well before 1000 AD, and the other six commence around 1000 AD.
2. It appears there was a more sparsely sampled original sampling rate by the published authors pre-1000 AD than post-1000 AD, creating some uncertainty with the earlier data.
3. The calculated $r_{PCC}$ data from the range of 200-1600 AD was consistently lower by about 0.20 than the data from the range of 1000-1600 AD.

A general overview of the data in Tables A12 through A22 (as shown in Supplementary Material, Appendix A) are summarized in Table 2.

Table 1. Summarizes the conditional $r_{PCC}$ and lag data for Data Set A and five transformational levels (Original, RA 50, RA 100, Loess 1, and Loess 2) for two data ranges (200-1600 AD and 1000-1600 AD). This summary is based on the results shown in tables A1-A11 in Supplementary Material, Appendix A.

| Summary of $r_{PCC}$ Analysis<br>Data Set A<br>No Lag $r_{PCC}$ and Maximum $r_{PCC}$ with Corresponding Lag<br>Five Transformation Levels and two Data Ranges (200-1600 AD, 1000-1600 AD) | | | | | | |
|---|---|---|---|---|---|---|
| | Average $r_{PCC}$(no lag) | Average $r_{PCC}$(max lag) | Average lag | Range $r_{PCC}$(no lag) | Range $r_{PCC}$ (max lag) | Range lag |
| Original | | | | | | |
| 200-1600 AD | -0.05 | 0.52 | 151 | -0.38 to 0.16 | 0.47 to 0.57 | 90 to 180 |
| 1000-1600 AD | 0.17 | 0.76 | 135 | -0.13 to 0.38 | 0.60 to 0.92 | 60 to 160 |
| RA 50 | | | | | | |
| 200-1600 AD | 0.02 | 0.66 | 152 | -0.37 to 0.27 | 0.57 to 0.79 | 120 to 180 |
| 1000-1600 AD | 0.30 | 0.87 | 132 | 0.07 to 0.60 | 0.77 to 0.96 | 60 to 170 |
| RA 100 | | | | | | |
| 200-1600 AD | 0.04 | 0.71 | 153 | -0.40 to 0.33 | 0.59 to 0.82 | 120 to 163 |
| 1000-1600 AD | 0.45 | 0.91 | 128 | 0.08 to 0.81 | 0.81 to 0.95 | 80 to 160 |
| Loess 1 | | | | | | |
| 200-1600 AD | -0.01 | 0.61 | 151 | -0.41 to 0.33 | 0.52 to 0.78 | 120 to 200 |
| 1000-1600 AD | 0.25 | 0.85 | 132 | -0.15 to 0.52 | 0.69 to 0.97 | 70 to 160 |
| Loess 2 | | | | | | |
| 200-1600 AD | 0.02 | 0.68 | 155 | -0.39 to 0.38 | 0.56 to 0.80 | 120 to 200 |
| 1000-1600 AD | 0.35 | 0.92 | 127 | -0.01 to 0.76 | 0.77 to 0.98 | 80 to 160 |
| Averages | | | | | | |
| 200-1600 AD | 0.00 | 0.64 | 152 | -0.39 to 0.29 | 0.54 to 0.75 | 114 to 184 |
| 1000-1600 AD | 0.30 | 0.86 | 131 | -0.03 to 0.61 | 0.73 to 0.96 | 70 to 162 |

Table 2. Summarizes the conditional $r_{PCC}$ and lag data for Data Set B and five transformational levels (Original, RA 50, RA 100, Loess 1, and Loess 2) for two data ranges (200-1600 AD and 1000-1600 AD). This summary is based on the results shown in tables A12-A22 in Supplementary Material, Appendix A.

Summary of $r_{PCC}$ Analysis
Data Set B
No Lag $r_{PCC}$ and Maximum $r_{PCC}$ with Corresponding Lag
Five Transformation Levels and two Data Ranges (200-1600 AD, 1000-1600 AD)

| | Average $r_{PCC}$ (no lag) | Average $r_{PCC}$ (max lag) | Average lag | Range $r_{PCC}$ (no lag) | Range $r_{PCC}$ (max lag) | Range lag |
|---|---|---|---|---|---|---|
| Original | | | | | | |
| 200-1600 AD | -0.24 | 0.41 | 154 | -0.47 to -0.10 | 0.25 to 0.48 | 150 to 160 |
| 1000-1600 AD | 0.08 | 0.59 | 128 | -0.23 to 0.64 | -0.10 to 0.87 | 100 to 200 |
| RA 50 | | | | | | |
| 200-1600 AD | -0.32 | 0.47 | 152 | -0.56 to 0.19 | 0.32 to 0.57 | 140 to 170 |
| 1000-1600 AD | 0.18 | 0.70 | 138 | -0.16 to 0.77 | 0.15 to 0.95 | 120 to 160 |
| RA 100 | | | | | | |
| 200-1600 AD | -0.33 | 0.50 | 154 | -0.57 to -0.19 | 0.36 to 0.60 | 140 to 170 |
| 1000-1600 AD | 0.30 | 0.74 | 125 | -0.19 to 0.87 | 0.19 to 0.96 | 70 to 160 |
| Loess 1 | | | | | | |
| 200-1600 AD | -0.32 | 0.47 | 154 | -0.56 to -0.17 | 0.44 to 0.57 | 130 to 180 |
| 1000-1600 AD | 0.09 | 0.71 | 132 | -0.37 to 0.69 | 0.15 to 0.95 | 70 to 180 |
| Loess 2 | | | | | | |
| 200-1600 AD | -0.32 | 0.52 | 161 | -0.55 to -0.17 | 0.38 to 0.64 | 140 to 190 |
| 1000-1600 AD | 0.19 | 0.77 | 118 | -0.41 to 0.88 | 0.26 to 0.98 | 50 to 180 |
| Averages | | | | | | |
| 200-1600 AD | -0.31 | 0.47 | 155 | -0.54 to -0.09 | 0.35 to 0.57 | 140 to 174 |
| 1000-1600 AD | 0.17 | 0.70 | 128 | -0.27 to 0.77 | 0.13 to 0.94 | 82 to 176 |

The data in Table 1 and Table 2 reveal the following observations:

1. The original data (Orig) $r_{PCC}$ (max) is consistently lower than the four smoothed transformations (RA 50, RA 100, Loess 1, and Loess2) by about 0.14 (200-1600 AD) and 0.13 (1000-1600 AD). $r_{PCC}$ (0-lag) is lower by about 0.07 (200-1600 AD) and 0.17 (1000-1600 AD). These numbers are from Data Set A. Data Set B shows the same trend with slightly smaller values. However, the Orig $r_{PCC}$ (max)is 0.52 and 0.76, respectively, for the longer and shorter ranges of Data Set A, which are Moderate and Strong correlations. For Data Set B, the Orig $r_{PCC}$ (max) values are 0.41 and 0.59 for the longer and shorter ranges respectively. Thus, the original data, without smoothing and with a larger noise component, still record significant conditional correlation values.
2. The RA 50 series is similar, but the values tend to lie between Orig and RA 100 which is consistent with the gradational nature of increasingly smooth character. The RA 50 $r_{PCC}$ (max) is 0.66 and 0.87, respectively, for the longer and shorter ranges of Data Set A, which are Moderate and Strong correlations. For Data Set B, the RA 50 $r_{PCC}$ (max) values are 0.47 and 0.70 for the longer and shorter ranges respectively.

3. The $r_{PCC}$ values (no lag) vs. the $r_{PCC}$ values (max lag) are always significantly lower for every transformation method, for both data ranges, and for every $CO_2$-temperature correlation pair. The average differential in Orig $r_{PCC}$ (max) (200-1600 AD) is 0.57 for Data Set A, and 0.65 for Data Set B. The average differential in Orig $r_{PCC}$ (max) (1000-1600 AD) is 0.59 for Data Set A, and 0.51 for Data Set B. The change in correlation strength is from None to Very Strong, thus emphasizing the lack of correlation from a statistical perspective for the no lag case.
4. While the average Orig $CO_2$ lag to temperature of both Data Sets A and B is about the same for the 200-1600 AD range, 151 and 154 yr respectively, and likewise for the 1000-1600 AD range, 135 and 128 yr, the range of lag is about 100 to 200 yr with a tighter cluster between 130 and 170 yr respectively. For the Orig data the average lag is about 153 yr and 132 yr, respectively, while for the RA 50 data the average lag is about 152 yr and 135 yr, respectively.
5. As shown below in the Original Charts (Fig. 1 and Fig. 2) of $CO_2$ and temperature, the most likely lag is about 150 yr based on prominent markers. Thus, the conditional $r_{PCC}$ (max) values for Original and RA 150 at the full data range of 200-1600 AD (156 and 152) seem to be a close match to the physical chart of the data even with a higher degree of noise component.
6. Observations regarding the shorter and younger range of 1000-1600 AD versus the longer range of 200-1600 AD:
    6.1. $r_{PCC}$ (max) lagged data for 1000-1600 AD has a consistently higher $r_{PCC}$ average differential of 0.23 compared to the 200-1600 AD range.
    6.2. While all of the $r_{PCC}$ values of the data with no lag are very low, 200-1600 AD is consistently lower than 1000-1600 AD: 0.07 at 0.47.
    6.3. The $CO_2$ lag to temperature is recoding about 23 yr higher for the longer range than the shorter range.
    6.4. The $r_{PCC}$ correlations may be somewhat lower for the 200-1600 AD period, although still showing at least Moderate strength of correlation, due to a probable lower sampling rate by the various researchers in the range of 1-1000 AD. Also, the Little Ice Age (LIA) is identified as ranging from 1300-1850 AD (Mann et al., 1999), but as shown in Fig. 1, temperature begins to steeply decline around 1100 AD and completes its rebound around 1900 AD. The dynamics of the LIA may have been a factor.
7. Running Average (RA 100) with significantly lower smoothing factor than Loess1 or Loess2, records similar $r_{PCC}$ values for the respective ranges of 200-1600 AD and 1000-1600 AD.
8. It is observed the $r_{PCC}$ for the longer range, ≈ 200 to 1600 AD, is always a bit lower than the $r_{PCC}$ for the shorter range (Table 1). There are several possible reasons for this result. The data sample distribution in most of the published studies was sparser in the years below 1000 AD. Having a longer-range extent will possibly introduce more inaccuracy and less precision. It is possible the driving process responsible for the 150-yr lag of $CO_2$ to temperature may fluctuate somewhat over time.
9. Loess 2 appears to show the highest $r_{PCC}$ compared to the other transformations.
10. Generally, regarding the different sources of data, there does not appear to be a significant difference among the $CO_2$ data sources or the temperature data sources with this view of the data. Two or three of the temperature sources in Data Set B do appear to be somewhat out of phase with the rest of the temperature data, although the major trends appear intact.
11. Given the influence of smoothing, preprocessing, and probable auto-correlation (Long-term memory), these $r_{PCC}$ correlations should be viewed as context-dependent indicators

rather than fixed or universal measures of the $CO_2$–temperature relationship. They should be interpreted comparatively rather than as intrinsic measures. The Statistical Validation Process described in Supplementary Material, Appendix B, should provide guidance as to whether the correlation analysis of individual pairs be considered significant.

### *3.2 Statistical Validation Framework (SVF) Summary*

Given the well-documented concerns regarding autocorrelation, long-range dependence (LRD), and smoothing-induced bias in paleoclimate time series, a dedicated Statistical Validation Framework (SVF) was developed and applied to all Pearson correlation results in this study. The SVF combines multiple diagnostic tests to safeguard against false-positive inferences and ensures that any reported associations between $CO_2$ and temperature meet rigorous statistical thresholds.

As outlined in the Methods section and detailed fully in Supplementary Material, Appendix B, the SVF includes seven validation categories: (1) autocorrelation testing (Durbin-Watson (Durbin & Watson, 1950), Breusch-Godfrey (Breusch, 1978; Godfrey, 1978), and Ljung-Box (Ljung & Box, 1978)); (2) Hurst exponent analysis using R/S, DFA, and GPH methods; (3) HAC (Heteroskedasticity and Autocorrelation Consistent) standard errors; (4) estimation of the effective sample size (Neff); (5) block permutation testing; (6) false discovery rate (FDR) correction; and (7) final significance classification based on joint criteria. The goal of the SVF is not to suppress correlation results but to distinguish robust signal from statistical artifact in the presence of serial correlation and LRD — concerns highlighted by Koskinas et al. (2022), Koutsoyiannis (2024c), and others.

Out of 64 primary $CO_2$–temperature pairs evaluated (across multiple lags and smoothing levels), 79 of 320 pairings passed at least one SVF statistical significance threshold, with Neff ≥ 10 or Neff ≥ 8. Most statistically reliable results ($r_{PCC}$ passing all SVF tests) occurred in unsmoothed or lightly smoothed datasets — especially the Original and Running Average 50 (RA 50) $CO_2$ series. A smaller number of valid results emerged from RA 100 and Loess-smoothed datasets, though these were treated with caution due to inflation risk. These outcomes reinforce the overall finding that correlation strength alone is not sufficient to infer significance without correcting for structural dependencies.

In order to reduce serial dependence and improve the reliability of statistical inference, all correlation analyses were performed on down-sampled series. All pairs were down-sampled by five subsets (every $1/10^{th}$, $1/20^{th}$, $1/30^{th}$, $1/40^{th}$, and $1/50^{th}$). Final selection of unique pairs was based on Neff value, down-sampling, and n (final sample size), and to some degree $r_{PCC}$. Some pairs required more aggressive down-sampling depending on autocorrelation structure and overall series length. While down-sampling helps mitigate inflation of $r_{PCC}$ due to autocorrelation, it can also reduce the number of observations (n) available for correlation. To preserve meaningful statistical power, the final selection of unique, SVF-passing pairs balanced multiple criteria — including correlation strength ($r_{PCC}$), effective sample size (Neff), and actual sample count (n) as shown in Table B4, Supplementary Material, Appendix B. In a few cases, a slightly smaller Neff value was accepted in favor of a higher n value, provided all SVF thresholds were still satisfied. This conservative approach prioritized statistical validity while ensuring that results were not driven by overly small sample sizes.

Later, sections of this paper will visually display selected $CO_2$–temperature pairs using smoothed Loess curves for interpretive clarity, but will explicitly annotate on each figure whether the underlying pair passed SVF criteria in its Original or RA 50 form. A summary comparison chart showing Original, RA 50, and Loess curves will also be provided to highlight their structural similarity and justify visual interpretation. In this way, SVF results are fully transparent and integrated, allowing readers to assess both statistical and visual coherence across all candidate relationships.

### *3.3 Structural Break or Regime Shift in the $CO_{2Lag}$ and Temperature Data at 1600 AD*

Unexpected behavior across the boundary of 1600 AD in the $CO_{2Lag}$ and temperature data, prompted testing for stability or non-stationarity in the $CO_2$–temperature relationship. Therefore, formal structural break analysis centered on 1600 AD was conducted. This breakpoint was hypothesized based on a marked reduction in correlation when extending from the 200–1600 AD segment to the full 200–1850 AD range. It is also about the time period where $CO_{2Lag}$ accelerated higher exponentially; temperature accelerated higher; and the nadir of the Little Ice Age occurs. Supplementary Material, Appendix C, details the application of three diagnostic tests: (1) the Chow test for structural discontinuity (Chow, 1960), (2) segmented Pearson correlation analysis, and (3) regression slope comparison across pre- and post-1600 intervals. Results show a highly significant F-statistic (F = 877.23) and an ~87% drop in regression slope post-break, alongside the collapse of full-span correlation ($r \approx -0.06$). These findings collectively indicate either a statistical phenomenon (structural break) or a large ecosystem change (regime shift) in system dynamics at 1600 AD, warranting the partitioning of subsequent analyses into distinct temporal phases. A detailed discussion with test results, about the structural break or regime shift, is presented in Supplementary Material, Appendix C.

### *3.4 Data Results - $CO_2$ vs. Temperature (1600-1850 AD)*

The data within the range of 1600-1850 AD was analyzed separately due to three previous outcomes:

1. The analysis of the entire range of $CO_2$ and temperature data from 200-1850 AD
2. The evidence of a structural break or regime shift in the data at 1600 AD shown in section 3.2
3. The analysis of the range of data from 200-1600 AD as shown in section 3.1

A more robust correlation analysis approach was conducted with one transformation level of the data, Running Average (50-yr centered). This was due to the structural break condition at about 1600 AD and the exceptional steep trending slopes of both $CO_2$ and temperature after 1600 AD. This approach calculated the following (Table A23 in Supplementary Material, Appendix A):

1. $r_{PCC}$ (no lag of $CO_2$ to temperature)
2. $r_{PCC}$ (maximum $r_{PCC}$) (calculated from -100 to +250 lag years in 5 yr intervals)
3. lag (lag interval with the maximum $r_{PCC}$)
4. Averages of each calculated parameter per $CO_2$ and temperature source

Three $CO_2$ sources and 6 temperature sources were utilized from this study.

The following steps were followed in deriving the results:

1. Cubic Transformation of $CO_2$ to enhance sensitivity to relative increases (Hyndman & Athanasopoulos, 2018).
2. The cubed $CO_2$ series was linearly detrended to remove long-term trends and better isolate internal variability (Granger & Newbold, 1974: Box et al., 2015).
3. Normalization of both $CO_2$ and temperature using min-max scaling to enable direct comparison. This technique facilitates comparative analysis, particularly when applying regression-based methods across differently scaled data (James et al., 2021).
4. Smoothing via a 50-yr Running Average to reduce high frequency variability. In correlation metrics smoothing improves stability while preserving decadal patterns of climate variability (von Storch & Zwiers, 1999).
5. Lag-alignment of $CO_2$ to temperature was calculated utilizing a lag range of -100 to 250 yr in 5-yr increments to determine the lag of the highest $r_{PCC}$ value. This both identifies the

lag and tests the hypothesis of a $CO_2$ to temperature of about 150 yr as observed with the data from 200-1600 AD (Granger, 1969; Mudelsee, 2010).

6. Pearsons Correlation Coefficients were calculated conditionally, in the same manner as for the data range of 200-1600 AD, since autocorrelation and long-term memory are issues that could inflate $r_{PCC}$ somewhat (Beran, 1994).

The data in 1600-1850 AD is similar to the range of 200-1600 AD in that it is autocorrelated and exhibits evidence of long-memory behavior, however based on the previous analysis shown in Supplementary Material, Appendix A, use of $r_{PCC}$ is considered conditionally acceptable for this study.

Referring to Table A23, in Supplementary Material, Appendix A, there are a few observations made for this RA 50 smoothing level data:

1. The average correlation is 0.85 at an average lag of 199 yr (range 130-250). This is a Very Strong correlation.
2. The average correlation is 0.29 at No Lag, indicating the hypothesis of $CO_2$ lagging temperature by about 150 yr is strong, and not the reverse, as popularly hypothesized.
3. The strongest lagged relationship is observed between the Juckes temperature series and Ahn $CO_2$ data ($r_{PCC} = 0.99$ at a lag of 210 yr).
4. Based on the data alone, it appears the relationship of $CO_2$ to temperature is not significantly different between the two ranges of data (200-1600 AD and 1600-1850 AD), even with the structural break at 1600 AD. $CO_2$ lags temperature by at least 150 yr, which effectively places all of the $CO_2$ data to present day as influenced centennially by temperature about 150 ys in the past.

### *3.5 Graphical Results - Original $CO_2$ and Temperature (200-1600 AD)*

Visual and correlation analysis of $CO_2$ versus temperature results are presented utilizing many of the widely recognized studies of $CO_2$ and temperature covering the past 2000 yr.

Conditional correlation analysis in the form of $r_{PCC}$ has been conducted on all of the data analyzed, and all 5 forms including the Original data (Orig), Running Average (RA 50); Running Average (RA 100); Loess 1 (lesser smoothing algorithm); and Loess 2 (greater smoothing algorithm). Maximum $r_{PCC}$ – lag analysis was also conducted and results are shown on Tables A1 through A22 in Supplementary Material, Appendix A.

As discussed in detail in the Supplementary Material, Appendix B, a robust statistical analysis, Statistical Validation Framework (SVF), has been conducted on all data in this study, and roughly 25% of the $r_{PCC}$ pairs passed statistical significance at either Robustly Significant or Tentatively Significant. Thus, all of the charts shown will identify this status. In many cases a chart will be presented at a higher smoothing factor, which itself has not passed the SVF, but one of its other variants has, and this status will be identified. For example, a Loess 2 chart may be shown (not passed), but it is a smoothed variant of an Orig or RA 50 that has passed the full SVF, meeting all criteria. Rather than formal inference, the purpose of the Loess 2 Chart would be to present an enhanced visual expression of the validated version illustrating the temporal and structural alignment in a visually compelling manner, not necessarily introducing an entirely new relationship. In these cases, the Loess 2 chart would be labelled as "conditional", based on the corresponding Orig or RA 50 SVF pass status. This illustrates that while high smoothing can visually enhance apparent alignment, formal inference must rely on statistical validation. This is consistent with best practices in statistical communication, where exploratory or supporting plots are distinguished from validated results (Kauffman et al., 2020; McGregor et al., 2013; Tufte, 2001; Gelman & Hill, 2006).

Fig. 1 shows a good example of the original data of $CO_2$ (Rubino et al., 2019) plotted against the original data of temperature (Ljungqvist, 2010) from about 1 to 2000 AD. Upon inspection, even with a noise component, it is apparent the two curves visually correlate very well with each other, but only if the $CO_2$ curve is time-shifted 150 yr earlier to correct for the $CO_2$ lag. Both the original $CO_2$ curve and the shifted $CO_2$ curves reflecting the lag are shown in the figure.

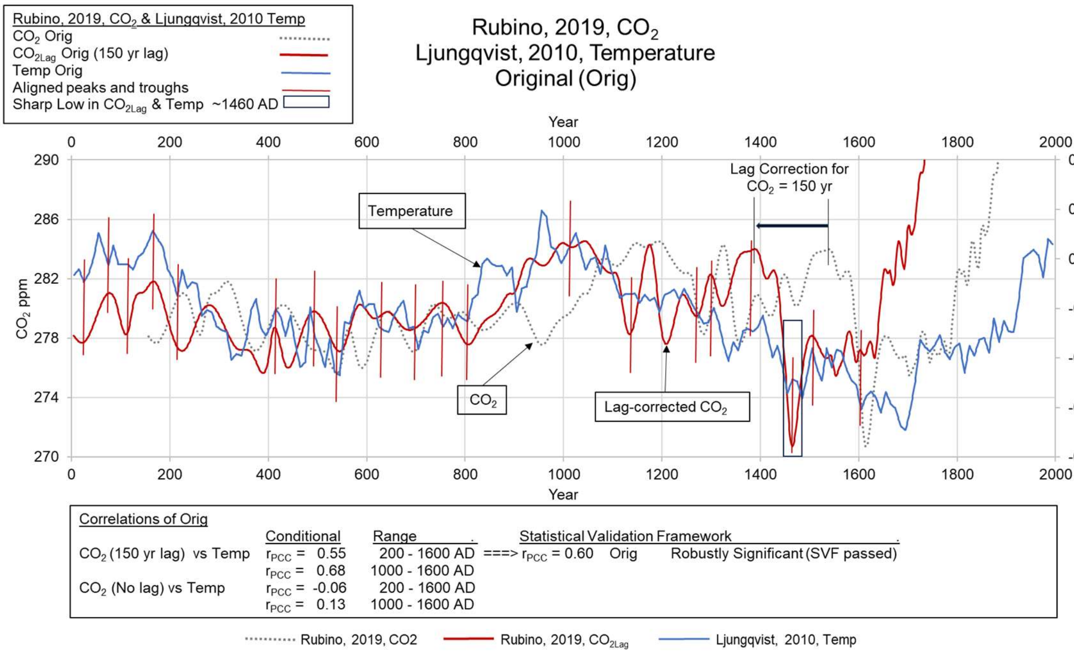

Correlations of Orig

| | Conditional | Range | | Statistical Validation Framework | | |
|---|---|---|---|---|---|---|
| $CO_2$ (150 yr lag) vs Temp | $r_{PCC}$ = 0.55 | 200 - 1600 AD | ===> | $r_{PCC}$ = 0.60 | Orig | Robustly Significant (SVF passed) |
| | $r_{PCC}$ = 0.68 | 1000 - 1600 AD | | | | |
| $CO_2$ (No lag) vs Temp | $r_{PCC}$ = -0.06 | 200 - 1600 AD | | | | |
| | $r_{PCC}$ = 0.13 | 1000 - 1600 AD | | | | |

*Figure 1. Original $CO_2$ and temperature data (from Rubino et al., 2019; Ljungqvist, 2010, respectively) are shown from 1 to 2000 AD along with the $CO_2$ curve shown with a 150-yr lag correction. Aligned peaks and troughs are depicted with thin red lines. A sharp low in $CO_{2Lag}$ and temperature are shown at about 1460 AD. $r_{PCC}$ is shown for lagged 150 yr and no lag for both ranges of 200-1600 AD and 1000-1600 AD. Orig for this pair is directly validated under SVF, and its correlation is presented here conditionally, supported by the corresponding result, Robustly Significant (SVF passed). The complete list of SVF passed pairs is in Supplementary Material, Appendix B, Table B4.*

Visual correlations covering peaks and troughs of 50-100 yr as well as 800-1000 yr are observed between the two curves of $CO_{2Lag}$ and temperature. Aligned peaks, or peak-clusters, are observed at about 80, 175, 410, 490, 590, 740, 920-1100, 1240, 1300, 1360-1420, and 1500-1575 AD. Correlative troughs can also be observed, in particular, the deep trough at about 1460 AD. At this year, with close precision, a deep trough is identified on almost every $CO_{2Lag}$ and temperature pair analyzed in this study.

At about 1775 AD for $CO_2$ and 1625 AD for $CO_{2Lag}$, the $CO_2$ curves take a sharp and exponentially high shift probably coinciding with the temperature curve which begins to increase more steeply, but at a much lower slope than $CO_2$. The Little Ice Age spanning from about 1100-1300 AD to about 1900 AD shows its latter upward temperature recovery from about 1700 to about 1900 AD, as it moves out of the low point of the Little Ice Age.

Fig. 1 also shows two broad trends of temperature: (1) peaks at about 100 AD and about 1000 AD with a trough at about 500 AD, and (2) peaks at about 1000 AD and about 2000 AD with a trough at about 1500 AD. These features may be associated with the 1000-yr cyclicity of earth climate indices and solar activity -- Eddy Cycle (Zhao et al., 2020). While there is not adequate length of data in the temperature records presented here to define a cycle of that nature, the amount of data that is present is consistent with the proposed, but not proven, Eddy cycle. However, below in this article, data is presented showing relative correlation between the temperature data curves and Total Solar Irradiance.

Fig. 2 shows the original data of $CO_2$ from (Rubino et al., 2019) plotted against the original data of temperature from Moberg et al. (2005) for the same period in the last 2000 yr. Similar to Fig. 1, the $CO_2$ curve and temperature curve in Fig. 2 correlate visually only when the $CO_2$ curve is shifted 150 yr.

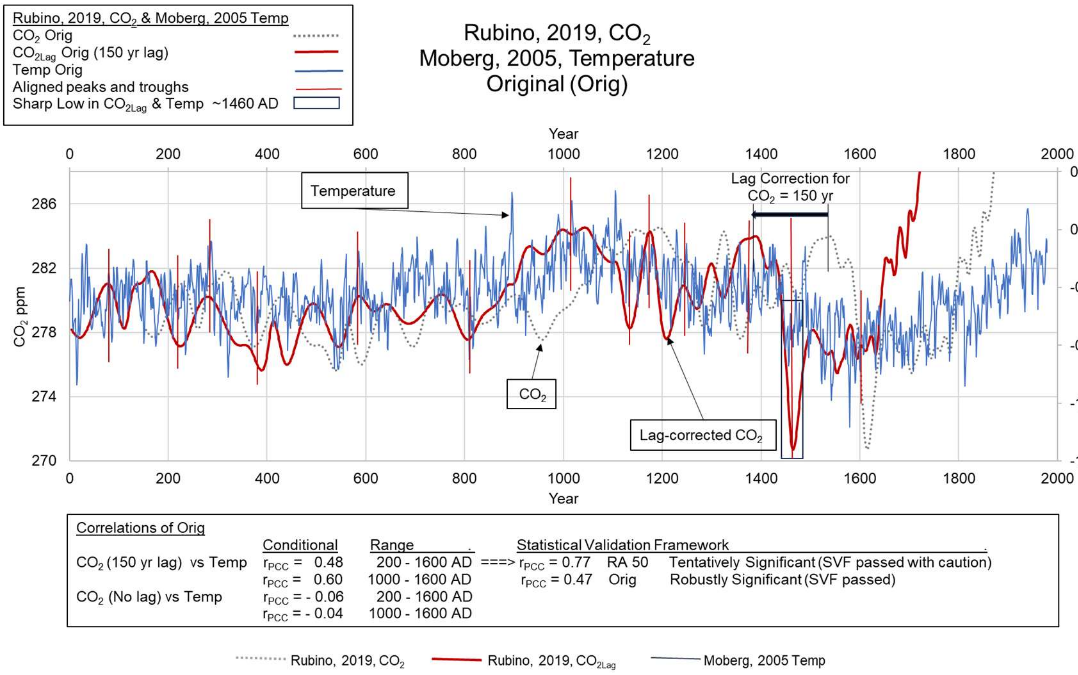

*Figure 2. Original $CO_2$ and temperature data (from Rubino et al., 2019; Moberg, 2005, respectively) are shown from 1 to 2000 AD along with the $CO_2$ curve shown with a 150-yr lag correction. Aligned peaks and troughs are depicted with thin red lines. A sharp low in $CO_{2Lag}$ and temperature are shown at about 1460 AD. $r_{PCC}$ is shown for $CO_2$ lagged 150 yr and no lag for both ranges of 200-1600 AD and 1000-1600 AD. Orig for this pair is directly validated under SVF, and its correlation is presented here conditionally, supported by the corresponding result, Robustly Significant (SVF passed). The variant, RA 50, is also SVF-validated at Tentaatively Significant, passed with caution. The complete list of SVF passed pairs is in Supplementary Material, Appendix B, Table B4.*

While evaluating the original published data included in Fig.1 and Fig. 2, even with a high noise-level component, certain key common observations can be made:

1. The $CO_{2Lag}$ of about 150 yr with temperature, is consistent and representative of all 64 original pairs of $CO_2$ versus temperature data in this study.
2. The $CO_{2Lag}$ curve is interrupted by a shift in the $CO_2$ curves at about 1600 AD (1750 AD on the $CO_2$ non-lagged curve). While $CO_2$ accelerates rapidly from this point, temperature climbs, but at a lower rate. This observation is consistent with all 64 data correlations.
3. Many peaks and troughs, and peak-trough clusters, of varying widths from 10 yr to 150 yr, appear to visually correlate between the $CO_{2Lag}$ and temperature curves.
4. There is a sharp notched decline of both $CO_{2Lag}$ and temperature at about 1460 AD with a width of 50 yr to 80 yr. This distinctive feature appears as a signature marker on all 64 correlations of $CO_{2Lag}$ and temperature.
5. A potential long cycle is observed on the temperature curves (shadowed by the $CO_{2Lag}$ curves) with peaks at about 100, 1000, and 2000 AD, and troughs at about 550 and 1500 AD, with a frequency cycle of about 1000 yr. This appears to very closely shadow the proposed Eddy Cycle for this range of data (Zhao et al., 2020). A longer data record showing these repeatable features with several major peaks and troughs would be desirable.

### 3.6. Graphical Results - Smoothed $CO_2$ and Temperature (200-1600 AD)

Fig. 3 presents five curves representing all smoothing transformation variants for a specific temperature series, (Hegerl, 2007), which shows the degree of variation in the charted curves typical of all of the series in the study. The Orig (violet) curve is the original published data which generally has more noise. However, this curve retains the sharper peaks and troughs which represent key markers, such as the marker at 1460 AD which is observed on almost all of the curves in this study: $CO_{2LAG}$ at 150 yr, temperature, and Total Solar Irradiance (TSI). The RA 50 (black) curve is the least-smoothed of the transformed curves, but retains the major peaks and troughs while shedding the minor noise. The RA 100 (red) curve is often very close to the Loess 1 (green) curve in character, and maintains the more major peaks and troughs while shedding the minor ones. The Loess 2 (blue) curve is the most smoothed, and generally reflects the more regional trends, while it smooths away the noise and smaller more granular features.

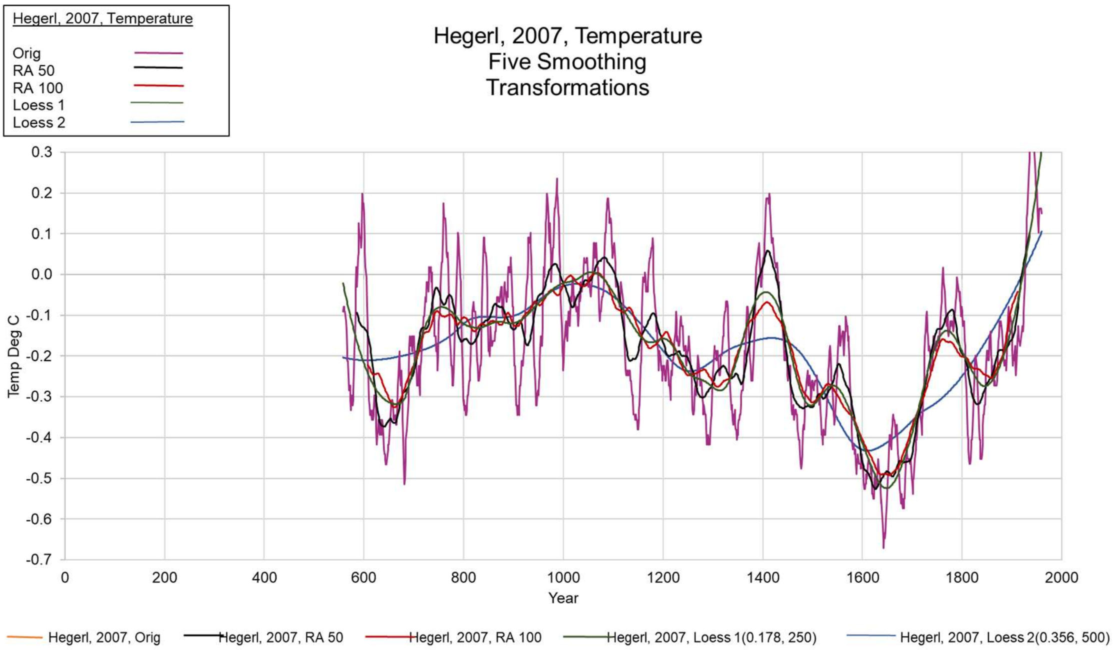

*Figure 3. Presents five forms of the temperature series, Hegerl et al., 2007: Original published data, Orig; Running Average centered on 50 yr, RA 50; Running Average centered on 100 yr, RA 100; smoothing algorithm, Loess 1 (Loess, 0.178, 250); and smoothing algorithm, Loess 2 (Loess, 0.356, 500).*

As displayed below in Fig. 4, on the Running Average (RA 50) chart, the visual correlation is excellent for the two curves — (1) Ljungqvist (2010) temperature (blue) and (2) Rubino et al. (2019) $CO_{2Lag}$ (red). The $CO_{2Lag}$ curve is time-shifted 150 yr earlier to correct for the lag. This is shown by the curves tracing each other from 200 to 1600 AD. The original $CO_2$ curve represented by a dashed light gray curve is clearly out of synch with the temperature curve. Several thin vertical red lines are drawn to highlight close orientation of many of the peaks and troughs showing more granular alignment. The general curvature aligned between the two curves over 2000 yr is easily apparent. From 1600 AD to about 1850 AD, the lagged-$CO_2$ and temperature curves also track on steep inclinations with $CO_{2lag}$ having a slightly steeper slope. Similar to the Original curves in Fig. 1, the visual correlation is excellent as are the conditional $r_{PCC}$ correlation numbers. For the data range 1000-1600 AD the $r_{PCC}$ is stronger. The comparison of the $CO_{2Lag}$ vs. no lag is striking with $r_{PCC}$ showing 0.81 and 0.28 for the data range of 1000-1600 AD and 0.67 and 0.06 for the data range of 200-1600 AD. This sharp differential of Strong correlation to No correlation agrees with the visual inspection of the chart where $CO_2$ is clearly offset by 150 yr. The running average smoothing, centered at 50 yr (RA 50), allows easier visual review than Orig, while the smoothing modifies the curve only slightly by removing noise, smaller inflections, and localized features. Although RA 50 smoothing for this pair is not directly validated under SVF, its correlation is presented here conditionally, supported by the corresponding Orig variant which passed full SVF criteria for statistical significance with Robustly Significant (SVF passed). The complete list of SVF passed pairs is in Supplementary Material, Appendix B, Table B4.

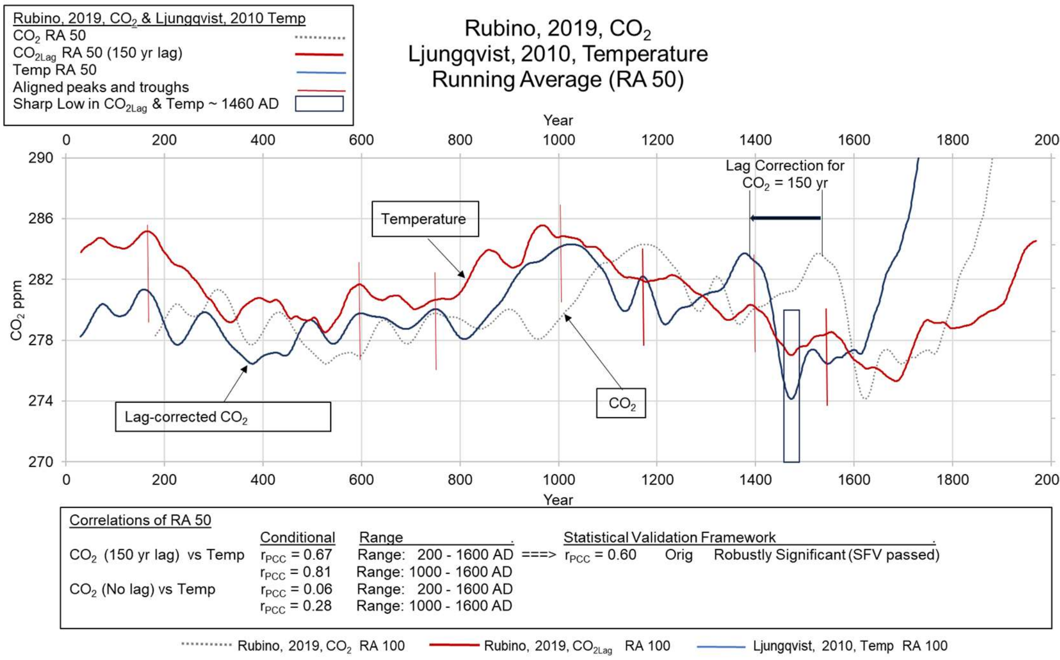

*Figure 4. Running Average smoothing, centered 50 yr, (RA 50), CO$_2$ and temperature data (from Rubino et al., 2019; Ljungqvist, 2010, respectively) are shown from 1 to 2000 AD along with the CO$_2$ curve shown with a 150-yr lag correction. Aligned peaks and troughs are depicted with thin red lines. $r_{PCC}$ is shown for 150-yr lag and no lag for both ranges of 200-1600 AD and 1000-1600 AD. Although RA 50 smoothing for this pair is not directly validated under SVF, its correlation is presented here conditionally, supported by the corresponding Orig variant which passed full SVF criteria for statistical significance with Robustly Significant (SVF passed). The complete list of SVF passed pairs is in Supplementary Material, Appendix B, Table B4.*

Another excellent example of visual correlation is a chart showing RA 100 smoothing with a Very Strong $r_{PCC}$, as observed in Fig. 5. Several thin vertical red lines are drawn to highlight key peaks and troughs. In this chart, Rubino et al. (2019) is compared to Yang et al. (2002). The continuous alignment over the 2000 yr is striking when comparing the temperature (blue) to CO$_{2Lag}$ (red) curves. The CO$_{2Lag}$ curve is corrected 150 yr from its original position shown by CO$_2$ (dotted gray). From 1600 AD to about 1850 AD, the lagged-CO$_2$ and temperature curves also track on steep inclinations with CO$_{2lag}$ having a slightly steeper slope. This is similar as observed in Fig. 4. For the data range, 1000-1600 AD, the $r_{PCC}$ is stronger. The comparison of the CO$_{2Lag}$ vs. no lag is impressive with $r_{PCC}$ showing 0.93 and 0.15 for the data range of 1000-1600 AD and 0.72 and 0.13 for the data range of 200-1600 AD. The Very Strong correlation to Weak correlation agrees with the visual review of the chart where CO$_2$ is clearly offset by 150 yr. Comparisons of $r_{PCC}$ should be considered conditional, as mentioned previously. Even though RA 100 is not directly validated under SVF, Orig and RA 50 for this pair are both directly validated, and the $r_{PCC}$ correlation is presented here conditionally, supported by the corresponding result, Robustly Significant (SVF passed). Smoothing visually enhances apparent alignment, but should be statistically validated for formal inference. The complete list of SVF passed pairs is in Supplementary Material, Appendix B, Table B4.

Loess smoothing was applied to all pairs of CO$_2$ and temperature as well as all pairs of CO$_{2Lag}$ and temperature in this study. Two levels of Loess were applied, somewhat subjectively. Loess 1 tends to be close to RA 100, while Loess 2 is smoother, and tends to eliminate more local features, accentuating the larger-scale features.

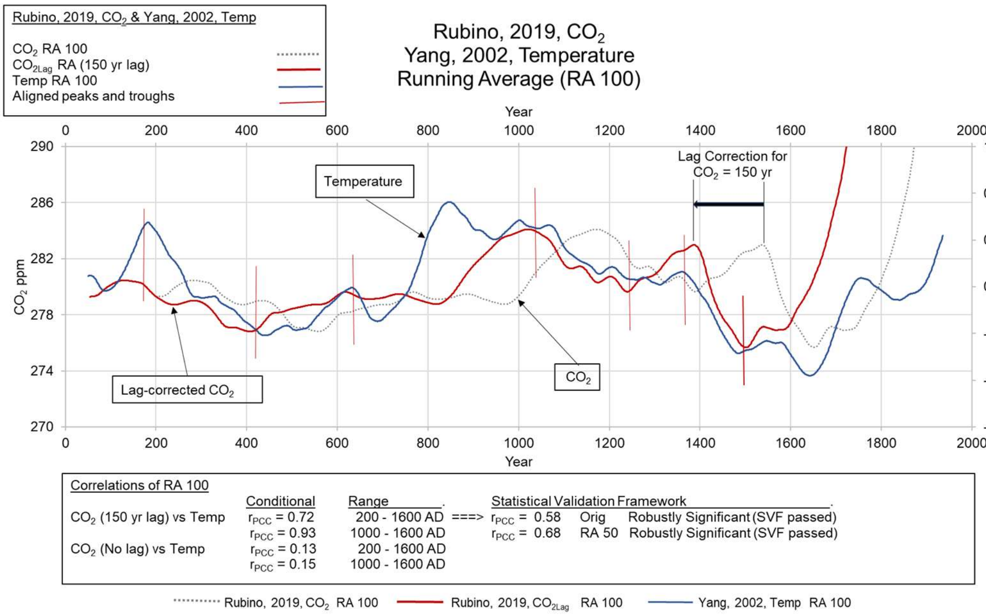

*Figure 5. Running Average smoothing, 100 yr, centered, $CO_2$ and temperature data (from Rubino et al., 2019; Yang et al., 2002, respectively) are shown from 1 to 2000 AD along with the $CO_2$ curve shown with a 150-yr lag correction. Aligned peaks and troughs are depicted with thin red lines. $r_{PCC}$ is shown for $CO_2$ lagged 150 yr and no lag for both ranges of 200-1600 AD and 1000-1600 AD. Although RA 100 is not directly validated under SVF, Orig and RA 50 for this pair are both directly validated, and the $r_{PCC}$ correlation is presented here conditionally, supported by the corresponding result, Robustly Significant (SVF passed). Smoothing visually enhances apparent alignment, but should be statistically validated for formal inference. The complete list of SVF passed pairs is in Supplementary Material, Appendix B, Table B4.*

As discussed previously, $r_{PCC}$ is used conditionally in this study due to autocorrelation and long-memory issues, although mitigated with various tests and methods (SVF). It should be noted that one of the concerns with autocorrelation and long-memory is an inflation of $r_{PCC}$, which is exhibited in the data, where $r_{PCC}$ is increasingly larger from Original to RA 100 to Loess 1 to Loess 2. However, visually comparing the curves where higher $r_{PCC}$ values are found does show commensurately closer visual correlation. Comparing the relative values of a maximum $r_{PCC}$ at an observed lag for $CO_{2Lag}$ against $r_{PCC}$ for the no lag case will not be an issue. It subjectively appears that the increase in $r_{PCC}$ as additional smoothing is applied, for the data in this study, is due to a combination of the two factors—some inflation due to autocorrelation and long memory effects and a resulting closer correlation for the broader more regional aspect. In either event the approach discussed previously in applying a battery of statistical tests associated with the Statistical Validation Framework appears to add confidence to using the $r_{PCC}$ data more quantitatively when the correlated pairs pass either as Robustly Significant (SVF passed) or Tentatively Significant (SVF passed with caution) (in Supplementary Material, Appendix B, Table B4).

Four typical examples of smoothed data are shown respectively in Fig. 6, based on Loess 2 smoothed data by Rubino et al. (2019) and Ljungqvist (2010), Fig. 7, based on Loess 2 smoothed data by Rubino et al. (2019) and Yang et al. (2002), Fig. 8, based on Loess 2 smoothed data by MacFarling Meure et al. (2006) and Hegerl et al. (2007), and Fig. 9, MacFarling Meure et al. (2006) and Yang et al. (2002). The smoothed curves show a very close visual relationship between $CO_{2Lag}$ and temperature. Large scale rolling peaks and troughs exhibit strong visible correlation, and the conditional correlation $r_{PCC}$ values are Very Strong as labelled on the figures. The $CO_{2Lag}$ curves have both been corrected by 175 (Fig. 6), 150 (Fig. 7), 120 (Fig. 8), and 150 (Fig. 9) yr for $CO_2$ lag, respectively, as indicated by correlation analysis as a function of lag correction (Tables A9 and A10, Supplementary Material, Appendix A).

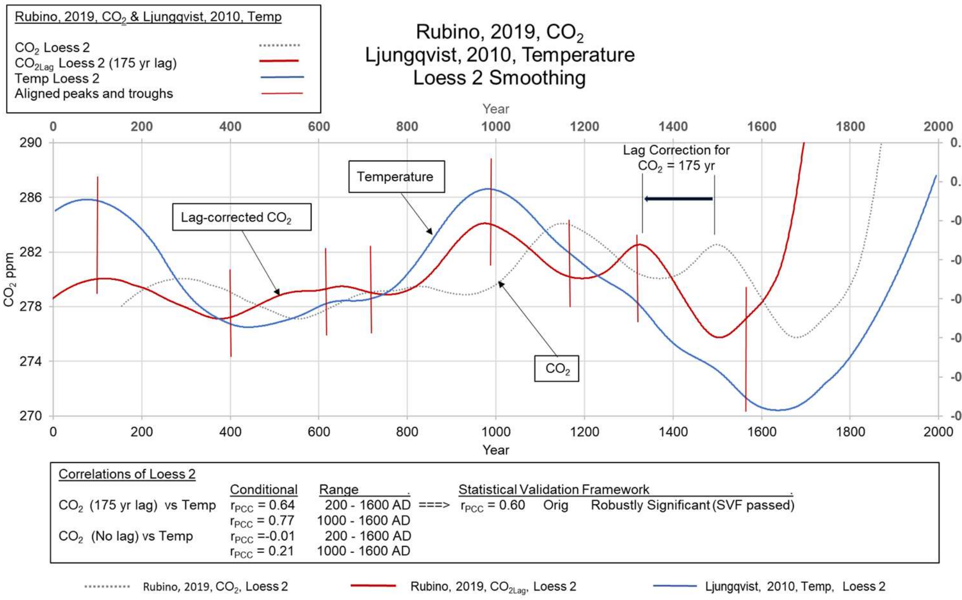

*Figure 6. Loess 2 smoothing, $CO_2$ and temperature data (from Rubino et al., 2019; Ljungqvist, 2010, respectively), are shown from 1 to 2000 AD along with the $CO_2$ curve shown with a 175 yr lag correction. Aligned peaks and troughs are depicted with thin red lines. $r_{PCC}$ is shown for $CO_{2Lag}$ lagged 175 yr and no lag for both ranges of 200-1600 AD and 1000-1600 AD. Although Loess 2 smoothing for this pair is not directly validated under SVF, its correlation is presented here conditionally, supported by the corresponding Orig variant which passed full SVF criteria for statistical significance with Robustly Significant (SVF passed). High smoothing visually enhances apparent alignment, but should be statistically validated for formal inference. The complete list of SVF passed pairs is in Supplementary Material, Appendix B, Table B4.*

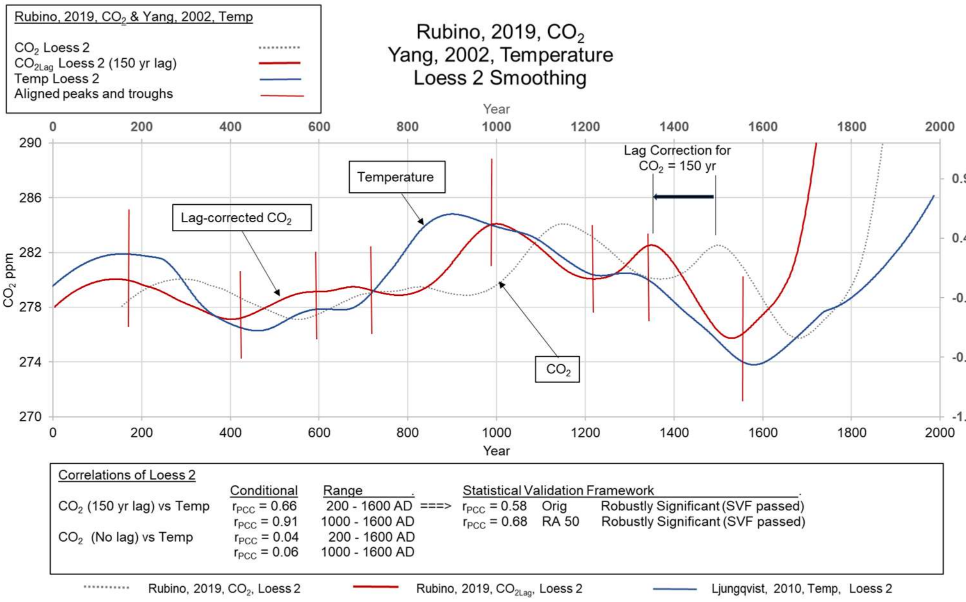

*Figure 7. Loess 2 smoothing, $CO_2$ and temperature data (from Rubino et al., 2019; Yang et al., 2002, respectively), are shown from 1 to 2000 AD along with the $CO_2$ curve shown with a 150-yr lag correction. Aligned peaks and troughs are depicted with thin red lines. $r_{PCC}$ is shown for $CO_{2Lag}$ lagged 150 yr and no lag for both ranges of 200-1600 AD and 1000-1600 AD. Although Loess 2 smoothing for this pair is not directly validated under SVF, its correlation is presented here conditionally, supported by the corresponding Orig and RA 50 variants which passed full SVF criteria for statistical significance with Robustly Significant (SVF passed). High smoothing visually enhances apparent alignment, but should be statistically validated for formal inference. The complete list of SVF passed pairs is in Supplementary Material, Appendix B, Table B4.*

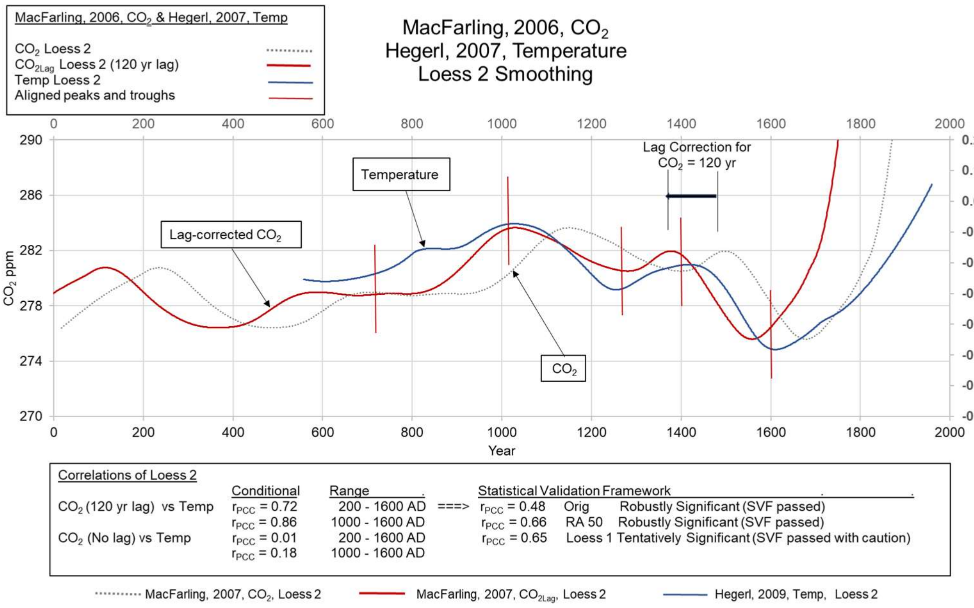

*Figure 8. Loess 2 smoothing, $CO_2$ and temperature data (from MacFarling Muere et al., 2006; Hegerl et al., 2007, respectively), are shown from 1 to 2000 AD along with the $CO_2$ curve shown with a 120-yr lag correction. Aligned peaks and troughs are depicted with thin red lines. $r_{PCC}$ is shown for $CO_{2Lag}$ lagged 120 yr and no lag for both ranges of 200-1600 AD and 1000-1600 AD. Although Loess 2 smoothing for this pair is not directly validated under SVF, its correlation is presented here conditionally, supported by the corresponding Orig and RA 50 variants which passed full SVF criteria for statistical significance with Robustly Significant (SVF passed). Its correlation is also supported by the corresponding Loess 1 variant which passed SVF criteria for statistical significance with Tentatively Significant (SVF passed with caution). High smoothing visually enhances apparent alignment, but should be statistically validated for formal inference. The complete list of SVF passed pairs is in Supplementary Material, Appendix B, Table B4.*

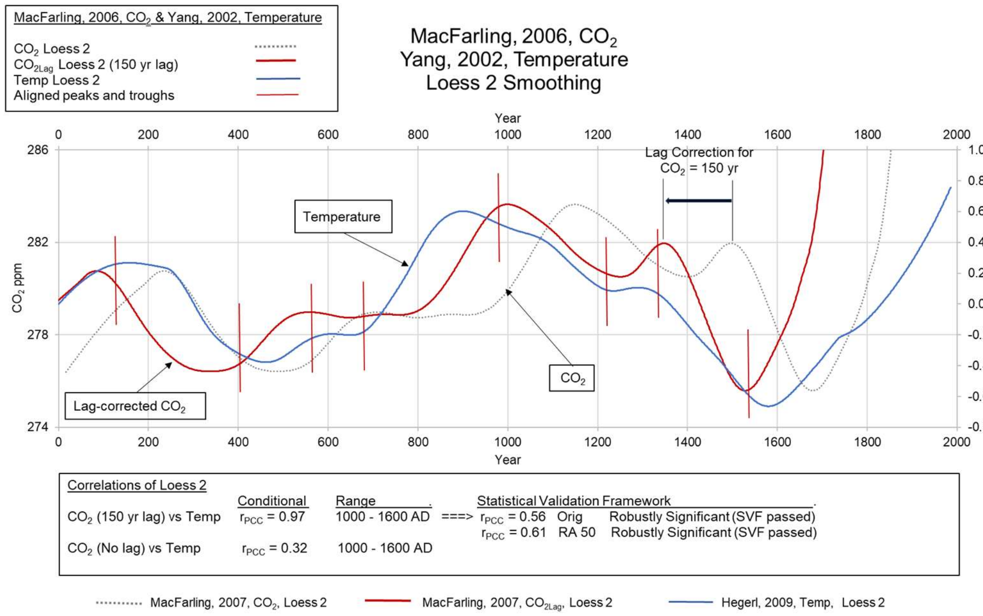

*Figure 9. Loess 2 smoothing, $CO_2$ and temperature data (from MacFarling Meure et al., 2006; Yang et al., 2002, respectively), are shown from 1 to 2000 AD along with the $CO_2$ curve shown with a 150-yr lag correction. Aligned peaks and troughs are depicted with thin red lines. $r_{PCC}$ is shown for $CO_{2Lag}$ lagged 150 yr and no lag for both ranges of 200-1600 AD and 1000-1600 AD. Although Loess 2 smoothing for this pair is not directly validated under SVF, its correlation is presented here conditionally, supported by the corresponding Orig and RA 50 variants which passed full SVF criteria for statistical significance with Robustly Significant (SVF passed). High smoothing visually enhances apparent alignment, but should be statistically validated for formal inference. The complete list of SVF passed pairs is in Supplementary Material, Appendix B, Table B4.*

On all four charts (Fig. 6, Fig. 7, Fig. 8, and Fig. 9) at about 1600 AD show an exponential rate of increase in $CO_{2Lag}$ and temperature, as does the corresponding $CO_2$ curve at about 1750 AD, whereas the temperature curve depicts a much smaller rate of increase. All four charts identify with one to two variant curves that have passed the SVF as Robustly Significant, while one chart added a third pass, Tentatively Significant, passed with caution. High smoothing visually enhances apparent alignment, but should be statistically validated for formal inference as thes charts signify. The complete list of SVF passed pairs is in Supplementary Material, Appendix B, Table B4.

Fig. 10 presents another chart of $CO_2$, $CO_{2Lag}$, and temperature with pairs at Loess 2 with a 130-yr lag of $CO_{2lag}$. This particular pair had three variants of which two have Robustly Significant (SVF passed) variants, Orig and RA 50. The other variant, RA 100, is Tentatively Significant (SVF passed with caution). The visual correlation is quite good, substantiating the $r_{PCC}$ and SVF results. This chart includes Rubino et al. (2019) $CO_2$ data and Hegerl et al. (2007) temperature data with excellent visual correlation and commensurate correlation data.

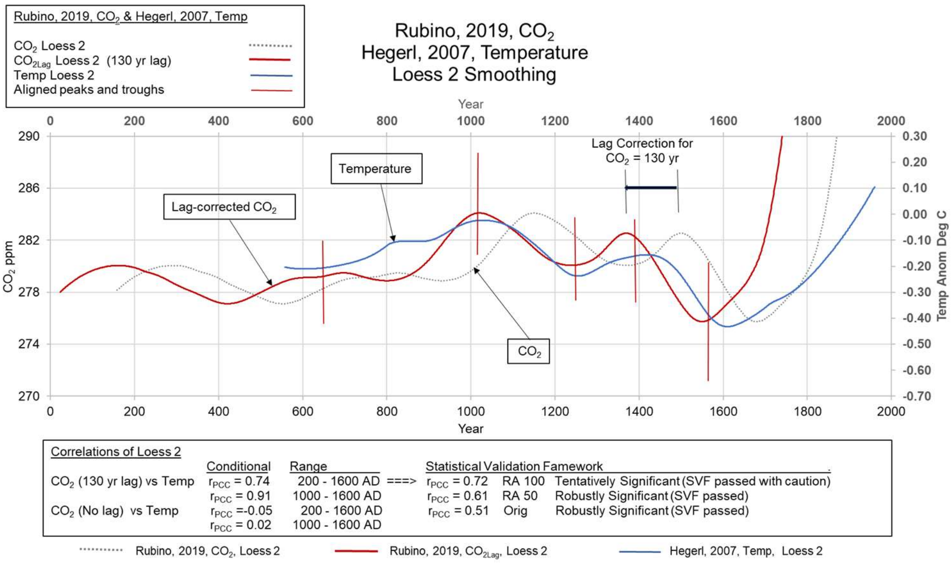

Correlations of Loess 2

| | Conditional | Range | | Statistical Validation Famework | | |
|---|---|---|---|---|---|---|
| $CO_2$ (130 yr lag) vs Temp | $r_{PCC} = 0.74$ | 200 - 1600 AD | ===> | $r_{PCC} = 0.72$ | RA 100 | Tentatively Significant (SVF passed with caution) |
| | $r_{PCC} = 0.91$ | 1000 - 1600 AD | | $r_{PCC} = 0.61$ | RA 50 | Robustly Significant (SVF passed) |
| $CO_2$ (No lag) vs Temp | $r_{PCC} = -0.05$ | 200 - 1600 AD | | $r_{PCC} = 0.51$ | Orig | Robustly Significant (SVF passed) |
| | $r_{PCC} = 0.02$ | 1000 - 1600 AD | | | | |

*Figure 10. Loess 2 smoothing, $CO_2$ and temperature data (from Rubino et al., 2019; Hegerl et al., 2007, respectively), are shown from 1 to 2000 AD along with the $CO_{2Lag}$ curve shown with a 130-yr lag correction. Aligned peaks and troughs are depicted with thin red lines. $r_{PCC}$ is shown for both analyzed ranges of 200-1600 AD and 1000-1600 AD. Although Loess2 for this pair is not directly validated under SVF, its correlation is presented here conditionally, supported by the corresponding variants RA 100, Tentatively Significant (SVF passed with caution), and RA 50 and Orig, both Robustly Significant (SVF passed).*

In summary, the graphical results for smoothed $CO_2$ and temperature data in the overall range of 200-1600 AD in this study, show a strong and reproducible visual correlation between temperature and $CO_2$ when it is $CO_2$ lag-corrected by about 150 yr. This relationship is consistent and continuous over the entire period and can be observed with the original published data and every variant tested (RA 50, RA 100, Loess 1, and Loess 2) for all combinations of 4 $CO_2$ series and 16 temperature series. Several combinations of $CO_2$ and temperature series are displayed the figures in this section of the report to show the consistency of correlation across the different published data.

Pearson's Correlation Coefficient was calculated for all pairs and variants as shown above, and with the confirmation of a significant number of pairs passing a rigorous Statistical Validation Framework process (in Supplementary Material, Appendix B), confidence can be placed in the results.

Although data was not included in this section above 1600 AD due to the structural break or regime shift discussed in Section 3.3, data results for range 1600-1850 are presented in Section

3.4, and graphical results for that data range are presented in Section 3.8.

### 3.7 Graphical Results – Smoothed Average $CO_2$ and Temperature (200-1600 AD)

All four $CO_{2Lag}$ smoothed data sets (Loess 2) identified in Table A10, Supplementary Material, Appendix A, were averaged to produce a composite $CO_{2Lag}$ curve. Eight temperature data sets (Loess 2) also shown on Table A10, Supplementary Material, Appendix A, were averaged to produce a composite temperature curve. Both the $CO_2$ and temperature were taken from Data Set A. The four $CO_{2Lag}$, eight temperature, composite $CO_{2Lag}$, and composite temperature curves are all shown on Fig. 11. The $CO_{2Lag}$ curves were corrected for $CO_2$ lag by 150 yr. Based on the temperature curves, warm periods and cool periods are shaded in light orange and light blue respectively. Key visually correlated peaks and troughs between $CO_{2Lag}$ and temperature are shown in red and blue dashed lines respectively. Named warm and cool periods over the last 2000 yr are identified along the base of Fig. 11 after Easterbrook (2016a).

Fig. 11 unambiguously shows the close visual relationship of the composite curves of $CO_{2Lag}$ (corrected for $CO_2$ lag by 150 yr) and composite temperature, as well as the non-lagged $CO_2$ curve, clearly out of phase with temperature. Conditional statistical correlation supports this observation with the following $r_{PCC}$ data:

| Year Range: | Data: | Correlation: | |
|---|---|---|---|
| 1000 – 1600 AD | $CO_{2Lag}$ (150-yr lag) | $r_{PCC} = 0.93$ | Very Strong |
| 1000 – 1600 AD | $CO_2$ (no lag) | $r_{PCC} = 0.05$ | None |
| 200 – 1600 AD | $CO_{2Lag}$ (150-yr lag) | $r_{PCC} = 0.73$ | Strong |
| 200 – 1600 AD | $CO_2$ (no lag) | $r_{PCC} = -0.07$ | None |

The averaged pairs of $CO_2$ and temperature contain similar autocorrelation and long memory issues that its underlying component series have, and there may be additional artificial inflation of correlation due to smoothing and aggregation. However, of the 64 pairs of combinations from Table A10, Supplementary Material, Appendix A, 60 pairs have variants (Orig and/or RA 50) that have passed the SVF process as mostly Robustly Significant. In the averaged case four average $CO_2$ and temperature pairs (Orig, RA 50, RA 100, and Loess 2) have been tested with the SVF, and one pair successfully passed – the Orig pair. The results are shown in Table 3.

Table 3. Results of the SVF testing for the Average $CO_2$ vs. Average Temperature records Data Set A are shown for the range, 200-1600 AD. $r_{PCC}$ is the Pearson's Correlation Coefficient; Samp Rate is the de-sampling rate to reduce the data points; n is the number of data points after de-sampling; Neff is the effective number of data points (Bretherton et al., 1999); Block-Perm-FDR p-values Grouped represents the process of using block permutations and grouped FDR (Fake Discovery Rate) showing p-values; HAC SE (Heteroskedasticity and Autocorrelation Consistent Standard Errors); and SVF Passing Category.

<table>
<tr><th colspan="9">Results of Statistical Validation Framework Testing<br>Average $CO_2$ vs. Average Temperature Correlation 200 -- 1600 AD</th></tr>
<tr><th>Avg $CO_2$ & Temp Pair</th><th>$r_{PCC}$</th><th>Samp Rate</th><th>n</th><th>Neff</th><th>Block-Perm-FDR p-value Grouped</th><th>Blocks Passed</th><th>HAC SE</th><th>SVF Passing Category</th></tr>
<tr><td>$CO_2$ & Temp (Orig)</td><td>0.63</td><td>20</td><td>71</td><td>13.5</td><td>$< 0.05$</td><td>1,5,10</td><td>2.91</td><td>Robustly Significant</td></tr>
<tr><td>$CO_2$ & Temp (RA 50)</td><td>0.68</td><td>20</td><td>71</td><td>5.8</td><td>$< 0.05$</td><td>1,5</td><td>4.55</td><td></td></tr>
<tr><td>$CO_2$ & Temp (RA 100)</td><td>0.71</td><td>30</td><td>47</td><td>4.7</td><td>$< 0.05$</td><td>1,5</td><td>4.89</td><td></td></tr>
<tr><td>$CO_2$ & Temp (Loess 2)</td><td>0,72</td><td>20</td><td>71</td><td>2.7</td><td>$< 0.05$</td><td>1,5,10</td><td>32.8</td><td></td></tr>
</table>

In Table 3 the Neff values on the Orig pair is strong, and the HAC SE value is commensurately low. Orig, RA 50, and RA 100, also passed on multiple blocks for FDR-grouped permutations p-value. The Neff values, being less than 8, are the primary reason for not passing SVF. Although Loess 2 for this averaged pair scenario is not directly validated under SVF, its correlation is presented here conditionally, supported by the corresponding Orig, passing Robustly Significant (SVF).

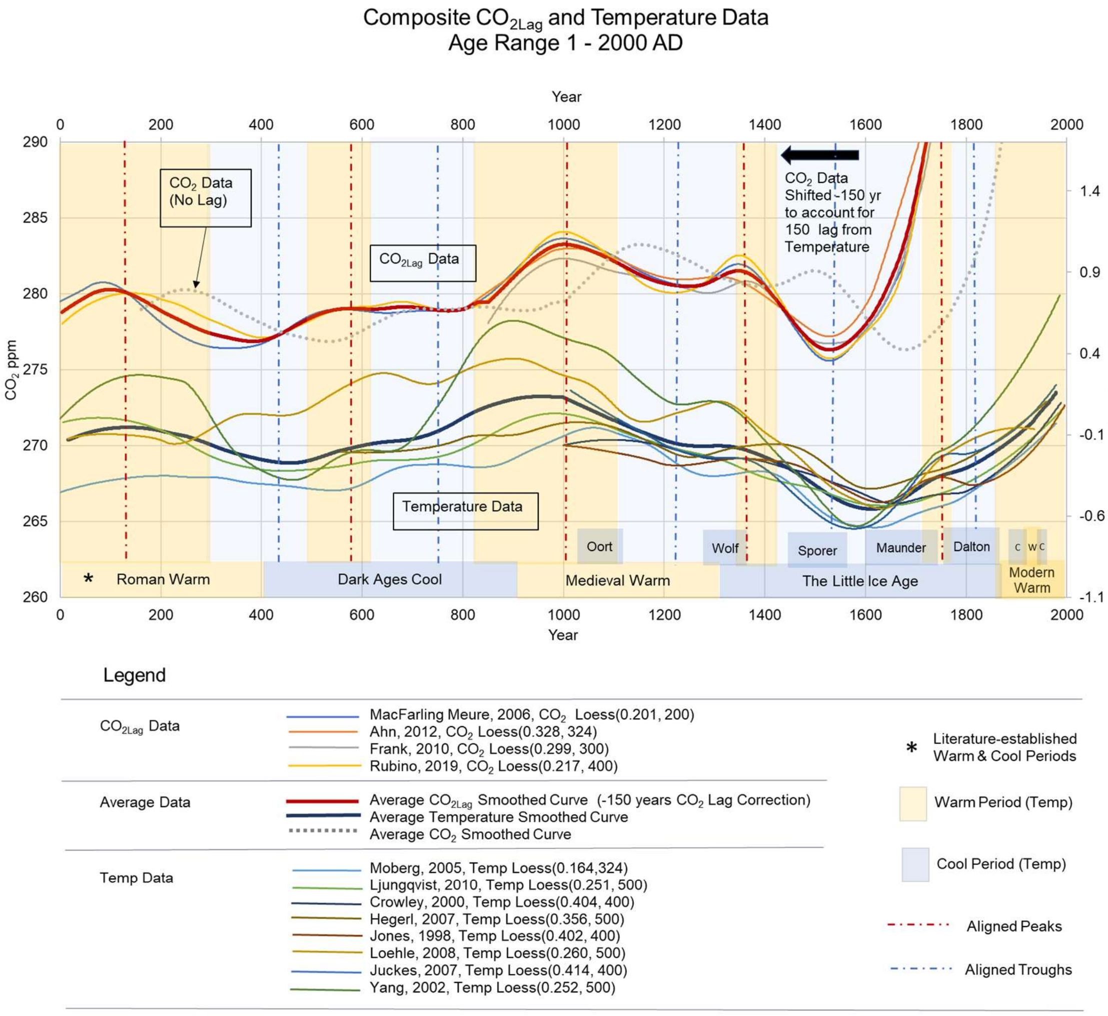

Composite & Average of $CO_{2LAG}$, and Temperature
Correlations of Loess 2

| | Conditional | Range | Statistical Validation Framework |
|---|---|---|---|
| $CO_{2Lag}$ (150 yr lag) vs Temp | $r_{PCC}$ = 0.73 | 200-1600 AD ===> | $r_{PCC}$ = 0.65 Orig Robustly Significant (SVF passed) |
| | $r_{PCC}$ = 0.95 | 1000-1600 AD | |
| $CO_2$ (No Lag) vs Temp | $r_{PCC}$ = 0.04 | 200-1600 AD | |
| | $r_{PCC}$ = 0.41 | 1000-1600 AD | |

*Figure 11. Smoothed Composite $CO_{2Lag}$, $CO_2$, and temperature data for the range of 1 to 2000 AD as well as average $CO_{2Lag}$, $CO_2$, and temperature. Cool and warm zones observed from this study are delineated as well as standard geologic-named cool and warm periods. Vertical red dashed lines identify visually correlated peaks between $CO_{2Lag}$ and temperature. Vertical blue dashed lines identify visually correlated troughs between $CO_{2Lag}$ and temperature. Averaged $r_{PCC}$ values are shown for the lagged $CO_2$ and non-lagged $CO_2$ cases. Although Loess2 for this Average pair is not directly validated under SVF, its correlation is presented here conditionally, supported by the corresponding variant Orig, as Robustly Significant (SVF passed). High smoothing visually enhances apparent alignment, but should be statistically validated for formal inference. References: $CO_2$: Ahn et al. (2012), Frank et al. (2010), MacFarling Meure et al. (2006), and Rubino et al. (2019); Temperature: Moberg et al. (2005), Ljungqvist (2010), Crowley (2000), Hegerl et al. (2007), Jones et al. (1998), Loehle and McCulloch (2008), Juckes et al. (2007), Yang et al. (2002).*

The average curves are shown without the composite curves for clarity on Fig. 12. The composite analysis confirms the individual analyses, both visually and statistically. Over the period of 1 to 1600 AD, $CO_2$ does not appear to control temperature in any manner. Rather, temperature appears to precede $CO_2$ in a closely coordinated process throughout the entire time period. This is shown by the visually coordinated curves of $CO_{2Lag}$ and temperature after the $CO_2$ lag correction of 150 yr. The Very Strong $r_{PCC}$ of 0.93 and 0.73 respectively for the two ranges analyzed, and the very low values of $r_{PCC}$ for the non-lagged $CO_2$ data of $r_{PCC} = 0.05$ and $r_{PCC} = 0.07$ also contribute in this confirmation.

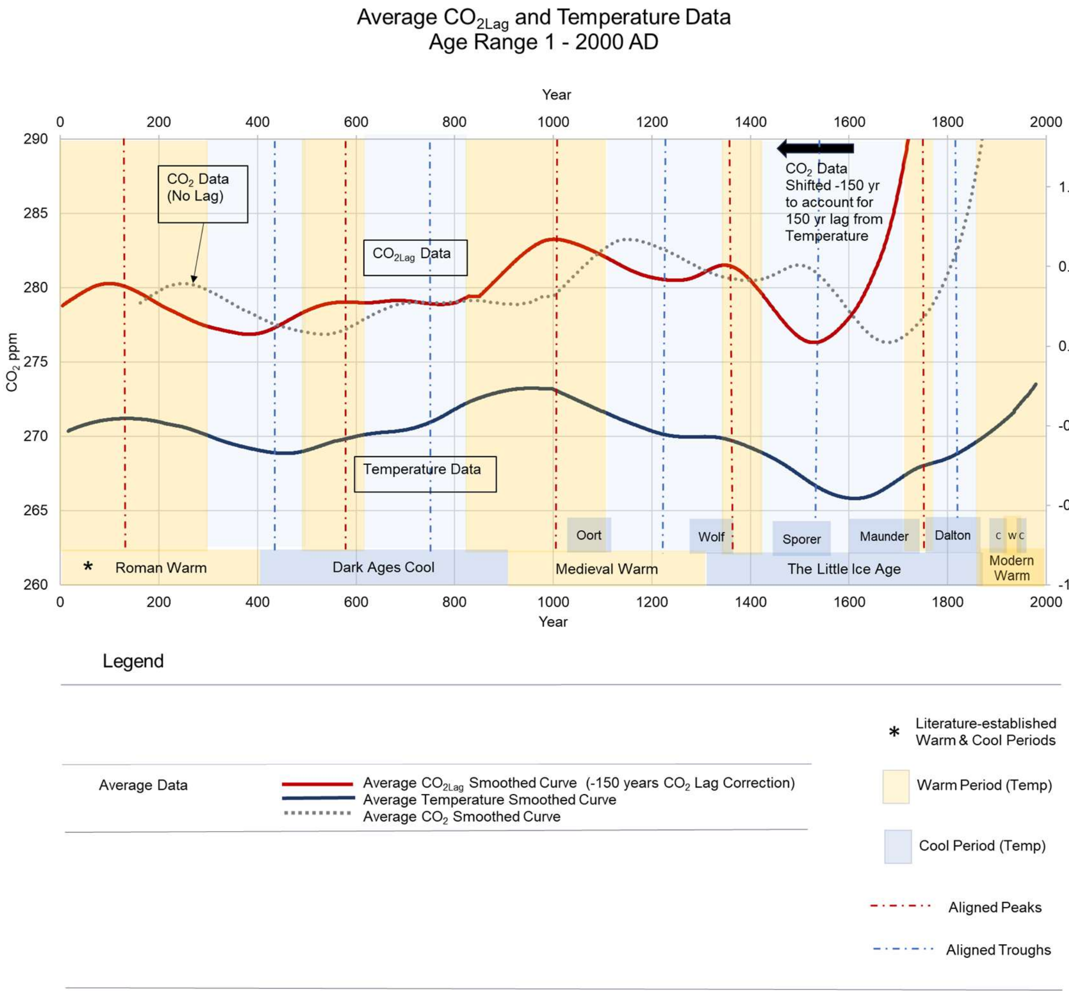

Composite & Average of $CO_{2LAG}$, and Temperature
Correlations of Loess 2

| | Conditional | Range | | Statistical Validation Framework | | |
|---|---|---|---|---|---|---|
| $CO_{2Lag}$ (150 yr lag) vs Temp | $r_{PCC}$ = 0.73 | 200-1600 AD | ===> | $r_{PCC}$ = 0.65 | Orig | Robustly Significant (SVF passed) |
| | $r_{PCC}$ = 0.95 | 1000-1600 AD | | | | |
| $CO_2$ (No Lag) vs Temp | $r_{PCC}$ = 0.04 | 200-1600 AD | | | | |
| | $r_{PCC}$ = 0.41 | 1000-1600 AD | | | | |

*Figure 12. Smoothed Average $CO_{2Lag}$, $CO_2$, and temperature data for the range of 1 to 2000 AD. Cool and warm zones observed from this study are delineated as well as standard geologic-named cool and warm periods. Vertical red dashed lines identify visually correlated peaks between $CO_{2Lag}$ and temperature. Vertical blue dashed lines identify visually correlated troughs between $CO_{2Lag}$ and temperature. Averaged $r_{PCC}$ values are shown for the lagged $CO_2$ and non-lagged $CO_2$ cases. Although Loess2 for this Average pair is not directly validated under SVF, its correlation is presented here conditionally, supported by the corresponding variant Orig, as Robustly Significant (SVF passed). High smoothing visually enhances apparent alignment, but should be statistically validated for formal inference. References: $CO_2$: Ahn et al. (2012), Frank et al. (2010), MacFarling Meure et al. (2006), and Rubino et al. (2019); Temperature: Moberg et al. (2005), Ljungqvist (2010), Crowley (2000), Hegerl et al. (2007), Jones et al. (1998), Loehle and McCulloch (2008), Juckes et al. (2007), Yang et al. (2002).*

### 3.8 Graphical Results – Smoothed $CO_2$ and Temperature (1600-1850 AD)

As discussed in Section 3.3 and detailed further in Supplementary Material, Appendix C, a structural break, consistent with a broader regime shift in climate dynamics, was identified around 1600 AD. This apparent state transition introduces a discontinuity in the statistical behavior of the system, particularly in the correlation between atmospheric $CO_2$ and temperature. For example, Pearson's correlation coefficients ($r_{PCC}$) are internally consistent within each period (e.g., 200–1600 AD and 1600–1850 AD), and even generally consistent between the two periods, but they degrade significantly when calculated across the boundary. Periods that span this breakpoint—such as 200–1650 AD or 200–1850 AD—show a marked decline in correlation strength, transitioning from strong to weak or nonsignificant values. To account for this discontinuity, the present study analyzes the two time periods separately:

1. a pre-break interval from 200–1600 AD, and
2. a post-break interval from 1600–1850 AD.

The upper bound of 1850 AD was selected based on the availability of robust correlation between $CO_2$ and temperature after applying a 150-yr lag correction to the $CO_2$ data—consistent with lag patterns observed throughout this study. Beyond 1850 (i.e., post-2000 when adjusted for lag), no valid comparisons can be drawn due to the absence of viable lag-corrected $CO_2$ data. This section presents the graphical and statistical analyses of the 1600–1850 AD interval, highlighting key patterns in the $CO_2$–temperature relationship during this climatically transitional period.

This section of the study investigates the conditional statistical association and visual graphical correlation between atmospheric $CO_2$ concentrations and multiple paleotemperature proxies over the period 1600-1850 AD by employing Running Average (RA 50) smoothing with a 50-yr centered window on all series. Three independent $CO_2$ records—Ahn et al. (2012), MacFarling Meure et al. (2006), and Rubino et al. (2019)—are analyzed against six established temperature reconstructions. Data results are shown in Supplementary Material, Appendix A, Table A23. Key findings are summarized below (average $r_{PCC}$ of each temperature vs. the three $CO_2$ series):

| Temperature | Average $r_{PCC}$ No Lag | Average $r_{PCC}$ Lag Max | Average Lag Years |
|---|---|---|---|
| Crowley (2000) | 0.25 | 0.90 | 170 |
| Hegerl (2007) | 0.46 | 0.96 | 183 |
| Juckes (2007) | 0.43 | 0.99 | 223 |
| Ljungqvist (2010) | 0.68 | 0.90 | 203 |
| Moberg (2005) | 0.63 | 0.90 | 163 |
| Yang (2002) | 0.46 | 0.92 | 193 |
| Overall Averages | 0.45 | 0.90 | 189 |

Significant points:

1. There is a significant increase between the No Lag and Lagged $r_{PCC}$ values – the average correlation is 2 times higher for lagged vs. no lagged scenarios. This is similar to the data from the data range 200-1600 AD.
2. The max $r_{PCC}$ values (0.90- 0.99) and the no lag $r_{PCC}$ (0.25 – 0.68) values are both within the close range of the $r_{PCC}$ values in the data range 200-1600 AD, albeit slightly higher.

As with other data in this study, the 1600-1850 AD data have been processed through the SVF to better understand the significance of the correlations. Table 4 depicts the results of the SVF. There is one $CO_2$ and temperature pair that passed the SVF in either of the two passing categories. Rubino $CO_2$ (Orig) vs. Moberg Temp (Orig) passed as Robustly Significant with a Neff value over 10 and group-block-permutation-FDR p-value < 0.05 in at least one block. It also had an $r_{PCC}$ = 0.54, sample size of 10, and HAC SE = 150.97. The HAC SE values were higher overall than the data from range 200-1600 AD possibly due to the regime change at 1600 AD and the exponentially increasing rates of increase for the $CO_2$ and temperature data commencing in this timeframe. Five of the pairs exhibited Neff between 5 and 7; passed the p-value test of Grouped-Block-Perm-FDR with values $< 0.05$; and all had reasonable strong sample sizes with $r_{PCC}$ between 0.52 and 0.80 (4 Orig and 1 RA 100). While these five pairs did not pass the stringent SVF, they exhibited strong parameters. The last three pairs are noteworthy from the perspective they had strong enough Neff values, but faltered in the Grouped-Block-Perm-FDR, which indicates strong Neff values alone are not enough.

As mentioned above, the goal of the SVF is not to suppress correlation results but to distinguish robust signal from statistical artifact in the presence of serial correlation and long-term memory issues. The results from 1600-1850 AD are consistent with those of 200-1600 AD, although there is a much lower pass rate probably related to regime change and rapid rise in $CO_2$ and temperature commencing in this time period. Along with the visual correlations shown below, the data does conditionally indicate some marginal significance (Santer et al., 2000; von Storch & Zwiers, 1999; Bretherton et al., 1999).

Table 4. Results of the SVF testing for the $CO_2$ vs. temperature records from Data Set A are shown for the range, 1600-1850 AD . $r_{PCC}$ is the Pearson's Correlation Coefficient; Samp Rate is the de-sampling rate to reduce the data points; n is the number of data points after de-sampling; Neff is the effective number of data points (Bretherton et al., 1999); Grouped-Block-Perm-FDR p-values represents the process of using block permutations and grouped FDR (Fake Discovery Rate) showing p-values; HAC SE (Heteroskedasticity and Autocorrelation Consistent Standard Errors); and SVF Passing Category.

Results of Statistical Validation Framework Testing
$CO_2$ vs. Temperature Correlations
1600 -- 1850 AD

| Avg $CO_2$ & Temp Pair | $r_{PCC}$ | Samp Rate | n | Neff | Grp-Block-Perm-FDR p-value | Blocks Passed | HAC SE | SVF Passing Category |
|---|---|---|---|---|---|---|---|---|
| Rubino $CO_2$ (Orig)<br>Moberg Temp (Orig) | 0.54 | 10 | 22 | 12.31 | < 0.05 | 1 | 150.97 | Robustly Significant |
| Ahn $CO_2$ (Orig) Hegerl Temp (Orig) | 0.84 | 10 | 16 | 6.18 | < 0.05 | 1 | 7.68 | - |
| MacFarling $CO_2$ (Orig)<br>Hegerl Temp (Orig) | 0.52 | 10 | 23 | 5.51 | < 0.05 | 1 | 152.85 | - |
| Ahn $CO_2$ (RA 100)<br>Moberg Temp (RA 100) | 0.80 | 10 | 11 | 5.51 | < 0.05 | 1 | 41.17 | - |
| Rubino $CO_2$ (Orig)<br>Hegerl Temp (Orig) | 0.71 | 10 | 22 | 5.32 | < 0.05 | 1 | 10.28 | - |
| Rubino $CO_2$ (Orig)<br>Crowley Temp (Orig) | 0.64 | 10 | 22 | 5.00 | < 0.05 | 1 | 34.61 | - |
| Ahn $CO_2$ (Orig)<br>Moberg Temp (Orig) | 0.18 | 10 | 16 | 14.02 | > 0.05 | - | 74.22 | - |
| MacFarling $CO_2$ (Orig)<br>Moberg Temp (Orig) | 0.39 | 10 | 23 | 13.16 | > 0.05 | - | 49.55 | - |
| MacFarling $CO_2$ (Orig)<br>Crowley Temp (Orig) | 0.35 | 30 | 8 | 8.18 | > 0.05 | - | 21.47 | - |

Figure 13 presents the transformed $CO_2$ and temperature series from Ahn et al. (2012) and Hegerl et al. (2007), respectively, for the period 1600–1850 AD as RA 50. The $CO_2$ series was cubed, detrended with linear regression, and normalized to a common scale from 0.0 to 1.0, and the x-axis extends from 1600 to 2000 AD to display the full temporal extent of the data, including lag alignment. The temperature series was normalized to match the $CO_2$ data. The purpose of this display style is due to the exponentially rising $CO_2$ and temperature curves. The transformation mollifies the chart without changing relationships to allow more character to be observed. The lag-adjusted $CO_2$ series ($CO_{2Lag}$, red), the unadjusted $CO_2$ series (gray dashed line), and the temperature series (blue) are plotted, with the $CO_{2Lag}$ offset by 170 yr. Vertical reference lines mark visually striking coincident peaks and troughs between $CO_{2Lag}$ and temperature, which are now visible due to the transformations. This alignment is quantitatively supported by a conditional Pearson correlation coefficient ($r_{PCC}$) of 0.95, compared to a much weaker correlation of 0.48 between the non-lagged $CO_2$ and temperature series. RA 50 for this pair is not directly validated under SVF, nor is its Orig variant. Its correlation is presented here conditionally, supported by SVF showing marginal significance with marginal Neff and passing FDR, and a related pair, Rubino $CO_2$ (Orig) and Moberg Temp (Orig), showing the corresponding variant, Orig, Robustly Significant (SVF passed). High smoothing visually enhances apparent alignment, but should be statistically validated for formal inference.

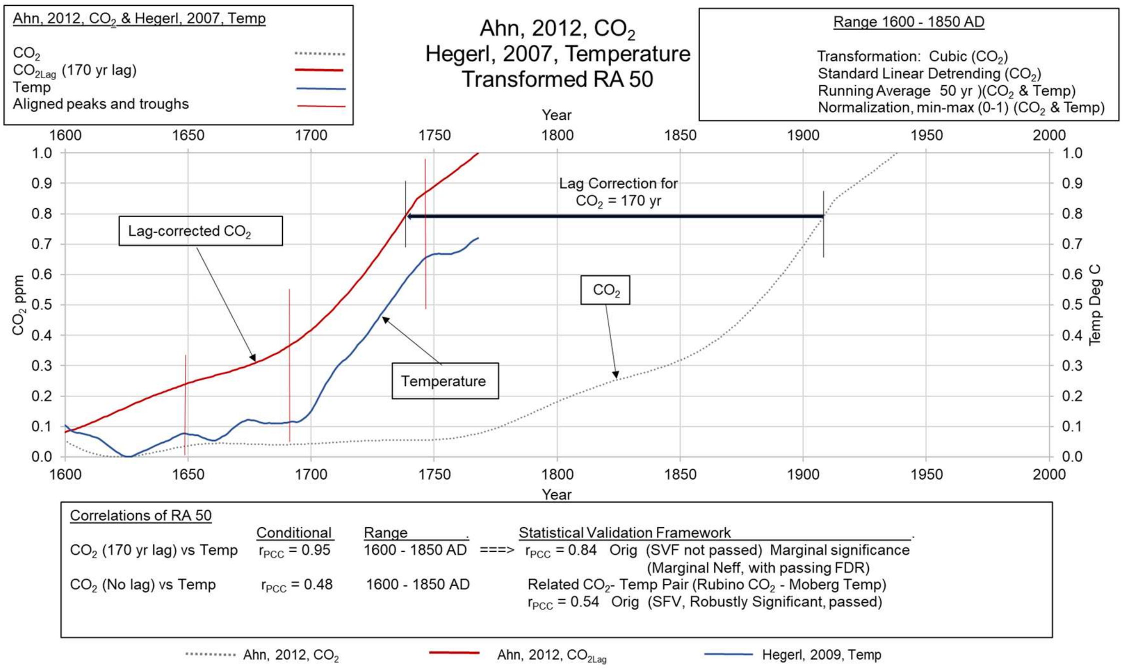

*Figure 13. Running Average, RA 50 smoothing, $CO_2$ and temperature data (from Ahn et al., 2012; Hegerl, 2007, respectively), are shown from 1600 to 2000 AD along with the $CO_2$ curve shown with a 170-yr lag correction. $CO_2$ is cubed, detrended with a linear regression, and normalized.between 0-1. Temperature is normalized between 0-1. Aligned peaks and troughs are depicted with thin red lines. Conditional maximum $r_{PCC}$ correlations at lag and $r_{PCC}$ at no lag are presented. Although RA 50 for this pair is not directly validated under SVF, nor is its Orig variant, its correlation is presented here conditionally, supported by SVF showing marginal significance with marginal Neff and passing FDR, and a related pair, Rubino $CO_2$ (Orig) and Moberg Temp (Orig), showing the corresponding variant, Orig, Robustly Significant (SVF passed). High smoothing visually enhances apparent alignment, but should be statistically validated for formal inference.*

Figure 14 displays a very similar chart to Figure 13. The transformed $CO_2$ and temperature series from Rubino et al. (2019) and Hegerl et al. (2007), respectively, for the period 1600–1850 AD. The $CO_2$ series was cubed, detrended with linear regression, and normalized to a common scale from 0.0 to 1.0, and the x-axis extends from 1600 to 2000 AD to display the full temporal extent of the data, including lag alignment. The temperature series was normalized from 0-1. The lag-adjusted $CO_2$ series ($CO_{2Lag}$, red), the unadjusted $CO_2$ series (gray dashed line), and the temperature series (blue) are plotted, with the $CO_{2Lag}$ off-set by 180 yr. Vertical reference lines mark visually striking coincident peaks and troughs between $CO_{2lag}$ and temperature, which are now visible due to the transformations. This alignment is quantitatively supported by a conditional Pearson correlation coefficient ($r_{PCC}$) of 0.97, compared to a weaker correlation of 0.43 between the non-lagged $CO_2$ and temperature series. Although RA 50 for this pair is not directly validated under SVF, nor is its Orig variant, its correlation is presented here conditionally, supported by SVF showing marginal significance with marginal Neff and passing FDR, and a related pair, Rubino $CO_2$ (Orig) and Moberg Temp (Orig), showing the corresponding variant, Orig, Robustly Significant (SVF passed). High smoothing visually enhances apparent alignment, but should be statistically validated for formal inference.

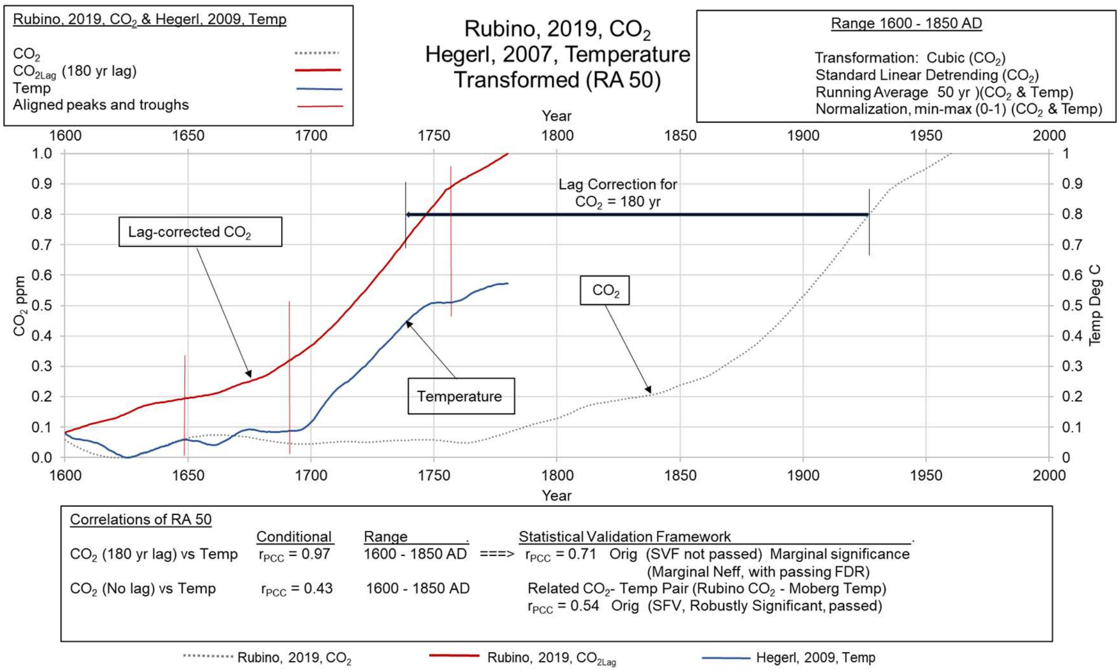

*Figure 14. Running Average, RA 50 smoothing, $CO_2$ and temperature data (from Rubino et al., 2019; Hegerl, 2007, respectively), are shown from 1600 to 2000 AD along with the $CO_2$ curve shown with a 180-yr lag correction. Aligned peaks and troughs are depicted with thin red lines. Conditional maximum $r_{PCC}$ correlations at lag and $r_{PCC}$ at no lag are presented. Although RA 50 for this pair is not directly validated under SVF, nor is its Orig variant, its correlation is presented here conditionally, supported by SVF showing marginal signifi-cance with marginal Neff and passing FDR, and a related pair, Rubino $CO_2$ (Orig) and Moberg Temp (Orig), showing the corresponding variant, Orig, Robustly Significant (SVF passed). High smoothing visually enhances apparent alignment, but should be statistically validated for formal inference.*

Fig. 15 displays the Pearson Correlation Coefficient, $r_{PCC}$, plotted against a range of $CO_2$ lag values (-100 to 250). The curve in this example shows a flat peak area ranging between $r_{PCC}$ of 0.90 and 0.92 between lags of 160 to 195 yr. $r_{PCC}$ drops off quickly in either direction before and after the flat peak.

These figures highlight the very strong relationship between lag-adjusted $CO_2$ and temperature, and reinforces a critical observation: once $CO_2$ is corrected for its lag (~170 to 180 yr), little comparable data remain in the late 20th and early 21st centuries to inform centennial or millennial-scale analyses. Notably, the more granular analyses by Koutsoyiannis (2024a), Humlum et al. (2013), Chylek et al. (2018b), and Adams and Piovesan (2005) report that $CO_2$ lags temperature by less than one year during the modern instrumental era. These studies typically assess monthly or annual fluctuations over relatively short time spans and likely capture dynamics distinct from those observed at centennial or millennial scales.

Therefore, the lag observed in the present study from 200-1600 AD and 1600-1850 AD (~150–170 yr) does not contradict the findings of these short-term studies. Rather, the consistent and strong correlation between $CO_{2lag}$ and temperature throughout the last 2000 yr—using annual resolution data—suggests a robust long-term relationship where temperature changes consistently precede $CO_2$ over centennial timescales.

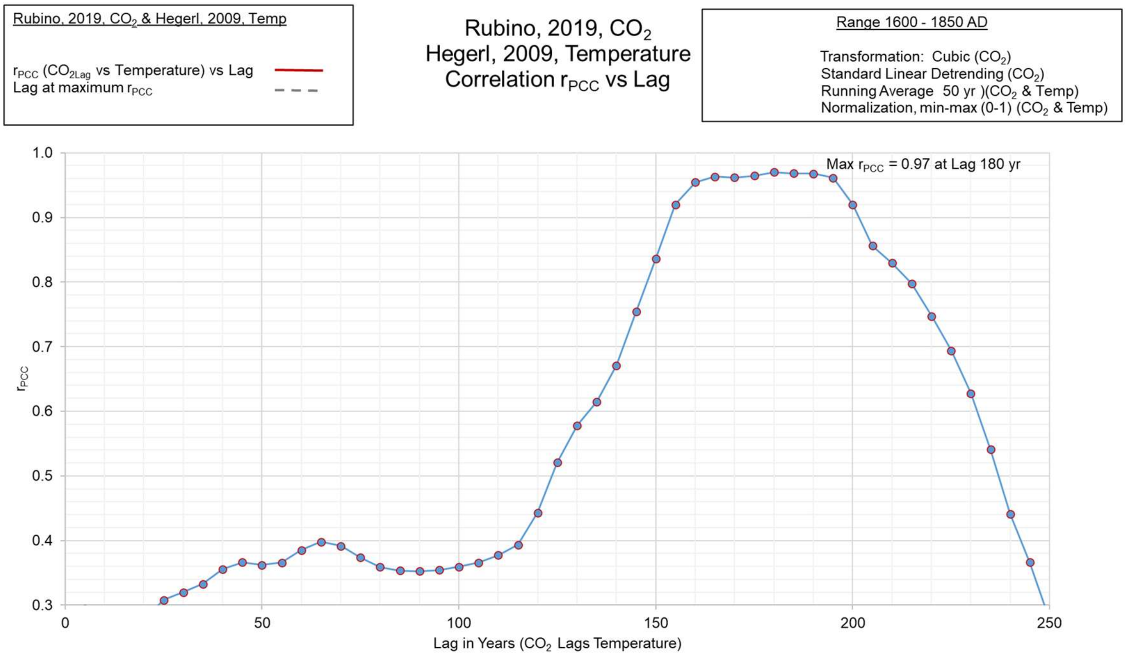

*Figure 15. Pearson Correlation Coefficient, $r_{PCC}$, is plotted against $CO_2$ lag corrections (-100 to 250, interval of 5 yr) for $CO_2$ (Rubino et al., 2019) and temperature (Hegerl et al., 2007). The peak of the curve depicting maximum correlation is at 180 yr of $CO_2$ lag correction. Correlation drops off in either direction rapidly after the flat peak area.*

### *3.9 Total Solar Irradiance (TSI) and Temperature (1-2000 AD)*

A comparative analysis was performed between multiple published reconstructions of Total Solar Irradiance (TSI) and temperature data spanning the past two millennia as detailed in Supplementary Material, Appendix D. Using conditional Pearson correlation coefficients with input on significance from the SVF, both visual and statistical congruence were identified across a broad array of TSI reconstructions (e.g., Scafetta & Bianchini, 2022; Scafetta, 2023; Lean, 2018; Shapiro et al., 2011; Wu et al., 2018; Steinhilber et al., 2009) and temperature datasets (e.g., Ljungqvist, 2010; Morice et al., 2012 [HadCRUT4]; Lenssen et al., 2024 [GISS]; Parker et al., 1992 [CET]). Similar to the previous conditional analysis of $CO_2$ and temperature, this analysis accounts for autocorrelation and long-term memory in paleoclimatic records. Given this caveat, Strong to Very Strong correlations were observed between TSI and global atmospheric temperature, reinforcing the hypothesis that TSI variability represents solar energy, which has been a persistent contributor to centennial-scale temperature dynamics. Integrating the TSI–temperature analysis alongside the $CO_2$–temperature analysis provides a more comprehensive perspective on the potential dynamic relationships among solar energy, surface temperature, and atmospheric $CO_2$.

## 4. Discussion

### *4.1 Atmospheric $CO_2$ Lags Temperature by 150 yr*

Results from both original and smoothed datasets—derived from visual inspection and correlation analysis—indicate that global atmospheric $CO_2$ lags atmospheric temperature by approximately 150 years over the period 1–1850 AD. Although the Industrial Revolution began around 1750 AD (Wilson, 2014), significant anthropogenic $CO_2$ emissions did not occur until roughly 1930 AD (Hoesly, 2018). This finding suggests that the observed lag is a natural process, as is the subsequent exponential increase in $CO_{2Lag}$ from ~1600 AD to the present in response to rising temperatures.

Because this analysis shows that $CO_2$ change has continuously followed temperature change throughout the Common Era—including 1850–2000 AD $CO_2$ changes that reflect temperature changes from 1700–1850—there is no evidence for a fundamental change in the $CO_2$–temperature relationship over the last 150 years.

Figures 11 and 12 summarize the smoothed $CO_{2Lag}$ and temperature curves, which visually track each other closely from 1–1600 AD. Figures 13 and 14 show a similar close correspondence from 1600–1775 AD. In all four figures, vertical dashed lines (red for peaks, blue for troughs) mark the synchronous occurrence of every identified peak and trough in $CO_{2Lag}$ and temperature over nearly 1800 years.

The combined evidence indicates that $CO_2$ does not exert a primary control on Earth's temperature over this time period; rather, it closely tracks temperature with a lag of ~150 yr. The analysis also reveals a structural break or regime shift around 1600 AD, coinciding with both the nadir of the Little Ice Age (Maunder Minimum) and a solar energy minimum, which corresponds to the observed temperature low and subsequent rapid increase in both temperature and lag-corrected $CO_2$. Between 1600 and 1850, the visual and statistical correlations between $CO_{2Lag}$ and temperature are strong.

The original $CO_2$ and temperature curves (Figs. 1–2), along with RA 50 (Fig. 4) and RA 100 (Fig. 5) series, strongly agree with the Loess smoothed-curve analyses (Figs. 6–10). All original datasets exhibit a pronounced concurrent drop in temperature and $CO_{2Lag}$ around 1460 AD, with a narrow 50–80 yr width. This distinct feature is only apparent after applying the −150 yr $CO_2$ lag correction and is further supported by:

1. Long-term patterns: The data suggest a possible millennial-scale cycle, with peaks near 100, 1000, and 2000 AD, and troughs around 550 and 1450 AD (~1000 yr frequency). Both $CO_{2Lag}$ and temperature appear to track this pattern, which aligns with proposed solar activity cycles such as the Eddy Cycle (Abreu et al., 2010; Zhao et al., 2020) and Hallstatt Cycle (Steinhilber et al., 2010). Longer datasets would be required to confirm a true cycle.
2. Shorter-term variability: Numerous visually correlated peaks, troughs, and peak–trough clusters are evident throughout 1–1850 AD, on timescales of 10–100 yr.

This mirrored relationship between $CO_{2Lag}$ and temperature appears at multiple temporal scales:

1. Macro-scale (~2000 yr): millennial cycles
2. Meso-scale (10–100 yr): decadal–centennial variability
3. Micro-scale (months): as documented by other studies

For example, Humlum et al. (2013) found that monthly $CO_2$ lags global SST by 11–12 mo and global air temperature by 9.5–10 mo (1980–2011 instrumental data). Monnin et al. (2001) identified a ~410 yr $CO_2$ lag during 11.2–17.0 kyr BP. Sharma and Karamanev (2021) reported a 1020–1080 yr lag over the last 650 kyr (max $r_{PCC} = 0.837$). Koutsoyiannis (2024a) demonstrated varying $CO_2$–temperature lags at multiple geologic periods, from 2.3 Myr in the Phanerozoic to 3–8 mo in the modern instrumental era.

Collectively, these findings, combined with the ~150 yr lag identified here, suggest that different but related processes drive the $CO_2$–temperature lag at different timescales. Humlum et al. (2013) proposed that near-surface ocean temperatures are a primary cause for short-term lags. The millennial-scale lag found by Sharma and Karamanev (2021) may reflect deeper ocean processes. Adams and Piovesan (2005) further proposed that monthly lags may involve internal biogeochemical cycles and tropical temperature influences.

## *4.2 Statistical Validation Framework*

The inclusion of $r_{PCC}$ analysis in concert with the visual correlation of $CO_{2Lag}$ (150 yr) and temperature and the visual correlation of TSI and temperature is based on a robust correlation testing framework, Statistical Validation Framework (SVF). It is implemented to assess statistical reliability of observed correlations between lag-adjusted atmospheric $CO_2$ proxies and temperature reconstructions as well as Total Solar Irradiance (TSI) and temperature. The analysis incorporates block permutation testing (10,000 iterations) across multiple block sizes, HAC-consistent standard errors, and both global and grouped FDR corrections to rigorously control for autocorrelation and long memory. Passing pairs were filtered based on effective sample size (Neff), yielding results classified as Robustly Significant (Neff $\geq$ 10) or Tentatively Significant (Neff 8–10), providing a conservative assessment of correlation reliability across time series with complex temporal structure. The SVF has successfully identified key correlation pairs that show significance through the camouflage of dependence, serial correlation, and long memory.

### *4.3 Role of the Oceans in the Relationship of $CO_2$ to Temperature*

Humlum et al. (2013) states that changes in ocean temperatures appear to explain most of the changes in atmospheric $CO_2$ during the 1980 to 2011 period, especially changes in Southern Ocean temperature.

Ocean processes and the carbon cycle are potential areas to investigate the possible explanations for the lag of $CO_2$ to temperature, especially deep ocean carbon sinks (Wang et al., 2024), atmospheric $CO_2$ ventilation (Yu et al., 2023), and the global ocean conveyor circulation (Toggweiler & Key, 2001). For the 150-yr $CO_2$ lag identified in this study, the answer may be related to deeper ocean processes as well as biogeochemical processes. It has been established by many researchers that $CO_2$, as part of the carbon cycle, is absorbed in the ocean as a carbon sink, when the temperature of the water is cool, and conversely, $CO_2$ is released into the atmosphere when the temperature of the water is warm (Easterbrook, 2016b), but the process is more complex as noted by (Wang et al., 2024), (Yu et al., 2023), and (Toggweiler & Key, 2001). Additional investigation is required to establish the process causing $CO_2$ to lag temperature, but the facts, as outlined in this study and the studies (Adams & Piovesan, 2005; Chylek et al., 2018b; Humlum et al., 2013; Monnin et al., 2001, Caillon et al., 2003; Mudelsee, 2001; Koutsoyiannis, 2024a; and Sharma & Karamanev, 2021), identify that $CO_2$ lags temperature at all major timeframes: months, tens of years, hundreds of years, hundred thousands of years, and even millions of years. These studies, as well as this study, also identify that $CO_2$ does not influence temperature.

### *4.4 Total Solar Energy (TSI) correlates with Temperature*

This study and others have established that atmospheric $CO_2$ lags both atmospheric and sea surface temperature. The next important question is the source of influence on the temperature of the oceans and atmosphere. Accordingly, this study has evaluated the data from several TSI papers and compared these with temperature data assessed in this study. The time period covers the last 2000 yr and the last few hundred years respectively.

Fig. D1, in Supplementary Material, Appendix D, defines a very close correlation between temperature (Ljungqvist, 2010) and TSI (Shapiro et al., 2011) as evidenced by the tight visual tracking and Very Strong conditional statistical correlation ($r_{PCC} = 0.79$ for the range of 5 to 1994 AD; $r_{PCC} = 0.91$ for the range of 1000 to 1994 AD). Causation cannot be proven from a chart such as this, but it is difficult to imagine how solar energy does not play a major role in control of atmospheric temperature from consistent results that span 2000 yr. It is probably a matter of determining the characteristics of the solar energy which is the major influencer. Fig. D2, in Supplementary Material, Appendix D, utilizing three different TSI studies (Steinhilber et al., 2010; Lean, 2018; Wu et al., 2018) shows TSI versus the Average Temperature curve (Fig. 12) taken from averaging temperature from eight temperature studies. While the visual correlation is quite compelling, and the correlation analysis is Strong ($r_{PCC} = 0.61$ to 0.62 for the range of 5 to 1994 AD; $r_{PCC} = 0.65$ to 0.75 for the range of 1000 to 1994 AD), the differences in Fig. D2, in Supplementary Material, Appendix D, compared to Fig. D1, in Supplementary Material, Appendix D, identify a slightly greater variability and less precision.

Switching the timeframe to the 250-yr range, Fig. 19 depicts TSI data from Scafetta (2023) compared to three temperature data sets collected instrumentally. These data are maintained by the Met Office Hadley Centre in Great Britain and are smoothed using Loess in this study: (1) HadCRUT4 (atmospheric temperature) (Morice et al., 2012), (2) HadSST3 (sea surface temperature) (Kennedy et al., 2011a; Kennedy et al., 2011b), and (3) CET (Legacy version) (atmospheric temperature of central England) (Parler et al., 1992). These data present as highly visually correlated on the chart and have a Very Strong statistical correlation ranging from $r_{PCC} = 0.84$ to $r_{PCC} = 0.92$. Thus, it appears the same results are evident regarding the close correlation of TSI and temperature both at very short and granular timeframes of 200 yr to longer periods of 2000 yr.

In Fig. D4, in Supplementary Material, Appendix D, all three temperature curves appear to trend sharply upward from about 1995 through 2023, whereas the TSI curve makes a significant lower turn. This appears to be somewhat discordant with the rest of the entire curve comparison from 1800 to present. One possible explanation has been proffered by several researchers as an artifact of five factors, especially for the years since 1995, which are:

1. Urban Heat Effect – a well-known result of temperature measurement stations being located in cities, airports, and urban areas exhibiting a significant increase of temperature over the ambient baselines as much as 0.45 degrees C. (Scafetta, 2021; Soon et al., 2023; Katata et al., 2023; Spencer, 2024; Watts, 2012)
2. Multiple questionable data adjustments since 2000 AD by organizations responsible for temperature repositories, such as NOAA, NASA, and Met Office Hadley Centre. The adjustments have typically increased parts of the temperature record by as much as 0.2 to 0.4 degrees C. (McKitrick, 2010; US Historical Climatological Network, 2024; Watts, 2012; Wallace et al., 2017)
3. Reduction of temperature stations by as much as 25% or more in mostly rural areas and a practice of populating the removed stations data with calculated estimates. (McKitrick, 2010; Wallace et al., 2017)
4. Natural temperature-enhanced forcing from large El Nino events (Douglass & Christy, 2009; Vinos, 2024b; Cobb et al., 2003)
5. An underwater volcanic eruption in 2022, Tonga, which increased water vapor in the global atmosphere by 10%, causing a sharp increase in global temperature, which will take several years to dissipate (Bielfeld, 2023; Vinos, 2024a; Vinos, 2024b; Lee & Wang, 2022).

The significant steep trough of TSI at about 1460 yr AD shown in Fig. 20 for all 4 TSI studies at a slight smoothing, is also replicated on all of the temperature and $CO_{2Lag}$ data sets shown in Fig. 1, Fig. 2, Fig. 4, and Fig. D5, in Supplementary Material, Appendix D. This marker, at 1460 AD, coupled with the overall visual and statistical correlations of these data, emphasize the relationship of these data to each other.

A strong correlation of TSI and atmospheric global temperature over a 2000-yr period is probably not a coincidence. Solar energy either plays an integral part in controlling temperature on the earth, or another forcing agent influences both solar energy and temperature. Perhaps, a third option is possible, where solar energy plays a major role in controlling temperature in concert with other agents (Scafetta, 2023). Some of these agents could include ocean and atmospheric pressure processes (D'Aleo & Easterbrook, 2016) such as the Atlantic Multidecadal Oscillation (AMO) (Knudsen et al., 2011), El Nino Southern Oscillation (ENSO) (Trenberth, 2016), or Thermohaline Ocean Circulation (THC) (Toggweiler & Key, 2001), among others (D'Aleo & Easterbrook, 2016). Cloudiness appears to be a significant contributor as well, as it appears to be controlled by solar magnetic modulation of cosmic rays (Svensmark et al., 2021; Svensmark et al., 2016; Svensmark, 2007). Volcanism also seems to correlate with temperature decreases as shown over the Little Ice Age (1250-1860 AD) (Wanner et al., 2022). On a larger scale, orbitally-driven insolation forcing, mainly precession and obliquity, can have influence (Wanner et al., 2022; Lorenz et al., 2006). Another indirect impact of TSI is solar-driven weakening of the jet stream causing colder temperatures in the northern hemisphere (Schwander et al. 2017; Moffa-Sanchez et al., 2014; Ineson et al., 2011). However, based on the strong visual and statistical correlations between TSI and temperature over short, medium, and longer time periods (2000 yr) shown in this study, it appears that solar energy is most probably a significant component, either directly or indirectly, in concert with other natural processes previously mentioned, controlling the temperature of the earth.

## 5. Conclusions

Atmospheric $CO_2$ clearly lags global temperature by about 150 yr over the timeframe of 1 to 1850 AD as shown by both visual and conditional statistical correlations (Very Strong) using all 16 atmospheric temperature studies compared with all 4 $CO_2$ studies for both original data and smoothed data.

Total Solar Irradiance (TSI) correlates both visually and statistically (conditional) with the data from the large number of temperature studies utilized in this paper:

1. Six TSI data sets compared to temperature from Ljungqvist (2010) and the Average Temperature from 8 atmospheric temperature studies over the last 2000 yr (Strong $r_{PCC}$).
2. Two additional TSI data sets compared to five shorter-term temperature data sets in the timeframe of 1850 to present (Very Strong $r_{PCC}$).

Along with many other correlated data curve artifacts such as peaks and troughs, a striking downward dip at the year, 1460 AD, is observed on all related data:

1. Atmospheric temperature
2. $CO_{2Lag}$ of 150 yr
3. Total Solar Irradiance

The Statistical Validation Framework (SFV) supported the conditional use of the $r_{PCC}$ values for comparative purposes based on a robust testing process taking into account dependence, autocorrelation, and long-term memory issues.

Atmospheric $CO_2$ does not precede temperature, nor does it control temperature as shown in this study over the last 2000 yr. The same conclusions have been reached in the study by Koutsoyiannis (2024a) coving several geologic time periods (e.g. Modern Period, Common Era, and Phanerozoic) over varying degree of $CO_2$ lag.; Humlum et al. (2013) for the monthly timeframe in the time period of 1980 to 2010, for 9 to 12 mo; Chylek et al. (2018b) between 1960 and 2016 for monthly data for 5 mo; and Adams and Piovesan (2005) between 1960 and 2004 for monthly data for 4 mo. The study by Sharma and Karamanev (2021) reached the conclusion $CO_2$ lags temperature by over 1000 yr over the last 650,000 yr.

It appears temperature, especially ocean temperature, plays a major and significant role in the consistent change of atmospheric $CO_2$, either directly or indirectly, with other oceanic processes. TSI correlates strongly with atmospheric temperature over the last 2000 yr ($r_{PCC}$ is Strong) and over the shorter period of the last 200 yr ($r_{PCC}$ is Very Strong) lending more evidence that solar energy plays a significant role in the temperature change of the earth.

Thus, a likely scenario for earth's climate change is driven by solar energy controlling temperature, directly or indirectly, and temperature controlling $CO_2$ somewhat modified by other climate factors. As such, this progression is likely influenced to some degree by several other wide-ranging processes from disparate sources such as: orbital-driven insolation forcing; vulcanism; change in cloudiness due to solar magnetic modulation of cosmic rays; planetary gravity; earth global and orbital mechanics; solar sub-processes; ocean circulation, oscillations, and cycles; atmospheric pressures; polar vortexes; solar-driven weakening of the jet stream; and others.

### Acknowledgements

This study could not have been accomplished without access to published data and international databases on temperature, atmospheric $CO_2$, and total solar irradiance. I am grateful to Dr. Ole Humlum for encouragement and informal discussion on this topic as well as peer reviewer, Professor Demetris Koutsoyiannis for structured, critical, and constructive evaluation which has hopefully led to more clarity, accuracy, focus, and scientific merit.

### Supplementary Material

Supplementary Material for this article includes Appendices A–D: (A) Data – Correlation Analysis of $CO_2$ vs. temperature, (B) Statistical Validation Framework, (C) Structural Break or Regime Shift at 1600 AD, and (D) Total Solar Irradiance and Temperature. It is available at Science of Climate Change online:
https://scienceofclimatechange.org/wp-content/uploads/SM-Vol5.3-Grabyan.pdf

### Declarations

This research did not receive any specific grant from funding agencies in the public, commercial, or not-for-profit sectors. The author declares that there are no known competing financial interests or personal relationships that could have appeared to influence the work reported in this paper.

**Editor**: H. Harde; **Reviewers**: D. Koutsoyiannis and anonymous.

## References

Abdussamatov, H., 2015. *Current Long-term Negative Average Annual Energy Balance of the Earth Leads to the New Little Ice Age*. Thermal Science, 19. S279-S288.

Abdussamatov, H., 2016. *The began quasi-centennial epoch of the New Little Ice Age*. In Abstract Book, Eleventh Annual Conference, “Plasma Physics in the Solar System”, February 15-19, 2016. Space Institute of the RAS, Moscow, p 187 (in Russian). https://doi.org/10.1016/B978-0-12-804588-6.00017-3.

Abreu, J. A., Beer, J., Ferriz-Mas, A., 2010. *Past and Future Solar Activity from Cosmogenic Radionuclides*. In Cranmer, S. R., Hoeksema, T. Kohl, J. L. (Ed.), 2010. SOHO-23: Understanding a Peculiar Solar Minimum ASP Conference Series, Vol 428. 287-295. https://www.aspbooks.org › publications › 428 › 287.pdf.

Adams, J. M., Piovesan, G., 2005. *Long series relationships between global interannual $CO_2$ increment and climate: Evidence for stability and change in role of the tropical and boreal-temperate zones.* Chemosphere, 59. 1595-1612. https://doi.org/10.1016/j.chemosphere.2005.03.064.

Ahn, J., Brook, E. J., Mitchell, L., Rosen, J., McConnell, J. R., Taylor K., Etheridge, D., Rubino, M., 2012, *Atmospheric $CO_2$ over the last 1000 years: A high-resolution record from the West Antarctic Ice Sheet (WAIS) Divide ice core.* Global Biogeocehmical Cycles, 26. GB2027, 1-11. https://doi.org/10.1029/2011GB004247.

Bard, E., Frank, M., 2006, *Climate change and solar variability: What's new under the sun?* Earth and Planetary Science Letters, 248, 1-2, 1-14. https://doi.org/10.1016/j.epsl.2006.06.016.

Bard, E., Raisbeck, G., Yiou, F., Jouzel, J., 2000. *Solar irradiance during the last 1200 years based on cosmogenic nuclides*. Tellus B: Chemical and Physical Meteorology, 52-3. 985-992. DOI: 10.3402/tellusb.v52i3.17080.

Benjamini, Y., Hochberg, Y., 1995. *Controlling the False Discovery Rate: A Practical and Powerful Approach to Multiple Testing*. Journal of the Royal Statistical Society: Series B (Methodological), 57(1), 289–300. https://www.jstor.org/stable/2346101.

Beran, J., 1994. *Statistics for long-memory processes.* Chapman and Hall. https://doi.org/10.1201/9780429488670.

Box, G. E., Jenkins, G. M., Reinsel, G. C., & Ljung, G. M. (2015). *Time Series Analysis: Forecasting and Control* (5th ed.). Wiley.

Bretherton, C. S., Smith, C., Wallace, J. M., 1999. *An Intercomparison of Methods for Finding Coupled Patterns in Climate Data*. Journal of Climate, 5(6), 541–560. https://doi.org/10.1175/1520-0442(1992)005<0541:AIOMFF>2.0.CO;2.

Breusch, T. S., 1978. *Testing for autocorrelation in dynamic linear models*. Australian Economic Papers, 17(31), 334–355. https://doi.org/10.1111/j.1467-8454.1978.tb00635.x.

Chapman and Hall/CRC. https://doi.org/10.1201/9781482295304.

Bielfeld, A., 2023, *The Tonga Eruption and its Effect on Earth.* News10NBC, November 29, 2023. https://www.whec.com/top-news/the-tonga-eruption-and-its-effect-on-earth/.

Caillon, N., Severinghaus, J. P., Jouzel, J., Barnola, J-M., Kang, J., Lipenkov, V. Y., 2003. *Timing of Atmospheric $CO_2$ and Antarctic Temperature Changes Across Glacial Terminations*. www.sciencemag.org, 299. 1728-1731. DOI: 10.1126/science.1078758.

Chow, G. C., 1960. *Tests of Equality Between Sets of Coefficients in Two Linear Regressions.* Econometrica, 28(3), 591–605. https://doi.org/10.2307/1910133.

Christy, J., Spencer, R., 2024a. *ESSC Global Temperature Report: August 2024*. The University of Alabama in Hunstville, 35, 5. 1-4. https://www.uah.edu/essc/weather-products/global-temperature-report.

Christy, J., Spencer, R., 2024b. *UAH Lower Troposphere Data, August 2024*. (accessed August 6, 2023). The University of Alabama in Hunstville. https://www.nsstc.uah.edu/data/msu/v6.0/tlt/uahncdc_lt_6.0.txt.

Chylek, P., Folland, C.K., Lesins, G., & Dubey, M.K., 2018a. *Ice core data evidence for a prominent near 20 year time lag of the Antarctic climate response to solar variability*. Geophysical Research Letters, 45, 11749–11756. https://doi.org/10.1029/2018GL079172.

Chylek, P., Tans, P., Christy, J., Dubey, M. K., 2018b. *The carbon cycle response to two El Nino types: an observational study*. Environmental Research Letters, 13. 024001, 1-8. DOI: 10.1088/1748-9326/aa9c5b.

Cobb, K. M., Charles, C. D., Cheng, H., Kastner, M. & Edwards, R. L. 2003. *El Niño/Southern Oscillation and tropical Pacific climate during the last millennium*. Nature 424, 271–276. DOI https://doi.org/10.1038/nature01779.

Covey, C., Thompson, S., Weissman, P., 1994, MacCracken, M., *Global Climatic Effects of Atmospheric Dust from an Asteroid or Comet Impact on Earth*. Global and Planetary Change, 10, 1-25. https://doi.org/10.1016/0921-8181(94)90020-5.

Cronin, T. M., Hayo, K., Thunell, R.C., Dwyer, G. S., Saenger, C., Willard, D.A., 2010. *The Medieval Climate Anomaly and Little Ice Age in Chesapeake Bay and the North Atlantic Ocean*. Palaeogeography, Palaeoclimatology, Palaeoecology, 297, 299-310. DOI: 10.1016/j.palaeo.2010.08.009.

Crowley, T. J., 2000. *Causes of Climate Change Over the Past 1000 Years*. Science, 289. 270-277. DOI: 10.1126/science.289.5477.270.

D'Aleo, J. S., Easterbrook, D. J., 2016. *Relationship of Multidecadal Global Temperatures to Multidecadal Oceanic Oscillations* (Chapter 11). In D. J. Easterbrook (Ed.), 2016. Evidence-Based Climate Science: Data Opposing $CO_2$ Emissions as the Primary Source of Global Warming (2nd ed.). Elsevier, 418 pp. 191-214. https://doi.org/10.1016/B978-0-12-804588-6.00011-2

D'Aleo, J. S., 2016. *Solar Changes and the Climate* (Chapter 15). In D. J. Easterbrook (Ed.),

2016. Evidence-Based Climate Science: Data Opposing $CO_2$ Emissions as the Primary Source of Global Warming (2nd ed.). Elsevier, 418 pp. 263-282. DOI: xxx.

Davis, W. J., 2017. *The Relationship between Atmospheric Carbon Dioxide Concentration and Global Temperature for the Last 425 Million Years*. Climate, 5. 76, 1-34.
DOI: 10.3390/cli5040076.

Dekan, K., 2021. *Volcanism and extreme climatic variability of the mid-13th century: Initiating the little Ice Age*, Little Ice Age. 1-9. DOI: 10.13140/RG.2.2.29018.36809.

Diebold, F. X., Rudebusch, G. D., 1991. *On the power of Dickey-Fuller tests against fractional alternatives*. Economics Letters, 35(2), 155–160. https://doi.org/10.1016/0165-1765(91)90067-T.

Doos, K., Nilsson, J., Nycander, J., Brodeau, L., Ballarotta, M., 2012. *The World Ocean Thermohaline Circulation*. Journal of Physical Oceanography, 42. 1445-1460.
DOI: https://doi.org/10.1175/JPO-D-11-0163.1.

Douglass, D. H., Clader, B. D., 2002. *Climate sensitivity of the Earth to solar irradiance*. Geophysical Research Letters, 29. 16, 33-1-33-4. https://doi.org/10.1029/2002GL015345.

Douglass, D. H., Christy, J., 2009. *Limits on $CO_2$ Climate Forcing from Recent Temperature Data of Earth*. Energy and Environment, 20, 1&2. https://doi.org/10.1260/095830509787689277.

Durbin, J., Watson, G. S., 1950. *Testing for serial correlation in least squares regression: I.* Biometrika, 37(3/4), 409–428. https://doi.org/10.1093/biomet/37.3-4.409.

Easterbrook, D. J., 2016a. *Cause of Global Climate Changes: Correlation of Global Temperature, Sunspots, Solar Irradiance, Cosmic Rays, and Radiocarbon and Berylium Production Rates (Chapter 14)*. In D. J. Easterbrook (Ed.), 2016. Evidence-Based Climate Science: Data Opposing $CO_2$ Emissions as the Primary Source of Global Warming (2nd ed.). Elsevier, 418 pp. 245-262. https://doi.org/10.1016/B978-0-12-804588-6.00014-8.

Easterbrook, D. J., 2016b. *Greenhouse Gases (Chapter 9)*. In D. J. Easterbrook (Ed.), 2016. Evidence-Based Climate Science: Data Opposing $CO_2$ Emissions as the Primary Source of Global Warming (2nd ed.). Elsevier, 418 pp. 163-173. https://doi.org/10.1016/B978-0-12-385956-3.10019-1.

Ermoli, I., Matthes, K., Wit, D., Krivova, N., Tourpali, K., Weber, M., Unruh, Y., Gray, L., Langematz, U., Pilewskie, P., Rozanov, E., Schmutz, W., Shapiro, A., Solanki, S., Woods, T., 2013, *Recent variability of the solar spectral irradiance and its impact on climate modelling.* Atmospheric Chemistry and Physics Discussions, 13. 3945-3977.
https://doi.org/10.5194/acp-13-3945-2013.

Esper, J., Cook, E., Schweingruber, F. H., 2002. *Low-Frequency Signals in Long Tree-Ring Chronologies for Reconstructing Past Temperature Variability*. Science, 295. 2250, 1-4. DOI: 10.1126/science.1066208.

Frank, D. C., Esper, J., Raible, C. C., Buntgen, U., Trouet, V., Stocker, B., Joos, F., 2010. *Ensemble reconstruction constraints on the global carbon cycle sensitivity to climate*. Nature, 463. 527-532. https://doi.org/10.1038/nature08769.

Gelman, A. & Hill, J. Data *Analysis Using Regression and Multilevel/Hierarchical Models*. (Cambridge Univ. Press, 2006). https://doi.org/10.1017/CBO9780511790942.

Geweke, J., Porter-Hudak, S., 1983. *The estimation and application of long memory time series models*. Journal of Time Series Analysis, **4**(4), 221–238. DOI: 10.1111/j.1467-9892.1983.tb00371.x.

Godfrey, L. G., 1978. *Testing for higher order serial correlation in regression equations when the regressors include lagged dependent variables*. Econometrica, 46(6), 1303–1310. https://doi.org/10.2307/1913835.

Gong, Y., Lu, J., Li, T., 2024. *The Impact of Annual Cycles on Anomalous Wind Meridional Structures of the ENSO*. Atmosphere, 15. 940, 1-10. DOI: 10.3390/atmos15080950.

Granger, C. W. J., 1969. *Investigating Causal Relations by Econometric Models and Cross-spectral Methods*. Econometrica, 37(3), 424–438. DOI: 10.2307/1912791.

Granger, C. W. J., & Newbold, P. (1974). *Spurious regressions in econometrics*. Journal of Econometrics, 2(2), 111–120. https://doi.org/10.1016/0304-4076(74)90034-7.

Granger, C. W. J., Joyeux, R., 1980. *An introduction to long-memory time series models and fractional differencing*. Journal of Time Series Analysis, 1(1), 15–29. https://doi.org/10.1111/j.1467-9892.1980.tb00297.x.

Gray, L. J., Beer, J., Geller, M., Haigh, J. D., Lockwood, M., Matthes, K., Cubasch, U., Fleitmann, D., Harrison, G., Hood, L., Luterbacher, J., Meehl, G. A., Shendell, D., van Geel, B., White, W., 2010. *Solar Influences on Climate*. Reviews of Geophysics, 48. RG4001, 1-53. https://doi.org/10.1029/2009RG000282.

Gray, S. T., Betancourt, J. L., Fastie, C. L., Jackson, S. T., 2003. *Patterns and sources of multidecadal oscillations in drought-sensitive tree-ring records from the central and southern Rocky Mountains*. Geophysical Research Letters, 30. 49, 1-4. DOI: 10.1029/2002GL016154.

Gray, W. M., 2012, *The Physical Flaws of the Global Warming Theory and Deep Ocean Circulation Changes as the Primary Climate Driver*. The Heartland Institute 7th International Conference on Climate Change (ICCC-7). 1-32. http://tropical.atmos.colostate.edu/Includes/Documents/Publications/gray2012.pdf.

Haigh, J., Winning, A., Toumi, R., Harder, J., 2010. *An influence of solar spectral variations on radiative forcing of climate*. Nature, 467. 696-699. https://doi.org/10.1038/nature09426.

Harris, C. R., Millman, K. J., van der Walt, S. J., Gommers, R., Virtanen, P., Cournapeau, D. et al., 2020. *Array programming with NumPy*. Nature, 585, 357–362. https://doi.org/10.1038/s41586-020-2649-2.

Hegerl, G. C., Crowley, T. J., Allen, M., Hyde, W. T., Pollack, H. N., Smerdon, J., Zorita, E., 2007. *Detection of Human Influence on a New, Validated 1500-Year Temperature Reconstruction*. Journal of Climate, 20. 650-666. https://doi.org/10.1175/JCLI4011.1.

Hoesly, R. M., Smith, S. J., Feng, L., Kilmont, Z., Janssens-Maenhout, G., Pitkanen, T., Selbert, J. J., Vu, L., Andres, R. J., Bolt, R. M., Bond, T. C., Dawidowski, L., Kholod, N., Kurokawa, J., Li, M., Liu, L., Lu, Z., Moura, M. C. P., O'Rourke, R., Zhang, Q., 2018. *Historical (1750–2014) anthropogenic emissions of reactive gases and aerosols from the Community Emissions Data System (CEDS)*. Geoscientific Model Development, 11, 369-408. https://doi.org/10.5194/gmd-11-369-2018.

Hoyt, D. V., Schatten, K. H., 1993. *A Discussion of Plausible Solar Irradiance Variations, 1700-1992*. Journal of Geophysical Research, 98. 18,895-18,906. https://doi.org/10.1029/93JA01944.

Hoyt, D. V., Schatten, K. H., 1997. *The Role of the Sun in Climate Change*. Oxford University Press, 279 pp. https://doi.org/10.1023/A:1006179829911.

Hunter, J. D., 2007. *Matplotlib: A 2D graphics environment*. Computing in Science & Engineering, 9 (3), 90–95. https://doi.org/10.1109/MCSE.2007.55.

Hyndman, R. J., & Athanasopoulos, G. (2018). *Forecasting: Principles and Practice* (2nd ed.). OTexts. https://otexts.com/fpp2/

Humlum, O., Stordahl, K., Solheim, J-E., 2013. *The phase relation between atmospheric carbon dioxide and global temperature*. Global and Planetary Change, 100. 51-69. http://dx.doi.org/10.1016/j.gloplacha.2012.08.008.

Hurst, H. E., 1951. *Long-term storage capacity of reservoirs*. Transactions of the American

Society of Civil Engineers, 116, 770–799.

Huybers, P. J., & Curry, W. B. (2006). *Links between annual, Milankovitch and continuum temperature variability*. Nature, 441(7091), 329–332. https://doi.org/10.1038/nature04745.

Imbrie, J., Boyle, E. A., Clemens, S. C., Duffy, A., Howard, W. R., Kukla, G., Kutzbach, J., Martinson, D. G., McIntyre, A., Mix, A. C., Molfino, B., Moreley, J. J., Peterson, L. C., Pisias, N. G., Prell, W. L., Raymo, M. E., Shackleton, N. J., Toggweiler, J. R., 1992. *On the Structure and Origin of Major Glaciation Cycles 1. Linear Responses to Milankovitch Forcing*. Paleoceanography, 7, 6, 701-738. https://doi.org/10.1029/92PA02253.

Ineson, S., Scaife, A. A., Knight, J. R., Manners, J. C., Dunstone, N. J., Gray, L. J., Haigh, J. D., 2011. *Solar forcing of winter climate variability in the Northern Hemisphere*. Nature Geoscience, 4. 753-757. https://doi.org/10.1038/ngeo1282.

James, G., Witten, D., Hastie, T., & Tibshirani, R. (2021). *An Introduction to Statistical Learning* (2nd ed.). Springer. https://doi.org/10.1007/978-1-0716-1418-1.

Jones, P. D., Briffa, K. R., Barnett, T. P., Tett, S. F. B., 1998. *High-resolution palaeoclimatic records for the last millennium: interpretation, integration and comparison with General Circulation Model control-run temperatures*. The Holocene, 8. 4, 455-471. https://doi.org/10.1191/095968398667194956.

Jones, P. D., & Mann, M. E. (2004). *Climate over past millennia*. Reviews of Geophysics, 42(2). https://doi.org/10.1029/2003RG000143

Juckes, M. N., Allen, M. R., Briffa, K. R., Esper, J., Hegerl, G. C., Moberg, A., Osborn, T. J., Weber, S. L., 2007. *Millennial temperature reconstruction intercomparison and evaluation*. Climate of the Past, 3. 591-609. https://doi.org/10.5194/cp-3-591-2007.

Katata, G., Connolly, R., O'Neill, P., 2023. *Evidence of Urban Blending in Homogenized Temperature Records in Japan and in the United States: Implications for the Reliability of Global Land Surface Air Temperature Data*. Journal of Applied Meteorology and Climatology, 62. 1095-1114. DOI: 10.1175/JAMC-D-22-0122.1.

Kennedy J.J., Rayner, N.A., Smith, R.O., Saunby, M. and Parker, D.E. (2011a). *Reassessing biases and other uncertainties in sea-surface temperature observations since 1850 part 1: Measurement and sampling errors*. J. Geophys. Res., 116, D14103, doi:10.1029/2010JD015218 (PDF 1Mb) (accessed August 6, 2023). https://www.metoffice.gov.uk/hadobs/hadsst3/data/HadSST.3.1.1.0/diagnostics/HadSST.3.1.1.0_annual_globe_ts.txt.

Kennedy J.J., Rayner, N.A., Smith, R.O., Saunby, M. and Parker, D.E. (2011b). *Reassessing biases and other uncertainties in sea-surface temperature observations since 1850 part 2: Biases and homogenization*. J. Geophys. Res., 116, D14104, doi:10.1029/2010JD015220. (PDF 1Mb) (accessed August 6, 2023). https://www.metoffice.gov.uk/hadobs/hadsst3/data/HadSST.3.1.1.0/diagnostics/HadSST.3.1.1.0_annual_globe_ts.txt.

Komitov, B., Kaftan, V., 2020. *The Volcanic and Solar Activity Relationship During the Last ~ 460 Years. Could a Significant Part of the "Sun-Climate" Relationship Goes Through Lithosphere?* In Georgieva, K., Kirov, B., Danov, D., 2020. Workshop "Solar Influences on the Magnetosphere, Ionosphere and Atmosphere", Book of Proceedings. Space Research and Technologies Institute Bulgarian Academy of Sciences, 135-140. DOI: 10.31401/WS.2020.proc.

Koscielny-Bunde, E., Bunde, A., Havlin, S., Roman, H. E., Goldreich, Y., Schellnhuber, H. J., 1998. *Indication of a universal persistence law governing atmospheric variability*. Physical Review Letters, 81(3), 729–732. https://doi.org/10.1103/PhysRevLett.81.729.

Koskinas, A., Zacharopoulou, E., Pouliasis, G., Deligiannis, I., Dimitriadis, P., Iliopoulou, T., Mamassis, N., and Koutsoyiannis, D., 2022. *Estimating the Statistical Significance of*

*Cross–Correlations between Hydroclimatic Processes in the Presence of Long–Range Dependence*, Earth, 3 (3), 1027-1041, doi:10.3390/earth3030059, 2022.

Kouwenberg, L., Wagner, R., Kurschner, W., Visscher, H., 2005, *Atmospheric* $CO_2$ *fluctuations during the last millennium reconstructed by stomatal frequency analysis of Tsuga heterophylla needles*. Geological Society of America, 33, No. 1, 33-36.

Koutsoyiannis, D., 2024a, *Stochastic assessment of temperature –* $CO_2$ *causal relationship in climate from the Phanerozoic through modern times*, Mathematical Biosciences and Engineering, 21 (7), 6560–6602, doi:10.3934/mbe.2024287.

Koutsoyiannis, D., 2024b, *The relationship between atmospheric temperature and carbon dioxide concentration*, Science of Climate Change, 4 (3), 39–59, doi:10.53234/scc202412/15, 2024b.

Koutsoyiannis, D., 2024c, *Stochastics of Hydroclimatic Extremes - A Cool Look at Risk*, Edition 4, ISBN: 978-618-85370-0-2, 400 pages, doi:10.57713/kallipos-1, Kallipos Open Academic Editions, Athens.

Koutsoyiannis, D. and Kundzewicz, Z. W., 2020, *Atmospheric temperature and* $CO_2$*: Hen-or-egg causality?*, Sci, 2 (4), 83, doi:10.3390/sci2040083.

Koutsoyiannis, D., Onof, C., Christofides, A., and Kundzewicz, Z. W., 2022a, *Revisiting causality using stochastics: 1.Theory*, Proceedings of The Royal Society A, 478 (2261), 20210835, doi:10.1098/rspa.2021.0835.

Koutsoyiannis, D., Onof, C., Christofides, A., and Kundzewicz, Z. W., 2022b, *Revisiting causality using stochastics: 2*. Applications, Proceedings of The Royal Society A, 478 (2261), 20210836, doi:10.1098/rspa.2021.0836.

Koutsoyiannis, D., Onof, C., Kundzewicz, Z. W., and Christofides, A., 2023, *On hens, eggs, temperatures and* $CO_2$*: Causal links in Earth's atmosphere*, Sci, 5 (3), 35, doi:10.3390/sci5030035.

Knudsen, M. F., Seidenkrantz, M. S., Jacobsen, B. H., Kuijpers, A., 2011. *Tracking the Atlantic Multidecadal Oscillation through the last 8,000 years.* Nature Communications, 10. 1038, Trenberth 1-9. https://doi.org/10.1038/ncomms1186.

Lean, J., 2000. *Evolution of the Sun's Spectral Irradiance Since the Maunder Minimum.* Geophysical Research Letters, 27. 16, 2425-2428. https://doi.org/10.1029/2000GL000043.

Lean, J. L., 2018. *Estimating Solar Irradiance Since 850 CE*. Earth and Space Science, 5. 133-149. https://doi.org/10.1002/2017EA000357.

Lee, J. and Wang, A., 2022. *Tonga Eruption Blasted Unprecedented Amount of Water Into Stratosphere*, August 2, 2022. Jet Propulsion Laboratory. https://www.nasa.gov/earth/tonga-eruption-blasted-unprecedented-amount-of-water-into-stratosphere/.

Lenssen, N., G.A. Schmidt, M. Hendrickson, P. Jacobs, M. Menne, and R. Ruedy, 2024: *A GISTEMPv4 observational uncertainty ensemble.* J. Geophys. Res. Atmos., 129, no. 17, e2023JD040179, doi:10.1029/2023JD040179.
https://data.giss.nasa.gov/gistemp/tabledata_v4/GLB.Ts+dSST.txt.

Li, Z., Chang, L., Lou, J., Shen, Y., Yan, H., 2022. *Multi-scale Analysis of the Relationships between Solar Activity,* $CO_2$ *and Global Surface Temperature*. Research in Astronomy and Astrophysics, 22. DOI 10.1088/1674-4527/ac8339.

Lin, J., Qian, T., 2022. *The Atlantic Multi-Decadal Oscillation*. Atmosphere-Ocean, 60. 3-4, 307-337. https://doi.org/10.1080/07055900.2022.2086847.

Ljung, G. M., Box, G. E. P., 1978. *On a measure of lack of fit in time series models.* Biometrika, 65(2), 297–303. https://doi.org/10.1093/biomet/65.2.297.

Ljungqvist, F. C., 2010, *A New Reconstruction of Temperature Variability in the Extra-Tropical Northern Hemisphere During the last Two Millennia*. Swedish Society for Anthropology and Geography, Series A. Sept 6. https://doi.org/10.1111/j.1468-0459.2010.00399.x.

Lockwood, M., Stamper, R., 1999. *Long-term drift of the coronal source magnetic flux and the total solar irradiance*. Geophysical Research Letters, 26. 16, 2461-2464. https://doi.org/10.1029/1999GL900485.

Loehle, C., McCulloch, J. H., 2008. *Correction to: A 2000-Year Global Temperature Reconstruction Based on Non-Tree Ring Proxies.* Energy & Environment, 19. 1, 92-100. https://www.jstor.org/stable/44397366.

Lorenz, S. J., Kim, J., Rimbu, N, Schneider, R. R., Lohmann, G., 2006. *Orbitally driven insolation forcing on Holocene climate trends: Evidence from alkenone data and climate modeling*. Paleoceanography, 21. PA1002. doi:10.1029/2005PA001152.

Lourens, L. J., Tuenter, E., 2016. *Chapter 25 – The Variation of the Earth's Movements (Orbital, Tilt and Precession)*. In T. Letcher (Ed.) Climate Change – Observed Impacts on Planet Earth (2nd ed.). Elsevier, 632 pp. 399-418. https://doi.org/10.1016/B978-0-444-63524-2.00025-7.

MacFarling Meure, C., Etheridge, D., Trudinger, C., Steele, P., Langenfelds, R., van Ommen, T., Smith, A., Elkins, J., 2006. *Law Dome $CO_2$, CH4 and N2O ice core records extended to 2000 years BP*. Geophysical Research Letters, 33. L14810, 1-5. https://doi.org/10.1029/2006GL026152.

Mann, M.E., Bradley, R.S., & Hughes, M.K., 1999. *Northern Hemisphere temperatures during the past millennium: Inferences, uncertainties, and limitations.* Geophysical Research Letters, 26(6), 759–762. https://doi.org/10.1029/1999GL900070.

Mann, M. E. (2004). *On smoothing potentially non-stationary climate time series*. Geophysical Research Letters, 31(7). https://doi.org/10.1029/2004GL019569.

Mann, M. E., Zhang, Z., Hughes, M. K., Bradley, R. S., Miller, S. K., Rutherford, S., Ni, F., 2008. *Proxy-based reconstructions of hemispheric and global surface temperature variations over the past two millennia*. Proceedings of the National Academy of Sciences, 105. 36, 1-6. https://doi.org/10.1073/pnas.0805721105.

Mann, M. E., Zhang, Z., Rutherford, S., Bradley, R. S., Hughes, M. K., Shindell, D., Ammann, C., Faluvegi, G., Ni, F., 2009. *Global Signatures and Dynamical Origins of the Little Ice Age and Medieval Climate Anomaly*. Science, 326. 1256-1260. DOI: 10.1126/science.1177303.

Marsh, G. E., 2014, *Interglacials, Milankovitch Cycles, Solar, Activity, and Carbon Dioxide*. Journal of Climatology, 2014. 345482, 1-7. https://doi.org/10.1155/2014/345482.

McGregor, H. V., Evans, M. N., Goosse, H., Leduc, G., Martrat, B., Addison, J. A., Mortyn, P. G., Oppo, D. W., Seidenkrantz, M. S., Sicre, M.-A., & Waelbroeck, C., 2013. *Robust global ocean cooling trend for the pre-industrial Common Era.* Nature Geoscience, 6(7), 615–620. DOI: 10.1038/ngeo1797.

McKinney, W., 2010. *Data structures for statistical computing in Python*. Proceedings of the 9th Python in Science Conference, 51–56. https://doi.org/10.25080/Majora-92bf1922-00a.

McKitrick, R., 2010. *A Critical Review of Global Surface Temperature Data Products*. SSRN, 6 August 2010. https://papers.ssrn.com/sol3/papers.cfm?abstract_id=1653928.

Middleton, D., 2011. *$CO_2$: Ice Cores vs. Plant Stomata.* https://wattsupwiththat.com/2010/12/26/co2-ice-cores-vs-plant-stomata/.

Microsoft Corporation, 2022. *Microsoft Excel, Version 2301, with Visual Basic for Applications*. Redmond, WA: Microsoft Corporation.

Moberg, A., Sonechkin, D. M., Holmgren, K., Datsenko, N. M., Karlen, W., 2005. *Highly variable Northern Hemisphere temperatures reconstructed from low- and high-resolution proxy data.* Nature, 3265. 1-5. DOI: 10.1038/nature03265.

Moffa-Sanchez, P., Born, A., Hall, I. R., Thornalley, D. J. R., Barker, S., 2014. *Solar forcing of North Atlantic surface temperature and salinity over the past millennium*. Nature Geoscience, 7. 275-278. https://doi.org/10.1038/ngeo2094.

Monnin, E., Indermuhle, A., Dallenbach., A, Fluckiger, J., Stauffer, B., Stocker, T. F. Raynaud, D., Barnola, J-M., 2001. *Atmospheric $CO_2$ Concentrations over the Last Glacial Termination.* www.sciencemag.org, 291. 112-114. DOI: 10.1126/science.291.5501.112.

Morice, C. P., J. J. Kennedy, N. A. Rayner, and P. D. Jones, 2012, *Quantifying uncertainties in global and regional temperature change using an ensemble of observational estimates: The HadCRUT4 dataset*. J. Geophys. Res., 117, D08101. (accessed August 6, 1923) doi:10.1029/2011JD017187.https://www.metoffice.gov.uk/hadobs/hadcrut4/data/current/time_series/HadCRUT.4.6.0.0.annual_ns_avg.txt.

Morner, N., 2012. *Planetary beat, solar wind and terrestrial climate*. In Borrega, C. D. E. and Cruz, A. F. B. (Ed.), 2012. Solar Wind: Emission, Technologies and Impacts. Nova Science Publishers. Inc., 987 pp. 47-66. https://novapublishers.com/shop/solar-wind-emission-technologies-and-impacts/.

Mudelsee, M., 2001. *The phase relations among atmospheric $CO_2$ content, temperature and global ice volume over the past 420 ka*. Quaternary Science Reviews, 20. 583-589. https://doi.org/10.1016/S0277-3791(00)00167-0. DOI 10.1007/s11207-016-0969-z.

Mudelsee, M., 2010. *Climate Time Series Analysis: Classical Statistical and Bootstrap Methods*. Springer. https://doi.org/10.1007/978-90-481-9482-7.

Mudelsee, M., 2014. Climate Time Series Analysis: Classical Statistical and Bootstrap Methods (2nd ed.) Springer. DOI: 10.1007/978-3-319-04450-7.

Muscheler, R., Adolphi, F., Herbst, K., Nilsson, A., 2016. *The Revised Sunspot Record in Comparison to Cosmogenic Radionuclide-Based Solar Activity Reconstructions*. Solar Physics, 291. 3025-3043.

Newey, W.K. and West, K.D. (1987) A simple, positive semi-definite, heteroskedasticity and autocorrelation consistent covariance matrix. Econometrica, 55(3), 703-708. DOI 10.3386/t0055.

Ogurtson, M. G., Nagovitsyn, A., Kocharov, G. E., Jungner, H., 2002. *Long-period cycles of the sun's activity recorded in direct solar data and proxies.* Solar Physics, 211. 371-394. https://doi.org/10.1023/A:1022411209257.

Parker, D.E., T.P. Legg, and C.K. Folland. 1992. *A new daily Central England Temperature Series*. 1772-1991. Int. J. Clim., Vol 12, pp 317-342 (PDF) (accessed August 6, 2023) https://www.metoffice.gov.uk/hadobs/hadcet/data/legacy/cetml1659on.dat.

Pearson, K., 1896. *Mathematical contributions to the theory of evolution. III. Regression, heredity, and panmixia*. Philosophical Transactions of the Royal Society of London. A, 187, 253–318. https://doi.org/10.1098/rsta.1896.0007.

Peltier Tech, 2024. Peltier Technical Services. Peltier Tech Website (https://peltiertech.com/documentation/loess/).

Peng, C. K., Buldyrev, S. V., Havlin, S., Simons, M., Stanley, H. E., & Goldberger, A. L., 1994. *Mosaic organization of DNA nucleotides*. Physical Review E, 49(2), 1685–1689. https://doi.org/10.1103/PhysRevE.49.1685.

Politis, D. N., & Romano, J. P., 1994. *The Stationary Bootstrap*. Journal of the American Statistical Association, 89(428), 1303–1313. DOI: 10.1080/01621459.1994.10476870.

Python Software Foundation, 2023. *Python Language Reference, version 3.10.*

https://www.python.org.

Quintessa Limited, 2020. *Graph Grabber v2.0.2*.

R Core Team, 2024. *R: A language and environment for statistical computing*. R Foundation for Statistical Computing, Vienna, Austria. https://www.R-project.org.

Roe, G., 2006. *In defense of Milankovitch.* Geophysical Research Letters, 33, L24703, 1-5. DOI: 10.1029/2006GL027817.

Rubino, M., Etheridge, D. M., Thornton, D. P., Howden, R., Allison, C. E., Francey, R. J., Langenfelds, R. L., Steele, L. P., Trudinger, C. M., Spencer, D. A., Curran, M. A. J., Ommen, T. D., Smith, A. M., 2019. *Revised records of atmospheric trace gases $CO_2$, CH4, N2O, and δ 13C-$CO_2$ over the last 2000 years from Law Dome, Antarctica.* Earth Systems Science Data, 11, 473-492. https://doi.org/10.5194/essd-11-473-2019.

Scafetta, N., 2021. *Detection of non-climatic biases in land surface temperature records by comparing climatic data and their model simulations.* Climate Dynamics, 56. 2959-2982. https://doi.org/10.1007/s00382-021-05626-x.

Scafetta, N., Bianchini, A., 2022. *The Planetary Theory of Solar Activity Variability: A Review*. Frontiers in Astronomy and Space Sciences, 9. 937930, 1-26. https://doi.org/10.3389/fspas.2022.937930.

Scafetta, N., 2023. *Empirical assessment of the role of the Sun in climate change using balanced multi-proxy solar records*. Geoscience Frontiers, 14. 101650, 1-19. https://doi.org/10.1016/j.gsf.2023.101650.

Schwander, M., Rohrer, M., Bronnimann, S., Malik, A., 2017. *Influence of solar variability on the occurrence of central European weather types from 1763 to 2009*. Climate of the Past, 13. 1199-1212. https://doi.org/10.5194/cp-13-1199-2017.

Schmutz, W. K., 2021. *Changes in the Total Solar Irradiance and climatic effects.* Journal Space Weather Space Climate, 11. 40, 1-13. https://doi.org/10.1051/swsc/2021016.

Shackleton, N. J., 2000. *The 100,000-Year Ice-Age Cycle Identified and Found to Lag Temperature, Carbon Dioxide, and Orbital Eccentricity*. Science, 289. 1897-1902. DOI: 10.1126/science.289.5486.1897.

Shapiro, A. I., Schmutz, W., Rozanov, E., Schoell, M., Haberreiter, M., Shapiro, A. V., Nyeki, S., 2011. *A new approach to the long-term reconstruction of the solar irradiance leads to large historical solar forcing*. Astronomy & Astrophysics, 529. A67, 1-8. https://doi.org/10.48550/arXiv.1102.4763.

Sharma, K., Karamanev, D., 2021. *Investigating the Historic Correlation between Atmospheric Carbon Dioxide Concentration and Global Temperature Change*. Ecological Engineering and Environmental Protection, 1. 5-16. DOI: 10.32006/eeep.2021.1.0516.

Shaviv, N. J., 2008. *Using the oceans as a calorimeter to quantify the solar radiative forcing*. Journal of Geophysical Research, 113. A11101, 1-13. doi:10.1029/2007JA012989.

Shaviv, N. J., Svensmark, H., Veizer, J., 2023, *The Phanerozoic climate*. Annals of the New York Academy of Sciences, 1519. 7-19. https://doi.org/10.1111/nyas.14920.

Solanki, S., Fligge, M., 1999, *A reconstruction of total solar irradiance since 1700.* Geophysical Research Letters, 26. 16, 2465-2468. https://doi.org/10.1029/1999GL900370.

Soon, W. H., 2009. *Solar Arctic-mediated Climate Variation on Multidecadal to Centennial Timescales: Empirical Evidence, Mechanistic Explanation, and Testable Consequences.* Physical Geography, 30. 144-184. https://doi.org/10.2747/0272-3646.30.2.144.

Soon, W., Connolly, R., Connolly, M., 2015. *Re-evaluating the role of solar variability on Northern Hemisphere temperature trends since the 19th century*. Earth-Science Reviews, 150. 409-

452. https://doi.org/10.1016/j.earscirev.2015.08.010.

Soon, W., Legates, D. R., 2013. *Solar irradiance modulation of Equator-to-Pole (Arctic) temperature gradients: Empirical evidence for climate variation on multi-decadal timescales.* Journal of Atmospheric and Solar-Terrestrial Physics, 93. 25-56. https://doi.org/10.1016/j.jastp.2012.11.015.

Soon, W., Connolly, R., Connolly, M., Akasofu, S., Baliunas, S., Berglund, J., Bianchini, A., Briggs, W., Butler, C., Cionco, R., Crok, M., Elias, A., Fedorov, V., Gervais, F., Harde, H., Henry, G., Hoyt, D., Humlum, O., Legates, D., Lupo. A., Maruyama, S., Moore, P., Ogurtsov, M., ÓhAiseadha, C., Oliveira, M., Park, S., Qiu, S., Quinn, G., Scafetta, N., Solheim, J., Steele, J., Szarka, L., Tanaka, H., Taylor, M. Vahrenholt, F., Velasco Herrera, V., Zhang, W., 2023. *The Detection and Attribution of Northern Hemisphere Land Surface Warming (1850–2018) in Terms of Human and Natural Factors: Challenges of Inadequate Data*. Climate, 11, 179. 1-36. https://doi.org/10.3390/cli11090179.

Spencer, R., 2024. *Recent UAH Research: Urban Heat Island Effects*. The University of Alabama in Huntsville. https://www.drroyspencer.com/2023/11/examples-from-our-new-uah-urban-heat-island-dataset/, June 15, 2024.

Stefani, F., Giesecke, A., Seilmayer, M., Stepanov, R., Weier, T., 2004. *Schwabe, Gleissberg, Suess-de Vries: Towards a Consistent Model of Planetary Synchronization of Solar Cycles*. Magnetohydrodynamics, 40. 1, 1-11. https://doi.org/10.48550/arXiv.1910.10383.

Steinhilber, F., Abreu, J. A., Beer, J, McCracken, K. G., 2010. *Interplanetary magnetic field during the past 9300 years inferred from cosmogenic radionuclides*. Journal of Geophysical Research, 115. A01104, 1-15.

Steinhilber, F., Beer, J., Frohlich, C., 2009. *Total solar irradiance during the Holocene*. Geophysical Research Letters, 36. L19704, 1-5. https://doi.org/10.1029/2009JA014193.

Stock, J. H., & Watson, M. W., 2003. *Introduction to Econometrics*. Addison-Wesley, Boston. 785 pp.

Svensmark, H., Friis-Christensen, E., 1997. Variation of cosmic ray flux and global cloud coverage-a missing link in solar-climate relationships. Journal of Atmospheric and Solar-Terrestrial Physics, 59. 11, 1225-1232. https://doi.org/10.1016/S1364-6826(97)00001-1

Svensmark, H., 1999. *Cosmic Rays and Earth's Climate*. Space Science Reviews, 93. 175-185. https://doi.org/10.1023/A:1026592411634.

Svensmark, H., 2007. *Cosmoclimatology: a new theory emerges*. Astronomy & Geophysics, 48. 1.18-1.24. https://doi.org/10.1111/j.1468-4004.2007.48118.x.

Svensmark, J., Enghoff, M. B., Shaviv, N. J., Svensmark, H., 2016. *The response of clouds and aerosols to cosmic ray decreases*. Journal of Geophysical Research: Space Physics, 121. 8152-8181. https://doi.org/10.1002/2016JA022689.

Svensmark, H., Svensmark, J., Enghoff, M. B., Shaviv, N. J., 2021. *Atmospheric ionization and cloud radiative forcing*. Scientific Reports, 11. 19668, 1-13. DOI: 10.1038/s41598-021-99033-1.

Svensmark, H., 2022. *Supernova Rates and Burial of Organic Matter*. Geophysical Research Letters, 48, e2021GL096376, 1-9. https://doi.org/10.1029/2021GL096376.

Toggweiler, J. R., Key, R. M., 2001. *Thermohaline Circulation*. Academic Press. 8 pp. https://doi.org/10.1016/B0-12-227090-8/00281-5.

Trenberth, K. E., 2016. *El Nino Southern Oscillation (ENSO)*. Elsevier, 12 pp. 1-12. https://doi.org/10.1016/B978-0-12-409548-9.04082-3.

US Historical Climatological Network, 2024, https://www.ncei.noaa.gov/data/ushcn/v25/.

Usoskin, I. G., Schussler, M., Solanki, S. K., Mursula, K., 2005. Solar activity, cosmic rays, and Earth's temperature: A millennium-scale comparison. Journal of Geophysical Research, 110. A10102, 1-11. https://doi.org/10.1029/2004JA010946.

Usoskin, I. G., Gallet, Y., Lopes, F., Kovaltsov, G. A., Hulot, G., 2016. *Solar activity during the Holocene: the Hallstatt cycle and its consequence for grand minima and maxima*. Astronomy & Geophysics, 587. A150, 1-10. DOI: 10.1051/0004-6361/201527295.

Vevard, C., Veizer, J., 2019. *On plate tectonics and ocean temperatures.* Geology, 47. 9, 881-885. https://doi.org/10.1130/G46376.1.

Vinos, J., 2024a, *Hunga-Tonga volcano: impact on record warming*. In Curry, J. A. (Ed), Climate Etc., https://judithcurry.com/2024/07/05/hunga-tonga-volcano-impact-on-record-warming/. July 5, 2024.

Vinos, J., 2024b, *Hunga Tonga volcano: impact on record warming*, in Watts, A., (Ed), Watts Up With That. https://wattsupwiththat.com/2024/07/09/hunga-tonga-volcano-impact-on-record-warming/. July 9, 2024.

Virtanen, P., Gommers, R., Oliphant, T. E., Haberland, M., Reddy, T., Cournapeau, D. et al., 2020. *SciPy 1.0: Fundamental algorithms for scientific computing in Python*. Nature Methods, 17 (3), 261–272. https://doi.org/10.1038/s41592-019-0686-2.

von Storch, H., Zwiers, F. W., 1999. *Statistical analysis in climate research.* Cambridge University Press. https://doi.org/10.1017/CBO9780511612336.

Wallace, J., D'Aleo, J., Idso, C., 2017. *On the Validity of NOAA, NASA and Hadley CRU Global Average Surface Temperature Data & The Validity of EPA's $CO_2$ - Endangerment Finding - Abridged Research Report*. Academia. https://www.academia.edu/33850726/On_the_Validty_of_NOAA_NASA_and_Hadley_CRU_Global_Average_Surface_Temperature_Data_and_The_Validity_of_EPAs_CO_2_Endangerment_Finding_Abridged_Research_Report. June, 2017.

Wang, G., Zhao, C., Zhang, M., Zhang, Y., Lin, M., Qiao, F., 2020. *The causality from solar irradiation to ocean heat content detected via multi-scale Liang–Kleeman information flow.* Scientific Reports, Nature Portfolio, 10. 17141, 1-9. https://doi.org/10.1038/s41598-020-74331-2.

Wang, Q., Ren, F., Li, R., 2024. *Uncovering the world's largest carbon sink—a profile of ocean carbon sinks research*. Environmental Science and Pollution Research, 31. 20362-20382. DOI: 10.1007/s11356-024-32161-z.

Wanner, H., Pfister, C., Neukom, R., 2022. *The variable European Little Ice Age*. Quaternary Science Reviews, 287. 107531. https://doi.org/10.1016/j.quascirev.2022.107531.

Watts, A. 2012, *An area and distance weighted analysis of the impacts of station 1 exposure on the U.S. Historical Climatology Network temperatures and 2 temperature trends.* In Watts, A. (Ed), Watts Up With That. https://wattsupwiththat.com/2012/07/29/press-release-2/. July 29, 2012.

White, W. B., Lean, J., Cayan, D. R., Dettinger, M. D., 1997. *Response of global upper ocean temperature to changing solar irradiance*. Journal of Geophysical Research, 102. C2, 3255-3266. https://doi.org/10.1029/96JC03549.

White, W. B., Dettinger, M. D., Cayan, D. R., 2000. *Global Average Upper Ocean Temperature Response to Changing Solar Irradiance: Exciting the Internal Decadal Mode.* Proceedings 1st Solar & Space Weather Euroconference. 125-132.

Wickham, H., 2016. *ggplot2: Elegant graphics for data analysis.* Springer-Verlag, New York. https://ggplot2.tidyverse.org.

Willson, R. C., Hudson, H. S., 1988. *Solar luminosity variations in solar cycle 21*. Nature, 332. 6167, 810-812. https://doi.org/10.1038/332810a0.

Willson, R. C., 1997. *Total Solar Irradiance Trend During Solar Cycles 21 and 22.* Science, 277. 1963-1965. DOI: 10.1126/science.277.5334.1963.

Willson, R. C., Mordvinov, A. V., 2003. *Secular total solar irradiance trend during solar cycles 21–23*. Geophysical Research Letters, 30. No. 5, 1199, 3-1 to 3-4. https://doi.org/10.1029/2002GL016038.

Wilson, Daniel C. S., 2014, *"Arnold Toynbee and the Industrial Revolution: The Science of History, Political Economy and the Machine Past."* History and Memory, vol. 26, no. 2, 2014, pp. 133–61. JSTOR, https://doi.org/10.2979/histmemo.26.2.133.

Wu, C. J., Krivova, N. A., Solanki, S. K., Usoskin, I. G., 2018. *Solar total and spectral irradiance reconstruction over the last 9000 years.* Astronomy & Astrophysics. 1-12. https://doi.org/10.1051/0004-6361/201832956.

Yang, B., Braeuning, A., Johnson, K. R., Yafeng, S., 2002. *General characteristics of temperature variation in China during the last two millennia*. Geophysical Research Letters, 29. No 9, 1324. 1-4. https://doi.org/10.1029/2001GL014485.

Yu, J., Anderson, R. F., Jin, Z. D., Ji, X., Thornalley, D. J. R., Wu, L., Thouveny, N., Cai, Y., Yan, L., Zhang, F., Menviel, L., Tian, J., Xie, X., Rohling, E. J., McManus, J. F., 2023. *Millennial atmospheric $CO_2$ changes linked to ocean ventilation modes over past 150,000 years*. Nature Geoscience, 16. 1166-1173. https://doi.org/10.1038/s41561-023-01297-x.

Zeileis, A., and Hothorn, T., 2002. *Diagnostic checking in regression relationships*. R News, 2 (3), 7–10. https://CRAN.R-project.org/package=lmtest.

Zeileis, A., and Grothendieck, G., 2005. *zoo: S3 infrastructure for regular and irregular time serie*s. Journal of Statistical Software, 14 (6), 1–27. https://doi.org/10.18637/jss.v014.i06.

Zhao, X., Soon, W., Herrera, V. M V., 2020. *Evidence for Solar Modulation on the Millennial-Scale Climate Change of Earth*. Universe, 6. 153, 1-9. https://doi.org/10.3390/universe6090153.

## Copyright References

Figure 1. Copyright note - Figure reproduced with permission from: (1) Rubino et al. (2019) – © CC By 4.0; (2) Ljungqvist (2010) - © The authors 2010, Geografiska Annaler: Series A © 2010 Swedish Society for Anthropology and Geography reprinted by permission of Informa UK Limited, trading as Taylor & Francis Group, www.tandfonline.com om behalf of Swedish Society for Anthropology and Geography.

Figure 2. Copyright note - Figure reproduced with permission from: (1) Rubino et al. (2019) – © CC By 4.0; (2) Moberg (2005) -- © 2005, Macmillan Magazines Ltd.

Figure 3. Copyright note - Figure reproduced with permission from: Hegerl et al. (2007) -- © American Meteorological Society.

Figure 4. Copyright note - Figure reproduced with smoothing with permission from: (1) Rubino et al. (2019) – © CC By 4.0; (2) Ljungqvist (2010) - © The authors 2010, Geografiska Annaler: Series A © 2010 Swedish Society for Anthropology and Geography reprinted by permission of Informa UK Limited, trading as Taylor & Francis Group, www.tandfonline.com om behalf of Swedish Society for Anthropology and Geography.

Figure 5. Copyright note - Figure reproduced with smoothing with permission from: (1) Rubino et al. (2019) – © CC By 4.0; (2) Yang et al. (2002) -- © 2024. American Geophysical Union.

Figure 6. Copyright note - Figure reproduced with smoothing with permission from: (1) Rubino et al. (2019) – © CC By 4.0; (2) Ljungqvist (2010) - © The authors 2010, Geografiska Annaler: Series A © 2010 Swedish Society for Anthropology and Geography reprinted by permission of Informa UK Limited, trading as Taylor & Francis Group, www.tandfonline.com om behalf of

Swedish Society for Anthropology and Geography.

Figure 7. Copyright note - Figure reproduced with smoothing with permission from: (1) Rubino et al. (2019) – © CC By 4.0; (2) Yang et al. (2002) -- © 2024. American Geophysical Union.

Figure 8. Copyright note – Figure reproduced with smoothing with permission from: (1) MacFarling Meure et al. (2006) -- © 2024 American Geophysical Union; (2) Hegerl et al. (2007) -- © American Meteorological Society.

Figure 9. Copyright note – Figure reproduced with smoothing with permission from: (1) MacFarling Meure et al. (2006) -- © 2024 American Geophysical Union; (2) Yang et al. (2002) -- © 2024. American Geophysical Union.

Figure 10. Copyright note - Figure reproduced with permission from: (1) Rubino et al. (2019) – © CC By 4.0; (2) Hegerl et al. (2007) -- © American Meteorological Society.

Figure 11. Copyright note - Figure reproduced with smoothing with permission from: (1) Ahn et al. (2012) – © 2024. American Geophysical Union; (2) Frank et al. (2010) – © 2005, Macmillan Magazines Ltd.; (3) MacFarling Meure et al. (2006) -- © 2024 American Geophysical Union; (4) Rubino et al. (2019) -- © CC By 4.0; (5) Moberg et al. (2005) -- © 2005, Macmillan Magazines Ltd.; (6) Ljungqvist (2010) -- © The authors 2010, Geografiska Annaler: Series A © 2010 Swedish Society for Anthropology and Geography reprinted by permission of Informa UK Limited, trading as Taylor & Francis Group, www.tandfonline.com om behalf of Swedish Society for Anthropology and Geography; (7) Crowley (2000) -- © 2024 American Association for the Advancement of Science; (8); Hegerl et al. (2007) -- © American Meteorological Society ; (9) Jones et al. (1998) -- © 1998, Sage Publications; (10) Loehle and McCulloch (2008) -- © Multi-Science Publishing Co. Ltd.; (11) Juckes et al. (2007) -- © CC By 4.0; (12) Yang et al. (2002) -- © 2024. American Geophysical Union.

Figure 12. Copyright note - Figure reproduced with smoothing with permission from: (1) Ahn et al. (2012) – © 2024. American Geophysical Union; (2) Frank et al. (2010) – © 2005, Macmillan Magazines Ltd.; (3) MacFarling Meure et al. (2006) -- © 2024 American Geophysical Union; (4) Rubino et al. (2019) -- © CC By 4.0; (5) Moberg et al. (2005) -- © 2005, Macmillan Magazines Ltd.; (6) Ljungqvist (2010) -- © The authors 2010, Geografiska Annaler: Series A © 2010 Swedish Society for Anthropology and Geography reprinted by permission of Informa UK Limited, trading as Taylor & Francis Group, www.tandfonline.com om behalf of Swedish Society for Anthropology and Geography; (7) Crowley (2000) -- © 2024 American Association for the Advancement of Science; (8); Hegerl et al. (2007) -- © American Meteorological Society ; (9) Jones et al. (1998) -- © 1998, Sage Publications; (10) Loehle and McCulloch (2008) -- © Multi-Science Publishing Co. Ltd.; (11) Juckes et al. (2007) -- © CC By 4.0; (12) Yang et al. (2002) -- © 2024. American Geophysical Union.

Figure 13. Copyright note - Figure reproduced as original and with smoothing with permission from: (1) Ahn et al. (2012) – © 2024. American Geophysical Union; (2) Hegerl et al. (2007) -- © American Meteorological Society.

Figure 14. Copyright note - Figure reproduced as original and with smoothing with permission from: (1) Rubino et al. (2019) -- © CC By 4.0; (2) Hegerl et al. (2007) -- © American Meteorological Society.

Figure 15. Copyright note - Figure reproduced as original and with smoothing with permission from: (1) Rubino et al. (2019) -- © CC By 4.0; (2) Hegerl et al. (2007) -- © American Meteorological Society.

*Research Article*

OPEN ACCESS

*SCC Publishing*
*Michelets vei 8 B*
*1366 Lysaker Norway*

*ISSN: 2703-9072*

*Correspondence:*
*ah@on.nl*

*Vol. 5.3 (2025)*
*pp. 81-106*

# Global Warming and the “impossible” Radiation Imbalance

*Ad Huijser*

## Abstract

Any perturbation in the radiative balance at the top of the atmosphere (TOA) that induces a net energy flux into- or out of Earth’s thermal system will result in a surface temperature response until a new equilibrium is reached. According to the Anthropogenic Global Warming (AGW) hypothesis which attributes global warming solely to rising concentrations of Greenhouse gases (GHGs), the observed increase in Earth’s radiative imbalance is entirely driven by anthropogenic GHG-emissions.

However, a comparison of the observed TOA radiation imbalance with the assumed GHG forcing trend reveals that the latter is insufficient to account for the former. This discrepancy persists even when using the relatively high radiative forcing values for $CO_2$ adopted by the Intergovernmental Panel on Climate Change (IPCC), thereby challenging the validity of attributing recent global warming exclusively to human-caused GHG emissions.

In this paper, Earth’s climate system is analyzed as a subsystem of the broader Earth Thermal System, allowing for the application of a "virtual balance" approach to distinguish between anthropogenic and other, natural contributions to global warming. Satellite-based TOA radiation data from the CERES program (since 2000), in conjunction with Ocean Heat Content (OHC) data from the ARGO float program (since 2004), indicate that natural forcings must also play a significant role. Specifically, the observed warming aligns with the net increase in incoming shortwave solar radiation ($SW_{IN}$), likely due to changes in cloud cover and surface albedo. Arguments suggesting that the $SW_{IN}$ trend is merely a feedback response to GHG-induced warming are shown to be quantitatively insufficient.

This analysis concludes that approximately two-thirds of the observed global warming must be attributed to natural factors that increase incoming solar radiation, with only one-third attributable to rising GHG-concentrations. Taken together, these findings imply a much lower climate sensitivity than suggested by IPCC-endorsed Global Circulation Models (GCMs).

**Keywords:** Global Warming; Radiation Imbalance; GHG-forcing; Climate Sensitivity; Ocean Heat Content.

Submitted 2025-07-19, Accepted 2025-08-22. https://doi.org/10.53234/scc202510/05

## 1. Introduction

In spring 2024, the Royal Dutch Metrological Institute (KNMI) published a new webpage centered around a picture of the growth in the radiation imbalance full of suggestive lines to make a claimed “acceleration” in *global warming* visible. Determining accelerations over periods of a few years in a climate with a relaxation time to changes of 3 to 5 years however, tends to speculation. The picture used, is taken from a paper with the title “*Global warming in the pipeline*” by Hansen *et al* [2]. These authors use even much longer relaxation times, based on the analyses of *Global Circulation Models* (GCMs). They claim that our climate is governed by processes strongly delaying the warming effects of forcings coupled to the growing concentration of *Greenhous gasses* (GHGs) like $CO_2$. Their paper warns for future warming, even if we stop with the anthropogenic emissions now. At the same time, it is used as a justification for the very high climate sensitivities and accordingly, long relaxation times that these GCMs deliver. To help explain the significant difference between their GCM’s output with much higher temperature trends than that are being (yet?) observed, they distinguish different climate sensitivities, a fast and a slow one. A rather complex concept for what is, at its core, a relatively simple thermal system.

This "relative simplicity" doesn't apply to localized weather phenomena, which even exhibit chaotic behavior. However, on a global scale and over longer periods of time, the average surface temperature of our climate system reacts similarly to that of a thermal system such as a pot of water on a stove: when the incoming heat is steady and below boiling, the system stabilizes when the heat loss (via radiation and convection) equals the input. Analogously, Earth's surface-atmosphere interface is the main absorber and emitter of heat. Reducing the "flame" (solar input) leads to cooling, regardless of the total heat already stored in the system. The system's average temperature will drop as well, as soon as the heating stops. So, no sign of any "*warming in the pipeline*" for such a simple system.

Yet Earth's climate system is inherently more complex due to its scale and the dynamics introduced by Earth's rotation and orbit. Solar heating occurs only half the time at any given location, and the Earth's surface is in constant rotation, with the solar heating peak moving at speeds of up to 0.5 km/s. Heat is therefore continuously redistributed across the globe via lateral atmospheric and oceanic flows. Averaged over time, these transports move heat from the Tropics (where most solar radiation is absorbed) to the Poles (which receive far less solar energy), with approximately 80% of the 5 PW carried by wind and the remainder by ocean currents [3]. These fluxes are partially equalizing the huge differences in the amount of incoming Solar radiation. Around the Equator, the radiation imbalance is highly positive, with about 40 W/m$^2$ more Sunlight coming in than Long-Wavelength radiation going out. Around the Poles we see the opposite, with a substantial negative balance in the order of about 100 W/m$^2$ by a higher flux out, than in. In average there is a (near) radiation balance that can be easily influenced by variations in both lateral heat flows. Consequently, changes in the amount of heat carried and/or changes in the path along which that heat is being transported, can easily influence the average surface temperature. Often, such changes are conveniently interpreted by AGW-proponents as being the result, rather than the cause of *global warming*. Those anthropogenic GHG-driven effects are by some even coupled to induce irreversible changes in our climate at so-called *tipping points*.

The two transport mechanisms, air and ocean, operate on different timescales. Air has a low specific heat capacity, but high wind speeds make it a fast medium for heat transfer. Oceans, by contrast, have a high specific heat capacity but move more slowly. The Atlantic Meridional Overturning Circulation (AMOC) with the well-known Gulf Stream carrying warm water from south to north, can reach speeds up to about 3 m/s. But its warm current remains largely confined to surface layers due to limited solar radiation penetration and gravity-induced stratification. With a path-lengths of up to 8,000 km and an average speed of 1.5 m/s, ocean heat takes approximately 2 months to travel from the Gulf of Mexico to the Arctic. This is comparable to the 1 to 2 months delay between solar input and temperature response in the annual cycle, suggesting that oceanic heat transport is part of the climate system's normal operation. Climate adaptation times from anthropogenic influences are estimated at 3 to 5 years. If "warming in the pipeline" exists, it must be buried in the much colder, deeper ocean layers.

ARGO float data since 2004 show substantial annual increases in Ocean Heat Content (OHC), sometimes expressed in mind-boggling terms such as $10^{22}$ joules per year (see Fig.1). While this may sound alarming [1,2], when converted to flux, it represents less than 1 W/m$^2$, a mere 0.6% of the average 160 W/m$^2$ of absorbed solar energy at the surface. All the rest is via evaporation, convection and ultimately by radiation sent back to space after globally being redistributed by wind and currents.

Although longwave *back-radiation* from the atmosphere penetrates only a few micrometers into ocean water, GHG-induced atmospheric warming will affect the ocean's top layer (~ 50 – 100 m thick) by affecting its cooling. Below this layer, temperatures drop rapidly, and any excess heat is stored in deeper ocean layers where it remains for centuries due to poor conductivity and stable stratification.

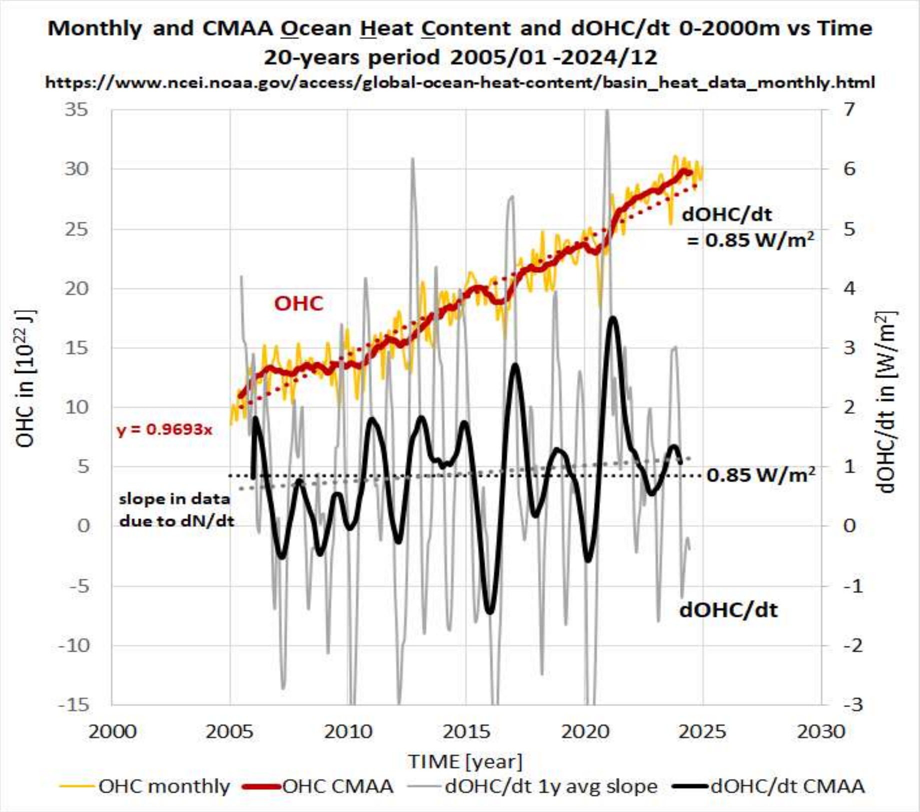

*Fig. 1. Ocean Heat Content (OHC) anomaly from 0–2000 meters over time, shown as 3-month and annual moving averages (CMAA), along with their time derivatives. Notable are the relatively large variations, likely reflecting the influence of El Niño events. The average radiative imbalance at the top of the atmosphere (TOA), estimated at 0.85 W/m², corresponds approximately to the midpoint of the time series (around 2015). Data: https://www.ncei.noaa.gov/access/global-ocean-heat-content/basin_heat_data.html [7].*

This raises the question: Why would extra GHGs that have only a limited effect on the 99.4% of the outgoing flux, have affected this 0.6% residue during a couple of decennia in such a way that we should be scared about all that "*warming in the pipeline*" as Hansen *et al.* [2] are warning us for? In the following sections, we examine data showing that observed trends in the radiation imbalance and OHC are better explained by the internal dynamics of the Earth's thermal system and natural forcings such as from increasing solar radiation, rather than solely by GHG emissions.

## 2. Climate balance in perspective

### 2.1. The ideal picture

A thermal system, such as a pot of water on a stove, reaches equilibrium when energy input matches energy loss. Analogously, Earth's thermal system absorbs shortwave (SW) solar radiation and emits longwave (LW) radiation. The average incoming solar flux at the top of the atmosphere is about 340 W/m², but due to Earth's albedo of 0.3, only about 240 W/m² enters the climate system. Although just 160 W/m² is actually absorbed at the surface, that $SW_{IN}$-flux determines the system's temperature, characterized by the averaged surface temperature $T_S$. This is reached when the cooling flux $LW_{OUT}$ sent to space equals the influx from the Sun $SW_{IN}$, resulting in a constant climate with $dT_S/dt = 0$.

In fact, our cooling is realized through the transfer of heat from the surface to space, by a combination of long-wavelength (LW) radiation, convection and latent heat by evaporation of water. During its path through the atmosphere, that integral flux is finally all transferred into radiation by GHGs, mainly water vapor and $CO_2$. That radiation leaves our climate system to space as $LW_{OUT}$ because there are no thermal flows possible anymore at TOA. We can forget here about the details of the transfer processes involved as changes in our climate's parameters are relatively small *i.e.,* in the order of 1% per century. Accordingly, they can all be linearized in a first-order approach as in the following analyses.

The dynamics of our climate balance is illustrated in Fig.2a using a resistor-capacitor (RC) circuit: the heat capacity (C) of the climate system is charged by an incoming solar flux ($SW_{IN}$) and discharges via a resistor (R), which represents all combined heat loss processes (LW radiation, convection and evaporation). The system reaches equilibrium when incoming $SW_{IN}$ and outgoing $LW_{OUT}$ fluxes match *i.e.,* when the radiation imbalance $N = (SW_{IN} - LW_{OUT}) = 0$. Climate's equilibrium surface temperature $T_0$, is then set by $SW_{IN}$ and R.

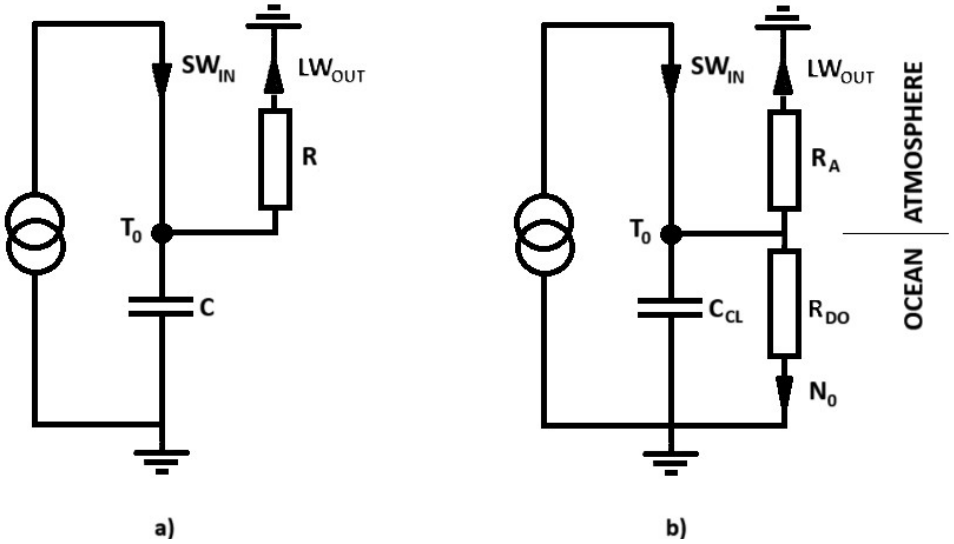

***Fig.2.*** *Schematic thermal circuit for our Earth' climate system, for illustration purposes only:*

a) *In its most rudimentary form consisting of a heat capacitor C shunted by a resistor R coupled to a source with constant flux $SW_{IN}$.*

b) *As a more realistic circuit where the heat capacity of our climate $C_{CL}$ is separated from the rest of the Earth' (almost infinite) heat capacity and where a small part $N_0$ of the incoming flux is "leaking" from the climate system through the resistor $R_{DO}$ to the deep ocean layers. $R_{DO}$ is much larger than the resistance of the atmosphere $R_A$ as $N_0$ is less than 0.6% of $SW_{IN}$ (see Section 2.3)*

Growing concentrations of GHGs increase the atmospheric resistance R to outgoing radiation, which upsets this balance. It is the background to the *Anthropogenic Global Warming* (AGW) hypothesis, promoted by the *International Panel on Climate Change* (IPCC) as the fundamental driver behind the observed warming since the beginning of the industrial era [8]. But, also changes in $SW_{IN}$ due to for instance clouds will have similar effect on the imbalance N, thus inducing a change in temperature necessary to regain balance. For a step-wise offset ΔN at t = 0, between incoming and outgoing radiation forcing the average temperature $T_0$ to change to a new equilibrium ($T_0 + \Delta T$), the respective time-paths for surface temperature T(t) and radiation imbalance N(t) for t > 0 are given by:

$$T(t) = T_0 + \Delta T\,\left(1 - exp(-t/\tau)\right) \qquad (1a)$$

$$N(t) = \Delta N\,\left(exp(-t/\tau)\right) \qquad (1b)$$

where $\tau = RC$ represents the relaxation time of the thermal system. For the new equilibrium temperature ($T_0 + \Delta T$) at $t \rightarrow \infty$, we can couple ΔT to ΔN according to:

$$\lambda\,\Delta T = \Delta N \qquad (2)$$

where λ is called a *feedback* parameter. Its inverse, ξ = 1/λ is our system’s *climate sensitivity* relating the ultimate temperature change ΔT to the original disturbance in the energy balance ΔN. The higher ξ, the larger the temperature’s reaction to a certain disturbance of the imbalance as the temperature at the surface “feeds” $LW_{OUT}$ in restoring its balance. Also, the more difficult the transfer from the surface to space, the longer it takes to restore the balance. In case of extra heating by the Sun, or reduced cooling by extra $CO_2$, the amount of energy fed to this thermal system to restore balance, equals τ ΔN. The amount of heat necessary to increase the temperature equals CΔT, yielding the important relation:

$$\tau = \frac{C}{\lambda} = \xi\, C \tag{3}$$

As the heat capacity of our climate system can be considered a given, the climate sensitivity scales with the relaxation time of our climate to disturbances. The relaxation time can a.o. be inferred from the various radiation components as measured at TOA by the CERES-program [9], as shown in Fig.3 with *Centered Moving Annual Averages* (CMAA) to remove cyclical/seasonal variation in the radiation components. The strong signal modulation with *peak-to-peak* times of roughly 3 years, must be indicative for the value of τ. This is far less than the 10 to 15 years for τ as the consequence of IPCC’s high climate sensitivity [8], or the even longer times as claimed by Hansen *et al* [2]. If those would be the reaction time of our climate to disturbances, the observed large variations in the radiation imbalance data as shown in Fig.3 would be completely flattened out.

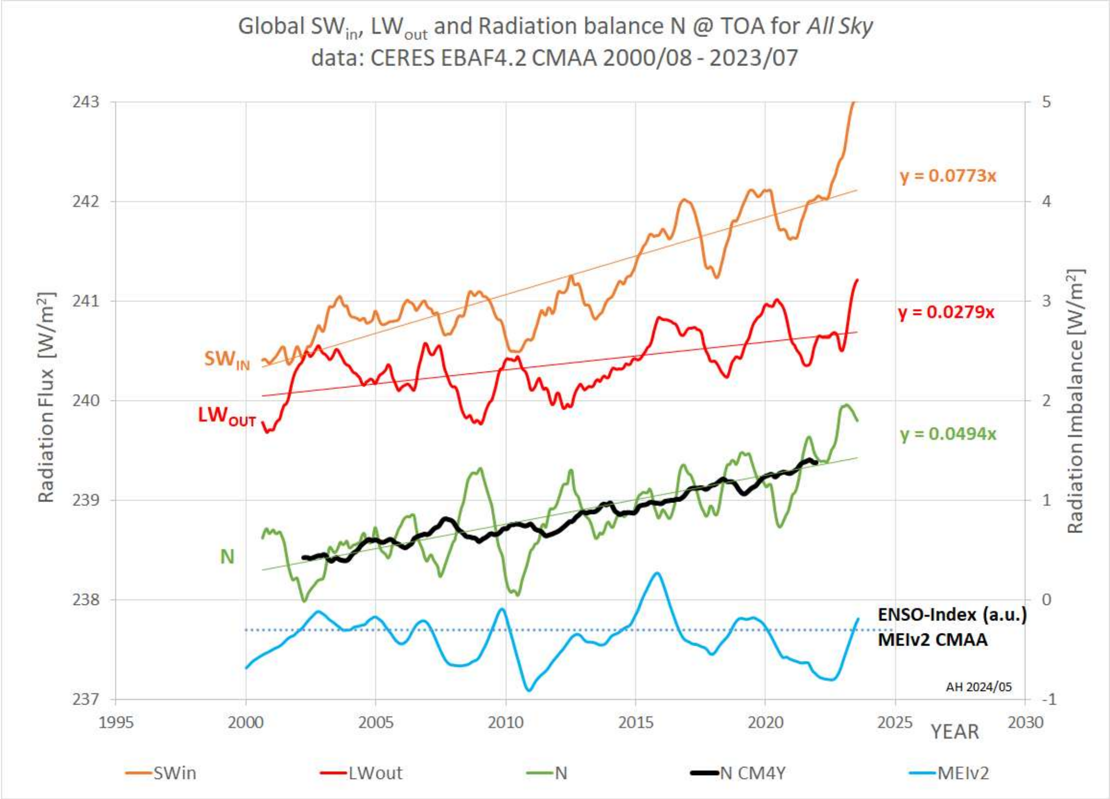

*Fig. 3. Centered Moving Annual Averages (CMAA) of the measured radiation components at the top of the atmosphere (TOA): incoming shortwave radiation $SW_{IN}$, outgoing longwave radiation $LW_{OUT}$, and their difference, the radiation imbalance N. Linear trends are indicated. For the radiation imbalance N, a 4-year moving average (CM4Y) is also shown, highlighting the effect of a 3–5 years climate relaxation time. In contrast, filtering with a longer time constant (10–15 years), as assumed under the Anthropogenic Global Warming (AGW) hypothesis, would largely suppress these variations. The ENSO MEIv2 index (as CMAA) is included to illustrate the strength of El Niño, which is primarily responsible for large fluctuations in cloud cover and, consequently, in radiation. Data sources: https://ceres.larc.nasa.gov/data [9]and https://psl.noaa.gov/enso/mei/ [10]*

### 2.2. Estimating our climates thermal capacity $C_{CL}$

The rather fast responses of our climate indicates that the thermal capacity of our climate must be much less than the capacity of the entire *Earth thermal system*. This climate heat capacity $C_{CL}$ depends on how sunlight is being absorbed, how that heat is transferred to the atmosphere and which part of it is being stored in either land or ocean.

At continental land-area, sunlight is absorbed only at the very surface where the generated heat is also in direct contact with the atmosphere. Seasonal temperature variations don't penetrate more that 1 to 2 meters deep in average and as a consequence, storage of heat is relatively small. Sunlight can penetrate pure water to several hundred meters deep, but in practice, penetration in the oceans is limited by scattering and absorption of organic and inorganic material. A good indication is the depth of the *euphotic* zone where algae and phytoplankton live, which need light to grow. In clear tropical waters where most of the sunlight hits our planet, this zone is 80 to 100 m deep [12].

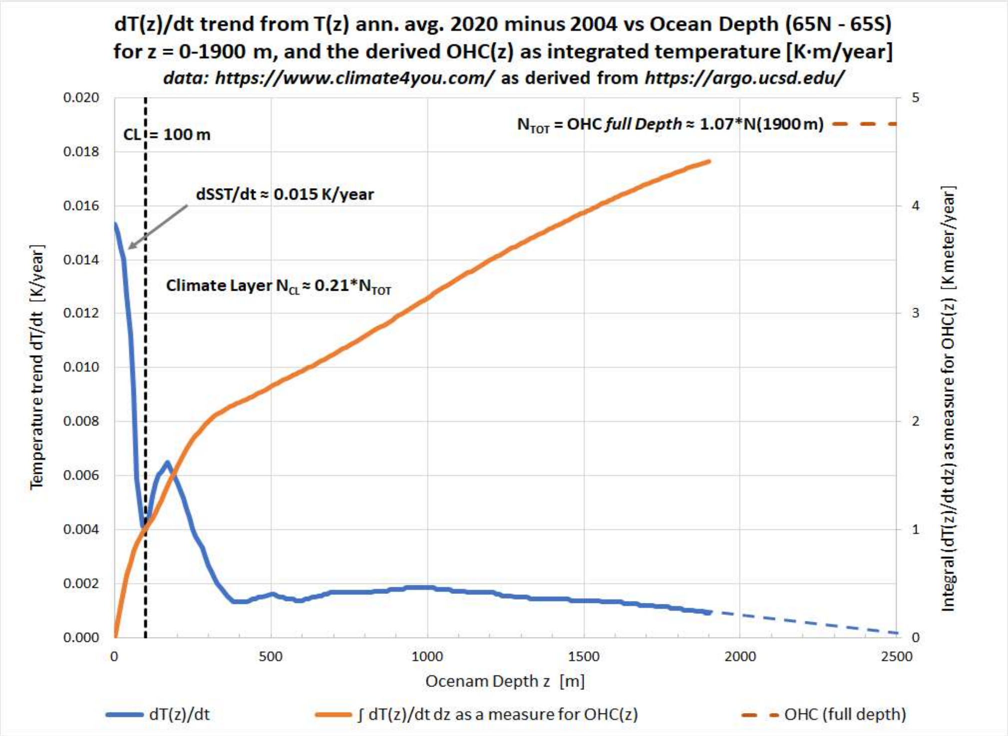

***Fig.4.*** *Average temperature trend dT(z)/dt (blue) between 2004 and 2020 as a function of depth (0-1900 meters), for oceans between 65ºS and 65 N. The surface temperature trend dSST/dt ≈ 0.015 K/year. The change in Ocean Heat Content (OHC) as a function of depth (orange) is obtained by integrating dT(z)/dt. The OHC over the full depth is estimated by extrapolation of dT(z)/dt below 1500 m. The temperature trend reveals a clear separation between the upper ocean (the "climate layer") and the deeper ocean. The climate layer is roughly 100 meters thick and stores about 20% of the total OHC. Temperature profile taken from https://www.climate4you.com/ (oceans) [14], based on https://argo.ucsd.edu/ [6]*

The equivalent thermal capacity of our oceans per unit area must therefore be much larger than that of land. As the equivalent heat capacity of our atmosphere equals only a few meters of water, this absorption zone of our oceans that also cover over 70% of the Earth's surface, is in first-order a good indicator for our climate's heat capacity $C_{CL}$.

Another important factor in our climate's heat capacity is how this ocean layer of absorbed heat is in contact with the atmosphere. Tides, wind, waves and convection continuously mix the top-layer of our oceans, by which heat is easily exchanged with the atmosphere. This *mixed-layer* is typically in the order of 25 - 100 m, dependent on season, latitude and on the definition of "*well-mixed*" [13]. Below this ~100 m thick top-layer, where hardly any light is being absorbed and the mixing process has stopped, ocean temperatures drop quickly with depth. As the oceans' vertical temperature gradient at that depth doesn't support conductive nor convective heat flows going upward, climate processes at the surface will thus become isolated from the rest of the Earth' thermal system.

Figure 4 with the *Change in Ocean Heat Content* vs. *Depth* over the period 2004 – 2020 obtained via the ARGO-floats [6,14], offers a good indication for the average climate capacity $C_{CL.}$ It shows the top layer with a high surface temperature change according to the observed global warming rate of about 0.015 K/year, and a steep cut off at about 100 m depth in line with the explanation above. Below the top layer, temperature effects are small and difficult to interpret, probably due to averaging over all kinds of temperature/depth profiles in the various oceans ranging from Tropical- to Polar regions.

A 100 m thick top-layer can be attributed to a climate heat capacity $C_{CL} \approx 13$ Wyear/m$^2$/K. That is consistent with a climate relaxation time $\tau \approx 4$ years in combination with the *Planck feedback parameter* $\lambda_{PL} = -3.3$ W/m$^2$/K according to relation (3): $\lambda_{PL} = -C_{CL}/\tau$ [4] (by convention $\lambda_{PL}$ has a negative value, but $\lambda = 1/\xi$ in the formulas applied here, is regarded as a positive parameter).

The split between top-layer and rest of the ocean looks physically visible in Fig.4, but in fact, $C_{CL}$ is no more than an "effective" climate heat capacity. Schwartz [5] calculates this effective heat capacity in a different way from a regression of OHC at various depths versus $T_S$. He concludes to a thermal capacity $C_{CL} = 14 \pm 6$ Wyear/m$^2$/K, equivalent to $110 \pm 50$ m thick climate layer. The relaxation time of $5 \pm 1$ years is derived from the autocorrelation of global mean sea surface temperatures. Taken together, he concludes from applying (3), to a climate sensitivity of $0.30 \pm 0.14$ K/W/m$^2$, in essence equal to the inverse of $-\lambda_{PL}$ as the outcome of [4]. Margins encompass the $C_{CL} = 13$ Wyear/m$^2$/K and $\tau = 4$ years as above, so we stick here to those values to remain consistent with earlier assessments [4].

A final remark on the heat involved in melting processes. Snow and ice increase the effective heat capacity of our climate as heat stored in this phase-transition cannot add anymore to warming. Processes like melting and freezing, occur at the atmosphere-surface interface and must be regarded as normal phenomena in our climate's natural reaction to warming or cooling. Therefore, they are supposed to be intrinsic to the "normal" climate sensitivity $\xi = 1/\lambda$.

### *2.3. A more realistic view on our climate's equilibrium and the radiation balance*

In case of a "perfect" equilibrium ($N = 0$, $dT_S/dt = 0$), all of the absorbed sunlight up to about 100 m deep, has to leave on the ocean-atmosphere interface again. However, deep oceans are still very cold with a stable, negative temperature gradient towards the bottom. This gradient will anyhow push some of the absorbed heat downwards. Therefore, even at a climate equilibrium with $dT_S/dt = 0$, we will observe $N > 0$. With the large heat capacity of the total ocean volume, that situation will not change easily, as it takes about 500 years with today's $N \approx +1$ W/m$^2$ to raise its average temperature just 1°C.

The Earth's climate system can thus be regarded as a subset of the total *Earth's thermal system* (ETS) responding to different relaxation times. The climate relaxes to a new equilibrium within 3–5 years, while the deeper oceans operate on multidecadal or even longer timescales, related to their respective thermal capacities C for the ETS, and $C_{CL}$ for the climate system.

The ratio $C/C_{CL}$ must be large. A first, too large estimate would be about 45 between the 4.5 km depth in average for our oceans and the 100 m top-layer of the oceans that interact in the climate processes with the atmosphere. The inner core of the Earth however, is still hot. This heat is flowing upwards to the surface where it is assumed to be somewhat less than 0.1 W/m$^2$ [11]. The heat capacity of the ETS must therefore be limited to the layer above the depth where this upward heat flow equals the downward flow from the absorbed sunlight. The OHC-data hint to a depth of the ETS-capacity somewhere between 1000 and 2000 m, with an ETS-relaxation time 10-20x the relaxation time $\tau$ of our climate *i.e,* about 40 to 80 years.

This split up between the climate system and the Earth' thermal system has been expressed in the circuit-scheme of Fig.2b where a large resistor is added not only to make the separation, but also the connection between these two thermal systems visible. Any surplus in the radiation imbalance N, goes partly into warming of the climate capacity $C_{CL}$, which we experience as *global warming*. The remaining part, the flux $N_0$, "leaks" through the large resistor $R_{DO}$ into the much larger heat capacity of the rest of the ETS. From the heat fluxes through both media (1 *vs* 240 W/m$^2$) we must conclude that $R_{DO} >> R_A$. Therefore, this decoupling doesn't make any difference for the surface temperature's set-point. The dynamics of the two thermal systems characterized by $\tau = R_A C_{CL}$ for our climate, and $R_A C$ for the ETS however, are completely different.

## 3. The "virtual balance" $N_0$ in the balancing act of our climate

The heat flux $N_0$, which leaks into the ocean's deeper layers (Section 2.3), does not contribute to the surface temperature and, by extension, to what we define as "climate." Still, it reflects a persistent offset in the Earth's radiation balance, even when surface temperatures appear stable *i.e.,* $dT_S/dt = 0$. This offset likely arises from slow changes in how heat is redistributed, either between top and bottom of the oceans and/or between Equator and Poles (see Section 1). Though part of the Earth's overall thermal system, $N_0$ acts as a *virtual balance* in the climate subsystem because it doesn't directly impact surface temperatures. This suggests that much of the observed increase in *Ocean Heat Content* isn't necessarily linked to changes in GHGs, as assumed in the AGW-hypothesis. Moreover, $N_0$ likely varies over time due to evolving wind patterns, changing ocean currents, or even local geothermal fluctuations [11].

This concept of a virtual balance lets us rethink the dynamics of our climate system under influence of an external forcing F(t) such as from extra GHGs and/or an increase in Solar flux. The driving force to change the surface temperature in order to restore balance is proportional to the deviation from equilibrium. By this concept, we can now separate the dynamics of the climate system from the much slower reacting Earth thermal system by considering deviations from that *virtual equilibrium* expressed as $(N(t) - N_0(t))$, by the following relation for disturbances of an equilibrium system:

$$\frac{d\big(N(t) - N_0(t)\big)}{dt} = \frac{dF(t)}{dt} - \frac{N(t) - N_0(t)}{\tau} \tag{4}$$

In the absence of external forcings (dF/dt = 0), N(t) relaxes back to $N_0(t)$ exponentially with a characteristic time τ according to (1b).

The driving force to restore equilibrium $(N(t) - N_0(t))$ is coupled to the surface temperature as in (2). So, the surface temperature $T_S$ that is applied here as characteristic for our climate, will rise according to $(N(t) - N_0(t))$ divided by the climate heat-capacity $C_{CL}$:

$$\frac{dT_S(t)}{dt} = \frac{N(t) - N_0(t)}{C_{CL}} \tag{5}$$

Here we assume a constant $C_{CL}$. If not, for example due to slow changes in the ocean top-layer, the term $T_S\, dC_{CL}/dt$ that we then have missed to account for in (5), will automatically be incorporated in $N_0(t)$. By rearranging (4) and applying (3) with $\lambda = C_{CL}/\tau$, we can now rewrite (4) as:

$$\frac{dN}{dt} = \frac{dN_0}{dt} + \frac{dF}{dt} - \lambda\frac{dT_S}{dt} \tag{6}$$

If $N_0(t)$ itself changes over time, $dN_0/dt$ in (4) becomes indistinguishable from external forcings and should be included in the trend of total forcings $dF_{TOT}/dt = dF/dt + dN_0/dt$, thus creating a well-known relation in climate literature:

$$\frac{dN}{dt} = \frac{dF_{TOT}}{dt} - \lambda\frac{dT_S}{dt} \tag{7}$$

In (6) and (7), time dependencies have been left out as these relations have only practical use in analyzing climate data when considering longer term trends. The trend indication dX/dt for a parameter X as applied here, stands in fact for the change ΔX over a period $\Delta t >> \tau$. In climate literature, one often uses (7) in this Δ-format:

$$\lambda \Delta T_S = \Delta F_{TOT} - \Delta N \tag{8}$$

to determine the climate sensitivity $\xi = 1/\lambda$ from the sum of all known forcings in $\Delta F_{TOT}$, the observed changes in imbalance ΔN and average temperature ΔT, over a certain period [15]. Calculation with (8) might underestimate the value for λ as one easily "forgets" the positive contribution $\Delta N_0$ in $\Delta F_{TOT}$.

## 4. Available data used in the analysis

### *4.1. Radiation data at TOA*

The most comprehensive radiation dataset is NASA's CERES-EBAF v4.2 [9]. For our analysis, we use monthly $SW_{IN}$, $LW_{OUT}$, and N data from 2000 onward, processed as *Centered Moving Annual Averages* (CMAA) to eliminate seasonal/cyclical effects and highlight long-term trends. These trends as shown in Fig.3 in units of [W/m²/year], are for the 23 years full 12 months period 2000/8 – 2023/7.

Satellite-based absolute radiation measurements with an uncertainty of about 3–5 W/m² per channel, are unfit to directly detect a radiation imbalance of about 1 W/m², as reported by NASA in Fig.3. Actually, this imbalance is calibrated using the time derivative of *Ocean Heat Content* dOHC/dt, as explained in Section 4.2. While the absolute values may be uncertain, the anomalies and trends in the CERES data are considered as being reliable, thanks to regular *in situ* calibration of the satellite sensors.

### *4.2. Ocean Heat Content (OHC) data*

The current radiation imbalance $N(t) \approx 0.85$ W/m², is estimated from dOHC/dt shown in Fig.1 [7]. *Ocean Heat Content* data are derived from vertical temperature measurements across the global oceans, collected by the ARGO float network [6]: a system of autonomous buoys that cycle to depths of ~2000 meters, measuring parameters like water temperature as they descend and ascend.

Figure 3 (along with Fig.1) reveals that short-term fluctuations in the TOA radiation imbalance don't always align with OHC trends. For example, the peak and dip around 2016 seen in OHC are not reflected in the TOA radiation imbalance data. However, those variations *do* appear in the incoming solar radiation $SW_{IN}$, which directly influences ocean heating. This correlation supports the inclusion of the term $dN_0/dt$ in (6), representing the heat flux into deeper ocean layers.

Figure 4 shows that heat continues to flow below 1900 meters, although modestly. A simple linear extrapolation suggests total OHC is about 1.10 times the measured OHC down to 1900 m. This correction factor (1.07) is applied to values derived from OHC, such as the calibrated absolute radiation imbalance in the CERES dataset, resulting in an updated estimate: $N \approx 0.94$ W/m². It does not apply to $dN/dt \approx 0.049$ W/m²/year however, as it comes directly from NASA's radiation measurements at TOA.

Figure 4 also shows that about 20% of the OHC change occurs in the top 100 meters of the ocean. This surface layer interacts strongly with the atmosphere and is therefore, not included in $N_0$, the flux into the deeper ocean. The energy flux absorbed in this *climate layer* $N_{CL} = (N - N_0) = C_{CL} dT_S/dt$, as required by conservation of energy. From Fig.4 we estimate a value for $N_{CL} \approx 0.20*1.1*0.85 \approx 0.19$ W/m², which implies $N_0 \approx 0.75$ W/m² (averaged over 2004 – 2023). *This value immediately shows, that $N_0$ is not near the thermal flux to the bottom as a result of the much warmer top-layer. The maximum in the average temperature gradient towards the bottom* *of the oceans of about 0.06 K/m as obtained from the ARGO-data, is found just under that top-layer. With a thermal conductivity coefficient of salty sea water around 15 °C of 0.58 W/K/m, we can only explain 0.035 W/m$^2$ i.e., a contribution of just 5% of the energy flux that heats the lower part of the oceans. So, most of that heat must come from absorbed solar radiation below the climate layer.*

### *4.3. Temperature trends*

To apply (6), we need a reliable estimate of the surface temperature trend. While many datasets exist, each with strengths and limitations [16], we focus in this paper on two key sources. The first is the HadCRUTv5 series from the UK Met Office [17], which shows a relatively high trend of *0.023 K/year* over the 2000–2023 period. This dataset is based on a mix of ground stations and buoys. Its global average is obtained through interpolation and homogenization algorithms. However, because many land-based stations are located near urban areas and airports, these records may be affected by local warming biases [19].

The second dataset is UAH-TLT from the Univ. of Alabama Earth System Science Center [18], based on satellite observations of microwave emissions from the *Lower Troposphere* (LT). It provides near-complete global coverage in a 1°x1° grid and shows a lower trend of *0.015 K/year* for this period.

Figure 4 shows that the sea surface temperature (SST) trend derived from ARGO data is approximately 0.015 K/year, closely matching the 0.0135 K/year trend in the ocean-only portion of the UAH-TLT dataset. In contrast, the HadSSTv4 dataset [20] (assumingly the ocean component of HadCRUTv5) shows a higher SST trend of 0.019 K/year, indicating a significant discrepancy. We don't know what causes this unexpected difference, but it is noteworthy since the ARGO floats are presumably part of the buoy network used in constructing the HadSSTv4 series.

### *4.4. Greenhouse gas forcings*

Since the start of CERES measurements in 2000, the concentration of greenhouse gases (GHGs), especially $CO_2$, has increased significantly. These concentrations have been reliably monitored since the early 1960s through daily observations, and the quality of these data is widely accepted.

Figure 5 shows the total atmospheric concentration of all *well-mixed* Greenhouse gasses, such as for instance Methane ($CH_4$), expressed as $CO_2$-equivalent by applying relative GHG-strengths [21]. For simplicity, we refer to this further on as "$CO_2$". Because $CO_2$-forcing is proportional to the logarithm of its concentration, a logarithmic scale is used on the vertical-axis. This reveals that $CO_2$ concentrations have followed a near-perfect exponential trend since the mid-1970s. Consequently, the forcing trend from GHGs ($dF_{GHG}/dt$) has remained approximately *constant* for over 4 decades, and it's unlikely to increase significantly. Net-zero initiatives in developed countries are slowing emission-growth, and global population, another major driver, is expected to stabilize later this century.

The actual forcing-trend $dF_{GHG}/dt$ depends on the value for the forcing from doubling the $CO_2$-concentration $F_{2xCO2}$ commonly expressed as:

$$\frac{dF_{GHG}}{dt} = F_{2xco_2}\frac{d}{dt}(\ln[CO_2])/\ln(2) \tag{9}$$

According to NASA's AGGI database [21] $dF_{GHG}/dt \approx 0.035$ W/m$^2$/year, indicating $F_{2xCO2} = 3.7$ W/m$^2$. IPCC, in its AR6 report [8], uses a slightly higher $RF_{2xCO2} = 3.9 \pm 0.5$ W/m$^2$, leading to a trend of *0.037 W/m$^2$/year*.

However, applied forcing strengths depend on the definition of radiative forcing (RF). The IPCC defines its RF at the *Top of the Troposphere* (TOT) where thermal fluxes are still present, whereas in (4)-(7) the forcing trends used, refer to the *Top of the Atmosphere* (TOA). This matters a lot, as IPCC’s definition excludes cooling effects of increasing GHGs in the *Stratosphere*, leading to systematically higher forcing values that may overstate surface warming considerably.

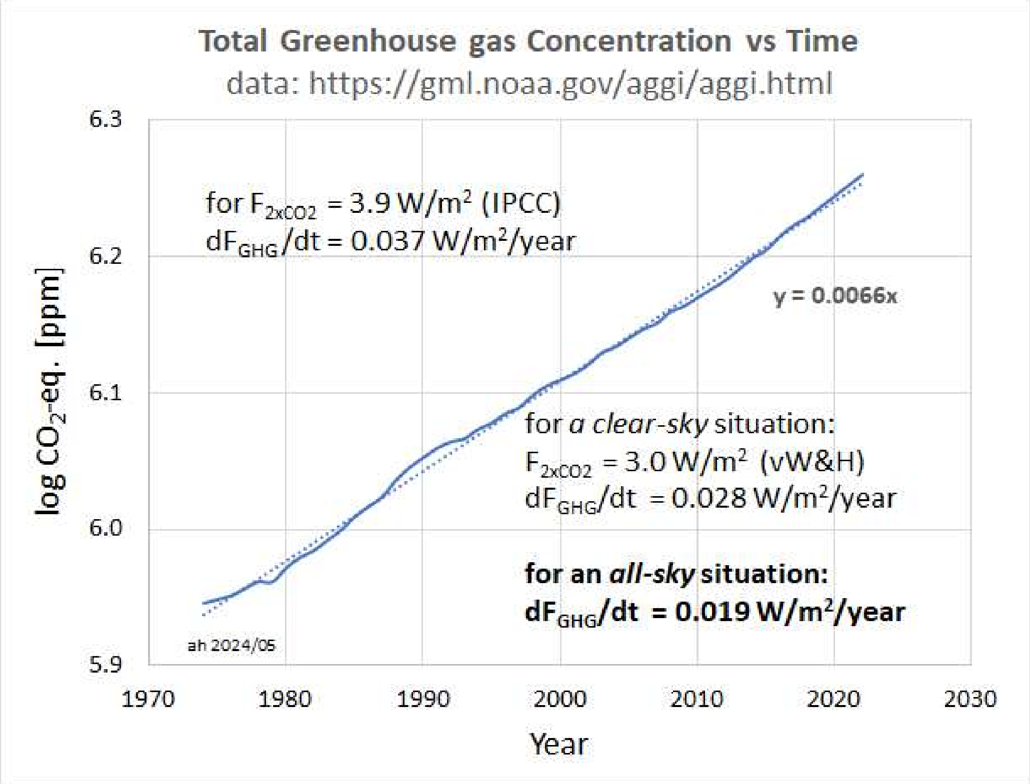

***Fig.5*** *Time evolution of the $CO_2$-equivalent concentration of all greenhouse gases (GHGs), based on data from [21]. The slope of this logarithmic plot indicates an almost constant radiative forcing trend over the past 40 years, in accordance with (9). With IPCC-AR6 “most likely” value of $RF_{2xCO2} \approx 3.9$ W/m²[8], it implies a GHG forcing trend $dF_{GHG}/dt = 0.037$ W/m²/year over the entire period. Using the recent "clear-sky" calculations by van Wijngaarden and Happer [22], the trend is ~0.028 W/m²/year. Accounting for the average ~2/3 cloud cover ("all-sky" conditions), the effective forcing trend is then significantly lowered to: $dF_{GHG}/dt \approx 0.019$ W/m²/year [25] (see the text for details).*

For comparison, Van Wijngaarden & Happer [22] report $F_{2xCO2} = 3.0$ W/m² at TOA based on thorough radiative transfer calculations. For RF according to the IPCC definition at TOT, they calculate 5.5 W/m², illustrating the significant cooling from GHGs in the Stratosphere. Rentsch [23], reports an experimental value of 2.65 W/m², based on analyzing 17 years of satellite based spectroscopic data.
These non-IPCC $F_{2xCO2}$ values are calculated/established under *clear-sky* conditions. But, on average, two-thirds of the Earth is covered by clouds, strongly modulating GHG effects. Clouds reduce outgoing radiative fluxes: only ~1/3 originates from the surface and fully "feels" GHG forcing over the entire atmospheric column. The other ~2/3 comes from *Top of Clouds* (TOC) levels. TOC radiation is not only lower (due to lower TOC-temperatures) but also traverses a thinner atmospheric layer, reducing the greenhouse effect. Although $CO_2$ is more effective above clouds where water vapor as a major overlapping absorber is nearly absent, the negative contribution due to the large cooling effect of GHGs in the Stratosphere however, remains constant by absence of clouds at those heights.

To estimate the net *all-sky* forcing, we can adjust *clear-sky* results using a "*Venetian blinds*" model [25] and *MODTRAN* simulations [24] applying TOC-temperature and -altitude from satellite data. This yields $F_{2xCO2} \leqq 2.0$ W/m², about half the value used in IPCC AR6 [8].
Although IPCC’s $RF_{2xCO2} = 3.9$ W/m² is defined at TOT, it most probably represents a real *all-sky* value, as it comes from GCM simulations that include cloud effects. Comparing it to the 5.5 W/m² as calculated for the *clear-sky* TOT-situation [22], yields a ratio of 0.71. Applying this ratio to the *clear-sky* calculated 3.0 W/m²/K at TOA, indicates an *all-sky* $F_{2xCO2} \approx 2.1$ W/m². This aligns well

with the 2.0 W/m² estimate from the *Venetian blinds* model [25], thus giving confidence in the *all-sky* forcing trend as derived via (9): ***$dF_{GHG}/dt \approx 0.019$ W/m²/year.***

## 5. Climate change in perspective

### 5.1. Splitting the Total Forcing Trend

In (7) all possible forcings trends at TOA including GHG-contributions $dF_{GHG}/dt$, were combined into a single term $dF_{TOT}/dt$. Since GHGs primarily act in the LW-channel, it is logical to split up the total forcing into: $dF_{TOT}/dt = dF_{NA}/dt + dF_{GHG}/dt$. Here the subscript "NA" refers to "natural" and/or "non-anthropogenic" contributions. This includes forcings in the SW-channel as *e.g.* from aerosols, changes in the Earth' *albedo*, either from changes in cloudiness or changes in the surface reflection, and changes in $N_0$, the heat disappearing into the deep ocean. Although clouds affect both SW and LW radiation, their "net" radiative impact described as the *Cloud Radiative Effect* (CRE) can be reasonably well attributed to the SW-channel only. We can therefore split up the total forcing even a step further into $dF_{TOT}/dt = dN_0/dt + dF_{SW}/dt + dF_{GHG}/dt$. Later on, in Section 8, we will discuss how $dF_{SW}/dt$ can be fully linked to the large observed incoming solar trend $dSW_{IN}/dt$ as shown in Fig.3. For now, it is just the trend of an unknown forcing in the SW-channel.

For the analysis we can rewrite (6) as:

$$\frac{dN}{dt} = \frac{dN_0}{dt} + \frac{dF_{SW}}{dt} + \frac{dF_{GHG}}{dt} - \lambda\frac{dT_S}{dt} \tag{10}$$

We could have kept $dN_0/dt$ as a "natural" forcing trend, "invisibly" included into $dF_{NA}/dt$. Its explicit treatment will prove important later.

### 5.2. Testing the AGW-GHG-only hypothesis

Suppose, we had no other forcings in our climate than those from GHGs as is basically assumed in IPCC's AGW-hypothesis. That would imply $dSW_{IN}/dt = dN_0/dt = 0$ and (10) simplifies to:

$$\frac{dN}{dt} = \frac{dF_{GHG}}{dt} - \lambda\frac{dT_S}{dt} \tag{11}$$

Since at present, $dT_S/dt > 0$ and $\lambda = C_{CL}/\tau > 0$ (*by definition*) we know for sure that according to (11): *$dN/dt < dF_{GHG}/dt$*. This is also to be expected in a stable system where the "effect" of a disturbance will be smaller than its "cause". The observed value for $dN/dt \approx +0.049$ W/m²/year according to the CERES-data (Fig.3) however, even exceeds the highest estimates for $dF_{GHG}/dt \approx 0.019 – 0.037$ W/m²/year (see Section 4.4 for the range). Even IPCC's large value for the trend in GHG-forcing cannot explain the trend in the observed radiation imbalance, at all. *It directly falsifies the AGW-hypothesis with GHGs as the sole drivers of Global Warming.*

### 5.3. The onset of Global Warming and the forcing dynamics at that time

There is another challenge to the "GHG-only" scenario. At some point in the mid-1970s, the global cooling trend during the previous decennia reversed, and the modern warming period began. At that "turning" point in temperature at $t = \zeta$, we must have had: $dT_S(\zeta)/dt = 0$ and $d^2T_S(\zeta)/dt^2 = 0$. According to (5) $dT_S/dt = 0$ implies $\mathbf{N(\zeta) = N_0(\zeta)}$, and $d^2T_S/dt^2 = 0$ requires*:* ***$dN(\zeta)/dt = dN_0(\zeta)/dt$.***

*With $C_{CL} > 0$, equation (11) delivers the important observation that: $dN(\zeta)/dt = dF_{GHG}(\zeta)/dt$.*

Figure 5 clearly shows a $dF_{GHG}/dt > 0$ at that time. So, if the AGW-hypothesis is correct, warming began with a positive trend in the radiation imbalance $dN(\zeta)/dt > 0$. As $dF_{GHG}/dt$ has been constant ever since, the rising temperature would have caused a declining imbalance ($d^2N/dt^2 < 0$)

eventually leading to dN/dt → 0 for t >> τ. This would imply, 50 years later, a climate in a *steady state* where the temperature would track the constant trend in GHG-forcing according to $\lambda dT_S/dt = dF_{GHG}/dt$. As then dN/dt = 0, we would observe a constant offset in the radiation imbalance given by $N = \tau\, dF_{GHG}/dt \approx 0.08 - 0.16$ W/m$^2$, depending on the choices for $F_{2xCO2}$ and τ. Accordingly, $dLW_{OUT}/dt = 0$ at a constant solar input as assumed in the AGW-hypothesis.

This is nowhere near the observed imbalance ~ 0.94 W/m$^2$, its large non-zero trend $dN/dt \approx 0.049$ W/m$^2$/year and $dLW_{OUT}/dt \approx 0.028$ W/m$^2$/year. It might explain the need for the IPCC to increase $F_{2xCO2}$ as much as possible, as well as to lengthen τ by increasing the climate sensitivity. But this introduces additional inconsistencies. Combining the observed imbalance and the high IPCC forcing trend, would indicate a relaxation time $\tau = N^*(dF_{GHG}/dt)^{-1} \approx 25$ years. If the imbalance began decreasing in the 1970s, it should even with this value have relaxed significantly by now to about 20% of its initial value $dN(\zeta)/dt = dF_{GHG}(\zeta)/dt$. Instead dN/dt as observed is still large, fully contradicting this expectation. Moreover, the AGW-*GHG-only* hypothesis can never explain the large $dLW_{OUT}/dt$ as observed.
The corresponding climate thermal capacity $C_{CL}$ would be $N^*(dT_S/dt)^{-1} \approx 40 - 60$ Wyear/m$^2$K, or equivalent to a *climate layer* of 300 - 450 meters thick. However, ARGO temperature-data show that seasonal variations don't penetrate much deeper than about 100 meters [14]. Below 200 meters, ocean temperatures are effectively decoupled from surface variations. That is consistent with the arguments in Section 2.4 about the parameters that determine the *climate layer* and the subsequent estimate for $C_{CL}$ of about 13 Wyear/m$^2$K *i.e.,* the heat capacity of a 100 m thick ocean layer.

### *5.4. Climate change and the important role of Solar Forcing*

In Section 5.2 we derived the two key conditions that must have been met at the transition point between the global cooling- and global warming regimes: $N(\zeta) = N_0(\zeta)$, and $dN(\zeta)/dt = dN_0(\zeta)/dt$. Substituting those into (10) that still contains all these components, gives a remarkable equality:

$$\frac{dF_{SW}}{dt} + \frac{dF_{GHG}}{dt} = 0 \qquad (12)$$

This implies that at t = ζ, the definitely positive forcing trend from GHGs was entirely offset by a negative trend in the forcing in the incoming solar channel *i.e.,* $dF_{SW}(\zeta)/dt \approx -0.019$ *W/m²/year*, or even more negative depending on the choice for $F_{2xCO2}$. However, as shown in Fig.3, it is unambiguous that the current trend in incoming radiation $dSW_{IN}/dt >> 0$, indicating that today's $dF_{SW}/dt > 0$.

*This leads us to conclude that the mid-1970s shift in climate change was not initiated by increasing GHG concentrations, but rather by a change in the trend of SW-channel forcings. During the preceding cooling period, rising CO₂ concentrations may have mitigated some of the cooling, but did not reverse it. Once the SW forcing trend turned positive, GHGs simply began to augment an already warming climate trend.*

### *5.5. The (near) "steady state" character of current climate change.*

Despite the ongoing changes in climate, the current state can be considered a "near" *steady-state.* The GHG forcing trend has been pretty constant for decades. Other forcings, primarily in the SW channel, are also likely to change slowly and can be approximated as having constant trends over decadal timescales. Similarly, despite yearly fluctuations, the surface temperature trend has remained fairly stable since 2000. This stability implies by the same logic as in Section 5.2, that $dT_S/dt$ is (near) constant, and according to (5) that $(N - N_0)$ is (near) constant too. This allows for a large dN/dt as observed, but also indicates that $dN_0/dt \approx dN/dt$. From the OHC-data (Fig.4) we estimate that since t = ζ when $dN_0(\zeta)/dt = dN(\zeta)/dt$, $dN_0/dt$ and dN/dt slowly developed to the present relation $dN_0/dt \approx 0.8^*dN/dt$. Inserting this in (10) results in:

$$\lambda \frac{dT_S}{dt} \approx \frac{dF_{SW}}{dt} + \frac{dF_{GHG}}{dt} - 0.2\,\frac{dN}{dt} \tag{13}$$

The 0.2*dN/dt cannot be neglected as it indicates the growing divergence in the order of about 10 mW/m$^2$/year. As a forcing, this is equivalent to a correction in the temperature trend of something like 3 – 10 mK/year, depending on the assumed climate sensitivity (see Section 6.1).

This analysis strengthens the conclusion that the increase in both N(t) and $N_0$(t) are not a direct consequence of greenhouse gas emissions, but rather of enhanced forcing in the SW-channel. The alleged accelerations in N(t) that triggered this study [1], must therefore be attributed to natural variations in the SW-channel, not GHGs. This also explains why we didn't include $dN_0/dt$ into the sum of forcing trends $dF_{TOT}/dt$ in (10). If we had assumed a full *steady state* with $d(N - N_0)/dt = 0$, we would have immediately noticed that (10) equals:

$$\lambda \frac{dT_S}{dt} = \frac{dF_{SW}}{dt} + \frac{dF_{GHG}}{dt} \tag{14}$$

A formula that we previously derived from a different perspective by perturbing the radiation fluxes in the SW- and LW-channels, going from one equilibrium to another. Begin and end state then both inherently satisfy the *steady state* condition $d(N - N_0)/dt = 0$. It was shown that based on the *Planck feedback* definition $1/\lambda_{PL} = -\partial T_S/\partial N$, the feedback parameter in (14) must then be $\lambda = -\lambda_{PL}$ [4].

Equation (14) determines the temperature trend in our climate due to slow changing forcings with a constant trend in either the SW- or LW-channel. These can be attributed to GHGs, aerosols or changes in cloudiness. In case the imbalance $d(N - N_0)/dt$ isn't fully relaxed to zero, the small remaining imbalance will be absorbed in a slightly different estimate for $dF_{SW}/dt$, keeping (14) still practically applicable. Using the relation $\lambda = C_{CL}/\tau$, we can rewrite (14) linking this sum of "external" forcings $dF_{EXT}/dt = dF_{SW}/dt + dF_{GHG}/dt$ to the OHC-trend for the *climate layer*:

$$C_{CL} \frac{dT_S}{dt} = (N - N_0) = N_{CL} = \tau\,\frac{dF_{EXT}}{dt} \tag{15}$$

The term $\tau\, dF_{EXT}/dt$ is the offset in the radiation imbalance N due to all external forcings $F_{EXT}$.

## 6. A comparative analysis of the data against different views on climate change

### *6.1. Input data-sets*

In this section, we apply the relations as derived in amongst others Section 5, to explore two contrasting perspectives on three fundamental parameters governing climate change: *climate sensitivity λ, temperature trend $dT_S/dt$* and *trend in GHG-forcing $dF_{GHG}/dt$.*

The first set, based upon IPCC's views and further referred to as the "*IPCC-set*", consists of:

> $\lambda = \lambda_{AGW} = 1.1$ W/m$^2$/K, $dT_S/dt = 0.023$ K/year and $dF_{GHG}/dt = 0.037$ W/m$^2$/year.
>
> For the *Equilibrium Climate Sensitivity* (ECS), IPCC reports 3 °C with a "*likely"* range of 2.5 – 4 °C. Their *best estimate* corresponds to $\lambda_{AGW} = 1.3$ W/m$^2$/K using ECS = $RF_{2xCO2}/\lambda_{AGW}$. For the simplicity of maintaining a clean 3x ratio with $\lambda_{PL}$, we adopted the midpoint of the *likely* range, in line with CMIP6 ESM as referred to by the IPCC [8].

The second set, further referred to as the "*NAT-set*" consists of quite different numbers with:

> $\lambda = -\lambda_{PL} = 3.3$ W/m$^2$/K, $dT_S/dt = 0.015$ K/year, and $dF_{GHG}/dt = 0.019$ W/m$^2$/year.
>
> Values originate from the analysis in [4], which initially also used IPCC's GHG-forcing trend ($dF_{GHG}/dt = 0.037$ W/m$^2$/year). That choice led then to a large mismatch with the observed *clear-sky* $dLW_{OUT}/dt$, prompting the *all-sky* recalculation for $F_{2xCO2}$ [25].

A fixed climate relaxation time $\tau = 4$ years is assumed for both sets. The consequence of IPCC's large climate sensitivity $1/\lambda_{AGW}$ is that with this constant $\tau$, the heat capacity of our climate $C_{CL}$ must become small. A shallow *climate layer* of about 30 meters is not very realistic, given the OHC-profile in Fig.4. To maintain consistency in the *IPCC-set* a longer relaxation time should be chosen ($\tau \approx 12$ years), or alternative combinations of $C_{CL}$ and $\tau$ such that $C_{CL}/\tau = \lambda_{AGW}$. As earlier discussed, a 12 years relaxation time doesn't seem realistic. In discussing the calculated results in Section 6.1, we will address the possible impact of this choice where applicable.

## *6.2. Data comparison and sensitivity sets as applied in Table 1*

For reference, Table 1 also includes a block of data derived from the observed OHC trends discussed in Section 5.2. Color-coding indicates which OHC-set parameters should be compared with the parameters calculated using (7) with $dF_{TOT}/dt = \lambda dT_S\, dt + dN/dt$ and (10), decomposing $dF_{TOT}/dt$ into $dF_{GHG}/dt$, $dF_{SW}/dt$ and $dN_0/dt$. Formulas used are indicated in the respective columns.

Climate sensitivity $\xi$, is generally expressed in its inverse as feedback parameter $\lambda$. It is by far the most controversial parameter and key differentiator between the two primary data sets. Their difference is so significant that exact values for the other parameters might be less critical. To illustrate how results depend on those parameters, we added to each climate sensitivity, also the temperature- and forcing trends of the other set. In this way we constructed 4 different sets. For the two primary sets, figures are shown in **bold** and for the two "hybrid combinations" in *italics*. Rows for these hybrids aren't colored in the table. They are not considered viable climate-scenarios but just added to make the sensitivity for certain parameter choices more visible.

***Table 1.*** *Summary of the radiation balance analysis for 4 scenarios. The two most relevant scenarios are the standard IPCC scenario (IPCC-set) and an alternative scenario (NAT-set) as described in the text. The primary input parameters include the inverse of the climate sensitivity $\lambda$, the trend in Greenhouse gas forcing $dF_{GHG}/dt$ and the observed surface temperature trend $dT_S/dt$. Using these parameters, various related components were calculated based on eq.(7) & (10), and where possible, compared with values derived from the Ocean Heat Content analysis in Sections 3 & 4. In the (colored) rows belonging to the two key scenarios, values are shown in* ***bold****; in the other scenarios, values are italicized. Identical color-coding is used to visually link corresponding values from the radiation balance and OHC analyses.*

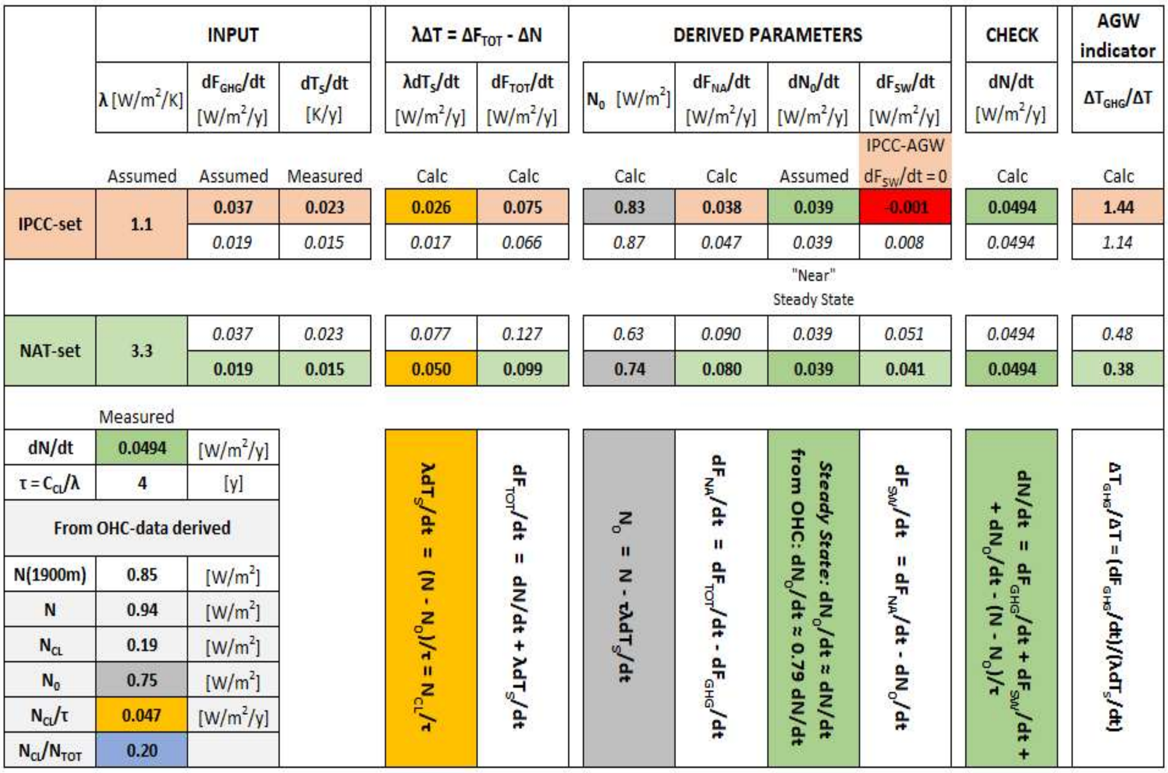

| | INPUT | | | $\lambda\Delta T = \Delta F_{TOT} - \Delta N$ | | DERIVED PARAMETERS | | | | CHECK | AGW indicator |
|---|---|---|---|---|---|---|---|---|---|---|---|
| | $\lambda$ [W/m²/K] | $dF_{GHG}/dt$ [W/m²/y] | $dT_S/dt$ [K/y] | $\lambda dT_S/dt$ [W/m²/y] | $dF_{TOT}/dt$ [W/m²/y] | $N_0$ [W/m²] | $dF_{NA}/dt$ [W/m²/y] | $dN_0/dt$ [W/m²/y] | $dF_{SW}/dt$ [W/m²/y] | $dN/dt$ [W/m²/y] | $\Delta T_{GHG}/\Delta T$ |
| | Assumed | Assumed | Measured | Calc | Calc | Calc | Calc | Assumed | IPCC-AGW<br>$dF_{SW}/dt = 0$ | Calc | Calc |
| IPCC-set | 1.1 | **0.037** | **0.023** | **0.026** | **0.075** | **0.83** | **0.038** | **0.039** | **-0.001** | **0.0494** | **1.44** |
| | | *0.019* | *0.015* | *0.017* | *0.066* | *0.87* | *0.047* | *0.039* | *0.008* | *0.0494* | *1.14* |
| | | | | | | | | "Near"<br>Steady State | | | |
| NAT-set | 3.3 | *0.037* | *0.023* | *0.077* | *0.127* | *0.63* | *0.090* | *0.039* | *0.051* | *0.0494* | *0.48* |
| | | **0.019** | **0.015** | **0.050** | **0.099** | **0.74** | **0.080** | **0.039** | **0.041** | **0.0494** | **0.38** |
| | | | | $\lambda dT_S/dt = (N - N_0)/\tau = N_{CL}/\tau$ | $dF_{TOT}/dt = dN/dt + \lambda dT_S/dt$ | $N_0 = N - \tau\lambda dT_S/dt$ | $dF_{NA}/dt = dF_{TOT}/dt - dF_{GHG}/dt$ | *Steady State:* $dN_0/dt \approx dN/dt$<br>from OHC: $dN_0/dt \approx 0.79\ dN/dt$ | $dF_{SW}/dt = dF_{NA}/dt - dN_0/dt$ | $dN/dt = dF_{GHG}/dt + dF_{SW}/dt + dN_0/dt - (N - N_0)/\tau$ | $\Delta T_{GHG}/\Delta T = (dF_{GHG}/dt)/(\lambda dT_S/dt)$ |

| | Measured | |
|---|---|---|
| $dN/dt$ | 0.0494 | [W/m²/y] |
| $\tau = C_{CL}/\lambda$ | 4 | [y] |
| From OHC-data derived | | |
| N(1900m) | 0.85 | [W/m²] |
| N | 0.94 | [W/m²] |
| $N_{CL}$ | 0.19 | [W/m²] |
| $N_0$ | 0.75 | [W/m²] |
| $N_{CL}/\tau$ | 0.047 | [W/m²/y] |
| $N_{CL}/N_{TOT}$ | 0.20 | |

### *6.3. Explaining/discussing the output parameters in Tabel 1*

In this section, we systematically explain each column in Table 1 and relate them to the output derived from OHC data, as shown in Figures 1 and 4. For the radiation imbalance trend, we use the CERES-EBAF4.2 dataset, as numerically illustrated in Fig.3.

- **$\lambda dT_S/dt$** expresses the climate response to the combined effect of all *forcings*. It is the warming of the *climate layer* through $\lambda dT_S/dt = N_{CL}/\tau$. In the *NAT-set*, using the *Planck feedback* parameter $-\lambda_{PL}$ this relationship is well satisfied. But in the *IPCC-set* using $\lambda_{AGW,}$ the expression does not match observations, unless the relaxation time $\tau$ is *increased*, or the heat content $N_{CL}$ *decreased*. These are contradictory adjustments: increasing $\tau$ implies a thicker, whereas lowering $N_{CL}$ requires a thinner *climate layer*. As $\lambda_{AGW} = C_{CL}/\tau$ is fixed and $C_{CL}$ scales with the layer thickness only, these opposing requirements create an internal inconsistency that cannot be resolved.
- **$dF_{TOT}/dt$** represents the trend in the sum of all *forcings,* calculated via $dF_{TOT}/dt = \lambda dT_S/dt + dN/dt$. Since both $dN/dt$ and $dT_S/dt$ are derived from observations, differences in the calculated $dF_{TOT}/dt$ are primarily due to the choice of $\lambda$. As expected, the *NAT-set* yields a slightly higher value than the *IPCC-set*. However, this difference is modest, especially considering the 3x difference in climate sensitivity between the two sets.
- **$N_0$** is the level of the virtual radiation balance as determined from the OHC-data and can also be calculated from the warming of the *climate layer* $C_{CL}dT_S/dt = N_{CL}$. The *IPCC-set* once again fails to match this value with its unrealistically thin climate layer due to the chosen $\lambda_{AGW}$. By contrast, the *NAT-set* aligns well with the OHC observations, consistent with the earlier finding above that the $\lambda dT_S/dt$ term is physically plausible.
- **$dF_{NA}/dt$** represents the portion of total forcing not attributable to GHGs. Under the AGW-hypothesis, which recognizes only anthropogenic GHGs as forcing agents, the *IPCC-set* necessarily implies: $dF_{NA}/dt = dN_0/dt$. This equality indeed holds in Table 1. However, this apparent agreement is misleading. In the AGW framework $dN_0/dt = 0$ *by definition*, because natural influences are excluded. By adjusting $dF_{GHG}/dt$ and $\lambda_{AGW}$, the energy balance equation $dF_{GHG}/dt = \lambda dT/dt + dN/dt$ according to the AGW-hypothesis, can always be satisfied. Section 5 already showed that such adjustments cannot overcome the fundamental requirement $dN/dt < dF_{GHG}/dt$, which remains a major unresolved issue in the IPCC's AGW-framework.

- **$dN_0/dt$** equals $dN/dt$ in a true *steady state.* However, given the possibility of slowly varying natural forcings and a non-constant $dT_S/dt$, the OHC data since 2004 suggest a constrained relationship: $dN_0/dt \approx 0.80{*}dN/dt$. In the *NAT-set*, this requires a small negative adjustment to the temperature trend of about –0.003 K/year. Because $dF_{TOT}/dt$ is fixed, that small negative contribution in (6) due to $dN_0/dt < dN/dt$, is offset by a corresponding increase in $dF_{SW}/dt$ in the next column. Such a minor correction will not lead to essentially different conclusions.

.

- **$dF_{SW}/dt$** is just the "residue" of $dF_{NA}/dt$ after subtracting $dF_{GHG}/dt$ and $dN_0/dt$. In the AGW-hypothesis of the IPCC, this is zero *by definition,* since natural or non-GHG forcings are excluded. In fact, using (11), this assumption even yields a slight *cooling* effect, despite the observed increase in incoming SW-radiation. This strongly undermines the *IPCC-set'*s credibility. The *NAT-set*, on the other hand, yields $dF_{SW}/dt \approx 0.041$ W/m$^2$/year, which aligns with the observed albedo changes (see Section 8) and contributes meaningfully to *global warming*.

- **dN/dt** serves as a consistency check, computed from the sum of previous components via (7). As expected, all values check out.

- **$\Delta T_{GHG}/\Delta T$** expresses the GHG-share in the observed *global warming* trend, calculated as $(dF_{GHG}/dt)/(\lambda dT_S/dt)$. It involves only the three parameters that most clearly distinguish the *NAT-set* from the *IPCC-set*: λ, $dT_S/dt$ and $dF_{GHG}/dt$. For the *NAT-set*, this ratio yields roughly 1/3rd anthropogenic and consequently, 2/3rd "natural" warming; consistent with the outcome of [4]. Even when using $\lambda_{PL}$ in combination with IPCC's high values for $dF_{GHG}/dt$ and $dT_S/dt$, the result still attributes over 50% to warming from natural origin. Thus, the critical discriminant is the climate sensitivity 1/λ and not so much $F_{2xCO2}$, the greenhouse gas strength. In contrast, the *IPCC-set* implies that 144% of the observed warming is of anthropogenic origin. Clearly, an impossible result unless a substantial, unrecognized *cooling* trend exists to offset this "overheating". Not a very plausible concept with an increasing solar radiation as observed. This again highlights how tuning of parameters like $\lambda_{AGW}$ and $RF_{2xCO2}$, to match a specific relationship can lead to implausible outcomes elsewhere in the system.

## 7. The consequences of the AGW-hypothesis under a "GHG-only" scenario

The preceding analysis highlights how the IPCC's assumptions diverge significantly from observed reality. While the IPCC model components may collectively reproduce the observed warming trend, they fail to individually align with key observational data, in particular the *Ocean Heat Content*.

A useful measure here, is the ratio $\Delta T_{GHG}/\Delta T$ which quantifies how much of the observed temperature change is attributable to greenhouse gases. In the context of (11), representing the "GHG-only" scenario central to the AGW hypothesis, this ratio should approach 1 if the IPCC narrative is correct. Demonstrating this equivalence is essential to validating IPCC's framework.

### 7.1. Varying the temperature trend $dT_S/dt$

We begin by examining the surface temperature trend $dT_S/dt$, which in the IPCC framework is set at 0.0234 K/year, consistent with NASA's CERES-EBAF v4.2 dataset. Its previous version, v4.1, used a lower trend of approximately 0.0186 K/year. In v4.2, updated in January 2024, the trend was suddenly aligned (for unclear reasons) with the HadCRUTv5 dataset (see Section 4.3).

While this higher trend is broadly consistent with UAH-TLT data over land [18], the global average from the same satellite series yields a lower 0.015 K/year, closely matching the sea surface temperature trend from ARGO floats (Fig. 1). If we were to adopt this lower value in the *IPCC-set*, the ratio $\Delta T_{GHG}/\Delta T$ would increase to approximately 2.2, since $dT_S/dt$ appears in the denominator. This might explain the IPCC's apparent preference for datasets with high warming trends. However, even with speculating about "accelerating" global warming, achieving $\Delta T_{GHG}/\Delta T = 1$ would require a trend of 0.034 K/year, well above what is currently observed or justifiable.

### 7.2. Adjusting climate sensitivity 1/λ

An alternative route is to increase climate sensitivity in the *IPCC-set*. This actually worsens the mismatch. To bring $\Delta T_{GHG}/\Delta T$ down to 1, we would need to decrease the climate sensitivity. This would imply a feedback parameter $\lambda \approx 1.6$ W/m²/K, corresponding to a climate sensitivity roughly twice the inverse of the *Planck feedback parameter* rather than three times larger. However, this value is not supported by *General Circulation Models* (GCMs), on which the *IPCC-set* is founded. In fact, the latest CMIP6 models tend toward even higher climate sensitivities than previous generations.

### *7.3. Modifying the GHG-forcing strength $F_{2xCO2}$*

The third option is to adjust the *forcing* strength $F_{2xCO2}$. IPCC-AR6 sets this value at 3.9 W/m$^2$ [8]. To satisfy $\Delta T_{GHG}/\Delta T = 1$, it should be lowered to about 2.7 W/m$^2$. Ignoring definitional nuances (see the discussion in Section 4.4), this required value is even lower than what is derived from *clear-sky* radiative transfer calculations [22].

### *7.4. Altering the climate relaxation time τ*

Finally, we could consider modifying the relaxation time $\tau = 4$ years, which influences several derived parameters (see Table 1). But this parameter **does not** affect the $\Delta T_{GHG}/\Delta T$ ratio. As such, it offers no pathway for reconciling the "*GHG-only*" scenario with the observed data.

## 8. The forcing trend $dF_{SW}/dt$ related to changes in incoming solar radiation $SW_{IN}$

### *8.1. Changes in cloudiness*

Section 6 showed that the *NAT-set* yields a residual forcing trend of approximately $dF_{SW}/dt \approx 0.041$ W/m$^2$/year. Regardless of the value of $F_{2xCO2}$, a constant GHG forcing trend ($dF_{GHG}/dt$) in the LW- channel should result in a constant $LW_{OUT}$, as established in Section 5. Observations (Fig. 3) on the contrary, reveal not only a significant positive trend in $dLW_{OUT}/dt$, but an even larger one in $dSW_{IN}/dt$.

The solar constant ($S_0$) remains nearly constant on an annual basis, as confirmed by CERES data over the past 23 years. Seasonal variations, however, are non-negligible. For instance, over 18 years, the average $S_0$ during spring (MAM) increased by about 0.2 W/m$^2$ compared to autumn (SON). During spring in the Northern Hemisphere, high-latitude regions received ~0.4 W/m$^2$ more solar radiation than their Southern Hemisphere counterparts. These variations likely result from orbital changes and, although often dismissed, they represent potential forcings of a similar magnitude as those of GHGs. In particular, they will influence the redistribution of heat as they affect the Northern- to Southern Hemisphere balance. Nevertheless, the observed increase in $SW_{IN}$ is primarily due to albedo changes, especially from clouds. Variations in $S_0$ are effectively embedded within the broader $dSW_{IN}/dt$ trend, but they do not explain its magnitude on their own.

### *8.2. The Cloud Radiative Effect (CRE)*

Clouds influence both SW and LW radiation fluxes in the same direction, but to different extents. This impact is known as the *Cloud Radiative Effect* (CRE). CERES data provides global average values: SW-CRE ≈ 45.2 W/m$^2$, and LW-CRE ≈ 25.6 W/m$^2$ respectively. These are derived from 20-years of radiation measurements under *clear-sky* (cs) and *all-sky* (as) conditions with 67% average cloud cover.

To estimate the net cloud-induced forcing from the $SW_{IN}$ trend, we multiply $dSW_{IN}/dt$ by the net-CRE factor, calculated as: (1 – LW-CRE/SW-CRE) ≈ 0.43 [9]. Changes in clouds and cloudiness are more than just cloud area-related effects as in this CRE. Changes in transparency, mostly for the SW-channel and changes in *Top of Cloud* (TOC) temperature for the LW-channel, contribute as well. While CERES offers some data on cloud area and TOC temperature, no robust method currently exists for incorporating these into an improved cloud forcing estimate. As such, $dSW_{IN}/dt$ remains our best proxy for quantifying the radiative effect of cloud changes.

Clouds also affect $dLW_{OUT}/dt$ through their shielding effect, influencing both $CO_2$ and water vapor forcing. The water vapor content in "*clear-sky*" conditions within an *all-sky* atmosphere, differs from that of a hypothetical Earth in a *clear-sky* equilibrium. Since a truly *clear-sky* Earth doesn't exist, interpreting the difference between *clear-sky* and *all-sky* $LW_{OUT}$ is inherently complex [25].

### *8.3. All-sky versus Clear-sky $SW_{IN}$ data*

$SW_{IN}$ is affected by more than clouds alone. Figure 3 shows only *all-sky* (*as*) data, but the *clear-sky* $SW_{IN}$(*cs*) has also increased over the same period by about 0.036 W/m²/year (see Fig. 2 in [4]). This trend likely follows changes in surface reflectivity, including snow/ice melt (*Surface Albedo* feedback), changes in land-use (urbanization), and *Global Greening* (by increased $CO_2$-levels?). To isolate the cloud-related effect, we subtract the *clear-sky (cs)* trend from the *all-sky (as)* value $dSW_{IN}(as)/dt \approx 0.077$ W/m²/year. Since 67% of Earth's surface is cloud-covered, only 1/3rd of this *clear-sky* trend affects the *all-sky* value, leaving a cloud-related $SW_{IN}$ trend ~ 0.065 W/m²/year. Multiplying this by the net-CRE factor gives a cloud-related SW forcing trend $dF_{SW}/dt$ of about $0.43 * 0.065 \approx 0.028$ W/m²/year.

This net-CRE ratio applied here, as well as $dSW_{IN}/dt$ are global averages. But regional discrepancies with $SW_{IN} >> LW_{OUT}$ around the Tropics and $SW_{IN} << LW_{OUT}$ in the Polar regions, do matter. Hence, both net-CRE and $dSW_{IN}/dt$ (*as – cs*) vary with latitude (see Fig. 6). The values in Fig. 6 are shown per unit area and must be cosine-weighted by latitude to yield a global average. The data suggests that the applied factor (0.43) may slightly underestimate the cloud forcing, so the derived 0.028 W/m²/year is likely conservative.

Finally, we have to add the *Surface Albedo* part of 0.012 W/m²/year again that we first subtracted to calculate the net forcing from $dSW_{IN}(as)/dt$, making $dF_{SW}/dt \approx 0.040$ *W/m²/year*.

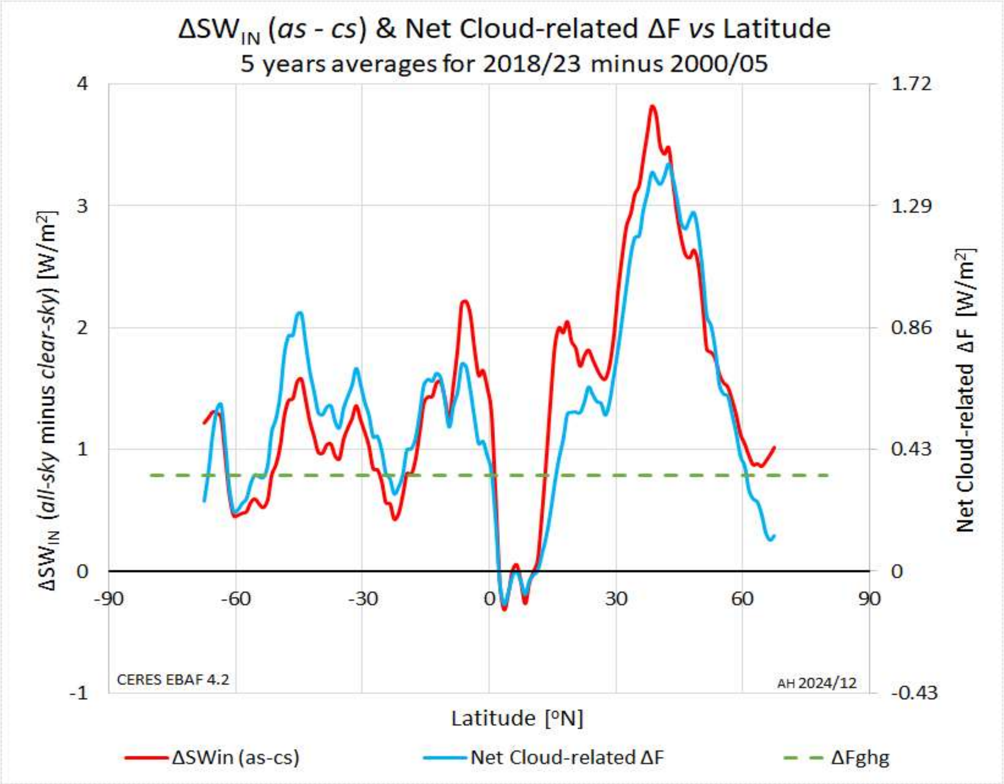

***Fig.6*** *Eighteen-year difference between 5-years averages of the latitude-dependent "all sky minus clear sky" incoming Solar radiation $\Delta SW_{IN}$ (as – cs) and the corresponding net cloud-related forcing $\Delta F_{SW}$ as calculated with the latitude dependent net-CRE ratio as described in Section 8. The respective vertical axes are scaled to match globally averaged net-CRE, demonstrating that this approach provides a good estimate of the global mean cloud-related forcing $\Delta F_{SW}$. The figure highlights that this forcing is predominantly a Northern Hemisphere phenomenon, with a peak in $\Delta F_{SW}$ of approximately 1.5 W/m². For comparison: the change in GHG forcing $\Delta F_{GHG}$ over the same period was as indicated, about 0.34W/m² (or 0.70 W/m² using IPCC's $RF_{2xCO2}$ forcing value).*
*Data source: https://ceres.larc.nasa.gov/data [9].*

### 8.4. Comparing $dF_{SW}/dt$ as derived from $SW_{IN}$ versus the calculated value from Tabel 1

The empirically derived $dF_{SW}/dt \approx 0.040$ W/m²/year aligns closely with the 0.041 W/m²/year obtained through the calculations used to construct Table 1. Considering the various assumptions and uncertainties involved in this derivation, this agreement is noteworthy and unlikely to be coincidental. Combining this with $dF_{GHG}/dt = 0.019$ W/m²/year and $\lambda = 3.3$ W/m²/K, we calculate with (13) a temperature trend $dT_S/dt \approx 0.015$ K/year. This is consistent with both the UAH-TLT satellite data and the SST trend, affirming the *NAT-set* as a reasonable model framework.

Figure 6 also illustrates that changes in cloudiness are more pronounced on the Northern Hemisphere, especially at mid-latitudes and over Western Europe. For example, the Dutch KNMI weather-station at Cabauw (51.87°N, 4.93°E), where all ground-level radiation components are monitored every 10 minutes, recorded an increase in solar radiation of almost +0.5 W/m²/year since 2000 [26]. Applying the 0.43 net-CRE factor (conservative for this latitude), we estimate a local forcing trend $dF_{SW}/dt \approx 0.2$ W/m²/year. This is an order of magnitude larger than the GHG-forcing (0.019–0.037 W/m²/year). Even with the IPCC values, GHGs can just account for about 16% of the warming at this station. The average temperature trend for this rural station located in a polder largely covered by grassland, is with ~ +0.043 K/year almost 3x the global average. This, nor the other trends mentioned above can be adequately explained by the IPCC's GHG-only model. As Section 9 will show, it also fails to explain the observed trend in $SW_{IN}$ at TOA.

## 9. Cloud-feedback as a possible origin of the forcing trend $dF_{SW}/dt$

The IPCC places strong emphasis on the role of *climate feedbacks* in amplifying the warming effect of greenhouse gases (GHGs) [8]. These feedbacks are considered secondary consequences of *Anthropogenic Global Warming*, driven by the initial temperature increase from GHGs. Among them, *Water-Vapor* feedback is the most significant. A warmer atmosphere holds more water vapor (approximately +7%/K) and since water vapor is a potent GHG, even a small warming from $CO_2$ can amplify itself through enhanced evaporation.

Other feedbacks recognized by the IPCC include *Lapse Rate*, *Surface Albedo*, and *Cloud* feedbacks [8], all of which are inherently tied to the presence and behavior of water in its various phases. Therefore, these feedbacks are natural responses to temperature changes, regardless of the original cause of warming, be it GHGs, incoming solar variability, or internal effects. They are not *additive* components to natural climate sensitivity, as treated by the IPCC, but rather integral parts of it [4].

In the energy balance framework discussed in Fig. 2, feedbacks manifest through a temperature sensitive R, thus influencing how quickly the system can return to equilibrium after a perturbation. Hence, their influence on temperature. However, through $\lambda = C_{CL}/\tau$, they are already incorporated in all applied equations in this paper through the value of $\tau$.

This conceptual distinction underlies the key difference in climate sensitivity assumptions between the *NAT-set* (natural feedback dominated, (near) Planck response) and the AGW/IPCC-set (strong positive feedbacks), as elaborated in [4].

### 9.1. Estimating the GHG-induced feedback contributions

In Section 8, we included the *Surface Albedo* feedback, changes in reflected solar radiation from the surface due to, for example, snowmelt or changes in vegetation. We didn’t distinguish whether these were caused by warming or other factors (e.g., *land use change* or *global greening*). In the IPCC framework, however, all feedbacks, including *Albedo* and *Cloud* feedbacks, are primarily presumed to be secondary effects of GHG-driven warming. This interpretation leads to the claim that the observed increase in incoming solar radiation ($SW_{IN}$) is not natural but is in itself a feedback effect from GHGs, caused by temperature-induced reductions in snow- and cloud cover.

To test this idea, we can estimate the contribution of temperature-driven feedbacks, specifically from *Surface Albedo* and *Cloud* changes, to the observed trend in $dF_{SW}/dt$ as calculated from $dSW_{IN}/dt$.

### 9.1.1. Surface Albedo feedback

From Table 1, the GHG-induced component of warming accounts for about 1/3rd of the total. Applying this to the *Albedo* feedback trend included in $dSW_{IN}/dt$ (~ 0.012 W/m²/year as shown in Section 8), the GHG-induced portion is only ~ *0.004 W/m²/year*. With a temperature trend of 0.015 K/year, it implies a *Surface Albedo* feedback parameter $\lambda_{SA} \approx 0.3$ W/m²/K, slightly lower than the IPCC's AR6 estimate. But even using their value $\lambda_{SA} = 0.35 \pm 0.25$ W/m²/K, gives a maximum contribution of only 0.005 W/m²/year to $dF_{SW}/dt$. That is still far too small to account for the observed trend.

### 9.1.2. Cloud feedback

For estimating the GHG-induced *Cloud* feedback, we have no other option than to use the IPCC's AR6 estimate for $\lambda_{CF} = 0.4 \pm 0.5$ W/m²/K as derived from GCMs [8]. The sum of all temperature driven *feedbacks* is about 2.2 W/m²/K of which 2/3rd has to be attributed to *Water-Vapor* feedback [4,8]. So, the high side of the range is very unlikely. On the low side of the range, negative values for $\lambda_{CF}$ will not help $SW_{IN}$ to increase, so we limit ourselves here to the center value. With the observed surface temperature trend $dT_S/dt = 0.015$ K/year, in line with SST trends over the predominantly oceanic cloud-forming regions, we calculate a *Cloud* feedback contribution of only 0.006 W/m²/year. With only one-third of the warming attributed to GHGs, the anthropogenic share of this feedback is roughly *0.002 W/m²/year*.

## 9.2. Combined feedback impact and implications

Combining these estimates for the GHG-induced *Surface Albedo* and *Cloud* feedbacks yield a contribution of only ~15% of the total $dF_{SW}/dt \approx 0.040$ W/m²/year as derived in Section 8.

Specifically, *Cloud feedback* alone accounts for just 5% of the total, meaning it is insufficient to explain the observed increase in $SW_{IN}$. Furthermore, it is notable that the *Cloud feedback* contribution is not even larger than that from the *Surface Albedo*, despite clouds playing a dominant role in radiative forcing and deliver about 50% of the normal Greenhouse Effect [25]. This might be due to the fact that not all *Surface Albedo* changes are temperature-driven. *Change of land-use* and *Global Greening* can occur independently of GHG-induced warming, yet still influence climate/temperatures.

In conclusion, the GHG-related *Surface Albedo* and *Cloud* feedbacks are far too weak to explain the observed trend in $SW_{IN}$. The majority of the trend must therefore be attributed to natural causes unrelated to GHG-induced warming. The resulting forcing trend $dF_{SW}/dt \approx 0.040$ W/m²/year as calculated in Section 8 using the observed $dSW_{IN}/dt$, matches well with the independently derived value of 0.041 W/m²/year from Section 7 and Table 1.

To estimate the purely natural contribution to global warming, we subtract the GHG-attributed share (about 0.006 W/m²/year) from the total $dF_{SW}/dt$, leaving a "net" natural forcing trend in the SW-channel of ≈ 0.035 W/m²/year. Given the GHG forcing trend $dF_{GHG}/dt \approx 0.019$ W/m²/year, this leads to the conclusion that *approximately 2/3rd of the observed global warming is of natural origin, and 1/3rd is due to anthropogenic cause such as the increase of e.g.* $CO_2$.

An alternative CERES-based analysis in [4] produced similarly, a 50/50 split, albeit assuming higher GHG-forcing trends. Even when using the IPCC GHG forcing values within the *NAT-set* (the "white row" in Table 1), natural contributions still dominate.

These findings indicate that the relative role of GHGs in observed warming depends more on the assumed climate sensitivity than on the absolute magnitude of GHG forcing. Of course, that is partly due to the observations that GHGs are not at all playing the dominant role in global warming, which IPCC attributes to them. As emphasized in [4], it is then the value of climate sensitivity and not necessarily the forcing strength that most strongly determines warming outcomes.

This analysis reinforces a fundamental point: climate feedbacks are not external modifiers of climate sensitivity; rather, they are inherent to the system. Their combined effect is already embedded in the climate response function. The IPCC's treatment of feedbacks as additive components used to "explain" high sensitivities in GCMs is conceptually flawed. Physically, Earth's climate is governed by the mass balance of water in all its phases: ice, snow, liquid, vapor, and clouds. The dynamics between these phases are temperature-sensitive, and they constitute the feedback processes. Feedbacks aren't just *add-ons* to the climate system, they *are* our climate.

## 10. Ocean Heat Content increase

In the introduction, the "*heat in the pipeline*" concept: the idea that heat stored in the deep, cold ocean layers could later resurface to significantly influence surface temperatures, was challenged. Without a substantial decrease in surface temperatures to reverse ocean stratification, this seems highly unlikely. Large and rapid temperature fluctuations during the pre-industrial era with rates up to plus, but also minus 0.05 K/year over several decennia as recorded in the *Central England Temperature* (CET) series [27], more than three times the rate observed today, further undermine the notion of a slow-release heat mechanism dominating surface temperature trends.

*Ocean Heat Content* must be related to solar energy. It is the prime source of energy heating the Earth thermal system. Almost 1 W/m$^2$ of that 240 W/m$^2$ solar flux that is in average entering the system, is presently remaining in the oceans. This is an order of magnitude larger than the estimated 0.1 W/m$^2$ of *geothermal heat* upwelling from the Earth inner core [11]. Extra greenhouse gasses don't add energy to the system, but just obstruct cooling. As shown in Section 5.3, this accounts for a radiation imbalance offset $\tau\ dF_{GHG}/dt$, or equivalent to a contribution to dOHC/dt of only about 0.08 W/m$^2$.

As redistribution of "*heat in the pipeline*" will not change the total OHC, roughly ¾ of the observed positive trend in OHC must at least be attributed to rising solar input. The oceans act in this way as our climate system's thermal buffer. It will mitigate warming during periods of increased solar input and dampen cooling when solar input declines, underscoring its critical role in Earth's climate stability.

Levitus *et al.* (2012) [28] combined OHC estimates back to 1955 to the data of the ARGO program as shown in Fig.7. Despite the high uncertainties in pre-ARGO ocean temperature measurements, it looks as if we had periods with a very strong positive +0.8 W/m$^2$ (1970-1980) as well as a very strong negative –0.7 W/m$^2$ radiation imbalance (1963-1970). But also, a period with an almost perfect radiation balance (1980-1990). Nevertheless, when averaged over the entire period from 1955 to 2010, the OHC trend to 2000 m depth corresponds to a positive net radiation imbalance of approximately +0.4 W/m$^2$. We also must have had a relatively high positive radiation imbalance before the turning point at $t = \zeta$, going from global cooling into a global warming regime. It all indicates to a positive radiation imbalance for most of the time, even before GHGs allegedly started to change our climate.

Reconstructed data in the AGGI database [21], show that GHG concentrations were already rising exponentially after WWII, implying a steady $dF_{GHG}/dt$ since at least 1955. Therefore, the almost constant forcing rate from GHGs cannot have triggered these abrupt radiation imbalance shifts as visible in Fig.7. So, the sudden variations around the early 1960s, 1970, 1980 and 1990, must have been triggered by natural events. Such rapid changes in OHC, as for instance around 1970, where N changes from a negative into a positive balance by +1.5 W/m$^2$ in about 4 years of time, also indicates a rather short climate relaxation time $\tau$. Again, this contradicts IPCC's high climate sensitivity value.

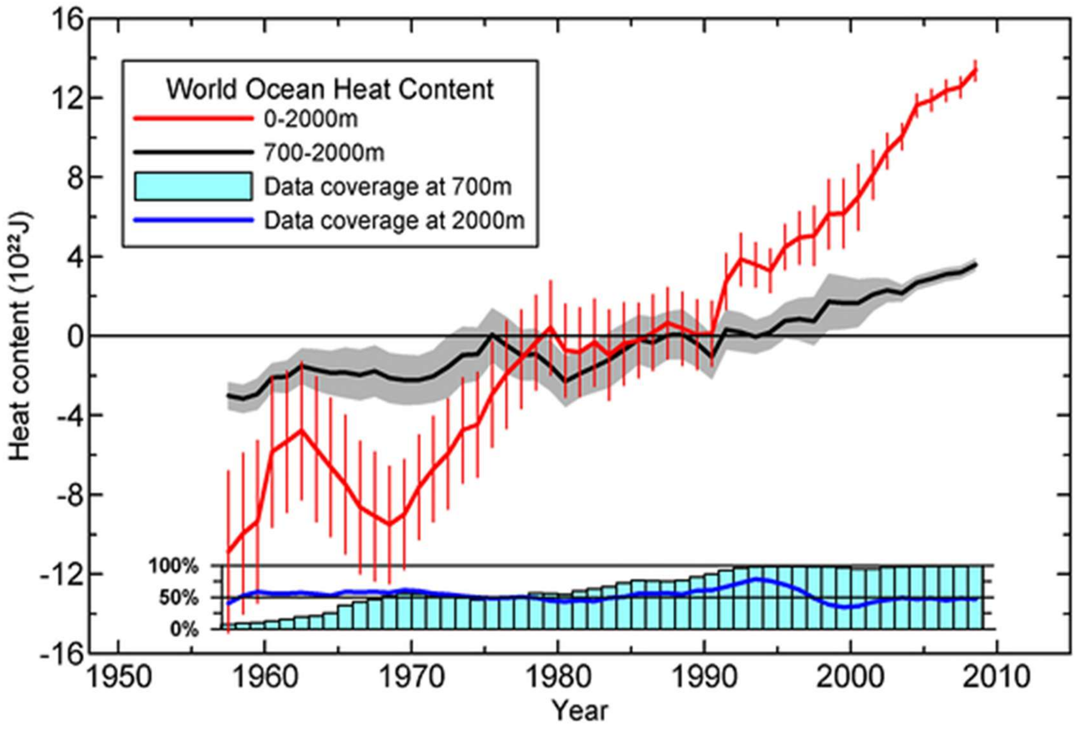

"Time series for the World Ocean of ocean heat content ($10^{22}$ J) for the 0–2000 m (red) and 700–2000 m (black) layers based on running pentadal (five-year) analyses. Reference period is 1955–2006. Each pentadal estimate is plotted at the midpoint of the 5-year period. The vertical bars represent +/−2.*S.E. about the pentadal estimate for the 0–2000 m estimates and the grey-shaded area represent +/−2.*S.E."

***Fig. 7.*** *Graph and part of its caption reproduced from Levitus et al. [28], showing estimates of Ocean Heat Content (OHC) since 1955, including the associated 2σ uncertainty range. At NOAA's Climate.gov, the 0–700 m OHC data are cited as evidence of greenhouse gas (GHG) effects, using the statement: "*More than 90 percent of the excess heat trapped in the Earth system due to human-caused global warming, has been absorbed by the oceans*".*

The strong downwards slope in the OHC before 1970 confirms the observation in Section 5.4 and expressed by (12) that around the turning point t = ζ, the forcing trend in the SW-channel had to be negative. Moreover, the rather slowly increasing 700-2000m OHC data in Fig.7 indicate that most of the fluctuations have occurred relatively close to the surface. Heat from *e.g. seafloor volcanism* as "warming from below", is expected to show up more pronounced in this 700-2000m OHC-profile. Although we cannot rule out *geothermal* influences [29], this observation makes them less likely.

As the OHC seems to be primarily coupled to $SW_{IN}$, the most plausible cause would involve rapid changes in SW-forcing. A sudden drop in cloud-cover might explain such changes, but no convincing observations could be found for the 1960-1980 period. Alternatively, changes in the latitudinal distribution of cloud-cover as illustrated by Fig.6, can result in similar radiative impacts due to the stark contrast between a positive radiation imbalance in the Tropics and a very negative imbalance at the Poles. The ENSO-oscillations in the Pacific Ocean around the equator are a typical example for such influences, as also illustrated in Fig.3 [10]. Shifts in cloud distribution are linked to changes in wind patterns and/or ocean currents, reinforcing the idea as indicated in Section 1, that even minor disruptions in horizontal heat transport can trigger major shifts in our climate's equilibrium [29, 30]. Sharp shifts in Earth's radiation imbalance like the one around 1970 as inferred from Fig.7, may even represent one of those alleged *tipping points*. But in this case, certainly not one triggered by GHGs. Ironically, some climate scientists in the early 1970s predicted an impending (Little) Ice Age [31].

While additional data (*e.g.* radiation measurements) are needed to draw firm conclusions, the available evidence already challenges the prevailing GHG-centric narrative again. GHG emissions, with their near constant forcing rate, cannot account for the timing nor the magnitude of historical OHC trends, as NOAA explicitly suggests [32]. Similarly, claims by KNMI that "accelerations" in radiation imbalance trends are GHG-driven [1], are not supported by data. And finally, the alarms around "*heat in the pipeline*" must be exaggerated if not totally misplaced. Given the similarities in radiation imbalance and GHG forcing rates around 1970 with today's situation, we must conclude that this assumed *heat* manifested itself at that time apparently as "*cooling in the pipeline*".

However, warnings for continued warming even if we immediately stop now with emitting GHGs are nevertheless, absolutely justified. Only, it isn't warming then from that *heat in the pipeline* due historical emissions that will boost our temperatures. Warming will continue to go on as long as *natural forcings* will be acting. These are already today's dominant drivers behind global temperature trends. And unfortunately, they will not be affected by the illusion of stopping global warming as created by implementing *Net-Zero* policies.

## 11. Summary and conclusions

This analysis demonstrates that a *global warming* scenario driven solely by *greenhouse gases* (GHGs) is inconsistent with more than 20 years of observations from space and of *Ocean Heat Content*. The standard *anthropogenic global warming* (AGW) hypothesis, which attributes all observed warming to rising GHG concentrations, particularly $CO_2$, cannot explain the observed trends. Instead, natural factors, especially long-term increase in incoming solar radiation, appear to play a significant and likely dominant role in global warming since the mid-1970s.

The observed increase in incoming solar radiation cannot be accounted for by the possible anthropogenic side effects of *Albedo*- and *Cloud*-feedback. All evidence points to the conclusion that this "natural" *forcing* with a trend of about 0.035 $W/m^2$/year is equal to, or even exceeds the greenhouse gas related *forcing* of about 0.019 $W/m^2$/year. Based on these values, only 1/3rd of the observed temperature trend can be of anthropogenic origin. The remaining 2/3rd must stem from *natural* changes in our climate system, or more broadly, in our entire Earth' thermal system.

Moreover, the observed increase in Earth's radiation imbalance appears to be largely unrelated to GHGs. Instead, it correlates strongly with natural processes driving increased incoming solar radiation. Claims of "acceleration" in the radiation imbalance due to GHG emissions are not supported by the trend in accurately measured GHG concentrations. If any acceleration in global warming is occurring, it is almost certainly driven by the increasing flux of solar energy—an inherently natural phenomenon not induced by greenhouse gases.

In summary, this analysis challenges the notion that GHGs are the primary drivers of recent climate change. It underscores the importance of accounting for natural variability, especially in solar input, when interpreting warming trends and evaluating climate models.

**Funding:** No funding received, nor solicited.

**Co-Editor:** Stein Storlie Bergsmark; **Reviewers:** Anonymous

## References

1. https://www.knmi.nl/over-het-knmi/nieuws/wat-iedereen-zou-moeten-weten-over-de-opwarming-van-de-aarde (in Dutch)
2. Hansen, J. *et al.* (2023)*, Global Warming in the Pipeline*, Oxford Open Climate Change, **3(1),** https://doi.org/10.1093/oxfclm/kgad008)

3. Trenberth K.E. and Caron J.M. (2001), *Estimates of Meridional Atmosphere and Ocean Heat Transports,* J. Climate **14**, 3433–3443, https://doi.org/10.1175/1520-0442(2001)014%3C3433:EOMAAO%3E2.0.CO;2
4. Huijser, A. (2024)**,** *Greenhouse Feedbacks are Intrinsic Properties of the Planck Feedback Parameter*, Science of Climate Change **4.2,** 89-113, https://doi.org/10.53234/scc202411/03
5. Schwartz, S. E. (2007), *Heat capacity, time constant, and sensitivity of Earth's climate system,* J. Geophys. Res., 112*,* https://doi.org/10.1029/2007JD008746
6. https://argo.ucsd.edu/
7. https://www.ncei.noaa.gov/access/global-ocean-heat-content/basin_heat_data.html
8. Climate Change (2021), *The Physical Science basis IPCC WG 1*, 6th Assessment Report, Technical Summary TS3.2 pg.93-97, http://www.ipcc.ch/report/ar6/wg1
9. https://ceres.larc.nasa.gov/data
10. ENSO MEIv2: *https://psl.noaa.gov/enso/mei/*
11. Pollack H.N., Hurter S.J. and Johnson J.R. (1993), *Heat flow from the Earth's interior: Analysis of the global data set*, Rev. Geophys. **31**, 267-280, https://doi.org/10.1029/93RG01249
12. https://www.britannica.com/science/marine-ecosystem#ref588433
13. Treguier A.M. *et al* (2023), *The mixed-layer depth in the Ocean Model Intercomparison Project (OMIP),* Geosci. Model Dev. **16**, 3849, https://doi.org/10.5194/gmd-16-3849-2023
14. https://www.climate4you.com/: the oceans paragraph
15. Lewis, N. & Curry, J. (2015), *The implications for climate sensitivity of AR5 forcing and heat uptake estimates.* Clim Dyn **45***,* 1009–1023 https://doi.org/10.1007/s00382-014-2342-y
16. For a good overview of the various temperature trends, their quality, pros/cons, etc., see https://www.climate4you.com/"global temperatures"
17. https://www.metoffice.gov.uk/hadobs/hadcrut5/data/HadCRUT.5.0.2.0/download.html
18. https://www.nsstc.uah.edu/climate/index.html
19. Spencer R., Christy J. & Braswell W. (2025), *Urban Heat Island Effects in U.S. Summer Surface Temperature Data, 1895-2023, accepted by JAMC in April 2025.* https://doi.org/10.1175/JAMC-D-23-0199.1
20. https://www.metoffice.gov.uk/hadobs/hadsst4/
21. https://data.giss.nasa.gov/modelforce/ in more detail: https://gml.noaa.gov/aggi/aggi.html
22. Van Wijngaarden W. & Happer W. (2021), *Relative Potency of Greenhouse Molecules*, https://doi.org/10.48550/arXiv.2103.16465
23. Rentsch C. (2021), *Radiative forcing by $CO_2$ observed at top of atmosphere from 2002 to 2019 (v2)*, https://doi.org/10.48550/arXiv.1911.10605 or https://essopenarchive.org/users/283962/articles/607772-radiative-forcing-by-co-observed-at-top-of-atmosphere-from-2002-2019
24. MODTRAN, https://climatemodels.uchicago.edu/modtran/
25. Huijser A., *unpublished results*
26. https://en.wikipedia.org/wiki/KNMI-mast_Cabauw
    KNMI's hourly and daily averaged data from station # 348: https://daggegevens.knmi.nl/
27. See the *Central England Temperature* (CET) series of temperatures measured using thermometers since1659, with decennia-long changes up to $|dT_S/dt| \approx 0.05$ K/year. https://hadleyserver.metoffice.gov.uk/hadcet/index.html

28. Levitus S. *et al* (2012), *World ocean heat content and thermosteric sea level change (0-2000 m), 1955-2010*, Geophys. Res. Lett. **39,** L10603 https://doi.org/10.1029/2012GL051106
29. Mullarney J.C., Griffiths R.W. and Hughes G.O. (2006), *The effects of geothermal heating on the ocean overturning circulation,* Geophys. Res. Lett. **33**, L02607 https://doi.org/10.1029/2005GL024956
30. Gray B.(2018), *Flaws in applying greenhouse warming to Climate Variability*, https://thegwpf.org/publications/bill-gray-flaws-in-applying-greenhouse-warming-to-climate-variability/
31. https://www.newscientist.com/article/mg19225822-300-the-ice-age-that-never-was/
32. https://www.climate.gov/news-features/understanding-climate/climate-change-ocean-heat-content

Research Article

SCC-Publishing

Michelets vei 8 B
1366 Lysaker, Norway

ISSN: 2703-9072

Correspondence:

frans.schrijver@gmail.com

Vol. 5.3 (2025) pp. 107 - 118

# Historical $CO_2$ levels in periods of global greening

Frans J. Schrijver

Independent Scientist, Hattem, Netherlands

## Abstract

The increased atmospheric $CO_2$ level is widely recognized as a primary driver of global greening (a 30% increase in GPP since 1900). It raises the question whether such an increased $CO_2$ level is also a necessary condition for a large GPP. This paper evaluates whether $CO_2$ levels during historical periods of similar or more greenness as today, are consistent with the widely held view that $CO_2$ levels remained below 300 ppm over the past 800,000 years, as indicated by Antarctic ice core records. Employing Mitscherlich's Law, the research models the global GPP response to increasing $CO_2$, based on the mean value of eight different long-term GPP datasets. It illustrates a diminishing return of vegetation associated with rising $CO_2$, as additional factors such as nutrient and water availability impose constraints on the fertilization effect. Due to this diminishing return the average residence time of $CO_2$ in the atmosphere increases significantly with higher GPP values. High $CO_2$ levels, similar to today's, were therefore necessary for comparable GPP during green periods like 10,000 years ago. A $CO_2$ concentration of 280 ppm would only be possible if nature's response to $CO_2$ were fundamentally different from what we observe today, with other constraining factors exceptionally more favorable. Natural fluctuations of the atmospheric $CO_2$ concentration can be well explained, based on the strong temperature dependence of the degeneration of carbon compounds that are stored in large quantities in the soil and the oceans.

**Keywords:** $CO_2$, atmosphere, greening, GPP, climate, global warming

Submitted 2025-07-20, Accepted 2025-10-06, https://doi.org/10.53234/scc202510/06

## 1. Introduction

Global greening refers to the observed increase in the amount of green vegetation, such as plants and trees, across the planet. The terrestrial Gross Primary Production (GPP) has gone up by more than 30% since 1900. Multiple studies have identified the growing atmospheric $CO_2$ concentration as the dominant driver of this greening (Haverd *et al.*, 2020; Lai *et al.*, 2024). The present level of greenness in terms of GPP is, however, not exceptional. In the history of the Earth there have been many fluctuations in the amount of vegetation. As an example, we use the situation 10,000 years ago, when there was 50% more forest area on the planet than there is today (Ritchie, 2021). In this study we investigate the relationship between the (historical) levels of greenness in terms of GPP and the atmospheric $CO_2$ concentration. The general accepted belief, based on ice core records of Antarctica, is that $CO_2$ levels were much lower than today, typically around 280 ppm and for a period of 800,000 years less than 300 ppm (Lüthi *et al.*, 2008; Bereiter *et al.*, 2015). We want to determine how likely it is that these low concentrations match with a level of greenness that is equal or higher than the present level, or if a higher atmospheric concentration is needed to explain historical GPP levels.

For carbon dioxide the atmosphere can be regarded as a well-mixed container with natural up and down fluxes to and from land and oceans. At any moment t in time the residence time $\tau(t)$ is defined as the average time $CO_2$ remains in the atmosphere in years and is equal to the total atmospheric $CO_2$ mass c(t) divided by the global down flux $d_G(t)$ per year, which leads to:

$$c(t) = d_G(t) \cdot \tau(t) \tag{1}$$

The recent global greening is reflected in the increase of the carbon fluxes to and from the atmosphere, and a longer residence time, since 1750. See Table 1. The down flux has increased by 29% and the residence time by 16%. Together they explain the increase with 50% of the $CO_2$ level (Schrijver, 2024).

Table 1: Changes in the carbon cycle since pre-industrial period (IPCC, 2021; Friedlingstein et al., 2023)

| | | *1750* | 2022 | *%* |
|---|---|---|---|---|
| $CO_2$ mass atmosphere | PgC | 591 | 885 | 50% |
| Natural emissions | $PgCyr^{-1}$ | 166 | 210 | 27% |
| Anthropogenic emissions | PgC | 0 | 11 | |
| Total emissions (up flux) | $PgCyr^{-1}$ | 166 | 221 | 33% |
| Total absorption (down flux) | $PgCyr^{-1}$ | 167 | 216 | 29% |
| Residence time | yr | 3.5 | 4.1 | 16% |

To draw conclusions on historical $CO_2$ concentrations, we must understand the impact of the global GPP to the down flux and to the residence time. The 2022 $CO_2$ level of 885 PgC is the result of a down flux of 216 $PgCyr^{-1}$, multiplied by the residence time of 4.1 years. If during periods of similar greenness in the past millennia the $CO_2$ level was only 590 PgC, it would imply a lower down flux and/or a shorter residence time at that time. To consider ice core records accurate, it is necessary to determine if a smaller down flux and/or a shorter residence time, combined with a high level of greenness, is reasonable.

## 2. GPP changes

The 'greening of the Earth' refers to the observed increase in the amount of green vegetation across large parts of the planet over the past decades. Long-term satellite records revealed a significant global greening of vegetated areas since the 1980s. In this contribution we refer to greening in terms of the increase in gross primary production (GPP), the rate of carbon fixation by photosynthesis. Global terrestrial GPP has gone up by more than 30% since 1900 (Haverd *et al.*, 2020; Lai *et al.*, 2024). A similar effect has been observed in the oceans, where increased levels of dissolved $CO_2$ lead to more photosynthesis by phytoplankton (Riebesell *et al.*, 2007)

The greening of the Earth is mostly the result of the increased $CO_2$ concentration, but estimates show large variations, from 44% (Chen *et al.*, 2022) to 86% (Haverd *et al.*, 2020). The most widely cited source estimates the $CO_2$ fertilization effect at approximately 70% (Zhu *et al.*, 2016). Other factors include nitrogen deposition (9%), climate warming (8%) and land cover change (4%)[1]. As atmospheric $CO_2$ concentrations have risen (now over 425 ppm, compared to ~280 ppm pre-industrially), plants can photosynthesize more effectively. $CO_2$ is a primary raw material for

---

[1] $CO_2$ is strictly speaking not a fertilizer as it is the primary raw material for photosynthesis. In the scientific literature there is, however, an abundant use of the term '$CO_2$ fertilization effect', that can be defined as the enhancement of photosynthesis and subsequent growth in many plants due to increasing levels of atmospheric carbon dioxide.

photosynthesis, so higher availability allows plants to grow faster and often use water more efficiently (by reducing stomatal conductance).

The major part of all $CO_2$ that directly or indirectly flows from the atmosphere to land and sea each year, is the result of photosynthesis. The photosynthesis of plants on land is responsible for almost all the terrestrial down flux, 120 - 130 $PgCyr^{-1}$. The photosynthesis of phytoplankton in the oceans is comparable with the GPP on land: 100 - 150 PgC $yr^{-1}$ (Huang *et al.*, 2021). This is larger than the $CO_2$ down flux to the oceans (80 - 90 PgC $yr^{-1}$), as it represents biological fixation of dissolved $CO_2$ within the ocean, which indirectly defines the exchange with the atmosphere. It is, however, clear that also in the oceans photosynthesis is an important component in the oceanic down flux.

Many studies though have found that the fertilization effect is weakening and greening is slowing down (Reich and Hobbie, 2013; Allen Jr., 2019; Terrer *et al.*, 2019; Wang *et al.*, 2020; Winkler *et al.*, 2021). The *ß*-factor is often used to characterize the plant response to increasing $CO_2$ concentration, where *ß* is defined as the relative increase in gross primary production (p) in response to an increase in atmospheric $CO_2$ concentration (c).

$$\beta = \frac{dp}{dc} \tag{2}$$

The global median *ß* during 1982 to 2015 was 16.1 ± 11.5% per 100 ppm, so 16% increase in photosynthesis per 100 ppm $CO_2$. Using multiple long-term satellite- and ground-based datasets, it was shown that global carbon fertilization effect declined across most terrestrial regions of the globe. During 1982 to 2015 ß decreased at a rate of $-0.92 \pm 0.12\%$ 100 $ppm^{-1}yr^{-1}$ (Wang *et al.*, 2020).

A declining *ß* means that the fertilization effect is weakening and greening is slowed down. The explanation is that further growth of the vegetation is constrained by other factors. An important factor is nutrient limitation. Plant growth is limited by the nutrient that is most scarce, not by the abundance of others. Even if $CO_2$ is super-abundant, plants cannot grow indefinitely if they don't have enough other essential nutrients like nitrogen or phosphorus. Also, the availability of sufficient water can be a limiting factor that slows down the growth rate. Another element is plant acclimation. Plants can physiologically adjust to sustained high $CO_2$, if they cannot use all the extra carbon for growth due to nutrient or other limitations.

We can apply Mitscherlich's Law, also known as the Law of Diminishing Returns in Agriculture, to describe the relationship between the application of a single variable input (e.g., fertilizer, water) to a fixed area of land and the resulting crop yield. The law states that the increase in crop yield due to an additional unit of input diminishes as more of that input is applied, assuming other factors (e.g., soil quality, sunlight) remain constant. The application of Mitscherlich’s Law has been demonstrated individual crop growth responses to rising atmospheric carbon dioxide, e.g. (Allen Jr., 2019).

## 3. Modelling Diminishing Returns

Here we have investigated the application of Mitscherlich’s Law to describe not just individual crop yields, but the global GPP as a whole in response to increasing $CO_2$ levels. It posits that the response (e.g., crop yield or vegetation growth) to an input (in this case the actual $CO_2$ concentration) increases rapidly at low input levels but approaches a maximum as the input continues to rise. For Earth's greening it can be written as follows.

$$\beta = \frac{dp}{dc} = B \cdot (A - p) \tag{3}$$

This equation says that the rate of GPP increase related to the $CO_2$ concentration is proportional to the gap between the maximum GPP and the current GPP, where:

*c* is the input level, in this case the actual $CO_2$ concentration,
*p* is the yield at input level c, in this case the gross primary production (GPP),
*A* is the attainable yield, in this case the maximum GPP (with other factors constant),
*B* is a constant related to the efficiency of the input ($CO_2$),
*ß* or dp/dc represents the rate at which yield (GPP) increases with respect to input ($CO_2$).

To investigate whether Mitscherlich can be applied to describe the greening of the Earth based on the $CO_2$ concentration, we apply the results of a study by (Wang *et al.*, 2024). This study investigated the global trends in terrestrial Gross Primary Productivity (GPP) and their driving factors over the past four decades, utilizing eight different GPP datasets, including BEPS GPP, CCDAS GPP, EC-LUE GPP, GIMMS GPP, LRF GPP, GPPNIRv, P-model GPP, and TRENDY GPP. The findings indicate a notable decrease in global GPP trends, from 0.43 $PgCyr^{-2}$ in 1982–1999 to 0.17 $PgCyr^{-2}$ in 2000–2016, a phenomenon observed across more than 68% of the terrestrial surface. This decline due to a reduced $CO_2$ fertilization effect was particularly evident in satellite-derived GPP data.

After solving the differential equation Mitscherlich's Law for the greening of the Earth can be written as follows (with $p_T$ as the terrestrial GPP).

$$p_{\mathrm{T}} = A(1 - \exp(-B(c - C_0)) \qquad (4)$$

Photosynthesis typically stops functioning at $CO_2$ concentrations below 150 ppm. So, this level can be regarded as a starting point in the equation, which is reflected in the value 318.6 PgC for $C_0$ (which is equal to 150 ppm). By matching the time series of the mean values of the 8 models with the actual concentration level in each year (Lan and Keeling, 2025), we were able to compare the $(c, p)$-values with Equation 4, as presented in Figure 1. Each blue dot represents a GPP value for the associated $CO_2$ value. With the use of the Non-linear Least Squares method we were able to find values for A and B that give the best fit for the given data. The red line shows the best fit line with an $R^2$ of 0.85.

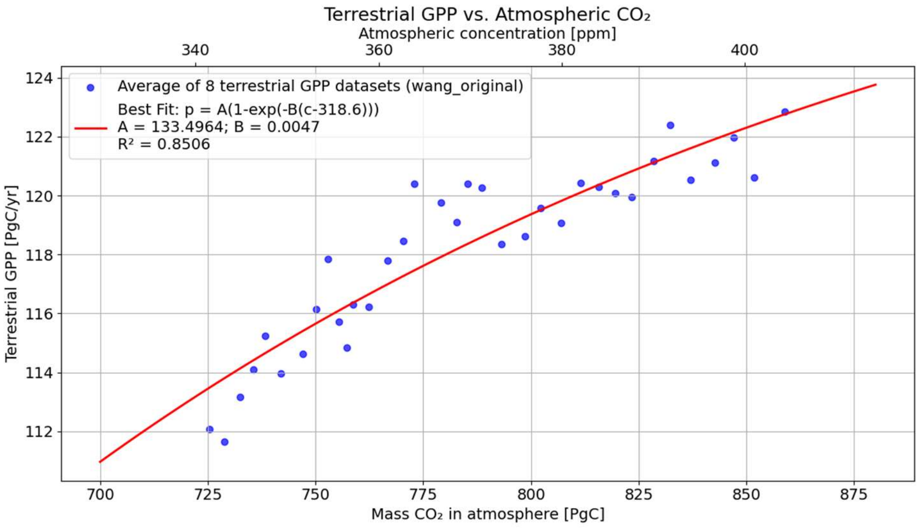

*Figure 1: The mean terrestrial GPP values of 8 long term models as a function of the actual CO₂ concentration in the atmosphere (blue dots). The red line represents the best fit line according to Mitscherlich's Law as given by equation 4.*

The available GPP data only relate to terrestrial absorptions, while we are interested in the total global GPP. We have, however, no reliable dataset for oceanic GPP changes in the past decades. Most studies on the fertilization effect are focused on terrestrial vegetation, supported by satellite observations. Global oceanic GPP trends are less straightforward than terrestrial trends and exhibit considerable regional and seasonal variability (Evans, Hales and Strutton, 2011).

Photosynthesis and respiration occur in water using dissolved $CO_2$, making it hard to distinguish biological processes from physio-chemical ones that interact with the atmosphere. Biological processes determine the dissolved $CO_2$ concentration and aquatic partial pressure ($pCO_2$), while the atmospheric exchange is driven by the difference in $pCO_2$ between the surface water and the atmosphere.

According to the 6th Assessment Report from the IPCC not just terrestrial, but also oceanic emissions have increased since pre-industrial times. Emissions from the oceans have increased from 54 $PgCyr^{-1}$ in 1750 (IPCC, 2021) up to 80 $PgCyr^{-1}$ (Friedlingstein *et al.*, 2023). The temperature dependence of physical-chemical processes (reduced solubility of $CO_2$ and temperature dependence of constants in the carbonate system) is 4 to 4.5% per degree Celsius, which is too small to explain this increase (Liu, Fukuda and Matsuda, 2006). This suggests that biological processes appear to cause changes to seawater $pCO_2$ that are more significant than the temperature effect on the solubility pump alone.

Although there is no direct measurement, a comparable fertilization effect may occur in marine environments due to the similar processes of carbon fixation involved. In Figure 2 we can see that we get a very good fit with the IPCC estimate for 1750 (IPCC, 2021) and the GCB figure (Friedlingstein *et al.*, 2023), if we assume an increase of oceanic photosynthesis that is proportional to the increase of terrestrial photosynthesis. Each blue dot in Figure 2 represents the sum of the terrestrial GPP value from the 8 models, and a proportional value for the oceanic GPP. The green squares are estimates from the IPCC and GCB of the down fluxes. The good fit with the red line based on Mitscherlich's Law confirms that the total GPP is close to the total down flux. Including the two extra data points in the dataset, results in a $R^2$ value of 0.94.

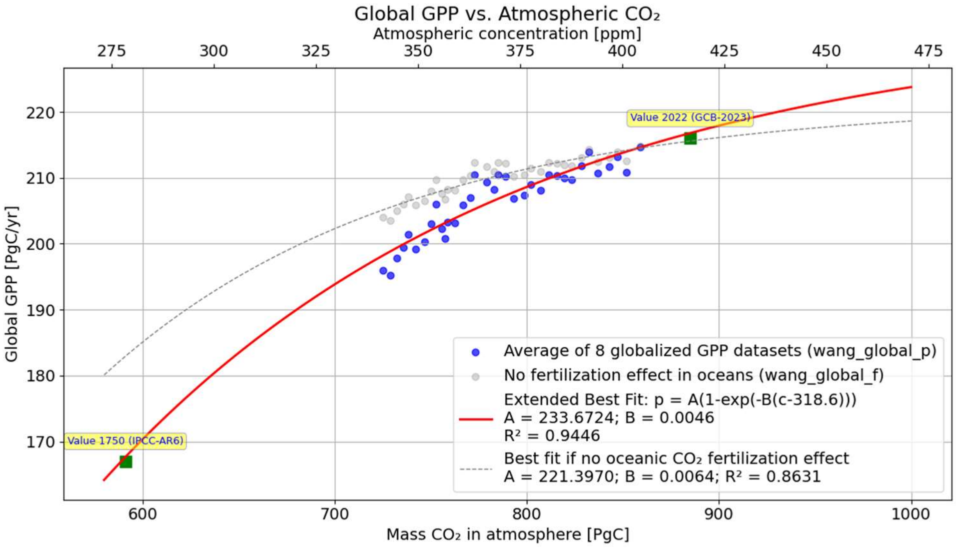

*Figure 2: Similar to Figure 1 with extended axes and an assumed proportional GPP change in the oceans. The two added datapoints give a good fit to the best fit line:1. $CO_2$ mass and down flux in 1750, based on IPCC-AR6 estimate (IPCC, 2021), and 2. the $CO_2$ mass and down flux in 2022, based on the Global Carbon Budget 2023 (Friedlingstein* et al.*, 2023). The gray dashed line and dots show the result if no $CO_2$ fertilization effect in the oceans is assumed.*

If we assume a smaller than proportional fertilization effect from the oceans, or even zero, we will get a best fit line that is more flat than the original one, but with a similar concave curve. In all cases the increase of the global down flux is slowing down compared to the increasing $CO_2$ concentration in the atmosphere. The gray dashed best fit line shows the most extreme case with no $CO_2$ fertilization effect in the oceans, so with a stable oceanic down flux, that does not change with $CO_2$ concentration.

Even though we only have terrestrial GPP data, we can easily show that in all cases an increasing terrestrial GPP leads to a larger global down flux (land + oceans) and a longer residence time, which together are consistent with a higher atmospheric $CO_2$ concentration.

The global down flux $d_G$ can be written as the sum of the flux to land $d_T$ and to the oceans $d_O$.

$$d_G = d_T + d_O = p_T + d_O \tag{5}$$

The terrestrial GPP ($p_T$) is almost equal to the terrestrial down flux ($d_T$). When $p_T$ increases under the influence of more $CO_2$, the global down flux will also increase, as long as the down flux to the oceans ($d_O$) is not decreasing under the influence of more $CO_2$.

The slowing down of the greening under the influence of diminishing returns, represented by the concave curve in Figures 1 and 2 instead of a straight line, indicates a longer residence. It can also be seen if we express the residence time $\tau$ as a function of the terrestrial greening $p_T$.

$$\tau = \frac{c}{d_G} = \frac{C_0 - \frac{1}{B}\ln\left(1 - \frac{p_T}{A}\right)}{p_T + d_O} \tag{6}$$

Since in Mitscherlich's law the maximum GPP is limited by the value $A$, the residence time will increase sharply at higher values of the terrestrial GPP, which we can see in Figure 4 (red line). The gray line shows the average residence time as a function of the terrestrial GPP if there is no $CO_2$ fertilization effect in the oceans, in which case the oceanic down flux is assumed stable in relation to varying GPP-values. This results in an even faster increase of the residence time.

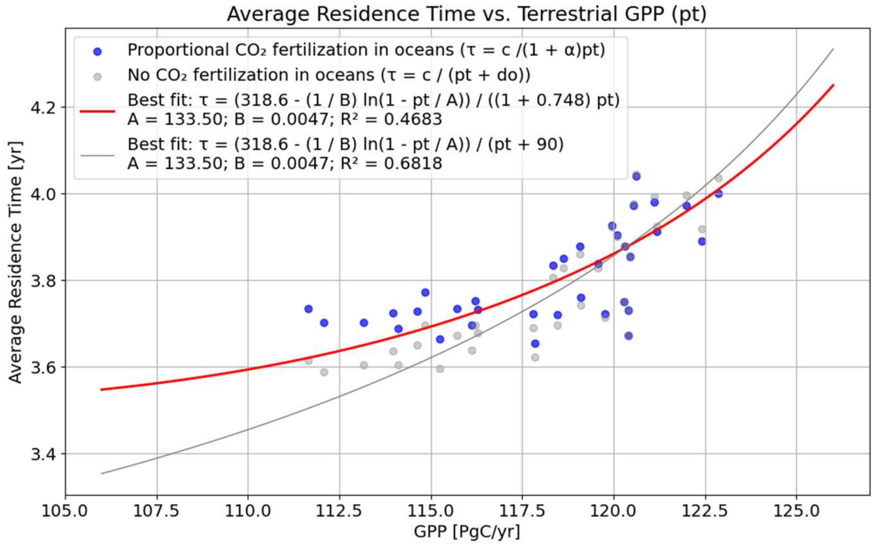

*Figure 4: The calculated average residence time of the original dataset as a function of the terrestrial GPP (blue dots). The red line represents the best fit line according to Equation 6. The gray line and dots assume no fertilization effect in the oceans.*

Constraining factors such as nutrient and water diminish the return of vegetation associated with rising $CO_2$. This effect translates into a longer residence time. Figure 4 shows that as a result of the diminished return, the average residence time of $CO_2$ in the atmosphere increases with higher GPP values. As the $CO_2$ mass in the atmosphere is proportional to both the down flux and the residence time, it is clear that a green Earth with a large GPP is inextricably linked to a high $CO_2$ concentration in the atmosphere. Around 10,000 years ago, forest cover was 50% greater than today (Ritchie, 2021). The land use change since that period as a result of human deforestation and agriculture, is illustrated in Figure 5. With a mean GPP of 2.0 $kgCm^{-2}yr^{-1}$ forests represent the most productive land cover, while grasslands and croplands on average reach 1.5 and 1.8

kgCm$^{-2}$yr$^{-1}$, respectively. When these GPP estimates are combined with the historical land use change, it follows that the global terrestrial GPP was 4.4% larger in that period than today (Krause *et al.*, 2022).

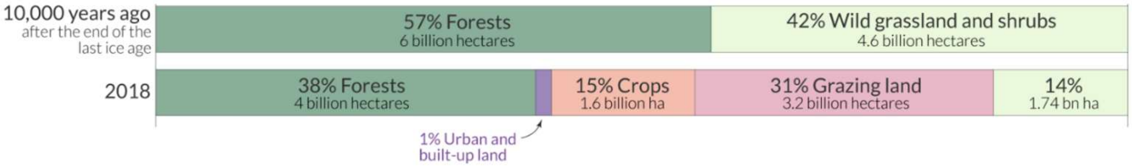

*Figure 5: Land use change over the past 10,000 years. Based on the average GPP values per square meter for forest, grassland and cropland, we can conclude that the total GPP 10,000 years ago was approximitly 4.4% larger than today. Image adapted from Our World in Data (Ritchie, 2021).*

Following Equation 6 and Figure 4, the residence time will increase relatively faster than the GPP, which implies that in that period the average residence time was at least as high as the current residence time of approximately 4.1 years, and thus also the amount of $CO_2$ in the atmosphere. We have no reason to believe that nature's response in terms of GPP to the actual $CO_2$ level was very different from today, so a shorter residence time is very unlikely. We can therefore conclude that global GPP 10,000 years ago was at least as high as today.

## 4. Discussion

It is obvious that the application of Mitscherlich's Law is a simplification of the complex processes that define the Earth's vegetation. The diminishing return is confirmed for individual plant species, where the application for the total GPP might raise new complexities, like global variability with different growth rates for the many ecosystems, nonlinear interactions and long-term effects (e.g. changes in the species composition) complicating the model. The available data from the 8 models show nevertheless a good fit, explaining that constraining factors like nutrient and water availability can be responsible for a slowdown of the greening. Apparently, the behavior of the sum of all vegetation does not fundamentally differ from that of individual plant species in this respect. It makes it evident that large GPP values lead to longer atmospheric residence times.

In a period without human disturbance and with the same or higher GPP as today, a $CO_2$ concentration of approximately 280 ppm would imply a residence time of approximately 2.7 years (590 PgC / 216 PgCyr$^{-1}$) or less. This would only be possible if nature's response to the $CO_2$ level were fundamentally different from what we observe today. $CO_2$ is one of the constraining factors that define the growth rate of vegetation. A larger GPP at low $CO_2$ levels would only be possible if other factors like sunshine, nutrient and water availability, were significantly more favorable than today. Especially in our example of 10,000 years ago, this is very unlikely. The deforestation and expanding agricultural land since that period is primarily the result of human activities (Ritchie, 2021). There is no indication that the other limiting factors have significantly changed.

As the present level of greenness is not exceptional in the history of the Earth, our results indicate that variations in atmospheric $CO_2$ concentrations up to levels comparable to or exceeding those observed today are possible. The view that human emissions are the only cause of rising atmospheric $CO_2$ levels is based on the assumption that, over decades or centuries, natural carbon fluxes tend to remain relatively balanced without significant human influence. The ocean and terrestrial carbon sinks are often defined by their capacity 'to absorb a part of the human caused $CO_2$ emissions'. Without these human emissions, the natural yearly fluxes would cancel each other out, maintaining a stable atmospheric concentration at a level of typically 280 ppm (IPCC, 2021; Friedlingstein *et al.*, 2023).

A precise balance between natural upward and downward fluxes is however unlikely. For plant respiration, you can argue that it is in some way related to the absorption of $CO_2$ by those same plants. But decomposition, the degeneration of carbon compounds that are stored in large quantities in the soil and the oceans, has only a delayed and indirect connection to current photosynthesis. There are different drivers for the most important fluxes to and from the atmosphere. For photosynthesis (down flux), the $CO_2$ concentration in the atmosphere is the most important driver. But for respiration (up flux), temperature is the most important driver, as long as enough organic carbon compounds are available. Bacterial processes responsible for the breakdown of organic material on and in the soil are exponentially related to temperature, with $Q_{10}$-values for soil respiration ranging from around 1.7 (approximately 5.4% per °C) to over 6 (approximately 20% per °C)(Luan *et al.*, 2013). Apart from the biological processes, the temperature dependence of physical-chemical processes in the seawater also causes additional emissions at higher temperatures (Liu, Fukuda and Matsuda, 2006; Takahashi *et al.*, 2009).

A period of rising temperatures can lead to more respiration from the large carbon buffers in the soil and oceans and thus a higher $CO_2$ concentration in the atmosphere and greening of the Earth. In a period of falling temperatures, the opposite effect can occur. As concluded by (Koutsoyiannis, 2024b): *"During cool periods, degradation slows more than photosynthesis, and this traps $CO_2$ into soil. During warm periods, carbon trapped in soils is released faster than photosynthesis can absorb it, and atmospheric $CO_2$ increases"*. The total carbon mass remains conserved within the Earth system, as substantial carbon reservoirs on land and in the oceans effectively buffer changes in carbon distribution. The changes in the buffers are very small compared to the total amount of 41,000 PgC (of which 3,100 PgC in the soil), a fortiori as the process of greening is relatively slow: 30% over a period of 120 years equals on average 0.2% per year.

More vegetation corresponds to higher $CO_2$ levels. This may appear contradictory, as plants absorb $CO_2$. However, greening is not the cause of the higher concentration but rather its result. The probable causality is summarized in Diagram 1.

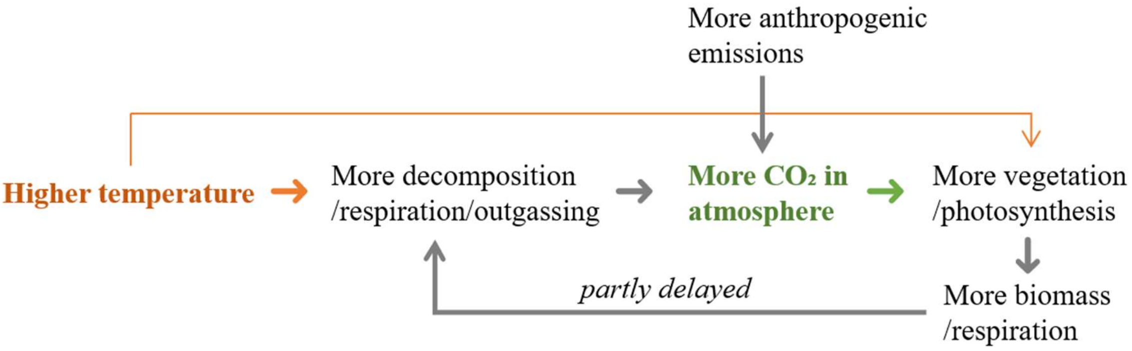

*Diagram 1: Simplified causality diagram that illustrates that the $CO_2$ concentration can change naturally, due to different drivers for the up flux and down flux. Global warming is the main driver (in orange) for more respiration and oceanic outgassing and has a (smaller) positive effect on global greening. The increased atmospheric concentration is the main driver (in green) for more photosynthesis and global greening, which results in more biomass and respiration. Increasing anthropogenic emissions can accelerate this process.*

Both higher temperatures and increasing anthropogenic emissions can lead to more $CO_2$ in the atmosphere, resulting in more photosynthesis and thus more vegetation. The effect is amplified, as more vegetation leads to more plant respiration and after some time biodegradation of the extra biomass. Increased temperatures also have a positive impact on the $CO_2$ outgassing of the oceans. Another element is the direct impact of temperature on global greening. Climate warming can enhance plant growth and extend the growing season in moderate and colder regions, but in tropical regions heat stress can reduce productivity. While less significant than $CO_2$ fertilization, the recent temperature increase resulted in a net positive contribution to global greening (Zhu *et al.*, 2016).

The important role of temperature in natural $CO_2$ fluctuations is supported by the proven unidirectional causal relationship between temperature and $CO_2$ (Koutsoyiannis *et al.*, 2023), and the developed mathematical framework that results in excellent agreement of the recent global warming with accurately measured $CO_2$ changes (Koutsoyiannis, 2024a). It also explains the abundance of vegetation 10,000 years ago, in the Holocene Thermal Maximum with relatively high temperatures.

In addition to global warming, human emissions have contributed to the greening process and so to the recent $CO_2$ rise. However, there is no need to assume a problematic ad hoc behavior for anthropogenic $CO_2$. According to the IPCC human emitted $CO_2$ accumulates and remains much longer in the atmosphere than natural $CO_2$, up to more than 100,000 years, which cannot be explained in the uncompartimented and well mixed atmosphere. Not the emissions, but the atmospheric concentration is the dominant driver for the uptake of $CO_2$ in the biosphere and through the oceans, which cannot differentiate based on the source of the $CO_2$ molecules.

## 5. Conclusions

Based on the relationship of the $CO_2$ concentration and the actual GPP values of 8 long term models, we showed that the global GPP response to increasing $CO_2$ follows Mitscherlich's Law, demonstrating diminishing returns. While $CO_2$ initially drives greening, its fertilization effect is slowing down due to limitations from other factors like nutrient availability and water. This implies that continued atmospheric $CO_2$ increases will lead to relatively smaller gains in GPP, and thus an increasingly longer $CO_2$ residence time. The global GPP is by far the most important component of the down flux to land and oceans. As the $CO_2$ concentration is proportional to the down flux and the residence time, a 'green Earth' is inextricably linked to high atmospheric $CO_2$ concentrations.

The current level of Earth's greenness is not extraordinary, suggesting that the present atmospheric $CO_2$ concentration is also not exceptional. This indicates that there have been natural variations in both GPP and $CO_2$ levels over time. These fluctuations are likely to occur, due to a combination of different drivers for the up and down flux and the large reservoirs of organic carbon in the soil and oceans. Rising temperatures increase the up flux to the atmosphere due to more terrestrial and oceanic respiration and more outgassing from oceans, leading to a higher atmospheric $CO_2$ level. This $CO_2$ level is the main driver for more greening and thus the down flux.

Human emissions have accelerated the greening process, but even if we assume that human emissions are the dominant cause for the recent $CO_2$ rise, it is still unlikely that historical $CO_2$ levels were as low as generally accepted. All assumptions discussed herein relate exclusively to how nature responds to changes in $CO_2$ levels, and do not address the underlying causes of increased $CO_2$ levels. A low $CO_2$ level of 590 PgC (280 ppm) combined with a similar high level of greenness would only be possible if nature's response to $CO_2$ were fundamentally different from what we observe today.

This conclusion contradicts the assumed low $CO_2$ concentrations in the past 800,000 years, based on the ice core records from Antarctica. In this context, we refrain from delving into the specifics of these records. However, it is important to acknowledge that ice core records are not direct measurements, but serve as proxies for historical $CO_2$ concentrations, which need correct interpretation and calibration, and which involve significant uncertainties. Several studies have raised serious questions regarding the accuracy and reliability of ice core data, especially with respect to the dissolvement of $CO_2$ in melting water the many years before the air bubbles in the ice are fully closed (Jaworowski, Segalstad and Ono, 1992; Jaworowski, Segelstad and Hisdsal, 1992; Harde, 2017).

The likelihood of higher $CO_2$ levels in the history of the Earth supports other studies that have identified temperature as a primary driver of the increase of the atmospheric $CO_2$ concentration (Harde, 2019; Berry, 2021; Koutsoyiannis, 2024a). The temperature dependence of the main fluxes to the atmosphere makes it unnecessary to assume an ad hoc behavior for human $CO_2$ in the atmosphere, with a deviant (much longer) residence time than other $CO_2$.

## Competing interests

The author declares that he has no conflict of interest.

## Data availability

This research uses no new data. The data sets used have been retrieved from the sources described in detail in the paper. All the calculations and charts are available in a Jupyter Notebook format, via GitHub, at https://github.com/fsch0203/historical_co2.

**Chief-Editor**: H. Harde, **Reviewers**: anonymous.

## References

Allen Jr., L.H., 2019: *Simplifying Crop Growth Response to Rising CO2 and Elevated Temperature*, Agricultural & Environmental Letters, 4(1), p. 190021. https://doi.org/10.2134/ael2019.06.0021.

Bereiter, B. *et al.*, 2015: *Revision of the EPICA Dome C CO2 record from 800 to 600 kyr before present*, Geophysical Research Letters, 42(2), pp. 542–549. https://doi.org/10.1002/2014GL061957.

Berry, E., 2021: *The impact of human CO2 on atmospheric CO2*, Science of Climate Change, 1.2, pp. 213–249. https://doi.org/10.53234/scc202112/13 (Accessed: 1 February 2023).

Chen, C. *et al.*, 2022: *CO2 fertilization of terrestrial photosynthesis inferred from site to global scales*, Proceedings of the National Academy of Sciences of the United States of America, 119(10), p. e2115627119. https://doi.org/10.1073/pnas.2115627119.

Evans, W., Hales, B. and Strutton, P.G., 2011: *Seasonal cycle of surface ocean pCO2 on the Oregon shelf*, Journal of Geophysical Research: Oceans, 116(C5). https://doi.org/10.1029/2010JC006625.

Friedlingstein, P. *et al.*, 2023: *Global Carbon Budget 2023*, Earth System Science Data, 15(12), pp. 5301–5369. https://doi.org/10.5194/essd-15-5301-2023.

Harde, H., 2017: *Reply to Comment on 'Scrutinizing the carbon cycle and CO2 residence time in the atmosphere'*. http://hharde.de/index_htm_files/Reply%202017-06-30.pdf (Accessed: 6 January 2023).

Harde, H., 2019: *What Humans Contribute to Atmospheric CO2: Comparison of Carbon Cycle Models with Observations*, Earth Sciences, 8(3), p. 139. https://doi.org/10.11648/j.earth.20190803.13.

Haverd, V. *et al.*, 2020: *Higher than expected CO2 fertilization inferred from leaf to global observations*, Global Change Biology, 26(4), pp. 2390–2402. https://doi.org/10.1111/gcb.14950.

Huang, Y. *et al.*, 2021: *Global Estimates of Marine Gross Primary Production Based on Machine Learning Upscaling of Field Observations*, Global Biogeochemical Cycles, 35(3), p. e2020GB006718. https://doi.org/10.1029/2020GB006718.

IPCC, 2021: *Climate Change 2021: The Physical Science Basis. Contribution of Working Group I to the Sixth Assessment Report of the Intergovernmental Panel on Climate Change.*

Cambridge, United Kingdom and New York, NY, USA: Cambridge University Press. https://doi.org/10.1017/9781009157896.

Jaworowski, Z., Segalstad, T.V. and Ono, N., 1992: *Do glaciers tell a true atmospheric CO2 story?*, Science of The Total Environment, 114, pp. 227–284. https://doi.org/10.1016/0048-9697(92)90428-U.

Jaworowski, Z., Segelstad, T.V. and Hisdsal, V., 1992: *Atmospheric CO2 and global warming: a critical review*. 2. rev. ed. Oslo: Norsk Polarinstitutt (Meddelelser / Norsk Polarinstitutt, 119). https://www.researchgate.net/publication/307215789_Atmospheric_CO2_and_global_warming_a_critical_review_2nd_edition.

Koutsoyiannis, D. *et al.*, 2023: *On Hens, Eggs, Temperatures and CO2: Causal Links in Earth's Atmosphere*, Sci, 5(3), p. 35. https://doi.org/10.3390/sci5030035.

Koutsoyiannis, D., 2024a: *Refined Reservoir Routing (RRR) and Its Application to Atmospheric Carbon Dioxide Balance*, Water, 16(17), p. 2402. https://doi.org/10.3390/w16172402.

Koutsoyiannis, D., 2024b: *Stochastic assessment of temperature–$CO_2$ causal relationship in climate from the Phanerozoic through modern times*, Mathematical Biosciences and Engineering, 21(7), pp. 6560–6602. https://doi.org/10.3934/mbe.2024287.

Krause, A. *et al.*, 2022: *Quantifying the impacts of land cover change on gross primary productivity globally*, Scientific Reports, 12(1), p. 18398. https://doi.org/10.1038/s41598-022-23120-0.

Lai, J. *et al.*, 2024: *Terrestrial photosynthesis inferred from plant carbonyl sulfide uptake*, Nature, 634(8035), pp. 855–861. https://doi.org/10.1038/s41586-024-08050-3.

Lan, X. and Keeling, R.F., 2025: *Trends in CO2 - NOAA Global Monitoring Laboratory*. https://gml.noaa.gov/ccgg/trends/data.html (Accessed: 11 July 2025).

Liu, Q., Fukuda, K. and Matsuda, T., 2006: *Study of Solution Process of Carbon Dioxide in Seawater*, Journal of The Japan Institute of Marine Engineering, 41, pp. 144–149. https://doi.org/10.5988/jime.41.SI_144.

Luan, J. *et al.*, 2013: *Factors Affecting Spatial Variation of Annual Apparent Q10 of Soil Respiration in Two Warm Temperate Forests*, PLoS ONE. Edited by B. Bond-Lamberty, 8(5), p. e64167. https://doi.org/10.1371/journal.pone.0064167.

Lüthi, D. *et al.*, 2008: *High-resolution carbon dioxide concentration record 650,000–800,000 years before present*, Nature, 453, pp. 379–382. https://doi.org/10.1038/nature06949.

Reich, P.B. and Hobbie, S.E., 2013: *Decade-long soil nitrogen constraint on the CO2 fertilization of plant biomass*, Nature Climate Change, 3(3), pp. 278–282. https://doi.org/10.1038/nclimate1694.

Riebesell, U. *et al.*, 2007: *Enhanced biological carbon consumption in a high CO2 ocean*, Nature, 450(7169), pp. 545–548. https://doi.org/10.1038/nature06267.

Ritchie, H., 2021: *The world has lost one-third of its forest, but an end of deforestation is possible*, Our World in Data. https://ourworldindata.org/world-lost-one-third-forests (Accessed: 23 June 2025).

Schrijver, F.J., 2024: *Impact of global greening on the natural atmospheric $CO_2$ level*, Science of Climate Change, 4(2), pp. 79–88. https://doi.org/10.53234/scc202411/02.

Takahashi, T. *et al.*, 2009: *Climatological mean and decadal change in surface ocean pCO2, and net sea–air CO2 flux over the global oceans*, Deep Sea Research Part II: Topical Studies in Oceanography, 56, pp. 554–577. https://doi.org/10.1016/j.dsr2.2008.12.009.

Terrer, C. *et al.*, 2019: *Nitrogen and phosphorus constrain the CO2 fertilization of global plant biomass*, Nature Climate Change, 9(9), pp. 684–689. https://doi.org/10.1038/s41558-019-0545-2.

Wang, S. *et al.*, 2020: *Recent global decline of CO2 fertilization effects on vegetation photosynthesis*, Science, 370(6522), pp. 1295–1300. https://doi.org/10.1126/science.abb7772.

Wang, Z. *et al.*, 2024: *Evolution of Global Terrestrial Gross Primary Productivity Trend*, Ecosystem Health and Sustainability, 10, p. 0278. https://doi.org/10.34133/ehs.0278.

Winkler, A.J. *et al.*, 2021: *Slowdown of the greening trend in natural vegetation with further rise in atmospheric $CO_2$*, Biogeosciences, 18(17), pp. 4985–5010. https://doi.org/10.5194/bg-18-4985-2021.

Zhu, Z. *et al.*, 2016: *Greening of the Earth and its drivers*, Nature Climate Change, 6, pp. 791–795. https://doi.org/10.1038/nclimate3004.

SCC Publishing
Michelets vei 8 B
1366 Lysaker Norway

ISSN: 2703-9072

Correspondence:

Les.coleman@unimelb.edu.au

Vol. 5.3 (2025)

pp. 119 - 134

*Research Article*

# Could $CO_2$ be the Principal Cause of Global Warming? A Finance Researcher Chimes In

*Les Coleman*

*Department of Finance, The University of Melbourne, Australia*

## Abstract

Earth's average annual temperature has increased by near 1.5$^0$C since the 19$^{th}$ century. This has been analysed principally through computer-based climate models built up from causal hypotheses. The resulting theory of anthropogenic climate change (ACC) has the central hypothesis that observed global warming is driven linearly by rising atmospheric concentrations of greenhouse gases (GHG), especially carbon dioxide ($CO_2$) from human activities. Analysis here adopts a statistical approach that examines warming from the perspective of a researcher in financial markets. The rationale is that climate and markets have much in common as complex, truly global systems with non-linear, hard-to-monitor external influences and multiple feedbacks; each is multidisciplinary; and much of the data in both disciplines is time series, for which it is notoriously difficult to establish cause and effect.

The principal finding is that the central hypothesis of ACC seems spurious, and due to simultaneous rises in global temperature and atmospheric $CO_2$ which independently follow unrelated, time trending variables. ACC is further questioned by the existence of joint test and missing variables problems. Exploring $CO_2$'s limited ability to explain warming by incorporating unsuspected forcers shows that humidity leads temperature and explains most of its increase; further, oceanic oscillations and cereal production are stronger explanators of temperature than $CO_2$.

This statistically-based study adds value to existing physics-based climate models through a complementary analytical perspective that tests the robustness of models to real world data. It concludes that human activity is contributing to global warming, but herding around the forcing role of carbon combustion has seen its influence exaggerated. This has obvious implications for the effectiveness of decarbonisation as a policy to manage global warming.

**Keywords:** climate change; ACC theory; hypothesis testing; econophysics; multidisciplinary research; temperature forcers

Submitted 2025-08-27, Accepted 2025-11-09, https://doi.org/10.53234/scc202510/09

## 1. Introduction

This study contributes to scientific investigation of changes in Earth's average temperature over recent decades by examining how well it is explained by the theory of anthropogenic climate change (ACC).

Analysis offers a complementary perspective to the principal research technique used by climate scientists which is computer models based on scientific hypotheses that are tuned to observed climate (Randall et al., 2019). It applies the type of statistical scrutiny that is common in finance research (e.g. Dougherty, 2011) to the central hypothesis of ACC which is that observed global warming is driven linearly by cumulative $CO_2$ emissions from human activities (Jarvis & Forster, 2024; Masson-Delmotte et al., 2021: page 28). Such an outside view enables a clear eyed examination of aspects of climate science that are not typically tested (Kahneman & Lovallo, 2003), which should lessen the risk of incorrect inferences and open new channels to detect unsuspected temperature forcers.

The statistical approach here has two further motivations. One is to extend an important aspect of the scientific method through replication studies and alternative analytical approaches that test whether a theory is robust and thus should be acted on (Armstrong & Green, 2022). To date, models have been the principal tool for understanding past, present and future climate; and there has been limited research along statistical lines. This dates to 1992 when the Intergovernmental Panel on Climate Change (IPCC) concluded that statistical shortcomings in temperature and other data required “a physical model that includes both the hypothesized forcing and the enhanced greenhouse forcing ... to make further progress” (Houghton, Callander, & Varney, 1992: 163). Since then the length and reliability of climate data have improved markedly.

The second motivation for this paper is that - although climate change is multidisciplinary - its science has faced minimal scrutiny from outside the discipline. Although climate and finance lie in different environments and institutional settings they have much in common. Both are complex, truly global systems with non-linear, hard-to-monitor external influences and multiple feedbacks; each is multidisciplinary with impacts on and from Earth’s environment, economy, society and demography; and much of the data in both disciplines is time series, for which it is notoriously difficult to establish cause and effect (Liang, 2014).

Such similarities established the field of econophysics which applies physics research practices to economics (Chakraborti, Toke, Patriarca, & Abergel, 2011). Its climate related literature includes examination of evaluation of climate change (Harris, Roach, & Codur, 2017; Keen, 2022; Nordhaus, 2019; Tol, 2024), the statistical aspects of relationships between climate variables (Carter, 2008; Kaufmann, Kauppi, & Stock, 2006b; McMillan & Wohar, 2013), reliability of climate models (Green & Soon, 2025; Scafetta, 2024), forecasts of climate change impacts (Burke, Dykema, Lobell, Miguel, & Satyanath, 2015), and decisions within IPCC reports (Green & Armstrong, 2007).

The intent of this analysis is to independently test ACC using field observations which provides rigor and so generates greater confidence leading to optimum climate policies.

## 2. Materials and methods

The research objective here is to evaluate core physical relationships behind the theory of anthropogenic climate change (ACC) as set out in the IPCC’s latest Assessment Report (AR6) (Masson-Delmotte et al., 2021: pages 6-7 and 28) which are that: the climate has warmed at a rate that is unprecedented in at least the last 2,000 years due to emissions from human activities including greenhouse gases (GHG: mainly $CO_2$, also methane, nitrous oxide and nitrogen oxides) and land use, and this is captured in a near-linear relationship between cumulative anthropogenic $CO_2$ emissions and global warming.

This is depicted in Figure 1.

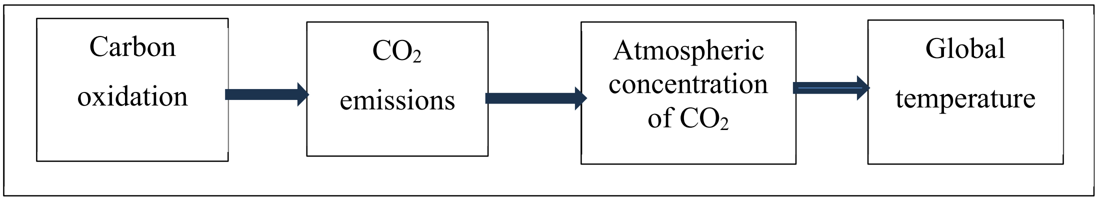

*Figure 1: Diagram of theory of anthropogenic climate change*

The most widely cited evidentiary support for this model is shown in Figure 2. The top chart supports the contention that “observed increases in well-mixed greenhouse gas (GHG) concentrations since around 1750 are unequivocally caused by human activities” (AR6, page 4). The lower chart supports the contention “that $CO_2$ and temperature covary” (AR6, page 44).

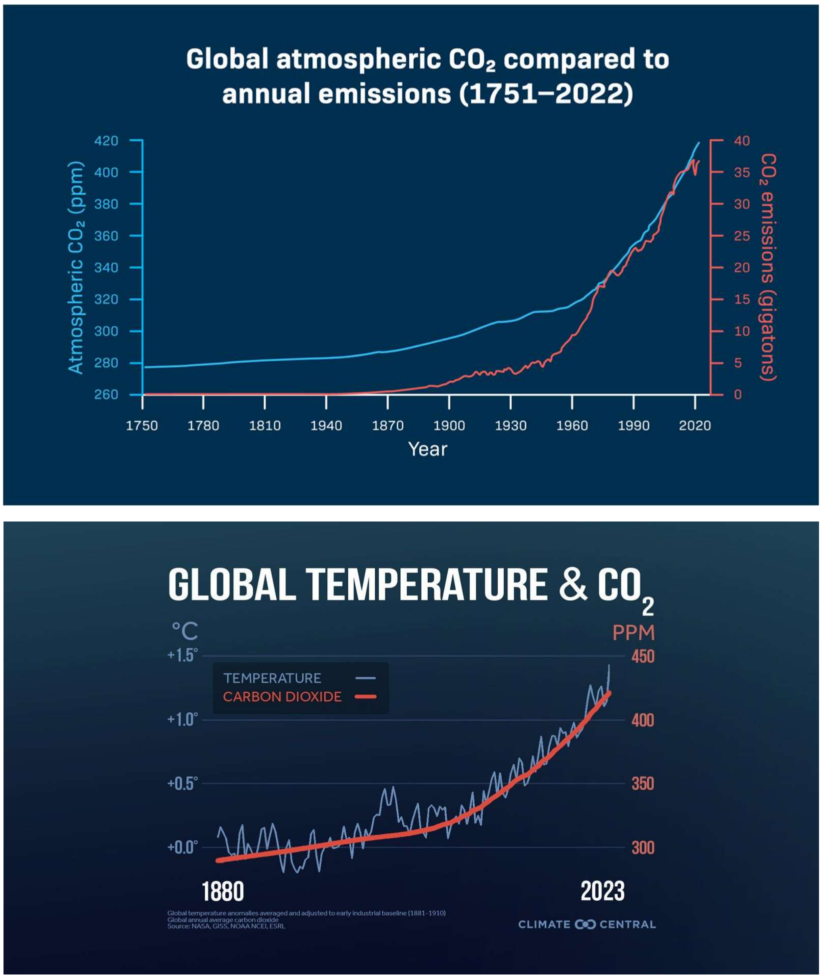

Global temperature anomalies averaged and adjusted to early industrial baseline (1881-1910)
Global annual average carbon dioxide
Source: NASA, GISS, NOAA NCEI, ESRL

*Figure 2. At top: Human emissions of CO2 and atmospheric concentration since start of the industrial revolution (NOAA, 2025). Below: CO2 and global temperature since the mid-19th century (LaPointe, 2024) (charts are in the public domain).*

A dominant component in each of $CO_2$ emissions, atmospheric $CO_2$ and global temperature is time. The possibility that this could lead to spurious correlations has been recognised by climate scientists since the 1980s (Houghton, Callander, & Varney, 1992: 163), but is all too rarely taken into account (Cummins, Stephenson, & Stott, 2022).

The research objective of this paper is to validate the key causal relationship underlying ACC using observed climate and related data, which involves testing four hypotheses (Bunge, 2017; Kampen, 2011):

> H1a. Correlation between atmospheric concentration of $CO_2$ and global temperature is not spurious
>
> H1b. Causality is clear in global warming so that global temperature consistently lags the independent, causal variable, $CO_2$ (or at least the two co-move, and $CO_2$ does not lag temperature)
>
> H2. The null hypothesis (that observed global warming would have occurred in the absence of emissions from human activities) can be tested independently of any assumptions
>
> H3. The $CO_2$-drives-warming hypothesis underlying ACC explains observed data (i.e. no missing variables)
>
> H4. Observed warming has no credible explanation other than that of rising atmospheric concentration of $CO_2$ and other greenhouse gases.

Analysis aims for reasonable statistical confidence ($p<0.05$), and uses adjusted R-squared as a measure of goodness of fit between hypothesised temperature forcers and observed temperature (Chen & Qi, 2023). It uses relatively simple statistical tools to avoid assumptions, and to ensure conclusions are accessible to a generalist audience. In addition, although not reliant on climate science, analysis seeks to remain grounded in the science by relying as much as possible on material from IPCC Assessment Reports.

Three analytical techniques will be used. The first is univariate linear OLS regression to determine best fits of global temperature (the dependent variable) against independent variables ($CO_2$ and other candidate temperature forcers) as per the following model:

$$Global\ temperature\ =\ \alpha_{\mathrm{n}} +\ \beta_{\mathrm{n}} \cdot\ Independent\ variable_{\mathrm{n}} \qquad (1)$$

where $\alpha_{\mathrm{n}}$and $\beta_{\mathrm{n}}$ are intercept and slope constants for forcing variable n.

The second technique examines the temperature-$CO_2$ relationship for spurious correlation, which arises between time series variables when correlations stem from their shared link to a third variable such as time. To illustrate this, consider two variables, global temperature, *T*, and atmospheric carbon dioxide concentration, *C*, that are linear functions of a third variable, *t*, as per the following:

$$T = a + b \cdot t\,, \qquad (2)$$

$$C = c + d \cdot t\,. \qquad (3)$$

Thus:

$$t = \frac{T-a}{b} = \frac{C-c}{d}\,, \qquad (4)$$

which makes it easy to see how *T* can seem to be a highly significant function of *C* solely because of their shared link to *t*.

The statistical solution is to validate correlation between the variables by establishing causation between changes in their levels (i.e. the current value minus its prior period value). If the co-movement between *T* and *C* reflects a true linear relationship such as:

$$T = g + h \cdot C \qquad (5)$$

Then:

$$\frac{\partial T}{\partial t} = constant \frac{\partial C}{\partial t} \qquad (6)$$

Thus, change in *C* should cause a proportional change in T, and both their changes and levels will co-vary in a constant, linear relationship.

The final technique tests for Granger causality, which was developed in economics and subsequently applied in other fields including climate change (Kampen, 2011; Kaufmann, Kauppi, & Stock, 2006a). The intuition is that causality (in the statistical, not scientific, sense) is demonstrated when forecasts of any variable based on its values in earlier periods can be improved by adding earlier value(s) of a second, causal variable. Consider the following equations:

$$Y_t =\ \alpha_1 +\ \beta_1 \cdot Y_{t-1} +\ \beta_2 \cdot Y_{t-2} \qquad (7)$$

$$Y_t =\ \alpha_1 +\ \beta_1 \cdot Y_{t-1} +\ \beta_2 \cdot Y_{t-2} +\ \beta_3 \cdot X_{t-1} +\ \beta_4 \cdot X_{t-2}\,. \qquad (8)$$

Variable *X* is said to Granger cause variable *Y* if equation (8) gives a better estimate of $Y_t$ than is given by equation (7).

Data used in the analysis are in the public domain, and details of definitions and sources are set out in Table 1. Analysis uses all available data during the period 1959 to 2024. The start year is chosen as the first full year when observational data for the key variable atmospheric concentration of carbon dioxide became continuously available from instrument observations.

Analysis employs EViews 13, which is an econometrics analytical package (S&P Global, 2024).

Table 1: Definitions and sources of data used in analysis and figures.

| Variable | Description | Source |
|---|---|---|
| Atlantic Multidecadal Oscillation (AMO) | Cyclical shifting of ocean temperatures in the North Atlantic | NOAA Physical Sciences Laboratory<br>https://www.psl.noaa.gov/data/timeseries/AMO/ |
| Cereal production | Global production of dry grains (barley, cereals, maize, millet, mixed grain, oats, rape seed, rice, rye, and wheat). | Annual data available since 1962 from Food and Agriculture Organization of the United Nations. https://www.fao.org/faostat/en/#data/QCL |
| Carbon dioxide ($CO_2$) | Anthropogenic emissions of carbon | From Global Carbon Budget 2024 (Friedlingstein et al., 2023) |
|  | Atmospheric concentration of $CO_2$ in ppm | Monthly since 1958 from Mauna Loa (https://gml.noaa.gov/ccgg/trends/data.html); and since about 1970 from Cape Grim, Australia (https://capegrim.csiro.au/) and Barrow (https://gml.noaa.gov/aftp/data/trace_gases/co2/flask/surface/txt/co2_brw_surface-flask_1_ccgg_month.txt). |
| Humidity | Annual mean specific humidity (water vapour as proportion of moist air by mass relative to 1981-2010). | Data available since 1974 from UK Met Office. https://climate.metoffice.cloud/humidity.html datasets |
| Temperature | Global temperature anomaly vs historical average ($^0$C). | Data available monthly since 1850 from: www.ncei.noaa.gov/access/monitoring/global-temperature-anomalies/anomalies; and https://www.metoffice.gov.uk/hadobs/hadcrut5/data/HadCRUT.5.0.2.0/download.html. Annual data are available from https://www.ncei.noaa.gov/access/monitoring/global-temperature-anomalies/anomalies. |

This section reports statistical evaluations of physical evidence relating to ACC's central premise that observed warming is driven linearly by accumulated atmospheric $CO_2$ from human-related carbon combustion. Analysis builds on previous work in climate science (e.g. Jolliffe & Stephenson, 2012; M. Nelson & Nelson, 2024; Nzotungicimpaye & Matthews, 2024; Von Storch & Zwiers, 2002; Zwiers & Von Storch, 2004) and economics (Green & Soon, 2025; May & Crok, 2024).

### *3.1 Possibly spurious relationship between global temperature and $CO_2$*

Most statistical tests assume that data have a constant, or stationary, mean and standard deviation, and thus oscillate around fixed values. A non-stationary distribution invalidates such analysis, and this statistical risk is quantified by testing time series for a unit root whose presence means they are not stationary. Table 2 shows the p-values from augmented Dickey-Fuller (ADF) tests and indicates that both temperature and $CO_2$ are non-stationary.

Table 2: p-values of unit root tests for temperature and $CO_2$.

| Variable | ADF test |
|---|---|
| Atmospheric $CO_2$ concentration | 0.999 |
| Global temperature | 0.999 |

Non-stationarity is common in economics whose data are dominated by time series, and researchers have managed this by analysing relationships between differences or changes in variables as well as between levels (e.g. Christian & Barrett, 2024; C. R. Nelson & Plosser, 1982). Differences are calculated for each observation by subtracting its previous value, which removes trends. For most data series, this makes the mean stationary and thus reliable in regression analysis that can unravel underlying dynamics.

This is done for atmospheric $CO_2$ and temperature since 1960 in Figure 3. As shown in the left chart, levels of atmospheric $CO_2$ and global temperature moved together. However, this was not true of their changes: annual change in $CO_2$ has accelerated while that for temperature continued at its long-term rate. If $CO_2$ were forcing global temperature, the latter‘s rate of change should also have quickened. Thus the correlation between temperature and $CO_2$ is likely spurious and cannot be relied on: this rejects hypothesis 1a that correlation between atmospheric concentration of $CO_2$ and global temperature is not spurious.

This conclusion matches that reached by others that $CO_2$ has, at best, a weak and probably spurious relationship with temperature (including Beenstock, Reingewertz, & Paldor, 2016; McMillan & Wohar, 2013). Alternatively the result is not inconsistent with a non-linear $CO_2$-temperature relationship that has also been suggested (e.g. Beenstock, Reingewertz, & Paldor, 2012; Jarvis & Forster, 2024).

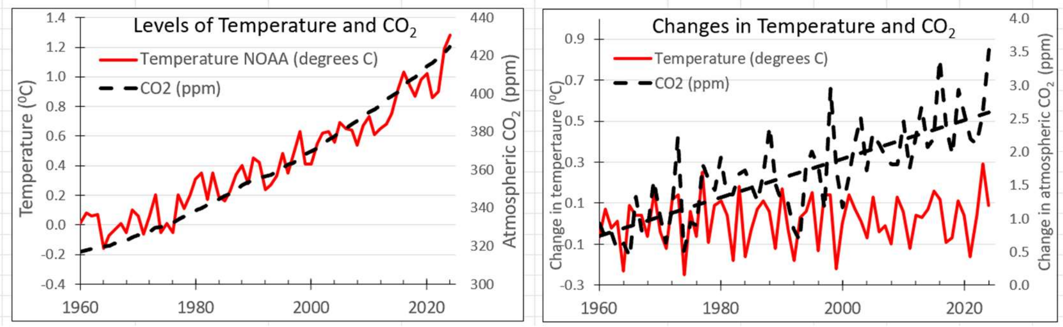

*Figure 3. Plots of levels and annual changes in atmospheric concentration of $CO_2$ and global temperature since 1960 (prepared by the author using data described in Table 1).*

In short, the central relationship of ACC appears to be spurious, and possibly due to shared time properties of atmospheric concentration of $CO_2$ and global temperature.

## *3.2 Causality in relationship between $CO_2$ and temperature*

The lead-lag relationship between $CO_2$ and temperature which is central to statistical causality of climate change is examined in Table 3 using annual data in univariate regressions of global temperature on atmospheric concentration of $CO_2$. The left half of the table analyses levels, and the right half analyses changes. The first column of the chart shows the $CO_2$ lead (where 1 means $CO_2$ leads temperature by one year), while other columns show slope and associated t-statistic and R-squared for values of levels and annual changes.

Table 3: Slope and associated t-statistic and R-squared from univariate regression of global temperature on atmospheric concentration of $CO_2$ as per eq.(1), where $\alpha_n$and $\beta_n$ are intercept and slope constants for forcing variable n. Covers levels and annual changes since instrumental data became available in 1958. The first column shows the $CO_2$ lead, where 1 means $CO_2$ leads temperature by one year. Level of significance: * < 0.05; ** < 0.01.

| $CO_2$ lead | Annual changes | | | | | |
|---|---|---|---|---|---|---|
| | Levels | | | Changes | | |
| | slope | t-stat | R-sqd | slope | t-stat | R-sqd |
| 2 | 0.011 ** | 27.4 | 0.92 | 0.007 | 0.32 | 0.00 |
| 1 | 0.011 ** | 27.8 | 0.92 | -0.038 | 1.74 | 0.03 |
| 0 | 0.010 ** | 28.7 | 0.93 | 0.057 ** | 2.89 | 0.11 |
| -1 | 0.010 ** | 28.3 | 0.93 | 0.064 ** | 3.27 | 0.13 |
| -2 | 0.010 ** | 26.7 | 0.92 | -0.021 | 1.01 | 0.00 |

Starting with levels in the left half of the Table , there are statistically strong ($p<0.01$) positive correlations between temperature and $CO_2$ at both leads and lags of up to at least two years. Thus there is no consistent cause and effect in this relationship which casts further doubt on causality as previously flagged (e.g. Davis, 2017; Koutsoyiannis, 2024).

Given the likely spurious relationship between levels of temperature and $CO_2$, a more telling test of the lead-lag relationship is shown in the right half of Table 3 which analyses the relationship between changes in global temperature and atmospheric concentration of $CO_2$. Neither one or two year-ahead $CO_2$ change has a statistically significant relationship with lagged temperature; concurrent values have a statistically significant ($p<0.01$) relationship so that temperature and $CO_2$ co-move; and there is a significant relationship between changes in year-ahead temperature and lagged $CO_2$. In short, changes in $CO_2$ do not consistently lead changes in temperature.

In unreported results, similar findings came from analysis of relationships between annual percentage changes in temperature and atmospheric $CO_2$.

Another perspective on ACC's $CO_2$ emissions-temperature relationship is that of Granger causality, which is examined in Table 4. Starting with levels of variables in panel A, temperature is strongly autocorrelated, and about 90 percent of future temperature is explained by its earlier values; adding previous levels of $CO_2$ slightly increases R-squared (or goodness of fit) from 89 to 93 percent.

Changes in variables are shown in panel B. Lagged values of temperature (i.e. $\beta_1$ and $\beta_2$) are highly significant ($p<0.01$). Adding previous values of change in $CO_2$ shows insignificant coefficients on $CO_2$ change; reduces the significance of $\beta_1$ and $\beta_2$; and cuts explanatory power of the model (i.e. R-squared) from 16 to 14 percent.

Thus $CO_2$ does not Granger cause temperature.

Table 4: Granger causality tests using eqs (7) and (8), where temperature is variable $Y$ and $CO_2$ is variable $X$. Level of significance: * < 0.05; ** < 0.01.

| | $\alpha_1$ | $\beta_1$ | $\beta_2$ | $\beta_3$ | $\beta_4$ | Adjusted R-sqd |
|---|---|---|---|---|---|---|
| Panel A: Levels of variables | | | | | | |
| Equation (7) | 0.0222 | 0.740 ** | 0.266 * | | | 0.888 |
| Equation (8) | -3.166 | 0.370 * | -0.232 | -0.038 | 0.049 | 0.928 |
| Panel B: Changes in variables | | | | | | |
| Equation (7) | 0.031 | -0.368 ** | -0.383 ** | | | 0.163 |
| Equation (8) | 0.013 | -0.336 * | -0.392 ** | -0.006 | 0.017 | 0.140 |

In terms of causality, $CO_2$ does not consistently lead temperature and changes in $CO_2$ do not Granger cause change in temperature. This rejects hypothesis 1b that causality is clear in global warming so that global temperature consistently lags the independent, causal variable, $CO_2$ (or at least the two co-move, and $CO_2$ does not lag temperature).

### 3.3 Robustness tests of the weak $CO_2$-warming link

This section repeats analysis in the previous section using annual temperature data since 1971 from the UK Met Office Hadley Centre observations dataset HadCRUT5 and NASA's GISS; along with $CO_2$ data for the second and third longest datasets from Barrow, Alaska and Cape Grim, Australia.

Figure 4 plots annual changes in various combinations of variables and shows the same pattern as Figure 3, namely that annual change in global temperature has been constant even though the annual change in atmospheric $CO_2$ has been increasing. Thus there is not a constant linear relationship between changes in any of the $CO_2$-temperature combinations, which confirms the relationship is likely spurious.

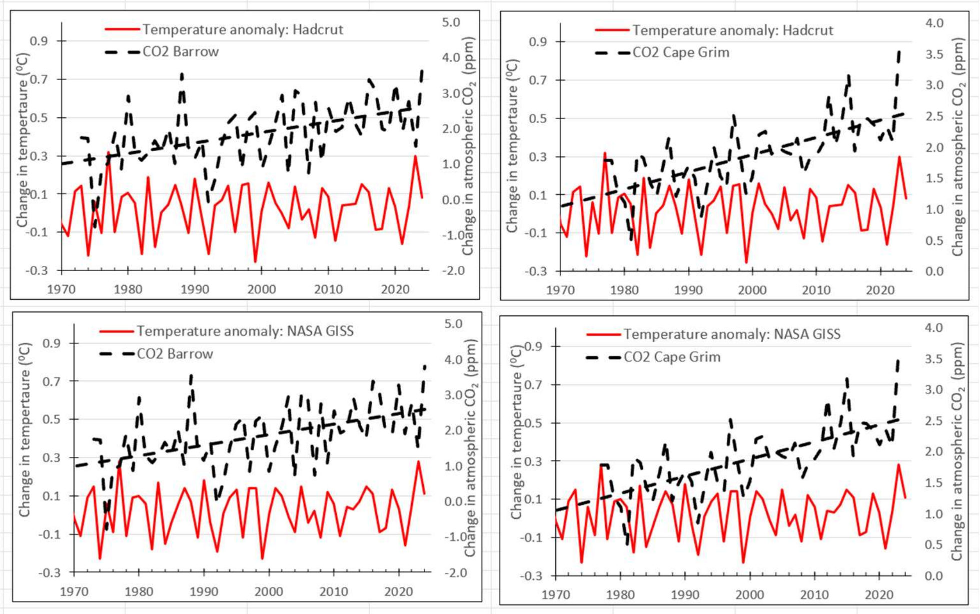

*Figure 4: Graphs of annual changes in global temperature using HadCRUT5 and NASA GISS temperature datasets, and in atmospheric concentrations of $CO_2$ from Barrow, Alaska and Cape Grim, Australia (prepared by the author using data described in Table 1).*

Table 5 reports slope and associated t-statistic from univariate regression as per equation (1) of annual changes in global temperature using HadCRUT5 and NASA GISS temperature datasets against changes in atmospheric concentrations of $CO_2$ from Barrow, Alaska and Cape Grim, Australia. The pattern here is similar to that in Table 3 where year-ahead $CO_2$ has no statistically significant ($p>0.05$) relationship with lagged temperature; concurrent values have statistically significant ($p<0.05$) relationships so that the temperature and $CO_2$ co-move; and there is a significant relationship ($p<0.01$-$0.05$) between changes in year-ahead temperature and lagged $CO_2$ in both periods. In short, changes in $CO_2$ lag changes in temperature rather than consistently leading, which confirms doubt on causality.

Table 5: Slope and associated t-statistic from univariate regression of temperature on $CO_2$ as per equation (1) for annual changes, since 1970s. The first column shows the $CO_2$ lead, where 1 means $CO_2$ leads temperature by one year. Level of significance: * < 0.05; ** < 0.01.

| | HadCRUT5 | | | | NASA GISS | | | |
|---|---|---|---|---|---|---|---|---|
| | Barrow | | Cape Grim | | Barrow | | Cape Grim | |
| $CO_2$ lead | slope | t-stat | slope | t-stat | slope | t-stat | slope | t-stat |
| 2 | 0.003 | 0.13 | -0.062 | 1.76 | 0.005 | 0.27 | -0.040 | 1.30 |
| 1 | -0.023 | 1.11 | 0.043 | 1.35 | -0.023 | 1.16 | -0.013 | 0.41 |
| 0 | -0.001 | 0.03 | 0.074 * | 2.30 | 0.003 | 0.13 | 0.073 * | 2.42 |
| -1 | 0.075 ** | 4.53 | -0.015 | 0.48 | 0.075 ** | 4.83 | 0.047 | 1.56 |
| -2 | -0.029 | 1.52 | -0.039 | 1.21 | -0.027 | 1.52 | -0.061 | 1.82 |

Table 6 repeats Granger causality tests using changes in variables. Lagged values of HadCRUT and GISS temperature (i.e. $\beta_1$ and $\beta_2$) are significant ($p<0.05$). Adding previous values of change in Barrow $CO_2$ reduces the significance of $\beta_1$ and $\beta_{2.}$; shows insignificant coefficients on $CO_2$ change; and cuts explanatory power of the models (i.e. R-squared falls). This robustness test further confirms that change in $CO_2$ does not Granger cause temperature.

Table 6: Granger causality tests using the equations(7) and (8), where change in temperature is variable $Y$ and change in atmospheric $CO_2$ is variable $X$. Level of significance: * < 0.05; ** < 0.01.

| | $\alpha_1$ | $\beta_1$ | $\beta_2$ | $\beta_3$ | $\beta_4$ | Adjusted R-sqd |
|---|---|---|---|---|---|---|
| Panel A: changes in HadCRUT temperature data and Barrow $CO_2$ data | | | | | | |
| Equation (7) | 0.041 | -0.387 ** | -0.342 * | | | 0.149 |
| Equation (8) | 0.054 | -0.395 ** | -0.345 * | -0.001 | -0.006 | 0.113 |
| Panel B: changes in GISS temperature data and Barrow $CO_2$ data | | | | | | |
| Equation (7) | 0.040 | -0.342 * | -0.343 * | | | 0.132 |
| Equation (8) | 0.042 | -0.346 * | -0.349 * | 0.001 | -0.02 | 0.093 |

In summary, robustness tests using additional data sets confirm earlier findings. In particular, annual change in various measures of atmospheric $CO_2$ has been steadily increasing but this has not altered the rate of change in global temperature, as would occur if $CO_2$ were forcing temperature. In addition, changes in $CO_2$ do not consistently lead temperature changes as also would occur if $CO_2$ were forcing temperature; rather, temperature leads one-year lagged change in $CO_2$. Nor do changes in $CO_2$ Granger cause change in temperature.

## 3.4 Testable, independent null hypothesis

The null hypothesis of ACC is that today's global temperature would have occurred in the absence of $CO_2$ emissions from human activities. To disprove this requires evidence that atmospheric $CO_2$ has driven temperature higher than its natural level. The typical approach is to fingerprint causes of warming using climate models that first incorporate only natural forcers (which are limited to solar radiation and volcanic activity: AR6, page 6) and then overlay anthropogenic forcings (Bindoff et al., 2013; Zhai, Zhou, & Chen, 2018). According to IPCC: "observed warming (1850-2019) is only reproduced in simulations including human influence" (AR6, page 516).

Two points arise here. First is that only two natural forcers are incorporated in models, whereas the literature reports many other natural influences on climate, including: Earth's orbital inclination (Muller & MacDonald, 1995); length of day (Lopes, Courtillot, Gibert, & Le Mouël, 2022); geomagnetism (Vares & Persinger, 2015); the Atlantic Multidecadal Oscillation (AMO) (Kerr, 2000) and Southern Oscillation (SOI) (Mazzarella, Giuliacci, & Scafetta, 2013); cloud seeding by cosmic radiation (Svensmark, 2007) and solar activity (Lockwood, 2012); humidity (Al-Ghussain, 2018) and changes in cloud structure (Dübal & Vahrenholt, 2021); and photosynthesis (Bender, Sowers, & Labeyrie, 1994) and plant physiology (McElwain & Steinthorsdottir, 2017).

In addition there are multiple studies depicting strong links between temperature and intuitively obvious anthropogenic forcers such as global population and GDP per capita (Coleman, 2023), as well as less certain forcers such as US postage costs (Green & Soon, 2025). This opens up a possible missing variables problem as discussed in the following section.

The second point is that models are tuned by altering their internal parameters to reduce mismatch between their output and observations (Hourdin et al., 2017). That is, all temperature change is attributed to anthropogenic forcing and just two natural forcings; and models' parameters are adjusted accordingly. The net is that computer-based climate models are built up from the assumption that $CO_2$ forces temperature, and then calibrated to match observed temperatures. This opens up what finance terms the joint test problem, which occurs when an hypothesis (i.e. that human carbon emissions cause warming) is tested using in-sample data and relies on the hypothesis being tested: any verification is tautological, which leads to herding around an uncertain conclusion and correlated scientific errors.

Testing the null hypothesis requires independent determination of anthropogenic components of temperature and atmospheric $CO_2$ over time (Hegerl & Zwiers, 2011). However, neither is directly observable, and experiments to determine them are impractical. Thus it is impractical to directly test whether warming is occurring naturally, which rejects hypothesis 2 that the null hypothesis of ACC (that observed global warming would have occurred in the absence of emissions from human activities) can be tested independently of any assumptions.

### 3.5 Alternative explanations of warming

Almost all scientific literature accepts that ACC explains warming (Lynas, Houlton, & Perry, 2021). The IPCC reports (AR6, pages v and 11): “it is unequivocal that human activities have heated our climate ... This warming is mainly due to increased GHG concentrations.” Other authorities agree, such as the American Geophysical Union whose ‘Position on climate change’ says that “there is no alterative [sic] explanation [to ACC] supported by convincing evidence” (AGU, 2019).

Conversely, statistical analysis above shows only weak causal relationship between atmospheric $CO_2$ and global temperature. In addition, the section above details multiple examples of natural and anthropogenic variables that are known to influence temperature, but are not included in models. This suggests the possibility of a missing variables problem where unsuspected forcers contribute to warming.

To demonstrate the potential impact of omitted forcers, Figure 5 plots levels and changes since 1960 of temperature against Atlantic Multidecadal Oscillation (AMO), global cereal production and specific humidity. For each forcer, levels appear strongly correlated with temperature; and changes are also strongly and linearly correlated with temperature, indicating the correlations are not spurious. These relationships are markedly different to that for atmospheric $CO_2$ and temperature, where - as shown in Figure 3 - changes do not co-move.

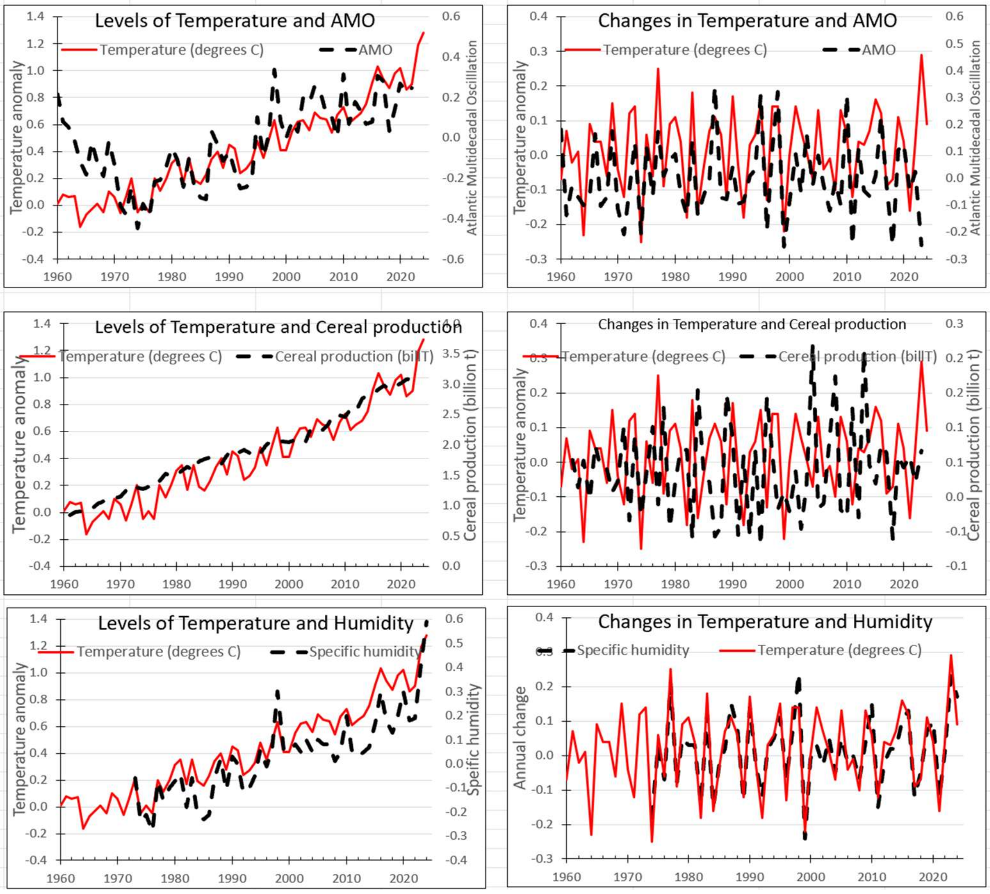

*Figure 5: Levels and changes in non-$CO_2$ related variables and NOAA temperature using available data since 1960. Top: temperature and Atlantic Multidecadal Oscillation (AMO); centre: temperature and global cereal production; bottom: global temperature and specific humidity. Graphs were prepared by the author using data with definitions and sources in Table 1.*

Table 7 quantifies the relationships in Figure 5. Panel A reports slope and t-statistic from linear regression of levels and changes since 1960 in NOAA temperature and in non-$CO_2$ forcers of Atlantic Multidecadal Oscillation (AMO), global cereal production and specific humidity. By comparison to values for $CO_2$ as a temperature forcer shown in Table 3 (slope and t-statistic, respectively for: level 0.010 and 28.7; and changes 0.057 and 2.89), statistical relationships for levels of non $CO_2$ forcers are almost as strong. However, using changes the statistical relationships between temperature and the non-$CO_2$ forcers are stronger than with $CO_2$.

Panel B reports Granger causality tests and shows that incorporating lagged values of each of Atlantic Multidecadal Oscillation (AMO), global cereal production and specific humidity considerably increases the explanatory power of lagged values of temperature, with the R-squared rising from 16.2 percent to 19-21 percent. This is around 1.5 times the explanatory power of $CO_2$.

Table 7. Statistical tests of relationships between changes in NOAA temperature and non-$CO_2$ forcers, namely Atlantic Multidecadal Oscillation (AMO), global cereal production and specific Panel A is linear regression of NOAA temperature against each forcer. Panel B is Granger causality test using the equations (7) and (8), where change in temperature is variable *Y* and changes in forcers are variable *X*. Level of significance: * < 0.05; ** < 0.01.

| Panel A: Linear regression of NOAA temperature against forcer | | | | | | |
|---|---|---|---|---|---|---|
| | Atlantic Multidecadal Oscillation | | Cereal production | | Humidity | |
| | slope | t-stat | slope | t-stat | slope | t-stat |
| Levels | 1.199 ** | 8.60 | 0.482 ** | 23.4 | 1.720 ** | 19.0 |
| Changes | 0.523 ** | 6.64 | -0.616 ** | 2.86 | 1.035 ** | 15.6 |

| Panel B: Granger causality test of changes in forcers | | | | | | |
|---|---|---|---|---|---|---|
| | $\alpha_1$ | $\beta_1$ | $\beta_2$ | $\beta_3$ | $\beta_4$ | Adjusted R-sqd |
| NOAA temperature | 0.031 | -0.368 ** | -0.383** | | | 0.162 |
| AMO | 0.026 | -0.304 | -0.228 | -0.184 | -0.180 | 0.203 |
| Cereal production | 0.004 | -0.295 * | -0.360 ** | 0.523 * | 0.192 | 0.210 |
| Humidity | 0.031 | 0.375 | -0.011 | -0.911 * | -0.335 | 0.191 |
| Atmospheric $CO_2$ | 0.013 | -0.336 * | -0.392 ** | -0.006 | 0.017 | 0.140 |

This section identifies three intuitively likely variables that can explain recent temperature rise better than atmospheric $CO_2$. The fact that ACC is not routinely tested against these and/or other alternative hypotheses is a significant shortcoming in its scientific methodology (Green & Soon, 2025).

ACC's confidence in $CO_2$ as the sole explanation for observed warming seems inconsistent with statistical uncertainties discussed in earlier sections; in addition the missing variables problem with ACC is obvious in light of $CO_2$ explaining far less of temperature change than other intuitively likely forcers of AMO, cereal production and humidity. This cautions that - although correlations between temperature and forcing variables are necessary for causality – there are many candidate variables. Simply choosing one is not a valid approach to proof.

This rejects hypothesis 4 that observed warming has no credible explanation other than that of rising atmospheric concentration of $CO_2$ and other greenhouse gases.

### *3.6 Summary*

To summarise the analysis above, it identifies several statistical shortcomings in ACC. The greatest is uncertainty in ACC's central hypothesis of a direct relationship between atmospheric $CO_2$ and global temperature, which is likely spurious such as would arise from shared time series properties of the variables. Moreover, incorporating lead-lag values in regressions shows that levels of temperature and $CO_2$ co-move with no evidence that $CO_2$ forces temperature; and analysis using changes shows that temperature leads one-year lagged change in $CO_2$. This conclusion is supported by Granger causality tests, and robustness tests using alternative temperature and $CO_2$ data sets.

In addition, ACC suffers the joint test problem that makes it impractical to dismiss the null hypothesis that warming would have occurred in the absence of higher atmospheric $CO_2$. The final statistical concern with ACC is a significant missing variables problem: global temperature has linear relationships since last century with multiple natural and anthropogenic variables that are stronger than the one with atmospheric $CO_2$.

Statistical relationships derived above suggest the explanatory model for global warming as shown in Figure 6. $CO_2$ emissions are driven by human population and industry; but emissions and atmospheric $CO_2$ have only weak influence on global temperature, which is driven more strongly by AMO, cereal production and/or humidity. As an aside, these links are statistically based, and no attempt is made here to explain the science behind them.

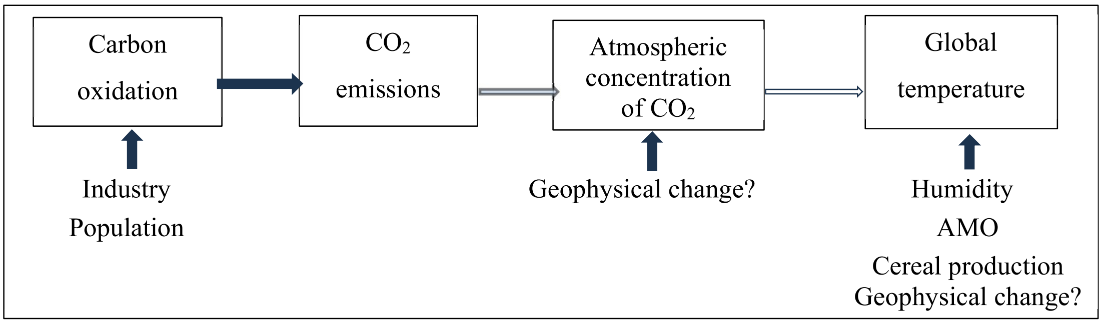

*Figure 6. Revised causal relationships leading to observed global warming.*

## 4. Discussion

A climate scientist commenting on this paper made several observations. First, analysis does not align with the climate discipline's science-based focus on physical mechanisms which establish $CO_2$ as a primary driver of recent global warming. Moreover, climate is affected by multiple external forcings, which are direct and indirect and time-, space- and scale- dependent and so introduce multiple causality pathways with non-linear, varying relationships. Thus drawing conclusions about ACC's credibility cannot rely on empirical studies or observational data, but requires examining its physical processes using global climate models.

This argument that models alone can be relied on is not, however, true of other disciplines, which are alert to implications of the retraction and replication literature (e.g. Ioannidis, 2005; Oransky, 2022), and make it a point to ensure that their theory is able to withstand multifaceted scrutiny. The last includes real world tests and analysis using a variety of tools and techniques applied by other disciplines in similar research environments, such as finance as conducted here.

The principal finding of this study is that the theory of anthropogenic climate change is not resilient to statistical analysis using real-world observations. In particular, the assumed linear relationship between global warming and atmospheric concentration of carbon dioxide is likely spurious and due to simultaneous, time-related rises in the two variables. In addition a number of natural and anthropogenic variables can explain warming better than $CO_2$, especially humidity which leads temperature and explains up to 80 percent of its variation. The last link is well-recognised, but is typically dismissed with the assertion that it is a feedback of GHG-induced warming. This requires re-assessment.

In short, the answer to the title's question is: No, $CO_2$ is at most a small contributor to observed warming. Given that the key hypothesis within ACC is not demonstrably valid, knowledge of its science seems incomplete. This opens up a number of other possible explanations for global warming such as: that climate sensitivity, or warming from a doubling in $CO_2$ concentration, is overstated; other factors are significant contributors to warming including Atlantic Multidecadal Oscillation, global cereal production and specific humidity; or another planetary scale human or geophysical phenomenon may be driving warming (Cohler, Legates, Soon, & Soon, 2025).

To close, evidence that elements of ACC do not withstand real world tests is troubling given strong public concern and high economic and social risk from climate change. More robust theory is essential to pave the way for optimum policy response to warming.

**Funding:** No funding of the work.

**Editor:** H. Harde, **Reviewers**: Anonymous

## References

AGU, 2019: Position Statement on Climate Change [Press release]. Retrieved from https://www.agu.org/share-and-advocate/share/policymakers/position-statements/position_climate

Al-Ghussain, L., 2018: *Global warming: review on driving forces and mitigation*. Environmental Progress & Sustainable Energy, 38 (1), 13-21.

Armstrong, J. S., & Green, K. C., 2022: *The Scientific Method: A guide to finding useful knowledge*. Cambridge UK: Cambridge University Press.

Beenstock, M., Reingewertz, Y., & Paldor, N., 2012: *Polynomial cointegration tests of anthropogenic impact on global warming*. Earth System Dynamics Discussions, 3 (2), 173-188.

Beenstock, M., Reingewertz, Y., & Paldor, N., 2016; *Testing the historic tracking of climate models*. International Journal of Forecasting, 32 (4), 1234-1246.

Bender, M., Sowers, T., & Labeyrie, L., 1994: *The Dole effect and its variations during the last 130,000 years as measured in the Vostok ice core*. Global Biogeochemical Cycles, 8 (3), 363-376.

Bindoff, N. L., Stott, P. A., Achutarao, K. M., Allen, M. R., Gillett, N., Gutzler, D., . . . Jain, S., 2013: *Detection and attribution of climate change: From global to regional*. In T. F. Stocker, D. Qin, & G.-K. Plattner (Eds.), *The Physical Science Basis. Contribution of Working Group I to the Fifth Assessment Report of the Intergovernmental Panel on Climate Change*. Cambridge: Cambridge University Press.

Bunge, M., 2017: *Causality and Modern Science*. New York: Routledge.

Burke, M., Dykema, J., Lobell, D. B., Miguel, E., & Satyanath, S., 2015: *Incorporating climate uncertainty into estimates of climate change impacts*. Review of Economics and Statistics, 97 (2), 461-471.

Carter, R. M., 2008: *Knock, knock: where is the evidence for dangerous human-caused global warming?* Economic analysis and policy, 38 (2).

Chakraborti, A., Toke, I. M., Patriarca, M., & Abergel, F., 2011: *Econophysics review: I. Empirical facts*. Quantitative Finance, 11 (7), 991-1012.

Chen, Q., & Qi, J., 2023: *How much should we trust R2 and adjusted R2: Evidence from regressions in top economics journals and Monte Carlo simulations*. Journal of Applied Economics, 26 (1), 2207326. doi:10.1080/15140326.2023.2207326

Christian, P., & Barrett, C. B., 2024: *Spurious regressions and panel IV estimation: Revisiting the causes of conflict*. The Economic Journal, 134 (659), 1069-1099.

Cohler, J., Legates, D., Soon, F., & Soon, W., 2025: *A critical reassessment of the anthropogenic $CO_2$-global warming hypothesis: Empirical evidence contradicts IPCC models and solar forcing assumptions*, Science of Climate Change, Vol. 5.1, pp. 13-28, https://doi.org/10.53234/SCC202501/06.

Coleman, L., 2023: *A strategic roadmap to thread global warming's risks*. Global Policy.

https://www.globalpolicyjournal.com/blog/21/09/2023/strategic-roadmap-thread-global-warmings-risks

Cummins, D. P., Stephenson, D. B., & Stott, P. A., 2022: *Could detection and attribution of climate change trends be spurious regression?* Climate Dynamics*,* 59 (9-10), 2785-2799.

Davis, W. J., 2017: *The relationship between atmospheric carbon dioxide concentration and global temperature for the last 425 million years*. Climate Dynamics*,* 5 (4), 76.

Dougherty, C. (2011). *Introduction to Econometrics* Oxford, UK: Oxford University Press.

Dübal, H.-R., & Vahrenholt, F., 2021: *Radiative energy flux variation from 2001–2020*. Atmosphere*,* 12 (10), 1297.

Friedlingstein, P., O'sullivan, M., Jones, M. W., Andrew, R. M., Bakker, D. C., Hauck, J., . . . Peters, G. P., 2023: *Global carbon budget 2023*. Earth System Science Data Discussions*,* 15 (12), 5301-5369.

Green, K. C., & Armstrong, J. S., 2007: *Global warming: Forecasts by scientists versus scientific forecasts*. Energy & environment*,* 18 (7), 997-1021.

Green, K. C., & Soon, W., 2025: *Are climate model forecasts useful for policy making? Effect of variable choice on reliability and predictive validity*. Science of Climate Change*,* Vol. 5.1, pp. 59 - 85, https://doi.org/10.53234/scc202501/07.

Harris, J., Roach, B., & Codur, A., 2017: *The Economics of Global Climate Change*. Somerville MA: Global Development And Environment Institute, Tufts University.

Hegerl, G., & Zwiers, F., 2011: *Use of models in detection and attribution of climate change*. Wiley Interdisciplinary Reviews: Climate Change*,* 2 (4), 570-591.

Houghton, J. T., Callander, B. A., & Varney, S. K., 1992: *Climate Change 1992: The Supplementary Report to the IPCC scientific assessment*. Cambridge UK: Cambridge University Press.

Hourdin, F., Mauritsen, T., Gettelman, A., Golaz, J.-C., Balaji, V., Duan, Q., . . . Qian, Y., 2017: *The art and science of climate model tuning*. Bulletin of the American Meteorological Society*,* 98 (3), 589-602.

Ioannidis, J. P., 2005: *Why most published research findings are false*. PLoS medicine*,* 2 (8), e124.

Jarvis, A., & Forster, P. M., 2024: *Estimated human-induced warming from a linear temperature and atmospheric $CO_2$ relationship*. Nature geoscience, 1-3.

Jolliffe, I. T., & Stephenson, D. B., 2012: *Forecast Verification: A practitioner's guide in atmospheric science*. NewYork: John Wiley & Sons.

Kahneman, D., & Lovallo, D., 2003: *Delusions of success: How optimism undermines executives' decisions*. Harvard Business Review*,* 81 (7), 56-63.

Kampen, J. K., 2011: *A methodological note on the making of causal statements in the debate on anthropogenic global warming*. Theoretical and Applied Climatology*,* 104, 423-427.

Kaufmann, R. K., Kauppi, H., & Stock, J. H., 2006a: *Emissions, concentrations, & temperature: a time series analysis*. Climatic Change*,* 77, 249-278.

Kaufmann, R. K., Kauppi, H., & Stock, J. H., 2006b: *The relationship between radiative forcing and temperature: what do statistical analyses of the instrumental temperature record measure?* Climatic Change*,* 77, 279-289.

Keen, S., 2022: *The appallingly bad neoclassical economics of climate change*. In B. Gills & J. Morgan (Eds.), Economics and Climate Emergency (pp. 79-107). London: Routledge.

Kerr, R. A., 2000: *A North Atlantic climate pacemaker for the centuries*. Science*,* 288 (5473), 1984-1985.

Koutsoyiannis, D. J., 2024: *Stochastic assessment of temperature–$CO_2$ causal relationship in climate from the Phanerozoic through modern times*. Mathematical Biosciences and Engineering, 21 (7), 6560-6602.

LaPointe, S., 2024: *The Greenhouse Effect and how humans enhance it*. 6News. https://cbs6albany.com/weather/weather-extra/the-greenhouse-effect-and-how-humans-enhance-it-climate-change

Liang, X. S., 2014: *Unraveling the cause-effect relation between time series*. Physical Review E: Statistical, Nonlinear & Soft Matter Physics, 90 (5), 052150.

Lockwood, M., 2012: *Solar influence on global and regional climates*. Surveys in Geophysics, 33 (3), 503-534.

Lopes, F., Courtillot, V., Gibert, D., & Le Mouël, J.-L., 2022: *Extending the range of Milankovic cycles and resulting global temperature variations to shorter periods (1–100 year range)*. Geosciences, 12 (12), 448.

Lynas, M., Houlton, B. Z., & Perry, S., 2021: *Greater than 99% consensus on human caused climate change in the peer-reviewed scientific literature*. Environmental Research Letters, 16 (11), 114005.

Masson-Delmotte, V., Zhai, P., Pirani, A., Connors, S. L., Péan, C., Berger, S., . . . Huang, M., 2021: *Climate Change 2021: The Physical Science Basis. Contribution of Working Group I to the Sixth Assessment Report of the Intergovernmental Panel on Climate Change*. Cambridge: Cambridge University Press.

May, A., & Crok, M., 2024: *Carbon dioxide and a warming climate are not problems*. American Journal of Economics and Sociology, 15.

Mazzarella, A., Giuliacci, A., & Scafetta, N., 2013: *Quantifying the Multivariate ENSO Index (MEI) coupling to $CO_2$ concentration and to the length of day variations*. Theoretical and Applied Climatology, 111, 601-607.

McElwain, J. C., & Steinthorsdottir, M., 2017: *Paleoecology, ploidy, paleoatmospheric composition, and developmental biology: A review of the multiple uses of fossil stomata*. Plant Physiology, 174 (2), 650-664.

McMillan, D. G., & Wohar, M. E., 2013: *The relationship between temperature and CO2 emissions: evidence from a short and very long dataset*. Applied Economics, 45 (26), 3683-3690.

Muller, R. A., & MacDonald, G., 1995: *Glacial cycles and orbital inclination*. Nature, 377 (6545), 107-108.

Nelson, C. R., & Plosser, C. R., 1982: *Trends and random walks in macroeconmic time series: some evidence and implications.* Journal of Monetary Economics, 10 (2), 139-162.

Nelson, M., & Nelson, D. B., 2024: *Decoupling $CO_2$ from climate change*. International Journal of Geosciences, 15 (3), 246-269.

NOAA, 2025: *Climate change: atmospheric carbon dioxide* [Press release] https://www.climate.gov/news-features/understanding-climate/climate-change-atmospheric-carbon-dioxide

Nordhaus, W., 2019: *Climate change: The ultimate challenge for economics*. American Economic Review, 109 (6), 1991-2014.

Nzotungicimpaye, C.-M., & Matthews, H. D., 2024: *Linking cumulative carbon emissions to observable climate impacts*. Environmental Research: Climate, 3 (3), 032001.

Oransky, I., 2022: *Retractions are increasing, but not enough*. Nature, 608 (7921), 9.

Randall, D. A., Bitz, C. M., Danabasoglu, G., Denning, A. S., Gent, P. R., Gettelman, A., . . . Pincus, R., 2019: *100 years of earth system model development*. Meteorological Monographs, 59, 12.11-12.66.

S&P Global., 2024: EViews Econometric Modeling Software. Retrieved from https://www.spglobal.com/marketintelligence/en/mi/products/eviews-econometric-modeling-analysis-software.html

Scafetta, N., 2024: *Impacts and risks of "realistic" global warming projections for the 21st century*. Geoscience Frontiers, 15 (2), 101774.

Svensmark, H., 2007: *Cosmoclimatology: A new theory emerges*. Astronomy & Geophysics, 48 (1), 1.18-11.24.

Tol, R. S., 2024: *A meta-analysis of the total economic impact of climate change*. Energy Policy, 185, 113922.

Vares, D. A., & Persinger, M. A., 2015: *Earth's diminishing magnetic dipole moment is driving global carbon dioxide levels and global warming*. International Journal of Geosciences, 6 (8), 846-852.

Von Storch, H., & Zwiers, F. W., 2002: *Statistical analysis in climate research*. Cambridge: Cambridge University Press.

Zhai, P., Zhou, B., & Chen, Y., 2018: *A review of climate change attribution studies*. Journal of Meteorological Research, 32 (5), 671-692.

Zwiers, F. W., & Von Storch, H., 2004: *On the role of statistics in climate research*. International Journal of Climatology: A Journal of the Royal Meteorological Society, 24 (6), 665-680.

Review Article

SCC Publishing
Michelets vei 8 B
1366 Lysaker Norway

ISSN: 2703-9072

Correspondence:
patrice.poyet.science@gmail.com

Vol. 5.3 (2025)
pp. 135-185

# Revisiting the Carbon Cycle

Camille Veyres[1], Jean-Claude Maurin[2], Patrice Poyet[3]

[1]Engineer, [2]Professor of Physics, [3]Docteur d'État ès Sciences

## Abstract

The stock-to-outflow ratio of $CO_2$ molecules in the atmosphere is about five years. Accordingly, only about 5.5% of the atmospheric $CO_2$ stock comes from fossil fuel emissions not yet absorbed by vegetation or oceans, while 94.5% originates from natural outgassing of oceans and soils. This interpretation is supported by the $\delta^{13}C$ record at Mauna Loa Observatory (MLO). The 50% increase in vegetation productivity since 1900 can be attributed to higher atmospheric $CO_2$ concentrations and a longer growing season. Decarbonization policies may therefore affect only 5.5% of atmospheric $CO_2$. Moreover, the strong month-by-month correlation, over nearly 800 months, between the increments of the $CO_2$ stock at MLO (altitude 3.4 km) and the sea-surface temperature (SST) anomaly in the inter-tropical zone shows that 94.5% of atmospheric $CO_2$ reflects the time-integrated effect of past surface temperatures, themselves determined by surface insolation. ARIMA time-series modeling further supports the correlation between 12-month increments of MLO $CO_2$ and SST. By contrast, there is no correlation ($R^2 = 0.01$) between the detrended 12-month $CO_2$ increments and fossil-fuel emissions. Simple models of carbon fluxes and stocks for the oceans, atmosphere, and vegetation & soils, assuming ocean degassing driven by inter-tropical SST, reproduce the observed time series atmospheric $CO_2$, $\delta^{13}C$ and vegetation productivity since 1900. In this context, IPCC theories and models based on concepts such as the Airborne Fraction, the Bern function, an adjustment time, the supposed persistence of 15–50% of fossil emissions in the atmosphere after 1000 years, a bottleneck between atmosphere and ocean, very low fluxes between surface and deep ocean, and Revelle's buffer factor, appear to be misleading constructs.

**Keywords:** Climate; $CO_2$; carbon cycle; ARIMA; ocean out-gassing; $^{13}C$; $^{14}C$; airborne fraction; Bern function; simple carbon cycle models

Submitted 2025-08-26, Accepted 2025-11-13. https://doi.org/10.53234/scc202510/10

## 1. Introduction

This contribution follows on from several important articles on the carbon cycle that have given rise to argumentative discussions (Salby & Harde, 2021a, 2021b, 2022a, 2022b; Berry, 2021; Harde, 2017, 2019; Köhler et al., 2018), after (Beenstock et al., 2012; Cawley, 2011; Essenhigh, 2009; Hocker, 2010; Pretis & Hendry, 2013). It incorporates results from (Campbell et al., 2017; Haverd et al., 2020; Koutsoyiannis, 2024a, 2024b; Lai et al., 2024; Levy et al., 2013; Segalstad, 1998) and of (Munshi, 2015, 2016a, 2016b, 2016c, 2017). A complete list of symbols and abbreviations used in this paper is provided in Appendix A.

## 2. Water, Carbon and Latent and Sensible Heat Cycles

Differences in insolation and temperature between the inter-tropical zone and the high latitudes result in the transfer of latent heat (evaporation, then condensation) and sensible heat (water, water vapor and $CO_2$) from the warm surface oceans to the cold surface oceans and to the continents, thanks to the turbulent motion of air and of surface oceans; the ocean is the main reservoir of water, of mobile carbon and of heat. The partial pressure of $CO_2$ in seawater varies as the power of 12.5 of the absolute temperature (in Kelvin) of this water (Sec. 8) and, for the same quantity of inorganic carbon per kg of seawater is, at 32°C, about 3.2 times greater than at 5°C. The contrast in sea surface temperatures means that there is an oceanic carbon degassing zone and an absorption zone separated by several thousand kilometers.

These out-gassing and absorption of the order of 100 Gt-C/yr between the atmosphere and the surface oceans are extensions of fluxes between the surface ocean and the deep ocean, as expressed by (Levy et al., 2013): "*We find that climatological physical fluxes of dissolved inorganic carbon (DIC) are two orders of magnitude larger than the other carbon fluxes and vary over the globe at smaller spatial scale. At temperate latitudes, the subduction of DIC and to a much lesser extent (< 10%) the sinking of particles maintain $CO_2$ undersaturation, whereas DIC is obducted back to the surface in the tropical band (75%) and Southern Ocean (25%). At the global scale, these two large counter-balancing fluxes of DIC amount to +275.5 Gt-C/yr for the supply by obduction and –264.5 Gt-C/yr for the removal by subduction which is 3 to 5 times larger than previous estimates*". These fluxes maintain the under-saturation or the supersaturation of surface seawater with respect to the air. These 275 Gt-C/yr have (finally!) been taken up by IPCC AR6 WG1, (Fig. 5.12, p. 700).

For a reservoir, as for a bank account, the inflow over 12 months equals the sum of the outflow and the change in the reservoir's content over that period. For atmospheric $CO_2$, the outflow is taken as one-fifth of the stock, consistent with the IPCC's estimate of a mean residence time of roughly 5 years (≈ 5 yr when the biospheric outflow is taken as NPP = GPP/2, versus ≈ 4 yr when using GPP, here GPP denotes gross primary production, i.e. total photosynthetic uptake before vegetation respiration): the natural degassing is therefore:

$$\text{degas}(t) = \frac{X(t)}{5\,yr} + \frac{\mathrm{d}X(t)}{\mathrm{d}t} - f_{\text{fossil}},\ \text{i.e. in ppm} \tag{1}$$

thus: 315/5 + 1 – 1 = 63 ppm/year in 1959 and 425/5 + 3.3 – 5 = 83.3 ppm/year in 2024. Over 66 years, +20.5 ppm/year for natural degassing versus +4 ppm/year for the inflow from fossil fuels; end 2024: 83.3 / (83.3 + 5) = 94.3% is the contribution of the natural degassing to the total inflow.

## 3. Tropical SSTs (20°S–20°N) Account for 83% of Post-1958 $CO_2$ Growth

The autotrophic respiration of plants is invisible from observatories at Mauna Loa (altitude 3397 m) or at South Pole (altitude 2837 m) far from any vegetation; at the surface on land 24-hour fluctuations in $CO_2$ air content of up to 100 ppm are common, e.g. in July in Luxembourg (Massen et al., 2005; Massen & Beck, 2011) with a diurnal minimum and a nocturnal maximum.

Table 1: The stock-to-outflow ratio, $X(t)$/absorb($t$), has been about five years since pre-industrial times.

| Carbon flows in Gt-C/year and atmospheric stocks in Gt-C | | | |
|---|---|---|---|
| | Pre-industrial | 1990 | 2024 |
| Absorption by ocean, i.e. $\text{absorb}_{\text{oce}}$ | 70 (IPCC, 2007) | 92 (IPCC, 2007) | 103 |
| Absorption by vegetation, i.e. $\text{absorb}_{\text{veg}}$ | 50 (Haverd et al., 2020) | 61 (IPCC, 2007) | 77 (Lai et al., 2024), 73 in 2016 (Haverd et al., 2020) |
| Atmospheric stock Gt-C (ppm in air), i.e. X(t) | 590 ? (278 ppm ?) | 754 (356 ppm) | 902 (425.3 ppm) |
| Stock-to-outflow ratio, i.e. $X(t)$ / absorb ($t$) | 4.9 years | 4.9 years | 5 years |

The area between 20°S and 20°N is three-quarters oceanic. Fig. 7.3.5 of (IPCC, 2007) for the year 1990 (360 ppm at MLO) and for the pre-industrial period suggests an average residence time of a $CO_2$ molecule in the atmosphere of about 5 years, i.e. a half-life of 3.5 years, since each year 20% of the $CO_2$ in the atmosphere is absorbed. IPCC (2001) §1.3 suggests a net carbon uptake by vegetation NPP (Net Primary Productivity) of the order of GPP/2, where GPP is Gross Primary Productivity. Haverd et al. (2020) estimate global GPP at 104 Gt-C/yr in 1900 and 146 Gt-C/yr in 2016, hence a "pre-industrial" NPP of 50 Gt-C/yr, 52 Gt-C/yr in 1900, 63 Gt-C/yr in 1990 and 73 Gt-C/yr in 2016, and according to Lai et al. (2024) 77 Gt-C/yr recently. These indications overlap with those of (Donohue et al., 2013; H. D. Graven et al., 2013; Nemani et al., 2003; Pretzsch et al., 2014; Zhu et al., 2016). Cawley (2011) adopts 5 years as did Essenhigh (2009) and Bolin (1960).

The total mass $X(t) = X_{\text{natural}}(t) + X_{\text{fossil}}(t)$ of carbon in the air, solution of $\mathrm{d}X(t)/\mathrm{d}t = f(t) - X(t)/5\text{yr}$, where $f(t)$ is the sum of the $f_{\text{fossil}}(t)$ in-flux from fossil fuels and of the $f_{\text{natural}}(t)$ in-flux from natural out-gassing by oceans and soils. This differential equation is linear, hence:

$$\frac{dX_{\text{fossil}}(t)}{\mathrm{d}t} = f_{\text{fossil}}(t) - \frac{X_{\text{fossil}}(t)}{5\ yr} \tag{2}$$

$$X_{\text{fossil}}(t) = \int_{t_0}^{t} e^{\frac{-(t-t')}{5\text{ yr}}} f_{\text{fossil}}(t')dt' \tag{3}$$

$$X_{\text{natural}}(t) = X(t) - X_{\text{fossil}}(t) \tag{4}$$

where $X(t)$ is based on $X_{\text{MLO}}$, series measured at the Mauna Loa Observatory since March 1958. Although $f_{\text{natural}}(t)$ is poorly known, $X_{\text{natural}}(t)$ is the difference between two precisely known quantities.

$f_{\text{fossil}}(t)$ comes from economic series: the CDIAC dataset (Boden et al., 2013) from 1751 to 2010 and, since 1965, the BP Statistical Review of World Energy (British Petroleum, annual editions) (with values increased by 5% to account for cement production), adjusted so as to coincide with the last 45 years of CDIAC. Emissions for a given year are dated to the middle of that year (e.g. emissions of the year 2020, recorded at date 2021.0, are to be dated 2020.5) or interpolated month by month between the dates 2020 and 2021. A +/– 5% seasonal modulation may be added (see carbonmonitor.org).

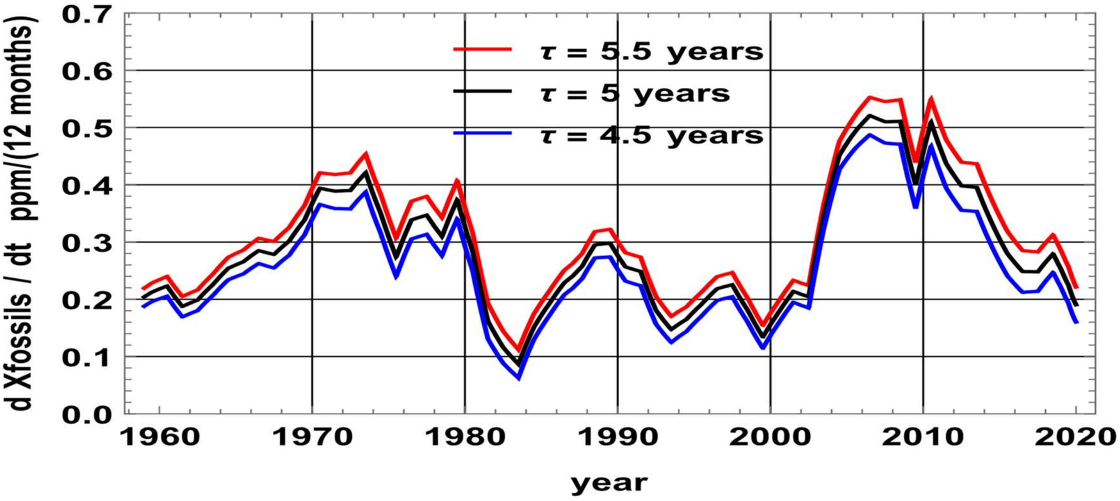

*Figure 1: Anthropogenic contribution* $\mathrm{d}X_{\text{fossil}}(t)/\mathrm{d}t$ *in ppm/yr to the annual atmospheric* $CO_2$ *increase computed for three residence times* $\tau$ *of the carbon dioxide in the atmosphere: 5.5 years, 5 years and 4.5 years.*

Figure 1 shows that carbon dioxide atmospheric residence times of 4.5 years or 5.5 years have almost no effect on the increments $\mathrm{d}X_{\text{fossil}}(t)/\mathrm{d}t$, which differ by less than 0.1 ppm / (12 months). Uncertainty over lifetime will therefore have little effect on the calculation of:

$$\frac{dX_{\text{natural}}(t)}{dt} = \frac{dX(t)}{dt} - \frac{dX_{\text{fossil}}(t)}{dt} \tag{5}$$

Figure 1 also shows the 1973-1974 crisis, the growth of natural gas in the 1980s and 1990s, and the growth of coal use in China and South-East Asia between 2000 and 2012; for the three lifetimes 5.5, 5 and 4.5 years, the 1959-2020 averages of $dX_{\text{fossil}}(t)/dt$ are 0.315 ppm/year, 0.287 ppm/year and 0.26 ppm/year.

To de-seasonalize the variations in atmospheric stock $X(t)$, we take 12-month increments centered in the middle of the 12 months: $dX(t)/dt$ is close to $X(t + 6$ months$) – X(t – 6$ months$)$. Figure 2 shows that the two stationary series MLO increments minus the fossil fuel stock increments (the black curve) and the blue curve[1] 3.17 (AT(t) + 0.25°C) where AT(t) is the sea surface temperature anomaly of the HadISST series between 20°S and 20°N correlate: between the dates 1958.7 and 2024.63, the correlation coefficient R of these series smoothed by a 3-month moving average is $R^2 = 0.795$, despite disturbances induced by several major volcanic eruptions (red curve in Figure 2) and a few mid-latitudes SST anomalies. Smoothing by a 12-month moving average yields $R^2 = 0.83$, but at the cost of losing some of the strength of the statistical test (Munshi, 2016c).

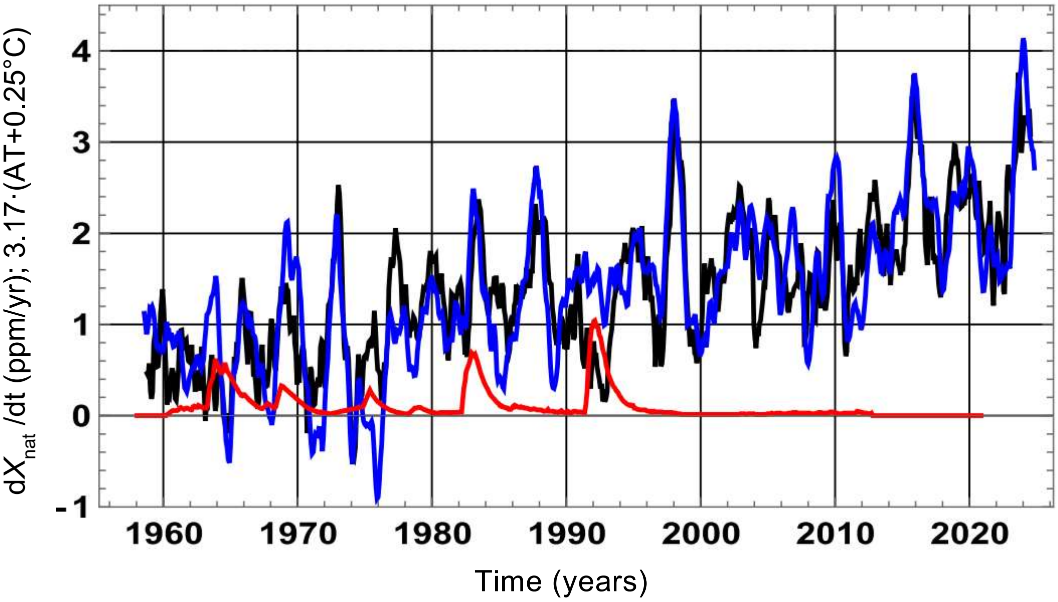

*Figure 2: Black curve: increments $X_{natural}(t + 6$ months$) – X_{natural}(t – 6$ months$)$ from the MLO series. Blue curve: 3.17 (AT(t) + 0.25°C) where AT(t) is the anomaly of the HadISST 20°S to 20°N series (Rayner et al., GRL), downloaded from knmi-climate explorer. The red curve shows 7× the stratospheric aerosol optical thickness at 550 nm, illustrating the cooling/insolation-reduction episodes associated with volcanic aerosols. Smoothing with a 3-month moving average has been applied. This figure independently confirms the relationship reported by Salby & Harde (2022a), i.e. see their Fig. 8.*

Between those dates $X_{\text{MLO}}$ went from 313.3 ppm to 422.9 ppm (+109.5 ppm), $X_{\text{fossil}}$ from 4.6 to 22.9 (+18.4 ppm), the sum of the monthly natural increments (the black curve) is 91.2 ppm, and the sum of the temperature effects (blue curve) is 91.7 ppm. Contributions to the total increase of $X_{\text{MLO}}$ are 16.7% (+18.4 ppm) for fossil fuel and 83.3%.for the Sea Surface Temperature controlled $X_{\text{natural}}$ increase.

With the whole HadISST series 1870 to end of 2024 the addition of the 1860 monthly increments

---

[1] This coefficient is the result of the ratio between the variation in the growth rate and the corresponding variation in temperature: 3.17 = Δ (increment over 12 months) / Δ temperature. An extended discussion of how the parameters of this type of equation are obtained is available in Maurin (2022), see Figure 3d.

given by: 3.17 ($AT_{SST}$ + 0.25°C) is 122.8 ppm, which added to the 280.2 ppm assumed at t = 1870 derived from a logistic approximation of observations at MLO:

$$X_{MLOlogis}(t) = 275 + \frac{555.7}{1 + e^{\frac{(2067-t)}{42.2\,yr}}} \quad \text{in ppm} \tag{6}$$

and to the 23 ppm from fossil fuels yields the 426 ppm observed at MLO at time 2025.0. The discrepancies between the blue and black curves of Figure 2 are small compared with the seasonal fluctuations, which at MLO are +9 ppm between September and April and –7 ppm from May to September.

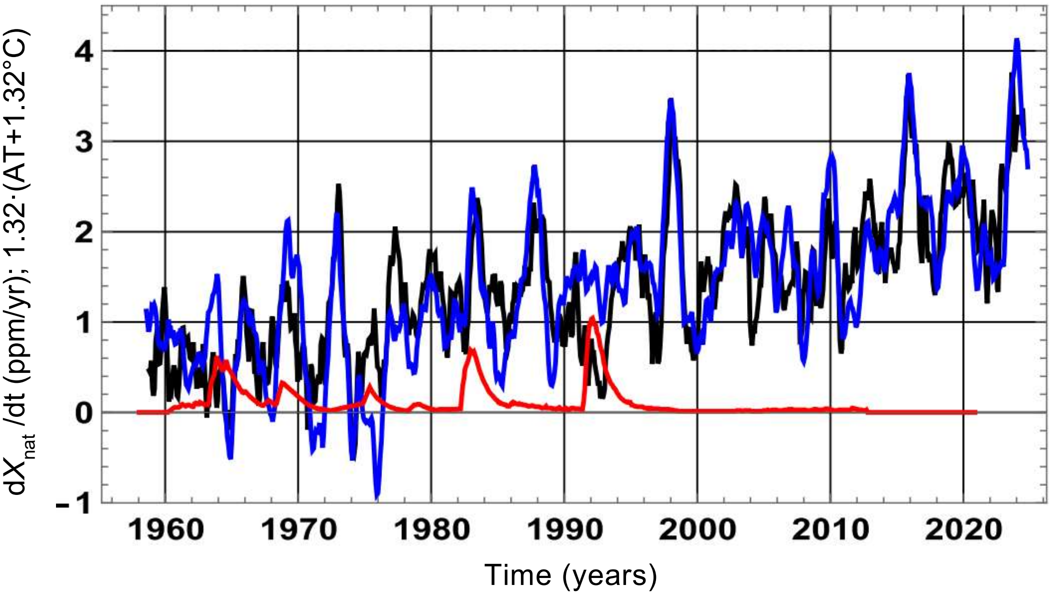

*Figure 3: As in Figure 2, but the blue curve here is 1.321 (AT(t) + 1.318°C), with AT(t) anomaly of the temperatures in the lower inter-tropical troposphere UAH MSU series starting in December 1978. No smoothing applied.*

With the UAH (University of Alabama in Huntsville) MSU (Microwave Sounding Unit) lower-troposphere temperature anomaly series for the inter-tropical band (20° S–20° N) (Spencer et al., 2017) UAH Version 6.0, shown here un-smoothed in Figure 3 , the correlation coefficient is $R^2$ = 0.66 and $R^2$ = 0.75 with a 4-month moving average. See also (Hocker, 2010). Between 1978.9 and 2024.0, the integral of the blue curve gives 77.3 ppm, added to the +12.6 ppm increase in the anthropogenic stock, is 89.9 ppm, close to the +90.5 ppm observed at MLO.

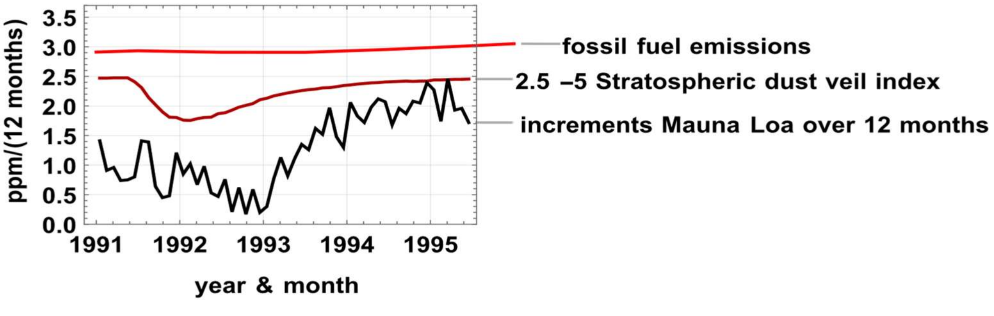

*Figure 4: Top red curve: $f_{fossil}(t)$ emissions in ppm/year. Bister (brownish) curve: 2 – 5 × stratospheric dust veil index. Black curve: ppm increments at MLO: 0.5 ppm/(12 months) during the 9 months centred on October 1992 and 2.2 ppm/(12 months) during the 9 months centred on October 1994.*

Figure 4 underlines the role of sea surface temperatures: from 1991 to end 1995, anthropogenic emissions were constant, but the 12-month increments of $X_{\mathrm{MLO}}(t)$ were 0.48 ppm/(12 months) over the 9 months centered on October 1992 (the eruption of Mount Pinatubo occurred in 1991), four times less than the 2.1 ppm/(12 months) over the 9 months centered on October 1994, after the end of the cooling brought by volcanic dust, which may have reduced inter-tropical outgassing and increased mid-latitude absorption.

## 4. No Correlation Between Anthropogenic Emissions and *X*(*t*) Increments

$f_{\mathrm{fossil}}(t)$ may be approximated by $f_{\mathrm{logis}}(t)$ = 17.92 Gt-C/yr / (1 + exp((2011–t)/29 yr)) and over 1950-2024 by $f_{\mathrm{fossil\ linear}}$(t) = 1.39 Gt-C/yr + 0.118 (–1950+ $t$) = 0.1183 ($t$ – 1938.23) Gt-C/yr, that is a linear trend $b$ = +0.056 ppm/yr. With linearly increasing emissions $b\ (t - t_0)$, a residence time of $\tau$ = 5 years for $CO_2$ molecules, $t - t_0$ large enough for $X(t_0)\exp(-(t-t_0)/\tau)$ to be negligible, $X_{\mathrm{fossil}}(t)$ is:

$$\int_{t_0}^{t} b\,(t'-t_0)\,e^{\frac{-(t-t')}{\tau}}\,\mathrm{d}t' = \tau\cdot b\left(t-t_0-\tau+\tau\cdot e^{\frac{-(t-t_0)}{\tau}}\right)\approx \tau\cdot b\cdot(t-t_0-\tau) \qquad (7)$$

The increment $X_{\mathrm{fossil}}(t) - X_{\mathrm{fossil}}(t\text{–}1)$ is $\tau \cdot b$ = 5 yr · 0.056 ppm/yr = 0.28 ppm or 0.59 Gt-C, this is the difference between the emissions of year $t$ and those of year $t$ – 5 yr.

The grey curve in Figure 5 shows the 12-month increments of $X_{\mathrm{MLO}}(t)$ observed since 1958; their average after 1995 is + 2.2 ppm/year, 7.9 times the + 0.28 ppm/year growth of the stock from fuels (average of the lower black curve of Figure 5).

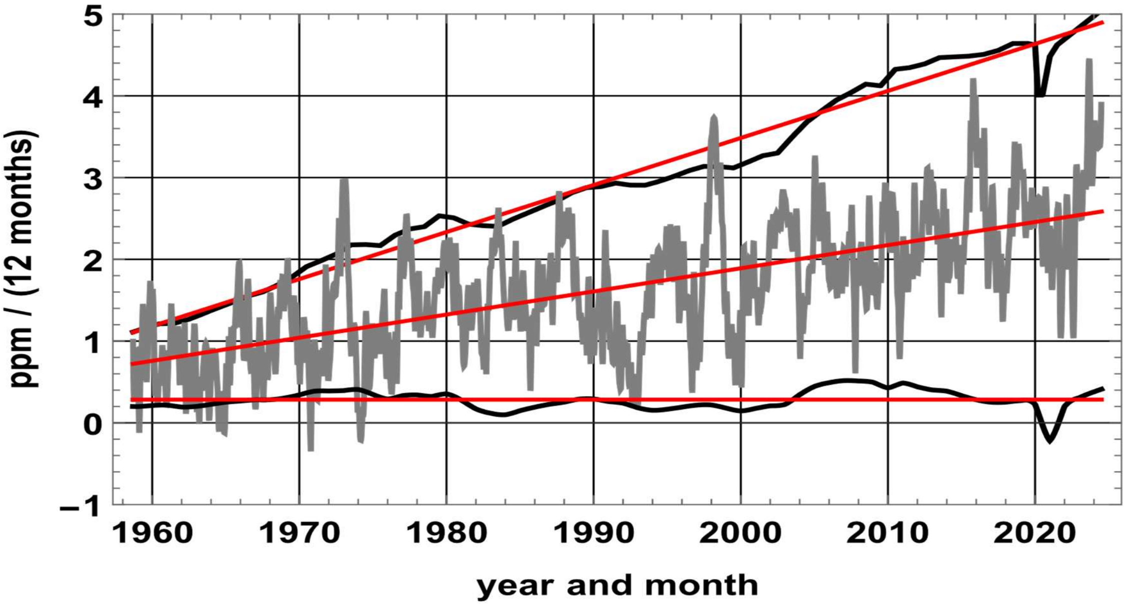

*Figure 5: From top to bottom, in ppm/(12 months): series of emissions from fossil fuels and cement plants (in black, an in-flow), series of ppm increments at MLO (in grey) and in black at bottom the time series of atmospheric stock increments $dX_{fossil}(t)/dt$ from fossil fuels and cement plants; the red lines are the linear trends in ppm with t=date: emissions from fossil fuels and cement plants = 0.0575 (t – 1939.45); increases in ppm at MLO = 2.57 – 0.028 (2024 – t); increases in atmospheric stocks dXfossil(t)/dt =0.283 + 0.000013 (t – 1959).*

A correlation can be sought only between weakly stationary series; to make a series stationary it may be derived with respect to time or its linear trend may be subtracted (Munshi, 2015, 2017; Podobnik & Stanley, 2008); Figure 6 shows the non-correlation between the series of the increments of annual averages of $X(t)$ and the series $f_{\mathrm{fossil}}(t)$ after subtraction from each series of its linear trend: the coefficient of determination $R^2$ is 0.026!

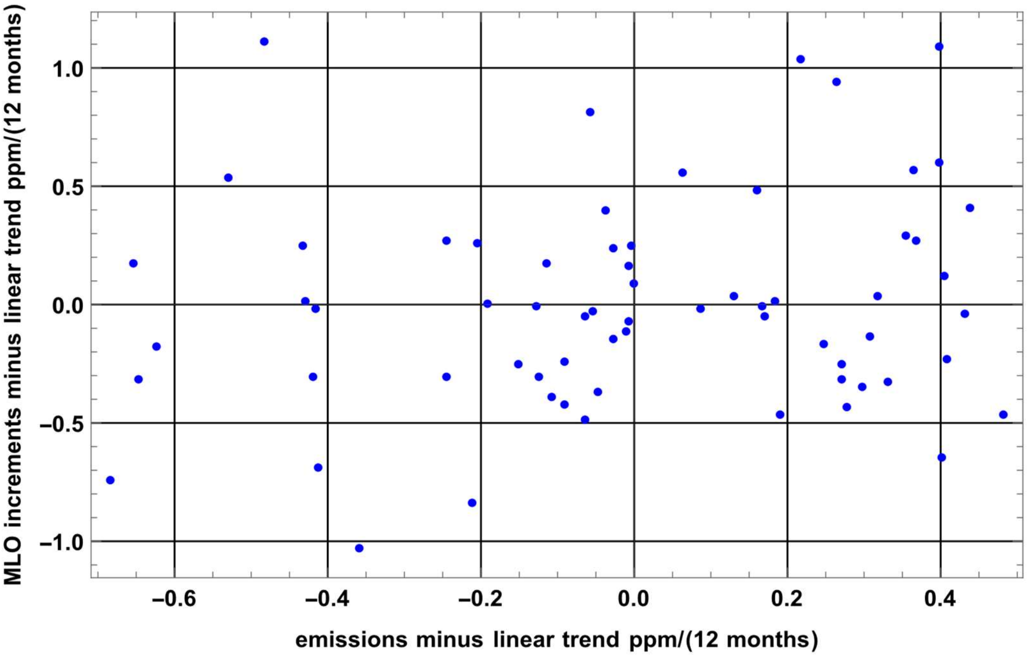

*Figure 6: Correlation between the year-on-year increments of the annual means at MLO (vertical axis) and the annual emissions $f_{fossil}(t)$ (horizontal axis), on series made stationary by subtracting their linear trend (detrended series). Coefficient of determination $R^2 = 0.026$.*

Munshi (2017) has shown that even with moving averages taken over 1, 2, 3, 4 and 5 years, the atmospheric $CO_2$ concentration is unresponsive to fossil fuel emissions. This is supported by the autocorrelations of the three series (Figure 7) fossil fuel emissions, increments $X_{\mathrm{MLO}}(t + 6 \text{ months}) - X_{\mathrm{MLO}}(t - 6 \text{ months})$ and inter-tropical sea surface temperatures anomaly.

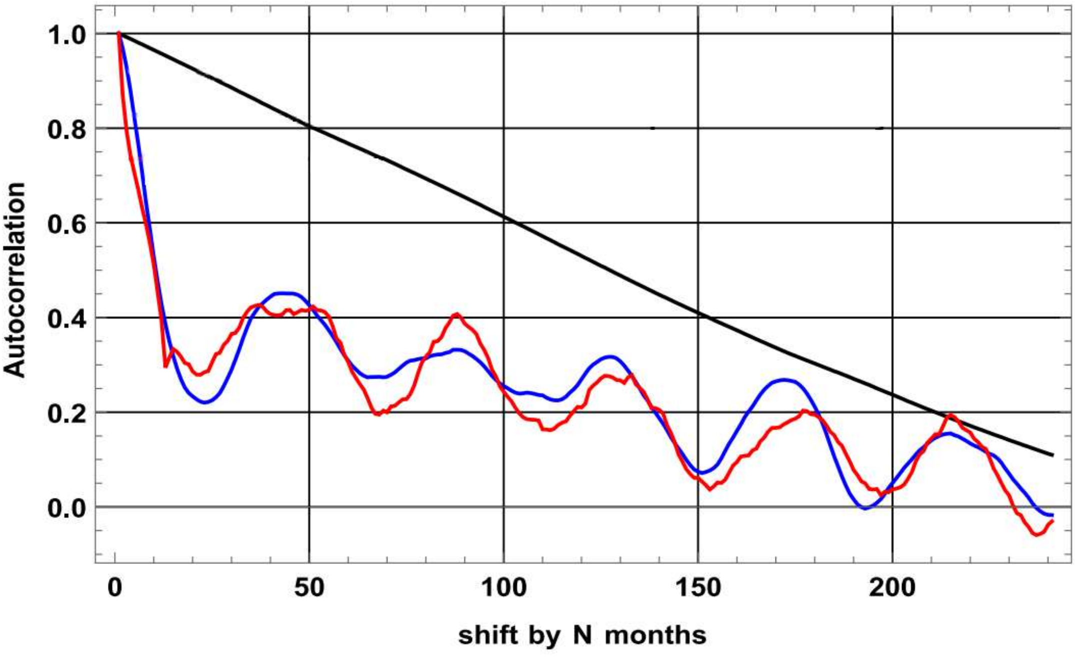

*Figure 7: Autocorrelations of the three time series: fossil fuel emissions (black curve), sea surface temperature anomaly of the inter-tropical degassing zone (blue curve) and ppm increments at MLO (red curve) X(t + 6 months) – X(t – 6 months).*

The uncertainties of the natural carbon fluxes (Table 1) are of the same order of magnitude as the fossil-fuel emissions. This alone should invite caution in drawing firm conclusions about the partitioning of sources and sinks. In addition, some budget closures, such as the balanced flux diagram in (IPCC, 2013) Fig. 6.1, rely on inferred fluxes that are adjusted to satisfy mass balance. It introduces a logical circularity[2], since the agreement is partly imposed rather than independently demonstrated. Thus, because the IPCC budget relies in part on inferred fluxes that are adjusted to close the mass balance, the resulting equilibrium is imposed by construction. As a consequence, the reported carbon budget does not independently demonstrate the underlying dynamics.

## 5. ARIMA Time Series : $X(t)$, $\Delta X(t)$, $f_{fossil}(t)$, SST Anomalies

### *5.1 ARIMA Time Series*

Understanding the dynamics of atmospheric $CO_2$ requires methods capable of distinguishing genuine causal structure from spurious correlations in trending data. In climatological and geophysical time series, non-stationarity and autocorrelation can easily produce misleading statistical relationships if not properly treated. Standard tools from econometrics and signal processing, including differencing, autocorrelation modeling, and ARIMA[3] (Autoregressive Integrated Moving Average) processes, are therefore essential for rigorous analysis of $CO_2$ records. These techniques explicitly account for persistence, serial dependence, and stochastic variability, ensuring that apparent associations are not artifacts of trend and memory in the data. Techniques for avoiding false correlations and for modeling time series are well known[4] e.g. (Maddala & Kim, 1998; Wolfram Research, 2012) and (Box et al., 2016).

Monthly $CO_2$ ppm series at MLO and SPO are ARIMA, I = 1. Modeling gives for SPO:

ARIMAProcess[0.109, {0.472, 0.079, 0.020, –0.126, –0.162, –0.177}, 1,{–0.478}, 0.042].

The equation for SPO is:

$(1 - L_1)\,(1 - 0.472\, L_1 - 0.079\, L_2 - 0.02\, L_3 + 0.126\, L_4 + 0.162\, L_5 + 0.177\, L_6)\, X(n) = 0.109 + e(n) - 0.478\, e(n-1)$

with Lm the shift operator by m months, $L(m)\, X(n) = X(n-m)$, e(n) a white noise of variance 0.042

Modeling gives for MLO:

ARIMAProcess[0.101, {0.772, –0.155, –0.219, –0.0248, –0.0129, –0.177}, 1, {–0.534}, 0.652]

Figure 8-a shows in blue and black the $X(t)$ series observed at MLO and SPO and their extensions, and as a curiosity, random draws in orange and red starting at the last historical point. Note that the increments $(1 - L_1)\, X(n) = X(n) - X(n-1)$ are ARMA stationary series.

Modeling MLO and SPO data as SARIMA, I=1, with seasonal variations gives for SPO:
$(1-L_1)\,(1-L_{12})\, X(n) = 0.00096 + (1 - 0.222\, L_{12})\, e(n)$, e(n) of variance 0.057 and a close equivalent for MLO: those random walks are plotted in Figure 8-b with blue and black forecasts and illustrative, non-significant random draws starting at the last historical point.

---

[2] When a system of fluxes is adjusted so that inflows and outflows balance by definition, the resulting "closure" does not constitute independent empirical verification. It reflects a *tautology*: the conclusion (balanced fluxes) is embedded in the premise (fluxes are inferred and adjusted to balance). This corresponds to the classical logical fallacy *petitio principii*, assuming what one seeks to prove. True empirical validation requires that mass balance emerge from independently measured fluxes and stocks, rather than from parameters tuned so that the balance necessarily holds.

[3] The ARIMA framework (Box et al., 2016) generalizes autoregressive and moving-average models to non-stationary series via differencing. It is a standard tool in econometrics and geophysical data analysis to separate signal from trend-driven pseudo-correlation.

[4] An introduction is given here: https://en.wikipedia.org/wiki/Autoregressive_integrated_moving_average

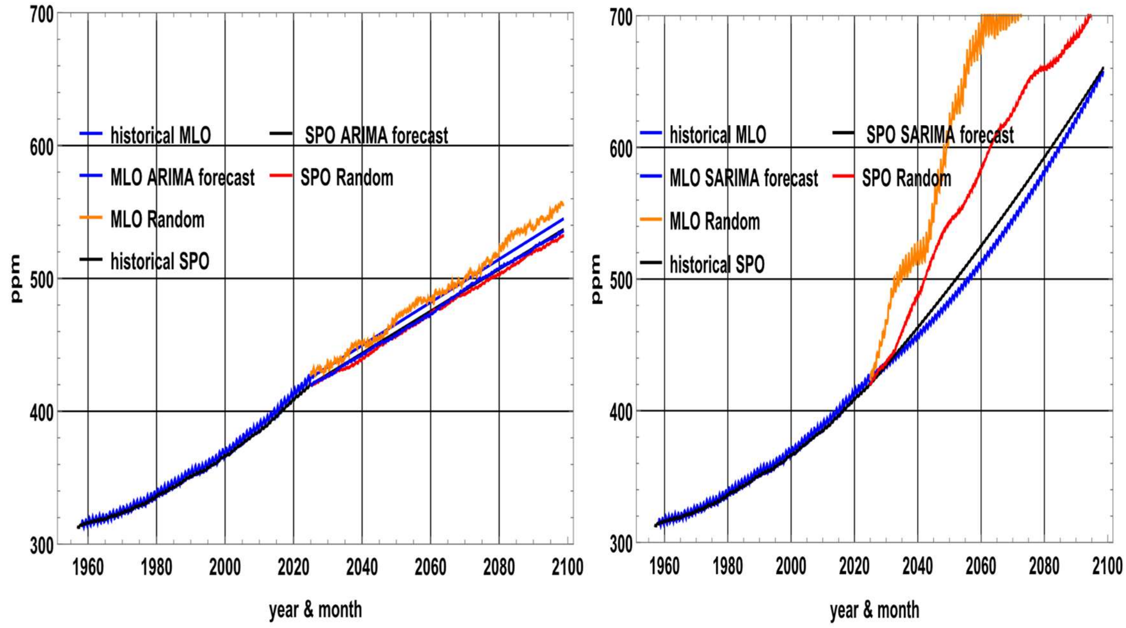

*Figure 8 a-b: Historical time series, forecasts and illustrative random draws of no predictive value. a) left: X(t) series at MLO and SPO as ARIMA I=1; b) right: ditto as SARIMA I=1 with seasonal variations.*

The series of increments $X(t + 6\text{ months}) - X(t - 6\text{ months})$ at MLO plotted on Figure 9-a is an autoregressive stationary moving average process ARMAProcess[0.214, {0.525, 0.346}, {0.255},0.162] that is $(1 - 0.525\, L_1 - 0.346\, L_2)\, X(n) = 0.214 + e(n) + 0.255\, e(n-1)$; the blue line forecast is the average of historical values; illustrative random draw is in orange.

Plotted in Figure 9-b are the annual emissions $f_{\text{fossil}}(t)$ since 1958; they are an I = 1, ARIMAProcess[0.124, {}, 1,{}, 0.0262] with e(n) of variance 0.026, $(1 - L_1)\, X(n) = 0.124 + e(n)$; plotted are a forecast, illustrative random draws from the last historical point and a logistic approximation of the series of emissions.

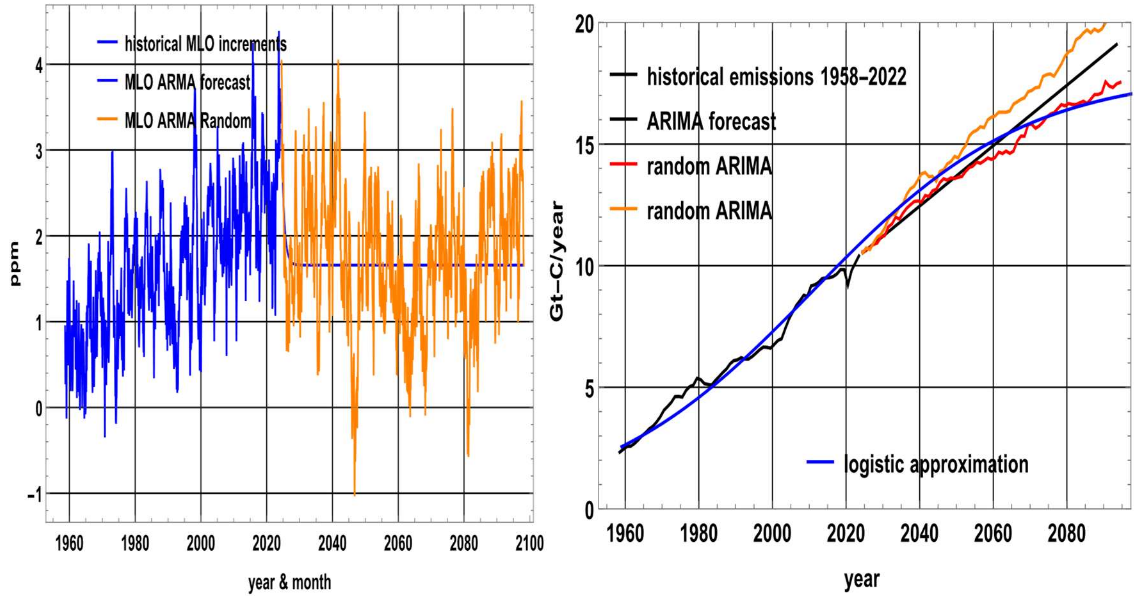

*Figure 9 a-b: Historical time series, forecasts and illustrative random draws of no predictive value. a) left: series of the X(t) increments at MLO as ARMA; b) right: series of fossil fuel and cement emissions since 1958 (I=1) as ARIMA I=1 and a logistic approximation of the historical series.*

The sea surface temperature (SST) anomaly between 20°S and 20°N (Figure 10-a since 1958 and 10-b since 1870, blue curve) is, since 1958 an ARMAProcess[–0.0, {0.971}, {–0.072, 0.051}, 0.0053] with a strong correlation from one month to the previous month but is not a random walk. $AT_{SST}(n) = 0.971\ AT_{SST}(n-1) + e(n) - 0.072\ e(n-1) + 0.051\ e(n-2)$ with e(n) variance 0.0053.

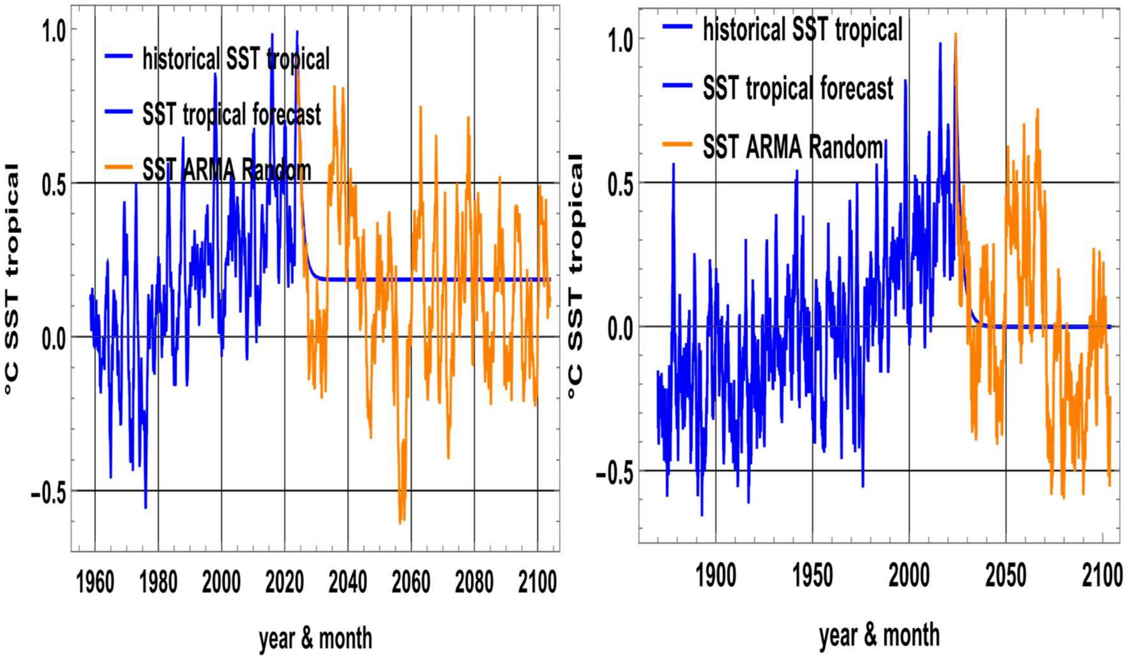

*Figure 10 a-b: a) left: $AT_{SST}$ temperature series as ARMA since mid-1958 with its "best forecast" (blue line) and illustrative random draws of no predictive value; b) right: $AT_{SST}$ ARMA series since 1870 with best forecast (blue line) and illustrative random draws of no predictive value.*

These exercises also show that the stationary series of $CO_2$ ppm increments (ARMA Figure 9-a) can be correlated with the stationary series of inter-tropical sea surface temperatures (Figure 2 and Figures 10-a-b) or with the inter-tropical lower troposphere temperature series (Figure 3), but not with the ARIMA I=1 series of fuel emissions (Figure 9-b) which must be detrended before a correlation with the stationary ARMA $AT_{SST}$ anomaly series can be tested (Figure 6).

If the ppm increments at MLO were proportional to fossil fuel emissions, which are ARIMA with I = 1, then the sum of these increments, i.e. the ppm series, should be ARIMA with I = 2; but it is I =1 as seen on Figure 8-a. **The Airborne Fraction conjecture is therefore false**.

### *5.2 Conclusions*

The equations:

$$\frac{\mathrm{d}X_{\mathrm{fossil}}(t)}{\mathrm{d}t} + \frac{X_{\mathrm{fossil}}(t)}{5\ yr} = f_{\mathrm{fossil}}(t) \tag{8}$$

$$\frac{\mathrm{d}X_{\mathrm{natural}}(t)}{\mathrm{d}t} = 3.17\ \mathrm{ppm/yr^2}(\mathrm{AT_{SST}}(t) + 0.25°\mathrm{C}) \tag{9}$$

$$X(t) = X_{\mathrm{natural}}(t) + X_{\mathrm{fossil}}(t) \tag{10}$$

reproduce the values observed at MLO. The computed and observed series since 1870 (the start of the temperature series) are plotted Figure 11. Taking into account the surface temperature series of the southern seas between 45°S and 60°S improves slightly the restitution of the observations.

*X*(*t*) in the atmosphere is therefore essentially the integral over the time of past inter-tropical temperatures, a consequence of these temperatures. Same conclusion was drawn by Salby & Harde (2022a).

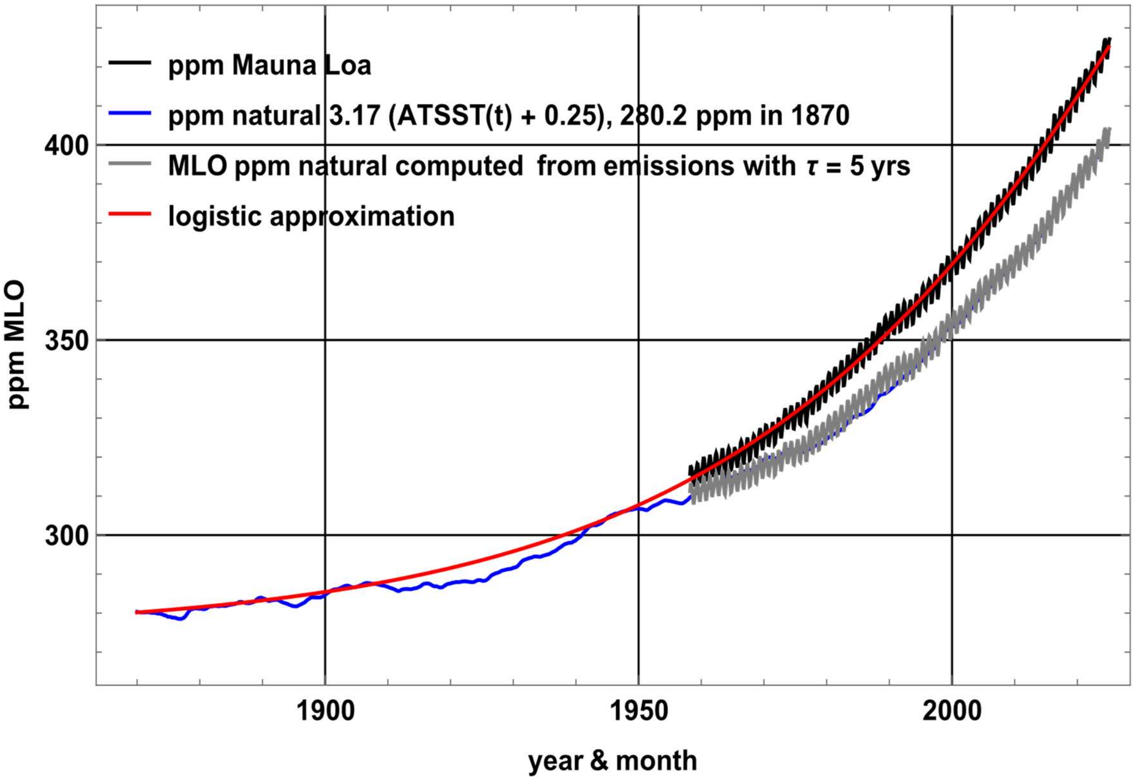

*Figure 11: Comparison of MLO observations and of their logistic approximation (red curve) with the values (in blue) computed with the inter-tropical temperature series $AT_{SST}(t)$ and with $f_{fossil}(t)$ since 1870.*

## 5.3 Some Misleading Tricks

### 5.3.1 Accumulations of Generally Positive Quantities

Two time series whose terms are accumulations of generally positive quantities always appear "visually" well correlated, even if these quantities are random. The effective sample size is reduced by the reuse of numbers, since the first number x1 is used n–1 times, x2 is used n–2 times...and the DF degrees of freedom become meaningless.

Let's quote Munshi (2016c): *"Therefore although strong correlation and regression coefficients can be computed from the time series of cumulative values, these statistics have no interpretation because they are illusory."* and *"Empirical evidence of the causal chain that links fossil fuel emissions to rising atmospheric $CO_2$ and a warming trend consists primarily of correlations between cumulative values (Kheshgi, 2005) (Canadell, 2007) (Botzen, 2008) (Brovkin, 2004) (Meinshausen, 2009) (Matthews, 2009) (Solomon, 2009) (Anderson, 2011) (Arora, 2011) (IPCC, 2007) (IPCC, 2014). However, this line of evidence is weakened by the spuriousness of correlations between cumulative values".*

Cumulative positive quantities can be seen, for example, in Fig. SPM. 10 (IPCC, 2021, p. 28), which claims that temperature is proportional to cumulative emissions (the starting point of this SPM 10 figure is probably 1876). Figure 12-a shows the HadCRUT4 series of monthly global temperature anomalies since 1850 (anomaly, i.e. in deviation from the mean of the same month taken over 1850-2025.0) versus cumulative emissions from fuels (horizontal axis), $R^2 = 0.86$.

This is a delusion: no correlation is possible between the emissions (not their cumulative values) and the annual temperature increments plotted in Figure 12-b right, $R^2 = 0.038$!

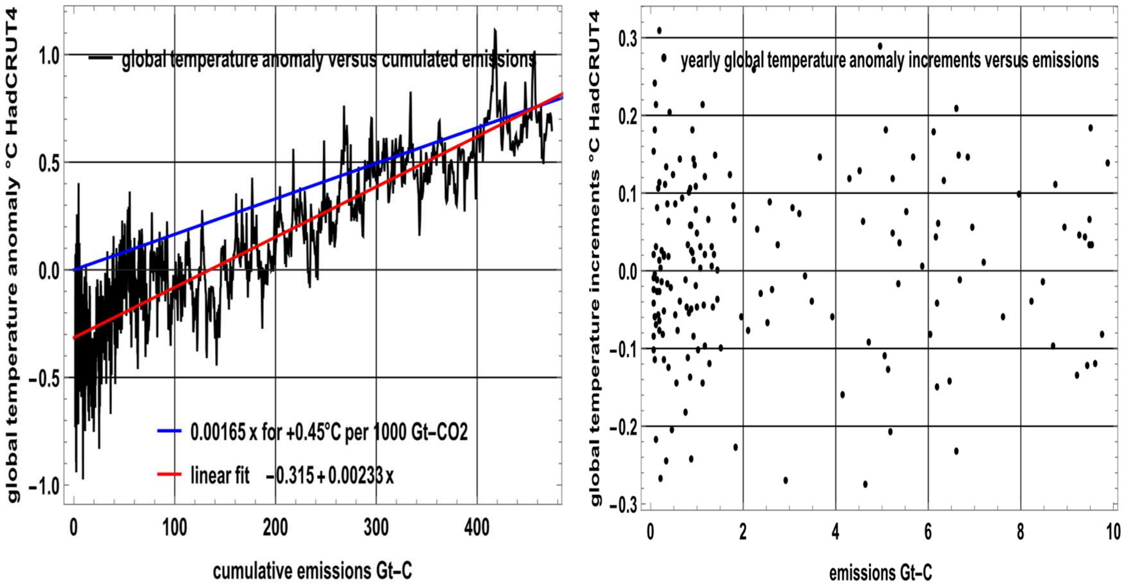

*Figure 12 a-b: a) left: On the ordinate, a monthly global temperature anomaly HadCRUT4 since 1850, and on the abscissa, cumulative $f_{fossil}(t)$ emissions from oil, coal and gas and cement plants at the date of the temperature anomaly; the blue line shows the IPCC formula in Fig. SPM10. AR6 (IPCC, 2021): +0.45°C/1000 Gt-$CO_2$ (i.e. +2°C compared with the average over 1850-2024 for a cumulative 1212 Gt-C); the red line is a linear fit 0.00233 × – 0.315: it is 0°C in 1974.8 for a cumulative 135 Gt-C and +2°C for 991 Gt-C; b) right: Increments of the HadCRUT4 annual mean global temperature series (y-axis) and yearly emissions (x-axis): R = 0.038, i.e. no correlation.*

Note in the IPCC accounting the importance of the LUC use (Land Use Changes), which before 1955 were far greater than the fossil fuel emissions (Figure 13-a), and of the choice of a starting date to give the impression of a "visual correlation": Figure 13-b begins in 1880 and looks better than Figure 12-a. Figures 12-a and 13-b are deceptive: a valid correlation can only be sought between the increments themselves (i.e. Figure 12-b), not between the cumulative values of the increments (Figures 12-a and 13-b)!

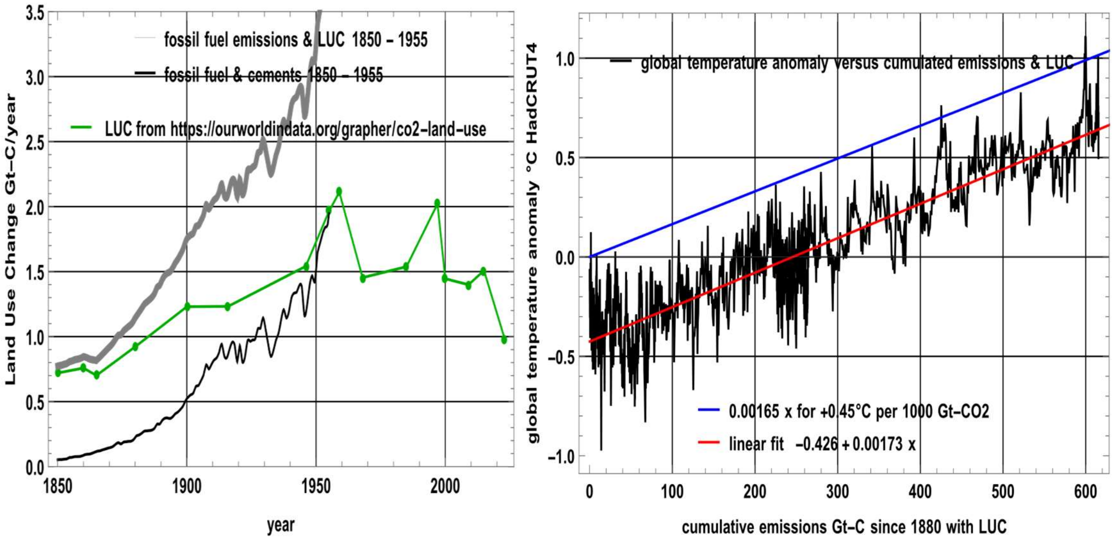

*Figure 13 a-b: a) left: Comparison of a series of LUC (green curve) with $f_{fossil}(t)$ (bottom black curve) before 1955; the top grey curve is the sum of LUC(t) + $f_{fossil}(t)$ used by the IPCC; b) right: As Figure 12-a but starting in 1880 (to hide the positive temperature anomalies seen at the beginning of the series such as +0.07°C in December 1852 on Figure 12-a, and with the addition of LUC to $f_{fossil}(t)$; the red linear fit is close to the blue (IPCC, 2021) +0.45°C for cumulative emissions of 1000 Gt-$CO_2$.*

### *5.3.2 Abusive Use of Smoothing by Moving Averages*

Two straight lines seem perfectly correlated (but that makes no statistical sense!), hence the use of moving averages over several years to give an air of visual verisimilitude to a non-existent causality, to find for example in (Hansen et al., 2013) an "Airborne Fraction" of emissions that would have remained perpetually in the air and accounted for all the growth in atmospheric $CO_2$ since pre-industrial times. The effective number of Degrees of Freedom (DF), for a series of length $n$ smoothed by a moving window of length $w$ becomes[5]:

$$\mathrm{DF} = \frac{n^2}{(n-w+1)w} - k \tag{11}$$

For a 60-year monthly series $n = 720$ and $w = 60$ (as often used for the Airborne Fraction), DF = 11 instead of 718. Beenstock et al. (2012) argued that regressions of global mean temperature on the logarithm of anthropogenic forcings lack statistical significance. For a discussion and subsequent exchange with Pretis & Hendry (2013), see Beenstock et al. (2013).

## 6. Carbon Cycle Calculations with Three Compartments

### *6.1 Stocks and Fluxes*

Stocker et al. (2013) i.e. (IPCC, 2013) state that carbon stocks and fluxes are known with uncertainties on the order of ~20% or more. Let us assume the following carbon stocks: approximately 38,000 Gt-C in the oceans and about 2,400 Gt-C in vegetation and soils in 1995. We further assume that the annual fluxes to the atmosphere are proportional to these pools, with magnitudes equal to a fraction $1/\tau_{oc}(t)$ of the ocean reservoir and $1/\tau_{tb}$ of the terrestrial biosphere reservoir (i.e. vegetation and soils). To remain consistent with the flux values reported in Fig. 2.1 of IPCC (1995) AR2, we take $\tau_{tb} = 40$ years, since 2400/40 = 60 Gt-C $\mathrm{yr}^{-1}$, and $\tau_{oc}(1995) = 413$ years, since $38000/413 \approx 92$ Gt-C $\mathrm{yr}^{-1}$.

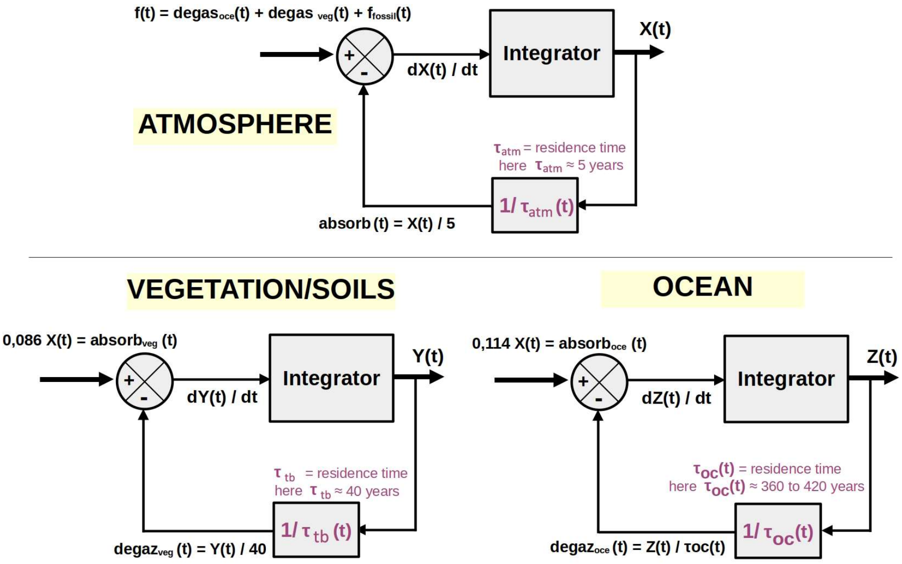

*Figure 14: Diagram of exchanges between reservoirs with four flows expressed as a fraction of the stock of the transferring reservoir.*

---

[5] The main term $n^2 / [(n - w + 1)\, w]$ gives the effective number of independent values after moving average smoothing. The "$-\, k$" corrects for parameters estimated from the series (typically $k = 1$ or 2). Thus $k$ is the number of fitted parameters (e.g. mean or trend).

Furthermore, to align with Haverd et al. (2020), we assume that annual fluxes from the atmosphere to the ocean and to vegetation correspond to 11.4% and 8.6% of the atmospheric carbon stock, respectively (see observations in Figure 17).

Hence three coupled differential equations with given initial values $X(t_0)$, $Y(t_0)$, $Z(t_0)$:

$$\begin{aligned} X'^{(t)} &= \frac{-X(t)}{\tau_{\mathrm{atm}}(t)} + \frac{Y(t)}{\tau_{\mathrm{tb}}(t)} + \frac{Z(t)}{\tau_{\mathrm{oc}}(t)} + f_{\mathrm{fossil}}(t) \\ Y'^{(t)} &= \frac{-Y(t)}{\tau_{\mathrm{tb}}(t)} + 0.086\, X(t) \\ Z'^{(t)} &= \frac{-Z(t)}{\tau_{\mathrm{oc}}(t)} + 0.114\, X(t) \end{aligned} \tag{12}$$

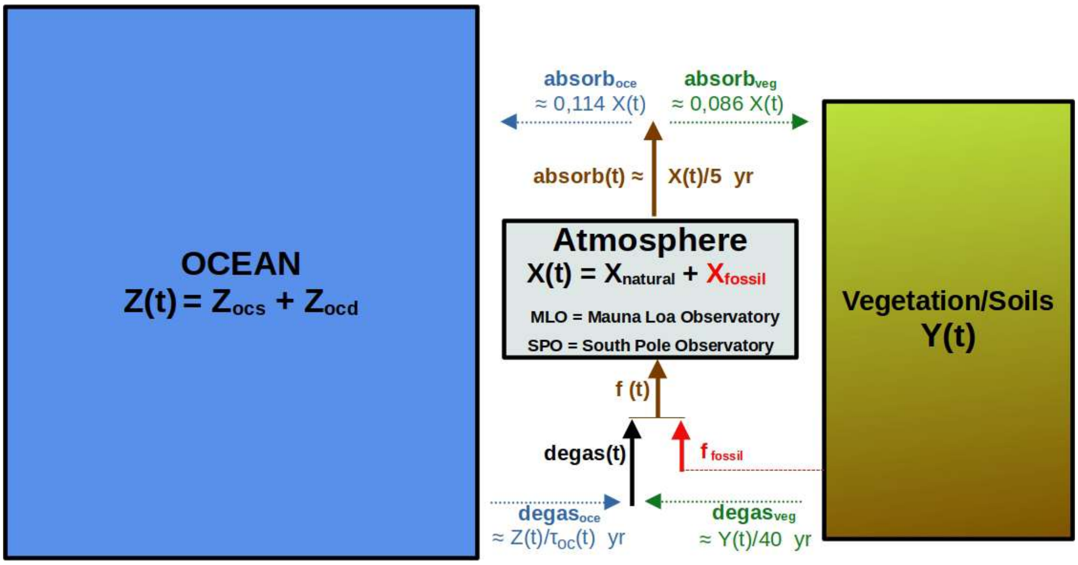

*Figure 15: Exchanges governed by the three coupled differential equations (12), corresponding to the diagram in Figure 14. All notation is defined in Appendix A.*

The exchanges of 275 Gt-C/year between the surface ocean and the deep oceans quoted in Sec. 2 above mean that the well mixed first 100 meters of the ocean is not separated from the rest of the ocean. Figure 16 shows what happens to a unit pulse of carbon into air at time $t_0 = 0$ ($f_{\mathrm{fossil}}(t) = 0$ for $t > 0$, $X(0) = 1$, $Y(0) = Z(0) = 0$) for $\tau_{\mathrm{oc}}(\mathrm{t}) = 360$ years: the black curve decreases as $\exp(-t/\tau_{\mathrm{atm}})$ during the first 10 years and tends towards 2.1% after 200 years, as the unit pulse of carbon is finally distributed between the three compartments in proportion to their masses, i.e. for the atmosphere: 875 / (875 + 2500 + 38000) = 2.1%. The black curve represents the mass of carbon that remains in the atmosphere, or returns to it after temporary residence in the other two reservoirs. It is well approximated by the impulse response[6]:

$$F1(t) = 0.021 + 0.928 \exp(-t\,/4.73\ \mathrm{yr}) + 0.0416 \exp(-t\,/70.46\ \mathrm{yr})$$

with F1(30) = 5%, F1(100) = 3.1%. *F1*($t$) is very different from Bern's impulse response of (IPCC, 2007) i.e. AR4 WG1 p. 213 note a)

---

[6] The black curve of Figure 16 takes into account anthropogenic $CO_2$ molecules that return to the atmosphere ("zombie" molecules after passing through the ocean and vegetation /soil compartments). If we did not take into account this return of 'zombie' molecules, we would have a simple decay in exp ($-t$/5yr). During the first 10 years, this return of 'zombie' molecules is negligible: we are close to exp($-t$/5yr). *F1*($t$) approximates this behavior: 4.73 years mainly concerns non-zombie molecules and 70.46 years concerns 'zombie' molecules (a mixture of $\tau_{\mathrm{tb}}$ =40 years for vegetation / soil and $\tau_{\mathrm{oc}}$= 360 years for the ocean).

$$FB(t) = 0.217 + 0.186\exp(-t/1.186\text{yr}) + 0.338\exp(-t/18.57\text{yr}) + 0.259\exp(-t/172.9\text{yr})$$

(red curve on Figure 16). The "vegetation & soils" compartment, shown in green on Figure 16, rapidly absorbs a part of the carbon pulse from the air, peaks at 34% at t = 14.4 years, before releasing its carbon: it still contains 9.2% of the initial pulse at t = 200 years and 6% in the long term. The “ocean” compartment, shown in blue in Figure 16, absorbs part of the carbon pulse present in the air even faster, then absorbs the excess carbon from vegetation & soils: it contains 92% of the carbon in the long term.

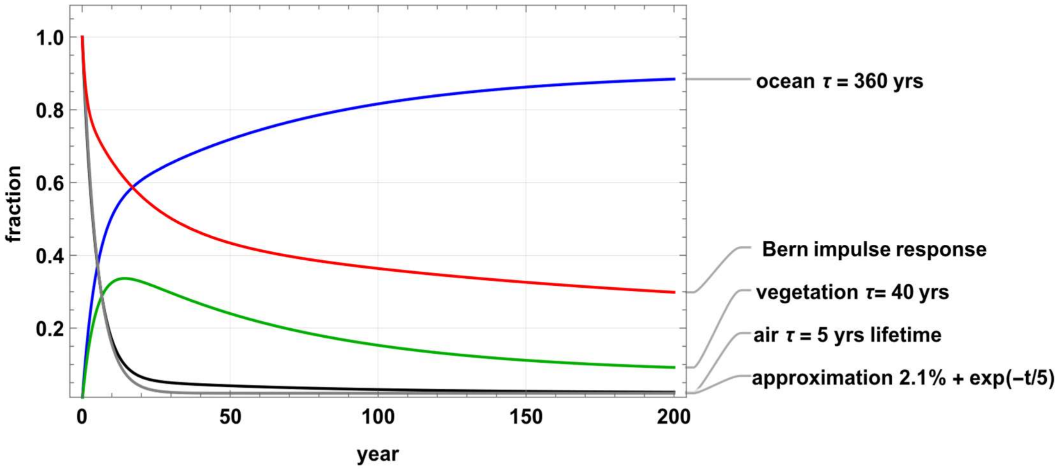

*Figure 16: Distribution between the three compartments of a unit pulse of carbon into the atmosphere at time t = 0. The black F1(t) curve and the grey 2.1% + exp(–t/$\tau_{atm}$) curve differ by at most 2.7%.*

The net flux absorbed by vegetation, its Net Primary Productivity NPP($t$) net of respiration is about GPP/2 (see Table 1); in Figure 17, the green curve from (Haverd et al., 2020) is the GPP over 1900 – 2016 extended with the indications of (Lai et al., 2024); this GPP is close to twice the 8.6% of $X(t)$ at MLO extended before 1959 by $X_{\text{MLOlogis}}(t)$ of equation (6). This justifies the parameters used in Figure 14: 0,086 $X(t)$ = absorb$_{\text{veg}}$(t) and (0,2 – 0,086) $X(t)$ = 0,0114 $X(t)$ = absorb$_{\text{oce}}$ (t).

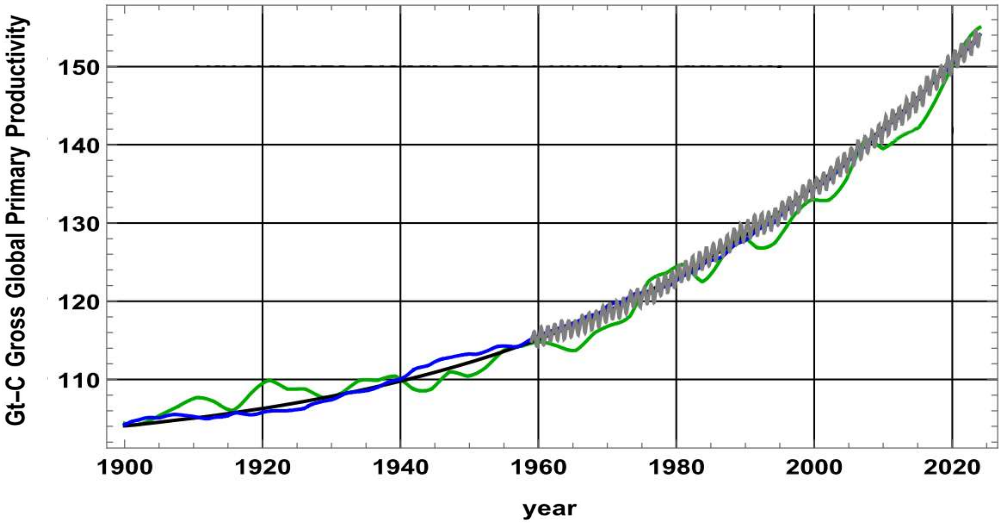

*Figure 17: The green curve is from (Haverd et al. 2020) and (Lai et al., 2024) the Global Gross Primary Productivity GPP of the vegetation in Gt-C/yr; the black curve is 2×8.6% × 2.12 of the ppm logistic $X_{MLOlogis}(t)$, the blue curve is 2×8.6% of the air carbon mass deduced from the series $f_{fossil}(t)$ and $AT_{SST}(t)$ (the inter-tropical sea surface temperatures anomaly) (plotted in ppm on Figure 11) and the grey curve is 2×8.6% of the X(t) series in Gt-C based on $X_{MLO}(t)$.*

### 6.2 Computation of Stocks and Fluxes

The three differential equations (12) of Subsec. 6.1 link the stocks of carbon in the air $X(t)$, in vegetation & soils $Y(t)$, and in the ocean $Z(t)$:
$X(t)$ is computed (see Subsec. 5.2) from the observed time series $AT_{SST}(t)$ for $X_{natural}(t)$ and $f_{fossil}(t)$ for $X_{fossil}(t)$,
$Y(t)$ is deduced from $dY(t)/dt + Y(t)/\tau_{tb} = NPP(t) = GPP(t)/2$ with Haverd et al.'s (2020) GPP($t$),
$Z(t) / \tau_{oc}(t)$ is $X'(t) + X(t)/\tau_{atm} - Y(t)/\tau_{tb} - f_{fossil}(t)$.

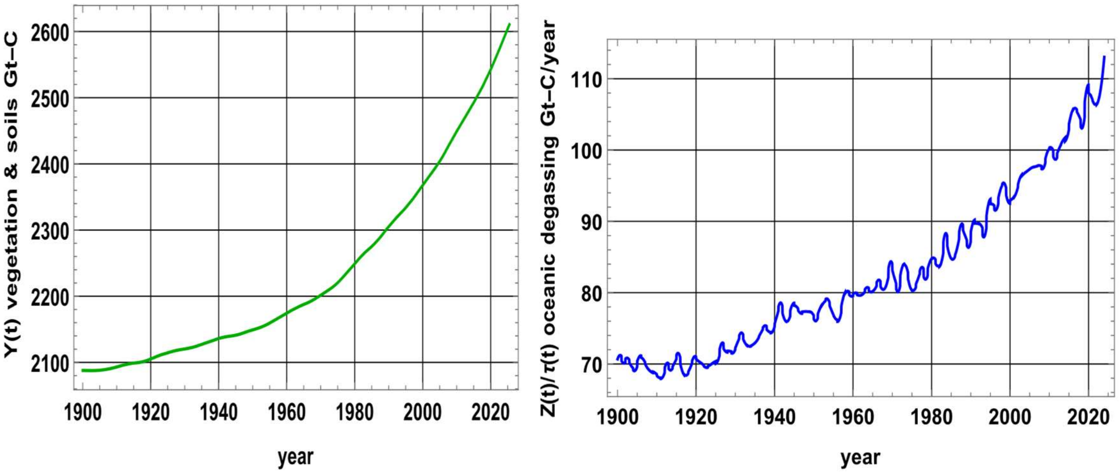

*Figure 18 a-b: a) left: Y(t) stock in vegetation and soil, the calculation uses the integral of GPP/2 according to Haverd et al. (2020) - see Figure 17; b) right: ocean degassing flux varying according to $Z(t)/\tau_{oc}(t)$.*

Cumulative ocean degassing over 1900-2025.0 is 10,350 Gt-C.
For vegetation and soils, Figure 18-a shows, with the GPP of Haverd et al. (2020) and Lai et al. (2024) plotted in Figure 17, $Y(1900)$ = 2088 Gt-C and $Y(2025)$ =2630 Gt-C.

IPCC's figures are:

- (AR2, Fig. 2.1) $Y(1989)$ = 2190 Gt-C with a Global NPP of 61 Gt-C/yr,
- (AR5, Fig. 7.3.5) $Y(1997)$ = 2261 Gt-C, GPP(1997) = 122 Gt-C/yr, $Y$(pre-industrial) = 2300 Gt-C and GPP(preindustrial) = 120 Gt-C/yr
- (AR6, Fig. 5.12) $Y(2013)$ = 2150 Gt-C, GPP(2013) = 142 Gt-C/yr, GPP (pre-industrial) = 113 Gt-C/yr.

Reducing the mean residence time in vegetation and soils from 40 years to 30 years reduces the $Y(2024)$ stock to 2300 Gt-C but has little effect on oceanic degassing, since $Y(1900)$ goes from 40 times to 30 times the NPP(1900): $Y(2024) - Y(1900)$ changes little.

### 6.3 Changes of the Stocks

Figure 19 shows the variations in the three carbon stocks and cumulative emissions between 1900 and 2025. The increases in atmospheric carbon (+297 Gt-C or +140 ppm) and in vegetation and soils (+542 Gt-C) result from the net contributions of the oceanic stock (−359 Gt-C) and fossil fuels (−480 Gt-C, of which approximately 50 Gt-C remain in the atmosphere, with the rest absorbed by vegetation and the oceans).

Since 1900, fossil fuel combustion has contributed a cumulative total of 480 Gt-C to stocks $X$, $Y$, and $Z$. Between 1900 and 2025, the inter-tropical ocean has released approximately 10,350 Gt-C (an average of 83 Gt-C $yr^{-1}$ over 125 years, according to Figure 18-b, right panel). However, the high-latitude ocean has absorbed 9,991 Gt-C, resulting in a net loss of 359 Gt-C from the ocean to the atmosphere and to vegetation/soils. Over the same period, the atmosphere gained 297 GtC and vegetation/soils gained 542 Gt-C.

In the absence of fossil fuel emissions (cumulative = 0 Gt-C), the atmospheric partial pressure of $CO_2$ would have increased more slowly, reaching 395 ppm instead of 425 ppm. This lower pressure would have promoted additional degassing in the inter-tropical ocean and reduced $CO_2$ absorption at high latitudes. In that case, the ocean would exhibit a net loss of 664 Gt-C (10,504 Gt-C degassed minus 9,840 Gt-C absorbed) to the atmosphere and vegetation/soils. The atmosphere would then have gained only 233 Gt-C and vegetation/soils only 431 Gt-C.

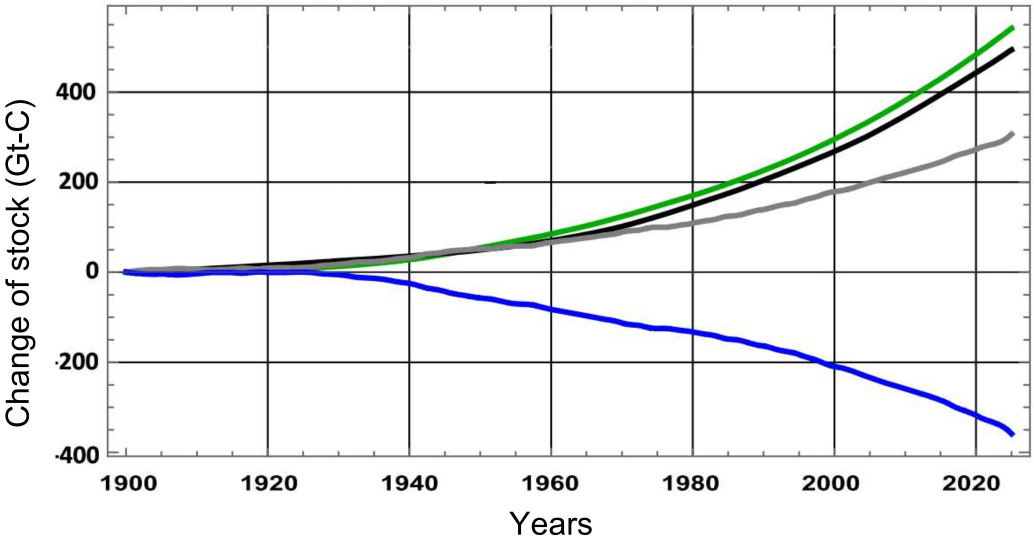

*Figure 19: Variations in Gt-C over 1900-2025 in atmospheric stocks X(t) (grey), vegetation and soil stocks Y(t) (green) and cumulative emissions since 1900 (black); in blue, the change of the oceanic stock Z(t) computed as the integral over time of $-Z(t)/\tau_{oc}(t) + 0.114\,X(t)$.*

### *6.4 A Glimpse at Decarbonization Policies in the EU-27*

The mean over 1980-2023 of the cost of weather-related catastrophes in EU-27 is € 16.8Bn/yr about 0.1% of the Gross Domestic Product (GDP) and the maximum over those 44 years has been € 63Bn/yr (EEA, 2024).

The EU "Fit For 55", –55% in 2030 with respect to 1990 emissions of 4.73 Gt-CO2/yr or 0.61 ppm/yr, aims at 2030 emissions of 0.27 ppm/yr with a further decline to 0 in 2050. The yearly cost of that policy is said to be over the next decades 5% to 10% of a 2024 EU GDP which is about € 17,900 Bn/yr, i.e. (≈1000 times the average cost of said catastrophes!).

$dX_{fossil}(t)/dt = f_{fossil}(t) - X_{fossil}(t)/5$ shows that the stock $X_{fossil}(2035)$ from EU emissions would be reduced from 1.6 ppm, if emissions were kept at their 2024 level, to 1.14 ppm that is minus 0.46 ppm. 0.46 ppm is about 5% of the seasonal increase of 8.6 ppm between the dates 2023.73 (end September) ($X_{MLO} = 418.4$ ppm) and 2024.42 (end April) ($X_{MLO} = 427$ ppm) and little more than one thousandth of $X_{MLO}$. Preventive measures (dams and retention basins, dykes, reservoirs, irrigation) account for less than one-thousandth of GDP per year, even in the Netherlands, and significantly reduce the impact of catastrophic floods. Mobile barriers on the Thames (closed 221 times since 1982) and on the Venice lagoon (78 barriers in service by 2020, raised about 28 times a year against the highest tides) effectively protect these cities.

## 7. On $^{13}C$ in the Atmosphere

The ratios of $^{13}C$ and $^{12}C$ isotopes of $CO_2$ in the air, observed continuously since 1980 at the Mauna Loa and at the South Pole observatories (at altitudes 2.8 km and 3.4 km) and far from any vegetation, confirm that only a few percent of carbon dioxide in the atmosphere come from fossil fuels. The marker $\delta^{13}C$ in units per mil (denoted ‰):

$$\delta^{13}C = \left( \frac{\left(^{13}C/^{12}C\right)_{\text{sample}}}{\left(^{13}C/^{12}C\right)_{\text{reference}}} - 1 \right) x1000\ ‰ \qquad (13)$$

is, for a mixture, approximately linear with respect to the quantities entering the mixture. Indeed for a mixture $X = X' + X''$, with markers $\delta$, $\delta'$ and $\delta''$ and $A = 1/\ (^{13}C/^{12}C)_{\text{reference}} = 1\ /\ 0.0112372$ for the VPDB reference, $\delta = A\ X_{13}/X_{12} - 1$, $\delta = (X'\ \delta' + X''\ \delta'' + X\ \delta'\ \delta''/(A+1))\ /\ (X + (X'\ \delta'' + X''\ \delta')\ /\ (A+1))$ or practically $(X'\ \delta' + X''\ \delta'')/X$ see note[7]. The $\delta^{13}C$ carbons of the fuels gas oil and coal are about –45, –28, –24.5 per mil with variations from deposit to deposit (Hu et al., 2021; Masood et al., 2022; Suto & Kawashima, 2016). The $\delta^{13}C$ of the mixture is slightly reduced by the flow from cement plants, and a small proportion of the hydrocarbons is used to make plastics (Figure 20-b).

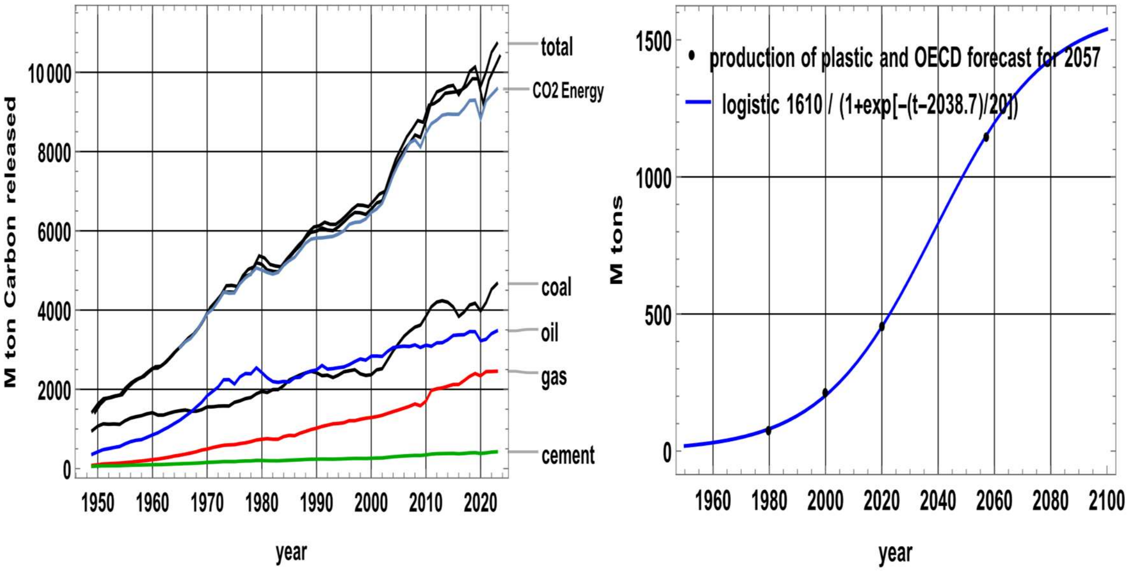

*Figure 20 a-b: a) left: Carbon (millions of tons) contained in gas, oil, coal and cement production, and the fraction used in energy production (Statistical review of World Energy Data 2023); b) right: Production of plastics in Mt/year past and extrapolated.*

Figure 21 shows estimates of the $\delta^{13}C_{\text{fossil}}(t)$. Over 45 years, the stock of fossil fuels has risen from 3.2% to 5.5% of the $CO_2$ in the air. We provide the computation of the *instantaneous atmospheric stock* of $CO_2$ originating from fossil sources (coal, oil, gas, cement) at a given time t. Each year's (or month's) emissions contribute to the current stock, but their influence *decays exponentially* with time due to natural absorption. For coal, the stock $X_{\text{coal}}(t)$ in the atmosphere at time t is the average of the previous emissions $f_{\text{coal}}(m)$ weighted by $e^{-(t-m)/5\text{ yr}}$. The variable $m$ represents the emission year (or time index) before t, that is, the time at which each individual emission $f_{\text{coal}}(m)$ occurred. So:

- $t$ = current year (or time of evaluation), e.g. 2024.05
- $m$ = past year (e.g. 1900, 1950, 2000, … up to $t$)
- $f_{\text{coal}}(m)$ = fossil $CO_2$ emissions from coal at time $m$

The exponential term $e^{-(t-m)/5\text{ yr}}$ is the weight expressing how much of the emission at time m still remains in the atmosphere at time $t$, assuming a 5-year e-folding decay time. The atmospheric

---

[7] The marker $\delta^{13}C$, expressed in per mil (‰), quantifies the relative abundance of $^{13}C$ to $^{12}C$ compared to a standard (VPDB). For mixtures, $\delta$ behaves approximately linearly because the $^{13}C/^{12}C$ ratio of the combined reservoir is a weighted average of the isotopic ratios of the individual components. The exact expression follows from mass balance on $^{13}C$ and $^{12}C$, but since $\delta$ values are small ($|\delta| \ll 1$), the higher-order terms in $\delta'\delta''/(A+1)$ are negligible, leading to the practical linear approximation $(X'\ \delta' + X''\ \delta'')/X$.

stock $X_{\text{coal}}(t)$ is obtained by summing all past emissions $f_{\text{coal}}(m)$, each diminished by an exponential factor that accounts for how much of it has been reabsorbed since it was emitted. Then, by combining the stocks from coal, oil, and gas, each with its own $\delta^{13}C$ signature, the weighted mean isotope ratio is:

$$\delta^{13}C_{\text{fossil}}(t) = \frac{\sum \delta^{13}\, C_i X_i(t)}{\sum X_i\,(t)} \tag{14}$$

The calculation for oil, gas and cement plants, i.e. the sum of stocks weighted by their own marker, for example $\delta^{13}C = \{-46, -28, -24.5\}$ for gas, oil and coal divided by the sum of stocks gives:

$\delta^{13}C_{\text{stock fossil}}(1980.05) = -27.9$ ‰ and $\delta^{13}C_{\text{stock fossil}}(2024.05) = -29.4$ ‰.

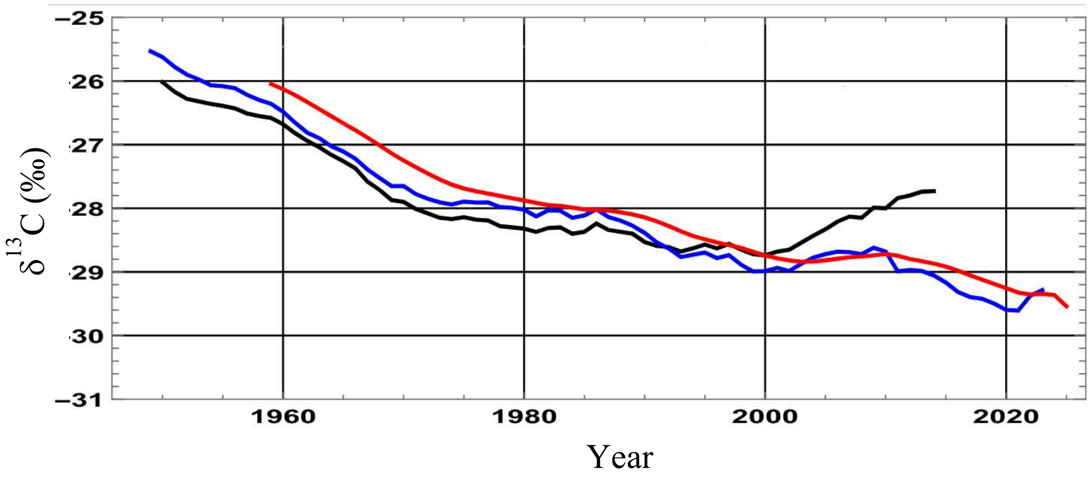

*Figure 21: δ13C estimates for the emissions from fuels and cement plants. Office of Scientific and Technical Information (OSTI), (https://data.ess-dive.lbl.gov/view/doi:10.3334/CDIAC/FFE.DB1013.2017), U.S. Department of Energy. Black curve is the "OSTI db1013 global", blue curve corresponds to the "computed energy and cements {-45, -28, -24.5}" and red curve is for "all gas and oil and coal".*

The $\delta^{13}C_{\text{stock natural}}(t)$ of the stock from natural out-gassing (which includes a small fraction of fossil carbon "zombie" recycled after absorption and out-gassing) is for instance:

$\delta^{13}C_{\text{stock natural}}(1980.05) = -6.84$‰ and $\delta^{13}C_{\text{stock natural}}(2024.05) = -7.5$‰ as

- at date 1980, 338 ppm (–7.52‰) = 11 ppm (–27.9‰) + 327 ppm (–6.84‰)
- at date 2024, 423 ppm (–8.68‰) = 22.8 ppm (–29.4‰) + 400 ppm (–7.5‰).

Figure 22-a shows:

1. in black, the $\delta^{13}C$ measured at Mauna Loa since 1980 and its 12-month moving average,
2. in grey, the $\delta^{13}C_{\text{stock natural}}$ that evolves slowly with the return to the atmosphere of "zombie" fossil fuel carbon absorbed by vegetation or oceans decades earlier, and its 12-month moving average.

The stock from natural out-gassing (grey curve in Figure 22-a) has the $\delta^{13}C$ signature of the ambient air some 60 years earlier, reflecting the average carbon transit times between absorption and out-gassing through the oceans and through vegetation and soils.

In the oceans, a relatively rapid movement on isopycnic surfaces close to the surface near 50°N and 1000 m deep in the inter-tropical zone could explain a transit in a century or less.

The Impulse Responses (Figure 16) give a sum of the carbon from fuels still in the atmosphere (for a 5-year lifetime) and of the fossil fuel "zombies" absorbed long ago and returned to air by out-gassing after sojourns in oceans and soils; subtracting all "fossil" carbons leaves a $\delta^{13}C$ between –6.6‰ (in 1980) and –7.1‰ (in 2024).

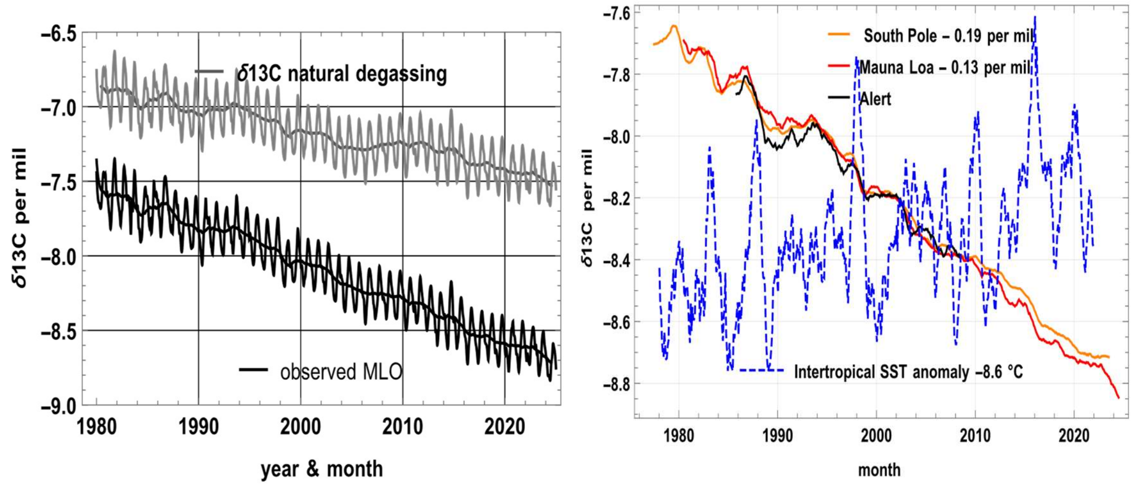

*Figure 22 a-b: a) left: Evolution of the atmospheric $\delta^{13}C$ (MLO observations in black) and in grey the $\delta^{13}C$ of the stock from natural out-gassing that is without the fossil fuels carbon still in the air for a lifetime of 5 years and their 12-month moving averages; b) right: Comparison of $\delta^{13}C$ observed at Alert (Alaska, 82°30'N & 62°21'W, 817 km from the North Pole), at Mauna Loa (19°28'N and 155°36'W, 3397 m) and at the South Pole (2937 m) with a 12-month moving average smoothing; the blue dashed line is the inter-tropical sea surface temperature anomaly shifted in ordinates by –8.6°C.*

Figure 23 compares the increments of $\delta^{13}C_{\text{stocknatural}}(t)$ and the sea surface temperatures of the inter-tropical zone: the $\delta^{13}$C of $CO_2$ degassed by the ocean is, according to (Quay et al., 2003, p. 4-12) Fig. 8 or (Roy-Barman & Jeandel, 2016, p. 110) Fig. 3.11, about –1.5‰ more negative than the $\delta^{13}$C of air: this may explain the peaks of negative values of the increments during times of strong out-gassing (Figure 2) that are the risers of the stairs on Figure 22.

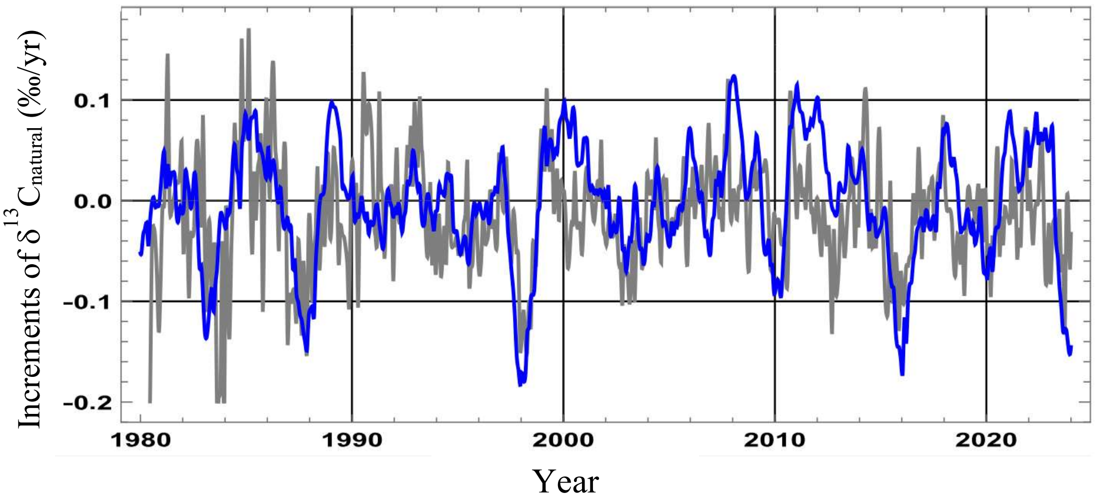

*Figure 23: In grey, increments of $\delta^{13}C_{\text{stock natural}}(t)$ in ‰ (12-month increments, centered in the middle of the 12 months to reduce the seasonal fluctuations) and in blue, 0.3 times the opposite of the inter-tropical sea surface temperature anomaly after subtracting its linear trend.*

Figure 24 shows (thick grey line at bottom) the $\delta^{13}C_{\text{stock natural}}$(t) (grey curve at top of Figure 22-a) shifted by +33.6): it decreases from August to May while MLO ppm (divided by 14, black curve) increase almost in phase with the mean inter-tropical SST (blue curve).

Koutsoyiannis (2024b) uses the Keeling plot of $\delta^{13}C(t)$ as a function of $1/X(t)$; adding to $X(t_0)$ of marker $\delta^{13}C_0$ a quantity $X(t) - X(t_0)$ of marker $\delta^{13}C_I$ gives to $X(t)$ the isotopic signature:

$$\delta^{13}C(t) = \delta^{13}C_I + (\delta^{13}C_0 - \delta^{13}C_I)\frac{X(t_0)}{X(t)} \tag{15}$$

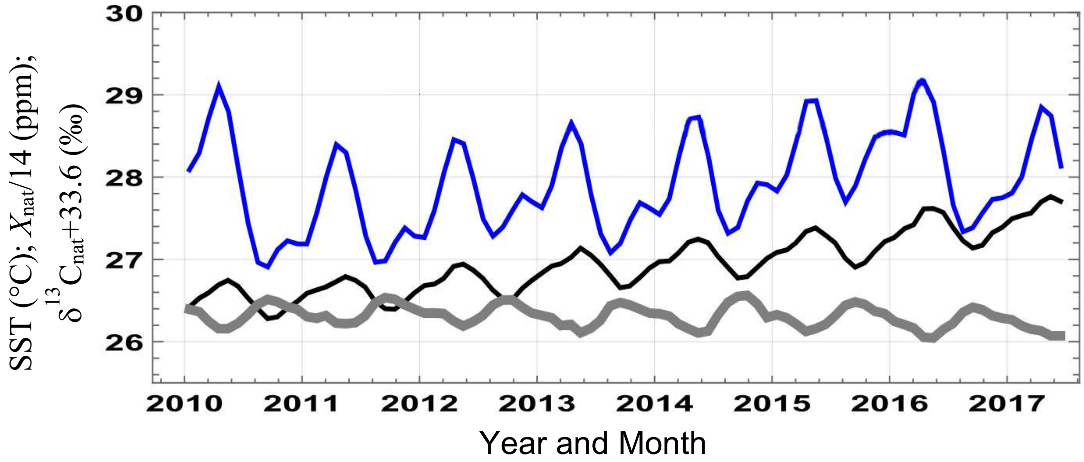

*Figure 24: Trends over 2010-2017 of the mean SST sea surface temperatures (in °C) between 20°S and 20°N (blue curve), $X_{natural}(t)/14$ at MLO (black curve) and 33.6 + $\delta^{13}C_{natural}(t)$ (thick grey line).*

Regression of $\delta^{13}C$ on the observations of $1/X(t)$ over a time interval gives the $\delta^{13}C_I$ as the *y*-intercept of the graph. For seasonal variations he finds $\delta^{13}C_D = -27.6‰$ during the two months with the highest photosynthesis (an atmospheric $CO_2$ decay phase) and various values of $\delta^{13}C_U$ during the two months of strongest atmospheric $CO_2$ growth phase, and for long-term variations $\delta^{13}C_I = -13.2‰$ even for reconstructions of $\delta^{13}C(t)$ going back to year 1520 (Böhm et al., 2002).

## 8. On Carbon in Seawater

An outflow from the ocean of 100 Gt-C/year over the 20°S-20°N zone (34% of the earth's surface), 75% oceanic, i.e. 130 M km², corresponds to an average flux of 64 moles-C/year/m². For seawater at 2 100 µmole-C/kg, an up-welling of 30 m/year is required, and three times more if only a third of the carbon that rises is degassed to the atmosphere. As seen in Sec. 2, and using equations (8) and (9) in Subsec. 5.2 these relations show that oceanic degassing (Figure 18-b) driven by $AT_{SST}(t)$ has provided the bulk of the growth in the atmospheric and vegetation and soil stocks: in 1960, oceanic degassing was 32 times the flux from "fossil fuels"; since 2010, it has been 11 times greater.

For the IPCC, changes in ocean degassing are absolutely taboo because it invalidates representations such as (IPCC, 2018, p. 105), Fig. 2.3: "*Temperature changes from 1850-1900 versus cumulative $CO_2$ emissions since 1st January 1876"* where cumulative human emissions are claimed to have caused:

1. all the increase in $CO_2$ and thus,
2. all the warming since 1876: "*Solid lines with dots reproduce the globally averaged near-surface air temperature response to cumulative $CO_2$ emissions plus non-$CO_2$ forcers as assessed in Figure SPM 10 of WGI AR5*."

The reality (Sec. 2 and 3 above) is that $AT_{SST}$ increased from 0.12 °C in 1959 to 0.97 °C in 2024 and accounts for 83% (+89 ppm) of the total increase (+107 ppm) in atmospheric $CO_2$ over that period. Moreover, the fraction of fuel-related emissions still remaining in the air (about 23 ppm out of 425 ppm at the end of 2024) cannot have any climatic effect. This negligible contribution of not more than 5.4% to the atmospheric $CO_2$ concentration is in full agreement with an independent line of reasoning and based on a residence (or absorption) time of $\tau = 3.8$ yr (see: Harde, 2025, Sec. 4, last paragraph).

### *8.1 Reminders*

[x] denotes the number of moles of compound x per kilogram of sea water.

The ocean is by far the main reservoir of circulating carbon, potentially inexhaustible if we consider the calcium carbonate in marine sediments. Seawater has everywhere almost the same composition (Dittmar principle, 1884) and contains in mole/kg: $H_2O$: 53.56, $Na^+$: 0.4685, $Mg^{2+}$: 0.05308, $Ca^{2+}$: 0.01028, $K^+$: 0.01021, $Sr^{2+}$: 0.00009, B: 0.00042, $Cl^-$: 0.54591, $SO_4^{2-}$: 0.02823, $CO_3^{2-}$ & $HCO_3^-$: 0.002, $Br^-$: 0.000842, $F^-$: 0.00007, i.e. 0.60561 moles per kg of positive charges excluding $H^+$ and 0.603282 moles of negative charges excluding carbonates, borates and OH.

The difference 605610 – 603282 = 2328 micro-moles/kg known as total alkalinity or TAlk, is also identical to $[HCO_3^-] + 2\,[CO_3^{2-}] + [B(OH)_4^-] + [OH^-] – [H^+]$.

Carbonate equilibria in seawater (Copin-Montégut, 1996; Dickson, 2010; Dickson et al., 2007) are described by five equilibrium constants that are functions of salinity and temperature; the fugacity $f_{CO_2}$ of $CO_2$ in the gas phase is derived as per (Zeebe & Wolf-Gladrow, 2001):

$$f_{CO_2} = \frac{[CO_2{}^*]}{k_0} \tag{16}$$

with:

- $[CO_2{}^*]$ = the equilibrium concentration of dissolved $CO_2(aq)$ in water, often in mol/kg or mol/l. The *[8] distinguishes it from total dissolved inorganic carbon (DIC = $CO_2 + HCO_3^- + CO_3^{2-}$).
- $k_0$ = the Henry's law solubility constant for $CO_2$ (temperature- and salinity-dependent).

Let $CO_2{}^*$ (a.k.a. $H_2CO_3^*$) denote dissolved molecular $CO_2$ plus carbonic acid:

$$CO_2^* \equiv CO_2(aq) + H_2CO_3 \tag{17}$$

Stoichiometric (salinity-dependent) equilibrium constants:

$$K_1^*, K_2^*, K_b^*, K_w \text{often in place of } k_{H_2O} \tag{18}$$

depend on *T*, *S*, and *P*; the asterisk distinguishes them from thermodynamic *K*'s based on activities, while $K_w$ instead of $k_{H2O}$ avoids confusion with water itself, either one or the other can be used. These constants are defined by the following relations (19):

$$\begin{aligned} [HCO_3^-] &= \frac{K_1^*[CO_2^*]}{[H^+]} \\ [CO_3^{2-}] &= \frac{K_2^*[HCO_3^-]}{[H^+]} \\ [B(OH)_4^-] &= \frac{K_b^*[B(OH)_3]}{[H^+]} \\ [H^+] &= \frac{K_w}{[OH^-]} \end{aligned} \tag{19}$$

The *pK* notation is also often used:

$$pK = -\log_{10}(K)\text{e.g.,}pK_1^* = pH - \log_{10}\big([HCO_3^-]/[\,CO_2^*]\big) \tag{20}$$

With the notations salinity *S*, and absolute temperature *T*, one can define $K_w\,(S,T)$ i.e. the ionic product of water in seawater at a given salinity and temperature, with $B_T(S)$, i.e. a salinity-dependent correction term and with $K_w^0\,(T)$ the ionic product in pure water at the given temperature:

$$K_w(S,T) = [H^+][OH^-] = K_w^0(T) + B_T(S) \tag{21}$$

$B_T(S)$ stands for the total boron concentration in seawater that is, the sum of all boron species (mostly boric acid $B(OH)_3$ and borate ion $B(OH)_4^-$). It is proportional to salinity, because boron

---

[8] The * is a conventional marker in geochemistry/ocean chemistry indicating the aqueous concentration of $CO_2$ in equilibrium with the atmosphere, not the whole carbonate system. $[CO_2{}^*]$ denotes the sum of dissolved molecular $CO_2$ and carbonic acid ($H_2CO_3$).

in seawater behaves conservatively (it scales linearly with the amount of dissolved salts) as defined by (Millero, 1995) as $B_T(S) = 1.188 \times 10^{-5}\, S$ mol kg$^{-1}$ or at typical ocean salinity with $S = 35$ kg/m$^3$, one gets $B_T(S) = 1.188 \times 10^{-5} \times 35 = 4.16 \times 10^{-4}$ mol kg$^{-1}$.

Once this is defined, the following relations apply with the notations "ln" as natural logarithm, $S = s$ kg/m$^3$ as salinity and $T = \vartheta$ K as temperature with $s$ and $\vartheta$ as their numerical values:

$$\begin{aligned}
\ln(k_0[T, S]) &= -60.240 + 93.451\,(100/\vartheta) + 23.358\,\ln(\vartheta/100) + \\
&\quad s\,[0.023 - 0.024\,(\vartheta/100) + 0.0047\,(\vartheta/100)^2] \\
\ln(k_b[T, S]) &= (-8966.9 - 2890.53\,s^{0.5} - 77.942\,s + 1.728\,s^{1.5} - 0.0996\,s^2)\,/\vartheta + 148.025 + \\
&\quad 137.194\,s^{0.5} + 1.621\,s + (-24.434 - 25.085\,s^{0.5} - 0.247\,s)\cdot\ln(\vartheta) + 0.053\,s^{0.5}\cdot\vartheta \\
\ln(k_1[T, S]) &= 2.837 - 2307.127/\vartheta - 1.553\,\ln(\vartheta) - (0.20760841 + 4.0484/\vartheta)\,s^{0.5} + \\
&\quad 0.085\,s - 0.007\,s^{1.5} + \ln(1 - 0.001\,s) \\
\ln(k_2[T, S]) &= -9.227 - 3351.611/\vartheta - 0.201\,\ln(\vartheta) - (0.107 + 23.972/\vartheta)\,s^{0.5} + \\
&\quad 0.113\,s - 0.008\,s^{1.5} + \ln(1 - 0.001\,s) \\
\ln(k_{H_2o}[T, S]) &= 148.965 - 13847.26/\vartheta - 23.652\,\ln(\vartheta) + \\
&\quad (-5.977 + 118.67/\vartheta + 1.049\,\ln(\vartheta))\,s^{0.5} - 0.016\,s
\end{aligned}$$

Same relations in (Dickson, 2010; Dickson et al., 2007), who use both decimal logarithms and Napierian logarithms.

DIC refers to dissolved inorganic carbon, DIC = $[CO_2] + [HCO_3^-] + [CO_3^{2-}]$ and TAlk is Total Alkalinity, the difference between the total charges of the major ions of dissolved salts excluding carbonates and borates, TAlk = $[HCO_3^-] + 2\,[CO_3^{2-}] + [B(OH)_4^-] + [OH^-] - [H^+]$.

Assuming that total boron $[B(OH)_3] + [B(OH)_4^-]$ is a fixed fraction $B_T$ of salinity $S$, we get $[B(OH)_4^-] = B_T[S]\,k_b\,/\,(k_b + [H^+])\cdot$ $x = [OH^-]$ is the solution close to $10^{-6}$ of the following equation (see Appendix B):

$$TAlk = \frac{\left(x\,k_1/K_{H_2O} + 2x^2 k_1\,k_2/K_{H_2O}^2\right)DIC}{1 + x\,k_1/K_{H_2O} + x^2 k_1\,k_2/K_{H_2O}^2} + B_T(S)\frac{x k_b}{K_{H_2O} + x k_b} - \frac{K_{H_2O}}{x} + x \qquad (22)$$

Figure 25 shows the temperature ranges corresponding to absorption (partial pressure of $CO_2$ in seawater less than say 425 µatm) and the temperature ranges for degassing, for example at more than 425 µatm. The dashed lines plot the simple approximation:

$$p_{CO_2\,\text{sea water}}(\mu\text{atm}) = 400\ \mu\text{atm}\ (\vartheta/\,299)^{12.5}\ (\text{DIC}_{\mu\text{mole/kg}}\,/\,2000)^{10.4}\ \ (2328/\ \text{TAlk}_{\mu\text{mole/kg}})^{10.3}$$

Seawater temperatures range from 32°C in some inter tropical zones to −1.5°C in salty waters at the edge of the pack ice (the global average of ocean surface temperatures oscillates between 290 K and 293 K, depending on the season).

With DIC and TAlk in µmol/kg and T in Kelvin, the pH is approximately given by this linear approximation (the regression coefficients therefore carry the corresponding inverse units so that the resulting pH remains dimensionless): $7.85 - 1.95 \times 10^{-3}\,(\text{DIC} - 2100) + 1.87 \times 10^{-3}\,(\text{TAlk} - 2328) - 1.59 \times 10^{-2}\,(T - 299)$; +1°K on T or +8 µmol/kg on the DIC have about the same effect: +18 µatm on the sea water partial pressure and –0.016 on the pH. Seawater temperatures over the Great Barrier Reef range from 24°C in winter to 30°C in summer.

Takahashi et al.'s (1993) formula (23) expresses the growth of $p_{CO_2\text{seawater}}$ with temperature:

$$\frac{pCO_2(T)}{pCO_2(T_{\text{ref}})} = \exp\,[0.043(T - T_{\text{ref}})] \qquad (23)$$

It is very close to the expression in $T^{12.5}$ (Figure 26).

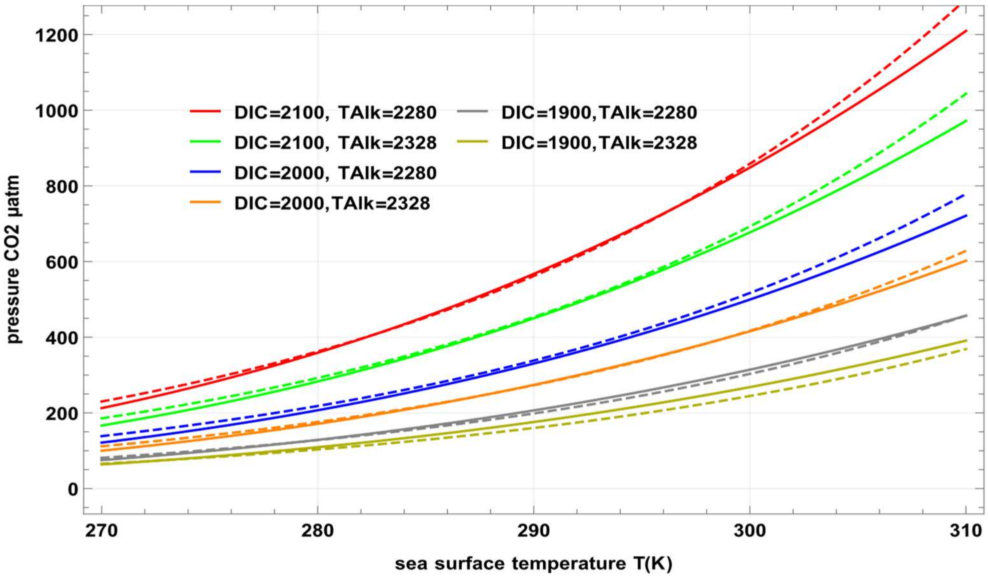

*Figure 25: Calculation according to (Copin-Montégut, 1996) of the partial pressure of* $CO_2$ *in seawater for various values of DIC, TAlk and T(K) at the surface; the dashed lines show the approximation* $400\,(T/299)^{12.5}\,(DIC/2000)^{10.4}\,(2328/TAlk)^{10.3}$ *with DIC µmol/kg and salinity S=35 g/l.*

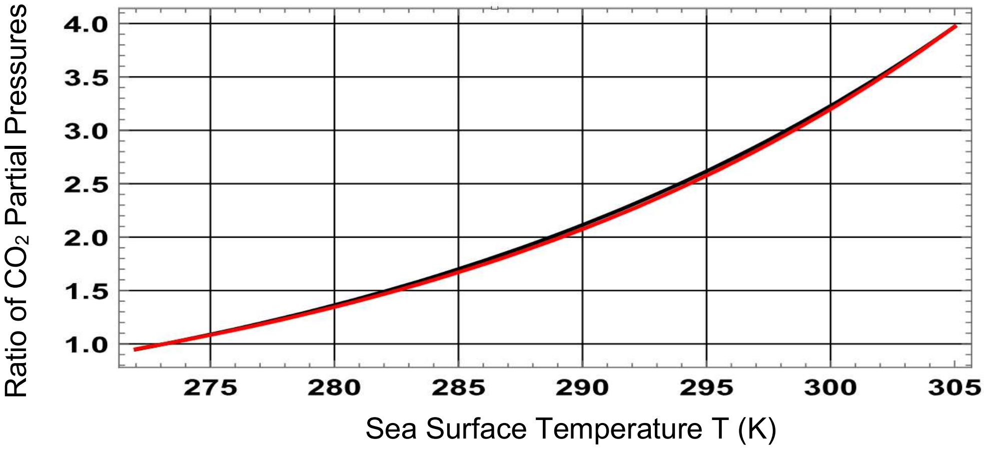

*Figure 26: Ratio of the CO2 partial pressures in seawater at temperature T to the partial pressure at 273.15 K: expressions in T12.5 and of Takahashi et al. (1993).*

The flux of carbon dioxide $F$ (in mol m$^{-2}$ s$^{-1}$ or mol m$^{-2}$ yr$^{-1}$) between the surface of the ocean and the air derives from the difference in partial pressures (Wanninkhof et al., 2013; Wanninkhof & McGillis, 1999) and is:

$$F = k \cdot K_0\left(pCO_2^{\text{seawater}} - pCO_2^{\text{air}}\right) \tag{24}$$

with $k$= 0.251 (Sc/660)$^{-0.5}$ <U$^2$> in m s$^{-1}$ and $K_0$ (in mol m$^{-3}$ Pa$^{-1}$ or mol m$^{-3}$ µatm$^{-1}$) is the $CO_2$ solubility in seawater (Henry's law constant) linking partial pressure to dissolved concentration. It is weakly dependent on salinity. Sc($t$) is the Schmidt number:

$$Sc(T) = 2073.1 - 125.62\,T + 3.6276\,T^2 - 0.043219\,T^3$$

where $T$ is the seawater temperature in °C, as used in the standard Schmidt number parameterizations (e.g., Wanninkhof 1992). The factor (Sc/660)$^{-0.5}$, where 660 is the Schmidt number of $CO_2$ at 20 °C, increases from 0.54 to 1.0 and 1.37 as $T$ increases from –1.5°C to +20°C and +32°C. <U$^2$> is the second-order moment of wind speed; according to Fig. 5 of Wanninkhof et al. (2013) it ranges from 30 m²/s² near the equator to 100 m²/s² at 50°N and perhaps 120 m²/s² or even 150 m²/s² at 50°S. Maps of $CO_2$ partial pressures in air and in surface water are shown in (Barry 2010).

A temperature change of +1°C increases partial pressure by 4.2% at 300 K (by 4.7% at 273 K): a difference ($p_{\mathrm{CO2water}} - p_{\mathrm{CO2air}}$) of (500 µatm – 420 µatm) becomes (521 µatm – 420 µatm) or +26% on the degassing, whereas a difference (430 µatm – 420 µatm) becomes (438 µatm – 420 µatm) with +80% on the degassing. The great variability of wind speed and of surface temperature, and intermittent oceanic eddies of small dimensions (km) that mix the water of the different layers, make it difficult to estimate fluxes.

### *8.2 The Depth of the Layer at 2250 µmol / kg is Probably Variable*

Many articles consider the boundary layer between water and air, the last hundred microns or centimeters [Bolin, 1960] or meters with many oceanographic measurements. But the degassed flow is determined by the difference between the DIC 100 m below the surface and that at the surface which is in quasi-equilibrium with the air.

The DIC at a depth of 100 m in the Atlantic, for example, is 2250 µmol/kg between 15°S and 15°N, and 2100 µmol/kg near 30°S and 40°N (Millero, 2007). At the surface, outgassing and absorption fluxes reduce the DIC to some 2000 µmol/kg (blue and orange curves Figure 25).

Measurements at the surface of the seas show a considerable variability in $p_{\mathrm{CO2\ sea\ water}}$ with mean annual values ranging from 250 µatm to 490 µatm depending on the site (air at MLO was then around 370 ppm), a seasonal amplitude of 60 µatm to 337 µatm near the coast, of 8 µatm to 71 µatm offshore and of 11 µatm to 178 µatm in coral reef areas (Sutton et al., 2019).

A very schematic division of the surface ocean into five geographical zones, the inter-tropical zone which degasses, two intermediate zones in equilibrium with the air and, finally, two zones closer to the poles which absorb $CO_2$ from the air, suggests that absorption depends on the temperature ratio of the last two zones: if $p_{\mathrm{CO2\ sea\ water}} = p_{\mathrm{CO2air}}$ at 35°N, $p_{\mathrm{CO2air}} - p_{\mathrm{CO2sea\ water}}$ at 50°N will be $p_{\mathrm{CO2air}}\,(1 - (T(50°\mathrm{N}) / T(35°\mathrm{N}))^{12{,}5})$, for example this difference is:

$$p_{\mathrm{CO2air}}\,(1 - ((273.15 + 5) / (273.15 + 20))^{12{,}5}) = 0.48\, p_{\mathrm{CO2air.}}$$

Depending on the strength of the carbon up-welling, the position of the layer at 2250 µmol/kg may be more or less close to the surface; it could have been near the surface during geological epochs with 1500 ppm or more in the air.

### *8.3 $CO_2$ Partial Pressures: No Static Air–Sea Equilibrium*

For {Talk = 2300 µmol /kg, S = 35 g/l} a static equilibrium with air at 400 ppm would require:

- at 0°C: DIC = 2184 µmol/kg or at 10°C: 2100 µmol/kg, while the observed DIC is 1950 to 2000 µmol/kg.
- at 30°C: DIC = 1939 µmol/kg, while the observed DIC is 2100 to 2000 µmol/kg in the surface waters feeding the inter-tropical out-gassing.

There can therefore be no static equilibrium between the surface ocean and the air; the permanent flows ocean to air in the tropics and air to ocean at mid and high latitudes, modulated by the ocean surface temperatures, are of the order of 100 Gt-C/year (Figure 18-b), extending the obduction and subduction quoted in Sec. 2. AR6 Fig. 5.12 of Masson-Delmotte et al. (2021) underestimates this flux at 80 Gt-C/year.

## 9. Insolation Controls Ocean Heat and Surface Temperatures

The heat capacity per m² of the first 300 m or 700 m of ocean is 120 or 280 times that of the entire air column above. Air can therefore hardly "warm the ocean". Donohoe et al. (2014) admit: "*climate models forced with $CO_2$ reveal that global energy accumulation is, instead, primarily caused by an increase in absorbed solar radiation (ASR)*". Indeed, thermal infrared emitted by the air is absorbed by a few tens of microns of liquid water and if its balance with thermal infrared emitted by the surface is positive, it contributes to evaporation.

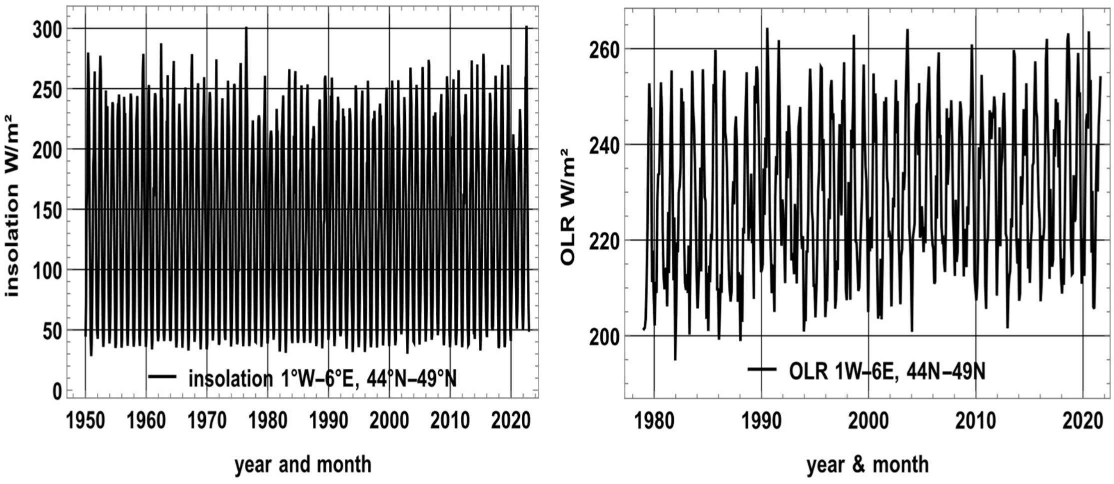

*Figure 27 a-b: a) left: Surface insolation over part of France: between 28 W/m² and 302 W/m²; b) right: Radiation delivered to the cosmos (OLR) over the same geographical area: i.e. between 200 W/m² and 260 W/m². Source: KNMI Climate Explorer.*

Long series of observations of surface insolation are available only over some land areas; Figure 27 compares over the same region the surface insolation and the OLR (Outgoing Longwave Radiation) supplied to the cosmos at the top of the atmosphere: the motion of the atmosphere and of its water vapor is driven by contrasting temperatures; it ensures that, outside polar zones in winter, the OLR is relatively uniform between 220 and 280 W/m².

Note that Hoogeveen et al. (2025), in their analysis of Earth's energy-imbalance observation series, did not find evidence for a greenhouse-gas effect, consistent with the conclusions of Nikolov & Zeller (2024).

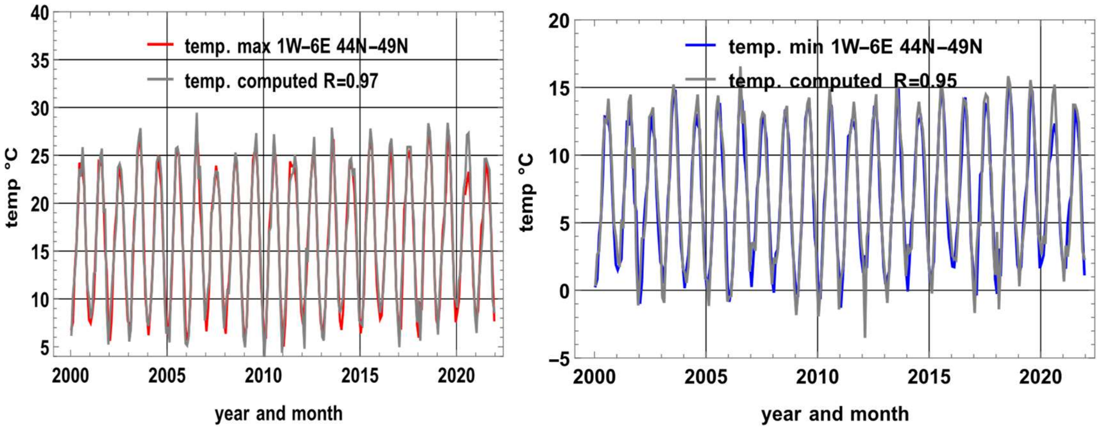

*Figure 28 a-b: Comparison of observed temperatures with values inferred from surface insolation. Source: KNMI Climate Explorer — NOAA/UD for OLR and E-OBS 23.1e (globrad) for surface solar radiation. a) left: temp. max. plotted against temp. computed; b) right: temp. min. plotted against temp. computed.*

The monthly averages $temp_{\max}(n)$ and $temp_{\min}(n)$ of the daily maximum and minimum temperatures observed during a month n, over a zone, may be computed from the surface insolation *insol*(n) over that zone during month n and the average temperatures $temp_{\max}(n-1)$ and $temp_{\min}(n-1)$ of the previous month (n–1). Here $temp_{\max}(n)$ and $temp_{\min}(n)$ are in °C, and *insol*(n) denotes the monthly mean surface insolation in W m$^{-2}$. The regression coefficients therefore carry the appropriate inverse units. For instance, Figure *28*,

$temp_{\max}(n) = 0.349 + 0.483\, temp_{\max}(n)\,(n-1) + 0.055\, \mathrm{insol}(n)$, standard deviation of the error $\sigma = 1.26$°C
$temp_{\min}\,(n) = -2.165 + 0.557\, temp_{\min}\,(n-1) + 0.0336\, \mathrm{insol}(n)$, standard deviation of the error $\sigma = 1.54$°C.

This supports the conclusion that the surface insolation drives the surface temperatures that drive the natural degassing (or absorption) of $CO_2$.

## 10. Examination of Some IPCC's Theories, Models and Conjectures

### 10.1 Introduction

A model is not a demonstration; it can only justify mechanisms if, and only if, all its results are consistent with all observations. Approximately reproducing the $X(t)$ curve is a necessary but by no means sufficient condition; the growth of the vegetation productivity (Figure 17) and the evolution of $\delta^{13}C$ must also be reproduced and the assumptions made must not be contrary to physics: see discussion in (Harde, 2019). The equations seen in Subsec. 5.2, i.e. (8), (9) and (10) meet these criteria.

Three different "theories", incompatible with each other and incompatible with the figures read on Fig. 6.1 p. 471 of the report (IPCC, 2013), rest on the concepts "*Airborne Fraction*", "*Bern-type impulse response*" and "*adjustment time*" that don't stand scrutiny (Poyet, 2022).

Any increase in natural outgassing since pre-industrial times would contradict the central assumption of the IPCC (2018) framework, namely that global temperature change is a function of the cumulative anthropogenic emissions $f_{\text{fossil}}(t)$ + LUC($t$) since 1876 (see their Fig. 1.2, p. 57; Fig. 2.3, p. 105). Figures 12-a (since 1850) and 13-b (since 1880) show curves of this kind, designed to make people believe in a false correlation like +0.45°C for +1000 Gt-$CO_2$ in cumulative emissions; Figure 12-b has shown that this is a deception.

### 10.2 Using $dpCO_2 / pCO_2$ vs. $dDIC / DIC$ to Suppress Circulating Fluxes

Stating that:

$$\frac{\mathrm{d}pCO_{2,\text{ seawater}}}{pCO_{2,\text{ seawater}}} = R\,\frac{\mathrm{d}DIC}{DIC} \tag{25}$$

is a ploy used to suppress the fluxes circulating permanently between oceans and atmosphere. For a Revelle factor $R = 12.5$, a doubling of the $CO_2$ pressure in the air and in surface water with $\mathrm{d}p_{CO2} = p_{CO2}$ implies an increase of dDIC of only 1/12.5 = 8% of the DIC; assuming a sea surface layer containing as much carbon as the atmosphere with little or no exchange with the deep ocean, more than 90% of the extra carbon injected into the atmosphere is said to remain in the air.

The contact between the oceans (361 million km², 71% of the Earth's surface) and the atmosphere has been modelled as a single point of contact at a mean ocean surface temperature, for example between 17.7°C and 18.3°C (Bolin & Eriksson, 1959; Joos, 2014; Joos et al., 1996: p. 402; Oeschger et al., 1975; Strassmann & Joos, 2018); this non-sense is used in so-called "models" to ignore the fluxes of about 100 Gt-C/year degassed (Figure 18-b) and absorbed by the surface oceans, and to pretend that the extra $CO_2$ from fuels remains perpetually in the air.

With respect to R, Wikipedia says[9]: "*The capacity of the ocean waters to take up surplus (anthropogenic) $CO_2$ is inversely proportional to the value of the Revelle factor.... The Revelle effect describes how only a small fraction of $p_{CO2}$ is present in ocean water when much larger amounts are added to the atmosphere"*. This is often said to be a "*buffering effect of sea water*". Egleston et al. (2010) describe these "*buffer factors"* in detail.

This deception is still used: Köhler et al. (2018) invoke Revelle and this relation 9 times on four pages.

With the approximation shown in Figure 25:
$p_{CO2\text{sea water}}$ (µatm ) = 400 µatm $(T / 299\text{ K})^{12.5}$ $(DIC_{\mu\text{mole/kg}} / 2000)^{10.4}$ $(2328 / TAlk_{\mu\text{mole/kg}})^{10.3}$
R= 10.4 (eq. 25). Revelle et al. (1965) take $R$= 12.5, various authors use $R$ between 8.5 and 14.

In reality, sea surface temperatures vary between +32°C and –1.8°C (Ventusky, 2025), giving a

---

[9] https://en.wikipedia.org/wiki/Revelle_factor

ratio 4.3 between the partial pressures computed with constant DIC and TAlk: therefore there is an inter-tropical zone that out-gasses (Figure 2) and colder sea surface zones that absorb, see maps in (Barry et al., 2010), with, as seen in Sec. 2, a permanent renewal of carbon in the surface ocean by obduction of 275 Gt-C/year where the ocean is degassing, and by subduction of almost as much to the depths where the ocean is absorbing.

*There is no static equilibrium without exchanges between reservoirs*. For $CO_2$, as for water vapor, substantial fluxes have always circulated continuously, driven by contrasts in temperature and insolation (Sec. 6 and 9 above).

Thus, the Revelle factor is deceptive because it assumes the ocean is a uniform, static reservoir, so that doubling atmospheric $CO_2$ would raise dissolved inorganic carbon (DIC) by only ~8%, suggesting over 90% of the extra $CO_2$ remains in the air, whereas in reality temperature contrasts drive continuous large-scale exchanges between tropical out-gassing and mid and high latitudes absorption.

## *10.3 Historical Information*

In 1957, continuous infrared measurements of $CO_2$ in air began with electronic equipment developed by Charles Keeling recruited by the Scripps Institution of Oceanography (Keeling et al., 2025). The MLO series began in March 1958. The variations of almost 100 ppm over 24 hours observed on land near growing vegetation and reported, e.g. by Massen et al. (2005), make the measurements on land more uncertain except when strong winds bring them closer to observations made 1 km or 2 km above land surface or sea level (Massen & Beck, 2011). Hence Keeling's choice of the South Pole and Mauna Loa observatories.

### *10.3.1 Bolin & Eriksson (1959)*

Bolin & Eriksson (1959) begin with: "*The dissociation equilibrium of carbon dioxide in the sea is discussed with particular emphasis on the buffering effect of sea water, when changes of the partial pressure of $CO_2$ in the gas phase take place. The results are used in a study of the changes of the carbon dioxide content of the atmosphere and the sea that occur as a result of release of $CO_2$ to the atmosphere by fossil fuel combustion. It is shown that the steady state considerations given by previous authors hereby are considerably modified.*" … "*However, by studying the $C^{14}$ distribution in the atmosphere and the sea and its variation in the atmosphere during the last 100 years as revealed by the ratio $C^{14}/C^{12}$ in wood one has been able to show that the exchange time between the atmosphere and the ocean is about 5 years (Craig,1957, 1958; Revelle and Suess, 1957; Arnold and Anderson, 1957; Rafter and Ferguson, 1958).*" … "*It has then been concluded by Revelle & Suess (1957) that most of the $CO_2$ due to combustion has been transferred into the ocean and that a net increase of $CO_2$ in the atmosphere of only a few percent has actually occurred*".

But then Bolin & Eriksson (1959) with *the buffering effect of sea water* try with a few pages of equations to make people believe that fuel emissions will remain forever in the atmosphere and will be the sole cause of the growth of $X(t)$. Bolin (1970) predicts between 375 ppm and 400 ppm in 2000 (at MLO it was 369 ppm in 2000).

Bolin & Eriksson (1959) reduce the system of three equations describing a static equilibrium between the atmosphere, the mixed layer at the surface of the ocean and the deep layer of the ocean, an equilibrium disturbed only by fossil emissions, to differential equations of order 3, one for each of the three compartments, with solutions of type: $a_0 + a_1 \exp(-t/b_1) + a_2 \exp(-t/b_2)$. Hence they assume that due to the "*buffering effect*" about 92% of the $CO_2$ from fossil fuels remain in the air. Vegetation is ignored.

With an exponential growth of fossil fuel emissions $4.96\times10^{-4}\cdot X(1880)\cdot\exp(0.029\cdot(t-1880))$, where $X(t)$ is the carbon mass in the atmosphere Bolin & Eriksson (1959) conclude that there will be between +25% and +40% more $CO_2$ in the air in 2000 than in 1880, and that "*The implications* *with regard to the radiational equilibrium of the earth in such a case may be considerable."*

### *10.3.2 Revelle et al. (1965)*

The report (Revelle et al., 1965) published by the US Presidency, entitled "*Carbon dioxide from fossil fuels – the invisible pollutant*", asserts that there is no exchange of carbon between the surface ocean (its 100 m deep "mixed" layer) and the deep ocean: "*In the past the usual scientific belief has been that by far the larger part of any added $CO_2$ would be absorbed in the ocean. This is undoubtedly true if we consider a sufficiently long time period, of the order of thousands or even perhaps hundreds of years ... but over shorter times only the uppermost layer takes part in exchanges with the air...*".

Revelle et al. (1965) use a remarkable circular reasoning to assume that half of all emissions remain perpetually in the air and devote four pages of their report to determining the masses of carbon $M$ in the ocean (limited to the surface ocean and rendered inoperative by Revelle's factor!), $A$ in the atmosphere and $B$ in the biomass that would support his assumption. Revelle et al. (1965) state that in 1959, 13.8% of the $CO_2$ in the atmosphere was from fossil fuels and that, with an exponential growth in "fossil" emissions at +3.2%/year (or +5%/year), fossil fuel $CO_2$ will contribute 57.04% (or 93.14%) of the $CO_2$ in the air in 2009.

This assumption of an exponential growth over 50 years, leading in 2009 to 4.8 times (or 11.5 times) the 2.4 Gt-C/year of 1959, is contradicted by the observations seen in Sec. 4: the "fossil fuel" emissions have grown almost linearly by 0.12 Gt-C/yr since 1950, not exponentially. With the 5-year lifetime seen in Sec. 2, the fraction of the atmospheric stock coming from fuels was 1.5% in 1959 and 4.8% in 2009, twelve and twenty times less than predicted by Revelle et al. (1965). Revelle et al. (1965) forecast "*+14% to +30% for the year 2000 compared with 1950*" (that is 385 ppm to 431 ppm significantly more than the 369 ppm observed at MLO in 2000), "*between +0.6°C and +4°C for +25% on atmospheric $CO_2$*" (+25% w.r.t 1965 is 398 ppm was observed in 2014), and these authors anticipate the melting of the Antarctic ice cap and other deleterious effects, as consequences of the use of fossil fuels.

Masson-Delmotte et al. (2021) have—implicitly—admitted the falsity of these assertions by showing Fig. 5.12 (p. 700 of AR6, WG1) the 275 Gt-C/year of Levy et al. (2013) between surface and deep oceans, obducted between the tropics and subducted at mid-latitudes.

### *10.3.3 Oeschger et al. (1975)*

Oeschger et al. (1975) still use the *Revelle factor* and state p. 180: "*Based on a preindustrial atmospheric $CO_2$ concentration in 1860 of 292 ppm, the $CO_2$ increase in 1970 amounted to 30 ppm. Comparison with the cumulative production of 54.9 ppm indicates that 55% of the fossil $CO_2$ produced until 1970 remained in the atmosphere.*" This is an introduction to the Bern Impulse response debunked in Subsec. 6.1 and on Figure 16 above.

### *10.3.4 Conservation Foundation (New York) (1963)*

Finally, let us mention the highly political program of the Conservation Foundation (New York), (1963), which became WWF in the 1990s: "*If all known reserves of fossil fuel were used within the next 500 years, a very reasonable assumption, and if the $CO_2$ system reaches $CaCO_3$ equilibrium (reducing atmospheric $CO_2$ to a minimum- a condition not likely to be reached for several thousand years) then the $CO_2$ content of the atmosphere would be four times what it is at present and the average surface temperature of the earth would have risen by 7°C. (The possible change if $CaCO_3$ equilibrium is not reached is 12.2°C). A change even half this great would be more than sufficient to cause vast changes in the climates of the earth; the polar ice caps would almost surely melt, inundating many densely settled coastal areas, including the cities of New York and London. If the temperature of the equatorial regions were to rise by this amount many life forms would be annihilated both on land and in the sea [...] Arousing public interest in the effects of the increase in atmospheric $CO_2$ is as much a problem as the lack of adequate data. The potentially dangerous* *increase of $CO_2$ due to the burning of fossil fuels is only one example of a failure to consider the consequences of industrialization and economic development."*

## 10.4 The Myth of a Permanent Airborne Fraction (AF)

### 10.4.1 The "Carbon Sink"

If **c**umulative fossil fuel emissions with Land Use Change (LUC) were the only cause of the growth of $X(t)$, then $\mathrm{d}X(t)/\mathrm{d}t = AF\, f_{\mathrm{fossil}}(t)$; a carbon sink, $sink(t)$, absorbs each year what has not remained in the atmosphere:

$$\begin{aligned} sink(t) &= f_{\mathrm{fossil}}(t) - \frac{\mathrm{d}X(t)}{\mathrm{d}t} \\ &= (1 - AF) f_{\mathrm{fossil}}(t) \\ &= absorb(t) - degas(t) \end{aligned} \tag{26}$$

Then natural absorption and degassing, 179 Gt-C/year and 175 Gt-C/year by mid-2023, with different physical causes, would be linked by a relation which, via $f_{\mathrm{fossil}}(t)$ (10.4 Gt-C/year in 2023), depends solely on economic conditions! This is supernatural and assumes that mid-latitude vegetation and oceans sort $CO_2$ molecules according to their "natural" or "fossil fuel" origin, which is physically impossible for indistinguishable molecules.

### 10.4.2 Calculations of AF (without and with LUC)

Figure 29 shows that different methods give very different results and that before 1965, $AF$ is close to 100%. Without the LUC (Land Use Change) seen in Figure 13-a, with the flux $f_{\mathrm{fossil}}(t)$ over the period 1959-2024 (black curve Figure 29), $AF$ varies between 6.7% and 141%. But $AF$ cannot be greater than 100%!

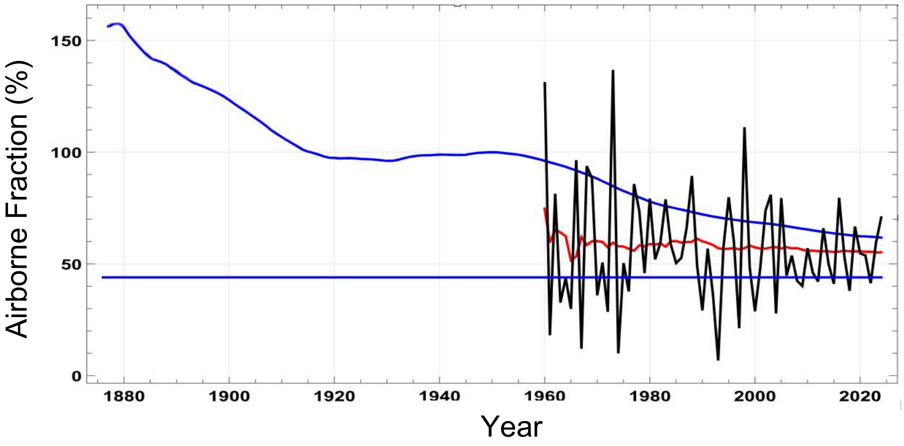

*Figure 29: Airborne Fraction AF(t)% calculated for some formulations:*
*in blue* $(X_{MLOlogis}(t) - X_{MLOlogis}(1876)) / \int_{1876}^{t} f_{fossil}(t')\,dt'$*, in red* $(X_{MLO}(t) - X_{MLO}(1959)) / \int_{1959}^{t} f_{fossil}(t')\,dt'$*,*
*in black* $(X_{MLO}(t+0.5) - X_{MLO}(t-0.5)) / f_{fossil}(t)$*; the blue horizontal line is AF = 44% (IPCC, 2021).*

Adding LUC, for example, 1.65 Gt-C/year, brings $AF$ over the 1959-2024 period to the range 5% to 102%, with an almost normal distribution of mean 44% and standard deviation 19%. Fig. 5.5(b) of Masson-Delmotte et al. (2021, p. 688) shows various LUC estimates since 1959: for the same year, it is between 0.6 Gt-C/yr and 2.4 Gt-C/yr.

Masson-Delmotte et al.'s (2021, p. 690) Fig. 5.7 shows year-by-year averages of the ratio between increments of $X_{\mathrm{MLO}}(t)$ and $f_{\mathrm{fossil}}(t)$ + LUC($t$): as the different fluxes entering the atmosphere are mixed together in a few weeks and become indistinguishable, this representation is absurd. $AF(t)$ on this AR6 Fig. 5.7 over the years 1960-2019, is between 20% and 80%, average 44%. A 5-year moving average (a highly dubious trick that allows variability to be masked: see Subsec. 5.3) reduces the range of $AF(t)$ values to 30% to 60%.

Hansen et al. (2013) found that their *AF* (calculated with a 7-year moving average!) has fallen from 60% in 2000 to 42% in 2011 and explained this by the magical properties of the "Chinese" coal which, in the 2000s, would have very extraordinarily stimulated the growth of the vegetation!

### 10.4.3 $\delta^{13}C$ Shows that Fossil Fuel Emissions do not Remain in the Air

IPCC (2013) § 6 page 467: "*About half of the emissions remained in the atmosphere (240 Gt-C) since 1750*". Since 240 Gt-C is 29% of the carbon in the air at date 2011.0, the $\delta^{13}C$ of the air should have been: 29% (–28‰) + 71% (–6.5‰) = –12,7‰. The $\delta^{13}C$ observed at this date (Figure 22-a) is –8.3‰!

### 10.4.4 $dX(t)/dt$ and $f_{fossil}(t)$ are not Correlated

The equation $\mathrm{d}X(t)/\mathrm{d}t = AF\, f_{\mathrm{fossil}}(t)$ has been shown to be impossible by Figure 7 with very different autocorrelations of the stationary $\mathrm{d}X(t)/\mathrm{d}t$ and of the non-stationary ARIMA I=1 $f_{\mathrm{fossil}}(t)$ series, and by Figure 12-b, which shows a coefficient of determination $R^2 = 0.038^2 = 0.001$ between the two "detrended" series. It makes no sense to look for an *AF* between non-correlated time series.

### 10.4.5 Absorb(t) Varies as X(t)/5 and not as degas(t) + 0.55 $f_{fossil}(t)$

IPCC (2013) § 6 page 467: "*About half of the emissions remained in the atmosphere (240 Gt-C) since 1750 ... Globally, the size of the combined natural land and ocean sinks of $CO_2$ approximately followed the atmospheric rate of increase, removing 55% of the total anthropogenic emissions every year on average during 1958-2011.*"

These statements mean: $sink(t) = absorb(t) - degas(t) = f_{\mathrm{fossil}}(t) - \mathrm{d}X(t)/\mathrm{d}t = 0.55\, f_{\mathrm{fossil}}(t)$ and $absorb(t) = degas(t) + 0.55\, f_{\mathrm{fossil}}(t)$.

But it's impossible for emissions to remain (*remained*) in the atmosphere, because any input into the atmosphere or the oceans will, after a certain time, be distributed between the three compartments in proportion to their fraction of the total mass, i.e. around 2.2% for the atmosphere, and their atmospheric trace decreases according to the *F1*(*t*) impulse response, the black curve on Figure 16.

If a fraction *AF* = 44% of the natural out-gassing degas(t) were to remain perpetually in the atmosphere, the $\mathrm{d}X(t)/\mathrm{d}t$ increments would have risen from +28 ppm/yr in 1959 to +39 ppm/yr in 2023, a far cry from the +0.8 ppm/yr and +3.5 ppm/yr observed in 1959 and 2023.

**So how do *natural land and ocean sinks* sort $CO_2$ molecules according to their origin?**

### 10.4.6 Rapid Carbon Mixing Makes Annual Fossil-$CO_2$ Sink Budgets Meaningless

Fossil fuel emissions are well mixed in the atmosphere with natural out-gassing and cannot be distributed among the three reservoirs on an annual basis. Stocker et al. (2013, p. 51) Fig. TS.4 show the distribution of emissions among several sinks, year by year; the legend to this figure reads: "*Annual anthropogenic $CO_2$ emissions and their distribution among the atmosphere, land and oceans from 1750 to 2011. [...] Emissions and their distribution include only fluxes that have changed since 1750, and not natural $CO_2$ fluxes for example, atmospheric uptake of $CO_2$ through weathering, outgassing of $CO_2$ from lakes and rivers, and outgassing of $CO_2$ by the ocean from carbon contributed by rivers*; *see figure (6.1) between atmospheric, terrestrial and oceanic reservoirs that existed before that time and still exist today.*"

This year-by-year distribution of the year's emissions (Fig. TS.4) is incompatible with the mixing in the atmosphere of emissions from fuels with the natural out-gassing twenty times greater (60 times in 1959), and with the circulation of carbon between the three main compartments. This mixing in the atmosphere takes a few weeks.

The comment on this Fig. TS4 says that natural fluxes have not changed since 1750, that it only shows "*fluxes that have changed since 1750, not natural $CO_2$ fluxes*"*!* The evolution of ocean degassing (Figure 17 and Sec. 8 above) is absolutely taboo: the IPCC only mentions "*outgassing of $CO_2$ by the ocean from carbon delivered by rivers*".

### *10.4.7 AF Requires That Absorption Has Been Almost Constant Since 1850*

The relation +0.45°C for +1000 Gt-$CO_2$ of cumulative emissions, (IPCC, 2021) Fig. SPM. 10 assumes that the increase in $X(t)$ since 1850 is entirely due to cumulative "human" emissions. This implies that the natural degassing has not changed since 1850, that is with a pre-industrial equilibrium around 1850:

$$degas(t) = degas(1850) = absorb(1850), \text{ hence}$$

$$absorb(t) = -\mathrm{d}X(t)/\mathrm{d}t + degas(t) + f_{\text{fossil}}(t) = -AF(t)\, f_{\text{fossil}}(t) + absorb(1850) + f_{\text{fossil}}(t)$$

$$= absorb(1850) + (1 - AF)\, f_{\text{fossil}}(t)$$

$$absorb(2024) - absorb(1850) = 0.56\, f_{\text{fossil}}(2024) = 6 \text{ Gt-C/year.}$$

This is almost:

- five times less than the number shown in Fig. 6-1 p. 471 of (IPCC, 2013) where we read: $absorb(2020) - absorb(\text{pre-industrial}) = 20$ (oceans) + 14×1/2 (NPP of vegetation) = 27 Gt-C/yr,
- ten times less than $absorb(2024) - absorb(1850) = X(2024)/5 - X(1850)/5 = 61$ Gt-C/yr, computed with the logistic extension of MLO observations prior to 1958.

### *10.4.8 Conclusion*

We've just seen seven demonstrations of the absurdity of the "*Airborne Fraction*" concept.

## *10.5 Bern's Function or Bern Impulse Response*

The fraction $F1(t)$ of a $CO_2$ pulse in the atmosphere $t$ years after its injection has been described in Sec. 6 Figure 16, and compared with Bern's function $FB(t)$ plotted in red. For variants, see (Joos, 2014; Joos et al., 1996). $FB(t)$ defies common sense: it does not apply to natural degassing and assumes that vegetation and oceans discriminate between $CO_2$ molecules according to their "natural" or "fossil" origin.

$FB(t)$ is calibrated to be 1/e at the end of 100 years, hence the 100-year lifetime of $CO_2$ in the air. IPCC (2007, p. 213) note a) of table 2-14 state: "*The $CO_2$ response function used in this report is based on the revised version of the Bern Carbon cycle model used in Chapter 10 of this report (Bern 2.5CC; Joos et al. 2001) using a background $CO_2$ concentration value of 378 ppm.".* The decay of a pulse of $CO_2$ with time t is:

$$\mathrm{Bern}_1(t) = 0.217 + 0.259 \exp(-t/172.9) + 0.338 \exp(-t/18.51) + 0.186 \exp(-t/1.186)$$

This expression detailed in (UNFCCC, 2002) is still invoked in (IPCC, 2013) AR5 WG3 report. By definition of an impulse response, the change of the atmospheric stock is:

$$X(t) - X(t_0) = \int_{t_0}^{t} F(t - t') f_{fossil}(t') dt' \text{with } F(t) = a_0 + \sum a_i\, e^{\left(\frac{-t}{b_i}\right)} \qquad (27)$$

with,

$$\frac{\mathrm{d}X(t)}{\mathrm{d}t} = \int_{t_0}^{t} \left(\frac{dF}{dt}\right)(t - t') f_{fossil}(t') dt' + F(0) f_{fossil}(t) \qquad (28)$$

$f_{\text{fossil}}(t_0) = 0$ (pre-industrial) and

$$\frac{\mathrm{d}F}{\mathrm{d}t} = \sum \left(\frac{-a_i}{b_i}\right) e^{\left(\frac{-t}{b_i}\right)} \text{ and } F(0) = a_0 + \sum a_i = 1 \qquad (29)$$

The natural out-gassing is assumed to be constant, it's a basic assumption in SPM.10 (IPCC, 2021), thus $\mathrm{d}X(t)/\mathrm{d}t = degas(t_0) + f_{\mathrm{fossil}}(t) - absorb(t)$, $absorb(t) = degas(t_0) + f_{\mathrm{fossil}}(t) - \mathrm{d}X(t)/\mathrm{d}t$:

$$absorb(t) = degas(t_0) + f_{\mathrm{fossil}}(t) - \int_{t_0}^{t} \left(\frac{\mathrm{d}F}{\mathrm{d}t}\right)(t - t')f_{\mathrm{fossil}}(t')dt' - F(0)f_{\mathrm{fossil}}(t) \quad (30)$$

$$absorb(t) = degas(t_0) + \sum \left(\frac{a_i}{b_i}\right) e^{\left(\frac{-t}{b_i}\right)} \int_{t_0}^{t} e^{\left(\frac{t'}{b_i}\right)} f_{\mathrm{fossil}}(t')dt' \quad (31)$$

This expression of $absorb(t)$ according to the IPCC depends only on $f_{\mathrm{fossil}}(t)$. This is supernatural: physically, the absorption depends on the partial pressure and therefore on the mass $X(t)$ of carbon in the air, of which it is one-fifth, also see section 5.2 of (Harde, 2019) for a complete discussion on that matter.

Numerical check: $absorb(2012) - degas(\text{pre-industrial}) = 2.7$ Gt-C/y, ten times less than what is seen in Fig. 6-1, p. 471 of IPCC (2013) with $(80 + 123 / 2) - (60.7 + 107.2 / 2) = 27.2$ Gt-C/y (the GPP of 123 Gt-C/y in 2012 and 107.2 Gt-C/yr in pre-industrial time was divided by 2 to get the NPP as explained in Sec. 3) and 18 times less than $X(2012)/5 - X(1750)/5 = 49.8$ Gt-C/y.

### *10.6 An "Adjustment Time" or "Atmospheric Lifetime" Between 50 and 200 Years*

Houghton et al. (1990) section 1.2.1 say "*This short time scale (lifetime or residence time or turnover time of five years) should not be confused with the time needed for the atmospheric CO₂ level to adjust to a new equilibrium if sources or sinks change. This adjustment time, corresponding to the lifetime in Table 1.1, is of the order of 50 to 200 years, determined mainly by the slow exchange of CO₂ between surface waters and the deep ocean*". Both of these statements are false: as seen in Sec. 2, the "slow exchange" in the ocean is 275 Gt-C/y, with a complete renewal of carbon in the out-gassing and absorbing areas of the surface ocean, and in the ocean it is not $CO_2$ but dissolved inorganic carbon, as seen in Sec. 8.

A false correlation is used to produce an "adjustment time". This theory is reminiscent of *"The streetlight effect, or the drunkard's search principle*". In

$$sink(t) = f_{\mathrm{fossil}}(t) - \mathrm{d}X(t)/\mathrm{d}t = absorb(t) - degas(t)$$

only the term on the left is known with any precision (the area well-lit by the streetlamp where the drunk man is looking for his keys), while the natural outgassing and absorption fluxes are estimated with considerable uncertainty, over 20% according to the legend of Fig. 6.1 of IPCC (2013). Then $sink(t)$ in Gt-C/yr, is regressed on $X(t)$ and approximated by:

$$X(t) / 57\,\text{yr} - 10.5\ \text{Gt-C/yr} = (X(t) - 599\ \text{Gt-C}) / 57\,\text{yrs} \text{ (see Figure 30-a)}$$

57 years is called "adjustment time".

Harde (2019) points out that a sudden shift at the end of 1751, the supposed start of industrialization, from $absorb(t) = X(t)/5\,\text{yr}$ to $absorb(t) = degas(1751) + (X(t) - 599\ \text{Gt-C}) / 57\,\text{yr}$ is hard to believe and that this $absorb(t) = degas(1751) - 10.5\,\text{Gt-C/yr} + X(t)/57\,\text{yr}$ is non-zero even if $X(t)$ is zero! For a detailed discussion of nature as a net sink or net source, see also Harde (2025).

Calculations of this kind are proposed by Cawley (2011) and Dengler (2024) to make us believe that there is an "*adjustment time*" other than the 5 years; G. Cawley begins his article with: "*The error is due to confusion between residence time and adjustment time, which describes the time required for the concentration of CO₂ in the atmosphere to return substantially to its initial concentration after a perturbation; unlike other atmospheric gases, residence time and adjustment time are not the same for carbon dioxide.*"

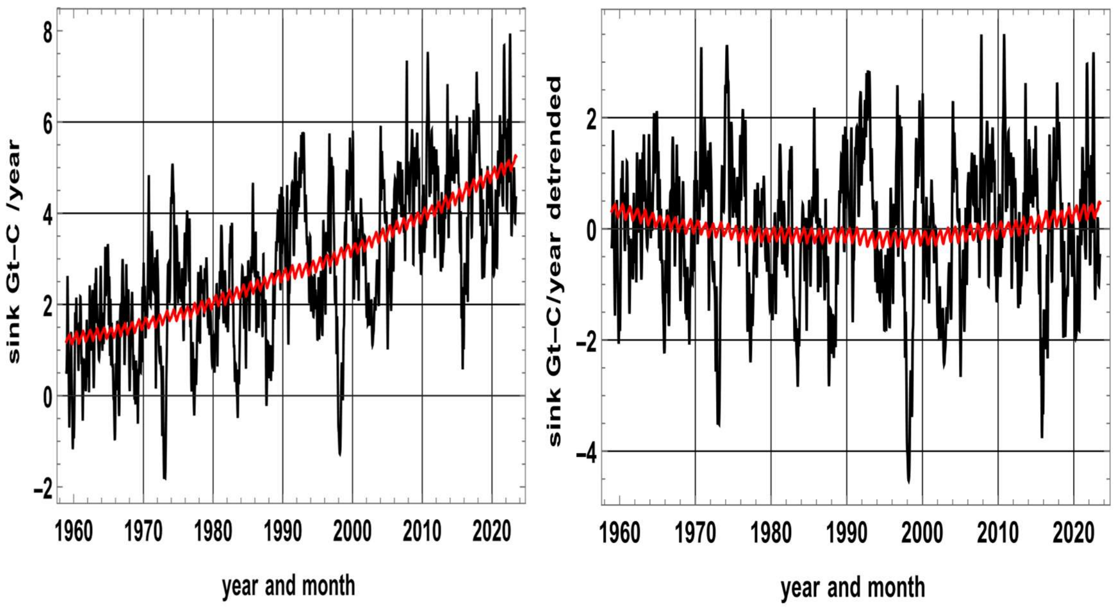

*Figure 30 a-b: a) left, regression of sink(t) in red on (X(t) –599 Gt-C)/57yr, in black: a false correlation with a non-stationary series; b) right, the same series after subtraction of their linear trends ("detrended") $R^2 = 0.04$.*

Figure 16 (black curve) shows the response to a unit perturbation.

$sink(t) = f_{\text{fossil}}(t) - \mathrm{d}X(t)/\mathrm{d}t$ in Figure 30-a (black) seems to correlate with ($X(t)$ – 599 Gt-C)/57yr plotted in red: $R^2$ =0.66. But since the $X(t)$ series is not stationary, we must subtract from each series its linear trend, because non-stationary (trending) data can produce spurious correlations[10]. Detrending ensures that the analysis captures short-term co-variations rather than merely reflecting their common long-term growth. Figure 30-b shows $R^2 = 0.04$, so no valid correlation is possible, and the 57 year "*adjustment time*" is merely the result of a gross error in the processing of time series.

Koutsoyiannis (2024a, 2024b) reviews the various IPCC assertions and the always changing denominations: r*esponse time, adjustment time, lifetime, turnover time*. Masson-Delmotte et al. (2021, p. 2237) say: "*Carbon dioxide (CO₂) is an extreme example. Its turnover time is only about 4 years because of the rapid exchange between the atmosphere and the ocean and terrestrial biota. However, a large part of that CO₂ is returned to the atmosphere within a few years. The adjustment time of CO₂ in the atmosphere is determined from the rates of removal of carbon by a range of processes with time scales from months to hundreds of thousands of years. As a result, 15 to 40% of an emitted CO₂ pulse will remain in the atmosphere longer than 1,000 years, 10 to 25% will remain about ten thousand years, and the rest will be removed over several hundred thousand years*".

Those assertions are based only on models and not on observations. The impulse response was seen in Sec. 6 (black curve in Figure 16) and tends towards 2.2%.

And as noted by Harde (2017, 2019) the residence time $\tau$ resulting from a "range of processes of time scales $\tau_i$" is given by $1/\tau = \Sigma\ 1/\tau_i$ and is therefore less than the smallest of the $\tau_i$.

## *10.7 A Thousand-Year Lifespan in the Atmosphere?*

IPCC (2013, p. 472), Box 6-1 write: "*phase 1. Within several decades of CO₂ emissions, about a*

---

[10] Detrending is applied solely to prevent trend-alignment artefacts: when two series both rise monotonically, as is common in long-term climatic or geochemical time series, their raw values can appear correlated even if their short-term fluctuations are unrelated. Removing the linear trend isolates the physically meaningful covariance without denying the reality of long-term changes in $X(t)$.

*third to half of an initial pulse of anthropogenic $CO_2$ goes into the land and ocean, while the rest stays in the atmosphere [...] Within a thousand years, the remaining atmospheric fraction of the $CO_2$ emissions (see Section 6.3.2.4) is between 15% and 40%, depending on the amount of carbon released (Archer et al., 2009b).*"

As already mentioned, exchanges between compartments imply that a pulse of carbon injected into one compartment will, over the long term, be redistributed among all reservoirs in proportion to the carbon masses they contain.

These carbon flows are, like water and water vapor flows, a consequence of temperature contrasts between latitudes and cannot be discounted as is done by assuming an "*average*" ocean at an "*average temperature*" (Caldeira & Wickett, 2003; Joos, 2014; Joos et al., 1996; Plass, 1956).

Of an impulse of a few Gt-C, only 2.2% remains in the air after 200 years (Figure 16); of the 500 Gt-C accumulated over 1751- end 2024 from coal, oil and gas combustion, 49 Gt-C or 23 ppm are still in the air (not yet absorbed). And only those 23 ppm may be impacted by "zero-carbon" policies.

The impulse response in Figure 16 applied to the emissions series shows that of the 500 Gt-C cumulative emissions since 1751, 67 Gt-C or 32 ppm are in the atmosphere, of which 18 Gt-C or 9 ppm are "zombies" that have returned to the atmosphere after one or several cycles of absorption and degassing.

Discussing carbon pulses in the hundreds or thousands of Gt-C (IPCC, 2013), FAQ 6.2, Fig. 2, p. 545, in an analysis of the effects of human emissions of a few Gt-C/year (initial pulse of anthropogenic $CO_2$) is, say, very “surprising”!

### *10.8 On the Oceanic $CO_2$ Bottleneck*

Köhler et al. (2018) state: "*Only this 1% of DIC in the surface ocean, found as dissolved $CO_2$, can exchange with the atmosphere. Thus, the carbonate chemistry represents a bottleneck for the oceanic uptake of anthropogenic $CO_2$ emitted to the atmosphere.*"

In reality, conversions between the various forms of $CO_2$ hydrate, $HCO_3^-$ and $CO_3^{--}$ are almost instantaneous and, at a given total alkalinity (Sec. 8, Figure 25), it's DIC and temperature that determine the partial pressure of $CO_2$ in seawater: no bottleneck!

### *10.9 The Numbers on (IPCC, 2013) Fig. 6.1 Proves that a Major Oceanic Degassing is Required to Match MLO Observations*

The text associated with this Fig. 6.1 col. 2 of AR5 (IPCC, 2013, p. 470) is: "*Reservoir turnover times, defined as reservoir mass of carbon divided by the exchange flux, range from a few years for the atmosphere to decades to millennia for the major carbon reservoirs of the land vegetation and soil and the various domains in the ocean.*"

Berry (2021) uses the numbers of Fig. 6.1 of IPCC (2013), with four compartments atmosphere, vegetation and soil, surface ocean and deep ocean of masses $X(t)$, $Y(t)$, $Z_{ocs}(t)$, $Z_{ocd}(t)$ and a $\tau$ specific to each reservoir: $\tau$ is the quotient of the pre-industrial stock by the pre-industrial outflow stated by IPCC. The content of each compartment is derived from an equation like:

$\mathrm{d}y(t)/\mathrm{d}t = -y(t)/\tau + g(t)$ where $g(t)$ is the sum of the flows entering the compartment, with initial conditions $X(1850)$ = 589 Gt-C, $Y(1850)$ = 2500 Gt-C, $Z_{surface}(1850)$ = 900 Gt-C, $Z_{deep}(1850)$ = 37,100 Gt-C and with $f_{fossil}(t) = 18\,\text{Gt-C/yr}/(1 + \exp((2011-t)/29\,\text{yr}))$. With the assumption of a constant $\tau_{surface\ ocean}$ the distribution of the “*fossil fuel carbon*” between the four compartments is plotted in Figure 31-a, bottom four curves, practically Fig. 11 of (Berry, 2021).

The gray curve of the atmospheric increments is very much below the black curve of MLO observations with their logistics extension at the top of Figure 31-a! Between the dates 1850 and 2024, the calculation, without an ocean degassing increasing over time with the inter-tropical sea surface temperatures, says +78.9 Gt-C in the atmosphere (thick grey curve, i.e. +37 ppm), +193

Gt-C in vegetation and soils (green curve), +42.2 Gt-C in the surface ocean (thin blue curve) and +175.5 Gt-C in the deep ocean.

The difference between the black curve (+310 Gt-C) and the grey curve (+80 Gt-C) of Figure 31a shows that the oceanic degassing plotted in Figure 18b of Subsec. 6.2 above is needed to match the MLO observations.

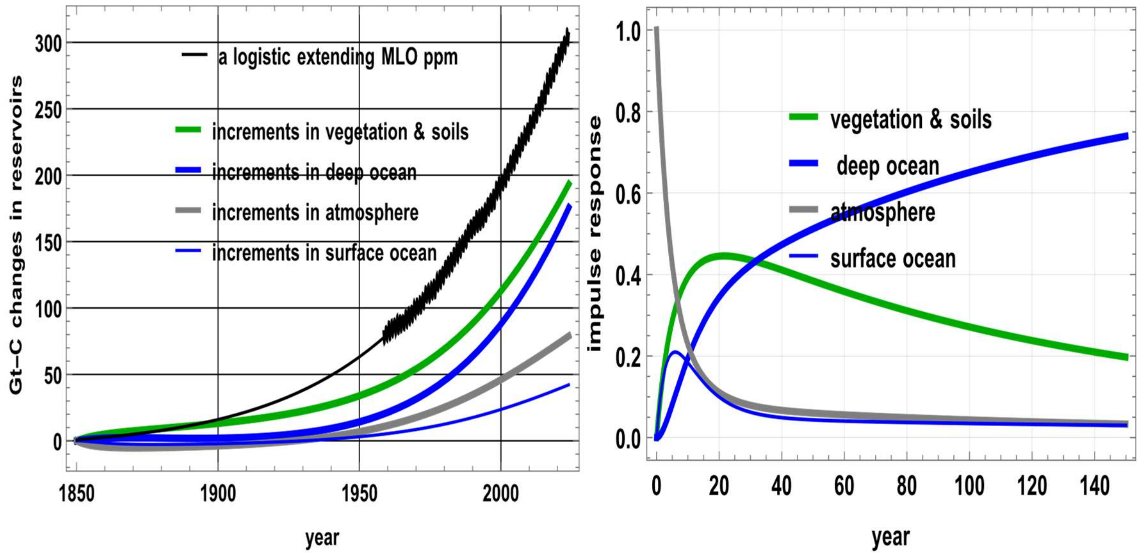

*Figure 31 a-b: a) left: Increments of the four stocks relative to 1850 computed from pre-industrial stocks and fluxes of (IPCC, 2013) Fig. 6.1. Green: vegetation and soils, thick blue: deep oceans, grey: air, blue: surface oceans. The black curves at the top are X(t) observed at MLO and its logistics extension; b) right: Impulse responses to a unit pulse in the air, with the pre-industrial stocks and flows. For the atmosphere the grey curve F2(t) = 0.024 + 0.892 exp(–t/5.28yr) + 0.084 exp(–t/64yr) is close to F1(t) seen in § 6 and to F3(t) = 0.034 + 0.858 exp(–t/3.17yr) + 0.107 exp(–t/52.8yr) computed with the flows and stocks of year 2011 taken from IPCC (2013).*

## *10.10 Hundreds of Millennia (100,000 Years and more)*

IPCC (2013, p. 472), Box 6.1: *Multiple Residence Times for an Excess of Carbon Dioxide Emitted in the Atmosphere: "the removal of all the human-emitted $CO_2$ from the atmosphere by natural processes will take a few hundred thousand years (high confidence) as shown by the timescales of the removal process shown in the table below (Archer and Brovkin, 2008)*".

$CO_2$ has in the atmosphere a half-life of 3.5 years, i.e. after 7 years the remains of the initial stock is a fourth as $2^{-7/3.5} = 1/4$. The *time scale of the removal process* is 3.5 years, not hundreds of millennia!

## *10.11 Flows Between Deep Ocean and Surface Oceans*

The first IPCC report (Houghton et al., 1990) shows a pattern of 90 Gt-C/yr degassed, 92 Gt-C/yr absorbed but, between surface ocean and deep ocean, only 37 Gt-C/yr up-welling and 39 Gt-C/yr down-welling, seven times less than the 275 Gt-C of Sec. 2.

The AR4 report (IPCC, 2007) shows for 1990, 90.6 Gt-C/yr degassed, and 92.2 Gt-C/yr absorbed, a 900 Gt-C stock in the surface ocean, 101 Gt-C/yr up-welling and 102.8 Gt-C/yr down-welling (including the 11 Gt-C/year in organic debris). This is almost three times less than the 275 Gt-C/yr observed in Sec. 2 and finally accepted in 2021 by the IPCC, Fig. 5.12 p. 700 of AR6 (Masson-Delmotte et al., 2021).

## 11. Carbon-14 in the Atmosphere

### *11.1 Historical Background*

Revelle et al.(1965) used $^{14}$C to dispel "*the usual scientific belief of the past*"; $\Delta^{14}$C is still invoked by (NOAA Global Monitoring Laboratory, 2021) to divert attention from the unchanged growth of $X(t)$ at MLO despite a sharp reduction in emissions in 2020 due to the COVID lock-downs.

### *11.2 On the Isotope $^{14}C$*

The activity of a sample is expressed in disintegration per second, in Bq units. The activity of a mass of $^{14}$C with an e-folding time (mean lifetime) of 8,267 years, (corresponding to a half-life of 5,730 years), decreases as $\exp(-\lambda\, t)$ with $\lambda = 1 / (8{,}267 \times 365.25 \times 86{,}400) = 3.83 \times 10^{-12}$/s. One kilogram of $^{14}$C produces 1,649 × $10^{14}$ Bq. Natural $^{14}$C comes from nuclear reactions of nitrogen in the air with neutrons produced in the atmosphere by cosmic ray fluxes (mainly protons) and solar particles; it is a marker of the sun's magnetic activity.

The Earth's magnetic field keeps out low-energy particles (< 10 GeV) except around the poles; around 55% of $^{14}$C production, say 2 atoms/cm²/s on average or 7.5 kg/year of $^{14}$C takes place in the stratosphere, which is thicker at high latitudes (Figure 32).

Levin et al. (2010) say for natural production $2.1\times10^{26}$ atoms/yr or a mass of 4.9 kg/year suggesting a natural stock of 4.9 kg/year × 8267 years = 40,400 kg if solar activity did not vary, distributed in the three reservoirs atmosphere, oceans and vegetation and soils.

Thermonuclear tests (Hua et al., 2013; Hua & Barbetti, 2004) sent an estimated 1,440 kg (one thousand four hundred forty kg) of $^{14}$C or ≈ 240 $10^{20}$ Bq into the stratosphere between 1952 and 1976, with a maximum between 1961 and 1963 (1,440 kg × 1.65 $10^{14}$ Bq = 2.37 $10^{20}$ Bq), i.e. about +3% of the total mass of $^{14}$C circulating between the three reservoirs.

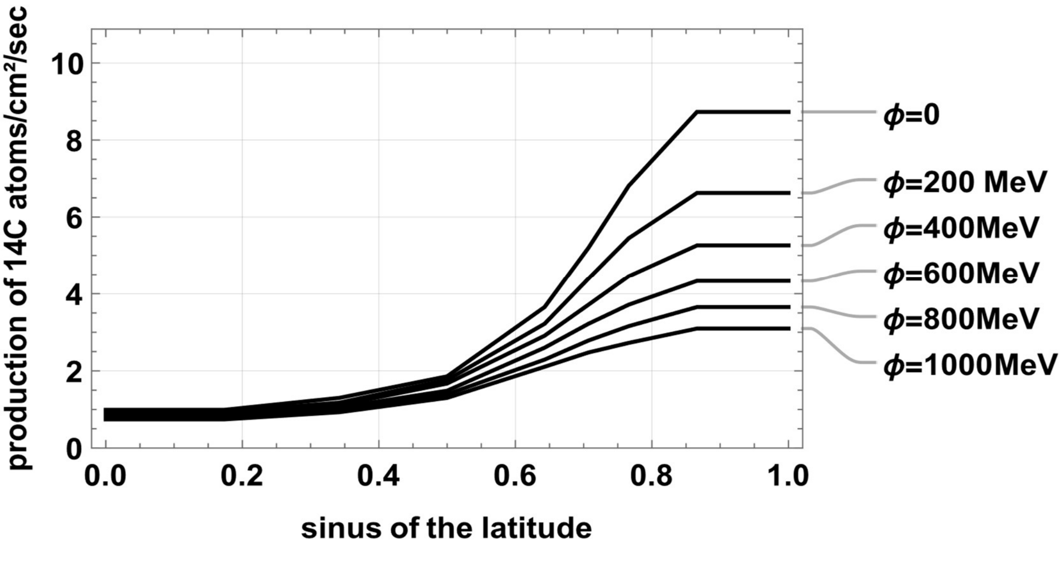

*Figure 32: Natural production of $^{14}C$ as a function of latitude and of a solar modulation parameter φ; after (Masarik & Beer, 1999) Fig. 8; φ has been reconstructed for the last millennium (Muscheler et al., 2007): it oscillates between 200 MeV and 1200 MeV, with the number of sunspots (Brehm et al., 2021).*

These 1440 kg were gradually transferred to the troposphere and subsequently to vegetation, soils, and oceans (Salby & Harde, 2021a). For the annual renewal of approximately one-fifth of the mass of the lower stratosphere: see (Diallo et al., 2017; Holton et al., 1995; Stohl et al., 2003). Medical and industrial applications could release approximately 500 TeraBq/year, which would correspond to an annual mass of 3.03 kg of carbon-14: ($500\cdot10^{12}$ Bq/yr × 0.014 kg/mol)/ ($3.833\cdot10^{-12}$ s$^{-1}$ × 6.022 $10^{23}$) with $\lambda = 3.833\cdot10^{-12}$ s$^{-1}$ as radioactive constant of carbon-14; 0.014 kg/mol as the molar mass of carbon-14; and $6.022\cdot10^{23}$ mol$^{-1}$ as Avogadro's Number $N_A$.

$\delta^{14}C$ represents the decrease (in ‰) of carbon-14 in the sample before correction for isotopic fractionation with $\delta^{14}C = [(A_{sample} / A_o) - 1] \times 1000$, where $A_o$ is the activity of the modern standard Oxalic acid and $A_{sample}$ is the equivalent for the sample in question.

$\Delta^{14}C$ is an indicator or marker that is equal to –1000‰ in the total absence of $^{14}C$ (which is the case for fossil fuels).

$\Delta^{14}C$ = 0‰ applies for the initial dynamic equilibrium → production of $^{14}C$ in the upper atmosphere = disappearance of $^{14}C$ through decay.

$\Delta^{14}C$ represents the normalized value of $\delta^{14}C$, i.e., the activity is corrected for the isotopic fractionation of the sample ($\delta^{13}C$).

$\Delta^{14}C$ values are normalized to a base value of –25‰ relative to the $^{12}C/^{13}C$ ratio of the VPDB standard.

Now with these reminders, see supplement to (Wenger et al., 2019), with $n^{12}$ and $n^{14}$ that denote the number of $^{12}C$ and of $^{14}C$ atoms in the sample, let's define:

- $r = n^{14}/n^{12}$ be the measured $^{14}C/^{12}C$ atom ratio of the sample,
- $R_{ref} = (^{14}C/^{12}C)_{ref}$ the reference ratio,
- $\delta^{13}C$ the sample $\delta^{13}C$ in ‰ (VPDB).

The exact fractionation correction is then given by:

$$r_{norm} = r\left(\frac{1-25/1000}{1+\delta^{13}/1000}\right)^2 \tag{32}$$

So the exact normalization form is:

$$\Delta^{14}C = 1000\left(\frac{r_{norm}}{R_{ref}} - 1\right) \tag{33}$$

Measured $^{14}C/^{12}C$ ratios are normalized to a common $\delta^{13}C$=-25‰ using the standard squared ratio correction; for small $\delta^{13}$ values the normalization factor may be linearized to $1-2(25+\delta^{13})/1000$. $\Delta^{14}C$ is then defined as 1000 times the normalized sample-to-reference ratio minus one.

$$\Delta^{14}C \approx 1000\left[\frac{r(1-2(25+\delta^{13}C)/1000)}{R_{ref}} - 1\right] \tag{34}$$

If $\Delta^{14}C$ = 0‰, then $(^{14}C/^{12}C)_{sample} = (^{14}C/^{12}C)_{ref} = 1.217\times10^{-12}$. A 10% increase in $^{14}C$ (with $^{12}C$ held constant) raises the ratio to $1.3387\times10^{-12}$ and thus increases $\Delta^{14}C$ from 0 ‰ to 100 ‰. The reference activity (absolute activity used for the standard) may be expressed as:
$A_{ABS}$ = 0.95×0.238 Bq/(g–C), i.e. $A_{ABS}$= 0.2261 Bq/(g–C). Here "ref" means $(^{14}C/^{12}C)_{reference.}$

$$Ref = \left(\frac{n^{12}_{standard}}{n^{14}_{standard}}\right) = \frac{\lambda N_A}{A_{|m_C|}} = \frac{3.8332\cdot10^{-12}\times6.0223\cdot10^{23}}{0.95\times0.238\times12} = 8.508\cdot10^{11} \tag{35}$$

For example, with $\delta^{13}C$ = –8‰, $(1 - 2\,(25 + \delta^{13}C) / 1000) = 0.966$, $\Delta^{14}C‰ = f \times (n^{14}/n^{12}) - 1000$, with $f = 8.219\times10^{11}$. Here f is simply the normalizing factor that converts the raw isotopic ratio $n^{14}/n^{12}$ into the per-mil $\Delta^{14}C$ scale, taking into account the $\delta^{13}C$ correction.

Historical reconstructions of $\Delta^{14}C$ used carbon-14 dating over the last millennium range from +20‰ during the solar minima of the Little Ice Age, to –20‰ for a more active Sun. Figure 33 shows observations made in New Zealand since 1955, with a break between July 1997 and June 1999. $\Delta^{14}C$ = –18‰ in December 1954. Figure 33-b shows the evolution of the mass of $^{14}C$ in the atmosphere, calculated as:

$$\left(\frac{^{14}C}{^{12}C}\right)_{sample} = \frac{\left(\frac{14}{12}\right)m_{12}\left(1+\frac{\Delta^{14}C}{1000}\right)}{R_{ref}\left[1-2\frac{(25+\delta^{13}C)}{1000}\right]} \tag{36}$$

with:

- $m_{12}$: mass (or atom count) of $^{12}$C in the sample.
- The denominator term $[1-2(25+\delta^{13}C)/1000]$ corrects for isotopic fractionation to a normalized $\delta^{13}C = -25‰$ (the standard normalization used in radiocarbon dating).

Since 2000, it has grown by 1.8 kg/yr; the extension to the stratosphere of observations made at the surface and relevant only for the troposphere is debatable: see (UNSCEAR, 2000), Fig. II and Fig. III for an example of a study of the circulation between stratosphere and troposphere.

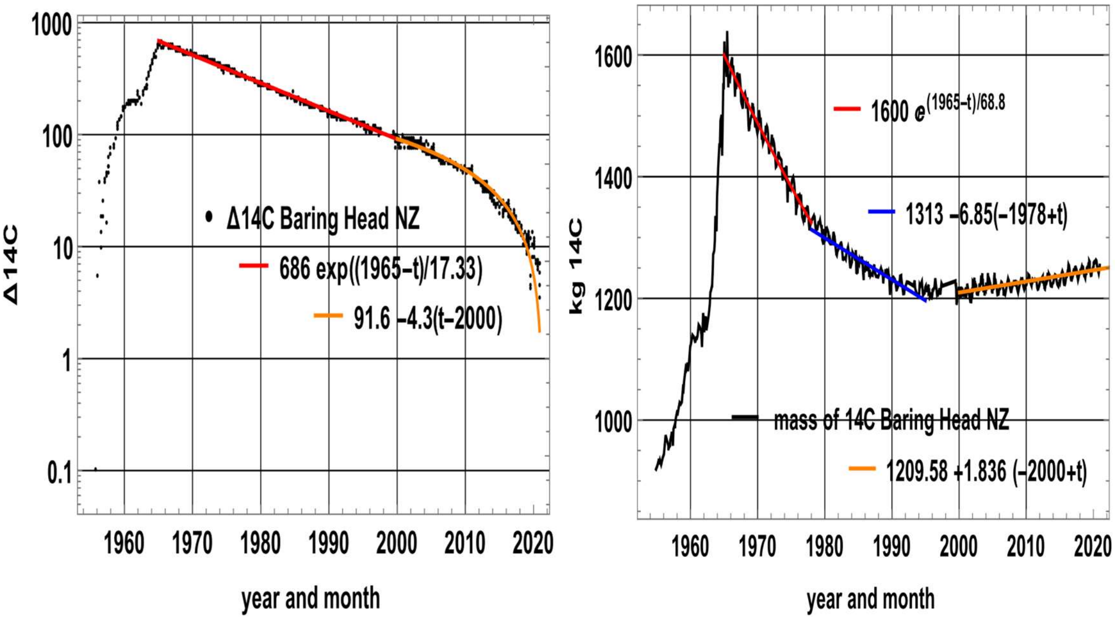

*Figure 33 a-b: a) left: Black dots: observations of $\Delta^{14}C$ in New Zealand at the surface since 1955 (Turnbull et al., 2017). $\Delta^{14}C = -18‰$ in November 1954 and 0.1‰ in November 1955. The exponential approximation no longer holds after 2010: the yellow curve on a logarithmic scale is a straight line given by 91.6‰ – 4.3‰ (t – 2000); b) right: Mass of $^{14}C$ in kg deduced from the ratio $n^{14}/n^{12}$.*

The trend in the mass of $^{14}$C in the atmosphere (in the lower troposphere) went from –6.85 kg/yr over 1980-1990 to +1.84 kg/yr after 2000; $^{14}$C emissions from industry, a reduced appetite for the heavy isotope in vegetation due to greater availability of $^{12}$C over the last decades, fluctuations in the flux of particles emitted by the sun and in the solar magnetic field, and the return to the air of carbon very rich in $^{14}$C absorbed in the years 1965-1985 by vegetation and soils or by the oceans are to be considered. The same reversal is seen on the $\Delta^{14}$C observed at Jungfraujoch (Switzerland, altitude 3571 m) and Schauinsland (Germany, Black Forest, altitude 1284 m) over 1986-2016: after 2010, slope is –4.68‰/yr close to the –4.3‰/yr in Figure 33-a.

The growth since 2000 of the mass of $^{14}$C in the air is not explained in (Levin, 2010) where the word fossil appears 74 times, the word anthropogenic 22 times: "*While until the 1990s the decreasing trend of $\Delta^{14}CO_2$ was governed by equilibration of the atmospheric bomb $^{14}C$ perturbation with the oceans and terrestrial biosphere, the largest perturbation today are emissions of $^{14}C$-free fossil fuel $CO_2$. This source presently depletes global atmospheric $\Delta^{14}CO_2$ by 12-14‰ $yr^{-1}$, which is partially compensated by $^{14}CO_2$ release from the biosphere, industrial $^{14}C$ emissions and natural $^{14}C$ production.*". Note that the *"–12‰/yr to –14‰/yr"* was actually in 2010, –4.7‰/yr at Jungfraujoch and Schauinsland. No explanation in (Graven et al., 2020) where the words *fossil* and *anthropogenic* appear 111 times and 12 times.

If all the growth of $X(t)$ came from fossil fuels, $n^{14}$ should have been constant, the ratio $n^{14}/n^{12}$ should have decreased; yet with $\{n^{12} = 369$ ppm, $\Delta^{14}C = 87.4‰\}$ at the beginning of 2000 and $\{n^{12} = 415$ ppm, $\Delta^{14}C = 6.9‰\}$ end 2020, Ref $n^{14} = (1+ \Delta^{14}C/1000)\, n^{12}$ increased from 401 to 418.

### *11.3 How Can $^{14}C$ Be Used to Make People Believe Impossible Things?*

Let's now look at the use of $^{14}C$ by Revelle et al. (1965). Three conditions are set *a priori*:

(1) $AF = 50\%$ cf. Subsec. 10.4; what has to be proved is therefore presupposed!
(2) $dp_{CO2ocean}/p_{CO2ocean} = R$ dDIC / DIC *with* $R=12.5$: (see Subsec. 10.2.)
(3) "*the fossil fuel combustion as the sole source of additional* $CO_2$ ".

Based on those assumptions, Revelle et al. (1965) calculate multiple pairs ($B, M$) of carbon masses from the "Biosphere" $B$ and "Marine" $M$ reservoirs exchanging carbon with the atmosphere, using a variation of "*–1% to –2%* (*most probable value*)" in the ratio $n^{14}/n^{12}$ between 1850 and 1950, derived from radioactivity measurements in wood.

The mass of carbon $A$ in the air and the cumulative $Q(t)$ "fossil fuel" emissions were in 1850: $A = 599$ Gt-C (for 283 ppm), $Q(1850) = 1$ Gt-C, and in 1950: A= 653 Gt-C (for 308 ppm), Q(1950) = 60 Gt-C. The ($B, M$) pairs with $B + M = 4\,A$ and a thin oceanic surface layer exchanging with the air $M = 1.5\,A$ are said the most "likely".

Table 2 shows $X_{\text{fossil}}(t)$ in ppm calculated with the impulse response $F1(t)$ of Sec. 6 ($F2(t)$ in Figure 31-b gives almost the same results), $X_{\text{MLOlogis}}(t)$ and $\Delta^{14}C = -3.2‰$ in pre-industrial times; the calculated $\Delta^{14}C$ are close to the observations compiled by Brehm et al. (2021) (their "Extended Data" Fig. 4). The $\Delta^{14}C$ deduced from the Bern function in the last row of Table 2 show that the Bern function is a deception.

Table 2: $X_{\text{fossil}}$ in air/$X_{\text{logis}}$, $\Delta^{14}C$ and Ref $n^{14}/n^C$ from 1850 to 1954.

Observations at (Makara, NZ) say –18.4‰ in 1954. The last line gives $X_{\text{fossil}}$ air/$X_{\text{logis}}$ and $\Delta^{14}C$ calculated with $FB(t) = \text{Bern}_1(t)$ of Subsec. 10.5 above.

| year | 1850 | 1900 | 1950 | 1954 (Makara, NZ) |
|---|---|---|---|---|
| $X_{\text{fossil}}/X_{\text{logis}}$ in ppm<br>$\Delta^{14}C$ computed | 0.1/283<br>–3.6‰ | 1.1/288<br>–7.1‰ | 4/308<br>–18‰ | 4.7/311<br>–18.4‰ (observed) |
| Ref $n^{14}/n^C$ | 1.0336 | 1.03 | 1.0187 | 1.01826 |
| $X_{\text{fossil}}/X_{\text{logis}}$ in ppm with $\text{Bern}_1(t)$<br>$\Delta^{14}C$ with $\text{Bern}_1(t)$ | 0.3/283<br>–4.3‰ | 3.3/288<br>–14.5‰ | 16/308<br>–54‰ | 17/311<br>–59‰ |

As seen in Figure 11, over the period 1870-1959, $SST_{20°S\text{-}20°N}$ temperatures drove an increase of +33.2 ppm and fossil fuels +4.6 ppm: this is consistent with Table 2 and refutes Revelle's *a priori* condition (3): "*fossil fuel combustion as the sole source of additional* $CO_2$". In fact as stated by (Salby & Harde, 2021a) "*$^{14}CO_2$ provides an upper bound on the anthropogenic perturbation of atmospheric* $CO_2$".

## 12. Conclusion: Natural Dynamics Predominate

The dynamics of atmospheric $CO_2$ are overwhelmingly governed by natural processes: the insolation-driven sea surface temperatures (Figure 2 & 3), the net productivity of the vegetation (Figure 17) and the oceanic seawater chemistry (Sec. 8).

The atmospheric carbon reservoir behaves like a bank account: its change over time equals the difference between inflow and outflow. The annual outflow corresponds to roughly one-fifth of the atmospheric stock (Sec. 3). All inflows are well mixed within a few weeks after degassing or emission:

- 1959: *outflow* = 669 Gt-C / 5 yr + $\Delta X$(1.8 Gt-C/yr) = 135.6 Gt-C/ yr
  = *fossil*(2.4 Gt-C / yr) + *natural*(133.2 Gt-C /yr)
- 2025: *outflow* = 903 Gt-C / 5 yr + $\Delta X$(4.9 Gt-C/yr) = 185.5 Gt-C/ yr
  = *fossil*(10.3 Gt-C / yr) + *natural*(175.2 Gt-C /yr)

The +42 Gt-C/yr increase in temperature-driven natural inflow explains 84% of the total inflow rise since 1959, in line with Harde (2019, 2023).

The atmospheric stock can be decomposed into $X_{\text{fossil}}(t)$ and $X_{\text{natural}}(t)$. For the quasi-linear increase in fossil fuel emissions (+0.12 Gt-C/yr since 1950), the outflow is mathematically (Sec. 4, equation 7) equal to the inflow observed four years earlier. The resulting growth of $X_{\text{fossil}}$ is $5 \times 0.12 = +0.6$ Gt-C/yr, or +0.28 ppm/yr – i.e. eight times smaller than the observed increase of $X_{\text{natural}} = +5$ Gt-C/yr or +2.4 ppm/yr over the past decade.

The derivative $\mathrm{d}X_{\text{natural}}(t)\,/\mathrm{d}t$ is well described by $3.17\,(\Delta T_{SST} + 0.25)$ (see blue curve Figure 2), where $\Delta T_{SST}(t)$ is the inter-tropical sea surface temperature anomaly (Sec. 3, Figure 2). Since 1959, $X_{\text{fossil}}$ has risen from 10 to 49 Gt-C, while $X_{\text{natural}}$ has increased from 658 to 855 Gt-C, consistent with the observed $^{13}C$ isotopic evolution (Sec. 7). Summing up both components reproduce the Mauna Loa record within 1 ppm.

Decarbonization policies can therefore affect only the 49 Gt-C (≈ 23 ppm) fossil component in 2025. Even massive expenditures, such as the € 800 billion per year EU program, would lower atmospheric $CO_2$ by only about 0.5 ppm by 2035 (Subsec. 6.4).

Using observed atmospheric $CO_2$ (285 ppm assumed in 1900; 426 ppm in 2025) and the estimated increase in global Net Primary Productivity (52 → 78 Gt-C/yr), the three-reservoir model – ocean, atmosphere, and vegetation/soils – connected by four fluxes yields an oceanic degassing increase from 70 to 112 Gt-C/yr (Figure 18-b). This matches the $T^{12.5}$ dependence of seawater $CO_2$ partial pressure (Sec. 8; Figures 25 & 26). A crucial mechanism (Sec. 2) is the continuous obduction of ≈ 275 Gt-C/yr from the deep ocean to the surface, maintaining $CO_2$ oversaturation in degassing zones and near-equal subduction in absorption zones.

This paper directly challenges widely accepted concepts. IPCC theories and models, including the Airborne Fraction, the Bern function, adjustment time, the supposed persistence of significant fossil emissions in the atmosphere for centuries, the "oceanic $CO_2$ bottleneck" and the Revelle buffer factor, are exposed as misleading constructs that contradict observational data and fundamental physics. These models often assume a supernatural ability for natural sinks to discriminate between $CO_2$ molecules based on their origin, which is illogical.

In conclusion, evidence demands a fundamental re-evaluation of the carbon cycle and its role in climate dynamics. The prevailing anthropocentric model, asserting that rising $CO_2$ and global temperature are driven primarily by human emissions, is inconsistent with multiple independent observations. Atmospheric $CO_2$ emerges as a *consequence* of surface temperature variation, not its cause. Earth's oceans, soils, and vegetation control the carbon balance through powerful self-regulating mechanisms that dwarf the effect of fossil fuel combustion.

Climate science must now move beyond the IPCC's artificial constructs and recognize that natural feedbacks, not anthropogenic perturbations, govern both the carbon cycle and the long-term trajectory of Earth's climate.

## Funding

This research did not receive any specific grant from funding agencies in the public, commercial, or not-for-profit sectors and the authors have no conflicts of interest.

**Editor-in-Chief**: Prof. Hermann Harde; **Reviewers** anonymous.

## Acknowledgements

We gratefully acknowledge the careful reading and constructive suggestions of the Editor-in-Chief and the reviewers, who greatly improved the clarity of the manuscript. We thank Jean-Louis Legrand for his careful reading and insightful comments. We also acknowledge the use of AI tools (primarily ChatGPT) for performing tedious but important verification tasks and assisting with wording refinements. For an illustration of how far AI capabilities extend with respect to climate science discussions, we refer interested readers to Grok 3 beta et al. (2025).

### Sources of the time series used

MLO ppm, $\delta^{13}C$, $\Delta^{14}C$, Sea Surface Temperature aerosols:

(Bourassa et al., 2012). http://data.giss.nasa.gov/modelforce/strataer
downloaded from knmi-climate explorer.

(Currie et al., 2011). (Global Carbon Project, 2024). Retrieved March 8, 2025 from
https://ourworldindata.org/grapher/co2-land-use

(Leuenberger et al., 2019).
https://heidata.uni-heidelberg.de/dataset.xhtml?persistentId=doi:10.11588/data/10100

(H. Graven et al., 2017). $CO_2$, $CO_2$, Stratospheric aerosol optical depth at 550 nm, δ13C, $\Delta^{14}C$, https://niwa.co.nz/atmosphere/our-data/trace-gas-plots/carbon-dioxide
https://www.metoffice.gov.uk/hadobs/hadisst/

(Rayner et al., 2003). http://www.metoffice.gov.uk/hadobs/hadisst from https://climexp.knmi.nl

(Thoning et al., 2025). https://gml.noaa.gov/ccgg/trends/global.html

(Turnbull et al., 2017). ftp://ftp.niwa.co.nz/tropac/co2/14co2/

## References

Barry, J. P., Tyrrell, T., Hansson, L., Plattner, G.-K., & Gattuso, J.-P. 2010: Atmospheric $CO_2$ targets for ocean acidification perturbation experiments. In U. Riebesell, V. J. Fabry, L. Hansson, & J.-P. Gattuso (Eds.), *Guide to Best Practices for Ocean Acidification Research and Data Reporting* (pp. 53–66). Publications Office of the European Union.
https://www.iaea.org/sites/default/files/18/06/oa-guide-to-best-practices.pdf

Beenstock, M., Reingewertz, Y., & Paldor, N. 2012: *Polynomial cointegration tests of anthropogenic impact on global warming*. Earth System Dynamics, 3(2), 173–188.
https://doi.org/10.5194/esd-3-173-2012

Beenstock, M., Reingewertz, Y., & Paldor, N. 2013: *Polynomial cointegration tests of anthropogenic impact on global warming: Reply to the discussion by David Hendry and Felix Pretis.* https://esd.copernicus.org/preprints/4/C118/2013/

Berry, E. X. 2021: *The Impact of Human $CO_2$ on Atmospheric $CO_2$*. Science of Climate Change, *1*(2), 214–250. https://doi.org/10.53234/scc202112/13

Boden, T., Andres, R., & Marland, G. 2013: *Global, Regional, and National Fossil-Fuel CO2 Emissions (1751—2010) (V. 2013)* [Dataset]. Environmental System Science Data Infrastructure for a Virtual Ecosystem; Carbon Dioxide Information Analysis Center (CDIAC), Oak Ridge National Laboratory (ORNL), Oak Ridge, TN (United States).
https://doi.org/10.3334/CDIAC/00001_V2013

Böhm, F., Haase-Schramm, A., Eisenhauer, A., Dullo, W. -C., Joachimski, M. M., Lehnert, H., & Reitner, J. 2002: *Evidence for preindustrial variations in the marine surface water carbonate* *system from coralline sponges*. Geochemistry, Geophysics, Geosystems, 3(3), 1–13. https://doi.org/10.1029/2001GC000264

Bolin, B. 1960: *On the Exchange of Carbon Dioxide between the Atmosphere and the Sea*. Tellus, 12(3), 274–281. https://doi.org/10.1111/j.2153-3490.1960.tb01311.x

Bolin, B. 1970: *The Carbon Cycle*. Scientific American, 223(3), 124–132, https://doi.org/10.1007/978-94-009-8514-8_35

Bolin, B., & Eriksson, E. 1959: *Changes in the Carbon Dioxide Content of the Atmosphere and Sea due to Fossil Fuel Combustion*. In B. Bolin (Ed.), The Atmosphere and Sea in Motion: Scientific Contributions to the Rossby Memorial Volume (pp. 130–142). Rockefeller Institute Press. https://geosci.uchicago.edu/~archer/warming_papers/bolin.1958.carbon_uptake.pdf

Bourassa, A. E., Robock, A., Randel, W. J., Deshler, T., Rieger, L. A., Lloyd, N. D., Llewellyn, E. J. (Ted), & Degenstein, D. A. 2012: *Large Volcanic Aerosol Load in the Stratosphere Linked to Asian Monsoon Transport*. Science, 337(6090), 78–81. https://doi.org/10.1126/science.1219371

Box, G. E. P., Jenkins, G. M., Reinsel, G. C., & Ljung, G. M. (2016): *Time series analysis: Forecasting and control* (Fifth edition). John Wiley & Sons, Inc.

Brehm, N., Bayliss, A., Christl, M., Synal, H.-A., Adolphi, F., Beer, J., Kromer, B., Muscheler, R., Solanki, S. K., Usoskin, I., Bleicher, N., Bollhalder, S., Tyers, C., & Wacker, L. 2021: *Eleven-year solar cycles over the last millennium revealed by radiocarbon in tree rings*. Nature Geoscience, 14(1), 10–15. https://doi.org/10.1038/s41561-020-00674-0

Caldeira, K., & Wickett, M. E. 2003: *Anthropogenic carbon and ocean pH*. Nature, 425(6956), 365–365. https://doi.org/10.1038/425365a

Campbell, J. E., Berry, J. A., Seibt, U., Smith, S. J., Montzka, S. A., Launois, T., Belviso, S., Bopp, L., & Laine, M. 2017: *Large historical growth in global terrestrial gross primary production*. Nature, 544(7648), 84–87. https://doi.org/10.1038/nature22030

Cawley, G. C. 2011: *On the Atmospheric Residence Time of Anthropogenically Sourced Carbon Dioxide*. Energy & Fuels, 25(11), 5503–5513. https://doi.org/10.1021/ef200914u

Conservation Foundation (New York). 1963: *Implications of rising carbon dioxide content of the atmosphere: A statement of trends and implications of carbon dioxide research reviewed at a conference of scientists*. The Conservation Foundation. https://babel.hathitrust.org/cgi/pt?id=mdp.39015004619030&view=1up&seq=1

Copin-Montégut, G. 1996: *Chimie de l'eau de mer*. Institut océanographique.

Currie, K. I., Brailsford, G., Nichol, S., Gomez, A., Sparks, R., Lassey, K. R., & Riedel, K. 2011: *Tropospheric* $^{14}CO_2$ *at Wellington, New Zealand: The world's longest record*. Biogeochemistry, 104(1–3), 5–22. https://doi.org/10.1007/s10533-009-9352-6

Dengler, J. 2024: *Improvements and Extension of the Linear Carbon Sink Model*. Atmosphere, 15(7), 743. https://doi.org/10.3390/atmos15070743

Diallo, M., Legras, B., Ray, E., Engel, A., & Añel, J. A. 2017: *Global distribution of* $CO_2$ *in the upper troposphere and stratosphere*. Atmospheric Chemistry and Physics, 17(6), 3861–3878. https://doi.org/10.5194/acp-17-3861-2017

Dickson, A. G. 2010: *The carbon dioxide system in seawater: Equilibrium chemistry and measurements*. In U. Riebesell, V. J. Fabry, L. Hansson, & J.-P. Gattuso (Eds.), Guide to Best Practices for Ocean Acidification Research and Data Reporting (pp. 17–40). Publications of the EU. https://www.researchgate.net/publication/284774361_The_carbon_dioxide_system_in_seawater_Equilibrium_chemistry_and_measurements

Dickson, A. G., Sabine, C. L., & Christian, J. R. 2007: *Guide to Best Practices for Ocean* $CO_2$

*Measurements* (p. 191) [PICES Special Publication 3; IOCCP Report number 8]. North Pacific Marine Science Organization.

Donohoe, A., Armour, K. C., Pendergrass, A. G., & Battisti, D. S. 2014: *Shortwave and longwave radiative contributions to global warming under increasing* $CO_2$. Proceedings of the National Academy of Sciences, 111(47), 16700–16705. https://doi.org/10.1073/pnas.1412190111

Donohue, R. J., Roderick, M. L., McVicar, T. R., & Farquhar, G. D. 2013: *Impact of* $CO_2$ *fertilization on maximum foliage cover across the globe's warm, arid environments*. Geophysical Research Letters, 40(12), 3031–3035. https://doi.org/10.1002/grl.50563

EEA. 2024: *Annual economic losses caused by weather- and climate-related extreme events in the EU Member States*. European Environment Agency. https://www.eea.europa.eu/en/analysis/indicators/annual-economic-losses-caused-by-weather-and-climate-related-extreme-events-in-the-eu-member-states/data-package.zip

Egleston, E. S., Sabine, C. L., & Morel, F. M. M. 2010: *Revelle revisited: Buffer factors that quantify the response of ocean chemistry to changes in DIC and alkalinity*. Global Biogeochemical Cycles, 24(1), 2008GB003407. https://doi.org/10.1029/2008GB003407

Essenhigh, R. H. 2009: *Potential Dependence of Global Warming on the Residence Time (RT) in the Atmosphere of Anthropogenically Sourced Carbon Dioxide*. Energy & Fuels, 23(5), 2773–2784. https://doi.org/10.1021/ef800581r

Global Carbon Project. 2024: *Global Carbon Budget (2024) – Annual* $CO_2$ *emissions from land-use change [dataset]*.

Graven, H., Allison, C. E., Etheridge, D. M., Hammer, S., Keeling, R. F., Levin, I., Meijer, H. A. J., Rubino, M., Tans, P. P., Trudinger, C. M., Vaughn, B. H., & White, J. W. C. 2017: *Compiled records of carbon isotopes in atmospheric* $CO_2$ *for historical simulations in CMIP6*. Geoscientific Model Development, 10(12), 4405–4417. https://doi.org/10.5194/gmd-10-4405-2017

Graven, H. D., Keeling, R. F., Piper, S. C., Patra, P. K., Stephens, B. B., Wofsy, S. C., Welp, L. R., Sweeney, C., Tans, P. P., Kelley, J. J., Daube, B. C., Kort, E. A., Santoni, G. W., & Bent, J. D. 2013: *Enhanced Seasonal Exchange of* $CO_2$ *by Northern Ecosystems Since 1960*. Science, 341(6150), 1085–1089. https://doi.org/10.1126/science.1239207

Graven, H., Keeling, R. F., & Rogelj, J. 2020: *Changes to Carbon Isotopes in Atmospheric* $CO_2$ *Over the Industrial Era and Into the Future*. Global Biogeochemical Cycles, 34(11), e2019GB006170. https://doi.org/10.1029/2019GB006170

Grok 3 beta, Cohler, J., Legates, D., Soon, F., & Soon, W. 2025: *A Critical Reassessment of the Anthropogenic* $CO_2$*-Global Warming Hypothesis*. Science of Climate Change, 5(1), 1–16. https://doi.org/10.53234/scc202501/06

Hansen, J., Kharecha, P., & Sato, M. 2013: *Climate forcing growth rates: Doubling down on our Faustian bargain*. Environmental Research Letters, 8(1), 011006. https://doi.org/10.1088/1748-9326/8/1/011006

Harde, H. 2017: *Scrutinizing the carbon cycle and* $CO_2$ *residence time in the atmosphere*. Global and Planetary Change, 152, 19–26. https://doi.org/10.1016/j.gloplacha.2017.02.009

Harde, H. 2019: *What Humans Contribute to Atmospheric* $CO_2$*: Comparison of Carbon Cycle Models with Observations*. Earth Sciences, 8(3), 139. https://doi.org/10.11648/j.earth.20190803.13

Harde, H. (2025). *Atmospheric CO2: What Physics Dictates*. Science of Climate Change, 5(4), 66–76. https://doi.org/10.53234/scc202511/12

Haverd, V., Smith, B., Canadell, J. G., Cuntz, M., Mikaloff-Fletcher, S., Farquhar, G., Woodgate, W., Briggs, P. R., & Trudinger, C. M. 2020: *Higher than expected* $CO_2$ *fertilization inferred from leaf to global observations*. Global Change Biology, 26(4), 2390–2402.

https://doi.org/10.1111/gcb.14950

Hocker, L. 2010, June 9: A study: *The temperature rise has caused the* $CO_2$ *Increase, not the other way around*. Watts Up With That? https://wattsupwiththat.com/2010/06/09/a-study-the-temperature-rise-has-caused-the-co2-increase-not-the-other-way-around/

Holton, J. R., Haynes, P. H., McIntyre, M. E., Douglass, A. R., Rood, R. B., & Pfister, L. 1995: *Stratosphere-troposphere exchange*. Reviews of Geophysics, 33(4), 403–439. https://doi.org/10.1029/95RG02097

Hoogeveen, J. J. A., Meirink, J. F., & Selten, F. M. 2025: *Likely breaks in cloud cover retrievals complicate attribution of the trend in the Earth Energy Imbalance*. Radiation/Atmospheric Modelling and Data Analysis/Troposphere/Physics (physical properties and processes). https://doi.org/10.5194/egusphere-2025-418

Houghton, J. T., Jenkins, G. J., & Ephraums, J. J. (Eds.). 1990: *Climate Change: The IPCC Scientific Assessment*. Cambridge University Press. https://archive.ipcc.ch/publications_and_data/publications_ipcc_first_assessment_1990_wg1.shtml

Hu, C., Xu, J., Liu, C., Chen, Y., Yang, D., Huang, W., Deng, L., Liu, S., Griffis, T. J., & Lee, X. 2021: *Anthropogenic and natural controls on atmospheric* $\delta^{13}$ *C-*$CO_2$ *variations in the Yangtze River delta: Insights from a carbon isotope modeling framework*. Atmospheric Chemistry and Physics, 21(13), 10015–10037. https://doi.org/10.5194/acp-21-10015-2021

Hua, Q., & Barbetti, M. 2004: *Review of Tropospheric Bomb*$^{14}$ *C Data for Carbon Cycle Modeling and Age Calibration Purposes*. Radiocarbon, 46(3), 1273–1298. https://doi.org/10.1017/S0033822200033142

Hua, Q., Barbetti, M., & Rakowski, A. Z. 2013: *Atmospheric Radiocarbon for the Period 1950–2010*. Radiocarbon, 55(4), 2059–2072. https://doi.org/10.2458/azu_js_rc.v55i2.16177

IPCC, 2001: The Carbon Cycle and Atmospheric Carbon Dioxide. In J. T. Houghton, Y. Ding, D. J. Griggs, M. Noguer, P. J. van der Linden, X. Dai, K. Maskell, & C. A. Johnson (Eds.), *Climate Change 2001: The Scientific Basis. Contribution of Working Group I to the Third Assessment Report of the Intergovernmental Panel on Climate Change* (pp. 191–197). Cambridge University Press. https://www.ipcc.ch/report/ar3/wg1/

IPCC, 2007: *Climate Change 2007: The Physical Science Basis. Contribution of Working Group I to the Fourth Assessment Report of the Intergovernmental Panel on Climate Change* (S. Solomon, D. Qin, M. Manning, Z. Chen, M. Marquis, K. B. Averyt, M. Tignor, & H. L. Miller, Eds.). Cambridge University Press. https://www.ipcc.ch/report/ar4/wg1/

IPCC, 2013: Stocker, T. F., Qin, D., Plattner, G.-K., Tignor, M., Allen, S. K., Boschung, J., Nauels, A., Xia, Y., Bex, V., & Midgley, P. M. (eds.). 2013: *Climate Change 2013: The Physical Science Basis. Contribution of Working Group I to the Fifth Assessment Report of the Intergovernmental Panel on Climate Change*. Cambridge University Press. https://www.ipcc.ch/report/ar5/wg1/

IPCC, 2018: *Global Warming of 1.5°C: An IPCC Special Report on the Impacts of Global Warming of 1.5°C Above Pre-Industrial Levels and Related Global Greenhouse Gas Emission Pathways, in the Context of Strengthening the Global Response to the Threat of Climate Change, Sustainable Development, and Efforts to Eradicate Poverty*. Cambridge University Press. https://www.ipcc.ch/sr15/download/

IPCC, 2021: Summary for Policymakers. In V. Masson-Delmotte, P. Zhai, A. Pirani, S. L. Connors, C. Péan, S. Berger, N. Caud, Y. Chen, L. Goldfarb, M. I. Gomis, M. Huang, K. Leitzell, E. Lonnoy, J. B. R. Matthews, T. K. Maycock, T. Waterfield, O. Yelekçi, R. Yu, & B. Zhou (Eds.), *Climate Change 2021: The Physical Science Basis. Contribution of Working Group I to the Sixth Assessment Report of the Intergovernmental Panel on Climate Change* (pp. 3–32). Cambridge University Press. https://doi.org/10.1017/9781009157896.001

Joos, F. 2014: *Climate and carbon cycle representation in Integrated Assessment Models*. http://hassler-j.iies.su.se/courses/climate/joos09.pdf

Joos, F., Bruno, M., Fink, R., Siegenthaler, U., Stocker, T. F., Le Quéré, C., & Sarmiento, J. L. 1996: *An efficient and accurate representation of complex oceanic and biospheric models of anthropogenic carbon uptake*. Tellus B: Chemical and Physical Meteorology, 48(3), 397. https://doi.org/10.3402/tellusb.v48i3.15921

Keeling, R. F., Piper, S. C., Bollenbacher, A. F., & Walker, S. J. 2025: *Scripps $CO_2$ Program: Monthly atmospheric $\delta^{13}C$ concentrations (per mil) derived from flask air samples, Mauna Loa Observatory, Hawaii*. Scripps Institution of Oceanography, University of California, San Diego. http://scrippsco2.ucsd.edu

Köhler, P., Hauck, J., Völker, C., Wolf-Gladrow, D. A., Butzin, M., Halpern, J. B., Rice, K., & Zeebe, R. E. 2018: Comment on " *Scrutinizing the carbon cycle and $CO_2$ residence time in the atmosphere*" by H. Harde. Global and Planetary Change, 164, 67–71. https://doi.org/10.1016/j.gloplacha.2017.09.015

Koutsoyiannis, D. 2024a: *Net Isotopic Signature of Atmospheric $CO_2$ Sources and Sinks: No Change since the Little Ice Age*. Sci, 6(1), 17. https://doi.org/10.3390/sci6010017

Koutsoyiannis, D. 2024b: *Refined Reservoir Routing (RRR) and Its Application to Atmospheric Carbon Dioxide Balance*. Water, 16(17), 2402. https://doi.org/10.3390/w16172402

Lai, J., Kooijmans, L. M. J., Sun, W., Lombardozzi, D., Campbell, J. E., Gu, L., Luo, Y., Kuai, L., & Sun, Y. 2024: *Terrestrial photosynthesis inferred from plant carbonyl sulfide uptake*. Nature, 634(8035), 855–861. https://doi.org/10.1038/s41586-024-08050-3

Leuenberger, M., Levin, I., & Hammer, S. 2019: *Long-term observations of $^{14}CO_2$ at Jungfraujoch* (Activity Report No. 2019). International Foundation High Altitude Research Stations Jungfraujoch and Gornergrat (HFSJG). https://www.hfsjg.ch/reports/2019/pdf/119_KUP_Leuenberger_Levin.pdf

Levin, I., Naegler, T., Kromer, B., Diehl, M., Francey, R. J., Gomez-Pelaez, A. J., Steele, L. P., Wagenbach, D., Weller, R., & Worthy, D. E. 2010: *Observations and modelling of the global distribution and long-term trend of atmospheric $^{14}CO_2$*. Tellus B: Chemical and Physical Meteorology, 62(1), 26. https://doi.org/10.1111/j.1600-0889.2009.00446.x

Levy, M., Bopp, L., Karleskind, P., Resplandy, L., Ethe, C., & Pinsard, F. 2013: *Physical pathways for carbon transfers between the surface mixed layer and the ocean interior*. Global Biogeochemical Cycles, 27(4), 1001–1012. https://doi.org/10.1002/gbc.20092

Maddala, G. S., & Kim, I.-M. 1998: *Unit Roots, Cointegration, and Structural Change*. Cambridge University Press.

Masarik, J., & Beer, J. 1999: *Simulation of particle fluxes and cosmogenic nuclide production in the Earth's atmosphere*. Journal of Geophysical Research: Atmospheres, 104(D10), 12099–12111. https://doi.org/10.1029/1998JD200091

Masood, N., Zafar, T., Hudson-Edwards, K. A., Rehman, H. U., & Farooqi, A. 2022: *Trace element geochemistry and stable isotopic (δ13C and δ15N) records of the Paleocene coals, Salt Range, Punjab, Pakistan*. International Journal of Mining Science and Technology, 32(3), 551–561. https://doi.org/10.1016/j.ijmst.2022.03.007

Massen, F., & Beck, E.-G. 2011: *Accurate Estimation of $CO_2$ Background Level from Near Ground Measurements at Non-Mixed Environments*. In W. Leal Filho (Ed.), *The Economic, Social and Political Elements of Climate Change*. Springer. https://doi.org/10.1007/978-3-642-14776-0

Massen, F., Kies, A., Harpes, N., & Students of the LCD+. 2005: *Seasonal and Diurnal $CO_2$ Patterns at Diekirch, LU, 2003–2005*. Lycée Classique de Diekirch. https://1315516fd2.clvawcdnwnd.com/a3651b7fada40d42bb0919787e9c4a73/200000621-d4b49d5ae6/diekirch.pdf

Masson-Delmotte, V., Zhai, P., Pirani, A., Connors, S. L., Péan, C., Berger, S., Caud, N., Chen, Y., Goldfarb, L., Gomis, M. I., Huang, M., Leitzell, K., Lonnoy, E., Matthews, J. B. R., Maycock, T. K., Waterfield, T., Yelekçi, O., Yu, R., & Zhou, B. (Eds.). (2021): *Climate Change 2021: The Physical Science Basis: Contribution of Working Group I to the Sixth Assessment Report of the Intergovernmental Panel on Climate Change*. Cambridge University Press. https://doi.org/10.1017/9781009157896

Maurin, J.-C. (2022, December 23): *$CO_2$ atmosphérique (2/3) Influence de la « température » sur la vitesse de croissance*. Science, climat et énergie. https://www.science-climat-energie.be/2022/12/23/co2-atmospherique-2-3/

Millero, F. J. 1995: *Thermodynamics of the carbon dioxide system in the oceans*. Geochimica et Cosmochimica Acta, 59(4), 661–677. https://doi.org/10.1016/0016-7037(94)00354-O

Millero, F. J. 2007: *The Marine Inorganic Carbon Cycle*. Chemical Reviews, 107(2), 308–341. https://doi.org/10.1021/cr0503557

Munshi, J. 2015: *Responsiveness of Atmospheric $CO_2$ to Anthropogenic Emissions: A Note*. SSRN Electronic Journal. https://doi.org/10.2139/ssrn.2642639

Munshi, J. 2016a: *Dilution of Atmospheric Radiocarbon $CO_2$ by Fossil Fuel Emissions*. SSRN Electronic Journal. https://doi.org/10.2139/ssrn.2770539

Munshi, J. 2016b: *Effective Sample Size of the Cumulative Values of a Time Series*. SSRN Electronic Journal. https://doi.org/10.2139/ssrn.2853163

Munshi, J. 2016c: *Illusory Statistical Power in Time Series Analysis*. SSRN Electronic Journal. https://doi.org/10.2139/ssrn.2878419

Munshi, J. 2017: *Responsiveness of Atmospheric $CO_2$ to Fossil Fuel Emissions: Updated*. SSRN Electronic Journal. https://doi.org/10.2139/ssrn.2997420

Muscheler, R., Joos, F., Beer, J., Müller, S. A., Vonmoos, M., & Snowball, I. 2007: *Solar activity during the last 1000yr inferred from radionuclide records*. Quaternary Science Reviews, 26(1–2), 82–97. https://doi.org/10.1016/j.quascirev.2006.07.012

Nemani, R. R., Keeling, C. D., Hashimoto, H., Jolly, W. M., Piper, S. C., Tucker, C. J., Myneni, R. B., & Running, S. W. 2003: *Climate-Driven Increases in Global Terrestrial Net Primary Production from 1982 to 1999*. Science, 300(5625), 1560–1563. https://doi.org/10.1126/science.1082750

Nikolov, N., & Zeller, K. F. 2024: *Roles of Earth's Albedo Variations and Top-of-the-Atmosphere Energy Imbalance in Recent Warming: New Insights from Satellite and Surface Observations*. Geomatics, 4(3), 311–341. https://doi.org/10.3390/geomatics4030017

NOAA Global Monitoring Laboratory. 2021: *Can We See a Change in the $CO_2$ Record Because of COVID-19?* https://gml.noaa.gov/ccgg/covid2.html

Oeschger, H., Siegenthaler, U., Schotterer, U., & Gugelmann, A. 1975: *A box diffusion model to study the carbon dioxide exchange in nature*. Tellus A: Dynamic Meteorology and Oceanography, 27(2), 168. https://doi.org/10.3402/tellusa.v27i2.9900

Plass, G. N. 1956: *The Carbon Dioxide Theory of Climatic Change*. Tellus, 8(2), 140–154. https://doi.org/10.1111/j.2153-3490.1956.tb01206.x

Podobnik, B., & Stanley, H. E. 2008: *Detrended Cross-Correlation Analysis: A New Method for Analyzing Two Nonstationary Time Series*. Physical Review Letters, 100(8), 084102. https://doi.org/10.1103/PhysRevLett.100.084102

Poyet, P. 2022: *The Rational Climate e-Book (2nd Edition)* (Version 2.31). Zenodo. https://doi.org/10.5281/zenodo.15575051

Pretis, F., & Hendry, D. F. 2013: *Comment on "Polynomial cointegration tests of anthropogenic impact on global warming*" by Beenstock et al. (2012) – *some hazards in econometric modelling of climate change*. Earth System Dynamics, 4(2), 375–384. https://doi.org/10.5194/esd-4-375-2013

Pretzsch, H., Biber, P., Schütze, G., Uhl, E., & Rötzer, T. 2014: *Forest stand growth dynamics in Central Europe have accelerated since 1870*. Nature Communications, 5(1), 4967. https://doi.org/10.1038/ncomms5967

Quay, P., Sonnerup, R., Westby, T., Stutsman, J., & McNichol, A. 2003: *Changes in the $^{13}C/^{12}C$ of dissolved inorganic carbon in the ocean as a tracer of anthropogenic $CO_2$ uptake*. Global Biogeochemical Cycles, 17(1). https://doi.org/10.1029/2001GB001817

Rayner, N. A., Parker, D. E., Horton, E. B., Folland, C. K., Alexander, L. V., Rowell, D. P., Kent, E. C., & Kaplan, A. 2003: *Global analyses of sea surface temperature, sea ice, and night marine air temperature since the late nineteenth century*. Journal of Geophysical Research: Atmospheres, 108(D14), 2002JD002670. https://doi.org/10.1029/2002JD002670

Revelle, R., Broecker, W., Craig, H., Keeling, C. D., & Smagorinsky, J. 1965: *Appendix Y4: Atmospheric Carbon Dioxide*. In *Restoring the Quality of Our Environment*. President's Science Advisory Committee. https://nsarchive.gwu.edu/document/31937-document-2-white-house-report-restoring-quality-our-environment-report-environmental

Revelle, R., & Suess, H. E. 1957: Carbon Dioxide Exchange Between Atmosphere and Ocean and the Question of an Increase of Atmospheric $CO_2$ during the Past Decades. *Tellus*, *9*(1), 18–27. https://doi.org/10.1111/j.2153-3490.1957.tb01849.x

Roy-Barman, M., & Jeandel, C. 2016: *$CO_2$ Exchanges between the Ocean and the Atmosphere*. In M. Roy-Barman & C. Jeandel, *Marine Geochemistry* (1st ed., pp. 235–264). Oxford University PressOxford. https://doi.org/10.1093/acprof:oso/9780198787495.003.0008

Salby, M., & Harde, H. (2021a): *Control of Atmospheric $CO_2$ Part I: Relation of Carbon 14 to the Removal of $CO_2$*. Science of Climate Change, 1(2), 177–196. https://doi.org/10.53234/scc202112/30

Salby, M., & Harde, H. 2021b: *Control of Atmospheric $CO_2$ Part II: Influence of Tropical Warming*. Science of Climate Change, 1(2), 197–213. https://doi.org/10.53234/scc202112/12

Salby, M., & Harde, H. 2022a: *Theory of Increasing Greenhouse Gases*. Science of Climate Change, 2(3), 212–238. https://doi.org/10.53234/scc202212/17

Salby, M., & Harde, H. 2022b: *What Causes Increasing Greenhouse Gases? Summary of a Trilogy*. Science of Climate Change, 2(3), 297–301. https://doi.org/10.53234/scc202212/16

Segalstad, T. V. 1998: *Carbon cycle modelling and the residence time of natural and anthropogenic atmospheric $CO_2$ on the construction of the "Greenhouse Effect Global Warming" dogma*. In R. Bate (Ed.), *Global Warming: The Continuing Debate* (pp. 184–219). European Science and Environment Forum (ESEF).

Spencer, R. W., Christy, J. R., & Braswell, W. D. 2017. *UAH Version 6 global satellite temperature products: Methodology and results*. Asia-Pacific Journal of Atmospheric Sciences, 53(1), 121–130. https://doi.org/10.1007/s13143-017-0010-y

Stocker, T. F., Qin, D., Plattner, G.-K., Tignor, M., Allen, S. K., Boschung, J., Nauels, A., Xia, Y., Bex, V., & Midgley, P. M. (eds.). 2013: *Climate Change 2013: The Physical Science Basis. Contribution of Working Group I to the Fifth Assessment Report of the Intergovernmental Panel on Climate Change*. Cambridge University Press. https://www.ipcc.ch/report/ar5/wg1/

Stohl, A., Bonasoni, P., Cristofanelli, P., Collins, W., Feichter, J., Frank, A., Forster, C., Gerasopoulos, E., Gäggeler, H., James, P., Kentarchos, T., Kromp-Kolb, H., Krüger, B., Land, C., Meloen, J., Papayannis, A., Priller, A., Seibert, P., Sprenger, M., … Zerefos, C. 2003: *Stratosphere-trop-*

*osphere exchange: A review, and what we have learned from STACCATO*. Journal of Geophysical Research: Atmospheres, 108 (D12), 2002JD002490. https://doi.org/10.1029/2002JD002490

Strassmann, K. M., & Joos, F. 2018: *The Bern Simple Climate Model (BernSCM) v1.0: An extensible and fully documented open-source re-implementation of the Bern reduced-form model for global carbon cycle-climate simulations* [Application/pdf]. https://doi.org/10.3929/ETHZ-B-000268290

Suto, N., & Kawashima, H. 2016: *Global mapping of carbon isotope ratios in coal*. Journal of Geochemical Exploration, *167*, 12–19. https://doi.org/10.1016/j.gexplo.2016.05.001

Sutton, A. J., Feely, R. A., Maenner-Jones, S., Musielwicz, S., Osborne, J., Dietrich, C., Monacci, N., Cross, J., Bott, R., Kozyr, A., Andersson, A. J., Bates, N. R., Cai, W.-J., Cronin, M. F., De Carlo, E. H., Hales, B., Howden, S. D., Lee, C. M., Manzello, D. P., … Weller, R. A. 2019: *Autonomous seawater p $CO_2$ and pH time series from 40 surface buoys and the emergence of anthropogenic trends*. Earth System Science Data, 11(1), 421–439. https://doi.org/10.5194/essd-11-421-2019

Takahashi, T., Olafsson, J., Goddard, J. G., Chipman, D. W., & Sutherland, S. C. 1993: *Seasonal variation of $CO_2$ and nutrients in the high-latitude surface oceans: A comparative study*. Global Biogeochemical Cycles, 7(4), 843–878. https://doi.org/10.1029/93GB02263

Thoning, K. W., Crotwell, A. M., & Mund, J. W. 2025: *Atmospheric Carbon Dioxide Dry Air Mole Fractions from continuous measurements at Mauna Loa, Hawaii, Barrow, Alaska, American Samoa and South Pole, 1973–present. Version 2025-04-26*. https://doi.org/10.15138/yaf1-bk21

Turnbull, J. C., Mikaloff Fletcher, S. E., Ansell, I., Brailsford, G. W., Moss, R. C., Norris, M. W., & Steinkamp, K. 2017: *Sixty years of radiocarbon dioxide measurements at Wellington, New Zealand: 1954–2014*. Atmospheric Chemistry and Physics, 17(23), 14771–14784. https://acp.copernicus.org/articles/17/14771/2017/acp-17-14771-2017.pdf https://doi.org/10.5194/acp-17-14771-2017

UNFCCC. 2002: *Parameters for tuning a simple carbon cycle model*. https://unfccc.int/resource/brazil/carbon.html

UNSCEAR. 2000: *Sources and Effects of Ionizing Radiation: UNSCEAR 2000 Report to the General Assembly, with Scientific Annexes. Volume I: Sources*. United Nations Scientific Committee on the Effects of Atomic Radiation. https://www.unscear.org/unscear/en/publications/2000_1.html

Ventusky. 2025: *Sea Surface Temperature Map*. https://www.ventusky.com/?p=9.0;-4.9;3&l=temperature-water

Wanninkhof, R., & McGillis, W. R. 1999: *A cubic relationship between air-sea $CO_2$ exchange and wind speed*. Geophysical Research Letters, 26(13), 1889–1892. https://doi.org/10.1029/1999GL900363

Wanninkhof, R., Park, G.-H., Takahashi, T., Sweeney, C., Feely, R., Nojiri, Y., Gruber, N., Doney, S. C., McKinley, G. A., Lenton, A., Le Quéré, C., Heinze, C., Schwinger, J., Graven, H., & Khatiwala, S. 2013: *Global ocean carbon uptake: Magnitude, variability and trends*. Biogeosciences, 10(3), 1983–2000. https://doi.org/10.5194/bg-10-1983-2013

Wenger, A., Pugsley, K., O'Doherty, S., Rigby, M., Manning, A. J., Lunt, M. F., & White, E. D. 2019: *Atmospheric radiocarbon measurements to quantify $CO_2$ emissions in the UK from 2014 to 2015*. Atmospheric Chemistry and Physics, 19(22), 14057–14070. https://doi.org/10.5194/acp-19-14057-2019

Wolfram Research. 2012: *UnitRootTest*. Wolfram Language & System Documentation Center. https://reference.wolfram.com/language/ref/UnitRootTest.html

Zeebe, R. E., & Wolf-Gladrow, D. A. 2001: *$CO_2$ in Seawater: Equilibrium, Kinetics, Isotopes* (Vol. 65). Elsevier Science (Gulf Professional Publishing). https://www.elsevier.com/books/co2-in-seawater-equilibrium-kinetics-isotopes/zeebe/978-0-444-50946-8

Zhu, Z., Piao, S., Myneni, R. B., Huang, M., Zeng, Z., Canadell, J. G., Ciais, P., Sitch, S., Friedlingstein, P., Arneth, A., Cao, C., Cheng, L., Kato, E., Koven, C., Li, Y., Lian, X., Liu, Y., Liu, R., Mao, J, Zeng, N. 2016: *Greening of the Earth and its drivers*. Nature Climate Change, 6(8), 791–795. https://doi.org/10.1038/nclimate3004

## Appendix A: List of Notations

*absorb*(*t*): annual carbon uptake by vegetation and oceans
*AF*: Airborne Fraction
AT(*t*): Temperature anomaly; $AT_{SST}(t)$ month-by-month mean inter-tropical sea surface temperature anomaly
*degas*(*t*): carbon released from oceans, vegetation and soils (excluding vegetation respiration over 24 hours)
*f*(*t*): total carbon flux entering the atmosphere,
$f_{fossil}(t)$ : carbon flux from fossil fuel emissions,
$f_{logis}(t)$ = 17.92 / (1 + exp((2011t)/29)) a logistic approximation of $f_{fossil}(t)$ whose integral over 1751-2025 is 500.6 Gt-C equal to the integral over the economic series of emissions from oil, coal and gas and cement plants
*Fx*(*t*): *F1*(*t*) (Sec. 6), *F2*(*t*) (Sec. 10.9, Fig. 31-b), *FB*(*t*) (Sec. 6.1, Fig. 16) : impulse response functions
GPP: Gross Primary Productivity (includes vegetation respiration)
Gt-C: gigaton carbon; 1 Gt-C = $10^{12}$ kg C; Gt-$CO_2$: gigaton $CO_2$; 1 ton $CO_2$ = 273 kg-C
MLO: Mauna Loa Observatory
NPP: Net Primary Productivity, i.e. Carbon uptake by vegetation with the 24-hour respiration subtracted
ppm: part per million number of molecules of one type per million molecules of air; 1 ppm $CO_2$ = 2.12 Gt-C
$p_{CO2air}$: partial pressures of $CO_2$ in the air (μatm)
$p_{CO2seawater}$: partial pressures of $CO_2$ in seawater (μatm)
*Q*(*t*): cumulative fossil fuel emissions up to time t
*R*: Revelle buffer factor between 9.5 to 12.5
Ref $^{13}C/^{12}C$: reference for ratio $^{13}C/^{12}C$ (VPDB[11])
Ref $^{14}C/^{12}C$: reference for ratio $^{14}C/^{12}C$ see note[12].
SPO: South Pole Observatory
$SST_{20°S-20°N}$: Sea Surface Temperature Sea surface temperature averaged between 20°S and 20°N
*X*(*t*): mass of carbon in the air
$X_{fossil}(t)$: mass of carbon in the air from fossil fuels
$X_{natural}(t)$: mass of carbon in the air from natural degassing
$X_{MLO}(t)$: content of carbon dioxide in the atmosphere observed at MLO
$X_{MLOlogis}(t)$ 275 + 555.72 / (1 + exp((2066.95 t)/ 42.16)) ppm extends $X_{MLO}$
*Y*(*t*): mass of carbon in vegetation & soil
*Z*(*t*): mass of carbon in the ocean

---

[11] $\delta^{13}C$ values are reported relative to the Vienna Pee Dee Belemnite (VPDB) standard, derived from a Cretaceous belemnite fossil from the Pee Dee Formation in South Carolina. See equation (13).

[12] For radiocarbon dating, the reference is usually Oxalic Acid I (HOx1) and II (HOx2) standards, normalized to $\delta^{13}C$ = –25‰ VPDB. $\Delta^{14}C$ (or $F^{14}C$) relative to an oxalic acid radiocarbon standard, but with $\delta^{13}C$ normalization to VPDB. VPDB is never used directly for radiocarbon $^{14}C/^{12}C$ — but it's still in the background, because radiocarbon results are corrected for isotopic fractionation using $\delta^{13}C$ vs. VPDB.

| | |
|---|---|
| $Z_{ocs}(t)$: | mass of carbon in the surface ocean |
| $Z_{ocd}(t)$: | mass of carbon in the deep ocean |
| $\tau(t)$: | ratio stock/out-flow for a reservoir (generally taken over 12 months) |

## Appendix B: TAlk Equation (22)

Let x=[OH$^-$]. Using $K_{H2O}$ for the water autoprotolysis constant (i.e. $K_w$), $k_1$, $k_2$ for the first and second dissociation constants of carbonic acid, $k_b$ for the borate dissociation constant, DIC for total dissolved inorganic carbon, and $B_T(S)$ for total boron (possibly scaled with salinity S), the total alkalinity equation can be written as equation (22), where TA (or TAlk) is the total alkalinity. Let's see what's the physical meaning of terms,

- First (fraction) term: carbonate alkalinity contribution from DIC, written in a form using [OH$^-$] via the relationships between [H$^+$], [OH$^-$], and the carbonate equilibria.
- Second term: borate alkalinity = $B_T(S)\times[B(OH)_4^-]$ expressed using [OH$^-$] (with $k_b$ and $K_{H2O}$ appearing because [H+]=$K_{H2O}$ /[OH$^-$]).
- Third and fourth terms: contributions from water autoprotolysis: $-K_{H2O}/x$ is $-$[H$^+$] (since [H+] = $K_{H2O}$/[OH−]), and +x is +[OH$^-$].

Now let's see what are the Units / dimensions used.

- x has units of mol·L$^{-1}$ (or mol·m$^{-3}$ depending on the concentration units used).
- $K_{H2O}$ has units such that $K_{H2O}$/x yields a concentration (same units as x). If SI is used: $K_{H2O}$ in (mol·m$^{-3}$)$^2$ so that [H$^+$]=$K_{H2O}$/[OH$^-$] has mol·m$^{-3}$ units, more commonly $K_w$ is given in (mol·L$^{-1}$)$^2$ or (mol·m$^{-3}$)$^2$; One needs to be consistent with DIC and TA units.
- DIC and TA must use the same concentration units as x (e.g. µmol·kg$^{-1}$, mmol·m$^{-3}$, etc.).

Solving for x:

- this equation (22) is nonlinear in x. The standard approach is to solve for x numerically (e.g. Newton–Raphson). Use the form above to compute F(x)−TAlk and its derivative for Newton.
- If one prefers to solve for [H$^+$] instead, substitute [H$^+$] = $K_{H2O}$/x and rewrite the equation in h=[H$^+$]; numerics can sometimes be more stable in h for very small/large values.

*SCC Publishing*
*Michelets vei 8 B*
*1366 Lysaker Norway*

*ISSN: 2703-9072*

*Correspondence:*

*aveollila@*
*yahoo.com*

*Vol. 5.3 (2025)*

*pp. 186 -206*

# Radiative Forcing of Water Vapour and its Use in Climate Models

*Antero Ollila*

*School of Engineering (Emer.), Aalto University, Espoo, Finland*

## Abstract

The positive feedback of water vapour has been the basic feature of General Circulation Models (GCMs), which approximately doubles the warming impacts of any other climate drivers. Some published scientific papers have shown that simple climate models without this feature can simulate the temperatures of the 2000s very well. On the other hand, the observed humidity observations revealed that it varies, but not according to the water feedback theory. There is a need for an optional method for calculating the warming impacts of water vapour. In this study, the radiative forcing (RF) value of water vapour for different atmospheric water amounts has been calculated by applying the line-by-line (LBL) method. A simple climate model by the author has been modified by implementing this dependency in the same way as for the other greenhouse (GH) gases. This model has been used for the simulations of absolute yearly temperature and humidity changes, as well as for decadal-long changes by applying CERES (Clouds and the Earth's Radiant Energy System) observations. These simulations reveal that humidity increases are strongly related to the primary energy changes of the absorbed solar radiation (ASR). The yearly temperature variations of the hemispheres show that water vapour increase has about a 14 % temperature impact and not about 100 % as assumed by the water feedback theory. This water vapour RF effect explains good results in simulating the high temperatures of the 2000s. The recent rapid warming during the 2000s is mainly caused by ASR variations, and this new calculation method can be applied in temperature simulations.

**Keywords**: positive water feedback**;** RF of water vapour; absorbed solar radiation; natural climate drivers; simple climate models; warming in the 2000s.

Submitted 2025-06-18, Accepted 2025-12-6, https://doi.org/10.53234/scc202510/11

## 1. Introduction

### *1.1 The solar activity changes over the 1850 – present period*

In the temperature simulations of the 2000s in this study, the role of the absorbed solar radiation (ASR) turns out to be significant. Therefore, it has been considered useful to carry out a short survey of research studies about solar activity changes over the period that the IPCC has applied in its own simulations by GCMs (General Climate Models) and in the CMIP6 (Coupled Model Intercomparison Project Phase 6) simulations.

Connolly et al. (2021) have carried out a comprehensive study consisting of 16 TSI and 5 temperature datasets. The TSI dataset included high-variability TSI estimates as well as low-variability datasets. Among the low-variability datasets is that of Matthes et al. (2017), which has been recommended to be applied in the CMIP6 simulations, and it is in line with the IPCC's general conclusion about the solar variation impacts being insignificant, as slow as ± 0.01 ºC (IPCC, 2021).

The results of Connolly et al. (2021) show that, applying high-variability TSI datasets like those of Hoyt & Schatten (1993) and Bard et al. (2000), most of the NH warming trend since the 19th century can be related to solar variability.

Stefani (2021) applied the multiregression method to correlate solar activity and logarithmic $CO_2$ concentration to sea surface temperature variations from 1850 to 2018. The geomagnetic aa index was applied as a proxy for solar activity changes. The correlation $R^2$ value of around 0.87 was for a climate sensitivity (of TCR type) in the range of 0.6 K to 1.6 K per doubling of $CO_2$. By eliminating the data of the last decade, the regression produced a significantly higher weight of the aa index.

Scafetta (2023) applied an energy balance model calibrated with a differential multilinear regression method in simulating the global temperature response from 1850 to 2020. He used anthropogenic, volcanic and solar climate drivers. As the solar proxies, he used three balanced multi-proxy TSI datasets combined from high-variability TSI records and the record of Matthes et al. (2017) as a reference, since it has been applied by the IPCC. The simulation results show that greater TSI variability matches more closely with the temperature records, implying that the ECS should be from 1.4 ºC to 2.8 ºC with a mean of 2.1 ºC.

Harde (2022) has applied his energy-radiation-balance model for the simulation of global temperature. He has integrated into his model the same feedbacks as in the CMIP6 model, and in addition to these, also convection and evaporation feedbacks. The best simulation result with a correlation factor of r = 0.95 was achieved with the ECS value of 0.68 °C and the TSI dataset of Hoyt & Schatten (1993). A convincing feature of this simulation was the accurate reproduction of the temperature peak of the 1930s and the strong temperature drop from the 50s to 80s.

It can be summarised that the published high-variability TSI estimates outnumber the low-variability TSI estimates, and the different types of analyses show that in simulations, they reproduce the observed temperature trends with much better accuracy than the low-variability TSI dataset applied in the CMIP6 simulations.

### *1.2 The theory of positive water feedback applied by the IPCC*

GCMs have an essential role in calculating global surface temperature changes. Manabe & Wetherald (1967) were the first to introduce positive water feedback. Their calculations showed only that water feedback doubles the original RF of $CO_2$. The consequence of this feature was the $\lambda$ value of the climate sensitivity parameter of 0.53 $K/(Wm^{-2})$ in their study. Without positive water feedback, the $\lambda$ value is about 0.27 $K/(Wm^{-2})$ as shown by Ollila (2023b). Manabe & Wetherald (1967) did not show that water feedback is a persistent property of the climate, even though many climate researchers think so. This feature became one of the essential features of GCMs already in the 1980s.

Positive water feedback is a cornerstone in any GCM and the simple model applied by the IPCC. The IPCC (2007) writes in AR4 that "*The positive water feedback doubles the radiative forcing of any GH gas".* The AR5 (IPCC 2013, p. 667) writes *"Therefore, although $CO_2$ is the main control knob on climate, water vapour is a strong and fast feedback that amplifies any initial forcing by a typical factor between two and three."* The fast feedback means that the response happens on the same timescale as any climate driver, and like $CO_2$ warms up the surface. The typical lifetime of water vapour in the atmosphere is about ten days.

The theoretical justification of positive water feedback is based on the equation of Clausius-Clapeyron (C-C), and this relationship has been referred to 36 times in AR6 (IPCC, 2021) as an explanation of water feedback in the lower atmosphere. This equation represents the pressure-temperature relationship in a saturated water vapour atmosphere. The C-C relation states that a 1-degree increase raises the water-holding capacity of the atmosphere by 6-7%. The actual amount of water in the atmosphere is given by the water-holding capacity times the relative humidity of the atmosphere. The real atmosphere is not saturated by water vapour, since the atmospheric humidity is around 70% and it varies greatly in different climate zones. Therefore, the theoretical basis is weak.

The C-C equation presupposes that there is enough energy to evaporate water while maintaining 100 % saturation in the gaseous atmosphere. This is not the case in the atmosphere.

The direct humidity and temperature measurements from 1980 onwards show no positive water feedback in the long run (Fig. 1). Reliable empirical conclusions about the water feedback can be drawn from the behaviour of the climate since 1979, after the worldwide use of the new humidity semiconductor technology Humicap® of Vaisala.

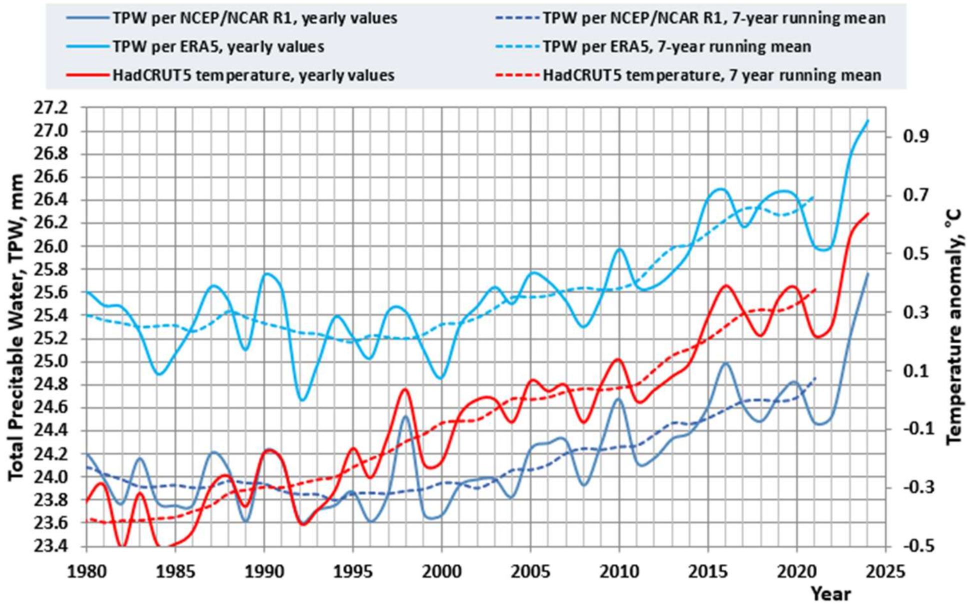

*Figure 1: The temperature trend (MetOffice, 2025) and Total Precipitable Water (NOAA, 2025a) trends according to two humidity measurements from 1980 to 2024. ERA5 stands for the fifth generation of the European Centre for Medium-Range Weather Forecasts (ECMWF) reanalysis for the global climate and weather. The NCEP/NCAR reanalysis is a joint project between the National Centers for Environmental Prediction (NCEP) and the National Center for Atmospheric Research (NCAR) in the United States.*

Wang et al. (2020) carried out an accuracy analysis on the five commonly used absolute humidity measurement data sets (precipitated water in millimetres = total precipitable water = TPW). They found that the smallest root mean square error of 1.45 mm was in JRA5 data, and the greatest was 3.34 mm in the NCEP/NCAR dataset for the period from 2016 to 2018 (NOAA 2025b). In the later analyses of this study, the humidity values of ERA5 have been applied.

These data sets have been depicted in Fig. 1 as yearly and 7-year running mean values. It can be noticed that the long-term value of temperature has increased by about 0.8 ºC from 1979 to 1994, but both TPW graph values show a negative trend (a 7-year running mean). These empirical trends of TPW versus temperature conflict with the positive water feedback theory. Trenberth et al. (2015) found that the three-dimensional Community Earth System Model (CESM), calculating a global surface mean temperature (GSMT) increase of 0.4 ºC from 2000-2014, was significantly greater than the observed 0.12 ºC. They concluded that the temperature pause was still a reality at the end of 2014. During the temperature pause, both TPW values showed a positive trend. Since 2014, both the temperature and TPW values have increased significantly, and in this sense, it is in line with the water feedback theory. The reasons for this change will be analysed later.

It is the common principle of science that a theory or a paradigm must pass through any experiment or test. Albert Einstein experienced a lot of criticism for his new theory of relativity. He responded to critics: "*No amount of experimentation can ever prove me right; a single experiment can prove me wrong.*" This same applies to the paradigm of positive water feedback applied by the IPCC.

### *1.3 Studies of water feedback and greenhouse effect magnitude by dissenting researchers*

Harde (2014; 2017) has carried out a theoretical analysis of the magnitudes of water vapour feedback based on the spectral lines of water and $CO_2$, which have overlapping absorption regions. He realises that the water spectral lines are already strongly saturated in the same way as $CO_2$ in this region. Therefore, by increasing water concentration, only the far wings of its spectral lines and weak absorption bands can further contribute to an additional absorption, which increases roughly logarithmically with the water vapour concentration. Water vapour concentration increases exponentially with rising temperature, but due to the C-C relation, the overall effect results in a linear increase in the absorptivities. Harde concluded that the water vapour feedback amplification is only 1.14 or 14 %, and not 2 or even more as reported by the IPCC in the AR5 (IPCC 2013). Harde (2022) applied this water feedback in his TSI and $CO_2$ simulations with good results.

Koutsoyiannis (2024) has carried out a comprehensive study about the GH effect and the magnitude of its contributors. The results based on MODTRAN calculations and mathematical analyses show that the contribution of $CO_2$ is 4 % – 5 %, and water and clouds dominate with a contribution of 87 % – 95 %. These results can be compared to other results, which are surprisingly few.

Schmidt et al (2010) have reported the $CO_2$ contribution as 19 %. Their calculation method is exceptional, since it is an average of two calculations: absorption change by removing $CO_2$ from the atmosphere, and calculating the absorption increase if $CO_2$, as it is the only GH gas in the atmosphere. The most common procedure is a so-called "single factor removal", which means that each GH gas has been removed from the atmospheric composition, and the reduced absorption amount is calculated for the total absorption in the atmosphere. The $CO_2$ contributions calculated with this method and applying the total absorption of 155-159 $Wm^{-2}$ of the terrestrial radiation are very close to each other: Schmidt et al. (2010) 14,9 %, Harde (2017) 15 %, and Ollila (2017) 14.9 %.

Ollila (2019) has found that the IPCC (2013; 2021) has its own definitions of the GH effect, which are not based on any scientific publication. He has proposed a new definition for the magnitude of the GH effect. It is based on the Earth's energy balance, which shows that the surplus of radiation energy on the surface in comparison to the net energy input from the sun is 510 – 240 $Wm^{-2}$ = 270 $Wm^{-2}$. By applying this figure, the contribution of $CO_2$ to the GH effect is only 7.4 %.

Koutsoyiannis (2024) has also calculated the relative strengths of water over $CO_2$ based on impacts on the upward and downward LW radiation changes in the atmosphere, and the corresponding values are 9.1 and 13.8, which means an average value of 11.9. It is interesting to note that the same value of Ollila (2017) is 11.8 based on the LW absorption in the atmosphere. It should be noted that the contribution calculations in the GH effect consider the total impact of a GH gas from its zero concentration to the present-day value. The relative strength calculations consider only relatively small concentration changes – typically 10 % increase - from the present values. Especially, the RF value of $CO_2$ is very nonlinear, but the water vapour RF value is close to linear dependency.

These different analyses show that the research studies of dissenting researchers concerning the strength and role of water and $CO_2$ deviate remarkably from the mainstream results.

### *1.4 Research study theories of the warming in the 2000s*

The temperature trend of the 2000s shows that there has been a so-called temperature pause from 2000 to 2014 and thereafter a relatively strong warming period with record-high temperatures in 2023 - 2024. Many different theories have been proposed for the reasons for the pause, and in the same way, different theories have been proposed for the present warming after 2014, since the

GH gases cannot explain the present warming.

Loeb et al. (2018) found a significant reduction of 0.83 Wm$^{-2}$ in global mean reflected SW flux at the TOA during the years 2014 - 2017. Ollila (2020) used the same CERES observations and identified that the SW anomaly forcing caused about 50 % of the El Niño temperature impact of 2015-2016. Ollila (2021) noticed that the GCMs can simulate current temperatures only if the SW anomaly of the 2000s has been omitted.

Harde (2022) has summarised research studies on the complicated nature of cloud feedback with observations that it is positive over the Pacific due to low-level cloud impacts and negative in the tropics. He has been able to formulate a mathematical equation connecting the cloud cover dependency on the TSI. Svensmark (2019) developed a comprehensive model about the mechanism between solar activity variations and cosmic radiation, which changes cloud formation through the generation rate of aerosols as water vapour condensation nuclei.

The later study of Loeb et al. (2021) has confirmed the earlier finding of Loeb et al. (2018) that low-level cloud reduction (the reduced albedo) has been the reason for increased ASR. Ollila (2023a) and Nikolev and Zeller (2024) have shown that the ASR anomaly variations can explain the major part of the temperature variations of the 2000s.

During the last few years, some research studies have been published, in which a common feature has been to identify anthropogenic reasons for the reduced albedo of the Earth. Due to new legislation, the sulphur emissions from the shipping industry have reduced, and the impacts have been at a maximum of 0.1 Wm$^{-2}$ according to Diamond (2023) and from 0.02 to 0.06 Wm$^{-2}$ according to Rantanen and Laaksonen (2024).

Hodnebrog et al. (2024) recognised the substantial diversity in aerosol Effective Radiative Forcing (ERF) among Coupled Model Intercomparison Project phase 6 (CMIP6) GCM models. For example, the decline of $SO_2$ emissions in China after 2007 is not accounted for in the earlier GCM simulations. They carried out a multi-model multi-ensemble approach, and they found that the ERF due to anthropogenic aerosol emission reductions has led to a $0.2 \pm 0.1$ Wm$^{-2}$ decade$^{-1}$ strengthening of the 2001–2019 imbalance trend.

Since the reduction of $SO_2$ aerosol has been the most significant in China, the temperature trends in China and the global temperature trend are depicted in Fig. 2.

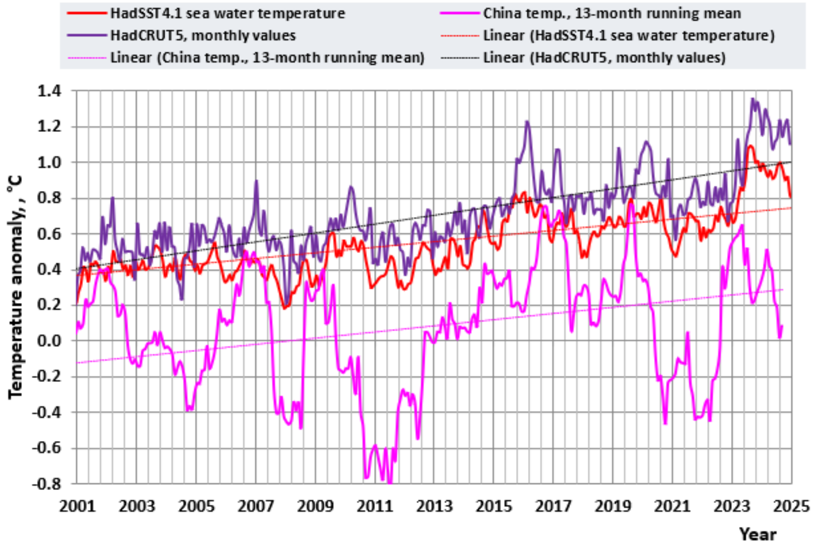

*Figure 2: The global temperature trend (MetOffice, 2024), the seawater temperature trend, HadSST.4.1 (Metoffice, 2025) and the temperature trend over China (NOAA, 2025b).*

The fluctuations of temperature trends in China are much greater than those in global temperatures, but the linear increase during the last 10 years is similar to the global sea surface temperature. Since the fluctuations are so great, some other factors are more probable reasons for temperature fluctuations than the aerosol reductions.

The Hunga Tonga–Hunga Ha‘apai submarine volcano eruption of magnitude VEI-5 in January 2022 created a strong water and ash plume reaching the stratosphere. Rantanen and Laaksonen (2024) have estimated the radiative warming effects of this eruption to be from 0.02 to 0.07 $Wm^{-2}$, and the estimate of Hansen et (2025) was negative, of -0.3 $Wm^{-2}$. Gupta et al. (2025) have studied in detail the water and sulphate impacts in the stratosphere, and they found that sulphates themselves and sulphate aerosols' interactions with humidity deplete the ozone layer, which leads to cooling. The net effect of the eruption was estimated to be $-0.10 \pm 0.02$ K in the southern hemisphere. It means that opposite results have been achieved.

Raghuraman et al. (2025) have shown that climate models have such a large internal variability that they can simulate high-temperature spikes, which happened in 1976 - 1977 and 2022 - 2023, without external forcing or changes in GH gas concentrations or aerosols. These events happened under special conditions connected to the change from the La Niña to the El Niño phase. It should be noted that this is a result of GCM simulations, and the real physical reason cannot be identified.

Ma et al. (2025) found that there has been a decline in ocean evaporation due to wind, even after 2017. This result is not in line with the TPW observations since the global humidity has increased steadily even after 2017 (Fig. 1), and it may be one of the explanations for the high temperatures of the years 2023 and 2024.

Myessignac et al. (2023) found that the climate feedback parameter – the reciprocal of the climate sensitivity parameter – is not constant but varies within the range from −3.2 to −1.0 $Wm^{-2}K^{-1}$ since 1970, the sea surface temperature, and is related to the phase of PDO (Pacific Decadal Oscillation). This result is in line with the information in Fig. 1. The PDO is a well-known general climate oscillation phenomenon, and there is no recognised increase of a warm phase during the 2000s, but there has been a cold phase after 2015 (NOAA 2025a).

The short-term temperature changes are distinctly related to the El Niño and La Niña events, which are caused by the regional changes of the ocean currents and winds in the tropical central and eastern Pacific Ocean. They initiate the temperature change, and the strong change in absolute humidity amplifies the change by a factor of about 100 percent of very strong El Niños (Ollila 2020). It is practically the same as the positive feedback used by the IPCC.

As we can see in the referred studies above, the proposed anthropogenic reasons are not strong in explaining the warming after the year 2015. But there is another strong climate driver, as originally found by Loeb et al. (2018), that the main reason is the reduction of the albedo, which has caused a strong increase in ASR. So far, there is no general explanation for the cloudiness decrease identified by Loeb et (2018), even though sulphate reductions have been proposed as an anthropogenic reason. Marsh and Svensmark (2000) have found a likely reason for cloudiness changes as they identified a relationship between the solar-modulated cosmic rays on global cloud cover (≤ 3 km).

The reasons for temperature changes in the 2000s are opposite to the findings of the latest reports of IPCC (2013, 2021), which show the aerosol-cloud radiation cooling effect from -0.82 $Wm^{-2}$ in 2011 to -1.00 $Wm^{-2}$ in 2019. A clear change happened in the 2000s, and the most common paradigm is that cloudiness now plays a major role in recent sudden temperature variations.

The main objection to using ASR as a climate driver in climate models is the claim that it is not an independent climate driver. It is well-known that ASR depends strongly on cloudiness, as shown by Loeb et al (2021). One can ask, is $CO_2$ an independent climate variable? It is not, since the yearly atmospheric $CO_2$ concentration increases only by about 45 % (IPCC 2021) in comparison to the value calculated from the actual fossil fuel emissions, but it varies yearly; the reason is deeply related to the $CO_2$ circulation between the atmosphere, the ocean, and the land plants. Since climate science is not capable of calculating ASR utilising cloud properties, it is well-established to use ASR as an independent climate driver for the time being. The real test can be found in temperature simulations of the short and long runs in Section 4.

These findings mean that there is a need to develop the RF value for water vapour in the same way as for the other GH gases. The author has not identified any RF equations for water, and therefore, he has carried out spectral analysis calculations to quantify the relationship between RF values and absolute humidity.

The present GCMs do not apply very well to temperature simulations of the 2000s, since they do not utilise direct CERES radiation observations and are poor at simulating ASR variations (Trenberth and Fasullo 2009; Stephens et al. 2022; IPCC 2013; IPCC 2021). The idea of GCMs has been that they should be capable of simulating also cloudiness changes, but so far, GCMs cannot do it.

Ollila (2023a) has not applied the positive water feedback in his simple climate models. Even though the water impact has been assumed to be constant, his simulation results during the 2000s are very close to the observed temperatures. This model has been named Ollila-1. In this study, a new version of Ollila-2 has been developed. The warming impact of water vapour in the Ollila-2 model is based on the RF values of water vapour, utilising the observed humidity concentrations in the atmosphere.

The objectives of this study are to develop the RF equation for atmospheric water vapour and to test the positive water feedback theory by applying the Ollila-2 model.

## 2. Materials and methods

### *2.1 Materials*

The temperature data are from NOAA (2025a), HadCRUT5 and HadSST.4.1 from MetOffice (2025), Berkeley (2025), and UAH (2025). The reflected shortwave radiation data for 1980 – 2001 are from ISCCP (2025), and the TSI (Total Solar Radiation) variations from the data set of Dewitte et al. (2022). The radiation data from 2001 onward are from the CERES (2025) satellite observations. The Oceanic Niño Index (ONI 2025) is from NOAA. In temperature simulations, humidity data are from NOAA (2025b) as well, and the GH gas concentrations are from NOAA (2025c). The RF equations for $CO_2$, $CH_4$, and $N_2O$ are from Ollila (2023b), and in the simple IPCC model, they are from the IPCC (2021). In LBL calculations, the Spectral Calculator tool of Gats Ins. (Gats 2025) was applied using the HITRAN database of version 2022 (HITRAN 2025).

### *2.2 Spectral Calculator application*

Spectral Calculator of Gats (2025) has been used in LBL calculations to simulate water vapour and other greenhouse (GH) gas concentration changes. The high-resolution transmission molecular absorption database of the Harvard-Smithsonian Center for Astrophysics (HITRAN 2025) was applied, which includes the water continuum model 2.52 MT_CKD of Mlawer et al. (2012). The polar summer profiles of the Spectral Calculator (Gats 2021) have been modified for temperature, pressure, and GH gas concentrations to correspond to the Average Global Atmosphere (AGA) profiles. These profiles have been tabulated in Appendix A, together with the global single profiles calculated as the combination of different climate zones. Appendix B is a summary of the calculation capabilities of the Spectral Calculator.

## 3. The radiative forcing of water vapour

The RF values of water vapour were calculated by varying the water vapour concentration $H_{TPW}$ from 4 mm to 41mm, and the $CO_2$ concentration from 330 ppm to 490 ppm. In the LBL calculations, the RF effects of water vapour are calculated based on the temperature, pressure, and water vapour concentration profiles of different climate zones, which are combined into one average climate atmospheric (AGA) profile. The $H_{TPW}$ value is a measure of the total water vapour amount in the atmosphere, which is available in atmospheric data sets (NOAA 2025a).

The calculations show that the impact of $CO_2$ concentration was minimal. The RF effect between the 330 ppm and 490 ppm was only 0.04 $Wm^{-2}$ on the RF value of water vapour. Since this is smaller than the estimated calculation accuracy, this effect was neglected.

The RF curve of absolute humidity $H_{TPW}$ variation from 4 to 41 mm has been depicted in Fig. 3. The fitting according to the second-order equation is (coefficient units $Wm^{-2}$, $Wm^{-2}mm^{-1}$, and $Wm^{-2}mm^{-2}$, respectively)

$$RF = -5.3526 + 1.5733 * H_{TPW} - 0.0156 * H_{TPW}{}^{2}\ [Wm^{-2}]. \qquad (1)$$

The coefficient of determination $R^2$ is 0.9959, and the standard error of the fitting is 0.89 $Wm^{-2}$.

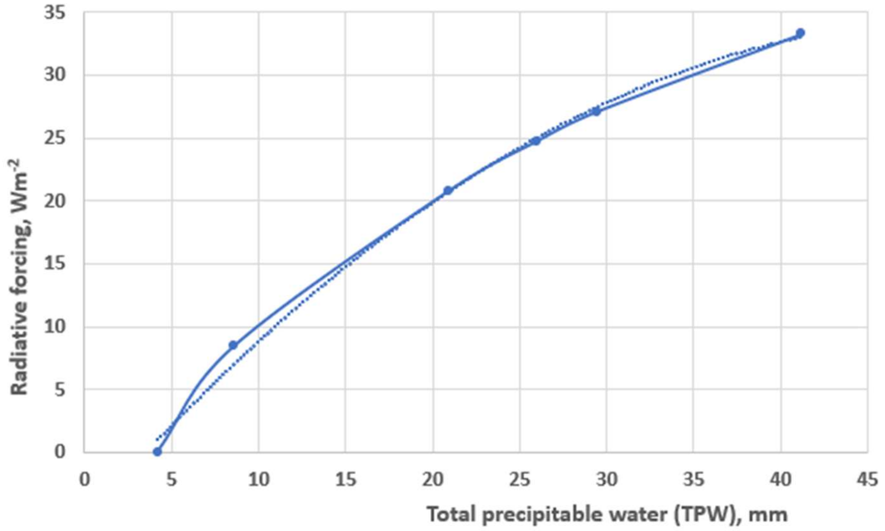

*Figure 3: The RF dependency RF according to the TPW values for the range from 4 mm to 41 mm. The dotted curve is the fitted curve.*

Since the $H_{TPW}$ range in the average global climate is much smaller, another equation was calculated applicable for the $H_{TPW}$ range from 20 mm to 30 mm, which has been depicted in Fig. 4.

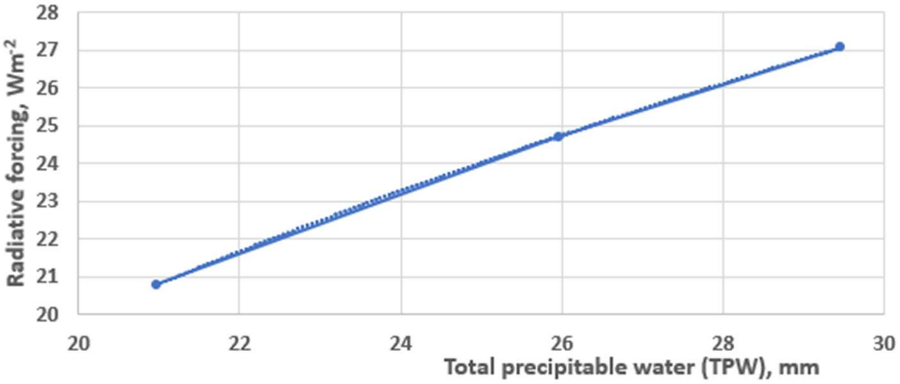

*Figure 4: The RF dependency RF according to the TPW values only for the narrow range from 21.0 mm to 29.5 mm. The dotted curve is the fitted curve.*

This fitting has a logarithmic dependency (coefficient units $Wm^{-2}$, and $Wm^{-2}$ $mm^{-2}$, respectively):

$$RF = -35.304 + 18.435 * \ln(H_{TPW}/1\,mm)\ [Wm^{-2}]. \qquad (2)$$

The dependency, according to equation (2), is practically linear, its coefficient of determination is $R^2 = 0.9999$, and the standard error of the fitting is 0.034 $Wm^{-2}$. These equations can partially explain why water vapour is a much stronger GH gas than $CO_2$. The strengths of water and carbon dioxide can be compared to each other in Fig. 5.

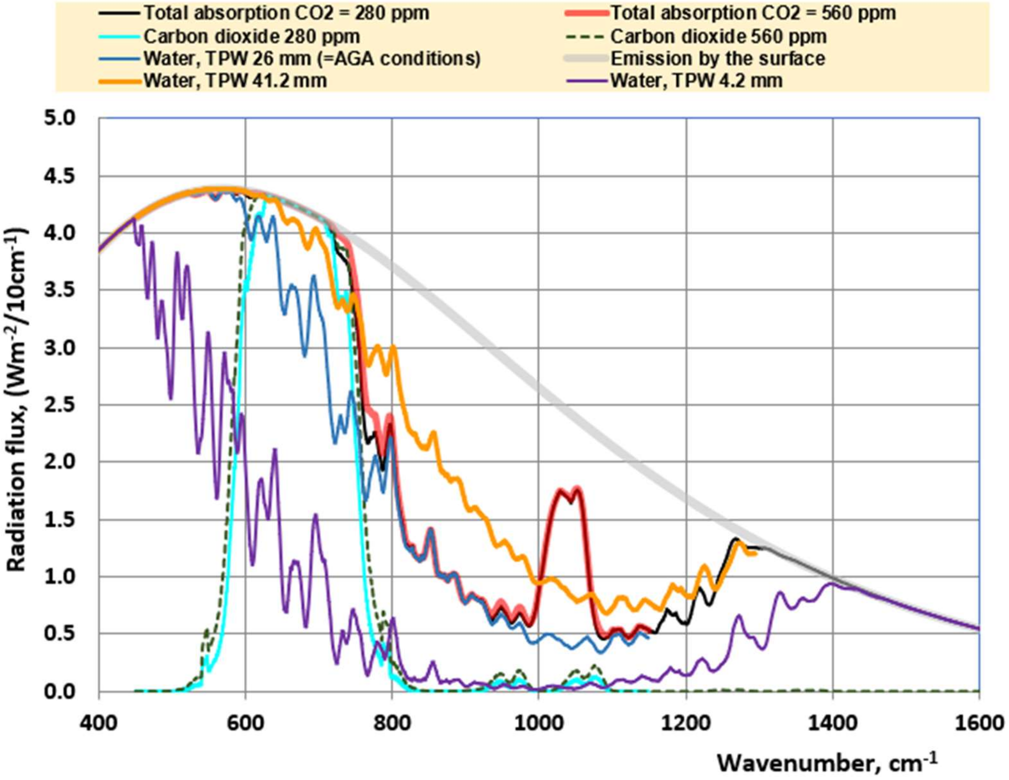

*Figure 5: The absorption graphs under different atmospheric conditions for average global atmospheric (AGA) conditions, when the surface temperature is 16.3ºC (289.5 K ). The $CO_2$ of 280 ppm (light green solid curve) and 560 ppm (dotted dark green curve) have been calculated, when $CO_2$ is the only GH gas in the atmosphere. The water vapour graphs of 4.2 TPW mm (purple curve), 26 mm TPW (blue curve), and 41.2 TPW mm (yellow curve) have been calculated under AGA conditions. The total absorption graphs (grey and red curves) have been calculated under AGA conditions. The emission graph corresponds to the surface temperature of 16.3 °C, assuming the emissivity factor to be 1.0.*

Fig. 5 illustrates the dominant role of water vapour under the average atmospheric conditions (AGA). Under tropical conditions, the role of $CO_2$ is insignificant, which can be noticed by comparing the water absorption curve (yellow) and the $CO_2$ absorption curve (green) to each other. The same conclusion can be drawn from total absorption curves when the $CO_2$ concentration increases from 280 ppm (black curve) to 560 ppm (red curve). This means a minimal warming effect of increasing $CO_2$ concentration in the tropical climate zone. Water vapour does not decrease significantly even in tropical conditions since its absorption increases in the wavelength zone of 7 µm - 14 µm, where the absorption effects of increasing $CO_2$ concentrations are much smaller.

## 4. Verification and validation

### *4.1 Verification of LBL calculations*

The validations of LBL calculations are not possible due to the too-small temperature effects under real climate conditions, but verification tests are possible.

Ollila (2023b) has shown that the LBL calculations carried out under average atmospheric conditions of 2008 – 2014 (detailed in Appendix C) resulted in the OLR flux of 272.0 $Wm^{-2}$ for the clear sky, which is almost the same as the CERES observed flux of 272.6 $Wm^{-2}$ during the same period (Huang and Chen 2020). The GH gas effects can be found to be in the same wavelength zones in both the calculated and the satellite-observed jagged curves. These results show that LBL calculations of this study are reliable, and the correct atmospheric composition has been applied.

### *4.2 The simple climate models applied in temperature simulations*

Three different simple climate models have been applied to temperature simulations, and they have the same common features, but the RF and temperature calculations are different.

The positive water feedback can be tested by applying simple climate models. In this study, a simple climate model has been applied as defined by IPCC (2013) on page 664

$$dT\text{s} = \lambda * \text{RF}, \tag{3}$$

where d*T*s is the global mean surface temperature change, and $\lambda$ is the climate sensitivity parameter. The warming impacts of climate drivers, which are in this study, ASR, and GHGs, including also water vapour, can be added together. This simplification is justified for simulations based on the graphs of Fig. 7.8 of the AR6 (IPCC, 2021), which show that the warming impacts of tropospheric aerosols, halogenated gases, ozone, and volcanic aerosols have been essentially constant during the 2000s.

The dynamic delays of RF values have been calculated by applying the first-order dynamic models as specified in the studies of Ollila (2020; 2021; 2023a). In this study, all the variables and the observed temperature were normalised to zero temperature effect for the period of 2003-2008.

The essential difference between the Ollila models and the IPCC simple model is the value of $\lambda$. The warming values of all climate drivers tabulated in Figures 7.6 and 7.7 in AR6 (IPCC 2021) are possible if the $\lambda$ value of 0.47 K/(Wm$^{-2}$) has been applied, which means the use of positive water feedback in the original GCM calculations.

The $\lambda$ without water feedback can be calculated from the energy balance of the Earth (Ollila 2023b) according to the equation

$$\lambda = T/(\text{SC}(1-\alpha)), \tag{4}$$

*T* is the emission temperature of the OLR radiation, SC is the solar constant, and $\alpha$ is the total albedo of the Earth. By applying the average CERES (2025) OLR flux values for the period 2008 - 2014, the SC is 1360.04 Wm$^{-2}$, $\alpha$ is 0.2916, and $\lambda$ is 0.265 K/(Wm$^{-2}$). The $\lambda$ value can be calculated for each month according to Eq. (4), and this has been applied in simulations of this study.

In the earlier model Ollila-1 (Ollila, 2021), the warming impact of the ENSO (El Niño and Southern Oscillation) effect was calculated by the equation first introduced by Trenberth and Fasullo (2013)

$$dT_{\text{ENSO}} = 0.1 * \text{ONI}, \tag{5}$$

where $dT_{\text{ENSO}}$ is the warming impact of the ENSO phenomenon applying a 5-month delay, and ONI is the Oceanic Niño Index (ONI 2024). In the Ollila-2 model, the ENSO effect has been replaced by the warming impact of water calculated on the $H_{\text{TPW}}$ basis and possible absorbed solar radiation (ASR) impacts.

In both Ollila models, the radiative forcings of $CO_2$, $CH_4$, and $N_2O$ have been calculated by the equations developed in the study of Ollila (2023b), and the same in the IPCC simple model are calculated using the equations of AR5 (IPCC 2013). The differences in the RF values of $CH_4$ and $N_2O$ are insignificant in these two cases.

In the temperature simulations, first-order dynamic models have been applied. The dynamical time constants for the ocean have been 2.74 months and for land 1.04 months (Stine et al. 2009). The responses of first-order dynamic models can be calculated in the discrete form by applying the so-called z-transform, which enables continuously changing input variables.

### *4.3 Water vapour warming impacts during the yearly temperature cycles*

The temperature of the Earth varies in the same way each year on both hemispheres. Only after 2020 has the NH temperature been increasing more rapidly than the SH temperature, and the reason is probably the ASR increase due to cloud cover changes on the NH hemisphere (Hansen et al., 2025). The variation is much greater than the temperature anomaly measurements indicate. The global absolute temperature varies from about 12.5 °C to 16.0 °C. The variation in the northern hemisphere (NH) is much greater, from about 9.5 °C to 22.0 °C, but in the southern hemisphere (SH), from about 10.0 °C to 16.0 °C. These observed temperature graphs have been depicted in Fig. 6, as well as the simulated temperatures by the Ollila-2 model.

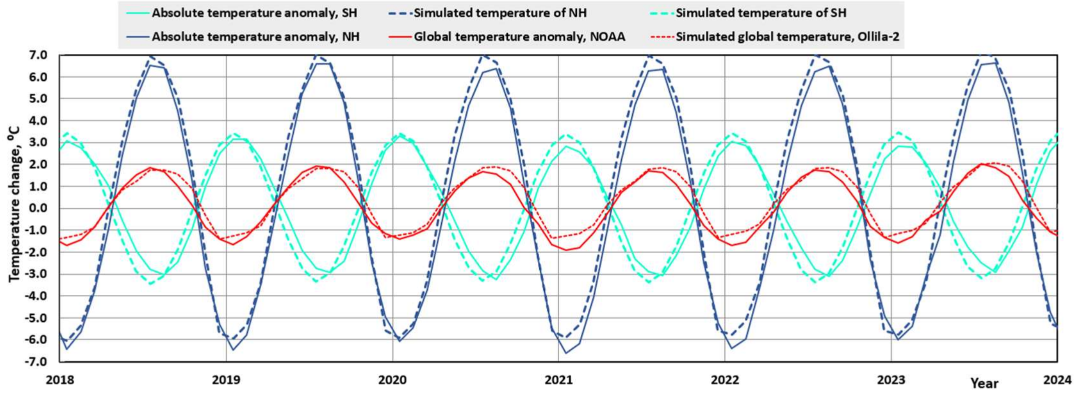

*Figure 6: The graphs of the observed (NOAA, 2025b) and simulated temperature yearly changes of NH, SH and the whole Earth by the Ollila-2 model. A one-month delay in temperatures from February to June due to the melting of ice and snow cover has been applied in the simulated NH temperatures.*

The graphs show that the Ollila-2 simulates the temperatures very well, even though the simulation step is relatively long, with one month. The maximum global temperature normally happens in July, even though the globe receives about 22 $Wm^{-2}$ more total solar radiation (TSI) in December-January than in June-July. Another decisive factor is the ratio of ocean and land. In the NH, the portion of the sea is 69 %, but in the SH it is 81 %. This means that the temperature variation is much smaller in the SH.

Since the dynamic delays and time constant differ between the hemispheres, the global temperature simulations have been carried out separately for both hemispheres, and the global simulation is the sum of these simulations (Fig. 7). The humidity changes, which should cause the positive water feedback, are fast changes happening at the same speed as the temperature changes.

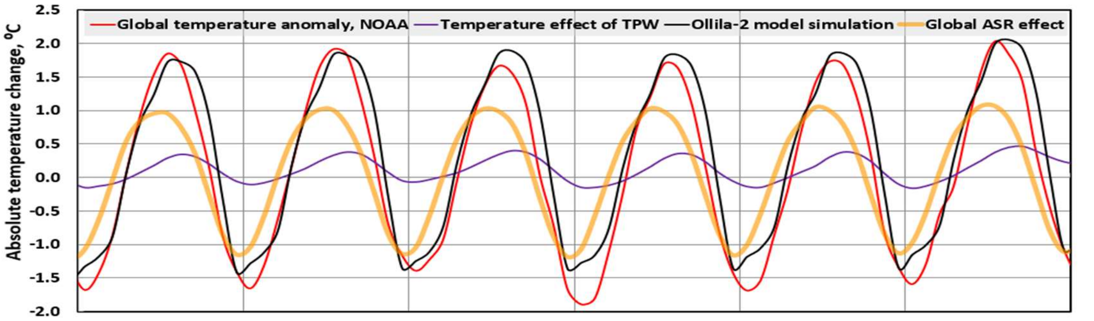

*Fig. 7: The graphs of the observed (NOAA) and simulated temperature anomalies of the globe.*

Also, the temperature impacts of ASR and water vapour ($H_{TPW}$) have been depicted. In Fig. 7, it can be noticed the fact that the ASR is the dominating climate driver of the Earth. The yearly temperature effect of GH gases according to IPCC science is only about 0.02 °C, and that is why it has not been depicted. The major finding of these simulations is that the temperature effect of water vapour variations is only from 12.8 % to 14.5% in addition to the ASR warming effect. This result is practically the same as that found by Harde (2017), that the water vapour feedback increases the climate sensitivity of the $CO_2$ impact by about 14 %. According to the positive water feedback theory, it should be about 100 %.

### *4.4 Temperature and radiation trends from 1980 onward*

The paradigm of the IPCC has been that GH gases are the climate drivers since industrialisation started in 1750. The temperature effect of GH gases, according to the IPCC, has been depicted in Fig. 8, and it has a similar linear trend as the global temperature.

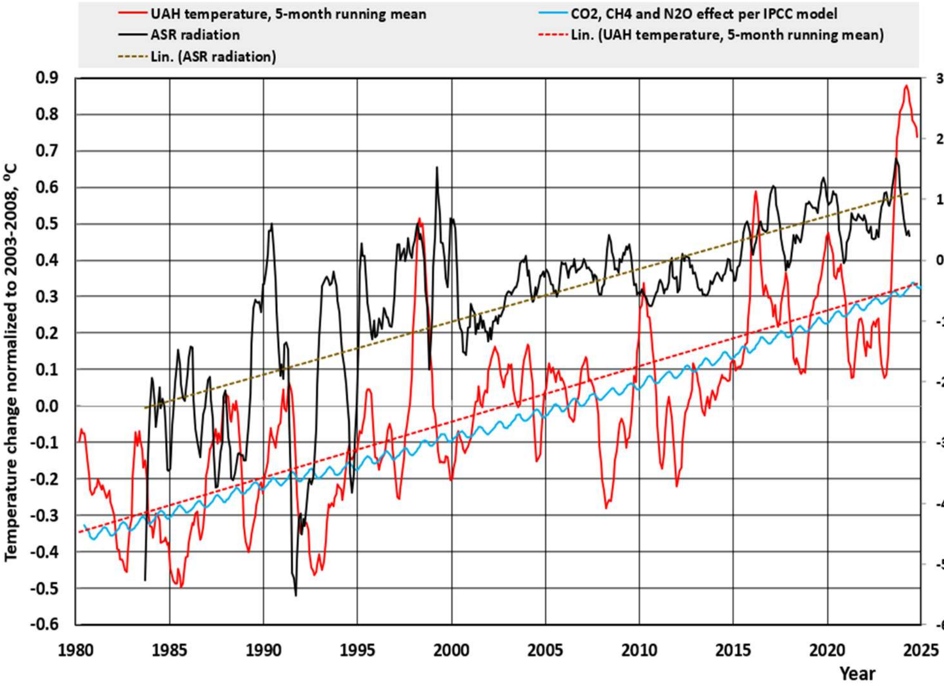

*Figure 8: The temperature trend from 1980 to 2025, together with the ASR radiation trend and the temperature effect of GH gases according to the IPCC.*

On the other hand, the ASR trend has the same kind of linear trend. The fluctuations of the ASR are very great based on the ISCCP data from 1983 to 2001, but the fluctuations are much smaller during the CERES satellite measurement period, which started in 2001, indicating a better measurement accuracy. It means that further analyses are needed to find out the roles of GH gases and the ASR changes in global warming.

### *4.5 Water vapour warming impacts during the 2000s*

The water feedback theory can be tested between 2001 and 2024, when the most accurate observations are available. It can also be expressed in the form that any surface temperature increase should include a water vapour impact corresponding to about 50 % of the total change. The temperature and humidity observations have been depicted in Fig. 9 together with major variables. During this short simulation period, the ENSO warming impacts must be included. The warming impact of ENSO originates from the absorbed solar energy, which is released in the El Niño phase, and then during the cooling period of La Niña, this energy is paid back.

It is easy to notice that the 50 % temperature anomaly (dotted lilac curve) does not vary according to the temperature effect of GH gases as implied by the positive water feedback theory by the IPCC. It should be noticed that according to AR6, $CO_2$ corresponds to about 80 % of the temperature increase from 1750 to 2019 (IPCC 2021). By judging with the eye, the ASR & ENSO effect has had the dominant role in the temperature increase after the year 2014.

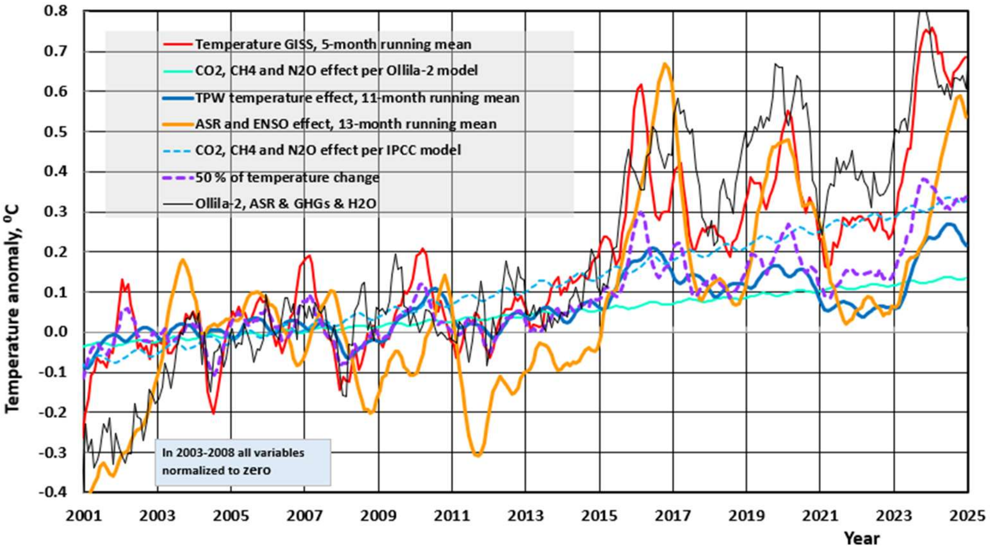

*Figure 9: The temperature effects of $CO_2$, $CH_4$, and $N_2O$ according to Ollila-2 (green solid curve) and IPCC models (dotted turquoise curve), water vapour (blue solid curve), and ASR+ENSO (brownish curve) have been depicted. The temperature anomaly (red curve) is according to the GISS (2025) data set calculated as a 5-month running mean. The lilac dotted curve illustrates the water vapour feedback effect caused by GH gases according to the C-C theory, which has doubled the original radiative forcings, and it is 50 % of the temperature curve. The warming impacts of ENSO have been calculated by Eq.(5). All variables have been normalised to zero in the period 2003-2008.*

One of the objectives of this study was to test the theory of positive water feedback. Two observation-based analyses have been carried out. The first one was the seasonal temperature variation analyses in section 4.3, which show that the $H_{TPW}$ temperature impact increases the absorbed solar radiation (ASR) effect by a factor of 1.14 and not by about 2 as assumed by the IPCC based on the C-C equation.

The theory in this study has been that the $H_{TPW}$ variations depend on the primary energy changes, which were tested during the period from 2010 to 2025. The most important energy input is the ASR, which has increased by 2.01 $Wm^{-2}$ from 2000 to the year 2023, which can be compared to the RF impact of 2.16 by $CO_2$ from 1750 to 2019 (IPCC 2021). The temperature effects of ASR and absolute humidity $H_{TPW}$ have been illustrated in Fig. 10.

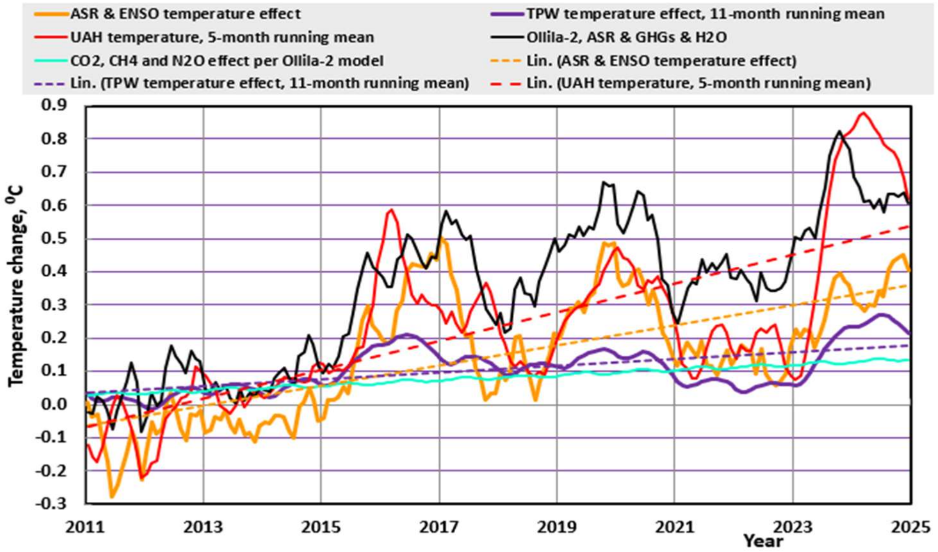

*Figure 10: The trend curves of UAH temperature, the temperature simulations of the Ollila-2 model, and the temperature effects of TPW absolute humidity, ASR & ENSO, and GH gases by the Ollila-2 model from 2011 to 2025.*

The $H_{TPW}$ curve seems to correlate quite well with the ASR&ENSO curve. By judging with the eye, the $H_{TPW}$ changes do not correlate with the impacts of GH gases. The multicorrelation coefficient of regression $R^2$ for the period 2005-2024 is 0.756 between the water vapour ($H_{TPW}$) and two variables, which are the temperature impacts of ASR&ENSO and the GH gases, according to the Ollila-2 model. The coefficient $R^2$ of the model with only ASR&ENSO is only slightly smaller, 0.688. It means that the $H_{TPW}$ values depend mainly on ASR and ENSO, which are the primary energy inputs.

The linear increases of temperature and $H_{TPW}$ temperature impacts from 2011 to 2025 are illustrated by the linear fittings of the actual trends in Fig. 10. The temperature increase has been 0.61 ºC, and the temperature increase of $H_{TPW}$ impact has been 0.14 ºC, which means a 23 % feedback effect on the primary temperature drivers (mainly ASR and ENSO). It is more than 14 % as concluded from the ASR impacts during the seasonal temperature changes in section 4.3. A plausible explanation is that during the period 2011-2025, there have been two strong climate disturbances, namely two very strong El Niños: 2015-2016 with an ONI value of 2.64, and 2023-2024 with an ONI value of 1.95. As found by Ollila (2020), about 50 % of the temperature effect of very strong El Niños results from the 100 % water feedback effect during these short-term intervals of about one year. These two strong El Niños have increased the average water feedback during this short period from its normal level 14 % to an observed value of 23 %.

### *4.6 Temperature simulations of the 2000s*

The temperature simulations during the 2000s have been carried out by applying the Ollila-2 model and the IPCC simple model (Fig. 11).

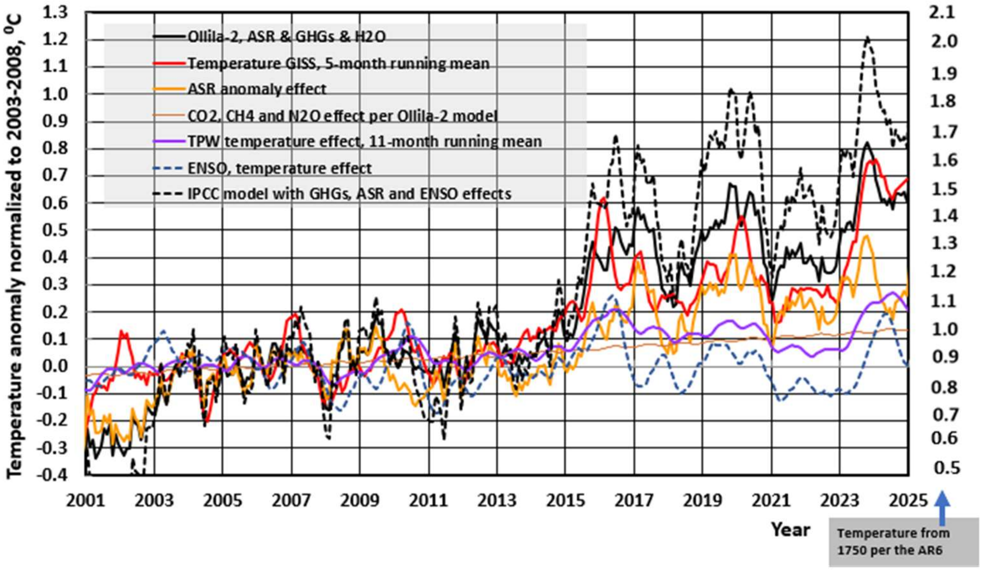

*Figure 11: The graphs of the Ollila-2 model and GISS temperature from 2001 to 2025. The warming impacts of the three major climate drivers of ASR, GHGs, and TPW have been depicted for the same period according to the Ollila-2 model, as well as the ENSO according to Eq. (5). The dashed black curve is the simulated temperature response applying the λ-value of 0.47 K/(Wm$^{-2}$) according to the IPCC (2021).*

The overall response of the Ollila-2 model is very good in comparison to observed temperature changes. By comparing the water vapour trend changes to the ENSO temperature changes, it is obvious that the major part of the ENSO effect happens through the changes in the atmospheric humidity and ASR changes. It can be noticed that the warming impacts of GH gases are very low. The ASR flux changes have had a major role in the temperature increase after the very strong El Niño in 2015-2016. The $H_{TPW}$ values have stayed at a record level after the El Niño of 2023-2024, and it seems to be the main reason, besides the ASR, for the very high temperatures of 2023 and 2024.

The temperature effects of the Ollila-2 model are based on the calculated RF effects of climate drivers. The effect of GH gases is minimal according to the RF values of both the Ollila-2 and IPCC simple models. The simulated temperature by the IPCC model starts to deviate from the observed temperature after El Niño 2015-2016. The reason is the increased ASR anomaly. Since the water feedback theory implies that water content should have a similar impact as the original ASR impact, the result is a far too high temperature response.

It should be noted that nature cannot separate whether the ASR impact is due to solar radiation changes or the albedo changes. If these changes cause temperature increases, the water feedback theory of the IPCC implies that this mechanism doubles the temperature impact. The ASR increase from 2011 to 2019 was 1.29 $Wm^{-2}$ according to CERES (2025) observations, which would increase the temperature by 0.6 ºC to about 1.9 ºC according to the IPCC science as described in section 1.3 (equation (3) with a $\lambda$ value of 0.47 $K/(Wm^{-2})$. Maybe this is a reason why there is no ASR anomaly impact in Figure 7.7 of AR6, since the GCM-calculated temperature would deviate significantly from the observed: 1.9 ºC versus 1.29 ºC. Another good reason is that the GCMs are not capable of calculating an ASR impact through cloud property impacts on albedo. This problem becomes even more distinct when thinking that the aerosol and cloud effect has decreased from -0.82 $Wm^{-2}$ in 2011 to -1.00 $Wm^{-2}$ in 2019 in Fig. 7.7 (IPCC 2021), but the real effect has been significantly positive as noted above. By applying the real RF warming impact of water, the temperature follows the observed temperature very well.

The correlation coefficient of the Ollila-2 model to the observed GISS temperature from 2005 to 2024 is 0.82. The most realistic measure of the models is the Mean Absolute Error (MAE), which is calculated by the equation

$$\mathrm{MAE} = \mathrm{ABS}(\mathrm{d}T_\mathrm{O} - \mathrm{d}T_\mathrm{C})/\mathrm{n}, \tag{6}$$

where ABS is a function calculating the absolute error between the observed temperature anomaly $T_\mathrm{O}$ and the model-simulated temperature anomaly $T_\mathrm{C}$, and n is the number of paired points. The MAE values calculated for the period from 2005 to December 2024 were 0.090°C for Ollila-2 and 0.183 °C for the IPCC model. These MAE values have been calculated from the original monthly values, even though the graphs in Fig. 10 have been smoothed by applying running mean values.

The greater MAE value of the IPCC model comes from the strong ASR flux increase after 2014, as noticed in Fig. 8, which overestimates the temperature response because of the water feedback mechanism of this model.

## 5. Discussion and conclusions

Water vapour is the most important GH gas since it has a major role in the GH effect. This effect varies based on the studies from 50 % (Schmidt et al. 2010) to 89-95 % (Koutsoyiannis 2024), and on the other hand, the $CO_2$ effect also varies in broad limits from about 4 % - 5 % (Koutsoyiannis 2024) to 33 % (Pierrehumbert 2010) as surveyed in section 1.3. For some reason, the IPCC does not report these key figures at all. The RF value of the water vapour, depending on its concentration in the atmosphere, shows that it is practically linear in global concentrations without a strong decreasing RF effect like in the equation of $CO_2$. This feature explains why water's capability to absorb infrared radiation in the wavelength zone 12 µm to 19 µm almost nullifies the warming impact of increased concentration of $CO_2$ in the tropics. The RF value equation of water, based on the $H_\mathrm{TPW}$ values, gives the possibility to treat water concentration changes in the same way as the other GH gases.

A rather solid conclusion of this study is that the $H_\mathrm{TPW}$ value seems to depend on the primary energy variations of the Earth. During the relatively short period of 25 years of this study, the most important climate driver in this respect is the absorbed solar radiation (ASR) and its variations. The ENSO temperature impact acts in the same way as the ASR effect. Together, these two variables (ASR and ENSO) explain the temperature variations and the significant increase in temperature of the 2000s.

Water amplification could not be found in the case of GH gases, or it was insignificant, but only for the preliminary energy input changes, like ASR and ENSO. This result is not very solid concerning the warming impacts of GH gases, since during this short period, the GH impacts are very small. Anyway, the maximum water feedback is only 14 % and not about 100 % for any climate radiative forcing. In practice, the best and simplest way to factor in the water feedback is to use the RF calculation based on the $H_{TPW}$ concentrations, since the water feedback is then automatically calculated according to its real impacts.

The ASR changes have been omitted in the GCM simulations of the AR6 (IPCC 2021) since these models have been constructed on the idea that ASR variations could be calculated through cloud property impacts. The simulation results of Ollila-2 simple climate models challenge the GCM models, which are based on the anthropogenic climate drivers only. Even though this is a short period, this model seems to give good results even when applied from the beginning of 1980.

In the year 2023, the global temperature increased about 0.28ºC, but the GH gases showed only an increase of about 0.02 ºC. Probably considering this fact, Schmidt (2024) wrote that GCMs cannot explain the high temperature of the year 2023, and it means that we are in uncharted territory. This study suggests two simple corrective measures applicable in all GCMs, which are the use of observed absorbed solar radiation (ASR) values and the concentration of water vapour for the calculation of the RF values in the same way as for other GH gases. In this way, the simulated temperatures are close enough to observations even by applying simple models.

The results of this paper challenge the water vapour feedback theory since the simulations show that the results using the RF of the water vapour are very good, instead of the water feedback theory of the C-C mechanism. It looks like the climate community is adhering to anthropogenic climate change, and they do not consider another paradigm, which leaves this question open for the time being.

**Funding:** No funds, grants, or other support were received.

**Editor**: Prof. Malamos; **Reviewers**: anonymous.

## References

Bard E, Raisbeck G, Yiou F, Jouzel J, 2000: *Solar irradiance during the last 1200 years based on cosmogenic nuclides*. Tellus 52B:985–992. https://doi.org/10.1034/j.1600-0889.2000.d01-7.x

Bellouin N, Boucher O, Haywood J, Shekar Reddy M, 2003: *Global estimate of aerosol direct radiative forcing from satellite measurements.* Nature 438:1138-1141.
DOI: 10.1038/nature04348

Berkley, 2025: *Temperature dataset*. https://berkeley-earth-temperature.s3.us-west-1.amazonaws.com/Global/Land_and_Ocean_complete.txt

CERES, NOAA, CERES EBAF-TOA Data, 2025:
https://ceres-tool.larc.nasa.gov/ord-tool/jsp/EBAFTOA42Selection.jsp

Connolly R, Soon W, Connolly M, Baliunas S, Berglund J, Butler CJ, Cionco RG, Elias AG, Fedorov VM, Harde H et al. (2021): *How much has the Sun influenced Northern Hemisphere temperature trends? An ongoing debate*. Res. Astron. Astrophys. 21(6):131.
https://iopscience.iop.org/article/10.1088/1674-4527/21/6/131?fbclid=IwaR0u-

Dewitte S, Cornelis J, Meftah M, 2022: *Centennial Total Solar Irradiance Variation*. Remote Sens. 14: 1072. https://doi.org/10.3390/rs14051072

Diamond MS, 2023: *Detection of large-scale cloud microphysical changes within a major* *shipping corridor after implementation of the International Maritime Organization 2020 fuel sulphur regulations.* ACP 23:8259–8269. https://doi.org/10.5194/acp-23-8259-2023

Gats, Gat Inc. 2025: *Spectral calculation tool*. https://www.spectralcalc.com/info/about

Gupta AK, Mittal T, Fauria KE, Bennartz R, Kok JF, 2022: *Hunga eruption cooled the southern hemisphere in 2022 and 2023.* Commun. Earth Environ. 6:240. https://doi.org/10.1038/s43247-025-02181-9

Harde H, 2014: *Advanced two-layer climate model for the assessment of global warming by* $CO_2$. Open Atm. Sc. J. 1(3):1-31. https://web.achive.org/web/20160429061756/http://www.scipublish.com/journals/ACC/papers/download/3001-846.pdf

Harde H, 2017: *Radiation Transfer Calculations and Assessment of Global Warming by* $CO_2$. Int. J. Atmos. Sci. 251034:1-30. https://doi.org/10.1155/2017/9251034

Harde H, 2022*: How Much CO2 and the Sun Contribute to Global Warming: Comparison of Simulated Temperature Trends with Last Century Observations.* Sci. Clim. Change. 2.2:105-133. https://doi.org/10.53234/scc202206/10

HITRAN, Harvard-Smithsonian Center for Astrophysics, 2024: *High-Resolution Transmission Molecular Absorption database.* https://www.cfa.harvard.edu/hitran/

Hodnebrog Ø, Myhre G, Jouan C, Andrews T, Forster PM, Jia H, Loeb NG, Olivié DJL, Paynter D, Quaas J, Raghuraman SP, Schulz M, 2024: *Recent reductions in aerosol emissions have increased Earth's energy imbalance.* Commun. Earth Environ. 5:166. https://www.nature.com/articles/s43247-024-01324-8

Hoyt DV, Schatten KH, 1993*: A discussion of plausible solar irradiance variations, 1700-1992.* J. Geophys. Res.: Space Phys. 98:18895–906. https://doi.org/10.1029/93JA01944

Huang B, Angel W, Boyer T, Cheng L, Chepuring G et al., 2018: *Evaluation SST analyses with independent ocean profile observation.* J. Clim. 36: 5015-5030. DOI: https://doi.org/10.1175/JCLI-D-17-0824.1

Huang X, Chen X, 2020: *A synergistic use of hyperspectral sounding and broadband radiometer observations from S-NPP and Aqua.* Fall 2020 NASA Sounder Science Team Meeting, October.

IPCC, AR4, 2007: Climate Change 2007, The Physical Science Basis, Cambridge Univ. Press, Cambridge, U.K., and New York. https://www.ipcc.ch/assessment-report/ar4/

IPCC, AR5, 2013: Climate Change 2013, The Physical Science Basis. Contribution of Working Group I to the Fifth Assessment Report of the Intergovernmental Panel on Climate Change. Cambridge Univ. Press, Cambridge, U.K., and New York. https://www.ipcc.ch/site/assets/uploads/2017/09/WG1AR5_Frontmatter_FINAL.pdf

IPCC, AR6, 2021: Climate Change 2021, The Physical Science Basis. Contribution of Working Group I to the Sixth Assessment Report of the Intergovernmental Panel on Climate Change. Cambridge Univ. Press, Cambridge, U.K., and New York. https://www.ipcc.ch/report/ar6/wg1/

ISCCP, The International Satellite Cloud Climatology Project, *FD data*, 2025. https://isccp.giss.nasa.gov/projects/flux/

Kiehl JT, Trenberth KE, 1997: *Earth's annual global mean energy budget*. Bull. Amer. Meteor. Soc 90: 311-323. DOI: https://doi.org/10.1175/1520-0477(1997)078<0197:EAGMEB>2.0.CO;2

Koutsoyiannis D, 2024: *Relative importance of carbon dioxide and water in the greenhouse effect: Does the tail wag the dog?* Sci. Clim. Change. 4.2:36-78. https://scienceofclimatechange.org/wp-content/uploads/SCC-Koutsoyiannis-DogTail-Nov-2024.pdf

Loeb NG, Thorsen TJ, Norris JR, Wang H, Su W, 2018: *Changes in Earth's energy budget during* *and after the "pause" in global warming: An observational perspective.* Climate 6, 62, https://www.mdpi.com/2225-1154/6/3/62

Loeb NG, Johnson GC, Thorsen TJ, Lyman JM, Rose FG, Kato S, 2021: *Satellite and ocean data reveal marked increase in Earth's heating rate.* Geophys. Res. Lett. 48, e2021GLO93047, https://doi.org/10.1029/2021GL093047

Ma N, Zhang Y, Yang Y, 2025: *Recent decline in global ocean evaporation due to wind stilling.* Geophys. Res. Lett. 5:e2024GL114256. https://doi.org/10.1029/2024GL114256

Manabe S, Wetherald RT, 1967: *Thermal equilibrium of the atmosphere with the given distribution of relative humidity*. J. Atm. Sci. 24(3):241-259. https://climate-dynamics.org/wp-content/uploads/2016/06/manabe67.pdf

Marsh ND, Svensmark H, 2000: *Low cloud properties influenced by cosmic rays.* Phys. Rev. Lett. 85(23), 5004–5007, DOI: https://doi.org/10.1103/PhysRevLett.85.5004

Matthes K, Funke B, Andersson ME, et al., 2017: *Solar forcing for CMIP6 (v3.2),* Geosci. Model Dev. 10:2247-2302. https://www.geosci-model-dev.net/10/2247/2017/gmd-10-2247-2017.pdf.

MetOffice, Met Office Hadley Centre, 2024: *Temperature data of HadCRUT5 and HadSST.4.1.* https://www.metoffice.gov.uk/hadobs/hadcrut5/data/HadCRUT.5.0.2.0/download.html

Mlawer EJ, Payne VH, Moncet J-L, Delamere JS, Alvarado MJ, Tobin DC, 2012: *Development and recent evaluation of MT CKD model of continuum absorption.* Philos. Trans. Math. Phys. Eng. Sci. A 370: 2520-2556. DOI: 10.1098/rsta.2011.0295

Meyssignac B, Chenal J, Loeb N, Guillaume-Castel R, Ribes A, 2023: *Time-variations of the climate feedback parameter λ are associated with the Pacific Decadal Oscillation*. Commun. Earth Environ. 4:241. https://doi.org/10.1038/s43247-023-00887-2

Nikolov N, Zeller NK, Roles of Earth's Albedo Variations and Top-of-the-Atmosphere Energy Imbalance in Recent Warming: New Insights from Satellite and Surface Observations. Geomatics 2024, 4(3), 311-341. https://doi.org/10.3390/geomatics4030017

NOAA, 2025a: *Pacific Decadal Oscillation (PDO).* https://psl.noaa.gov/pdo/

NOAA, Global Monitoring Laboratory (GML) of the National Oceanic and Atmospheric Administration, 2025b: *Web-based Reanalysis Intercomparison Tool: Monthly/Seasonal Time-Series.* https://psl.noaa.gov/data/atmoswrit/timeseries/index.html

NOAA, Global Monitoring Laboratory (GML) of the National Oceanic and Atmospheric Administration, 2025b: *Web-based Reanalysis Intercomparison Tool: Monthly/Seasonal Time-Series.* https://psl.noaa.gov/data/atmoswrit/timeseries/index.html0

NOAA, Global Monitoring Laboratory (GML) of the National Oceanic and Atmospheric Administration, 2025c: *Carbon dioxide, methane and nitrogen oxide concentrations*. https://gml.noaa.gov/ccgg/trends/

Ohmura A, 2001: *Physical Basis for the Temperature-Based Melt-Index Method*. J. Appl. Meteorol. Climatol. 40:754-76. DOI:https://doi.org/10.1175/1520-450(2001)040<0753:PBFTTB>2.0.CO;2

Ollila A, 2017*:* Warming effect reanalysis of greenhouse gases and clouds. PSIJ 13(2):1-13. https://journalpsij.com/index.php/PSIJ/article/view/374

Ollila A, 2019: The effect definition. PSIJ 23(2):1-5. https://doi.org/10.9734/psij/2019/v23i230149

Ollila A, 2020: *The pause end and major temperature impacts during super El Niños are due to shortwave radiation anomalies.* PSIJ 24(2):1-20. DOI: 10.9734/psij/2020/v24i230174

Ollila A, 2021: *Global Circulation Models (GCMs) simulate the current temperatures only if the* *shortwave radiation anomaly of the 2000s has been omitted*. Curr. J. App. Sci. Techn. 42(46):111-183. DOI: 10.9734/cjast/2021/v40i1731433

Ollila A, 2023a: *The 2023 record temperatures: correlation to absorbed shortwave radiation anomaly.* Sci. Clim. Change 4.1:74-87. DOI: 10.53234/scc202403/15

Ollila A, 2023b: *Radiative forcing and climate sensitivity of carbon dioxide ($CO_2$) fine-tuned with CERES data.* Curr. J. App. Sci. Techn. 40(17):45-52. DOI: 10.9734/cjast/2023/v42i464300

ONI, NOAA, 2025: *Oceanic Niño Index (ONI).* https://ggweather.com/enso/oni.htm

Pierrehumbert RT, 2010: *Infrared radiation and planetary temperature*. Phys. Today 64(1):33-38.

Raghuraman SP, Soden B, Clement A, Vecchi G, Menemenlis S, Yang W, 2024: *The 2023 global warming spike was driven by the El Niño–Southern Oscillation*. Atm. Phys. Chem. 24:11275-112823.

Rantanen M, Laaksonen A, 2024: *The jump in global temperatures in September 2023 is extremely unlikely due to internal climate variability alone*. npj Clim. Atmos. Sci, 7:34.

Scafetta N, 2023: *Empirical assessment of the role of the Sun in climate change using balanced multi-proxy solar records.* GSF 14(6):101650. https://doi.org/10.1016/j.gsf.2023.101650

Schmidt GA, Ruedy RA, Miller RL, Lacis AA, 2010: *Attribution of the present-day total greenhouse effect.* J. Geophys. Res. 115:D20106. https://doi.org/10.1029/2010JD014287

Schmidt GA, 2024: *Climate models can't explain 2023's huge heat anomaly – we could be in uncharted territory*. Nature: 627. https://www.nature.com/articles/s41612-024-00582-9

Stefani F, 2021: *Solar and Anthropogenic Influences on Climate: Regression Analysis and Tentative Predictions*. Climate 2021, 9, 163. https://doi.org/10.3390/cli9110163

Stephens GL, Hakuba MZ, Kato S, Gettelman A, Dufresne J-L, Andrews T, Cole JNS, Willen U, Mauritsen T, 2022: *The changing nature of Earth's reflected sunlight*. Proc. R. Soc. A 478:20220053. https://royalsocietypublishing.org/doi/pdf/10.1098/rspa.2022.0053

Stine AR, Huybers P, Fung IY, 2009: *Changes in the phase of annual cycle of surface temperature*. Nature 457:435-441. https://www.nature.com/articles/nature07675

Svensmark H, 2019: *FORCE MAJEURE - The Sun's Role in Climate Change*, The Global

Warming Policy Foundation, ISBN 978-0-9931190-9-5.

Trenberth KE, Fassullo JT, 2009: *Global warming due to increasing absorbed solar radiation.* Geophys. Res. Lett. 36: L07706. https://doi.org/10.1029/2009GL037527

Trenberth KE, Zhang Y, Fassullo JT, 2015: *Relationships among top-of-atmosphere radiation and atmospheric state variables in observations and CESM.* J. Geophys. Res. A. 120:10074-10090. https://doi.org/10.1002/2015JD023381

UAH, 2024: *Global temperature anomaly data set*. https://www.nsstc.uah.edu/data/msu/v6.0/tlt/uahncdc_lt_6.0.txt

Wang S, Xu T, Nie W, Jiang C, Yang Y, Fang Z, Li M, Zhang Z, 2020: *Evaluation of Precipitable Water Vapor from Five Reanalysis Products with Ground-Based GNSS Observations*. Remote Sensing, 12(11), 1817–1835. https://doi.org/10.3390/rs12111817

Wild M, Folini D, Schär C et al., 2013: *The global energy balance from a surface perspective.* Clim. Dyn. 40, 3107–3134. https://doi.org/10.1007/s00382-012-1569-8

Zhang T, Rossow WB, Lacis AA, Oinas V, 2004: *Calculations of radiative fluxes from the top of atmosphere based on ISCCP and other global data sets: Refinements of the radiative model and the input data*. J. Geo. Res. 109:1149-1165. https://doi.org/10.1029/2003JD004457

## Appendix A. The average climate profiles applied in the LBL calculations

The climate zones are the five zones available in the Spectral Calculator application: tropical, midlatitude summer (ML-S), midlatitude winter (ML-W), polar summer (Polar-S), and polar winter (Polar-W). US Standard (US Stand) is the average atmospheric condition above the USA continent, and it has not been applied in these calculations. The weighing factors in calculating the average global profiles are 0.391 for the tropics, 0.461 for the midlatitude zone, and 0.148 for the polar zone. The profiles have been tabulated to the average altitude of 11 km of the troposphere, since thereafter the climate zone differences are insignificant.

| **Average global atmosphere - AGA** | | | |
|---|---|---|---|
| **Altitude** | **Temperature** | **Pressure** | **Humidity** |
| km | Kelvin | mbar | g/m3 |
| 0 | 288.23 | 1013.90 | 11.06 |
| 1 | 283.68 | 900.23 | 7.36 |
| 2 | 278.84 | 797.91 | 5.16 |
| 3 | 274.45 | 705.34 | 3.33 |
| 4 | 268.29 | 622.01 | 2.10 |
| 5 | 262.00 | 547.05 | 1.24 |
| 6 | 255.58 | 479.54 | 0.67 |
| 7 | 249.10 | 418.88 | 0.36 |
| 8 | 242.58 | 364.78 | 0.16 |
| 9 | 236.31 | 316.37 | 0.05 |
| 10 | 230.36 | 273.62 | 0.01 |
| 11 | 226.02 | 235.71 | 0.00 |
| | | **Total, prcm** | **2.6** |

Polar Summer (Polar-S) profiles have been applied in simulations. The water content of this climate profile has been adjusted by multiplying the profile values by 1.2384, which makes the total amount of precipitable water (prcm) 2.6 cm, which is the average water content of the atmosphere.

## Appendix B. The capabilities of the Spectral Calculator

Ollila (2017) has calculated the global total absorption value using these five different climate zones to be 307.53 $Wm^{-2}$ in the troposphere. The same value applying the adjusted Polar summer profiles is 305.98 $Wm^{-2}$, which is only 0.5 % smaller. It can be estimated that this small difference does not affect RF calculations. Since the one profile calculation is so close to the five profile results, it is justifiable to use it in all LBL calculations in this study.

The Spectral Calculator LBL code, together with the HITRAN (2024) database, has been applied in numerous calculations without finding any problems or errors according to Gats (2024). The number of spectral lines originates from the HITRAN database, and spectra up to one million points can be calculated. The atmosphere is modelled as graduated concentric spherical shells. The number of shells depends on the path length and altitude range. For example, a path from the ground to 120 km (the top of our Spectral Calculator atmospheres) is split into 19 shells: 250 meters thick at the surface, growing to 10 km thick at high altitudes.

The author has applied this tool for calculating the $CO_2$ contribution in the GH effect by applying the US Standard Atmosphere 1976 with 12% water reduction, and the result is 27%, almost the same as the 26% calculated by Kiehl and Trenberth (1997) with the same atmospheric conditions.

Schmidt et al. (2010) have calculated that the $CO_2$ contribution to the GH effect is 14 % corresponding to 21.7 Wm$^{-2}$ absorption, and the same figures of the author applying the Spectral Calculator are 12.7 % / 20.1 Wm$^{-2}$ using the GH effect magnitudes of 155 and 157.7 Wm$^{-2}$, respectively. Also, the total LW absorptions according to the altitude with the Spectral Calculator are the same as reported by Ohmura (2001): 1 km 90 %, 2 km 95 %, and 11 km 98 %.

The average global cloud layer is at an altitude from 1.5 km to 4.1 km (Wang et al., 2000), and the LW absorption by $CO_2$ has been completed below 1 km (Ollila, 2017). Thus, clear sky LW radiation reduction for a specific $CO_2$ concentration is accurate enough for the cloudy sky reduction, but the reduction of OLR flux due to cloud absorption is needed, which is proportional to $OLR_{clear}$ according to the coefficient $R_c$.

## Appendix C. The atmospheric conditions applied in the LBL calculations

In this study, the radiation flux of the clouds and the CERES (2024) data have been applied as reference material during the pause period from 2008 to 2014. This period has been selected since there are no exceptional climate events, and it is long enough for filtering out small deviations. The total precipitable water (TPW) amount has been 2.6 cm, carbon dioxide 393 ppm, methane concentration 1.803 ppm, and nitrogen oxide concentration 324 ppb at the surface level.

The surface-emitted LW flux is 398 Wm$^{-2}$ according to the Earth's energy balance, applying the CERES radiation flux data (Wild et al., 2013). This flux value corresponds to Planck's temperature of 16.3 °C. Huang et al. (2018) have analysed five sea surface temperature (SST) datasets. During the pause from 2000 to 2014, the SST values varied from 18.1 °C to 18.5 °C. Since the oceans cover 70 % of the Earth's area, it means the real surface temperature is essentially higher than 15 °C, normally used as the global temperature estimate. The cloud fraction of this period has been 0.674 (CERES, 2024).

The average CERES observed OLR values in Wm$^{-2}$ for this period are 240.038 for all-sky and 267.940 for clear sky, and the cloud fraction has been 0.674. The cloudy sky value is not readily available, but it can be calculated using the equation of Bellouin et al. (2003):

$$OLR_{all\text{-}sky} = 0.674 * OLR_{cloudy} + 0.326 * OLR_{clear} \qquad \text{(a)}$$

According to this equation, OLR for a cloudy sky is 226.54 Wm$^{-2}$. The clear sky flux of 268 Wm$^{-2}$ at the TOA is the sum of 186 Wm$^{-2}$ radiated from the atmosphere and 82 Wm$^{-2}$ transmitted through the atmosphere. When the sky turns from a clear sky to a cloudy sky, the changes in radiation fluxes happen immediately. The transmittance flux of 82 Wm$^{-2}$ disappears, and the atmosphere-radiated OLR of 226 Wm$^{-2}$ becomes about 15.5 % smaller than the same of clear sky. This change is caused by the LW radiation absorption by clouds, which has an essential role in the GH effect.

The accurate ratio of $OLR_{cloudy}$ to $OLR_{clear}$ during the period 2008-2014 is 0.8455, which has been marked by $R_c$ in this study. The author has used $R_c$ in calculating the cloudy sky OLR values from the LBL calculated $OLR_{clear}$ values, which are needed in RF calculations of $CO_2$.

The absorption effect of $CO_2$ happens below the 1 km altitude since the $CO_2$ is so a strong absorber in its waveband zone. The global surface temperature of cloudy sky conditions is about 0.1 °C higher than the all-sky conditions (Zhang et al., 2004). The explanation is that the reradiation from clouds increases more than the SW radiation to the surface decreases during relatively short periods of cloudy sky conditions (about two days of three are cloudy).

Essay

# On the Residence Time of $CO_2$ in the Atmosphere and the Carbon Mass Balance

Raimund Müller

Edertal, Germany

SCC-Publishing

Michelets vei 8 B
1366 Lysaker, Norway

ISSN: 2703-9072

Correspondence:
mueller.raimund@
outlook.com

Vol. 5.3 (2025)
pp. 207-212

## Abstract

The impression is gained that there is still no conclusive physical description of the global behavior of $CO_2$ absorption/emission in the various reservoirs. There is a growing group that is convinced, the residence time of $CO_2$ in the atmosphere is approximately 4 years. Another group assumes a significantly longer residence time of 30 years or more. Finding a common consensus between both sides appears difficult.

An attempt is made here to provide an approach. It can be viewed as a complement to other articles recently published in Science of Climate Change. We assume that there is a regular exchange of $CO_2$ between the reservoirs, both in terms of absorption and emission. Without anthropogenic emissions, absorption and emission balance each other.

The approach assumes an equilibrium of $CO_2$ concentrations between the various reservoirs. Any additional amount of $CO_2$ introduced into the system is distributed in a constant ratio among the reservoirs.

**Keywords:** e-time τ; global carbon cycle; absorption $S_{LAND}$ and $S_{OCEAN.}$; $CO_2$-equilibrium and equivalence principle, communication tubes

Submitted 2025-05-29, Accepted 2025-10-20, https://doi.org/10.53234/scc202510/07

## 1. Introduction

Most scientists represented by the IPCC believe that the $CO_2$ increase from 280 ppmv to 420 ppmv is solely anthropogenic, justifying this with a residence time according to the Bern Model.

However, in recent years, a growing number of scientists (Roth [1], Berry [2], Schrijver [3]) have cast doubt on this view, especially since the Bern Model contradicts the Equivalence Principle [12] and has no physical basis. The IPCC's previous predictions have never come true.

Prof. Feynman once taught: If the prediction is wrong, the assumption is necessarily wrong. The assumption that 50% of anthropogenic emissions remain in the atmosphere must therefore also be questioned.

This statement addresses two points.

1. The evidence provided by Mueller [5] that the absorption of the oceans and land areas relative to the $CO_2$ concentration has been constant for 270 years, has several implications. Firstly, according to the Equivalence Principle [12], anthropogenically produced $CO_2$ has the same residence time as natural $CO_2$. Secondly, the result can be determined as a state of equilibrium between the Earth's reservoirs.
2. Due to this state of equilibrium between the atmosphere, the ocean, and biomass, the assumption that a stable atmospheric $CO_2$ concentration can be maintained if anthropogenic $CO_2$ emissions are halved is untenable. Any additional amount of $CO_2$ introduced into the system is distributed in a constant ratio among the reservoirs.

In this article, I base my analysis on the statistical analysis of the constancy of ocean absorption and land biomass according to Müller [5]. This demonstrates the equilibrium state in the Earth's $CO_2$ system. On the other hand, since $CO_2$ concentrations have increased by 50% since 1850, but the equilibrium has been maintained, it must be possible to draw conclusions from this.

## 2. On the Absorption of Reservoirs

The absorption of $CO_2$ in the ocean and in biomass is constant relative to the respective $CO_2$ concentration in the atmosphere. This demonstrates the validity of Henry's Law for the ocean and the linearity of plant growth with atmospheric $CO_2$ concentrations up to 450 ppmv (Hamburg Education Server [6]) (see Fig. 2).

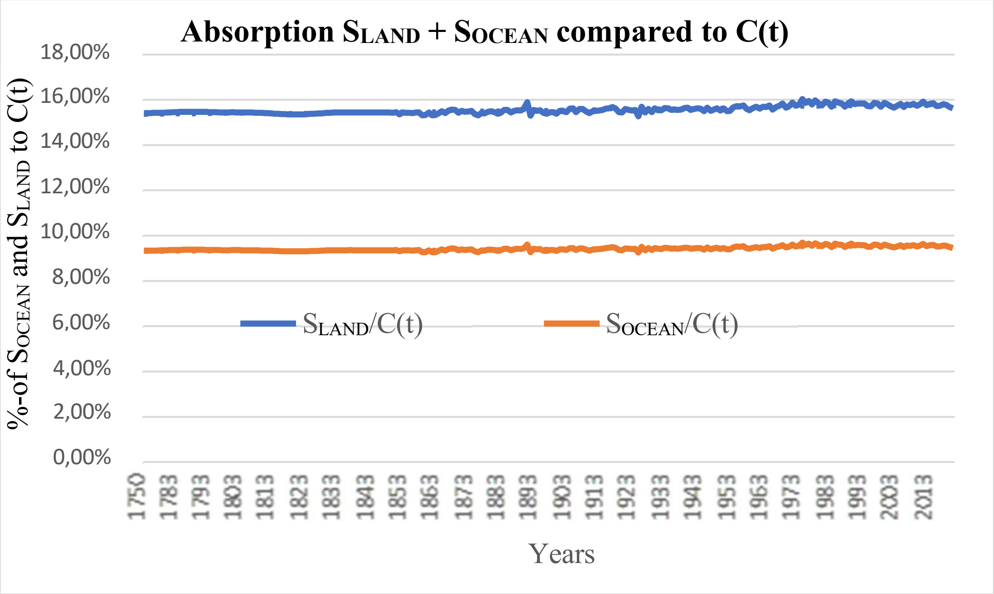

*Fig. 1: The relative total absorption on ocean and on land stays constant over 270 years [5].*

According to the IPCC AR6 [7] Chapter 5 Fig. 5.12, at the beginning of industrialization, the $CO_2$ concentration was 278 ppmv or 591 GtC. IPCC says, the e-time (equal to residence time) is about 4 years, corresponding to a total annual emission of approximately 165.9 GtC/a. Today, we have 50% more $CO_2$, which is 420 ppmv or 890 GtC. In IPCC AR5, WG1 Chapter 6, p. 472, Box 6.1 the residence time for the anthropogenic component is within several decades and a few thousands of years. Many scientific theories propose an e-time of 30 years.

This means, however, if the 591 GtC in 1750 have a residence time of less than 4 years in the atmosphere (165.9 GtC/a according to the IPCC [7]), the anthropogenic 298 GtC (889 GtC – 591 GtC) remain with a residence time of 30 years, i.e., an annual absorption of 11 GtC/a. We should therefore have a total annual absorption of 165,9 GtC/a from the old stock and 11 GtC/a from the anthropogenic 289 GtC, a total of 176,9 GtC/a plus new emissions. (According to the IPCC, the emission in 2020 is approximately 216.2 GtC. With this value, the residence time would have to be approximately 4 years.)

This contradicts the proportionality of Henry's Law and the measured higher biomass, which is also approximately proportional to $CO_2$ concentration. Despite a 50% higher partial pressure, absorption would be almost constant (from 165,9 GtC to 176,9 GtC) over 30 years with residence time $\tau = 30$ years. The assertion that the anthropogenic $CO_2$ content remains in the atmosphere longer than the natural $CO_2$ content thus rejects Henry's Law, as well as the linearity of $CO_2$ absorption by plants in relation to $CO_2$ partial pressure. However, both phenomena are scientifically recognized.

With a 50% higher partial pressure, according to Henry's Law, the oceans would have to emit and absorb 50% more. The oceans account for approximately 32% of global emissions. In 1750, the oceans ($S_{OCEAN}$) absorbed approximately 54.8 GtC/a, and the biomass/land ($S_{LAND}$) absorbed 111.1 GtC/a. (see IPCC Chapter 5 Figure 5.12 [7]). For reasons of proportionality, an additional $CO_2$ exchange of approximately 27.4 GtC/a would have to occur from the oceans (the IPCC is correct here), resulting in a total $CO_2$ exchange of the ocean of approximately 82.2 GtC/a.

Table:1 Absorption by $S_{OCEAN}$ and $S_{LAND}$ according to the principle of proportionality.

| Absorption (GtC) | 1750 | 2020 |
|---|---|---|
| $S_{OCEAN}$ | 54,8 | 82,2 |
| $S_{LAND}$ | 111,1 | 166,6 |
| Total | 165,9 | 248,8 |

Due to the higher biomass according to NASA and Tiexi [8] of at least 44% by 2016, an additional $S_{LAND}$ emission of 48.8 GtC/a would have to occur. For 2020, we also assume 50% for proportionality reasons, which would then be 55.5 GtC (although the IPCC only reports 29 GtC) – together with the current figure, this would amount to 166.6 GtC/a. Therefore, $S_{LAND}$ + $S_{OCEAN}$ is 166.6 GtC/a + 82.2 GtC/a = 248.8 GtC/a.

If these assumptions are incorrect, the following is true: Since the biomass has clearly increased significantly according to several scientific reports, the only option is a correction of Henry's Law – or the residence time is not constant. In this case, the measurement data from the Global Carbon Budget must be questioned. For example, if biomass did not increase by 50% but only by 35% with a 50% increase in $CO_2$, then in Fig. 1 $S_{LAND}$ would have to decrease by 1.5% to about 14% - which is obviously not the case.

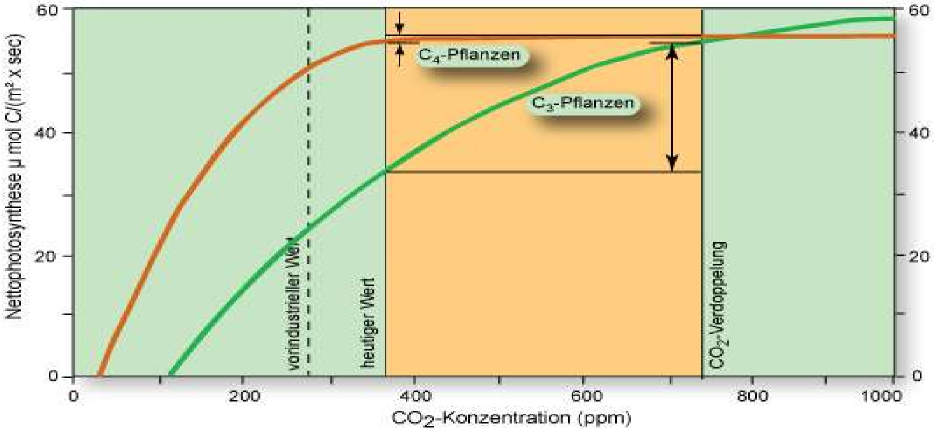

*Fig. 2 the increase of C3-plants for 280 ppmv to 400 ppmv is up to 35% C4-Plants up to 55%, proofed by Taylor et al.[9].*

This results in an average residence time, including the 298 GtC from anthropogenic emissions, of less than four years. A residence time of anthropogenic emissions of 30 years or more is therefore invalid.

Let's examine the sources of anthropogenic emissions in more detail. If the anthropogenic share is defined as $E_{FF}$(10 GtC) + $E_{LUC}$(3 GtC) + $E_{BMV}$(14 GtC), then this requires an additional annual emission of 27 GtC/a for 2020, or a total of 248.8 GtC/a + 27 GtC/a = 275.8 GtC/a. Fossil emissions therefore account for 4% of total emissions, while total anthropogenic emissions amount to 10.8% of total emissions.

Definition and Datasource – Skrable [4], Global Carbon Budget, 2021[10]:

$E_{FF}$: Human Carbon is from burning carbon fuels and producing cement
$E_{LUC}$: Land Carbon is from human-caused land-use-change
$E_{BMV}$: Burned Biomass caused by human activity
$E_{OT}$: Emission by ocean temperature increase

As explained in Müller [5], the absorption rate relative to the partial pressure has remained constant for 270 years in both the ocean and the land. We therefore have a constant equilibrium between ocean, land, and atmosphere, similar to communicating tubes. Of the 27 GtC/a emissions, 4.4 GtC/a remain in the atmosphere, 7.3 GtC/a enter the ocean, and 15.3 GtC enters the biomass/land. However, according to the Mauna Loa database, an average of 5.2 GtC remained in the atmosphere annually between 2010 and 2020.

The claim that the airborne fraction of approximately 50% of anthropogenic emissions remain in the atmosphere is misleading. Compared to the natural equilibrium, in addition to purely fossil emissions $E_{FF}$, there are additional emissions ($E_{LUC}$ + $E_{BMV}$). Strictly speaking, this also includes $E_{OT}$, the additional outgassing of $CO_2$ from the ocean due to its warming according to Henry's Law (approximately 5 GtC in 2020). With the same ratio, the theoretically remaining portion in the atmosphere agrees with the measured values from Mauna Loa.

## 3. The Net-Zero Thesis

If – as preferred in public debate – $E_{OT}$, $E_{LUC}$, and $E_{BMV}$ are attributed to natural $CO_2$ sources (as is the 1 GtC produced by the respiration of 8 billion people), and only fossil emissions are considered as an increase in $CO_2$ concentration, one could argue:

The annual increase in atmospheric $CO_2$ concentration (assuming fossil emissions of 10 GtC/a) in recent years has been 2.44 ppmv, or 5.2 GtC/a. It is claimed that keeping the current carbon concentration constant would be possible, if we reduced fossil emissions from 10 GtC/a by 5.2 GtC/a. Total anthropogenic emissions should therefore remain at 4.8 GtC/a. The current $CO_2$ concentration in the atmosphere would then remain constant, with the excess being absorbed by the ocean and the biosphere.

This means that there is no equilibrium between all three reservoirs. This, however, contradicts the equilibrium principle between the three reservoirs described above, as well as Henry's Law and the linearity principle of biomass growth. The equilibrium principle implies that a portion of each additional emission remains in the atmosphere.

*Summary:*

The following statement is false:

With an annual additional anthropogenic emission of 10 GtC, 5.2 GtC/a remains in the atmosphere, 3.3 GtC is absorbed on land, and 1.5 GtC in the ocean.

The correct statement would be: the total non-natural emissions from the disturbed equilibrium are the above 27 GtC + 5 GtC from $E_{OT}$. So 32 GtC. Of this, 5.2 GtC remains in the atmosphere, 18.2 GtC on land, and 8.6 GtC in the ocean.

The constant ratio of the distribution is thus 16.25% : 56.87% : 26.88%.

The soil's $CO_2$ budget has not yet been taken into account. As of 2020, it contains 1500 $GtCO_2$ (410 GtC).

## 4. Carbon Balance Compared with Data from the IPCC and Global Carbon Budget

If we combine Tayler's study[9] for a 30% increase in biomass from 1850 to 2000 with Tiexi's [8] new study of a 14% increase between 2000 and 2016, we have a biomass increase of at least 44%. (1% per year). For 2020 – here the data apply to the ocean, and C(2020) = 420 – we propose a 50% increase with a linear absorption in the ocean and land.

With the following assumptions, according to the IPCC:

In 1750: The atmosphere had 591 GtC. For respiration, see Table 1. Biomass was 520 GtC (IPCC indicates between 450 GtC and 650 GtC), and the residence time is less than 4 years. The surface ocean had 900 GtC in 1750.

In 2020: The atmosphere had 889 GtC. The land biosphere probably has 780 GtC today (+50%). Since absorption remained constant at $S_{LAND}$ (see Figure 1), it follows that land biomass must have increased by 50%, i.e., by 260 GtC.

According to the author's theory, the surface ocean has absorbed 50% more, or 450 GtC, of which a portion has entered the deep sea. A calculation based on the respective Revelle factor (Müller [5]) gives approximately 110 GtC (24%). This leaves 1250 GtC in the surface ocean. The total increase in all four reservoirs by 2020 was 298 GtC + 260 GtC + 340 GtC + 110 GtC = 1008 GtC.

However, only 463 GtC were emitted anthropogenically from fossil fuels by 2019. This is 45% of the carbon balance.

Table 2: C-Budget

| Absorption GtC | C-Budget 1750 | *Sur Plus* 2020 |
|---|---|---|
| $S_{Ocean}$ | 900 | 340 |
| $S_{Land}$ | 520 | 260 |
| $S_{Air}$ | 591 | 298 |
| $S_{Deep\ Sea}$ | 37100 | 110 |
| Total | 39111 | 1008 |

The IPCC and Global Carbon Budget provide different figures:

IPCC:

Atmosphere +279 GtC, Biosphere +239 GtC, and Deep Sea +173 GtC equals 691 GtC.
No data is available on absorption in the ocean.

Global Carbon Budget:

The Global Carbon Budget reports total emissions from $E_{FF}$ and $E_{LUC}$ as 463 GtC + 195 GtC = 658 GtC. This results in a deficit of 350 GtC to 545 GtC.

## 5. Summary

Both the total $CO_2$ emissions reported by the IPCC for 2020, as well as the biomass increase and increased $CO_2$ absorption by the oceans, rule out a residence time of anthropogenic $CO_2$ of more than four years.

The principle of equilibrium between reservoirs does not allow for the net-zero thesis. Any additional $CO_2$ inputs are distributed among the reservoirs in a fixed ratio.

The question also arises as to why, according to the Global Carbon Budget 2023, the ocean has absorbed so little $CO_2$, which contradicts Henry's Law.

Furthermore, the above considerations raise the question, where 500 GtC come from. This does not take into account the change of $CO_2$ stored in the upper soil layer. $E_{BMV}$ and $E_{OT}$ could explain a part of it.

We therefore know that the IPCC's assumptions and fundamentals are wrong. But we also know that many unanswered questions remain.

The share of biomass in atmospheric $CO_2$ in 1850 was approximately 66%, or 182 ppmv. A 50% increase would add up to an additional 90 ppmv. A 1°C warming of the ocean as well as soil respiration could explain the shortfall to 140 ppmv. The discussion about $CO_2$ would then be irrelevant.

**Funding**
This research did not receive any specific grant from funding agencies in the public, commercial, or not-for-profit sectors.

**Acknowledgments**

I thank the editor and the reviewers for critical reading the manuscript and important advices.

## References

1. Roth, Eike, 2025: *About the Origin of $CO_2$ in the Atmosphere,* Science of Climate Change, Vol. 5.1, pp. 1-14, https://doi.org/10.53234/scc202501/05.
2. Berry, Edwin, 2023: *How to find climate truth,* Sience of Climate Change, Vol. 3.1,pp. 68-91. https://doi.org/10.53234/scc202301/21.
3. Schrijver, Frans, 2024: *Impact of global greening on the natural atmospheric $CO_2$ level,* Science of Climate Change, Vol. 4.2 pp. 79-88, https://doi.org/10.53234/scc202411/02.
4. Skrable, Kenneth, et al.: 2022: *World Atmospheric $CO_2$, its 14C Specific Activity, Non-Fossil Component, Anthropogenic Fossil Component and Emissions (1750 -2018),* Health Physics Society. https://doi.org/10.1097/HP.0000000000001485
5. Müller, Raimund, 2023: *Estimation of e-Time for $CO_2$ and Revelle Factor,* Science of Climate Change, Vol. 3.3 pp. 327-345, https://doi.org/10.53234/scc202308/06,
6. Hamburger Bildungsserver: *Die zentrale Plattform für Lehrende und Lernende.* (hamburg.de) https://bildungsserver.hamburg.de/resource/blob/265480/01e4f121413e4a2949efa062dd85ca65/2007-vegetation-data.pdf
7. IPCC AR6 WGI, Chapter 5, p. 700
8. Tiexi, Cheng, 2024: *The global greening continues despite increased drought stress since 2000*, ScienceDirekt, Vol. 49, e02791, https://www.sciencedirect.com/science/article/pii/S2351989423004262
9. Taylor, Charles, Schlenker, 2021: *Environmental drivers of agricultural productivity growth: $CO_2$ fertilisation of US field crops*, NATIONAL BUREAU OF ECONOMIC RESEARCH 1050 Massachusetts Avenue Cambridge, MA 02138. https://www.nber.org/papers/w29320
10. Global Carbon Budget, 2021, https://www.globalcarbonproject.org/carbonbudget/archive/2021/GCP_CarbonBudget_2021.pdf
11. Harde, Hermann, 2023: *Understanding Increasing $CO_2$*, Science of Climate Change, Vol. 3.4 pp. 369-374, https://doi.org/10.53234/scc202310/12.
12. Harde, Hermann, 2019: *What Humans Contribute to atmospheric $CO_2$: Comparison of Carbon Cycle Models with Observations*, https://doi.org/10.11648/j.earth.20190803.13

SCC-Publishing

Michelets vei 8 B
1366 Lysaker, Norway

ISSN: 2703-9072

Correspondence:
ajsadar@geneva.edu

Vol. 5.3 (2025)
pp. 213-216

Commentary

# Frightening Climate Story Lacks Depth of Climate Knowledge

Anthony J. Sadar[1]

Geneva College, Beaver Falls, PA

## Abstract

This commentary is a conflation and revision of the author's essays previously published in the *American Thinker* and the *Washington Times*. To counter climate anxiety, this treatise reflects the limited predictions of climate models, particularly the atmosphere's temperature profile, where models are not merely uncertain but also show a common warming bias relative to observations. Also, regarding the physics, how precipitation will change with warming is not sufficiently understood. This suggests that models can seriously misrepresent certain fundamental feedback processes.

**Keywords:** Climate modeling; climate outlooks.

Submitted 2025-10-31, Accepted 2025-11-09. https://doi.org/10.53234/scc202510/08

## Commentary

Terror in the troposphere is alive and well on US college campuses as revealed by former vice-president Kamala Harris during an October 2025 interview. According to Ms. Harris, her goddaughter, a junior in college, was experiencing climate anxiety, as were other students on campuses in the US and abroad.

The angst is not surprising. For decades, the narrative of impending global climate catastrophe has trudged ahead nearly unimpeded through academia. Politicians and professional societies joined the steady march along the way. Mainstream media dutifully disseminated the descending doom.

However, now a broader, less frightening view of the climate is emerging as a perspective that challenges the climate story status quo is gaining more attention.

For instance, more of the public are learning that the claimed and predicted global climate calamities are considerably overblown. (Note the recent epiphany of philanthropist Bill Gates, who according to the Associated Press (AP), still "thinks climate change is a serious problem but it won't be the end of civilization." Mr. Gates is refocusing his attention on the critical matter of reducing human suffering (McDermott, 2025).

The overestimation is because a large part of the airy disaster saga can be found in its edifice fashioned by modelling. In science, modelling produces a tentative representation of an observation or condition based on interpretation of available information.

Atmospheric modelling is typically of the mathematical kind. Such modelling involves sophisticated equations which necessitate assumptions and limitations and contain measured and approximated input quantities.

Most of my forty years of professional practice encompassed mathematical modelling of the

---

[1] The author is a Certified Consulting Meteorologist and an adjunct associate professor of science at Geneva College, Beaver Falls, PA. He is also co-author of *Environmental Risk Communication: Principles and Practices for Industry* (CRC Press).

dispersion of air pollutants. The air pollution models combined sources of contaminants (industrial smokestacks) with adverse weather conditions (stagnant air) and critical receptors (vulnerable communities) to produce a reasonable estimate of worst-case air pollution impacts.

This sort of modelling focused on predicting harmful effects over relatively short time frames (hours to one year) and on tight space scales (dozens of square meters to several square kilometers).

Compare this example of small-scale weather simulation to its large-scale global climate analogue.

Both modelling methods attempt to faithfully replicate reality. And as understanding of the atmosphere increased and computer capacity expanded, both methods yielded dramatically improved outcomes. Both rely on careful, unbiased observations and interpretations of adequate scientific data. And both produce useful results to guide decisions involving public health and safety. These are some of the positive portions of modelling.

There are some negative parts.

Models typically lack adequate spatial resolution to capture small but potentially critical aspects of the atmosphere. Spatial inadequacy includes not just horizontal stretches across the earth's surface but its vertical expanse as well. And, within this three-dimensional space, constant changes are occurring with temperature, moisture, wind, pressure, and energy.

Lack of complete information and knowledge of the chemistry and physics of the air leads to serious uncertainties of future conditions. This is true for small-scale air-pollution modelling and even more so for global climate modelling. The atmosphere is inherently complex as is its modelling and the increase in time and distance affects forecast accuracy.

Yet, although changes that occur in the atmosphere occur in three dimensions, so much thinking on climate change happens on a two-dimensional level.

Certainly, academic and government studies delve into the dimensional complexity of the airy environment, but the study results seem to be delivered and interpreted in a simplistic way.

Take climate conclusions derived from the U.N. Intergovernmental Panel on Climate Change (IPCC) report. The IPCC report is the bible of climate change collective wisdom and its latest edition is the Sixth Assessment Report (AR6).

The synthesis of the full lengthy report to AR6 was released March 2023. And even though there are thousands of pages of mainly technical material including peer-reviewed references in the full multi-year state-of-the-science AR6, the relatively brief synthesis is typically heavily influenced by politics, highlighting the *governmental* portion of the Intergovernmental Panel on Climate Change.

From the skewed IPCC synthesis reports and similar politically biased narratives, many in the public, politicians, and news media conclude:

> The Earth's air temperature is rising to dangerous levels; this rise is mainly due to increasing levels of carbon dioxide in the atmosphere; the release of carbon dioxide by burning fossil fuels must end, as soon as possible; without cessation of fossil fuel use, much of life on Earth will die.

Some form of this "settled science" diatribe has been repeated almost *ad nauseum* for decades. Schooling from K-16 and into graduate education has been saturated with this mantra. Nevertheless, the reality of atmospheric science is far from this "two-dimensional" thinking. What is actually known is not so simple nor settled.

Like the air itself, a third dimension must be added to common climate-change thinking that includes the depth of the atmosphere.

This expanded, three-dimensional perspective derives from atmospheric modeling which is used to explore the dynamics of the global air and to forecast its future conditions. But even sophisticated mathematical climate modeling still lacks sufficient equations to match actual climate conditions.

The mismatch between model output and reality is recognized in *A Critical Review of Impacts of Greenhouse Gas Emissions on the U.S. Climate*, a July 2025 US Department of Energy report authored by five accomplished professionals in the fields of atmospheric science, physics, and economics. Although this document is facing challenges, its section on the "Vertical temperature profile mismatch" alerts the reader not only to the dramatic mismatch between model results and actual measurements, but also the fact that the atmosphere is three-dimensional and more complex than most people realize. Thus:

> "[t]he atmosphere's temperature profile is a case where [climate] models are not merely uncertain but also show a common warming bias relative to observations. This suggests that they misrepresent certain fundamental feedback processes" (US DOE, 2025).

My own peer-reviewed research which included 30-years (1991 - 2020) of low-level temperature conditions derived from southwest Pennsylvania twice-daily balloon-launch data confirms that changes in the lowest layer of the Earth's air defy incontrovertible conclusions. My study investigated atmospheric changes that impact the dispersal of air pollutants near the ground (Sadar, 2022, with additional discussion in Sadar, 2024).

These changes also relate directly to climate change mechanics because changes to the trends in near-surface temperature along with moisture content have a profound effect on the Earth's hydrologic (water) cycle.

Notably, perhaps the most uncertain of the feedback processes mentioned in the *Critical Review* is related to the water cycle.

Water in all its forms -- as solid ice and snow, as liquid cloud droplets, precipitation, and fog, and as invisible vapor -- continuously cycles its modes and in the process absorbs or releases energy. Water vapor and clouds account for most of the greenhouse effect.

In the recent book *Climate and Energy: The Case for Realism*, one of the US DOE *Critical Review* authors, climatologist Roy Spencer, noted that precipitation processes that restrict the accumulation of water vapor in the atmosphere:

> "are not known in enough detail to predict how the weak direct-warming effect of [carbon dioxide] will be either amplified or reduced by precipitation limits on water vapor. Climate models only crudely represent the conversion from water vapor to precipitation…. The actual physics that will determine how precipitation will change with warming are not even understood, let alone represented in climate models" (Beisner et al., 2024).

Clearly there is still a lot to be investigated about the workings of the atmosphere. And nuanced science must continue to be disseminated and understood regardless of politicized storylines that imply two-dimensional simplicity to the three-dimensional complexity of the climate.

Regardless, models as sophisticated tools in the scientist's toolbox are enormously beneficial. Air dispersion models have helped us to understand and reduce air contaminant concentrations. Climate models have greatly improved awareness of atmospheric dynamics and potential long-term changes.

This critique does not denigrate atmospheric modeling in any way or at any level, small or large. Rather it is more of a cautionary tale to reduce bombastic certitude and to add much-needed humility to the quantitative and qualitative analysis of the atmosphere. In the real world of heat and humidity, wind and pressure, land and sea, mountain and valley, no one knows with sufficient clarity the end of the climate story or even its subsequent chapters in the decades ahead.

As the saying goes, "there are two sides to every story." For the longest time the scary side with a cacophony of climate calamity had been the one pandered to students and the general public. But now it appears that, to the betterment of science and the serenity of society, the other side -- a less frightening, more realistic side -- of the complicated climate story is being given a fair public hearing.

**Chief-Editor**: H. Harde

## References

Beisner, E.C.; Legates, D.R., Editors, 2024, *Climate and Energy: The Case for Realism*, Washington, D.C.: Regnery Publishing.

McDermott, J., 2025: *Bill Gates calls for climate fight to shift focus from curbing emissions to reducing human suffering*, Associated Press (AP), Oct. 28. https://apnews.com/article/bill-gates-climate-change-united-nations-4108f76e746d1e3e13845f33b8ae7007.

Sadar, A.J., 2022: *Climatology and trends of morning and evening temperature inversions in southwestern Pennsylvania with air quality implications*, Environ. Sci. Pollut. Res., 29, 49411-49421, https://doi.org/10.1007/s11356-022-20504-7.

Sadar, A.J., 2024: *Will Climate Change Crush Air Quality by Boosting Temperature Inversions, or Not?* Science of Climate Change, Vol. 4.1, pp. 107-109, https://scienceofclimatechange.org.

US Department of Energy (US DOE), 2025: *A Critical Review of Impacts of Greenhouse Gas Emissions on the U.S. Climate*, US DOE Climate Working Group, https://www.energy.gov/sites/default/files/2025-07/DOE_Critical_Review_of_Impacts_of_GHG_Emissions_on_the_US_Climate_July_2025.pdf.